Surface Plasmon Enhanced,
Coupled and Controlled Fluorescence

Surface Plasmon Enhanced, Coupled and Controlled Fluorescence

Edited by Chris D. Geddes

WILEY

Copyright © 2017 by John Wiley & Sons, Inc. All rights reserved 2017

Published by John Wiley & Sons, Inc., Hoboken, New Jersey
Published simultaneously in Canada

No part of this publication may be reproduced, stored in a retrieval system, or transmitted in any form or by any means, electronic, mechanical, photocopying, recording, scanning, or otherwise, except as permitted under Section 107 or 108 of the 1976 United States Copyright Act, without either the prior written permission of the Publisher, or authorization through payment of the appropriate per-copy fee to the Copyright Clearance Center, Inc., 222 Rosewood Drive, Danvers, MA 01923, (978) 750-8400, fax (978) 750-4470, or on the web at www.copyright.com. Requests to the Publisher for permission should be addressed to the Permissions Department, John Wiley & Sons, Inc., 111 River Street, Hoboken, NJ 07030, (201) 748-6011, fax (201) 748-6008, or online at http://www.wiley.com/go/permissions.

Limit of Liability/Disclaimer of Warranty: While the publisher and author have used their best efforts in preparing this book, they make no representations or warranties with respect to the accuracy or completeness of the contents of this book and specifically disclaim any implied warranties of merchantability or fitness for a particular purpose. No warranty may be created or extended by sales representatives or written sales materials. The advice and strategies contained herein may not be suitable for your situation. You should consult with a professional where appropriate. Neither the publisher nor author shall be liable for any loss of profit or any other commercial damages, including but not limited to special, incidental, consequential, or other damages.

For general information on our other products and services or for technical support, please contact our Customer Care Department within the United States at (800) 762-2974, outside the United States at (317) 572-3993 or fax (317) 572-4002.

Wiley also publishes its books in a variety of electronic formats. Some content that appears in print may not be available in electronic formats. For more information about Wiley products, visit our web site at www.wiley.com.

Library of Congress Cataloging-in-Publication Data:

Names: Geddes, Chris D., editor.
Title: Surface plasmon enhanced, coupled, and controlled fluorescence / edited by Chris D Geddes.
Description: Hoboken, New Jersey : John Wiley & Sons, Inc., [2017] | Includes bibliographical references and index.
Identifiers: LCCN 2016052144 | ISBN 9781118027936 (cloth) | ISBN 9781119324829 (epub)
Subjects: LCSH: Fluorescence. | Fluorescence spectroscopy. | Surface plasmon resonance. | Plasmons (Physics)
Classification: LCC QC477 .S87 2017 | DDC 535/.352–dc23
LC record available at https://lccn.loc.gov/2016052144

Cover image credit:
Background: Patrick Llewelyn-Davies/Gettyimages
Middle: Courtesy of the editor

Printed in the United States of America

10 9 8 7 6 5 4 3 2 1

Contents

List of Contributors *xi*
Preface *xv*

1 Plasmonic-Fluorescent and Magnetic-Fluorescent Composite Nanoparticle as Multifunctional Cellular Probe *1*
Arindam Saha, SK Basiruddin, and Nikhil Ranjan Jana
1.1 Introduction *1*
1.2 Synthesis Design of Composite Nanoparticle *2*
1.2.1 Method 1: Polyacrylate Coating-Based Composite of Nanoparticle and Organic Dye *3*
1.2.2 Method 2: Polyacrylate Coating-Based Composite of Two Different Nanoparticles *3*
1.2.3 Method 3: Ligand Exchange Approach-Based Composite of Two Different Nanoparticles *4*
1.3 Property of Composite Nanoparticles *5*
1.3.1 Optical Property *5*
1.3.2 Fluorophore Lifetime Study *7*
1.4 Functionalization and Labeling Application of Composite Nanoparticle *8*
1.5 Conclusion *8*

2 Compatibility of Metal-Induced Fluorescence Enhancement with Applications in Analytical Chemistry and Biosensing *13*
Fang Xie, Wei Deng, and Ewa M. Goldys
2.1 Introduction *13*
2.2 Homogeneous Protein Sensing MIFE Substrates *14*
2.2.1 Core–Shell Approach *14*
2.2.2 Homogeneous Large Au Nanoparticle Substrates *16*
2.2.3 Commercial Klarite™ Substrate *18*
2.3 Ag Fractal Structures *19*
2.3.1 Reasons for High Enhancement Factors in Nanowire Structures *19*
2.3.2 Ag Dendritic Structure—Homogeneous Silver Fractal *22*
2.4 MIFE with Membranes for Protein Dot Blots *25*
2.5 MIFE with Flow Cytometry Beads and Single Particle Imaging *30*

3 Plasmonic Enhancement of Molecule-Doped Core–Shell and Nanoshell on Molecular Fluorescence *37*
Jiunn-Woei Liaw, Chuan-Li Liu, Chong-Yu Jiang, and Mao-Kuen Kuo
3.1 Introduction *37*
3.2 Theory *38*
3.2.1 Plane Wave Interacting with an Multilayered Sphere *39*
3.2.2 Excited Dipole Interacting with a Multilayered Sphere *40*
3.2.3 EF on Fluorescence *40*
3.3 Numerical Results and Discussion *41*
3.3.1 Core–Shell *41*

3.3.1.1 Au@SiO_2 *41*
3.3.1.2 Ag@SiO_2 *46*
3.3.2 Nanoshelled Nanocavity *50*
3.3.2.1 Au NS *50*
3.3.2.2 Ag NS *52*
3.3.3 NS@SiO_2 *53*
3.3.3.1 Au NS@SiO_2 *54*
3.3.3.2 Ag NS@SiO_2 *58*
3.4 Conclusion *66*

4 Controlling Metal-Enhanced Fluorescence Using Bimetallic Nanoparticles *73*
Debosruti Dutta, Sanchari Chowdhury, Chi Ta Yang, Venkat R. Bhethanabotla, and Babu Joseph
4.1 Introduction *73*
4.2 Experimental Methods *74*
4.2.1 Synthesis *74*
4.2.1.1 NP Synthesis by Sputtering and Annealing *74*
4.2.1.2 Nanoparticle Synthesis by the Polyol Process *74*
4.2.2 Particle Characterization *75*
4.2.3 Fluorescence Spectroscopy *76*
4.2.3.1 On Sputtered and Annealed Ag–Cu NPs *76*
4.2.3.2 On Ag–Cu NPs Synthesized with the Polyol Process *79*
4.3 Theoretical Modeling *79*
4.3.1 Modeling SPR Using Mie Theory *79*
4.3.2 Modeling of Metal-Enhanced Fluorescence Modified Gersten–Nitzan Model *81*
4.3.3 Modeling MEF Using Finite-Difference Time-Domain (FDTD) Calculations *85*
4.4 Conclusion and Future Directions *87*

5 Roles of Surface Plasmon Polaritons in Fluorescence Enhancement *91*
K. F. Chan, K. C. Hui, J. Li, C. H. Fok, and H. C. Ong
5.1 Introduction *91*
5.1.1 Surface Plasmon-Mediated Emission *91*
5.1.2 Excitation of Propagating and Localized Surface Plasmon Polaritons in Periodic Metallic Arrays *93*
5.1.3 Surface Plasmon-Mediated Emission from Periodic Arrays *95*
5.2 Experimental *95*
5.2.1 Sample Preparation *95*
5.2.2 Optical Characterizations *96*
5.3 Result and Discussion *97*
5.3.1 The Decay Lifetimes of Metallic Hole Arrays *97*
5.3.2 Dependence of Decay Lifetime on Hole Size *98*
5.3.3 Comparison between Dispersion Relation and PL Mapping *100*
5.3.4 Comparison of the Coupling Rate Γ_B of Different SPP Modes *102*
5.3.5 Photoluminescence Dependence on Hole Size *104*
5.3.6 Dependence of Fluorescence Decay Lifetime on Hole Size *105*
5.4 Conclusions *107*

6 Fluorescence Excitation, Decay, and Energy Transfer in the Vicinity of Thin Dielectric/Metal/Dielectric Layers near Their Surface Plasmon Polariton Cutoff Frequency *111*
Kareem Elsayad and Katrin G. Heinze
6.1 Introduction *111*
6.2 Background *111*
6.3 Theory *112*
6.4 Summary *120*

7 Metal-Enhanced Fluorescence in Biosensing Applications *121*
Ruoyun Lin, Chenxi Li, Yang Chen, Feng Liu, and Na Li
7.1 Introduction *121*
7.2 Substrates *121*
7.3 Distance Control *128*
7.4 Summary and Outlook *132*

8 Long-Range Metal-Enhanced Fluorescence *137*
Ofer Kedem
8.1 Introduction *137*
8.2 Collective Effects in NP Films *138*
8.3 Investigations of Metal–Fluorophore Interactions at Long Separations *138*
8.3.1 Distance-Dependent Fluorescence of Tris(bipyridine)ruthenium(II) on Supported Plasmonic Gold NP Ensembles *138*
8.3.2 Lifetime *139*
8.3.3 Intensity *141*
8.3.4 Emission Wavelength and Linewidth *143*
8.4 Conclusions *146*

9 Evolution, Stabilization, and Tuning of Metal-Enhanced Fluorescence in Aqueous Solution *151*
Jayasmita Jana, Mainak Ganguly, and Tarasankar Pal
9.1 Introduction *151*
9.1.1 Coinage Metal Nanoparticles in Metal-Enhanced Fluorescence *153*
9.2 Metal-Enhanced Fluorescence in Solution Phase *154*
9.2.1 Metal-Enhanced Fluorescence from Metal(0) in Solution *154*
9.2.1.1 Silver- and Gold-Enhanced Fluorescence *154*
9.2.1.2 Selectivity for Silver-Enhanced Fluorescence *157*
9.2.1.3 Silver-Enhanced Fluorescence in Diiminic Schiff Bases *161*
9.2.1.4 Copper-Enhanced Fluorescence *165*
9.2.1.5 Tuning of Metal-Enhanced Fluorescence *166*
9.3 Applications of Metal-Enhanced Fluorescence *169*
9.3.1 Sensing of Biomolecules *169*
9.3.2 Sensing of Toxic Metals *171*
9.4 Conclusion *174*

10 Distance and Location-Dependent Surface Plasmon Resonance-Enhanced Photoluminescence in Tailored Nanostructures *179*
Saji Thomas Kochuveedu and Dong Ha Kim
10.1 Introduction *179*
10.2 Effect of SPR in PL *181*
10.2.1 Photoluminescence *181*
10.2.1.1 Radiative Decay in MEF *181*
10.2.1.2 Nonradiative Decay in MEF *182*
10.2.2 Enhancement of Emission by SPR *182*
10.2.2.1 Resonance Energy Transfer *182*
10.2.2.2 NFE Mechanism *183*
10.2.3 Quenching of Emission by SPR *184*
10.3 Effect of SPR in FRET *185*
10.3.1 FRET *185*
10.3.2 SPR-Induced Enhanced FRET *188*
10.3.3 Effect of the Position, Concentration, and Size of Plasmonic Nanostructures in FRET System *189*
10.4 Conclusions and Outlook *191*

11 Fluorescence Quenching by Plasmonic Silver Nanoparticles *197*
M. Umadevi
11.1 Metal Nanoparticles *197*
11.2 Fluorescence Quenching *197*
11.3 Mechanism behind Quenching *198*

12 AgO_x Thin Film for Surface-Enhanced Raman Spectroscopy *203*
Ming Lun Tseng, Cheng Hung Chu, Jie Chen, Kuang Sheng Chung, and Din Ping Tsai
12.1 Introduction *203*
12.1.1 SERS on the Laser-Treated AgO_x Thin Film *203*
12.1.1.1 Experimental Method *203*
12.1.1.2 Tunabe SERS Enhancement *204*
12.1.1.3 SERS-Active Nanostructure Made on Flexible Substrate *205*
12.1.2 Annealed AgO_x Thin Film for SERS *206*
12.2 Conclusion *206*

13 Plasmon-Enhanced Two-Photon Excitation Fluorescence and Biomedical Applications *211*
Taishi Zhang, Tingting Zhao, Peiyan Yuan, and Qing-Hua Xu
13.1 Introduction *211*
13.2 Metal–Chromophore Interactions *212*
13.3 Plasmon-Enhanced One-Photon Excitation Fluorescence *214*
13.4 Plasmon-Enhanced Two-Photon Excitation Fluorescence *215*
13.5 Conclusions and Outlook *220*

14 Fluorescence Biosensors Utilizing Grating-Assisted Plasmonic Amplification *227*
Koji Toma, Mana Toma, Martin Bauch, Simone Hageneder, and Jakub Dostalek
14.1 Introduction *227*
14.2 SPCE in Vicinity to Metallic Surface *227*
14.3 SPCE Utilizing SP Waves with Small Losses *230*
14.4 Nondiffractive Grating Structures for Angular Control of SPCE *232*
14.5 Diffractive Grating Structures for Angular Control of SPCE *234*
14.6 Implementation of Grating-Assisted SPCE to Biosensors *236*
14.7 Summary *237*

15 Surface Plasmon-Coupled Emission: Emerging Paradigms and Challenges for Bioapplication *241*
Shuo-Hui Cao, Yan-Yun Zhai, Kai-Xin Xie, and Yao-Qun Li
15.1 Introduction *241*
15.2 Properties of SPCE *242*
15.3 Current Developments of SPCE in Bioanalysis *243*
15.3.1 New Substrates Designing for Biochip *243*
15.3.2 Optical Switch for Biosensing *244*
15.3.3 Full-Coupling Effect for Bioapplication *245*
15.3.4 Hot-Spot Nanostructure-Based Biosensor *248*
15.3.5 Imaging Apparatus for High-Throughput Detection *249*
15.3.6 Waveguide Mode SPCE to Widen Detection Region *251*
15.4 Perspectives *252*

16 Plasmon-Enhanced Luminescence with Shell-Isolated Nanoparticles *257*
Sabrina A. Camacho, Pedro H. B. Aoki, Osvaldo N. Oliveira, Jr, Carlos J. L. Constantino, and Ricardo F. Aroca
16.1 Introduction *257*
16.2 Synthesis of Shell-Isolated Nanoparticles *259*
16.2.1 Nanosphere Au-SHINs *259*
16.2.2 Nanorod Au-SHINs *260*
16.3 Plasmon-Enhanced Luminescence in Liquid Media *262*
16.4 Enhanced Luminescence on Solid Surfaces and Spectral Profile Modification *265*
16.4.1 SHINEF on Langmuir–Blodgett Films *266*

17 Controlled and Enhanced Fluorescence Using Plasmonic Nanocavities *271*
Gleb M. Akselrod, David R. Smith, and Maiken H. Mikkelsen
17.1 Introduction to Plasmonic Nanocavities *271*
17.2 Summary of Fabrication *272*
17.3 Properties of the Nanocavity *273*
17.3.1 Nanocavity Resonances *273*
17.3.2 Tuning the Resonance *274*
17.3.3 Directional Scattering and Emission *276*
17.4 Theory of Emitters Coupled to Nanocavity *277*
17.4.1 Simulation of Nanocavity *278*
17.4.2 Enhancement in the Spontaneous Emission Rate *278*
17.5 Absorption Enhancement *280*
17.6 Purcell Enhancement *282*
17.7 Ultrafast Spontaneous Emission *286*
17.8 Harnessing Multiple Resonances for Fluorescence Enhancement *288*
17.9 Conclusions and Outlook *291*

18 Plasmonic Enhancement of UV Fluorescence *295*
Xiaojin Jiao, Yunshan Wang, and Steve Blair
18.1 Introduction *295*
18.2 Plasmonic Enhancement *295*
18.3 Analytical Description of PE of Fluorescence *296*
18.4 Overview of Research on Plasmon-Enhanced UV Fluorescence *297*
18.4.1 Material Selection *297*
18.4.2 Structure Choice *301*
18.4.3 Experimental Measurement *303*
18.4.3.1 Characterization of SPR Properties *303*
18.4.3.2 Fluorescence Enhancement *304*
18.4.3.3 Lifetime Measurement *305*
18.4.3.4 Toward Quantitative Florescence Analysis *305*
18.5 Summary *306*

Index *309*

List of Contributors

Gleb M. Akselrod
Center for Metamaterials and Integrated Plasmonics and Department of Electrical and Computer Engineering
Duke University
Durham, NC
USA

Pedro H. B. Aoki
São Carlos Institute of Physics
University of São Paulo
São Carlos
Brazil

Ricardo F. Aroca
Faculdade de Ciências e Tecnologia
UNESP Universidade Estadual Paulista
Presidente Prudente
Brazil

Saji Thomas Kochuveedu
Institute of Applied Physics
Johannes Kepler University
Altenbergerstraße, Austria and Department of Chemistry and Nano Science
School of Natural Sciences
Ewha Womans University, Seoul, Korea

SK Basiruddin
Centre for Advanced Materials
Indian Association for the Cultivation of Science
Kolkata, India

Martin Bauch
Energy Department
AIT—Austrian Institute of Technology
Vienna, Austria

Venkat R. Bhethanabotla
Department of Chemical & Biomedical Engineering
University of South Florida
Tampa, FL, USA

Steve Blair
Department of Electrical and Computer Engineering
University of Utah, Salt Lake City, USA

Sabrina A. Camacho
Faculdade de Ciências e Tecnologia
UNESP Universidade Estadual Paulista
Presidente Prudente
Brazil

Shuo-Hui Cao
Department of Chemistry and the MOE Key Laboratory of Spectrochemical Analysis & Instrumentation
College of Chemistry and Chemical Engineering
Xiamen University
Xiamen, China

K. F. Chan
Department of Physics
The Chinese University of Hong Kong
Sha Tin, Hong Kong

Jie Chen
Department of Physics
National Taiwan University
Taipei, Taiwan

Yang Chen
Institute of Analytical Chemistry
Peking University, Beijing, China

Sanchari Chowdhury
Department of Chemical & Biomedical Engineering
University of South Florida
Tampa, FL, USA

Cheng Hung Chu
Department of Physics
National Taiwan University
Taipei, Taiwan
and

Research Center for Applied Sciences
Academia Sinica
Taipei
Taiwan

Kuang Sheng Chung
Department of Physics
National Taiwan University
Taipei, Taiwan

Carlos J. L. Constantino
Faculdade de Ciências e Tecnologia
UNESP Universidade Estadual Paulista
Presidente Prudente
Brazil

Wei Deng
ARC Centre for Nanoscale BioPhotonics
Macquarie University, Sydney, Australia

Jakub Dostalek
Biosensor Technologies
AIT—Austrian Institute of Technology
Vienna, Austria

Debosruti Dutta
Department of Chemical & Biomedical Engineering
University of South Florida
Tampa, FL, USA

Kareem Elsayad
Advanced Microscopy
Vienna Biocenter Core Facilities (VBCF)
Vienna, Austria

C. H. Fok
Department of Physics
The Chinese University of Hong Kong
Sha Tin, Hong Kong

Mainak Ganguly
Department of Chemistry
Furman University
Greenville, SC, USA

Ewa M. Goldys
ARC Centre for Nanoscale BioPhotonics
Macquarie University, Sydney, Australia

Maiken H. Mikkelsen
Department of Physics, Metamaterials and Integrated Plasmonics, and Department of Electrical and Computer Engineering
Duke University
Durham, NC, USA

Simone Hageneder
Biosensor Technologies
AIT—Austrian Institute of Technology
Vienna, Austria

Katrin G. Heinze
Rudolf Virchow Center
DFG Research Center for Experimental Biomedicine
University of Würzburg
Würzburg, Germany

K. C. Hui
Department of Physics
The Chinese University of Hong Kong
Sha Tin, Hong Kong

Jayasmita Jana
Department of Chemistry
Indian Institute of Technology
Kharagpur, India

Nikhil Ranjan Jana
Centre for Advanced Materials
Indian Association for the Cultivation of Science
Kolkata, India

Chong-Yu Jiang
Institute of Applied Mechanics
National Taiwan University
Taipei, Taiwan, ROC

Xiaojin Jiao
Department of Electrical and Computer Engineering, University of Utah
Salt Lake City, USA

Babu Joseph
Department of Chemical & Biomedical Engineering
University of South Florida
Tampa, FL, USA

Ofer Kedem
Center for Bio-Inspired Energy Science
Northwestern University
Evanston, IL, USA

Dong Ha Kim
Department of Chemistry and Nano Science
School of Natural Sciences
Ewha Womans University, Seoul, Korea

Mao-Kuen Kuo
Institute of Applied Mechanics
National Taiwan University
Taipei, Taiwan, ROC

Chenxi Li
Key Laboratory of Bioorganic Chemistry
and Molecular Engineering of Ministry
of Education
Peking University
Beijing, China

J. Li
Department of Physics
The Chinese University of Hong Kong
Sha Tin, Hong Kong

Na Li
College of Chemistry and Molecular Engineering
Peking University, Beijing, China

Yao-Qun Li
Department of Chemistry and the MOE Key
Laboratory of Spectrochemical Analysis &
Instrumentation
College of Chemistry and Chemical Engineering
Xiamen University
Xiamen, China

Jiunn-Woei Liaw
Department of Mechanical Engineering
Chang Gung University
Taoyuan, Taiwan, ROC

Ruoyun Lin
Beijing National Laboratory for Molecular
Sciences (BNLMS)
Peking University
Beijing, China

Chuan-Li Liu
Institute of Applied Mechanics
National Taiwan University
Taipei, Taiwan, ROC

Feng Liu
College of Chemistry and Molecular Engineering
Peking University
Beijing, China

Osvaldo N. Oliveira, Jr.
São Carlos Institute of Physics
University of São Paulo
São Carlos, Brazil

H. C. Ong
Department of Physics
The Chinese University of Hong Kong
Sha Tin, Hong Kong

Tarasankar Pal
Department of Chemistry, Indian Institute of
Technology, Kharagpur
India

Arindam Saha
Centre for Advanced Materials
Indian Association for the Cultivation of Science
Kolkata, India

David R. Smith
Department of Electrical and Computer
Engineering, Center for Metamaterials and
Integrated Plasmonics and Department of Physics
Duke University
Durham, NC, USA

Koji Toma
Department of Biomedical Devices and
Instrumentation
Institute of Biomaterials and Bioengineering
Tokyo Medical and Dental University
Tokyo, Japan

Mana Toma
Department of Applied Chemistry for
Environment
School of Science and Technology
Kwansei Gakuin University
Sanda, Japan

Din Ping Tsai
Department of Physics
National Taiwan University
Taipei, Taiwan
and
Research Center for Applied Sciences
Academia Sinica
Taipei, Taiwan

Ming Lun Tseng
Department of Physics
National Taiwan University
Taipei, Taiwan

M. Umadevi
Department of Physics
Mother Teresa Women's University
Kodaikanal, India

Yunshan Wang
Department of Electrical and Computer Engineering
University of Utah, Salt Lake City, USA

Fang Xie
Faculty of Engineering, Department of Materials
Imperial College, London, UK

Kai-Xin Xie
Department of Chemistry and the MOE Key Laboratory of Spectrochemical Analysis & Instrumentation
College of Chemistry and Chemical Engineering
Xiamen University
Xiamen, China

Qing-Hua Xu
Department of Chemistry
National University of Singapore
Singapore, Singapore

Chi Ta Yang
Department of Chemical & Biomedical Engineering
University of South Florida
Tampa, FL, USA

Peiyan Yuan
Department of Chemistry
National University of Singapore
Singapore, Singapore

Yan-Yun Zhai
Department of Chemistry and the MOE Key Laboratory of Spectrochemical Analysis & Instrumentation
College of Chemistry and Chemical Engineering
Xiamen University
Xiamen, China

Taishi Zhang
Department of Chemistry
National University of Singapore
Singapore, Singapore

Tingting Zhao
Department of Chemistry
National University of Singapore
Singapore, Singapore

Preface

In the last 20 years or so, we have seen the discovery and growth of a new area of science, namely, *fluorescence-based plasmonics*. This new and exciting area of science has already started to change the way we think about and use fluorescence spectroscopy today but is in stark contrast to how we have all traditionally utilized fluorescence. For example, for nearly 130 years, up until the early 1980s, we had considered fluorophores as simple far-field free-space emitters, transmitting into a nonconducting and transparent medium. As a fluorescence community we have collectively continued down this thought path and developed numerous approaches for imaging, approaches in the analytical sciences, synthesized fluorophores that are fluorescence-sensitive to a vast array of analytes or biomolecules, and even developed highly sensitive and ultrafast instrumentation to undertake the most challenging of physiological/cellular measurements. Subsequently, far-field fluorescence spectroscopy has become entrenched in the life sciences today, with many research labs housing instrumentation, which, many years back, was considered highly specialized but is today considered routine technology. Even our etymology has changed. I remember back in the 1990s how we all referred to single molecule studies as "single molecule detection," as it was arduous at best to study single molecules. Today, "single molecule spectroscopy" has been transformative in cellular and mechanistic biology, with many of the highly complex confocal microscopes, for the most part, *turnkey* today. Our achievements as a fluorescence community have also been gratefully acknowledged by a worldwide audience, with two Nobel Prizes in Chemistry in recent years, one in 2008 for the discovery and use of green fluorescent protein (GFP) and, more recently in 2014, awarded for super resolution microscopy.

However, in the near field, for fluorophores in close proximity, less than one wavelength of light away, from either Noble metal nanoparticles, nanoparticle-comprised films, or even continuous films, our explorative journey as a community is only just beginning. The merging of fluorescence spectroscopy with plasmonics has created a new area of science, *fluorescence-based plasmonics*, that is just as exciting to researchers today, as early fluorescence likely was to the pioneers of the day.

Today, much of the work on *fluorescent-based plasmonics* has been focused on using surface plasmons and their associated e-fields for enhancing fluorescence signatures. This has been referred to as surface-enhanced fluorescence, plasmon-enhanced fluorescence, and most popularly as metal-enhanced fluorescence (MEF), which was in fact a name I first coined in the research literature myself in 2002 and subsequently was the title of the first edited volume on the topic, which precedes this Wiley volume (published in 2010). In addition, surface plasmons have also been widely used for 30 years to enhance both Raman (SERS) and more recently IR signatures, which have led to the introduction of more generalized terms, such as "surface plasmon-enhanced spectroscopies." In addition to enhanced fluorescence, surface plasmons have additionally been shown to couple fluorescence; transport and reradiate coupled quanta; provide for spatially localized excitation (MEF–EVE effect); and even pump both singlet and/or triplet states to promote a variety of photochemistries, to name but just a few applications. Subsequently, in this continuation volume from my 2010 volume *Metal-Enhanced Fluorescence*, I have invited leading researchers to contribute invited chapters with the hope of both updating us on the latest developments in metal-enhanced fluorescence while at the same time introducing us to some of the latest developments in fluorescence-based plasmonics.

Finally in closing, I would like to thank the authors for their excellent and timely contributions and for the Wiley editors, Michael Leventhal, Katherine Clark, and Bob Esposito for the help in putting this volume together.

Best
Professor Chris D. Geddes, FRSC
The Institute of Fluorescence
University of Maryland, Baltimore County
Baltimore, USA
February 16, 2016.

1

Plasmonic-Fluorescent and Magnetic-Fluorescent Composite Nanoparticle as Multifunctional Cellular Probe

Arindam Saha, SK Basiruddin, and Nikhil Ranjan Jana

Centre for Advanced Materials, Indian Association for the Cultivation of Science, Kolkata, India

1.1 Introduction

The interaction of fluorophore with metal has been a field of research since many decades. In 1970s, Drexhage found that fluorophore located near the metallic surfaces shows oscillations of the emissive lifetime depending on the distance from the metal surface [1, 2]. After this finding, many theoretical [3–9] and practical researches were directed in this field [10–16]. Now it is well known that when a metal surface interacts with an excited-state fluorophore, two phenomena can take place, either the fluorescence of the fluorophore is enhanced or it is quenched. When a metal stays very close to the fluorophore, typically within 20 nm, the electrons from the excited fluorophore transfer to the metal and hence result in fluorescence quenching. But when the metal surface stays 20–50 nm away from the fluorophore, the excited electrons of fluorophore interact differently with the metal electrons and it results in an increase in the rate of fluorescence decay as well as the rate of excitation. The effect is enhancement of fluorescence with decreased lifetime and increased photostability. This phenomenon is termed as metal-enhanced fluorescence (MEF) [14, 17, 18]. Most of this MEF has been observed for silver island film [17, 19–26], silver colloids [27–29], other silver nanostructures [30, 31], gold [32–35], iron oxide [36], tin [37], platinum [38], aluminium [39], and so on. Among different metals, nanosize silver and gold are studied more frequently as they have plasmonic properties in the visible region arising due to collective oscillations of surface electrons and that can significantly modulate the MEF properties.

Different options of a fluorophore under proper excitation are shown in Scheme 1.1. According to the aforementioned diagram, when a fluorophore is excited with an appropriate energy, it reaches to a higher electronic level and then undergoes decay in both radiative and non-radiative ways. Here Γ indicates the rate of radiative decay; K_{nr} is the rate of non-radiative decay and rate of quenching collectively. When the fluorophore is within the distance of 20 nm from the metal surface, then $K_{nr} > \Gamma$ and as a result both quantum yield (QY) (Q_0) and lifetime (τ_0) decrease. But when the distance between the metal surface and fluorophore is typically between 20 and 50 nm, $\Gamma > K_{nr}$ and hence Q_0 increases but τ_0 decreases, which is indicated by MEF. Since the lifetime decreases, the fluorophore remains in the excited state for a shorter time period and their chance of non-radiative decay or other excited state reaction is decreased that results in increased photostability [18, 23, 40–42]. When the distance is larger than 50 nm, there is preferably no interaction between the fluorophore and metal surface.

In fluorescence-based experiments (e.g., sensor application, cellular imaging, molecular probe design), metal-induced quenching is a critical drawback [43] and difficult to overcome completely. However, this quenching effect has been exploited as "Turn Off" detection of analyte in many cases, although this type of sensor design is neither specific nor accurate since many other factors can influence the quenching phenomenon. Alternative "Turn On" sensor design is of utmost importance where the presence of analyte is more selectively detected by the fluorescence enhancement effect [44]. In cellular imaging, the conventionally used molecular dyes often undergo photobleaching and hence long-term tracking of cellular activities is difficult. Although new dyes have been developed with reduced photobleaching properties, the quenching of the dye under complex cellular environment is unavoidable that often hinders the

Surface Plasmon Enhanced, Coupled and Controlled Fluorescence, First Edition. Edited by Chris D. Geddes.
© 2017 John Wiley & Sons, Inc. Published 2017 by John Wiley & Sons, Inc.

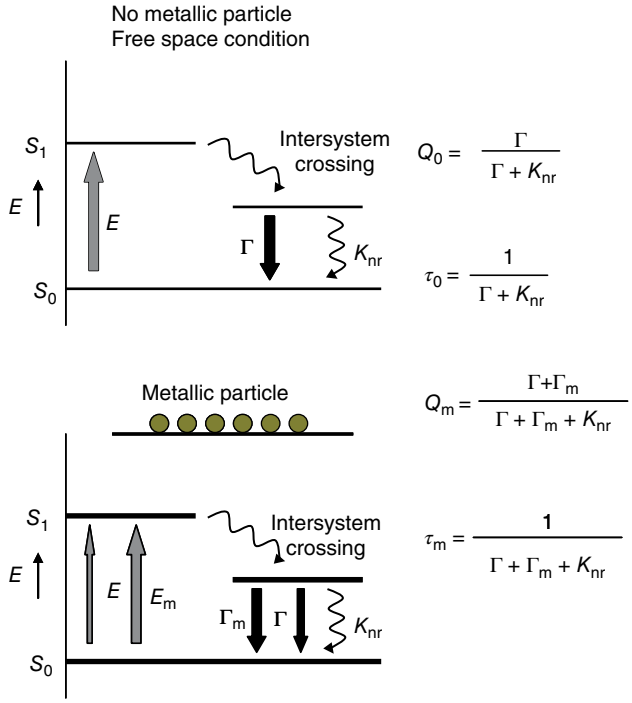

Scheme 1.1 Different options of electron–hole recombination within a fluorophore. Here E and E_m are energy of excitation for fluorophore and metal plasmon.

imaging. Various semiconductors and other fluorescent nanoparticles are emerging as promising alternatives, but toxicity issues question their application potential for *in vivo* imaging and long-time cellular tracking [45–48].

The most adverse effect of metal-induced quenching occurs in the preparation of multifunctional probe, which is one of the current research directions. Various multifunctional probes composed of metallic and fluorescent components have been developed and many are still under development stages. These probes can be used for multiple applications like sensing, detection, imaging, and separation [49–55]. However, synthesis of these probes is a major challenge since the metal-based plasmonic or magnetic component in the composite system quenches the fluorescence of the fluorophore component. In order to solve this problem, various methods have been developed via tuning the separation distance between fluorescent components and quencher components, and in some selected cases MEFs are also observed [56–64].

We are interested in the development of noble metal nanoparticle-based hybrid nanoprobes composed of plasmonic and fluorescent components so that they can be used for different cellular labeling applications. Although noble metal nanoparticles have tunable optical property due to surface plasmon, their strong quenching property creates a difficulty in making hybrid nanoprobes. Thus appropriate methods need to be developed for synthesis, keeping optimum separation distance between the plasmonic and fluorescent components. In addition the methods should be simple and cost effective with options for various functionalizations. We have developed different methods to prepare different plasmonic-fluorescent nanoprobes that are composed of gold/silver nanoparticles of different sizes/shapes as plasmonic components and fluorescein or CdSe/ZnS quantum dots (QDs) as fluorescent components [65–68]. In addition to plasmonic-fluorescent hybrid nanoparticle, we are also developing magnetic metal oxide-based magnetic-fluorescent hybrid nanoparticles that can be used for magnetic separation applications [67, 68]. In all these hybrid nanoprobes, the fluorescence of the fluorophore component is partially quenched with the final QY ranging between 7 and 20%. These hybrid nanoparticles can be used for both fluorescence and plasmon-based imaging probes. Here we will summarize different approaches for their synthesis, functionalization, and application potential.

1.2 Synthesis Design of Composite Nanoparticle

Our research goal is to develop synthetic approach for plasmonic-fluorescent, magnetic-fluorescent, magnetic-plasmonic, or a combination of all the three components and applications of all these composites in various biomedical fields, such as cellular imaging, cellular

targeting and separation, protein detection, and study of carbohydrate–protein interaction. Here we will mainly focus on fluorescence-based composite materials. There are three general steps in the synthesis of these composite nanoparticles. First, high-quality hydrophobic nanoparticles, such as Au, Ag, CdSe/ZnS, and iron oxide; and hydrophilic nanoparticles, such as Au nanorod, Ag plate, Ag-coated Au nanorod have been synthesized by different reported methods [69–73]. Next, these as-synthesized nanoparticles are converted into polyacrylate-coated water-soluble nanoparticles when needed, using the reported methods [74–76]. Finally, composite materials have been synthesized using three different approaches shown in Scheme 1.2. Table 1.1 summarizes all types of composite nanoparticles prepared by these approaches along with their properties.

1.2.1 Method 1: Polyacrylate Coating-Based Composite of Nanoparticle and Organic Dye

This method can be employed for the preparation of plasmonic-fluorescent and magnetic-fluorescent composite nanoparticles between nanoparticle and organic dye [65, 66]. The preparation method is very similar to polyacrylate coating of nanoparticles with a modification where fluorescein methacrylate monomer is added along with other acrylate monomers so that fluorescein can be incorporated in the polyacrylate backbone. In this method IGEPAL cyclohexane-based reverse micelle solution has been used as a medium where hydrophobic nanoparticles and hydrophilic acryl monomers can be dissolved. The role of reverse micelle is to initiate the polyacrylate coating in homogeneous condition to minimize particle–particle aggregation during coating processes. The polymerization is initiated in the presence of an initiator ammonium persulfate under basic condition (*N*,*N*,*N*′,*N*′ tetramethylethylenediamine) and under inert atmosphere. The polymerization is stopped after 1 h by adding ethanol that precipitated the particles. The precipitated particles are washed with chloroform and ethanol and finally dissolved in fresh water. To further purify the composite system from free polymer, salt-induced precipitation and redispersion technique have been adapted followed by dialysis [65].

In the reaction condition, fluorescein methacrylate and other acryl monomers undergo simultaneous polymerization and are coated on the nanoparticle surface making 5–10 nm shells. Since the polymerization is random, fluorescein molecules are attached randomly on the polymeric coating backbone making a distance distribution between fluorescein and core nanoparticle. Different polymers forming acryl monomer can be used to provide different chemical functional groups on the coating backbone and on the nanoparticle surface. For example, *N*-(3-aminopropyl)methacrylamide hydrochloride has been used to provide primary amine functionality, acrylic acid for carboxylate functionality, poly(ethylene glycol) methacrylate for polyethylene glycol functionality, and methylene *bis*acrylamide is used to crosslink the polymer for a robust coating.

1.2.2 Method 2: Polyacrylate Coating-Based Composite of Two Different Nanoparticles

This method is useful for the synthesis of magnetic-fluorescent and plasmonic-fluorescent composite nanoparticles using two different nanoparticle components [67]. Here inorganic semiconductor nanoparticles are employed as fluorescent components and metal or metal oxides are used as plasmonic or magnetic components. The semiconductor nanoparticles of CdSe with ZnS shell QD have been prepared in different sizes ranging from 2 to 6 nm using the colloidal chemical synthesis method reported earlier [69]. These semiconductor nanoparticles have sizes less than the excitonic Bohr radius showing the quantum confinement effect and the bandgap between valence band and conduction band can be tuned by changing the particle size. The smaller the size higher the bandgap and hence the emission maxima blueshifted. Hence by tuning the size, we can have nanoparticles of various emissions (e.g., red, yellow, green). Other component nanoparticles such as gold, silver, and iron oxide in the size range of 5–50 nm have been prepared using standard methods. All the as-synthesized nanoparticles are purified from free surfactants and dispersed in solvents prior to their use.

Composite nanoparticle synthesis approach is very similar to polyacrylate coating method described in Method 1, except that two nanoparticles are used during polyacrylate coating. In this method both the nanoparticles are taken in reverse micelle along with polymer-forming monomer precursors, and polymerization is performed in that condition so that both nanoparticles are encapsulated inside a common polymeric shell. Since the reverse micelle is a dynamic assembly, the polymerization process can randomly trap different nanoparticles inside a single polymeric shell with the formation of a composite nanoparticle. The composition of composite can be controlled by varying the concentration ratio of the two nanoparticles. The polymer shell structure and functionality can be controlled by using different polymer precursors. Adjusting the polymerization condition composite

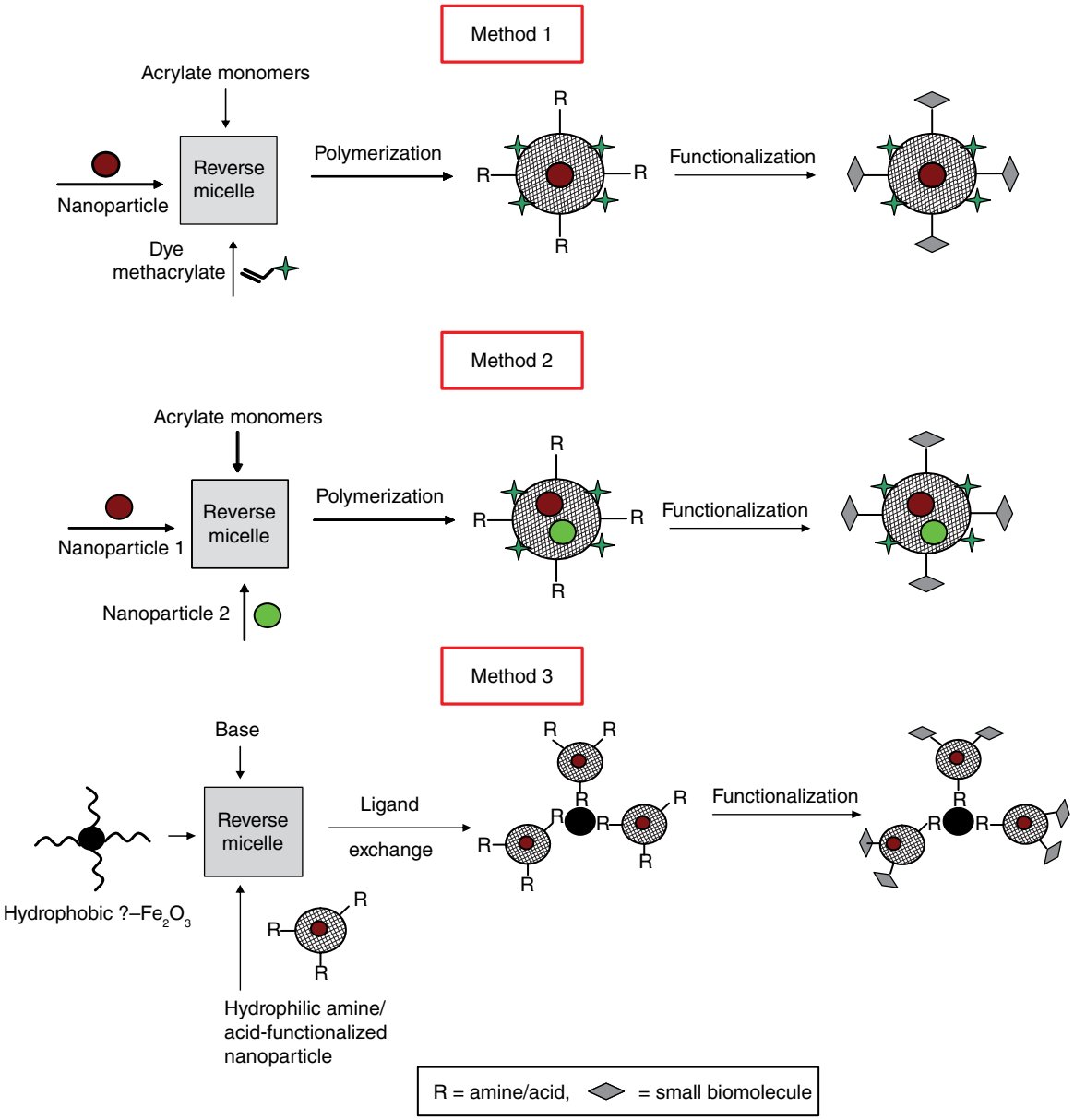

Scheme 1.2 Different synthesis approaches for multifunctional nanoparticle.

nanoparticle can be prepared having good water solubility and with 8–20% fluorescence QY. These composite nanoparticles can be purified by methods described in Method 1.

1.2.3 Method 3: Ligand Exchange Approach-Based Composite of Two Different Nanoparticles

This method is useful for the preparation of magnetic-fluorescent and magnetic-plasmonic nanocomposites, and here we will discuss only magnetic-fluorescent nanocomposites [68]. The ligand exchange approach is well known for the conversion of hydrophobic nanoparticle into hydrophilic nanoparticle. In this method, a thiol-based hydrophilic molecule is mixed with hydrophobic surfactant-capped gold or QD nanoparticle. As thiols have strong interaction with Au or Zn surface, they adsorb on the nanoparticle surface by replacing hydrophobic surfactants, making water-soluble nanoparticles. Thus conventional ligand exchange involves exchange of ligands on a nanoparticle surface. Here we have extended the ligand exchange approach involving two nanoparticles where ligands present on

Table 1.1 Summary of different composite nanoparticles along with their properties and application potentials.

Composite composition	Composite property	Preparation method	Overall size (nm)	Quantum yield (%)	Application
Au–fluorescein	Plasmonic and fluorescent	Method 1	20–40	16	Dual imaging (fluorescence and dark field), protein detection
Ag–fluorescein	Plasmonic and fluorescent	Method 1	20–40	12	Dual imaging (fluorescence and dark field), protein detection, antibacterial activity
Au nanorod–fluorescein	Plasmonic and fluorescent	Method 1	<100	9	Dual imaging (fluorescence and dark field), protein detection, photothermal therapy
Ag-coated Au nanorod–fluorescein	Plasmonic and fluorescent	Method 1	~65	8	Dual imaging (fluorescence and dark field), SERS[a]-based detection
γ-Fe_2O_3–fluorescein	Magnetic and fluorescent	Method 1	20–40	20	Fluorescence imaging, magnetic separation, MRI
γ-Fe_2O_3-CdSe/ZnS	Magnetic and fluorescent	Methods 2 and 3	50–80 (Method 2)	8–20	Fluorescence imaging, magnetic separation, MRI
			20–30 (Method 3)		

[a] SERS, surface-enhanced Raman scattering.

the surface of one nanoparticle replace the ligand present on another nanoparticle surface. Specifically we have mixed two types of nanoparticles, one coated with hydrophobic ligands and the other coated with hydrophilic ligands. The hydrophilic coating is exposed with surface chemical functionality that has strong affinity to other nanoparticle and thus replaces the hydrophobic ligands of the other nanoparticle. These processes lead to the formation of a composite nanoparticle.

We have used surfactant-coated hydrophobic iron oxide nanoparticle and polyacrylate-coated hydrophilic QD for this work. Polyacrylate-coated QDs are synthesized using the technique mentioned previously. This coating provides surface amine/acid group on QD nanoparticle surface. In contrast hydrophobic iron oxide nanoparticle has a long-chain fatty acid/amine capping. For the ligand exchange, the hydrophobic iron oxide is first dissolved in reverse micelle and then hydrophilic QDs are added under basic condition. At this condition long-chain fatty acid/amine capping on iron oxide surface is replaced by the surface amine/acid of polyacrylate-coated QDs. Next, ethanol is added to precipitate the hybrid material. The supernatant is decanted, and the precipitate has been washed repeatedly with cyclohexane and chloroform. This washing step removes any free hydrophobic γ-Fe_2O_3 as they are soluble in cyclohexane and chloroform. During each washing step, the hybrid materials are magnetically separated from the solution. This magnetic separation removes any free hydrophilic nanoparticle from the hybrid particle. After these washing steps, the hybrid materials have been dried in air and finally dissolved in water or a buffer solution.

The success of this process depends on the type of long-chain ligand on iron oxide surface and the type of surface functional group on QDs. Proper adjustment of these two factors results in efficient ligand exchange to produce magnetic-fluorescent composite nanoparticles. It is also possible to control the number of QDs on the iron oxide surface by adjusting the ratio of two nanoparticle concentrations and by controlling the amine/acid on the polyacrylate backbone of QDs. The fluorescence QY of the composites depends on the amount of QD over each iron oxide nanoparticle surface and typically varies from 8 to 20%. Composite nanoparticle produced by this approach can be further functionalized using the primary amine/carboxylate present on the QD surface.

1.3 Property of Composite Nanoparticles

1.3.1 Optical Property

We have prepared plasmonic-fluorescent (Au, Ag, Au nanorod, and Ag plate as plasmonic component) and magnetic-fluorescent (γ-Fe_2O_3 and Fe_3O_4 as magnetic component) composite materials using the aforementioned three different approaches (Table 1.1). All these hybrid nanoparticles are water soluble with good colloidal stability in various buffer media. Figure 1.1 shows

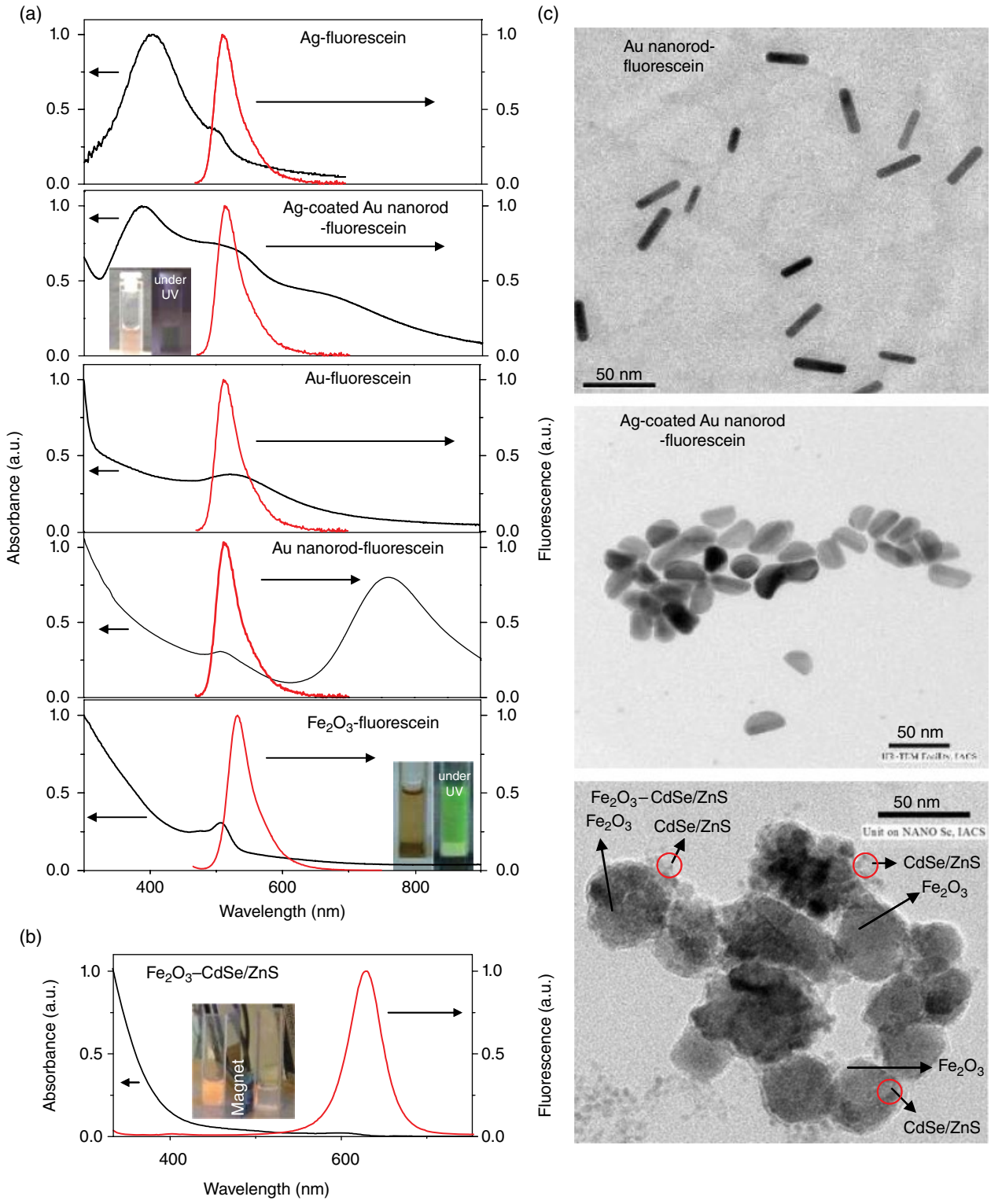

Figure 1.1 UV–Vis and fluorescence spectra of fluorescein-based composite nanomaterials (inset digital images of plasmonic-fluorescent and magnetic-fluorescent composites along with normal light and UV light and/or magnetic separation under UV light) (a), UV–Vis and fluorescence spectra of QD-based composite nanomaterials (b), and TEM image of Au nanorod–fluorescein, Ag-coated Au nanorod–fluorescein, and γ-Fe_2O_3–CdSe/ZnS composite (c).

representative ultraviolet (UV)–visible (Vis) and photoluminescence spectra of different plasmonic-fluorescent and magnetic-fluorescent nanoparticles showing plasmonic-fluorescent and magnetic-fluorescent properties (Figure 1.1). In the UV–Vis spectra of Au–fluorescein, the peak at around 530 nm is due to plasmonic property of Au nanoparticles, and the peak around 510 nm is due to the absorbance of fluorescein. Due to this fluorescein absorption, the plasmonic peak of Au becomes broad. In the case of Ag-fluorescein, two peaks are observed in the UV–Vis spectra—510 nm peak corresponds to fluorescein absorption, and 410 nm peak corresponds to plasmonic absorption of Ag nanoparticles. In Au nanorod–fluorescein, two peaks of Au nanorod are observed at 520 and 800 nm, which are due to transverse and longitudinal oscillation of plasmonic electrons along the nanorod's short and long axes, respectively. But the peak at 520 nm broadens due to fluorescein absorption. The Ag-coated Au nanorod–fluorescein composites show three distinct humps corresponding to plasmonic peaks of Ag and Au in 400–800 nm regions. In case of iron oxide-fluorescein only, the fluorescein absorption peak is observed since iron oxide does not have any absorption in the visible region. In all these plasmonic-fluorescent composite nanoparticles, the photoluminescence spectra show the characteristic green emission of fluorescein with a peak at around 528 nm. The digital images show plasmonic color under normal light and characteristic green emission under UV light irradiation. The QY of these composite nanoparticles is calculated using fluorescein as a standard (95% QY). The concentration of fluorescein is calculated from the absorption spectra of hybrid nanoparticles in both acidic and basic pH. Fluorescein shows no absorption at 500 nm in acidic pH but shows significant absorption in basic pH, and this fact has been used to calculate the fluorescein concentration. Fluorescence QY is calculated as 12% for Ag– fluorescein, 16% for Au–fluorescein, 9% for Au nanorod–fluorescein, 8% for Ag-coated Au nanorod–fluorescein, and ~20% for iron oxide–fluorescein.

Semiconductor nanoparticle QD-based composites (iron oxide QD and Au nanorod QD) show fluorescent properties characteristic of semiconductor nanoparticle. In Figure 1.1b UV–Vis spectrum and photoluminescence property of such particles have been shown. In the UV–Vis spectrum, a small hump at 600 nm corresponds to QD's first excitonic peak, which arises due to the transition of electrons from the highest energy level of valence band to the lowest energy level of conduction band. When these composites are excited using 350 nm light, it produces sharp emission spectra centered around 630 nm, which arises due to electron–hole recombination. Magnetic property of these composites can be realized from the digital image showing magnetic separation of these particles under magnet once their colloidal stability is lowered by adding salt. These composite nanoparticles also show fluorescence QY in the range of 8–20%, depending on the size of QD used.

1.3.2 Fluorophore Lifetime Study

The fluorescence QY data suggests that fluorophores in composite nanoparticle are distributed around metal/metal oxide keeping a separation distance so that the fluorescence is not completely quenched. In order to understand in more detail the nature of interaction between fluorophore and metal/metal oxide, we performed lifetime measurements of fluorophore in the composite nanoparticle. Figure 1.2 shows a representative result of the lifetime study. Analyzing the fluorescent lifetime data of the plasmonic-fluorescent nanocomposites, we have found that lifetime decreases and decay curve fits with the multiple exponential, compared to single exponential fitting for fluorescein. For example, fluorescein itself has an average lifetime of ~4.4 ns, but in composites

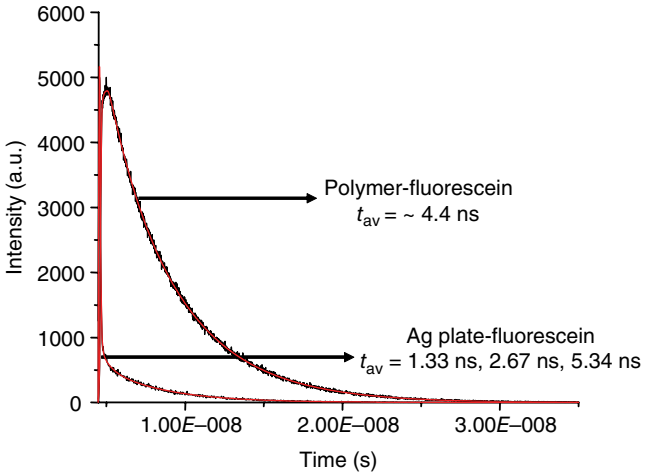

Figure 1.2 Lifetime data for polymer fluorescein that is best fitted in a single exponential curve and for Ag plate–fluorescein composite that best fitted in three exponential curves with decreased lifetime. Dotted line corresponds to experimental data and bold line corresponds to fitting curve.

the decay curve best fits with three exponentials with the decrease in average lifetime. In case of Ag–fluorescein, the average lifetimes are 0.46, 2.43, and 4.12 ns; for Au–fluorescein, they are 0.05, 0.88, and 3.47 ns; for Au nanorod–fluorescein, the values are 0.2, 1.8, and 3.6 ns; and for Ag plate–fluorescein, the values are 1.33, 2.67, and 5.34 ns. Lowering of average lifetime and decrease in fluorescence QY in all these samples suggest a significant quenching effect of fluorophore fluorescence. Three different lifetimes suggest that the fluorophores are at various distances from the plasmonic nanoparticles and greater the distance from the core, the higher the average lifetime is. This distance-dependent distribution of fluorophore results in the partial quenching effect. Similar type of lifetime data has also been observed in case of other QD-based composite nanoparticles suggesting that the behavior of fluorescent dye or fluorescent nanoparticle (QDs) in composite nanoparticles is similar. Nevertheless, the final composite contains sufficient fluorescence for multifunctional application.

1.4 Functionalization and Labeling Application of Composite Nanoparticle

The composite nanomaterials prepared by various methods are water soluble with the scope for further functionalization. In TEM study of fluorescein-based composite nanoparticle, the core nanoparticles can be visualized but the fluorescein-incorporated polyacrylate shell is invisible unless proper staining is performed (Figure 1.1c). Similarly, for two nanoparticle-based composites, both nanoparticles can be detected in TEM but not their polymer shells (Figure 1.1c). DLS study offers the hydrodynamic diameter of these composite nanomaterials including the polymer shells and the overall size ranges between 20 and 80 nm (Table 1.1). These composite nanoparticles have been functionalized with various biomolecules such as glucose, oleyl, vancomycin, TAT peptide, and so on. Standard conjugation chemistries like glutaraldehyde-based coupling, *N*-succinimidyl 4-(maleimidomethyl)cyclohexanecarboxylate (SMCC)-based conjugation, and 1-ethyl-3-(3-dimethylaminopropyl)carbodiimide (EDC) coupling [68, 74] have been applied for covalent conjugation with a nanoparticle. In most of these works, the primary amine functional groups present on the composite nanoparticle surface have been used for conjugation chemistry.

These composite nanoparticles have potential multifunctional applications. For example, a plasmonic-fluorescent nanoparticle can be used as a dual imaging probe such as fluorescence imaging using fluorescent component and scattering-based dark field imaging using a plasmonic component or imaging and detection probe such as fluorescence-based imaging and plasmon-based detection [65, 66]. The magnetic-fluorescent nanoparticle can be used for fluorescence-based imaging and magnetic separation [67, 68]. We have used functionalized composite nanoparticles for multifunctional cellular imaging and cell separation applications. Oleyl functionalization offers cell membrane targeting, TAT functionalization offers increased cellular internalization, and glucose or vancomycin functionalization offers specific cell targeting and labeling [65–68]. When imaged under fluorescence microscope, labelled cells show bright fluorescence due to fluorophore components, and both fluorescein dye and QD are photostable for long-term cellular imaging [65, 67]. Similarly, the dark field imaging shows bright colors of labeled cells due to plasmonic components (Figure 1.3). Magnetic separation of labeled cells has also been studied when magnetic component is present in the composite nanoparticle. We have also extended this work for bacteria imaging and separation using vancomycin-functionalized magnetic-fluorescent composites [67] (Figure 1.3).

Specific detection of protein has been performed using glucose-functionalized nanocomposites via specific interaction with glycoprotein concanavalin A (Con A). Con A has four binding sites for glucose, which upon interaction with glucose crosslink the particles and causes precipitation of particles from the solution [66]. The glucose-functionalized Au nanorod–fluorescein composite responds to a very small change in Con A concentration, since the longitudinal peak of Au nanorod is very sensitive to aggregation. This probe can be extended for imaging of glycoprotein in cellular environment or magnetic separation of glycoprotein from extracellular environment. These examples show that the composite nanoparticle can be used for a variety of multifunctional applications such as optical detection and imaging or separation.

1.5 Conclusion

Metal-induced fluorescence quenching is a major drawback in numerous fluorescence-based applications, particularly in multifunctional composite probe design. In contrast, MEF, which can be observed for an optimum distance between fluorophore and metal, has a great potential in overcoming this quenching problem.

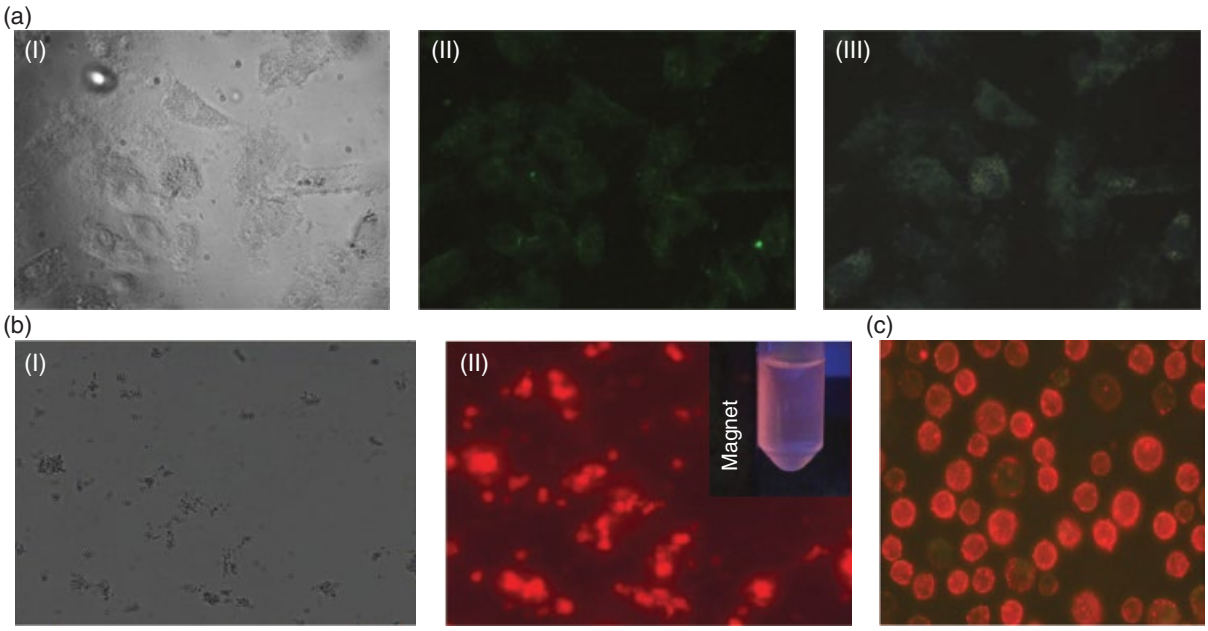

Figure 1.3 (a) H9C2 cells treated with oleyl-functionalized Au nanorod–fluorescein composite. (I) Bright field image, (II) fluorescence image, and (III) dark field image. (b) *Bacillus subtilis* bacteria treated with vancomycin-functionalized γ-Fe_2O_3–CdSe/ZnS nanocomposite (I) bright field image and (II) fluorescence image (inset magnetic separation of bacteria). (c) Fluorescence image of EAC cell treated with oleyl-functionalized γ-Fe_2O_3–CdSe/ZnS nanocomposite. (*See insert for color representation of this figure.*)

However, very limited success has been achieved in this direction due to the difficulty in controlling the distance between fluorophore and metal. We have designed three different strategies for the synthesis of multifunctional composite nanoparticles that overcome the quenching problem completely. The designs are such that fluorophores are distributed at various distances from the core metallic particle and only partial quenching of the fluorophores is observed in average. The resultant composite nanoparticle can be used as multifunctional probes for different biomedical applications. We have applied these probes for dual imaging, imaging-separation, and detection-separation applications.

Acknowledgments

The authors would like to thank DST and DBT, Government of India, for financial support. AS and SB acknowledge CSIR, India, for research fellowship.

References

1 Drexhage, K. H. *J. Lumin.* **1970**, *12*, 693.
2 Drexhage, K. H. *Progress in Optics, Vol. XII*; Wolf, E., Ed.; North Holland Publishing Company: Amsterdam, **1974**.
3 Tews, K. H. *J. Lumin.* **1974**, *9*, 223.
4 Chance, R. R.; Prock, A.; Silbey, R. *J. Chem. Phys.* **1974**, *60*, 2744.
5 Persson, B. N. J. *J. Phys. C, Solid State Phys.* **1978**, *11*, 4251.
6 Gersten, J.; Nitzan, A. *J. Chem. Phys.* **1981**, *75*, 1139.
7 Ruppin, R. *J. Chem. Phys.* **1982**, *76*, 1681.
8 Barnes, W. L. *J. Mod. Opt.* **1998**, *45*, 661.
9 Das, P. C.; Puri, A. *Phys. Rev. B* **2002**, *65*, 155416/1.
10 Adams, A.; Rendell, R. W.; Garnett, R. W.; Hansma, P. K.; Metiu, H. *Opt. Commun.* **1980**, *34*, 417.
11 Weitz, D. A.; Garoff, S.; Hanson, C. D.; Gramila, T. *J. Opt. Lett.* **1982**, *7*, 89.
12 Leitner, A.; Lippitsch, M. E.; Draxler, S.; Riegler, M.; Aussenegg, F. R. *Appl. Phys. B* **1985**, *36*, 105.
13 Aussenegg, F. R.; Leitner, A.; Lippitsch, M. E.; Reinisch, H.; Riegler, M. *Surf. Sci.* **1987**, *139*, 935.
14 Sokolov, K.; Chumanov, G.; Cotton, T. M. *Anal. Chem.* **1998**, *70*, 3898.
15 Tarcha, P. J.; De Saja-Gonzalez, J.; Rodriguez-Llorente, S.; Aroca, R. *Appl. Spectrosc.* **1999**, *53*, 43.
16 De Saja-Gonzalez, J.; Aroca, R.; Nagao, Y.; De Saja, J. A. *Spectrochim. Acta A* **1997**, *53*, 173.
17 Lakowicz, J. R. *Anal. Biochem.* **2001**, *298*, 1.
18 Geddes, C. D.; Lakowicz, J. R. *J. Fluores.* **2002**, *12*, 121.
19 Lakowicz, J. R.; Shen, Y.; D'Auria, S.; Malicka, J.; Fang, J.; Gryczynski, Z.; Gryczynski, I. *Anal. Biochem.* **2002**, *301*, 261.

20 Gryczynski, I.; Malicka, J.; Holder, E.; DiCesare, N.; Lakowicz, J. R. *Chem. Phys. Lett.* **2002**, *372*, 409.

21 Lakowicz, J. R.; Maliwal, B. P.; Malicka, J.; Gryczynski, Z.; Gryczynski, I. *J. Fluoresc.* **2002**, *12*, 431.

22 Gryczynski, I.; Malicka, J.; Shen, Y.; Gryczynski, Z.; Lakowicz, J. R. *J. Phys. Chem. B* **2002**, *106*, 2191.

23 Malicka, J.; Gryczynski, I.; Gryczynski, Z.; Lakowicz, J. R. *Anal. Biochem.* **2003**, *315*, 57.

24 Lakowicz, J. R.; Malicka, J.; D'Auria, S.; Gryczynski, I. *Anal. Biochem.* **2003**, *320*, 13.

25 Malicka, J.; Gryczynski, I.; Lakowicz, J. R. *Anal. Chem.* **2003**, *75*, 4408.

26 Malicka, J.; Gryczynski, I.; Maliwal, B. P.; Fang, J.; Lakowicz, J. R. *Biopolymers* **2003**, *72*, 96.

27 Maliwal, B. P.; Malicka, J.; Gryczynski, I.; Gryczynski, Z.; Lakowicz, J. R. *Biopolymers* **2003**, *70*, 585.

28 Geddes, C. D.; Cao, H.; Gryczynski, I.; Gryczynski, Z.; Fang, J.; Lakowicz, J. R. *J. Phys. Chem. A* **2003**, *107*,3443.

29 Lukomska, J.; Malicka, J.; Gryczynski, I.; Lakowicz, J. R. *J. Fluoresc.* **2004**, *14*, 417.

30 Parfenov, A.; Gryczynski, I.; Malicka, J.; Geddes, C. D.; Lakowicz, J. R. *J. Phys. Chem. B* **2003**, *107*, 8829.

31 Geddes, C. D.; Parfenov, A.; Lakowicz, J. R. *Appl. Spectrosc.* **2003**, *57*, 526.

32 Pompa, P. P.; Martiradonna, L.; Della Torre, A.; Della Sala, F.; Manna, L.; De Vittorio, M.; Calabi, F.; Cingolani, R.; Rinaldi, R. *Nature Nanotechnol.* **2006**, *1*, 126.

33 Zhang, J.; Lakowicz, J. R. Opt. Express **2006**, *15*, 2598.

34 Fu, Y.; Zhang, J.; Lakowicz, J. R. *J. Am. Chem. Soc.* **2010**, *132*, 5540.

35 Hwang, A.; Smolyaninov, I. I.; Davis, C. C. *Nano Lett.*, **2010**, *10*, 813.

36 Zhang, Y.; Padhyay, A.; Sevilleja, J. E.; Guerrant, R. L.; Geddes, C. D. *J. Phys. Chem. C* **2010**, *114*, 7575.

37 Zhang, Y.; Dragan, A.; Geddes, C. D. *J. Appl. Phys.* **2010**, *107*, 024302.

38 Ray, K.; Chowdhury, M. H.; Lakowicz, J. R. *Chem. Phys. Lett.* **2008**, *465*, 92.

39 Chowdhury, M. H.; Ray, K.; Gray, S. K.; Pond, J.; Lakowicz, J. R. Proceedings of SPIE—the International Society for Optical Engineering, **2010**, *7577*, 75770O.

40 Ray, K.; Szmacinski, H.; Enderlein, J.; Lakowicz, J. R. *Appl. Phys. Lett.* **2007**, *90*, 251116.

41 Gryczynski, I.; Malicka, J.; Nowaczyk, K.; Gryczynski, Z.; Lakowicz, J. R. *J. Phys. Chem. B* **2004**, *108*, 12073.

42 Fu, Y.; Lakowicz, J. R. *Laser Photon. Rev.* **2009**, *3*, 221.

43 Zhang, J.; Badugu, R.; Lakowicz, J. R. *Plasmonics*, **2007**, *3*, 3.

44 Tan, S. S.; Kim, S. J.; Kool, E. T. *J. Am. Chem. Soc.* **2011**, *133*, 2664.

45 Hoshino, A.; Fujioka, K.; Oku, T.; Suga, M.; Sasaki, Y. F.; Ohta, T.; Yasuhara, M.; Suzuki, K.; Yamamoto, K. *Nano Lett.* **2004**, *4*, 2163.

46 Derfus, A. M.; Chan, W. C. W.; Bhatia, S. N. *Nano Lett.* **2004**, *4*, 11.

47 Kirchner, C.; Liedl, T.; Kudera, S.; Pellegrino, T.; Javier, A. M.; Gaub, H. E.; Stoelzle, S.; Fertig, N.; Parak, W. *J. Nano Lett.* **2005**, *5*, 331.

48 Bentzen, E. L.; Tomlinson, I. D.; Mason, J.; Gresch, P.; Warnement, M. R.; D. Wright, D.; Sanders-Bush, E.; Blakely, R.; Rosenthal, S. *J. Bioconjugate Chem.* **2005**, *16*, 1488.

49 Wang, D.; He, J.; Rosenzweig, N.; Rosenzweig, Z. *Nano Lett.* **2004**, *4*, 409.

50 Sathe, T. R.; Agrawal, A.; Nie, S. *Anal. Chem.* **2006**, *78*, 5627.

51 Selvan, S. T.; Patra, P. K.; Ang, C. Y.; Ying, J. Y. *Angew Chem. Int. Ed.* **2007**, *46*, 2448.

52 Park, J.-H.; von Maltzahn, G.; Ruoslahti, E.; Bhatia, S. N.; Sailor, J. M. *Angew Chem. Int. Ed.* **2008**, *47*, 7284.

53 Kim, J.; Kim, H. S.; Lee, N.; Kim, T.; Kim, H.; Yu, T.; Song, I. C.; Moon, W. K.; Hyeon, T. *Angew Chem. Int. Ed.* **2008**, *47*, 8438.

54 Stoeva, S. I.; Lee, J.-S.; Smith, J. E.; Rosen, S. T.; Mirkin, C. A. *J. Am. Chem. Soc.* **2006**, *128*, 8378.

55 Gole, A.; Agarwal, N.; Nagaria, P.; Wyatt, M. D.; Murphy, C. *J. Chem. Commun.* **2008**, *46*, 6140.

56 Zhang, J.; Fu, Y.; Li, G.; Nowaczyk, K.; Zhao, R. Y.; Lakowicz, J. R. *Biochem. Biophys. Res. Commun.* **2010**, *400*, 111.

57 Lakowicz, J. R.; Malicka, J.; Gryczynski, I.; Gryczynski, Z. *Biochem. Biophys. Res. Commun.* **2003**, *307*, 435.

58 Badugu, R.; Lakowicz, J. R.; Geddes, C. D. *J. Am. Chem. Soc.* **2005**, *127*, 3635.

59 Zhang, J.; Fu, Y.; Liang, D.; Zhao, R. Y.; Lakowicz, J. R. *Langmuir* **2008**, *24*, 12452.

60 Aslan, K.; Wu, M.; Lakowicz, J. R.; Geddes, C. D. *J. Am. Chem. Soc.* **2007**, *129*, 1524.

61 Malicka, J.; Gryczynski, I.; Geddes, C. D.; Lakowicz, J. R. *J. Biomed. Opt.* **2003**, *8*, 472.

62 Aslan, K.; Lakowicz, J. R.; Szmacinski, H.; Geddes, C. D. *J. Fluores.*, **2004**, *1*, 677.

63 Aslan, K.; Huang, J.; Wilson, G. M.; Geddes, C. D. *J. Am. Chem. Soc.* **2006**, *128*, 4206.

64 Zhang, J.; Fu, Y.; Liang, D.; Nowaczyk, K.; Zhao, R. Y.; Lakowicz, J. R. *Nano Lett.*, **2008**, *8*, 1179.

65 Saha, A.; Basiruddin, SK.; Sarkar, R.; Pradhan, N.; Jana, N. R. *J. Phys. Chem. C* **2009**, *113*, 18492.

66 Basiruddin, SK.; Saha, A.; Pradhan, N.; Jana, N. R. *Langmuir* **2010**, *26*, 7475.

67 Basiruddin, SK.; Saha, A.; Sarkar, R.; Majumder, M.; Jana, N. R. *Nanoscale*, **2010**, *2*, 2561.

68 Saha, A.; Basiruddin, SK.; Pradhan, N.; Jana, N. R. *Langmuir* **2010**, *26*, 4351.

69 Li, J. J.; Wang, Y. A.; Guo, W.; Keay, J. C.; Mishima, T. D.; Johnson, M. B.; Peng, X. *J. Am. Chem. Soc.* **2003**, *125*, 12567.

70 Jana, N. R.; Peng, X. *J. Am. Chem. Soc.* **2003**, *125*, 14280.

71 Jana, N. R.; Chen, Y.; Peng, X. *Chem. Mater.* **2004**, *16*, 3931.

72 Jana, N. R. *Small* **2005**, *1*, 875.

73 Jiang, J.; Gu, H.; Shao, H.; Devlin, E.; Papaefthymiou, G. C.; Ying, J. Y. *Adv. Mater.* **2008**, *20*, 4403.

74 Wei, Y.; Jana, N. R.; Tan, S.; Ying, J. Y. *Bioconjugate Chem.* **2009**, *20*, 1752.

75 Tan, S. J.; Jana, N. R.; Gao, S.; Patra, P. K.; Ying, J. Y. *Chem. Mater.* **2010**, *22*, 2239.

76 Basiruddin, SK.; Saha, A.; Pradhan N.; Jana, N. R. *J. Phys. Chem. C*, **2010**, *114*, 11009.

2

Compatibility of Metal-Induced Fluorescence Enhancement with Applications in Analytical Chemistry and Biosensing

Fang Xie[1], *Wei Deng*[2], *and Ewa M. Goldys*[2]

[1] *Faculty of Engineering, Department of Materials, Imperial College, London, UK*
[2] *ARC Centre for Nanoscale BioPhotonics, Macquarie University, Sydney, Australia*

2.1 Introduction

A wide variety of chemical and biological analyses is based on the use of fluorescence for reporting of specific molecular events [1–3]. Signal intensity is frequently a challenge, and hence the interest in techniques that produce increased fluorescence signals from the available amount of fluorophores, such as metal-induced fluorescence enhancement (MIFE), has been intensely investigated [4–6]. Significant effort has been expended on understanding the foundations of this effect and different schemes where the effect can be observed. A number of excellent review papers describe recent results in this now quite mature area [4, 6–8]. Much of this work alongside with the key issues such as the role of localized plasmons in metals in relationship to fluorophore excitations is very well covered in the present volume; these will not be repeated here.

Our group has been developing and investigating fluorescence enhancement with a view to introduce this technology in real applications whenever they offer an advantage. We summarized our MIFE work in two reviews [9, 10]. Our program addresses the problem of compatibility of MIFE with practical technologies used in biosensing. This issue is rarely a focus of academic studies. One of the important applications of MIFE is in protein sensing, for example, by using immunoassays [11]. Immunoassays work by the principle of highly specific antibody–antigen recognition. The antibody is usually immobilized on a substrate such as glass slide. Fluorescently labeled antigen analyte in the examined sample conjugates to that antibody and adheres to glass slide, while all other simultaneously labeled proteins in the sample can be washed away (Figure 2.1). Here, MIFE enables the substrate used as a sensing platform to play an active role where specialized metal nanostructures deposited on glass produce an increased fluorescence signal of the fluorescent label compared to standard unmodified glass substrates. However metal nanostructures developed by our predecessors often suffered from limited uniformity. Responding to this need we developed several approaches to develop homogeneous assay substrates and demonstrated their utility for protein sensing [12, 13]. The metal-enhancement technology has also been applied to an alternative format of key significance in biotechnology, such as membranes [14, 15]. Membranes are used as substrates in a leading commercial technology of lateral flow assays [16] and are also commonly used in western blots and in immunodiagnostic devices [17].

Flow cytometry is also an important analytical method, commonly used in biotechnology. In this technique, fluorescently labeled analyte molecules are specifically conjugated to the micrometer size beads, which are also fluorescent. The bead color and the color of the fluorescent label of analyte molecules are different. The fluorescence from the beads and the analyte are then read out as the beads (with conjugated analytes) move in a single file through the laser focus. Co-registration of two brief fluorescence signals (from a bead and the analyte label on the same bead) signals the presence of analyte molecules. Flow cytometry poses significant challenges for fluorescence detection due to high speed of beads as they move through laser focus, which limits the time for fluorescence readout. Correspondingly, for ultrasensitive detection the analyte fluorescence needs to be amplified. We addressed this problem by developing fluorescence-enhancing flow cytometry beads whose utility was demonstrated in the flow cytometry experiments [18]. We describe our results in more detail in the following text (section 2.5).

Surface Plasmon Enhanced, Coupled and Controlled Fluorescence, First Edition. Edited by Chris D. Geddes.
© 2017 John Wiley & Sons, Inc. Published 2017 by John Wiley & Sons, Inc.

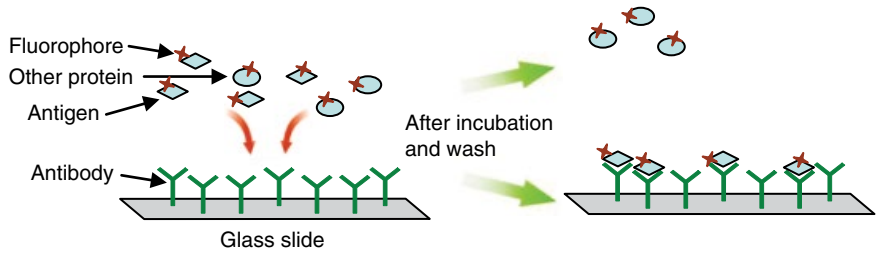

Figure 2.1 Schematic illustration of immunoassay on a glass slide. (*See insert for color representation of this figure.*)

2.2 Homogeneous Protein Sensing MIFE Substrates

2.2.1 Core–Shell Approach

Homogeneous substrates have been investigated in References [12] and [13]. In Ref. [12] we took advantage of the fact that homogeneous layers of gold nanoparticles can be deposited on glass slides with ease. However it is preferred to use silver for MIFE, due to reduced absorption in the visible compared with gold. We combined the advantages of these two materials by coating the Au nanoparticles with silver. Silver was deposited on the Au colloid-coated surface, which was immobilized on a glass surface by covalent binding. By varying the silver enhancing time, the sizes of these nanoparticles could be varied from about 10 nm to several hundred nanometers, while homogeneous distribution was maintained. Fluorescence enhancement was then quantified by using an FITC-HSA monolayer. Depending on the size of these Ag/Au nanoparticles, the fluorescence of FITC was either quenched, unaffected, or enhanced in comparison to the controls, where fluorescence was due solely to the same FITC-HSA monolayer on a bare glass surfaces. The Au core–Ag shell nanostructures produced after 3-min silver enhancing time had an enhancement factor of 13-fold, suggesting that this system can yield technologically promising substrates for fluorescence enhancement assays (Figures 2.2 and 2.3).

One of the important advantages of substrates prepared in this way was macroscopic uniformity of the surface, unlike in many competing methods, due to monodisperse Au seed on the glass surface and isotopic growth of silver on the Au colloid surface. The chemistry required for their preparation was also undemanding. In brief, a self-assembled Au colloid nanoparticle monolayer on glass was formed by firstly functionalizing the glass surface with (3-aminopropyl)-trimethoxysilane (APTMS) and then immersing into Au colloid solution. Depending on the time and concentration of the Au colloid solution employed, Au nanoparticle layers with various interparticle distances were formed on the glass surface. The surfaces were immersed in a silver enhancer solution to form Au core–Ag shell containing nanostructures. Depending on the time employed during the silver enhancing step, the size of these nanoparticles can range from 10 nm to several hundred nanometers. Binding of FITC-HSA to the silvered surface, or, in control experiments, to the glass surface, was accomplished by incubating the surfaces in a 10 μM FITC-HSA solution overnight at 4°C, followed by rinsing with buffer to remove the unbound materials. The enhancement factor obtained when using the silver was determined as the ratio of fluorescence intensity on silver to fluorescence intensity on glass, given both surfaces are known to have almost equal monolayer coverage.

The resulting structures were characterized by a range of methods. SEM images (Figure 2.2a–c) show the size and the surface morphology of the Au core–Ag shell nanoparticles as MIFE substrates. The silver coating appeared to be initially homogeneous over the Au core and with increasing enhancing time formed the nanoflower-shaped particles. The average particle sizes, calculated from 100 particles, with 1 and 3 min silver enhancing time are about 19 and 47 nm, respectively.

Laser scanning microscopy at 488 nm excitation wavelength demonstrated the enhancement of fluorescence emission in the areas containing the nanoparticles as well as the bare glass surface without the nanoparticles. The enhancement factor was determined as the ratio of fluorescence intensity on silver to fluorescence intensity on glass based on the fluorescence spectra. The origin of this enhancement obtained using appropriate size Ag nanoparticles is attributed to the effect of increased excitation rate from the locally enhanced electromagnetic field by interaction of incident light with the nanoparticles and a higher quantum yield from an increase of the intrinsic decay rate of the fluorophore. Homogeneous core–shell nanoparticles presented here could significantly improve the sensitivity of fluorescence-based biological assays and also could be utilized in high-throughput screening and drug discovery.

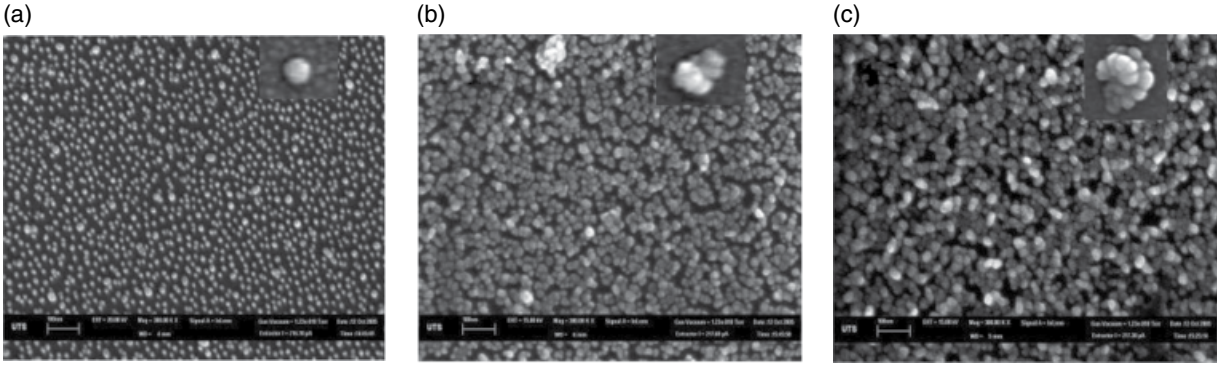

Figure 2.2 An SEM image of (a) 9 nm Au colloid; (b) Au core–Ag shell nanoparticles after 1 min silver enhancing step (~19 nm); and (c) Au core–Ag shell nanoparticles 3 min silver enhancing step (~47 nm); insets show the morphology of individual particles. Xie *et al*. [12]. Reproduced with permission of American Chemical Society.

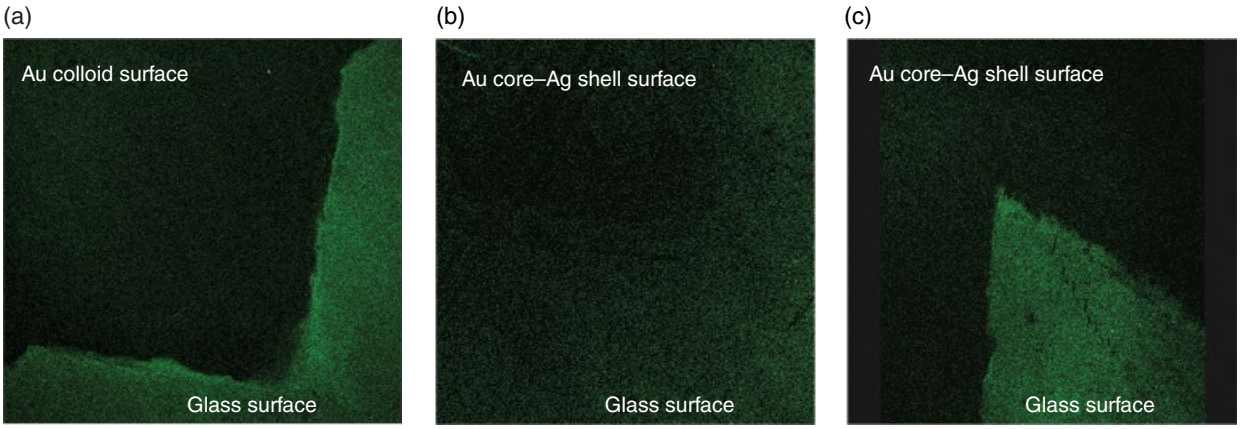

Figure 2.3 Laser scanning microscopy image of FITC-HSA monolayer on both nanoparticles and glass surface; excitation: 488 nm, emission collection 520–560 nm; (a) 9 nm Au colloid as MEF substrate, quench; (b) Au core–Ag shell nanoparticles 1 min silver enhancing step (nanoparticles size: 19 nm) as an MEF substrate, almost no effect; (c) Au core–Ag shell nanoparticles after 3 min silver enhancing step (nanoparticles size: 47 nm) as an MEF substrate, clear enhancement. Xie *et al*. [12]. Reproduced with permission of American Chemical Society.

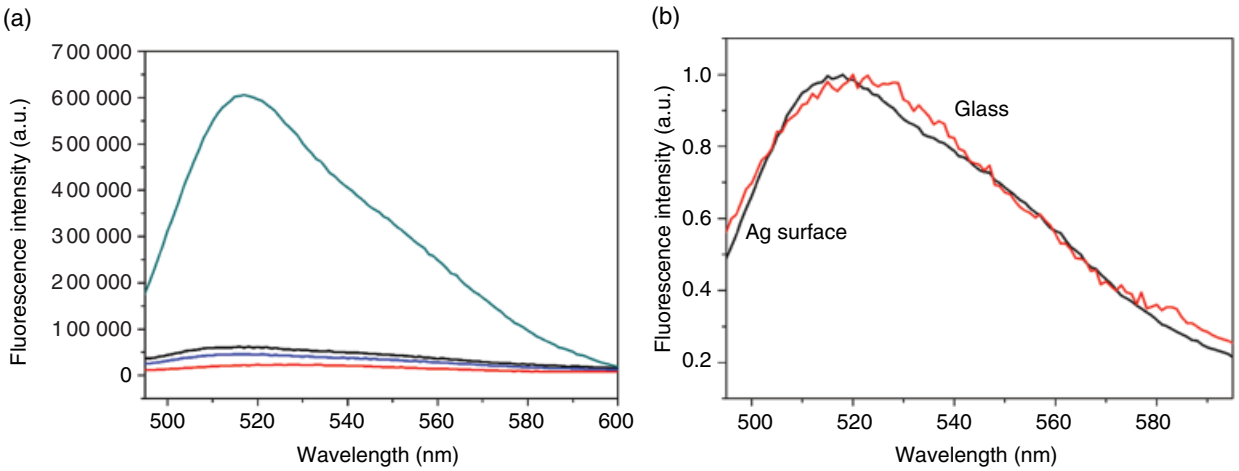

Figure 2.4 (a) Fluorescence emission intensity of FITC-HSA (from top to bottom): on substrate with 3 min silver enhancing time, on substrate with 1 min silver enhancing time, on clean glass surface, and on Au colloid monolayer; (b) normalized emission spectra of FITC-HSA on glass and on Au core–Ag shell nanoparticles with 3 min silver enhancing time. Xie *et al*. [12]. Reproduced with permission of American Chemical Society.

2.2.2 Homogeneous Large Au Nanoparticle Substrates

Metal enhancement by using colloidal Au nanoparticles has been reported prior to this work, but limited enhancement factors have been achieved, in the order of 3-fold only [19]. However, the use of gold is attractive, because gold surfaces resist oxidation much better compared with Ag and remain stable for many months after preparation. Importantly, gold-based substrates such as Au colloids can be produced with well controlled and homogeneous coverage. Therefore, in the second approach, we investigated fluorescence enhancement induced by Au-based substrates [13].

The core idea was to use specially synthesized large size and dense gold colloids as these are able to induce an appreciable enhancement of fluorescence. Au colloids 40, 59, and 81 nm in radius were homogeneously deposited on glass substrates with varying average particle distances and interparticle coupling. The fluorescence enhancement was examined by using self-assembled monolayers of epicocconone (Deep Purple™)-bovine serum albumin (DP-BSA). The highest observed fluorescence enhancement for DP-BSA was 15 times with the 162 nm Au colloid, and an average interparticle distance of 67 nm, as shown in the fluorescence spectra (Figure 2.5), was recorded for samples with various particle sizes and interparticle distances.

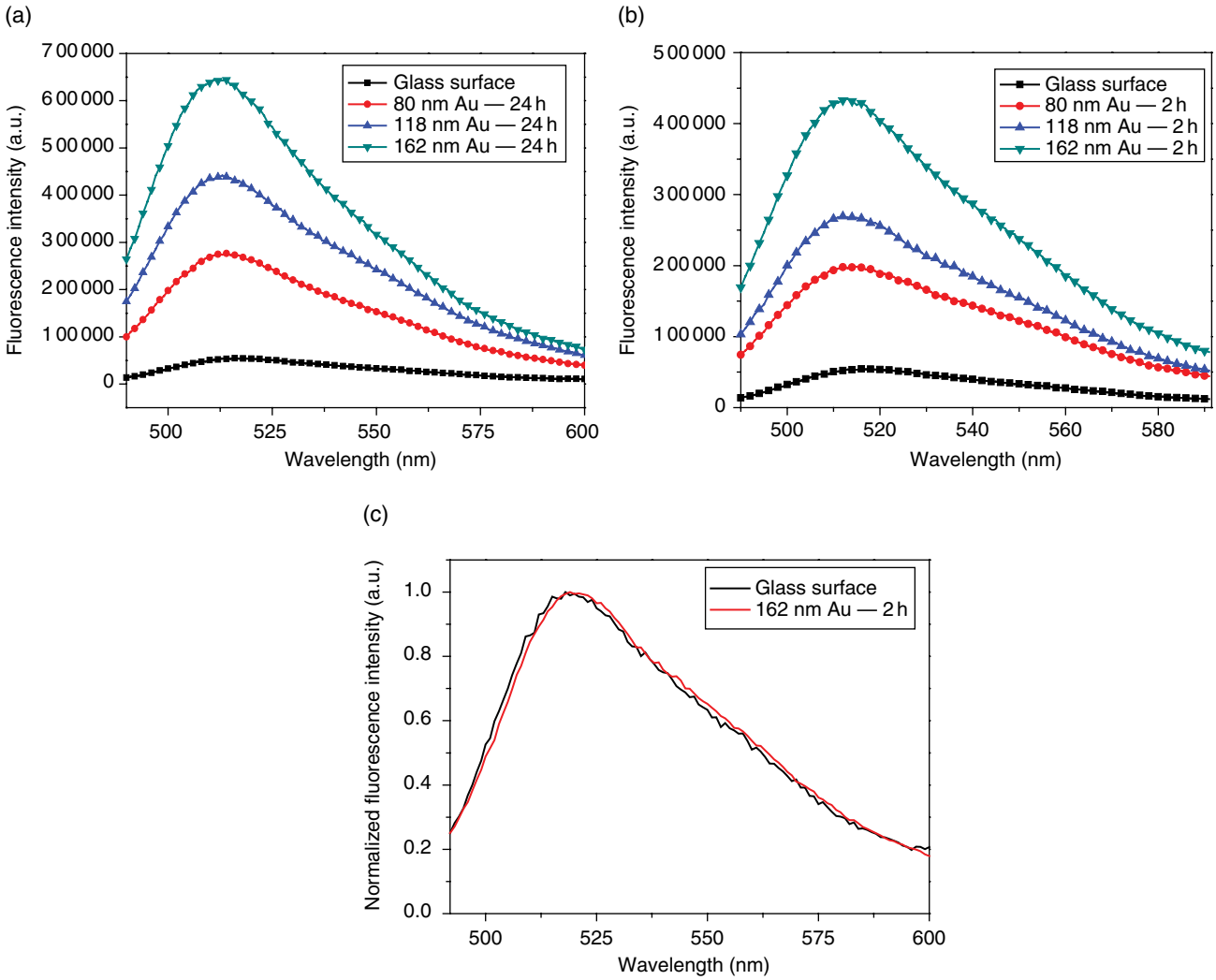

Figure 2.5 Fluorescence emission intensity of FITC-HSA: (a) on substrate with 2 h incubation time (from top to bottom): 162 nm Au colloid; 118 nm Au colloid; and 80 nm Au colloid. (b) On substrate with 24 h incubation time (from top to bottom): 162 nm Au colloid; 118 nm Au colloid; and 80 nm Au colloid. (c) Normalized emission spectra of FITC-HSA on glass and on metallic surface. Xie *et al*. [13]. Reproduced with permission of American Chemical Society.

The origin of fluorescence enhancement in these structures is the result of two effects: an increase of a local electromagnetic field near gold nanoparticles, leading to increased excitation rate of fluorophores, and an increase of the radiative decay rate Γ of fluorophores close to metal nanostructures, reflected both in the fluorescence lifetime and quantum yield, referred as "emission enhancement." The local electromagnetic field enhancement produces a higher excitation rate, but it does not change the lifetime of the fluorophore; this effect is referred as "excitation enhancement." For the DP-BSA monolayers that can be excited by a pulsed 405 nm laser, we have been able to investigate the lifetimes making it possible to examine these two effects separately. The fluorescence lifetime images for each sample were collected in the region with an Au colloid-coated triangle area and the surrounding glass surface used as a control. Figure 2.6 shows the results for the sample with 118 nm Au colloid incubated for 24 h. The average lifetime for each pixel is displayed as a map, which shows the homogeneity of the mean lifetime distributions on glass surface and colloid-coated surface, respectively. These average lifetime distributions for the colloid-coated part and control glass surface clearly demonstrate a significant decrease in the lifetime of a colloid-coated surface.

Tables 2.1 and 2.2 demonstrate strong variations of fluorescence enhancement with both interparticle distance and particle size. Both interparticle distance and size play a significant role in the total fluorescence enhancement induced by metal, and fluorescence can be dramatically enhanced when the particles of appropriate size are brought close enough to enable the effective coupling and localization of the electromagnetic field. We have thus shown that Au colloids with appropriate size and optimized interparticle distance can produce promising substrates for fluorescence enhancement with outstanding macroscopic homogeneity.

Table 2.1 Lifetime measurements for each sample and the calculated values of rate (Γ_m/Γ), yield ratios (Q_m/Q), and modified quantum yield Q_m; τ is the average lifetime value of the control sample (2.6 ns).

Sample	τ/τ_m	Γ_m/Γ	$Q_m/Q = E_{em}$	Q_m
162 nm Au—24 h	8.9	39.5	4.55	0.91
118 nm Au—24 h	8.6	38.0	4.42	0.90
80 nm Au—24 h	7.2	31.0	4.40	0.89
162 nm Au—2 h	4.1	15.5	4.00	0.80
118 nm Au—2 h	3.2	11.0	3.75	0.75
80 nm Au—2 h	2.4	7.3	3.35	0.67

Dankwart *et al.* [11]. Reproduced with the permission of John Wiley & Sons.

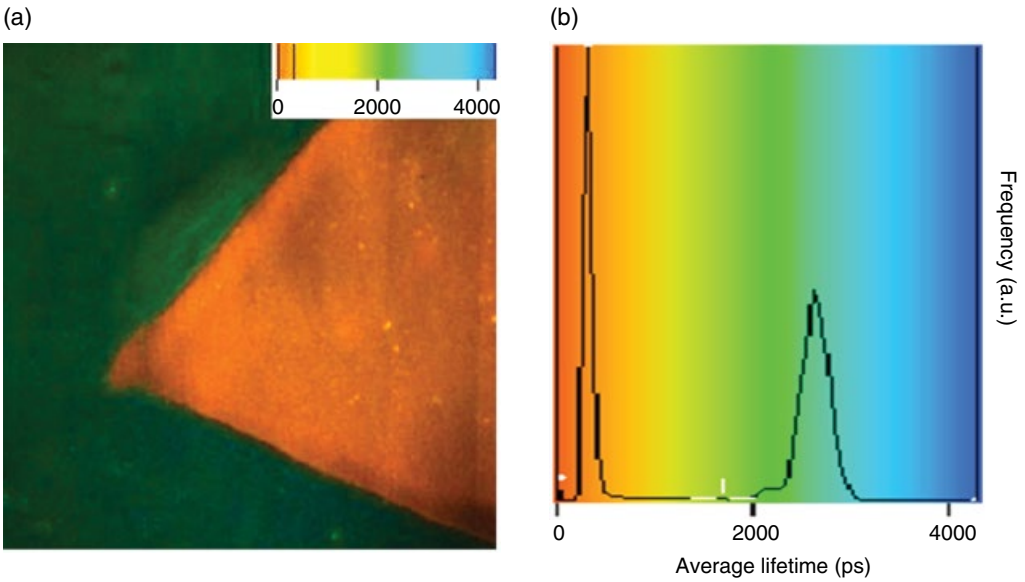

Figure 2.6 (a) A color-coded lifetime image for the sample with 162 nm Au colloid after 24 h deposition (the color-coded fluorescence lifetime scale bar is displayed on top-right corner); the triangle is the colloid-coated monolayer, and the surrounding area is clean glass surface. The entire sample is covered with a fluorescent DP-BSA monolayer. (b) Distribution of the average lifetime obtained in the FLIM data analysis for metallic and glass area of the same sample. Image area is 2.5 mm × 2.5 mm. Xie *et al.* [13]. Reproduced with permission of American Chemical Society.

Table 2.2 Values of excitation enhancement (E_{ex}) and emission enhancement (E_{em}) for each sample.

Sample	Enhancement factor (E_t)	Emission enhancement (E_{em})	Excitation enhancement (E_{ex})
162 nm Au—2 h	7.5	4.00	1.88
118 nm Au—2 h	6.70	3.75	1.78
80 nm Au—2 h	5.70	3.35	1.70
162 nm Au—24 h	15.80	4.55	3.47
118 nm Au—24 h	11.30	4.42	2.56
80 nm Au—24 h	9.40	4.40	2.14

Xie *et al.* [13]. Reproduced with the permission of American Chemical Society.

2.2.3 Commercial Klarite™ Substrate

We also investigated a commercial periodic metal nanostructure (Klarite), originally developed as a uniform SERS substrate [20]. The structure is made of etched silicon with pyramidal pits, coated with a thin gold layer. The geometry of this structure was optimized to provide high Raman enhancement. We investigated this substrate by evaluating radiative rates of fluorophores in complex metal environments where we demonstrated the effect of increased radiative rates in regions of localized surface plasmons. The method for assessing radiative emission rates of the fluorophores was by fluorescence lifetime and cathodoluminescence measurements. By using this approach, we identified and quantified the increased radiative rate of Deep Purple (DP) fluorophore in inverted pyramidal pits of Klarite (Figure 2.7) compared with the radiative rate of the same fluorophore on planar gold. This increased rate is attributed to the effect of localized surface plasmons preferentially concentrated in the pits of these arrays.

This study was carried out by using protein monolayers of bovine serum albumin (BSA) labeled with a fluorophore DP (Amersham) in form of a conjugate (DP-BSA). The BSA increases the distance of fluorophores to the metal surface, which should exceed 5 nm to prevent quenching. The DP-BSA monolayer was formed by covalently binding BSA onto gold surface using functional molecule 11-mercaptoundecanoic acid (MUA) and then conjugating to DP fluorophore [21].

The results of lifetime and cathodoluminescence measurements provided information about the radiative rates in the various regions of the structure. The ratio of the radiative rates is equal to the ratio of quantum yields

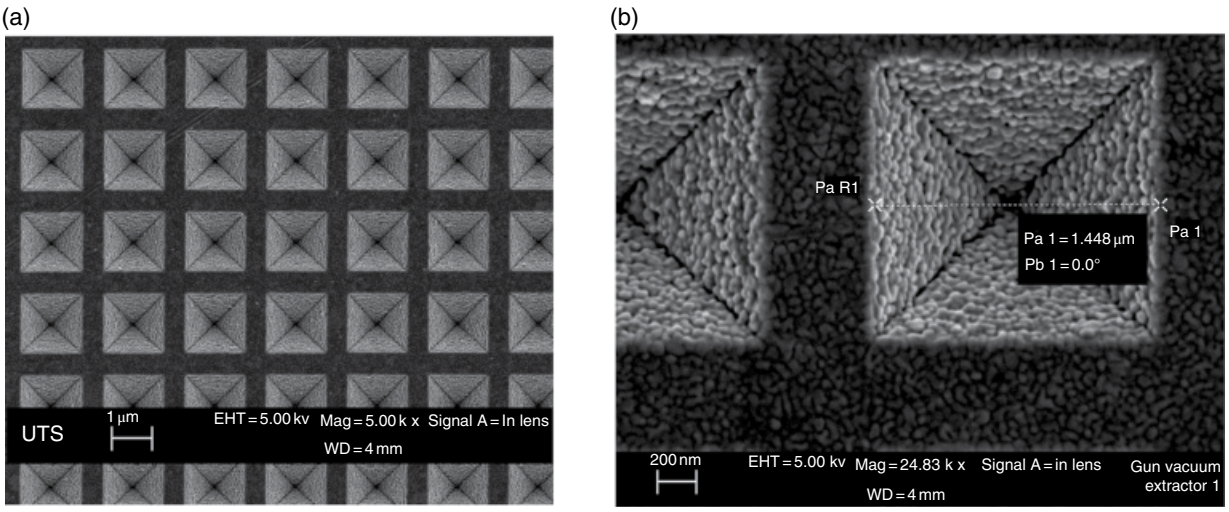

Figure 2.7 SEM images of Klarite substrate with nanostructured arrays under (a) low and (b) high magnification. The nanostructured arrays consist of a square lattice of inverted square pyramidal pits with a pitch of 2 µm. The pyramid faces are oriented at an inclination of 35.3 to the normal. Xie *et al.* [20]. Reproduced with permission of Elsevier.

divided by the ratio of the average lifetime. FLIM images of DP-BSA monolayers deposited on Klarite as well as on the adjacent plain gold surface were examined. Figure 2.8 shows the distributions of the calculated values of average lifetime where we can clearly observe two main peaks at 0.63 ns, originated from the pits and 1.23 ns in the flat unpatterned area and a smaller subsidiary feature. Cathodoluminescence characterization of the Klarite substrate was carried out to quantify the ratio of the fluorophore quantum yields on various surface regions. As shown in Figure 2.9, the ratio of quantum yields on pits and on flat surfaces is about 1.56. We emphasize that geometrical factors alone do not affect the observed intensity variations.

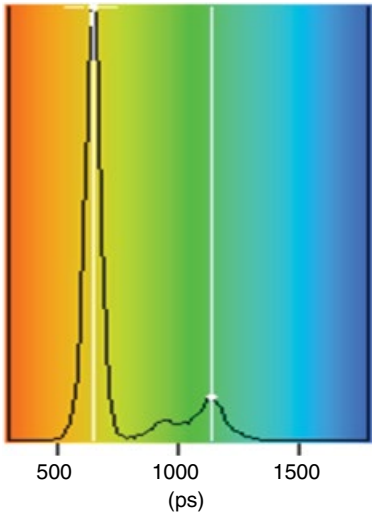

Figure 2.8 Distribution of average lifetimes on Klarite substrate. The sharp minimum at 0.63 ns corresponds to the pits, and the maximum at around 1.23 ns originates from pixel lifetimes in flat areas. For comparison, the average lifetime of a DP monolayer on flat glass is 1.37 ns. Xie *et al*. [20]. Reproduced with permission of Elsevier.

The substitution of the measured values produces the ratio of radiative rates of approximately 3. Spontaneous decay of an excited fluorophore arises from its interaction with the ground state of the quantized electromagnetic field [22]. The rate at which this occurs is affected by the local density of field modes [23]. Thus our observed enhancement of radiative rate in the pits indicates an increase in the local density of states consistent with the Klarite structure showing the surface-enhanced Raman effect. The structure under investigation is designed to produce localized plasmon modes at near IR frequencies [21]. Our observation of only moderate enhancement of radiative rate in the pits is consistent with the imperfect match between the peak emission of DP and the plasmon resonance energy for this structure [24]. Our cathodoluminescence-based method to determine radiative rates makes it possible to fine-tune plasmonic structure design to control the radiative properties of fluorophores.

2.3 Ag Fractal Structures

2.3.1 Reasons for High Enhancement Factors in Nanowire Structures

In addition to the homogeneous substrates described before, we also investigated fluorescence enhancement in an electrodeposited silver structure with a fractal architecture [25]. Although these structures are nonuniform, this study shed light on reasons for their

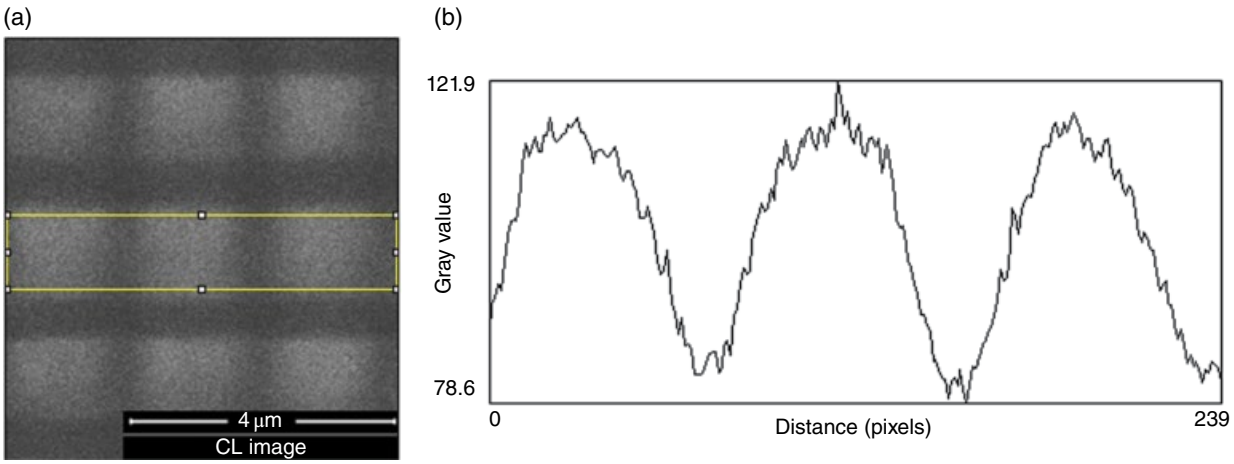

Figure 2.9 (a) Panchromatic cathodoluminescence images of the structure shown in Figure 2.7. (b) Intensity averaged over a width of a single pit as a function of distance. Xie *et al*. [20]. Reproducd with permission of Elsevier.

high (up to a factor of 57) fluorescence amplification factor, which is correlated with structure thickness.

Silver structures were prepared in the following fashion: two pieces of silver foil were placed apart between two cleaned microscope slides held by tape. The gap between two microscope slides was filled with deionized (DI) water (pH 6.4). A direct current of 100 μA was passed between two silver foil electrodes for 20 min, and during that time the voltage typically dropped from 12 V to about 6 V as the structures grew starting from the cathode. Both types produced closely similar results.

The HSA-FITC complex was selected for fluorescent enhancement study because FITC-labeled HSA spontaneously binds to glass and silver and can produce complete coverage. The size of the HSA molecule of 4 nm is close to the optimal distance for fluorescence enhancement of the FITC molecules. Binding of FITC-HSA to the silvered surface, or to the glass surface (in control experiments), was accomplished by incubating the surfaces in a 10 μM FITC-HSA solution overnight at 4°C, followed by rinsing with buffer to remove the unbound materials.

Figure 2.10a shows a representative laser scanning microscopy image of a silver structure coated with a fluorescent monolayer. The confocal *z*-stack measurements were used to estimate the overall thickness of the structure, which was in the order of a few micrometers. The spectral emission characteristics for the fluorophores bound to the silver structure and control samples with the same fluorophores bound to clean glass were identical. A dark area at the top of the fluorescence image was selected to estimate the average signal from glass coated with the same fluorescent monolayer. This average signal was used to calculate the fluorescence enhancement of the whole image. Figure 2.10b shows the corresponding transmission image of the same area of the structure. In this image we observe a varying density of silver with darker areas corresponding to locations where more silver was deposited. The "fractal" character of the silver structures is clearly observed. All the examined silver structures grown showed high and nonuniform fluorescence enhancement, with selected regions where the fluorescence enhancement factor was as high as 57. These highly intense regions tend to occupy only a small fraction of the structure area. The nonuniformity of fluorescence was characterized by digitally coloring the areas with an enhancement larger than 17 (Figure 2.10e) and 33 (Figure 2.10f) by setting the image threshold at the appropriate values. In these images the dark areas with a magnification of 17 and beyond cover about 30% and those with a magnification of 33 and beyond cover only 3% of the structure.

The optical transmission image of the structure (Figure 2.10b) provides information about the three-dimensional (3D) arrangement of the silver structure. This image is characterized by varying gray color with gray values between 0 (black) and 255 (white). The gradation of gray in the observed transmission image reflects the overall thickness of silver. Inspection of Figure 2.10a and b strongly suggests that the fluorescence amplification is higher in regions of lower transmission. To examine this further, we calculated the spatial correlation between these images (Figure 2.10c), which unambiguously shows that high and medium fluorescence intensity and very low/low transmission values are clearly correlated. The saturation shown at the right-hand corner corresponds to those areas of the slide, which were not covered by silver. We thus conclude that more substantial silver deposits promote fluorescence amplification and the effect seems to be gradual.

ESEM was carried out to study the silver structures (Figure 2.11a and b), which shows a loose arrangement of silver nanowires several micrometers in length and with similar radii ~50–100 nm in diameter. Assuming the ESEM image is representative of the entire volume of the structure, the surface area can be estimated to be proportional to the thickness of the deposit and to the area density of the nanowires and inversely proportional to the nanowire radius. The image also clearly shows tips of the nanowires, which can act as antennas and effectively emit radiation when coupled to fluorophores. Although a fraction of fluorophores deposited at such a surface is unable to emit light directly toward the observer, their light may contribute to the overall fluorescence through multiple scattering. Consequently, thicker structures with larger surface areas produce more fluorescence.

The FLIM images of fluorescent monolayers deposited within the silver structures were recorded to study the fluorescence lifetime of two regions: (i) a thin region with dense but visibly discontinuous branches and (ii) a thick region, which under the optical microscope appeared to contain a dense silver layer. As a control we used a region outside of the structure where no apparent silver could be observed. The fluorescence decay curves collected in each pixel could be satisfactorily fitted using a model with two decay times t_1 and t_2, from which an average value is calculated using the weighting a_1 and a_2 for each of the decay components. Figure 2.12 shows the distributions of calculated values of the average lifetime (t_m). These results clearly indicate that the fluorescence lifetime for the fluorophores deposited over the silver is significantly reduced, from about 1.6 ns to less

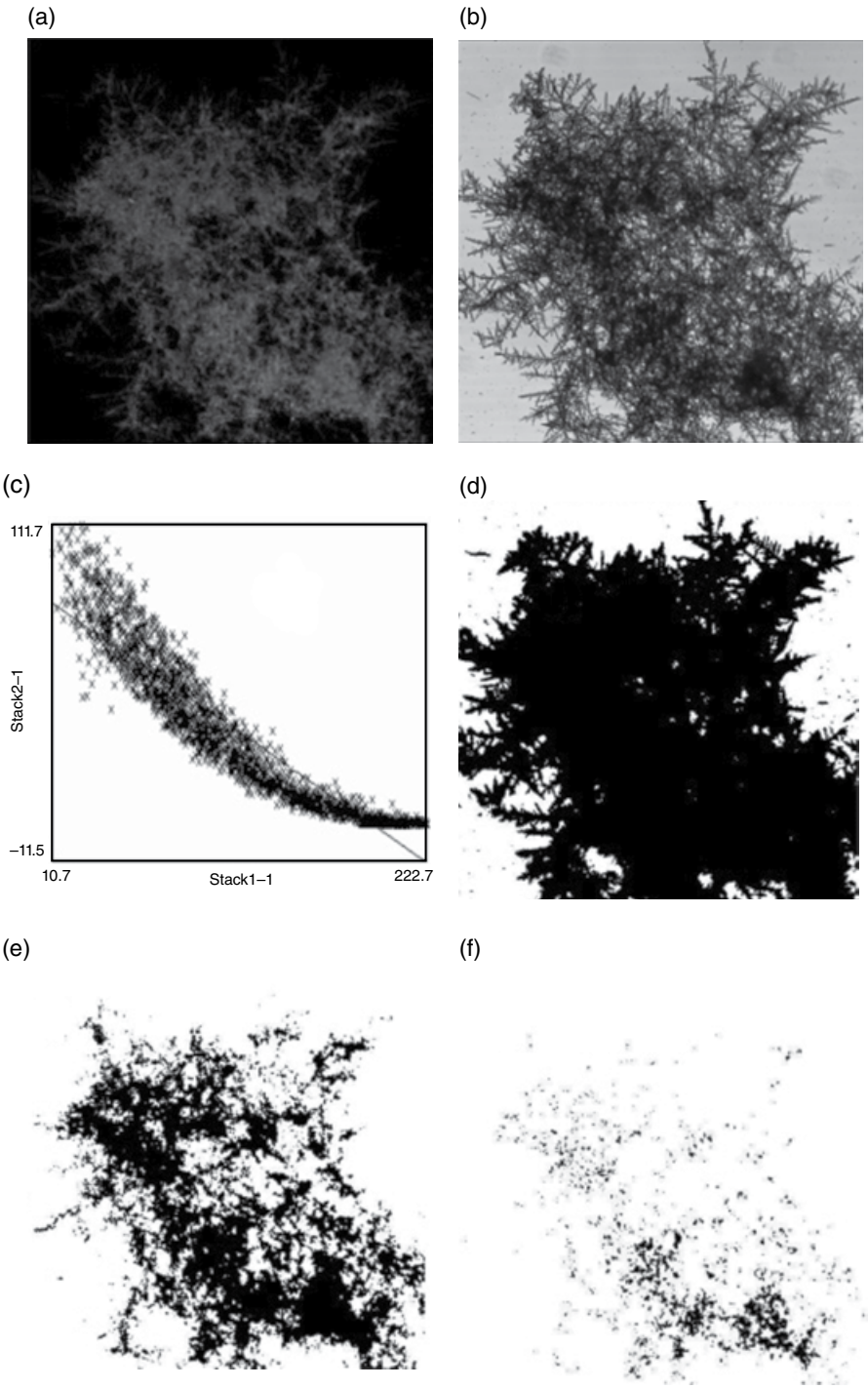

Figure 2.10 (a) Laser scanning microscopy image of a fluorescent protein monolayer on an electrodeposited silver structure, (b) transmission image of the same region of the structure, and (c) pixel-to-pixel correlation of gray values between the two images. The transmission intensity is displayed on the *x*-axis with the black color corresponding to low readings (near 0) and the white areas of uncovered glass corresponding to high *x* values, near 255. The fluorescence intensity (*y*-axis) is displayed in a similar fashion with black near 0 and highly fluorescent regions at high *y* values. Linearity improves in the upper left corner where fluorescence is high and transmission low. Saturation is observed on bare glass, not covered with fractals. (d) Regions of the same structure with fluorescence amplification >1. (e) Regions where fluorescence amplification is >17. (f) Regions with fluorescence amplification >33. The image size in (a–f) is 170 µm by 170 µm. Goldys *et al*. [25]. Reproduced with the permission of American Chemical Society.

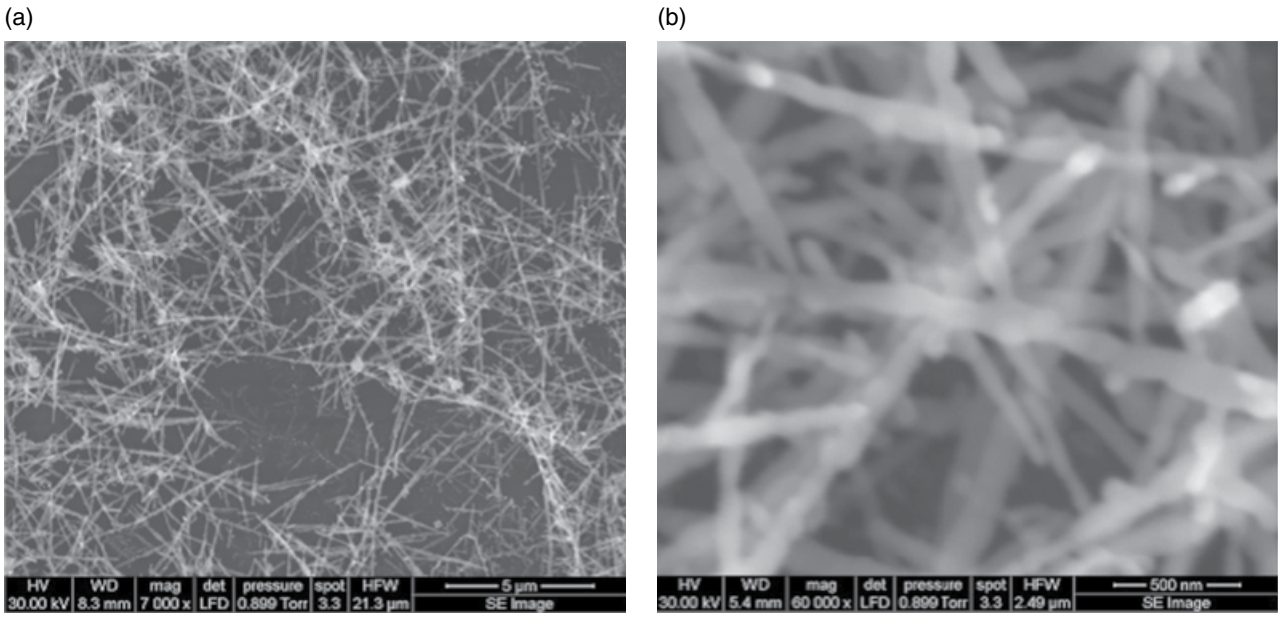

Figure 2.11 ESEM images of the silver structures: (a) magnification ×7000, bar represents 5 µm and (b) magnification ×60 000, bar represents 500 nm. Goldys *et al*. [25]. Reproduced with the permission of American Chemical Society.

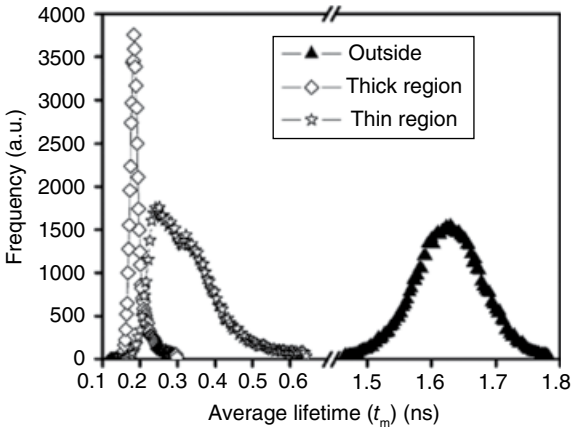

Figure 2.12 Distributions of the average lifetime obtained in the FLIM data analysis for thick fractal (diamonds), thin fractal (stars), and control sample with no silver coverage (triangles). Goldys *et al*. [25]. Reproduced with the permission of American Chemical Society.

than 0.194 ns in thin areas and about 0.155 ns in thick areas. With the FLIM system response in the order of 30 ps, the observed values are well within the range of our experimental capabilities and accuracy. Such a strong decrease of the fluorescence lifetime is consistent with the effect of fluorescence amplification in the proximity of metal.

The presented results suggest that the effects of a decreased lifetime and fluorescence amplification in the presence of metal occur gradually and become stronger as the amount of metal in close proximity to the fluorophore increases. It suggests that the high level of fluorescence amplification from the structures can be attributed to several effects. First, the open architecture of the structure in the ESEM image greatly increased the total surface area owing to the random stacking of nanowires. The second factor that contributes to fluorescence enhancement is the electric dipole moment for electron resonance oscillations along such wires that is greatly enhanced compared to more spherical nanoparticles, and any coupling of the optical transitions in the fluorophore molecules to these vibrations may result in antenna effects where the coupled radiation is effectively reemitted to free space. Third, the well-established effect of metal enhancement continues to take place as evidenced by the greatly reduced fluorescence lifetime. Other effects such as partially relieved self-quenching and possibly increased excitation rate due to an enhanced electric field also make a contribution. With all these cooperating effects, the fluorescence amplification can reach high values.

2.3.2 Ag Dendritic Structure—Homogeneous Silver Fractal

Au/Ag or their core–shell nanoparticles produce homogeneous substrates; however, the fluorescence enhancement factor is relatively low (about 10 times) [11, 12]. Silver fractal structures exhibit very high

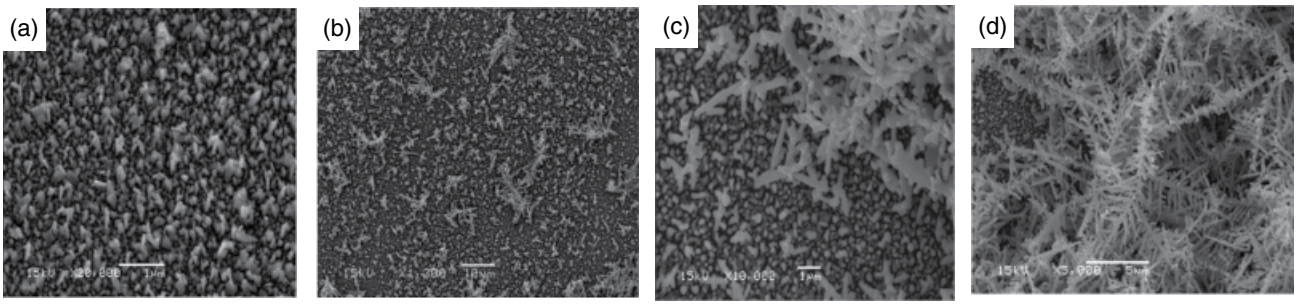

Figure 2.13 SEM images of the silicon wafer with silver dendrites grown at 50°C by self-assembled electroless deposition at various times and different magnifications: (a) 20 s, (b) 30 s, (c) 1 min, (d) 2 min. Drozdowicz *et al*. [26]. Reproduced with the permission of American Chemical Society.

fluorescence enhancement (about 57 times) [25], but their nonuniformity limits practical applications. Therefore, we investigated an alternative method to produce uniform silver dendritic nanostructures for enhanced fluorescence by electroless deposition approach [26]. We have been able to show that these metal-modified surfaces have high enhancement factors between 30 and 40 times, observed by binding a protein BSA labeled with the fluorescent dye DP. Such silicon-based structures with high fluorescence enhancement factors are suitable for integration with lab-on-chip and biosensing microelectronic devices.

Silver nanostructures were produced on silicon wafers using self-assembled electroless deposition by galvanic exchange. Briefly, cleaned p-type silicon wafer fragments (1 × 2 cm) were etched in a diluted solution of 0.5% HF at room temperature for 10 min. The samples were rinsed in DI water and then in methanol and blow dried with compressed nitrogen. Following that, half of the area was masked with a chemical/temperature resistant 3M adhesive type and etched in a 5.0 mol/L HF solution containing 0.02 mol/L silver nitrate at 40°C for 20 s, 30 s, 1 min, and 2 min, respectively. After the etching process, the tape was removed, and silicon fragments were rinsed with DI water and methanol alcohol and blown dry with nitrogen.

The formation of silver deposits via an electroless deposition is based on a self-assembled localized microscopic electrochemical cell model. In this model, initially, both silicon etching and silver deposition occur simultaneously at the Si surface where Si–Si bonds in the crystal lattice act as a reducing agent for the Ag^+ ions in solution. The Ag^+ ions in the vicinity of the silicon surface capture electrons from the valence band in silicon and form a deposit of silver nuclei that are uniformly distributed on the surface of the silicon wafer. With further deposition, SiO_2 begins to be formed under these silver nanoclusters, and it is subsequently etched away by HF. The silver nanoclusters and the surrounding Si areas act, respectively, as local cathodes and anodes, leading to electroless dendritic growth of silver deposits. Figure 2.13 shows the evolution of surface morphology. Initially, silver nanoclusters deposited for only 20 s show a variety of different shapes including oblate, prolate, and also some triangular prisms with relatively uniform size in the range 50–100 nm (Figure 2.13a). With increasing reaction time, some elongated nanoparticles start to form and evolve toward small ramified clusters (Figure 2.13b). As the deposition process continues (Figure 2.13c), tree-like 3D silver structures are formed with clearly defined branches that continue to grow further away from the surface and finally detach from it almost completely. At later stages of deposition (Figure 2.13d), the initial, isolated nuclei are no longer observed and the structures form a dense 3D deposit.

Binding of the DP-BSA monolayer to the surface was carried out by adding 50 µL of 10 µg/mL BSA solution to the silver structures/silicon surfaces, which were derivatized with poly-L-lysine to ensure effective binding of BSA, and incubating overnight at 4°C, followed by rinsing in 0.01 M PBS buffer to remove the unbound BSA molecules. DP fluorophore was then conjugated to BSA monolayers by adding 50 µL of 1:200 DP-buffered solution at pH 7 to the surfaces and incubation of the modified substrate for 1 h at room temperature. Unconjugated DP was removed by rinsing the substrate with a solution of 15% methanol and 7.5% acetic acid. The DP-BSA fluorescent monolayer makes it possible to quantitatively compare the fluorescence intensity of fluorophore-protein conjugates with and without various silver fractal nanostructures on silicon after background signal subtraction and correction for differences in surface coverage.

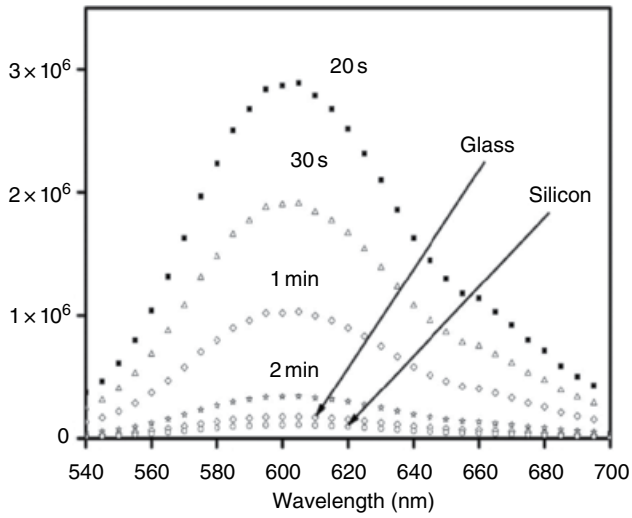

Figure 2.14 Fluorescence emission spectra of the DP-BSA conjugate monolayer on dendritic silver nanostructures on silicon substrates at various times of electroless deposition and on a glass slide and silicon used as a reference. Excitation wavelength: 520 nm. Drozdowicz *et al*. [26]. Reproduced with the permission of American Chemical Society.

Fluorescence measurements of DP-BSA monolayers bound to the silver fractals deposited on silicon have been carried out to establish fluorescence enhancement. As the albumin proteins generate a complete monolayer about 4 nm thick and poly-L-lysine forms a monolayer of about 7 nm thickness, the combined spacing of about 10 nm provides the optimum condition for metal plasmon-mediated fluorescence enhancement by minimizing nonradiative decay channels, which otherwise can lead to fluorescence quenching at small distances < 4nm. It also provides separation from the silicon substrate, which significantly reduces fluorescence quenching observed at small distances due to efficient energy transfer to the semiconductor. The DP dye was chosen, as it becomes fluorescent only when bound to proteins, and, as such, does not contribute to fluorescence when unconjugated.

The results are presented in Figure 2.14. The graphs show a well-established fluorescence spectrum of DP fluorophores bound to proteins. The control DP-BSA monolayers deposited on silicon without the fractal layer showed slightly quenched fluorescence (~80% of the integrated emission intensity) as compared with the same monolayer deposited on a glass substrate. From the spectra, it shows that, at 20 s growth time, the observed intensity was 26.3 times higher than that for the DP-BSA monolayer deposited on silicon; subsequently, it decreased to 17.4, 9.4, and 3.1 at 30 s, 1 min, and 2 min growth time, respectively, which were averaged over relatively large areas of 1 mm × 2 mm. The enhancement factors at various growth times were also derived from the fluorescence intensity images produced during the FLIM data acquisition at 405 nm excitation with fluorescence detection in the 500–700 nm range. Their values also listed in Table 2.1 were 38.5, 27.2, 11.1, and 4.2 for samples with silver fractals grown for 20 s, 30 s, 1 min, and 2 min, respectively, slightly higher than obtained earlier, which were measured by averaging from much smaller areas of about 0.25 mm^2 in size. The fluorescence intensity image of one such area excited at 405 nm and the respective fluorescence intensity profile for the sample with silver deposition for 20 s are shown in Figure 2.15a, which shows good uniformity of fluorescence enhancement.

Fluorescence lifetime measurements provide insights into fluorescence decay rates, thus we could further investigate the both effect of excitation enhancement and emission enhancement. The results of average lifetime distributions for samples grown at various times are presented in Figure 2.16; these data were taken on samples covered in half by the silver fractal, with the other half presenting an unmodified silicon surface, both coated with a DP-BSA monolayer. The lifetimes shown in Table 2.3 are all shorter than the DP lifetime in the control sample. Also, we observe that both the fluorescence enhancement factor and lifetime follow exactly opposite trends with the shortest lifetime (for 20 s growth) correlating with the highest enhancement factor, which indicates that the effect of metal-nanostructure-mediated fluorescence enhancement takes place in the present nanostructures.

The experimentally measured fluorescence lifetime ratios for DP-BSA fluorophore on silver fractal and unmodified silicon surfaces for various silver fractal growth times as well as the calculated parameters such as the radiative rates, quantum yield ratios, emission enhancements, and quantum yield Q_m modified by the metallic surface are listed in Table 2.3. The highest fluorescence enhancement was observed in samples with silver fractal grown for 20 s where an

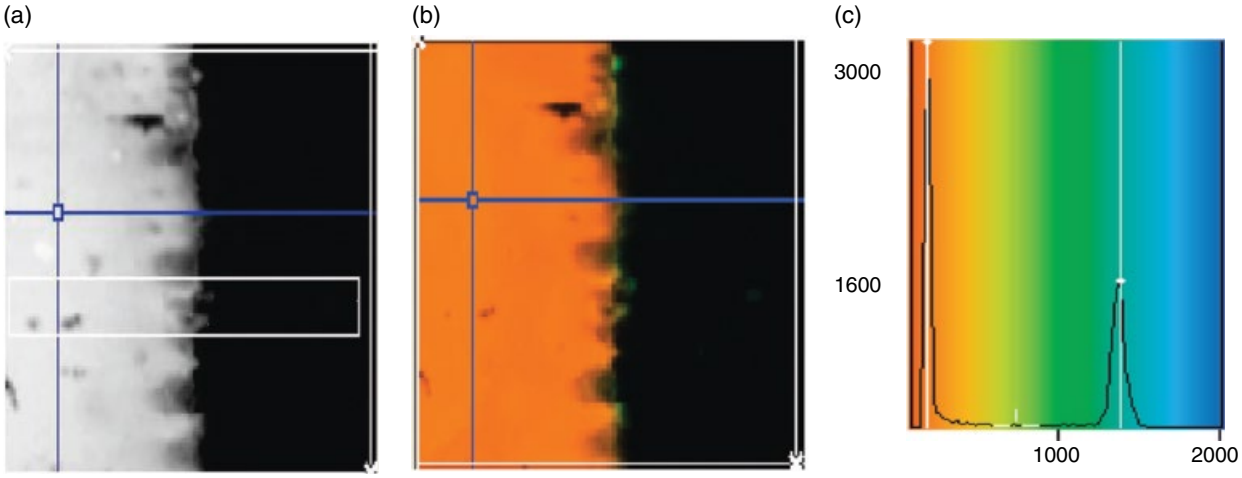

Figure 2.15 Fluorescence intensity image and color-coded FLIM image from the DP-BSA monolayer on the silicon sample with silver fractal deposited for 20 s. The silver fractal area is bright, and the dark region is the clean silicon surface. The images were collected using a 10× magnification objective and 405 nm laser diode excitation. The size of the analyzed region is about 1500 µm × 1500 µm. (a) Intensity image. The selected region (white rectangle) was used for the fluorescence intensity profile shown in Figure 2.6a. (b) FLIM image. (c) Lifetime distribution graph for image b. Drozdowicz *et al*. [26]. Reproduced with the permission of American Chemical Society.

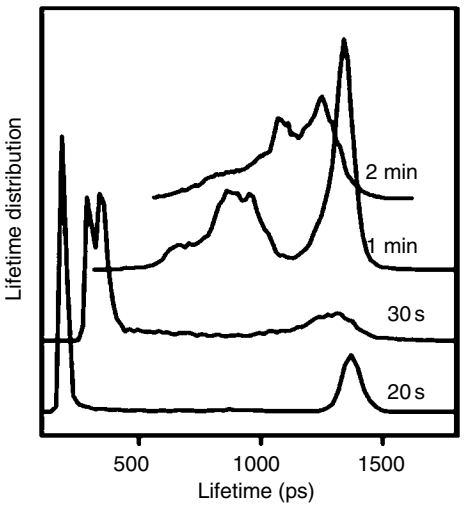

Figure 2.16 Distribution of the average lifetime obtained in the FLIM data analysis for silver fractal and silicon areas of the samples with fractal grown for 20 s, 30 s, 1 min, and 2 min. The image areas used were 2 mm × 2 mm, and the plots are vertically shifted for clarity. Drozdowicz *et al*. [26]. Reproduced with the permission of American Chemical Society.

average enhancement factor of 38.5 was measured. This phenomenon of decreasing enhancement with longer deposition could be explained as follows: The LSPR of the 20 s deposit is expected to overlap strongly with the fluorescence emission of DP (peak at 600 nm), thus very high emission enhancement of the fluorescence. The silver nanoparticles forming silver fractal at longer growth times produce elongated branches, and it is expected that the plasmon resonance of longer deposits will be red shifted, making the overlap less significant, causing the fluorescence to decrease. The calculations indicate that the major contribution to the intensity enhancement comes from the emission enhancement, which is almost twice as high as the excitation enhancement, and its effect becomes less pronounced as the fractal growth progresses.

In summary, Ag dendritic structure produced by electroless deposition shows the fluorescence enhancement factor of the order of 40. The main advantage of such structures shows very good macroscopic uniformity. It also demonstrates that strong fluorescence enhancement of fluorophores in close proximity to silver nanostructures deposited directly on silicon is achievable. Several technologies such as DNA microarrays, lab-on-chip, or ELISA in proteomics use can potentially use a silicon substrate as a solid surface for deposition of probes (reporters). The proposed method can be easily integrated with silicon sensor device processing, and, as such, it is promising for various improved biological and medical-sensing applications.

2.4 MIFE with Membranes for Protein Dot Blots

Following our successful demonstrations of fluorescence enhancement on flat surface such as glass and silicon surfaces (two-dimensional (2D) surfaces), we

Table 2.3 Lifetime measurements for each sample and the calculated values of lifetime (τ/τ_m), radiative rate (Γ_m/Γ), and quantum yield ratios on silver fractal versus unprocessed silicon surfaces (Q_m/Q) as well as modified quantum yield Q_m; τ is the average lifetime value of the control silicon sample (1.37 ± 0.02 ns).

Sample	τ_m (ps)	τ/τ_m	Γ_m/Γ	$E_{em} = Q_m/Q$	Q_m
20 s	182 ± 30	7.5 ± 0.4	61.94 ± 8.0	8.36 ± 1.0	0.88 ± 0.06
30 s	305 ± 30	4.5 ± 0.4	33.13 ± 5.0	7.60 ± 1.0	0.80 ± 0.06
1 min	855 ± 50	1.6 ± 0.3	5.70 ± 0.8	4.19 ± 0.5	0.44 ± 0.04
2 min	1054 ± 80	1.3 ± 0.4	2.84 ± 0.3	2.96 ± 0.5	0.31 ± 0.02

Drozdowicz *et al.* [26]. Reproduced with the permission of American Chemical Society.

further investigated the feasibility of applying such methodology to 3D structures such as membranes [27], as detection and identification of low abundance biomarker proteins is frequently based on various types of membrane-based devices. Lowering of the protein detection limits is vital in commercial applications such as lateral flow assays and in western blots widely used in proteomics, which currently suffer from insufficient detection sensitivity and low retention for small 2–5 kDa proteins.

In our study reported in Ref. [27], two types of metal nanoparticles (gold colloids and silver fractals) were deposited onto a range of commonly used types of membranes including polyvinylidene fluoride (PVDF). Due to strong affinity of proteins to noble metals, such modified membranes have the potential to effectively capture trace proteins preventing their loss. The membrane performance in protein dot blots was evaluated using the protein–fluorophore conjugates. The metal nanoparticles increase light extinction by metals, which is balanced by increased fluorescence, so that the effective fluorescence signal is unchanged. This feature combined with the capture of proteins by the nanoparticles embedded in the membrane increases the detection limit of membrane assays.

For Au colloid-modified PVDF membrane, three colloids with average particle size of 50, 70, and 95 nm were used. The colloid density used in the membrane modification experiments was established from the amount of reagents used and was in the order of 10^{10} particles/mL. The samples were immersed in 1.5 mL Au nanoparticle solutions for varying periods of time (0.5 h, 1 h, 2 h, 4 h, 6 h, and overnight). After immersion for long enough to achieve color saturation, one set of sample was again immersed in a fresh solution until saturation. The amount of nanoparticles deposited in the membranes for each incubation condition were estimated and listed in Table 2.4. As seen in Figure 2.17, some membrane regions are densely covered with particles, while other regions are not coated. A simple calculation, using the total membrane area and density of particles, makes it possible to estimate the average distance between 95 nm particles in PVDF membrane incubated to saturation to be of the order of 4000 nm and much larger to that observed in Figure 2.17b. Due to relatively large surface area in these membranes, it is difficult to coat them with gold particles at very high densities throughout the entire thickness of the membrane.

Table 2.4 Area density of nanoparticles in the modified membranes.

Gold colloid size (nm)	Density after overnight incubation (mm^2)	Density after incubation to saturation in 2 × 1.5 mL (mm^2)
50	5.3×10^6	1.1×10^7
70	1.9×10^6	3.9×10^6
95	7.7×10^5	1.5×10^6

Xie *et al.* [27]. Reproduced with the permission of Springer.

The procedure to deposit silver fractal on membranes was adopted from References [28–30]. Briefly, a sandwich structure was assembled, where a piece of membrane soaked in aqueous 0.50 M silver nitrate was inserted between two clean glass slides. Two silver electrodes were inserted between the glass slides and positioned on the membrane. The deposition time was 20 min with the applied voltage of about 10 V. After silver deposition the membranes were rinsed in DI water and dried in the dark. As shown in Figure 2.18, silver fractals deposited on all membranes formed tree-like structures. Close inspection of their branches indicates that their thickness is almost constant over the entire aggregate, and each small "needle" in the "tree-like" branch is composed from small particles of similar size that have undergone agglomeration. The growth of the dendrites is understood to occur as described by the diffusion-limited aggregation model [31]. Each silver fractal on membranes appears to be composed from aggregates of very small

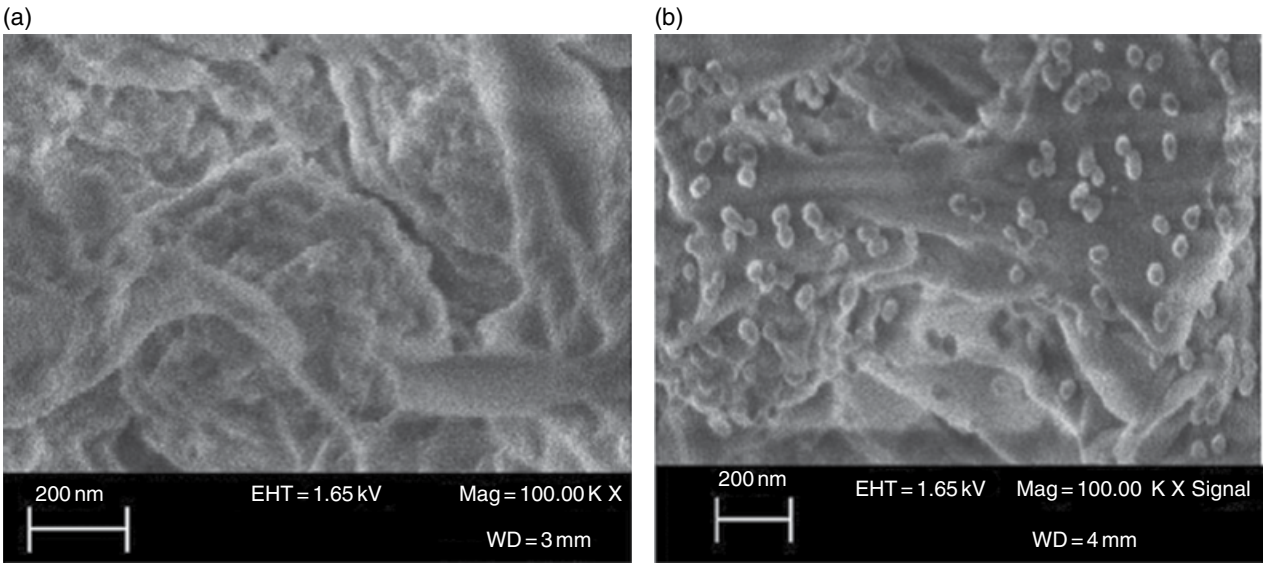

Figure 2.17 SEM images of the PVDF membrane incubated overnight in 50 nm Au colloid: (a) membrane before incubation and (b) membrane with gold nanoparticles. Xie *et al*. [27]. Reproduced with the permission of Springer.

individual seed particles of about 20–30 nm diameter. The membrane 2043A, characterized by the lowest value of the Klemm parameter, is expected to suppress the diffusion of silver most strongly. The preferred growth mode of silver fractals on this membrane was achieved by addition of new silver deposits to the existing sites, rather than by forming the new ones. The fractal structure on this membrane is flat (2D), strongly attached to the surface, with a well-pronounced "tree-like" structure and long, dense "needles" regularly branching out. The fractals grown on the remaining membranes, where diffusion is not so limited, also have "needle-like" structures oriented to the stems but with shorter, more 3D, and less uniform and denser branches. In these fractals, a typical thickness of the individual silver needles is about 80–100 nm.

The BSA sample of 25 ng/10 μL concentration was used to dot blot on PVDF membrane incubated with gold nanoparticles. These membranes were prewetted by loading 20 μL of methanol prior to loading with the 10 μL protein aliquot. The membranes fully dried in air were then ready for DP staining. For the membranes with silver fractal deposition, a different dot blotting protocol was used. Instead of depositing BSA and then staining using DP dye, dots of various concentrations of FITC-HSA conjugate were formed on the membranes and analyzed using the Typhoon scanner. The results of dot blot for membranes incubated with the three types of nanoparticles are presented in Figure 2.19. The fluorescence intensity was linear with BSA concentration, with no noticeable offset indicating a very small intrinsic fluorescence of the membrane, and a very desirable characteristic for applications involving fluorescence. A quantitative analysis of the dot blots was carried out (Figure 2.20) by measuring the average fluorescence signal from the dot blot after background subtraction. The results show a diminishing contrast between the dot blot and the membrane with increasing Au colloid. This varying ratio indicates that, instead of enhancement, fluorescence intensity was reduced when the PVDF membranes were modified with Au colloid. This effect persisted for each size of Au colloids. Moreover, the effective signal from the blot also decreased with increasing incubation time, but their ratio remained comparable to the same quantity in unmodified membranes. The additional lifetime measurements showed that there was negligible lifetime reduction of DP on the modified PVDF, suggesting the absence of emission enhancement, one of the components of total fluorescence enhancement [32]. The absence of fluorescence enhancement could be explained by the following reasons. Firstly, the distribution pattern of the BSA protein molecules may be unfavorable for easy observation of fluorescence enhancement. A large percentage of BSA may stay inside the membrane, instead of on the surface of membrane. Second, Au colloid may physically block the excitation laser to reach the fluorophore inside the membranes. Third, the laser light may reach the cross section of the membrane; however, Au colloid may physically block the emission light from DP molecules inside the membranes.

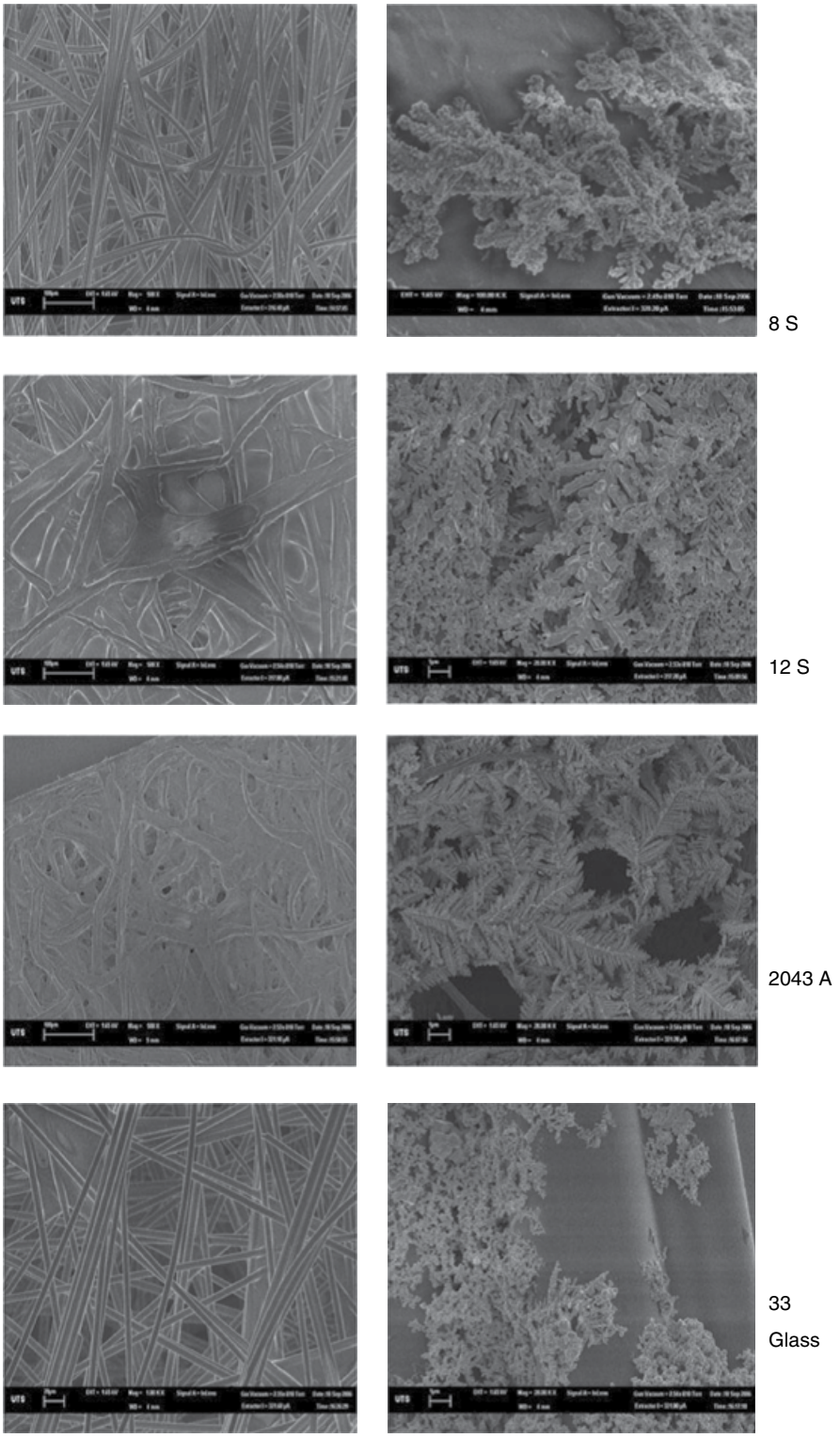

Figure 2.18 SEM images of silver fractal structures deposited on various membranes as listed in the image (20 min deposition time). The images on the left show the morphology of the uncoated membrane, and those on the right show the membranes after deposition of silver fractal structures. Xie *et al.* [27]. Reproduced with the permission of Springer.

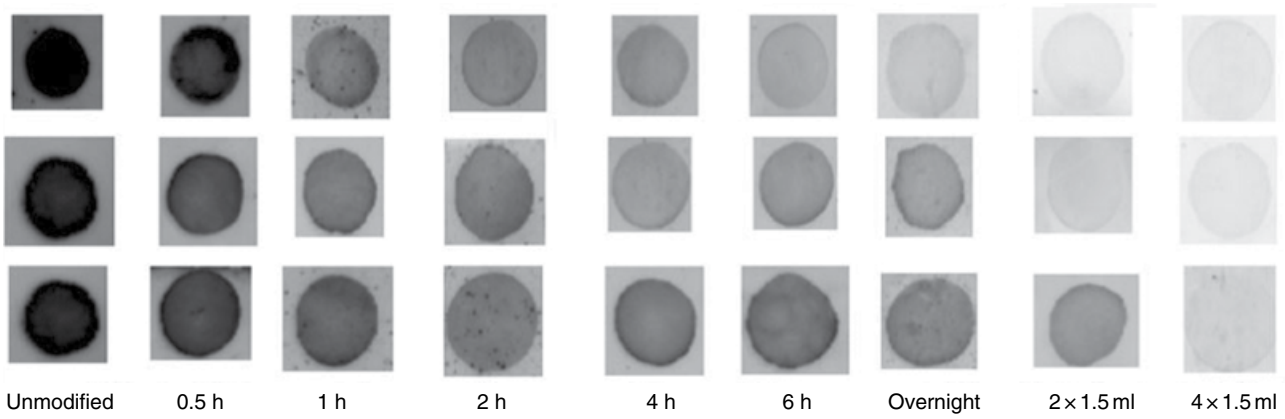

Figure 2.19 A series of dot blots on PVDF membranes modified with Au nanoparticles with varying incubation times. Top row 50 nm, middle row 75 nm, and bottom row 95 nm. The incubation times vary from left to right: unmodified control sample, 0.5 h, 1 h, 2 h, 4 h, 6 h, overnight, 2 × 1.5 mL to saturation, 4 × 1.5 mL to saturation. In each case, 25 ng per 10 µL of BSA was deposited and stained with DP. Xie *et al*. [27]. Reproduced with the permission of Springer.

Figure 2.20 Fluorescence intensity of membrane samples with varying incubation times in gold colloids and spotted with BSA–DP. Black squares indicate total fluorescence intensity in protein spot, gray squares refer to background intensity which is fluorescence intensity outside the protein spot, gray triangles represent absolute intensity (a difference of total and background intensity). Xie *et al*. [27]. Reproduced with the permission of Springer.

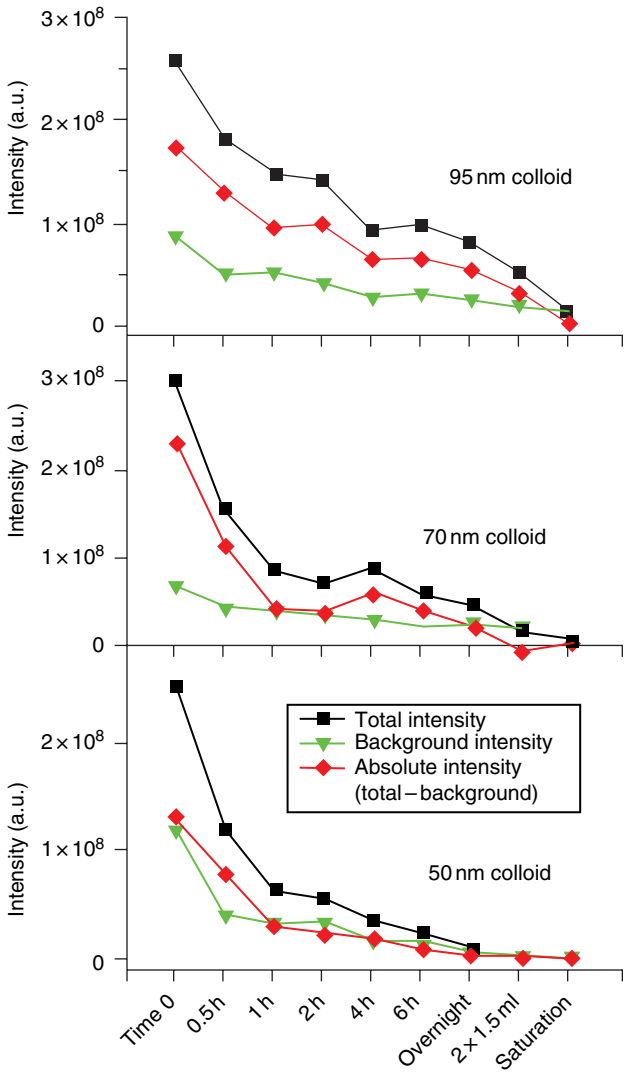

The dot blot results on silver fractal structures are similar to those on Au colloid-modified membranes. All the modified membranes had lower fluorescence intensity in areas without dot blots; this is a desirable feature for sensitive fluorescence detection. Also all dot blots on modified membranes had lower fluorescence intensity than on unmodified membranes. The fluorescence intensity difference between the blot region and away from it was smaller on modified membrane, but their ratio was largely comparable to the same quantity in unmodified membranes.

In summary, PVDF membranes can be modified by simple incubation with a gold colloid solution to a surface density in the order of 10^7 per mm^2. A method was developed to deposit silver fractal structures on membrane support. Further we established the effect of these modifications on the fluorescence detection on such membranes. All the examined membranes showed a reduced background fluorescence, which originated mostly from their upper layer, approximately few tens of micrometers. Dot blot results showed that the fluorescent intensity of the blots is reduced, as is their effective fluorescent signal; however, the ratio of the blot signal to the background signal after modification remains comparable to the unmodified membranes. Given that metal nanoparticles embedded in the membrane show other highly desirable properties, such as the ability to capture low-molecular-weight proteins, this modification can facilitate more sensitive fluorescence-based bioassays and other biochemical procedures.

2.5 MIFE with Flow Cytometry Beads and Single Particle Imaging

Our work describes the preparation of silver nanostructure-coated silica microspheres and their characterization and applications in the flow cytometry bead immunoassay and cell imaging [18, 33]. In our method, a seed Au colloid was first covalently bound to APTMS-modified silica beads (400 nm and 5 μm diameter), followed by silver nanostructure overcoating. To test the ability of such nanostructured surfaces to enhance fluorescence signal, we used a model immunoassay, rabbit immunoglobulin G (IgG)–IgG rabbit antibody, labeled with Alexa Fluor 430. Subsequently, we demonstrated the flow cytometry readout of this immunoassay and have shown that it was enhanced, by examining the fluorescence intensity histograms of beads with and without Ag nanostructures. Furthermore, we demonstrated that such silver nanostructures can also be used to improve brightness in a bioimaging experiment with BHHCT-Eu^{3+}-labeled environmental microorganisms, *Giardia* cysts. These 6 μm wide, 9 μm long, and ~0.5 μm thick pathogens were imaged by using 365 nm wavelength UV LED excitation in a time-gated fluorescence microscope.

The Au colloid was firstly synthesized by boiling gold solution containing 0.25 mM $HAuCl_4$ and 0.25 mM trisodium citrate in the presence of 0.01 M $NaBH_4$ solution under constant stirring. Silica–Au assemblies were then prepared using APTMS in the process, which allows gold particles binding to silica surface. For the deposition of silver nanostructures on silica beads, we used here the silver enhancer solutions to cause growth of silver nanostructures on the gold "seeds." In a typical immunoassay, rabbit IgG was firstly bound to the surface of a glass slide pre-coated with silver nanostructure-coated silica beads. The glass slide was then incubated for 2 h with anti-rabbit IgG–Alexa Fluor 430 conjugate, followed by a rinse before measurement. The reference experiment was also carried out under the same experimental conditions, apart from pure silica beads being used instead of silver nanostructure-coated ones. For the cell imaging, the *Giardia lamblia* solution was mixed with mouse anti-*Giardia* antibody, biotinylated goat anti-mouse IgG antibody and streptavidin (SA)-labeled europium chelate (BHHCT-Eu^{3+}). After incubation for 24 h at room temperature, the cysts were washed with distilled water several times to remove the unreacted conjugates. At the same time, the glass slides were filled with solutions of pure and Ag nanostructure-coated silica beads. After silica bead solution dried in air, the *Giardia* cysts were added to the slide for fluorescence microscopy imaging.

Figure 2.21 shows a typical SEM image of beads coated with silver nanostructures. We found that 400 nm silica beads with 3 min silver nanostructure coating had a high and even coverage. In order to assess the effect of silver nanostructures on fluorescence amplification, we carried out a model immunoassay with a fluorescently labeled antibody. The results in Figure 2.22 show that such structures clearly enhanced fluorescence of Alexa Fluor 430, with ~8.5-fold increase in fluorescence intensity, compared to that of the sample without Ag nanostructure coating. In the case of large 5 μm silver-coated silica beads, about 10-fold increase in fluorescence intensity was observed in the sample with silver coating.

For a more complete characterization of the effect of metal nanostructures on the fluorescence, we carried out the measurements of fluorescence lifetimes. As discussed in the literature, metal-enhanced fluorescence is accompanied by an increase in the quantum yield and a decrease in the lifetime of a fluorophore

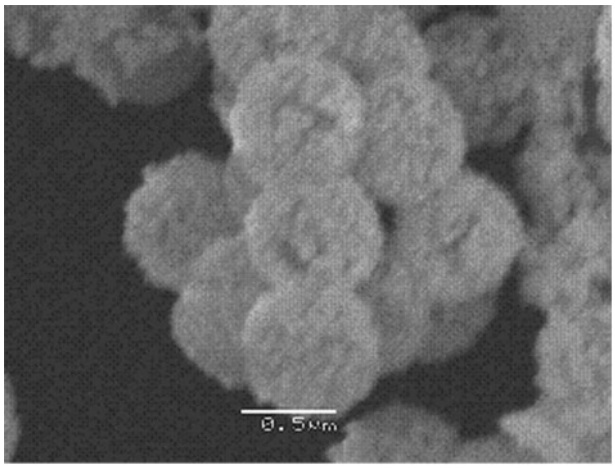

Figure 2.21 A typical SEM image of silica beads with Ag nanostructures. Deng *et al*. [18]. Reproduced with the permission of American Chemical Society.

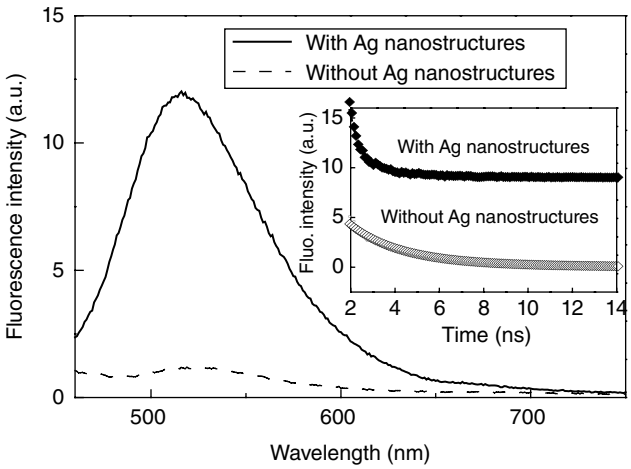

Figure 2.22 Fluorescence intensities from the pure silica beads (dashed line) and silver nanostructure-coated silica beads (solid line). Inset shows the corresponding fluorescence lifetime decay curves of Alexa Fluor 430. Deng *et al*. [18]. Reproduced with the permission of American Chemical Society.

located in the proximity of the metallic nanoparticles. In order to confirm the enhancement mechanism, we measured the lifetime of Alexa Fluor 430 on the 400 nm silica surface with and without silver nanostructures. The decay curves shown in the inset of Figure 2.22 demonstrate a reduction of fluorescence lifetime due to the silver nanostructures. These decay curves were fitted by a double exponential function with two characteristic lifetime components. In the sample without silver enhancement, the Alexa Fluor 430 had an average lifetime of about 2.50 ns. With Ag enhancement, the average lifetime of Alexa Fluor 430, 0.70 ns, was obtained. Such reduced lifetime has two major implications: higher photostability and higher relative quantum yield (number of emitted photons per unit time under the same excitation conditions). Both properties make it possible to use shorter exposure time or obtain higher signal to noise for comparable exposure times, thus increasing sensitivity and detectivity in any fluorescence measurements, including flow cytometry and cell imaging.

We further carried out a flow cytometry experiment on our bead immunoassay with and without Ag nanostructures. The flow cytometry results show ~3 and ~3.7-fold fluorescence enhancement (Figure 2.23) for silver nanostructure-coated 400 nm silica beads and 5 μm silica beads, respectively. These values were lower than previously observed for the same beads deposited on glass slides (8.5 and 10.1). We propose the following explanation for this difference. The excitation wavelengths in the spectroscopy and flow cytometry experiments were slightly different, 430 nm for spectroscopy measurements and 488 nm in flow cytometry measurements. In addition, the absorption spectra of Ag nanostructure-coated silica beads measured on dried slides showed the plasmon resonance band maximum in 375–380 nm range. This wavelength range is expected to enhance the excitation/emission of our model fluorophore Alexa Fluor 430 more strongly at 430 nm excitation wavelength than at the 488 nm excitation wavelength used in flow cytometry experiments.

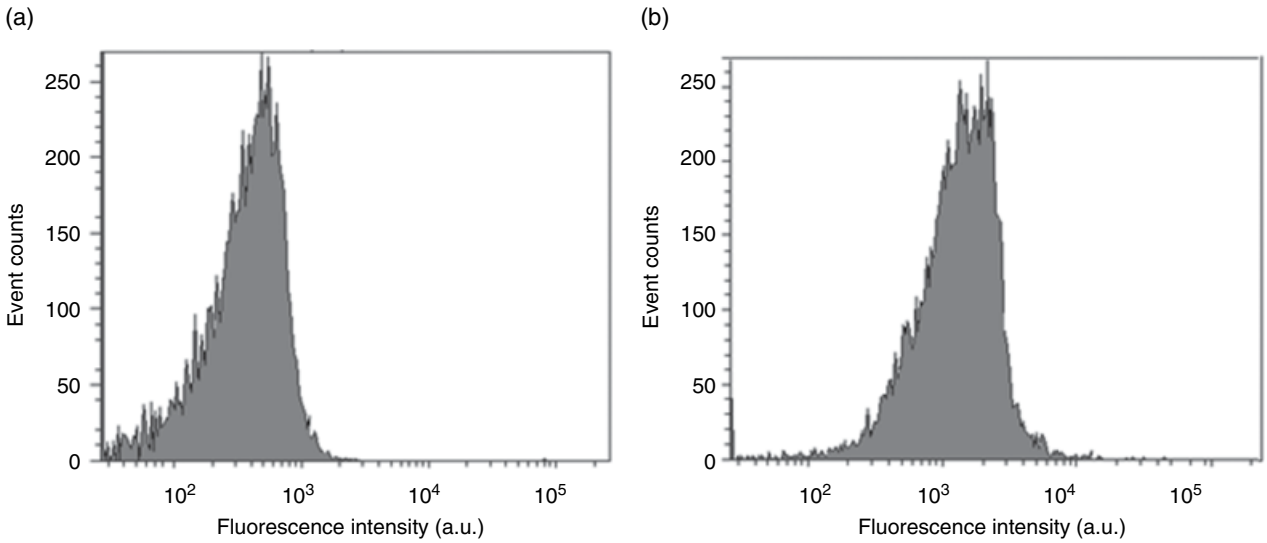

Figure 2.23 Signal intensity histograms of 5 μm silica beads without (a) and with Ag nanostructures (b) based on flow cytometry readout. Deng *et al*. [18]. Reproduced with the permission of American Chemical Society.

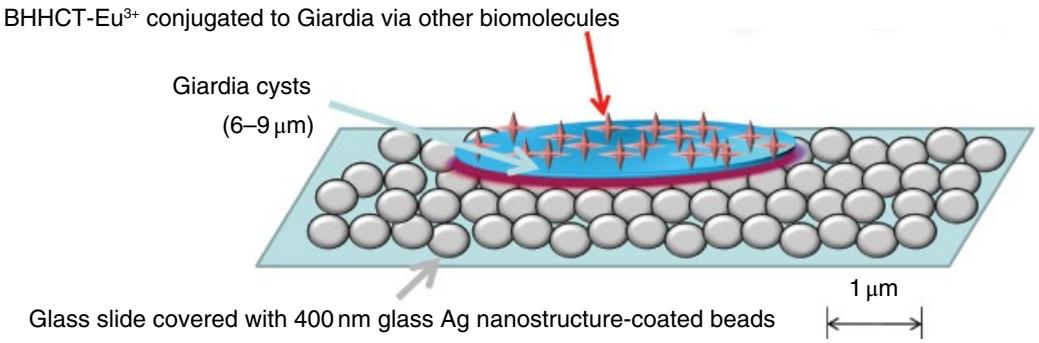
BHHCT-Eu3+ conjugated to Giardia via other biomolecules
Giardia cysts
(6–9 μm)
1 μm
Glass slide covered with 400 nm glass Ag nanostructure-coated beads

Figure 2.24 Schematic illustration of bioimaging with silver-enhanced beads.

For the cell imaging with the metal-coated beads, we used a model microorganism *Giardia lamblia* where SA-labeled BHHCT-Eu^{3+} was attached to the cell surface. The organisms were placed on silver nanostructure-coated silica beads as shown in Figure 2.24. In this case, an appropriate approach was required to analyze fluorescence signals obtained from these cells as they do not have exactly same sizes and shapes, and also the labeling of each cell tends to be nonuniform. We have therefore collected signals from a number of cells to obtain statistically meaningful results. In order to eliminate the effect of variability of cell shapes, sizes, and local variations of labeling efficiency, the image pixel intensity distribution was investigated on both Ag-coated and uncoated regions using the "histogram" function of Image J. From the corresponding intensity histogram, we found the mean image signal is increased 2-fold (Figure 2.25a). The representative cell images with and without Ag nanostructure-coated silica beads were shown in Figure 2.25b. The observed lower enhancement factor obtained in the cell imaging compared to the immunoassay is attributed to the following reasons. First, it is known that the fluorescence enhancement is most pronounced only when the fluorophore is localized at an optimal distance close to the surface of metal nanostructures that is in the range of 5–30 nm [34, 35]. In our experiment on the biological cells, the distances of fluorophore molecules to metal nanostructures cover a much wider range. The excitation enhancement is thus averaged over the cell thickness, resulting in the lower average enhancement. In addition, emission enhancement plays an important role for the very thin samples. However, the strength of the emission enhancement decreases as the distance from the metal nanostructures increases [36]. Therefore,

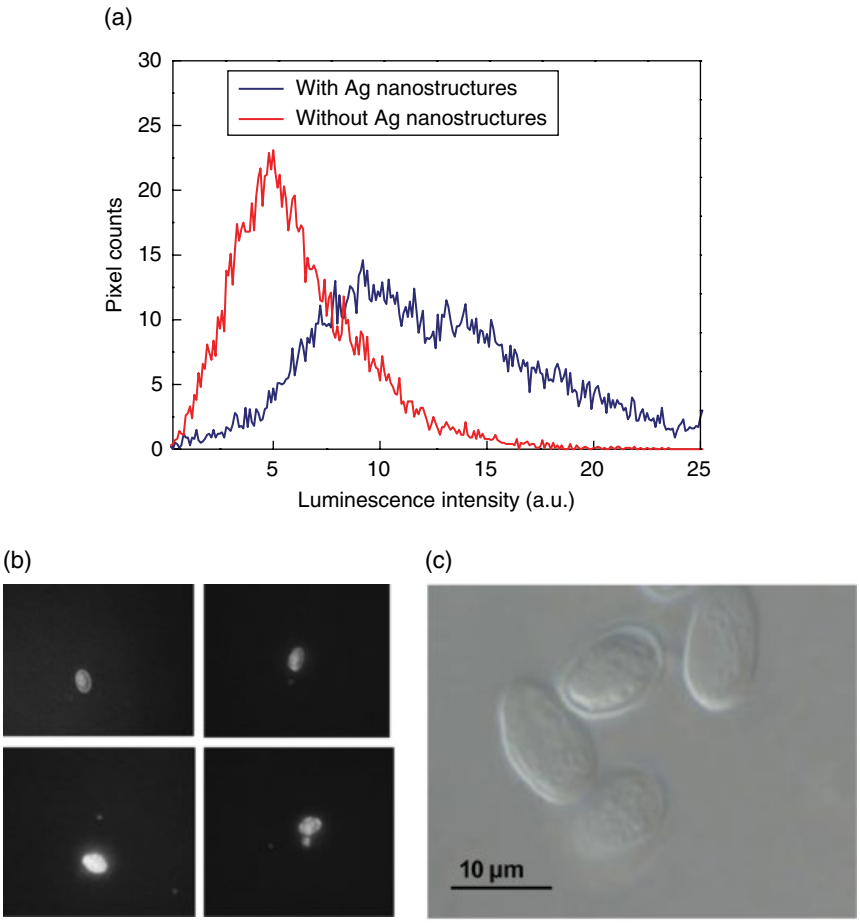

Figure 2.25 Signal intensity histograms of stained Giardia lamblia cells on the pure silica beads (gray line) as reference and with Ag nanostructures (black line) (a), representative images of Giardia cysts stained by BHHCT-Eu^{3+} on the silica beads without (upper panel) and with Ag nanostructures (lower panel) (b), and the DIC image of Giardia cysts (c). Deng *et al*. [33]. Reproduced with the permission of American Chemical Society.

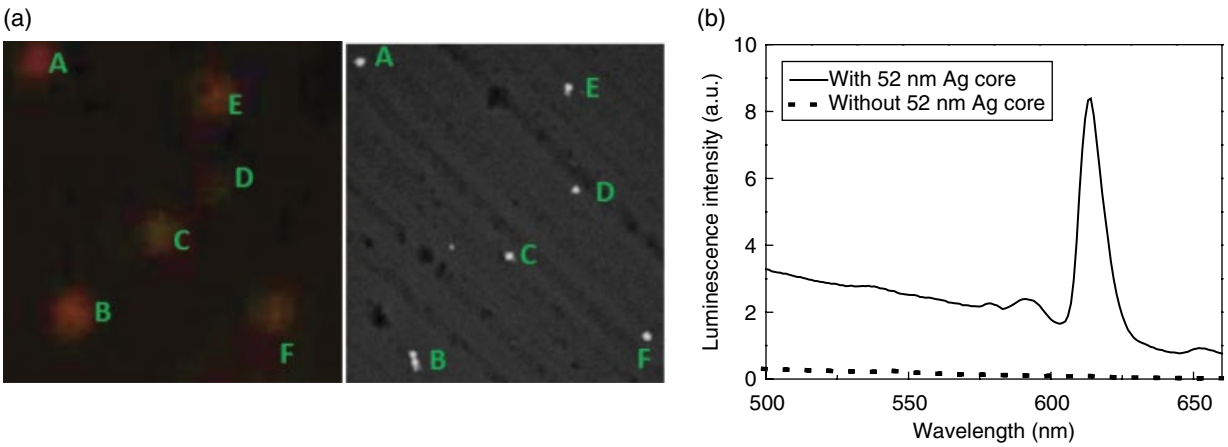

Figure 2.26 (a) Images of single BHHCT-Eu-DPBT-doped Ag@SiO_2 nanoparticles with 25 nm silica shell and 52 nm Ag core (left panel: the fluorescence image taken at ×60 magnification in a time-gated fluorescence microscope at 10 s exposure time; right panel: the TEM image at the same magnification as the fluorescence image). (b) Luminescence spectra of nanoparticle-labeled antibody after bioassay. Solid line: BHHCT-Eu-DPBT-doped Ag@SiO_2 with 12 nm silica shell and 52 nm Ag core; dotted line: BHHCT-Eu-DPBT-doped hollow nanoparticles with 12 nm silica shell and without 52 nm Ag core. Deng *et al*. [37]. Reproduced with the permission of John Wiley & Sons.

the observed signal enhancement in cell imaging is mainly caused by the increase of the fluorophore excitation rate.

The culmination of our studies was the development of an optimized biosensing probe for ultrasensitive detection [37]. In this study, we encapsulated a europium (Eu) dye in plasmonic Ag@SiO_2 nanoparticles comprising an Ag core and an undoped silica shell, followed by another ultrathin shell conjugated with a fluorophore BHHCT-Eu-DPBT. We designed our chemistry to modify both the silver-fluorophore distance and the Ag core size. The Ag core size is controlled by the growth of citrate-reduced silver colloids using metal deposition. The thickness of the first silica shell was varied by using different amounts of tetraethyl orthosilicate (TEOS), which is able to produce silica sols on the surface of silver nanoparticles. To facilitate this reaction ammonia is added as a catalyst for hydrolysis and condensation of TEOS. Once the silver core has been covered with the first shell, 3-aminopropyl(triethoxy)silane (APS)-linked BHHCT-Eu-DPBT (APS-BHHCT-Eu-DPBT) was then covalently linked and embedded in second, <3 nm thick exterior silica shell. Due to the MIFE effect, these nanoparticles doped with Eu were bright enough to be observed individually (Figure 2.26a). In order to further demonstrate the utility of these nanoparticles in biological applications, we carried out a fluorescent bioassay using SA–biotin binding. The nanoparticles were first conjugated with biotinylated IgG antibodies and then bound to the SA-coated glass slide. The fluorescence intensity was enhanced by ~120 times at high excitation intensity of 32.3 mW/cm^2 by comparing with the control sample without the silver core at the same experimental conditions (Figure 2.26b). The fluorescence lifetimes of these plasmonic nanoparticles were in the range of milliseconds, which is much longer than cellular autofluorescence. This difference enables the application of our nanoprobes in ultrasensitive, background-free time-gating fluorescence detection.

References

1 Weiss S., *Science 283*, 5408, 1676–1683 (**1999**).
2 Orrit M., Bernard J., *Phys. Rev. Lett. 65*, 2716–2719 (**1990**).
3 Sevick-Muraca E.M., Houston J.P., Gurfinkel M., *Curr. Opin. Chem. Biol. 6*, 5, 642–650 (**2002**).
4 Lakowicz J. R., *Anal. Biochem. 298*, 1–24 (**2001**).
5 Lakowicz J.R., Shen Y., D'Auria S., Malicka J., Fang J., Gryczynski Z., Gryczynski I., *Anal. Biochem. 301*, 261–277 (**2002**).
6 Geddes C.D., Lakowicz J.R., *J. Fluoresc. 12*, 121–129 (**2002**).
7 Aslan K., Gryczynski I., Malicka J., Matveeva E., Lakowicz J.R., Geddes C.D., *Curr. Opin. Biotechnol. 16*, 55–62 (**2005**).
8 Aslan K., Lakowicz J.R., Szmacinski H., Geddes C.D., *J. Fluoresc. 14*, 677–679 (**2004**).
9 Deng W., Xie F., Baltarac H.T.M.C.M., Goldys E.M., *et al*. *Phys. Chem. Chem. Phys. 15*, 15695–15708 (**2013**).
10 Deng W., Goldys E., *Langmuir 28*, 10152–10163 (**2012**).
11 Dankwart A., *Encyclopedia of Analytical Chemistry: Applications, Theory and Instrumentation*, Ed. Meyers R.A., John Wiley & Sons, ISBN: 978-0-470-97333-2 (**2011**) (**2001**).
12 Xie F., Baker M.S., Goldys E.M., *J. Phys. Chem. B 110*, 46, 23085–23091 (**2006**).
13 Xie F., Baker M.S., Goldys E.M., *Chem. Mater. 20*, 5, 1788–1797 (**2008**).
14 Marques P.A.A.P., Noguiera H.I.S., Pinto R.J.B., Neto C.P., *J. Raman Spectrosc. 39*, 439–443 (**2008**).
15 Muniz-Miranda M., Innocenti M., *Appl. Surf. Sci. 226*, 125–131 (**2004**).
16 Nagatani N., Tanaka R., Yuhi T., Endo T., Kerman K., Takamura Y., Tamiya E., *Sci. Technol. Adv. Mater. 7*, 270–275 (**2006**).
17 Duchesne L., Fernig D.G., *Anal. Biochem. 362*, 287–289 (**2007**).
18 Deng W., Drozdowicz-Tomsia K., Jin D., Goldys E.M., *Anal. Chem. 81*, 7248–7255 (**2009**).
19 Aslan K., Malyn S.N., Geddes C.D., *J. Fluoresc. 17*, 7–13 (**2007**).
20 Xie F., Drozdowicz-Tomsia K., Goldys E.M., *Chem. Phys. Lett. 466*, 4–6, 186–188 (**2008**).
21 Coghlan D.R., Mackintosh J.A., Karuso P., *Org. Lett. 7*, 2401 (**2005**).
22 Milloni P.W., *The Quantum Vacuum*, Boston, MA, Academic Press, **1994** (chapter 4).
23 Perney N.M.B., Baumberg J.J., *Opt. Express 14* 847 (**2006**).
24 Perney N. M. B., Baumberg J. J., Zoorob M. E., Charlton M. D. B., Mahnkopf S., Netti C. M., *Opt. Express 14*, 847–857 (**2006**).
25 Goldys E.M., Drozdowicz-Tomsia K., Xie F., Shtoyko T., Matveeva E., Gryczynski I., Gryczynski Z., *J. Am. Chem. Soc. 129*, 40, 12117–12122 (**2007**).
26 Drozdowicz-Tomsia K., Xie F., Goldys E.M., *J. Phys. Chem. C 114*, 3, 1562–1569 (**2010**).
27 Xie F., Shtoyko T., Drozdowicz-Tomsia K., Goldys E.M., *J. Nanopart. Res., 13*, 2, 613–624 (**2011**).
28 Geddes C.D., Parfenov A., Gryczynski I., Lakowicz J.R., *J. Phys. Chem. B*, *107*, 9989–9993 (**2003**).

29 Geddes C.D., Parfenov A., Roll D., Gryczynski I., Malicka J., Lakowicz J.R., *J. Fluoresc. 13*, 119–122 (**2003**).

30 Shtoyko T., Matveeva E.G., Chang I.F., Gryczynski Z., Goldys E., Gryczynski I., *Anal. Chem. 80* 1962–1966 (**2008**).

31 Witten T.A., Sander L.M., *Phys. Rev. Lett. 47*, 1400–1403 (**1981**).

32 Lakowicz J.R., *Anal. Biochem. 324*, 153–169 (**2004**).

33 Deng W., Jin D., Drozdowicz-Tomsia K., Yuan J., Goldys E., *Langmuir 26*, 10036–10043 (**2010**).

34 Zhang J., Malicka J., Gryczynski I., Leonenko Z., Lakowicz J.R., *J. Phys. Chem. B 109*, 7969–7975 (**2005**).

35 Mertens H., Koenderink A., Polman A., *Phys. Rev. B 76*, 115123 (**2007**).

36 Moal E., Fort E., Lévêque-Fort S., Cordelières F., Fontaine-Aupart M., Ricolleau C., *Biophys. J.*, *92*, 2150–2161 (**2007**).

37 Deng W., Jin D., Drozdowicz-Tomsia K., Yuan J., Wu J., Goldys E., *Adv. Mater. 23*, 4649–4654 (**2011**).

3

Plasmonic Enhancement of Molecule-Doped Core–Shell and Nanoshell on Molecular Fluorescence

Jiunn-Woei Liaw[1], Chuan-Li Liu[2], Chong-Yu Jiang[2], and Mao-Kuen Kuo[2]

[1] *Department of Mechanical Engineering, Chang Gung University, Taoyuan, Taiwan, ROC*
[2] *Institute of Applied Mechanics, National Taiwan University, Taipei, Taiwan, ROC*

3.1 Introduction

In the past decades, a variety of Au or Ag nanoparticles (NPs) have been synthesized, for example, spherical NP [1], nanorod (NR) [2–4], nanocube [5], and so on. Moreover, the composite nanostructures have also been developed, for example, core–shell [6], nanoshell (NS) [7], and nanomatryushka [8]. The two important applications of these nanostructures are the surface-enhanced Raman scattering (SERS) [9–14] and the surface-enhanced fluorescence (SEF) [15] (or called metal-enhanced fluorescence [16]) by utilizing their surface plasmon resonance (SPR). Due to the SPR, a collective motion of free electrons in these metallic nanostructures is formed, and the local electric field is enhanced when irradiated by an excitation light. Although a few reports have demonstrated the strong plasmonic enhancement on molecular fluorescence [17–33], some reports have shown an opposite result—serious quenching [34–38]. In addition, the SEF factors estimated by numerical methods are usually larger than that of experiment. These contradictions and discrepancies imply that a more detailed discussion on SEF is needed.

Recently, the molecule-doped core–shell ($Au@SiO_2$ or $Ag@SiO_2$) has been widely used for SEF, where the molecules are embedded in the outer silica layer [25–28]. Using this structure, the distance between the metal NP and the molecules is controllable, and sometimes a spacer is added in between the NP and molecule-doped layer to avoid the quenching. The SPR band of a core–shell is slightly redshifted from that of a bare NP due to the higher permittivity of silica relative to the surrounding medium. On the other hand, NS possesses a merit that its SPR is tunable by adjusting the thickness of metal shell or the core size [7]. Moreover, the SPR modes of NS are more versatile than those of metallic NP, for example, the dipole, quadrupole, sextupole, and octupole modes [39–45]. In particular, the dipole mode of NS is redshifted from that of metallic NP. Therefore, NS can be used to enhance the near-infrared (NIR) fluorescence of nearby molecules [30–32]. Furthermore, the molecule-doped Au $NS@SiO_2$ has been developed to confine the molecules in the outer silica layer [33]. On the other hand, a nanocavity of Ag NS for enhancing the fluorescence of a single molecule encapsulated in the silica core has been proposed [46, 47]. Recently, Ag NS encapsulating a molecule in the silica core has been developed to enhance the fluorescence of $Ru(bpy)_3^{2+}$ [48] or Eu(III) complex [49]. In addition, Au NS has been used for enhancing the photoluminescence of a quantum dot encapsulated at the center [50]. It was also shown that the lifetime of fluorophore embedded in Ag NS is dramatically reduced by the SPR of NS to prevent photobleaching of dye [48, 49]. Actually, the reduction of fluorescence lifetime by metal nanostructure is an important feature of SEF [51, 52]. Moreover, using the gap mode of a dimer structure for SERS [9] and SEF [53–68] has also attracted a lot of attention. Recently, the SPR-enhanced Förster resonance energy transfer (FRET) [51, 69, 70] between a donor and an acceptor, for example, by using the core–shell [71] or NS [72], has been studied. In addition, a novel nanostructure of surface plasmon amplification by stimulated emission of radiation (*spaser*) has been proposed, where Ag NS is covered by a gain medium (e.g., quantum dots or dyes) or contains a gain medium in the core [73–75]. The main idea of *spaser* is to use the energy coupling between the spontaneous emission of the gain medium and the SPR mode of the Ag NS for inducing and amplifying coherent lights. Based on this concept, a *spaser*-based nanolaser has been demonstrated by

Surface Plasmon Enhanced, Coupled and Controlled Fluorescence, First Edition. Edited by Chris D. Geddes.
© 2017 John Wiley & Sons, Inc. Published 2017 by John Wiley & Sons, Inc.

utilizing dyes-doped core–shell ($Au@SiO_2$) irradiated by a laser of 488 nm to generate a narrowband coherent light of 531 nm. The wavelength of this coherent light is just in the overlapped regime of the SPR band of the Au NP, the emission spectrum of OG-488 dye, and the tail of the excitation spectrum of the dye [76]. Although the intensity of this emission was much weaker than the dye's fluorescence for a practical application, the research has shown the possibility to realize *spaser*. Except these applications of metal NPs mentioned earlier, there are the other applications related to the SPR, for example, the photothermal therapy [77–79], the photoacoustic imaging [80–84], and the two-photon luminescence of metal NPs [85–88] irradiated by femtosecond laser. In short, these current developments in SEF [89–122] have shown the potential for practical applications.

In this chapter, the plasmonic enhancement on molecular fluorescence of three types of spherical nanostructures will be analyzed and discussed: core–shell [123, 124], NS [125], and silica-coated NS [126, 127]. The first one is the molecule-doped core–shell, which is a metal (Au or Ag) NP coated by a silica layer, denoted by $Au@SiO_2$ or $Ag@SiO_2$. The molecule is embedded within the outer silica layer of core–shell. Another one is the molecule-doped NS, a silica core coated by a metal layer, where the molecule is encapsulated in the silica core. The other one is a molecule-doped $NS@SiO_2$, a NS coated by a silica layer, where the molecule is embedded in the outer silica layer. Since the cause of SEF is due to the SPR of these nanostructures, their SPR modes will be particularly analyzed, and the corresponding near-field amplification on the electric field will also be discussed. Moreover, the dependence of the fluorescence enhancement on the molecular location and orientation will be illustrated, particularly at the SPR modes. Furthermore, the overall performance of a large number of these NPs will be discussed. In addition, the Stokes-shift effects of the fluorescence excitation and emission wavelengths on the enhancement will also be discussed.

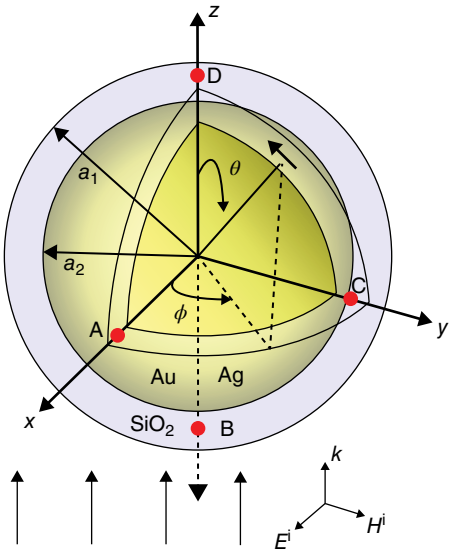

Figure 3.1 Configuration of a molecule-doped core–shell ($Au@SiO_2$ or $Ag@SiO_2$) irradiated by a plane wave. The radii of metal core and silica shell are denoted by a_2 and a_1, respectively. Points A, B, C, and D are four typical locations for a single molecule embedded in the middle of the outer silica shell. (*See insert for color representation of this figure.*)

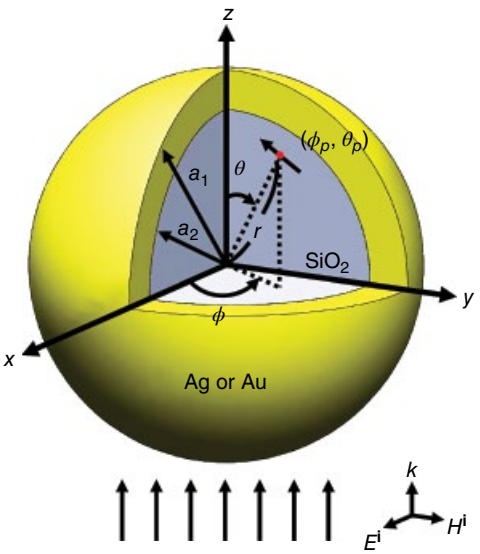

Figure 3.2 Configuration of metal (Ag or Au) NS with an encapsulated molecule (dipole) in the silica core irradiated by a polarized plane wave. The radii of silica core and metal shell are denoted by a_2 and a_1, respectively.

3.2 Theory

In the following text, three types of spherical nanostructures will be analyzed. Figure 3.1 shows the configuration of a molecule-doped core–shell ($Au@SiO_2$ or $Ag@SiO_2$) irradiated by a plane wave, where the radii of metal core and silica shell are denoted by a_2 and a_1, respectively. The configuration of Au or Ag NS encapsulating a molecule within the silica core is shown in Figure 3.2, where the outer radii of the NS and the silica core are denoted by a_1 and a_2. Figure 3.3 shows the configuration of a molecule-doped $NS@SiO_2$, where the molecule is embedded in the outer silica layer. The outer radii of the silica shell, the NS, and the silica core are denoted by a_1, a_2, and a_3, respectively. To analyze the plasmonic enhancement of these core–shells or NSs on the fluorescence of a

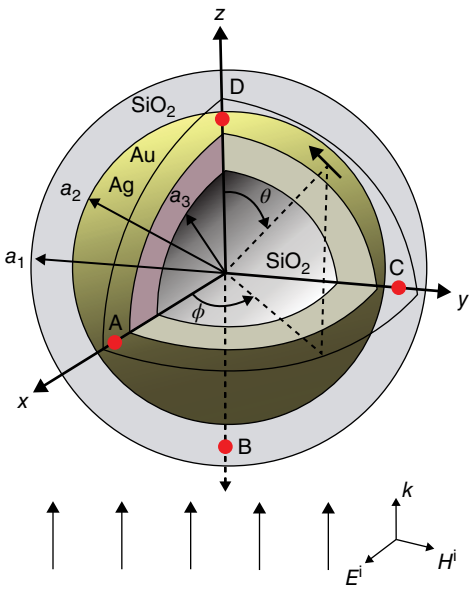

Figure 3.3 Configuration of Ag NS@SiO_2 with molecules (electric dipoles) embedded in the outer silica shell irradiated by an incident *x*-polarized plane wave. The outer radii of silica shell, the Ag NS, and the silica core are denoted by a_1, a_2, and a_3, respectively. Points A, B, C, and D are four typical locations of a single molecule embedded in the middle of the outer silica shell.

nearby molecule, the process of molecular fluorescence is simply divided into two stages: the excitation and the emission stage [18, 64, 95, 128]. In addition, the classical electromagnetic (EM) theory (Maxwell's equations) is used for the analysis of each stage. For the former, the electric field around these multilayered spheres induced by the illumination of an incident plane wave will be analyzed by using the Mie theory [114]. In particular, the excitation rate for exciting a nearby molecule will be studied. Once the molecule is excited, it is regarded as an electric dipole to emit the fluorescence in the presence of the nanostructure at the emission stage. The dyadic Green's functions [129, 130] for a single multilayered sphere are derived to calculate the radiative and nonradiative powers of this dipole in the presence of metal nanostructure. After that, the apparent quantum yield will be calculated to present the efficiency of emission under the influence of these nanostructures. Finally, the enhancement factor (EF) will be used to evaluate the performance of SEF [18, 95, 128]. Moreover, the average enhancement factor (AEF) [123–127] will be proposed to assess the overall SEF performance of a large number of NPs or NSs. Without loss of generality, the incident plane wave is assumed to propagate along the *z*-axis with *x*-polarization for the three cases. The origin of the coordinate is located at the center of the core–shell or NS. Moreover, these nanostructures are assumed dilute. Hence, the multi-scattering of light with multi-NPs is neglected for the dilute colloid. In addition, the interaction of multimolecular fluorescence, for example, self-quenching, is also neglected.

3.2.1 Plane Wave Interacting with an Multilayered Sphere

At the excitation stage, the EM field induced by an incident plane wave interacting with the nanostructure is concerned. Due to the SPR of the metal nanostructure, the near-field electric field around the structure is enhanced to raise the probability of exciting a nearby molecule. The general Mie theory [114] is used to calculate the EM field induced by the interaction of a plane wave with a multilayered sphere (core–shell, NS, and NS@ SiO_2) at a specific excitation wavelength, λ_{ex}. The excitation rate $\Psi(\mathbf{e}_p, \mathbf{x}_d; \lambda_{ex})$ for a molecule located at $\mathbf{x}_d$ with a unit dipole moment $\mathbf{e}_p$ is defined as

$$\Psi\left(\mathbf{e}_p, \mathbf{x}_d; \lambda_{ex}\right) = \frac{\left|\mathbf{E}\left(\mathbf{x}_d; \lambda_{ex}\right) \cdot \mathbf{e}_p\right|^2}{\left|\mathbf{E}^i\right|^2} \tag{3.1}$$

where $\mathbf{E}$ is the total electric field and $|\mathbf{E}^i|^2$ is the intensity of the incident wave. Here the superscript "i" denotes the incident part, and "s" the scattering part. The total fields are $\mathbf{E} = \mathbf{E}^i + \mathbf{E}^s$ and $\mathbf{H} = \mathbf{H}^i + \mathbf{H}^s$. In order to identify the SPR mode of the nanostructure, the scattering cross section (SCS), absorption cross section (ACS), and extinction cross section (ECS) are needed to calculate in advance; ECS = SCS + ACS. These parameters are useful to choose an optimal excitation wavelength for inducing a maximum excitation rate. First, the scattering power of a nanostructure irradiated by a plane wave in terms of the surface integral of Poynting vector $\mathbf{E}^s \times \bar{\mathbf{H}}^s$ is defined

$$P_s = \frac{1}{2}\mathrm{Re}\left\{\int_{S_0} \mathbf{E}^s \times \bar{\mathbf{H}}^s \cdot d\mathbf{a}\right\} \tag{3.2}$$

where S_0 is any simple closed surface enclosing the whole nanostructure and the dipole and Re denotes the real part. Here the complex conjugate of $\mathbf{H}^s$ field is taken for the Poynting vector. Similarly, the absorption power is defined as

$$P_a = -\frac{1}{2}\mathrm{Re}\left\{\int_{S_1} \mathbf{E} \times \bar{\mathbf{H}} \cdot d\mathbf{a}\right\} \tag{3.3}$$

where the Poynting vector of the total field is used and S_1 is the outer surface of the nanostructure. The normalized SCS (C_s) and ACS (C_a) are defined as

$$C_s = \frac{P_s}{AS^i} \tag{3.4}$$

$$C_a = \frac{P_a}{AS^i} \tag{3.5}$$

where A is the cross section of the nanostructure and S^i is

$$S^i = \frac{1}{2}\left|\mathbf{E}^i \times \mathbf{H}^i\right| \tag{3.6}$$

Moreover, the normalized ECS (C_e) is the sum of C_s and C_a.

3.2.2 Excited Dipole Interacting with a Multilayered Sphere

At the emission stage, the excited molecule is modeled as an electric dipole emitting the fluorescence at a specific emission wavelength. The dipole's radiative and nonradiative powers under the influence of the nearby nanostructure are concerned. Based on Refs. [129, 130], the dyadic Green's functions of multilayered sphere are derived for core–shell, NS, and NS@SiO_2; two sets of Green's functions of a unit radial dipole and a tangential dipole are derived. Therefore, the total EM field generated by any arbitrarily oriented dipole in the presence of the nearby nanostructure can be obtained systematically by using the linear combinations of the EM fields of these analytical Green's functions. The solutions are expressed in series forms of spherical wave functions at any specific emission wavelength λ_{em}. We use the superscript "d" to denote the EM field induced by the electric dipole. The radiative power of an electric dipole, located at $\mathbf{x}_d$ with a unit dipole moment $\mathbf{e}_p$, in the presence of an NP at an emission wavelength λ_{em} is expressed in terms of the Poynting vector $\mathbf{E}^d \times \bar{\mathbf{H}}^d$ as

$$P_r\left(\mathbf{x}_d, \mathbf{e}_p; \lambda_{em}\right) = \frac{1}{2}\mathrm{Re}\left\{\int_{S_0} \mathbf{E}^d \times \bar{\mathbf{H}}^d \cdot d\mathbf{a}\right\} \tag{3.7}$$

where S_0 is any simple closed surface enclosing the whole nanostructure and the dipole and Re denotes the real part. The complex conjugate of **H** field is taken for the Poynting vector. Similarly, the nonradiative power, which is the dissipation power in metal, is defined as

$$P_{nr}\left(\mathbf{x}_d, \mathbf{e}_p; \lambda_{em}\right) = -\frac{1}{2}\mathrm{Re}\left\{\int_{S_1} \mathbf{E}^d \times \bar{\mathbf{H}}^d \cdot d\mathbf{a}\right\} \tag{3.8}$$

where S_1 is the outer surface of the nanostructure. Hence, the apparent quantum yield $\eta(\mathbf{x}_d, \mathbf{e}_p; \lambda_{em})$, which is the efficiency of the emission of a dipole in the presence of a nearby nanostructure, is defined as

$$\eta\left(\mathbf{e}_p, \mathbf{x}_d; \lambda_{em}\right) = \frac{P_r}{P_r + P_{nr}} \tag{3.9}$$

where $0 \le \eta \le 1$.

3.2.3 EF on Fluorescence

Subsequently, the EF [18, 64, 95, 128] for the whole fluorescence process is defined as the product of the excitation rate of the excitation stage and the apparent quantum yield of the emission stage:

$$\alpha(\mathbf{e}_p, \mathbf{x}_d; \lambda_{ex}, \lambda_{em}) = \Psi(\mathbf{e}_p, \mathbf{x}_d; \lambda_{ex}) \cdot \eta(\mathbf{e}_p, \mathbf{x}_d; \lambda_{em}) \tag{3.10}$$

Since the dipole moment of a molecule is in an arbitrary orientation $\mathbf{e}_p$, the mean enhancement factor (MEF), $\alpha_M(\mathbf{x}_d; \lambda_{ex}, \lambda_{em})$, at the position $\mathbf{x}_d$ is defined as the average of EF over all possible orientations $\mathbf{e}_p$:

$$\alpha_M\left(\mathbf{x}_d; \lambda_{ec}, \lambda_{em}\right) = \frac{1}{4\pi}\int_0^{4\pi} \alpha\left(\mathbf{e}_p, \mathbf{x}_d; \lambda_{ex}, \lambda_{em}\right) d\Omega_p \tag{3.11}$$

where Ω_p is the solid angle of dipole's orientation and then $d\Omega_p$ in terms of spherical coordinates is $d\Omega_p = \sin\theta_p d\theta_p\, d\varphi_p$. Moreover, the effective enhancement factor (EEF), α_E, is defined as the ratio of MEF of the nanostructure encapsulating a dipole to MEF of the medium without the nanostructure on an arbitrarily oriented free dipole. For the latter, since the apparent quantum yield is unit one, its MEF is 1/3 considering the random orientation of $\mathbf{e}_p$ with respect to the polarization of the incident light. Therefore EEF, $\alpha_E(\mathbf{x}_d; \lambda_{ex}, \lambda_{em})$, is expressed as

$$\alpha_E\left(\mathbf{x}_d; \lambda_{ex}, \lambda_{em}\right) = \frac{3}{4\pi}\int_0^{4\pi} \alpha\left(\mathbf{e}_p, \mathbf{x}_d; \lambda_{ex}, \lambda_{em}\right) d\Omega_p \tag{3.12}$$

Furthermore, if a monolayer of molecules is uniformly embedded with the same distance r from the center, the AEF, $\hat{\alpha}_A$, is defined as

$$\hat{\alpha}_A\left(r; \lambda_{ex}, \lambda_{em}\right) = \frac{1}{4\pi}\int_0^{4\pi} \alpha_E\left(\mathbf{x}_d; \lambda_{ex}, \lambda_{em}\right) d\Omega \tag{3.13}$$

where Ω is the solid angle of molecular position $\mathbf{x}_d$ in the spherical coordinates, $d\Omega = \sin\theta d\theta d\varphi$.

Furthermore, for an NS encapsulating a molecule randomly located inside the silica core, the AEF of the entire core is defined as

$$\alpha_A(\lambda_{ex},\lambda_{em}) = \frac{4\pi}{V_0}\int_0^{a_2} \hat{\alpha}_A(r;\lambda_{ex},\lambda_{em}) r^2 dr \quad (3.14)$$

where $r = |\mathbf{x}_d|$ and the volume of the core is $V_0 = 4\pi a_2^3/3$. In contrast, for the core–shell (Au or Ag@SiO_2) and NS@SiO_2 encapsulating a molecule randomly doped in the outer silica layer, the AEF of the entire silica layer is further defined as

$$\alpha_A(\lambda_{ex},\lambda_{em}) = \frac{4\pi}{V_0}\int_{a_2}^{a_1} \hat{\alpha}_A(r;\lambda_{ex},\lambda_{em}) r^2 dr \quad (3.15)$$

where $r = |\mathbf{x}_d|$ and $V_0 = 4\pi\left(a_1^3 - a_2^3\right)/3$. Because of the Stokes shift of a real fluorescence, the emission wavelength is always longer than the excitation wavelength, that is, $\lambda_{em} \geq \lambda_{ex}$.

3.3 Numerical Results and Discussion

In this section, the SPR modes (particularly the dipole and quadrupole modes) of core–shell (Au@SiO_2 or Ag@SiO_2), NS, and NS@SiO_2 will be identified first by using the far-field ECS and the near-field electric field. For a typical wavelength near the dipole mode, the EF of each type of NPs on the fluorescence of an arbitrarily oriented and located molecule embedded within the silica shell or core will be calculated first. The molecule is modeled as an electric dipole. Subsequently, AEF is obtained by averaging the individual EF over all possible orientations and positions of the electric dipoles. The AEF of these NPs is used to estimate the overall performance of a large number of NPs. The frequency-dependent permittivity of Au and Ag is referred to Ref. [131]. The surrounding medium is assumed to be water.

3.3.1 Core–Shell

In this section, the EF and EEF of core–shell (Au@SiO_2 or Ag@SiO_2) on molecular fluorescence will be discussed to illustrate that the SEF is dependent on the molecular location and orientation. The major works are referred to Ref. [123, 124]. In addition, the role of the SPR modes of core–shell, particularly the dipole mode, playing on SEF will be discussed. The configuration of core–shell is shown in Figure 3.1. The thickness of the silica shell is denoted by t_S; $t_S = a_1 - a_2$, where a_1 and a_2 are the outer radii of the silica shell and the metal core, respectively. Moreover, the frequency-dependent AEF of core–shell will be discussed to present the overall effect of a large number of core–shells.

3.3.1.1 Au@SiO_2

Consider a core–shell Au@SiO_2 submerged in water irradiated by a polarized plane wave, where a single molecule is doped within the outer silica layer [123]. The ECSs of Au@SiO_2 of $t_s = 25$ nm with different core radii a_2 (40, 50, 60 nm) irradiated by a plane wave are shown in Figure 3.4. The major SPR band of Au@SiO_2 belongs to the dipole mode. The peaks of SPR band are at 570 nm, 590 nm, and 620 nm corresponding to these cases of $a_2 = 40$ nm, 50 nm, and 60 nm, respectively. The SPR band (the dipole mode) of Au NP is broad. The local electric field around Au@SiO_2 can be enhanced when Au@SiO_2 is irradiated by a plane wave of wavelength within this regime. For example, the electric fields and the cross sections of $|\mathbf{E}_r|$ and $|\mathbf{E}_\theta|$ in the xz-plane of Au@SiO_2 irradiated by a plane wave of 633 nm are shown in Figure 3.5a and b, where $[t_S, a_2] = [25,50]$ nm.

Furthermore, the EF at four typical points (A, B, C, and D) with the same distance ($d = 12.5$ nm) to the surface of Au core is analyzed. If the molecule is located at point A on the lateral side of the core–shell for illumination, the spherical plot of EF of the core–shell versus the dipole orientations looks like a dumbbell, as shown in Figure 3.6a. The xz-plane cross section of Figure 3.6a is shown in Figure 3.6b. The optimal orientation at point A is in x-direction, which is the polarization direction of the incident plane

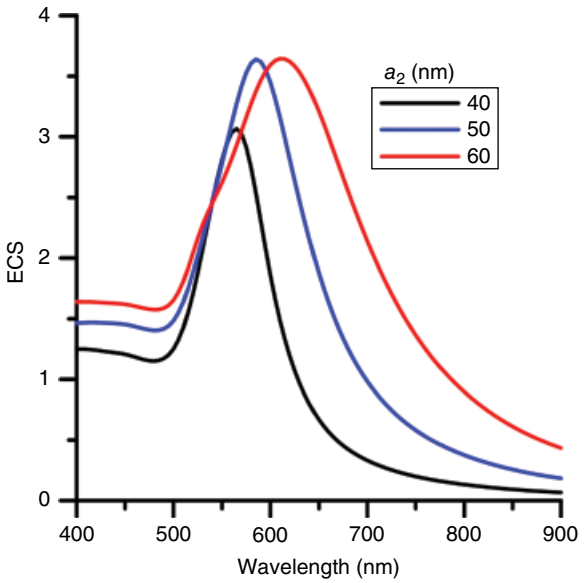

Figure 3.4 ECSs versus wavelengths for core–shell Au@SiO_2 of $t_s = 25$ nm with various a_2 (40, 50, 60 nm) in water.

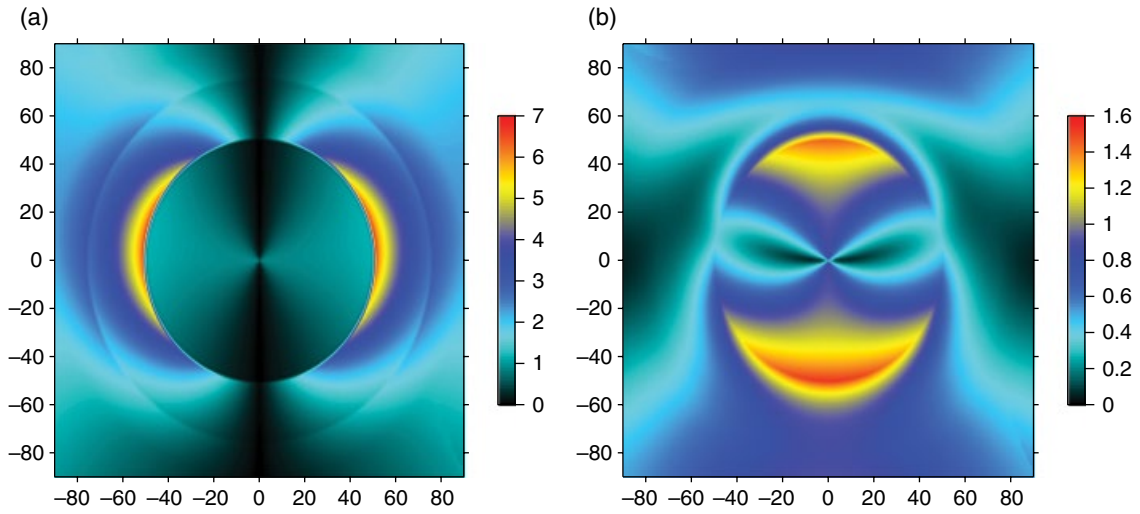

Figure 3.5 (a) $|\mathbf{E}_r|$ and (b) $|\mathbf{E}_\theta|$ in the *xz*-plane cross section of Au@SiO_2 in water irradiated by a plane wave of 633 nm at the dipole mode, where $[t_s, a_2] = [25,50]$ nm.

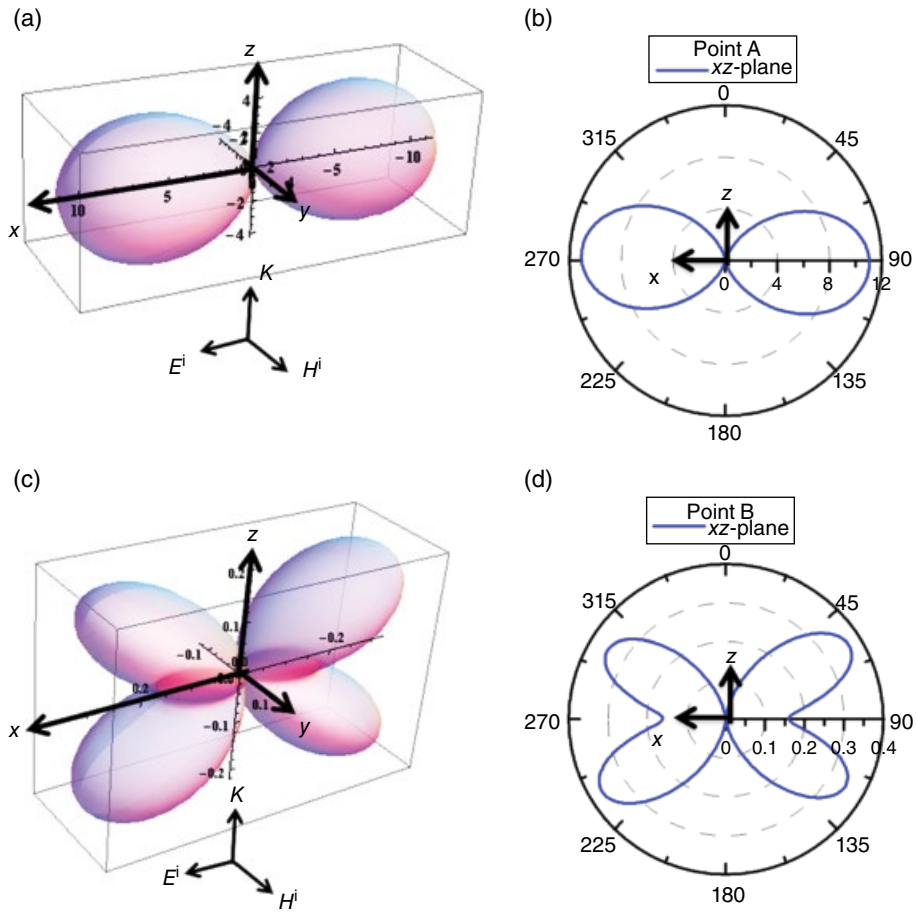

Figure 3.6 (a) Spherical plot of the 3D profile of EF versus dipole orientations at $\lambda_{ex} = \lambda_{em} = 633$ nm for a core–shell Au@SiO_2 ($[t_s, a_2] = [25,50]$ nm) containing a molecule located at point A. (b) The *xz*-plane cross sections of (a), (c), (e), and (g) are EFs at points B, C, and D. (d), (f), and (h) are the *xz*-plane or *xy*-plane cross sections of (c), (e), and (g), respectively [123].

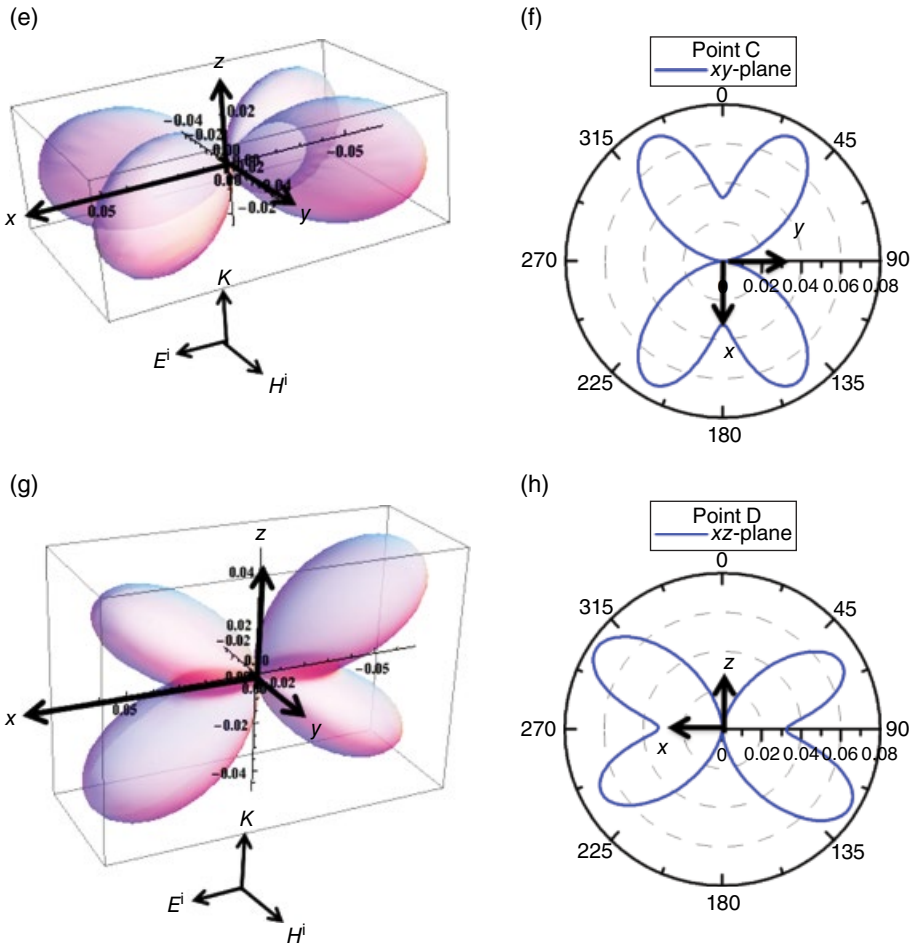

Figure 3.6 (*Continued*)

wave. If the molecule is located at point B on the front side of the core–shell for illumination, the three-dimensional (3D) profile of EF becomes a butterfly, as depicted in Figure 3.6c. The *xz*-plane cross section of this profile is plotted in Figure 3.6d. The spherical plot of EF at point C is shown in Figure 3.6e and f, and that at point D, on the back side of Ag NS, is shown in Figure 3.6g and h. Furthermore, the 3D spherical plot of EEF for a molecule at various positions with the same distance ($d = 12.5$ nm) from the surface of Au core at $\lambda_{ex} = \lambda_{em} = 633$ nm is shown in Figure 3.7a. In this 3D profile, the distance of each point of the profile to the center represents the magnitude of EEF for the position vector. The *xy*-plane, *yz*-plane, and *xz*-plane cross sections of Figure 3.7a are shown in Figure 3.7b, c, and d, respectively. The EEF at point A is 9.561, and EEF at point B is 0.374. The EEF at point C is 0.077, much less than that of point A. Due to the *x*-polarized incident light, the SPR oscillation of the dipole mode makes the electric field at point A much stronger than that at point C. This 3D profile also illustrates that EEF is sensitive to the relative position of molecule not only to the core–shell but also to the polarization of the incident wave. The minimum EEF occurs at point D (0.077) on the back side of the core–shell, and the maximum EEF (10.03) does not occur at point A but at A′ with 12° away from point A, as shown in Figure 3.7b. The AEF of the core–shell on the fluorescence of a monolayer of molecules embedded at $d = 12.5$ nm is 3.262.

Subsequently, the distribution of AEF versus distance d between the molecule-doped layer ($t_s = 25$ nm) and Au core ($a_2 = 50$ nm) at $\lambda_{ex} = \lambda_{em} = 633$ nm is shown in Figure 3.8. The AEF of the entire shell is 2.626. Figure 3.8 indicates that the maximum AEF (3.35) is obtained if $d = 10.5$ nm. When the molecule is too close to Au core (say $d < 4$ nm), a strong fluorescence energy transfer between the excited molecule and Au NP occurs, resulting in a severe dissipation of fluorescence in Au. Consequently, AEF is less than unit one; that is, a quenching phenomenon is induced. Thus, adding an appropriate silica spacer in between Au core and

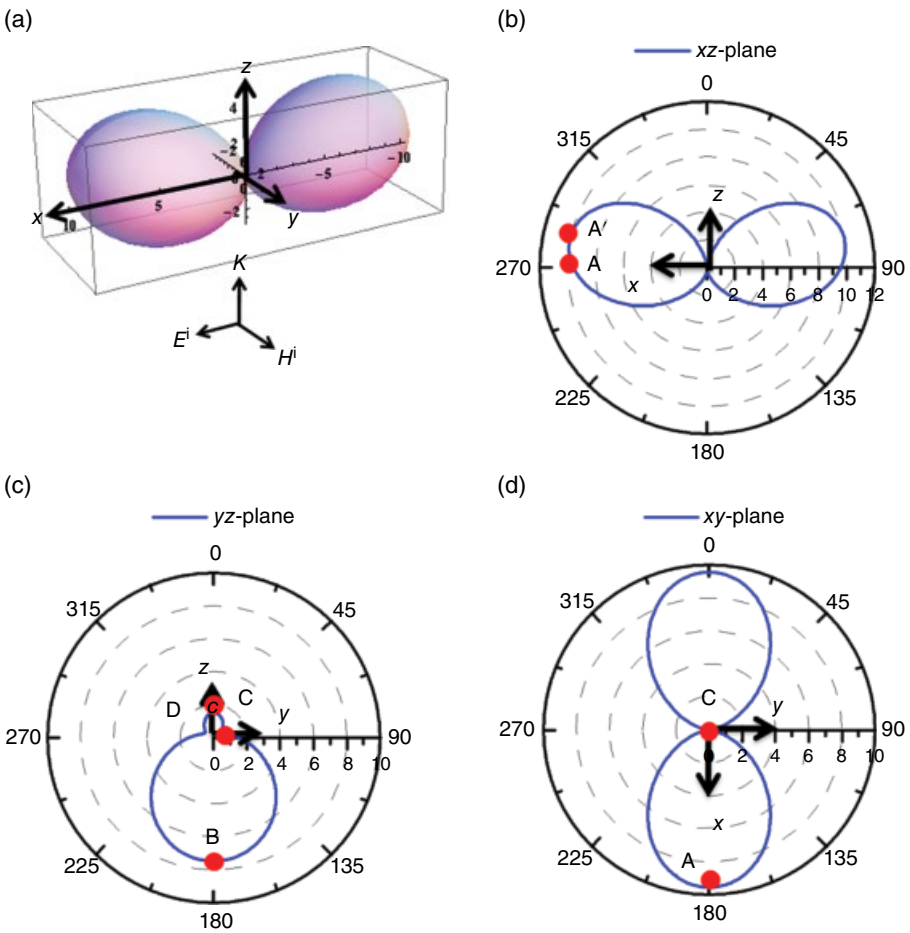

Figure 3.7 (a) Spherical plot of the 3D profile of EEF versus molecular positions for Au@SiO_2 ($[t_s,a_2]=[25,50]$nm) at $\lambda_{ex}=\lambda_{em}=633$nm, where these molecules are embedded in the middle layer of the shell ($d=12.5$ nm). (b) The *xz*-plane, (c) the *yz*-plane, and (d) the *xy*-plane cross sections of (a). AEF on this monolayer of molecules is 3.262 [123].

molecule-doped layer is necessary to improve the AEF. For example, using a silica spacer of $d_0=5$nm, AEF can be raised to 2.892 for the aforementioned case, compared with the value of 2.626 without spacer.

The AEFs versus wavelength for Au@SiO_2 of $t_s=25$ nm with different a_2 are shown in Figure 3.9. It illustrates that there is an optimal a_2, about 50–60 nm, for obtaining a maximum AEF within a broadband regime (600–700 nm). In addition, for a larger core–shell, AEF spectrum is redshifted and becomes less, as shown in Figure 3.9. In contrast, for a smaller Au core ($a_2<30$ nm), Au@SiO_2 always exhibits a quenching, rather than an enhancement, on fluorescence within the spectrum of 400–900 nm.

Subsequently, the Stokes-shift effect between the fluorescence excitation and emission spectra on AEF will be discussed further. Figure 3.9 has shown that AEFs of a smaller Au NP (e.g., $a_2=20$ and 30 nm) are always less than unit one in the whole spectrum (400–900 nm) for the non-Stokes-shift case, that is, a quenching rather than enhancement. Therefore, only the AEFs of bigger Au NP (e.g., $a_2=50$ nm) on the fluorescence with the Stokes shift will be discussed. The curves of AEF versus the emission wavelength λ_{em} for Au@SiO_2 of $a_2=50$nm and $t_s=25$nm irradiated by different lasers ($\lambda_{ex}=488$, 514, 561, 633, and 671 nm) are depicted in Figure 3.10a. The results of $a_2=60$nm are shown in Figure 3.10b. Figure 3.10 demonstrates that Au@SiO_2 behaves as a low-pass filter and amplifier with a cutoff wavelength of 590 nm. This is to say that Au@SiO_2 is only beneficial to those molecules with excitation and emission wavelengths longer than the SPR band of Au core (≈560 nm). This is because the interband transition of Au NP causes a severe dissipation of fluorescence in the region of $\lambda<560$ nm. Moreover, AEF depends on the size of Au core. The maximum AEF of $a_2=50$nm is obtained by a 633-nm laser irradiating, while the maximum one of $a_2=60$nm is obtained by a 671-nm laser. In addition, AEF depends on the molecule. For example,

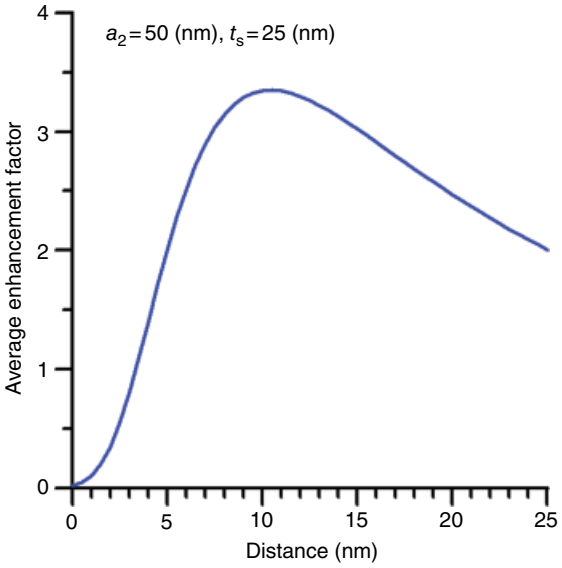

Figure 3.8 Distribution of AEF versus distances d between the molecules layer and Au core of Au@SiO_2 ($[t_s,a_2]=[25,50]$ nm) at $\lambda_{ex}=\lambda_{em}=633$ nm. The maximum AEF (3.35) is at $d=10.5$ nm. The AEF of the entire shell is 2.626 [123].

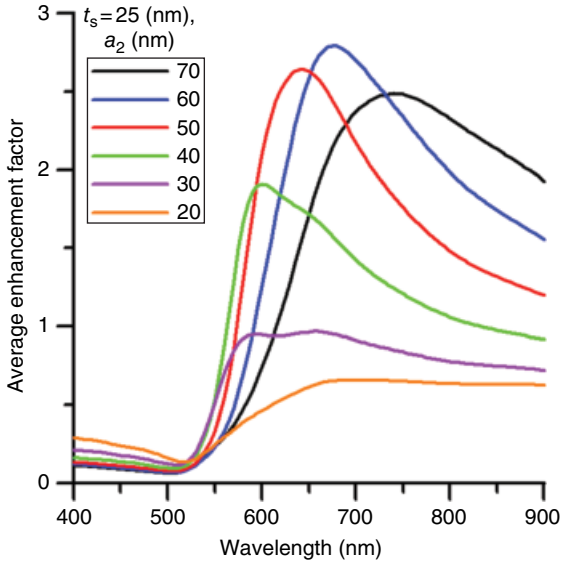

Figure 3.9 AEF versus wavelengths for Au@SiO_2 of $t_s=25$ nm with various a_2 in water [123].

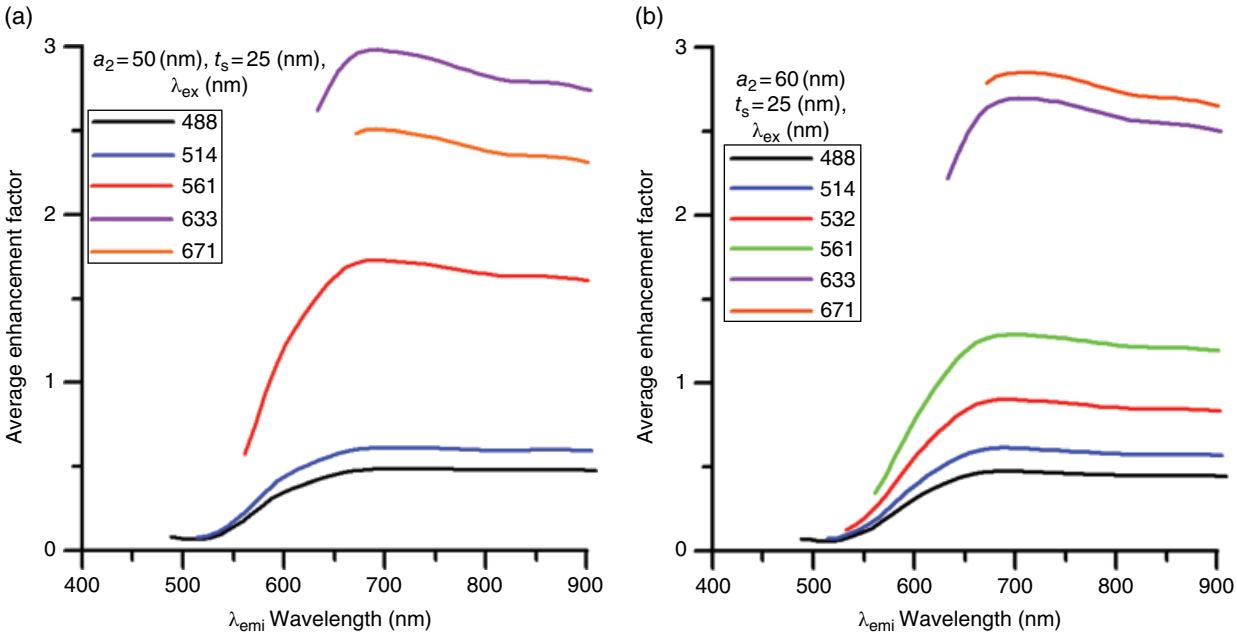

Figure 3.10 (a) AEF versus emission wavelengths λ_{em} for a molecule-doped Au@SiO_2 of $[t_s,a_2]=[25,50]$ nm irradiated by different lasers ($\lambda_{ex}=488$ nm, 514 nm, 561 nm, 633 nm, 671 nm). (b) AEF for a larger Au@SiO_2 of $[t_s,a_2]=[25,60]$ nm [123].

for FITC-doped Au@SiO_2 ($[t_s,a_2]=[25,50]$ nm), AEF is 0.15 at $\lambda_{ex}=488$ nm, $\lambda_{em}=520$ nm, and for Rhodamine 6G-doped Au@SiO_2 of the same size, AEF is 0.192 at $[\lambda_{ex},\lambda_{em}]=[514,554]$ nm. For both cases, a quenching on florescence is caused by Au@SiO_2. In contrast, for Alexa 633-doped Au@SiO_2 of optimized size ($[t_s,a_2]=[25,50]$ nm), AEF is 2.844 at $[\lambda_{ex},\lambda_{em}]=[633,653]$ nm. Similarly, for Cy 5.5-doped Au@SiO_2 of optimized size ($[t_s,a_2]=[25,60]$ nm), AEF is 2.844 at $[\lambda_{ex},\lambda_{em}]=[671,691]$ nm. Moreover, to enhance NIR fluorescence (e.g., ICG), Au NS [25, 26] can be adopted, instead of Au@SiO_2.

3.3.1.2 $Ag@SiO_2$

Consider core–shell $Ag@SiO_2$ submerged in water irradiated by a polarized plane wave [124]. The ECSs of $Ag@SiO_2$ of $t_s = 15$ nm with different core radii a_2 (20, 25, 30 nm) irradiated by a plane wave are shown in Figure 3.11. Figure 3.11 indicates that there are two SPR bands corresponding to the dipole mode and the quadrupole mode. For the dipole mode, the peaks of different sized $Ag@SiO_2$ are at 410 nm, 420 nm, and 435 nm for $a_2 = 20$ nm, 25 nm, and 30 nm, respectively. This implies that the dipole mode is redshifted as the Ag core increases. Moreover, the bandwidth of the dipole mode becomes broader as the core increases. In contrast, for the quadrupole mode, the peaks are almost the same at 380 nm for the three different cases but become sharper as the core increases. For example, the electric fields, the cross sections of $|\mathbf{E}_r|$ and $|\mathbf{E}_\theta|$ in the xz-plane, of $Ag@SiO_2$ irradiated by an x-polarized plane wave of 420 nm are shown in Figure 3.12a and b, where $[t_s, a_2] = [15,25]$ nm. Figure 3.12 exhibits the pattern of the dipole mode.

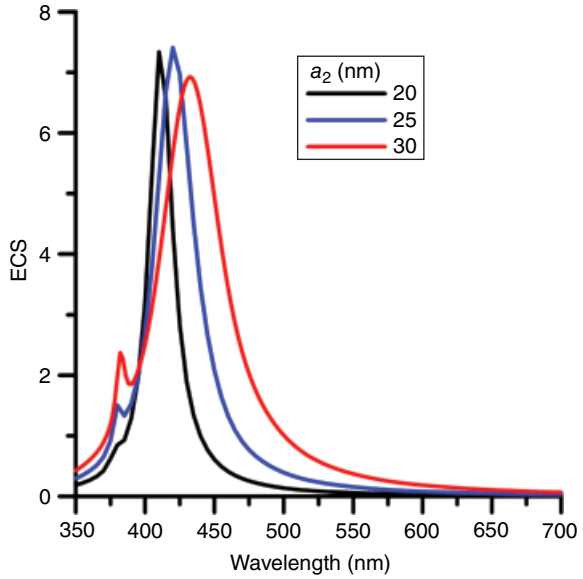

Figure 3.11 ECSs of $Ag@SiO_2$ of $t_s = 15$ nm with different core radii a_2 (20, 25, 30 nm) irradiated by a plane wave.

Furthermore, we assume there is no Stokes shift between the excitation and the emission spectra of molecules; that is, $\lambda_{em} = \lambda_{ex}$. Consider a typical $Ag@SiO_2$ of $[t_s, a_2] = [15,25]$ nm containing a single molecule embedded in the middle of the silica shell, as shown in Figure 3.1. The EFs at four typical positions (points A, B, C, and D) with a distance ($d = 7.5$ nm) to the surface of Ag core are analyzed at 420 nm, which is exactly at the dipole mode of $Ag@SiO_2$. The 3D spherical plot of the EF for an electric dipole versus the dipole orientations at point A is depicted in Figure 3.13a, which is like a dumbbell. The xz-plane cross section of this profile is shown in Figure 3.13b. The maximum EF of point A is obtained when the dipole's orientation is along the x-axis, parallel to the polarization of the incident light. The 3D spherical plots of EF at points B, C, and D are shown in Figure 3.13c, e, and g, respectively, and Figure 3.13d, f, and h corresponds to their xz-plane or xy-plane cross sections. Figure 3.13 illustrates that EF is dependent on the molecular location and orientation. Furthermore, we average the EF of all possible orientations at each point to obtain EEF. Subsequently, we consider a monolayer of molecules with a fixed distance ($d = 7.5$ nm) to the surface of Ag core. The 3D spherical

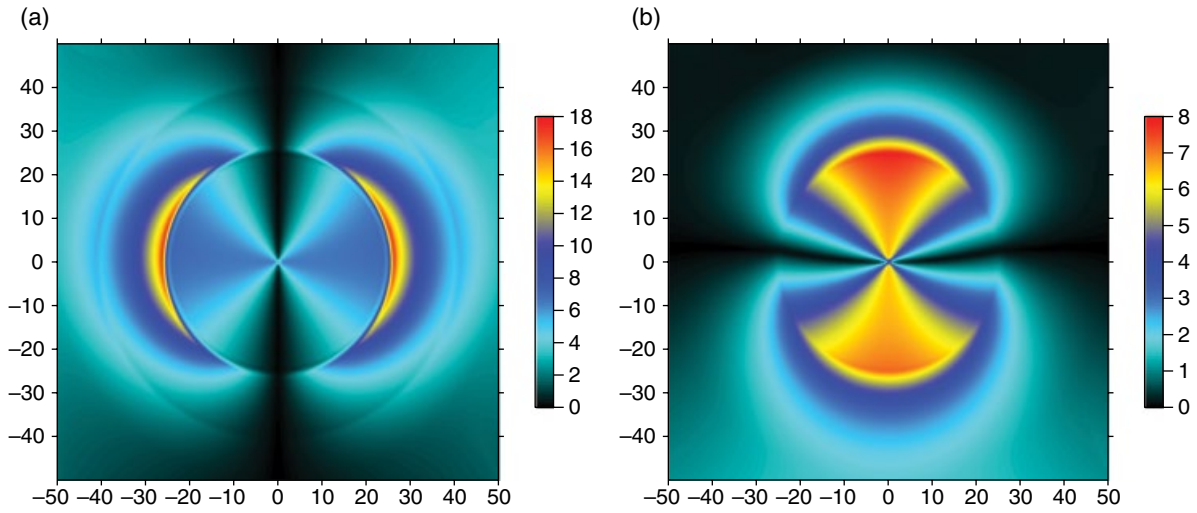

Figure 3.12 (a) The cross section of $|\mathbf{E}_r|$ and (b) $|\mathbf{E}_\theta|$ in the xz-plane of $Ag@SiO_2$ in water irradiated by a plane wave of 420 nm at the dipole mode, where $[t_s, a_2] = [15,25]$ nm.

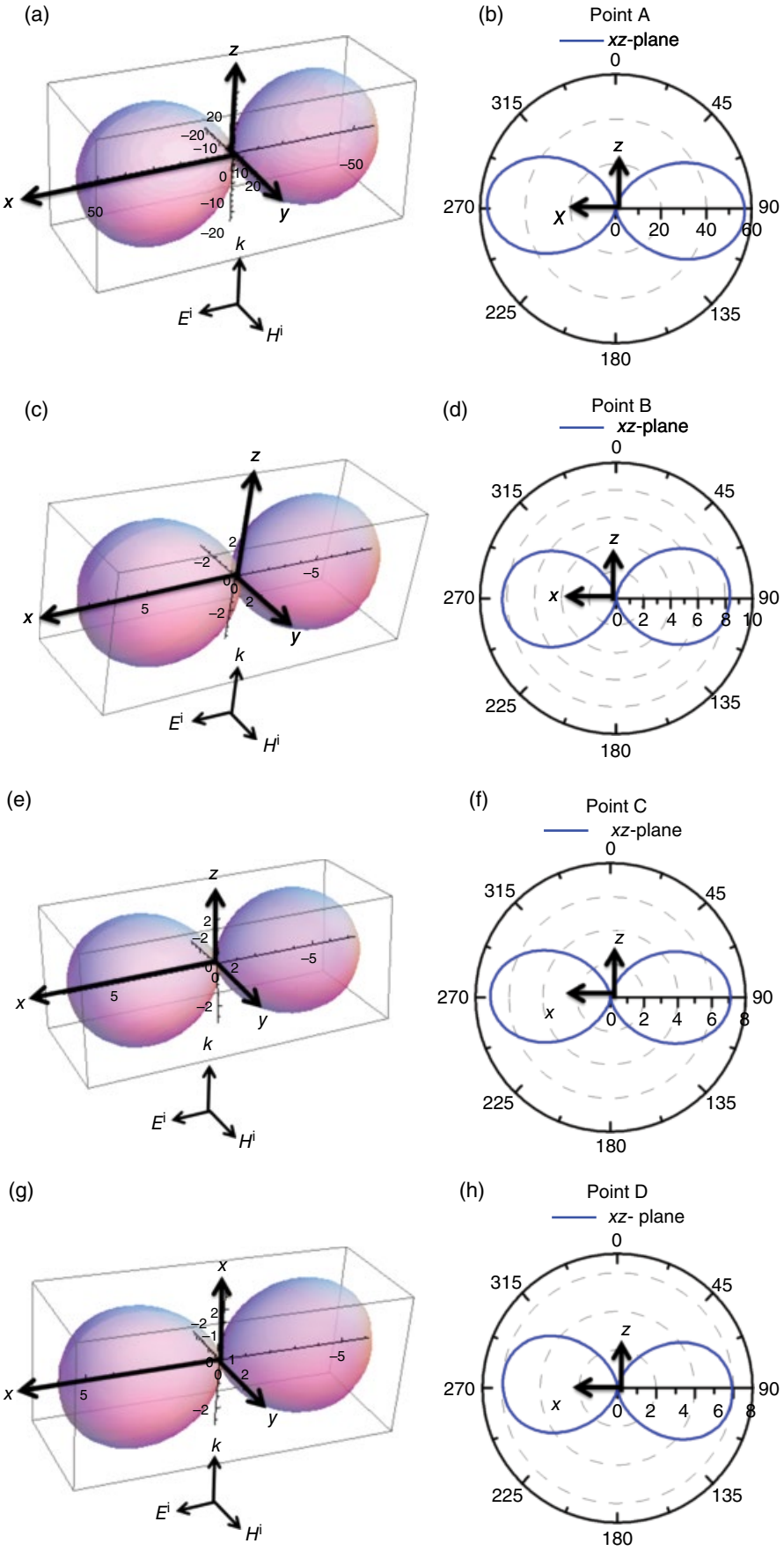

Figure 3.13 (a) 3D profile of EF versus dipole orientations at $\lambda_{ex} = \lambda_{em} = 420$ nm for a core–shell Ag@SiO_2 ($[t_S, a_2] = [15, 25]$nm) containing a molecule located at point A. (b) The *xz*-plane cross sections of (a), (c), (e), and (g) are EF at points B, C, and D. (d), (f), and (h) are the *xz*-plane or *xy*-plane cross sections of (c), (e), and (g), respectively [124].

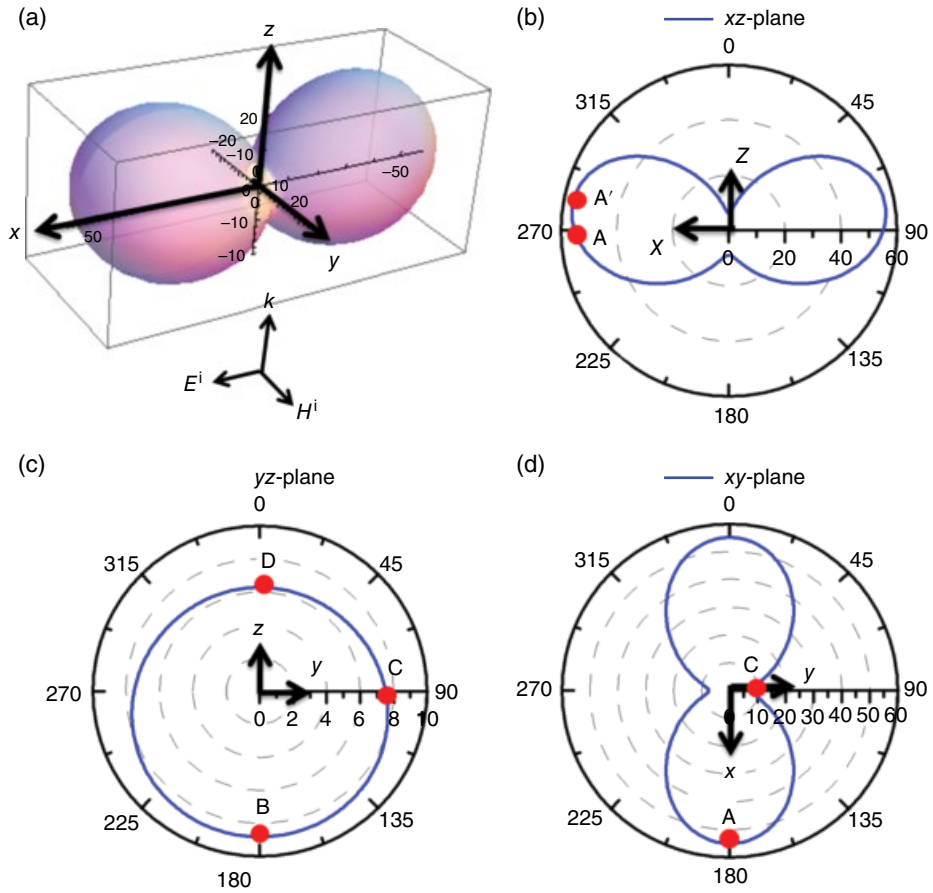

Figure 3.14 (a) 3D profile of EEF versus molecule positions for a core–shell ($[t_s,a_2]=[15,25]$ nm) at $\lambda_{ex}=\lambda_{em}=420$ nm, where molecules locate at the middle layer of the shell ($d=7.5$ nm). (b) The *xz*-plane, (c) the *yz*-plane, and (d) the *xy*-plane cross sections of (a). AEF is 23.485 [124].

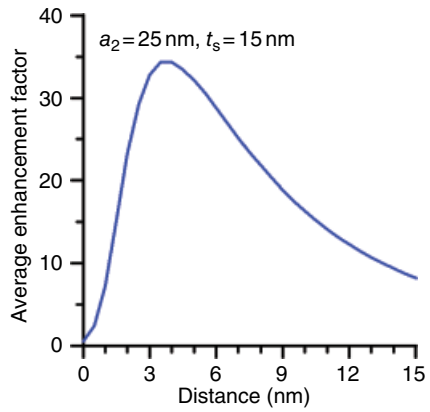

Figure 3.15 AEF versus distances *d* between the molecule layer and the Ag core of a core–shell ($[t_s,a_2]=[15,25]$nm) at $\lambda_{ex}=\lambda_{em}=420$nm. The maximum AEF (34.37) is at $d=4$ nm. The AEF of the entire shell is 18.78 [124].

plot of the EEF versus the molecular positions at $\lambda_{ex}=\lambda_{em}=420$ nm is depicted in Figure 3.14a. The *xz*-, *yz*-, and *xy*-plane cross sections of EEF are shown in Figure 3.14b, c, and d, respectively. Although both points A and C are on the equator of the Ag@SiO_2, the EEF (7.51) of point C is much less than EEF (55.05) of point A, as shown in Figure 3.14d. This is because the polarization of the incident plane wave is in *x*-direction and the wavelength is at the dipole mode of the Ag@SiO_2. Therefore, the SPR oscillation makes the electric field at point A much stronger than that at point C. Figure 3.14a and c shows that the minimum EEF (6.281) occurs at point D and the maximum EEF (56.55) occurs at point A′, with an angle 10° away from point A, as shown in Figure 3.14b. The EEF at point B is 8.819. Moreover, the AEF of Figure 3.14a is 23.485 for $d=7.5$ nm at $\lambda_{ex}=420$ nm.

Moreover, we consider the effect of the distance between the monolayer of molecules and the Ag core on AEF. Figure 3.15 shows the AEF versus d at $\lambda_{ex}=\lambda_{em}=420$ nm, where $[t_s,a_2]=[15,25]$ nm. The

AEF of the entire shell is 18.78. The maximum AEF (34.37) occurs at $d = 4$ nm. In addition, the AEF is less than one, when $d < 1$ nm. It indicates that a quenching phenomenon will be caused for those molecules within this area.

The AEF versus wavelengths is shown in Figure 3.16 for Ag@SiO_2 of $t_s = 15$ nm with different core radii a_2. Figure 3.16 indicates there is an optimal a_2, about 20 nm, for obtaining a narrowband (400–430 nm) AEF with a maximum peak at 420 nm. Moreover, the smaller the Ag core, the narrower the spectrum of AEF. If the radius of the Ag core is larger than 40 nm, the AEF spectrum of Ag@SiO_2 is partitioned into two bands: a narrow shorter-wavelength band (quadrupole mode) and a broad longer-wavelength band (dipole mode). However, for a larger Ag@SiO_2, the AEF in both bands becomes smaller, as shown in Figure 3.16.

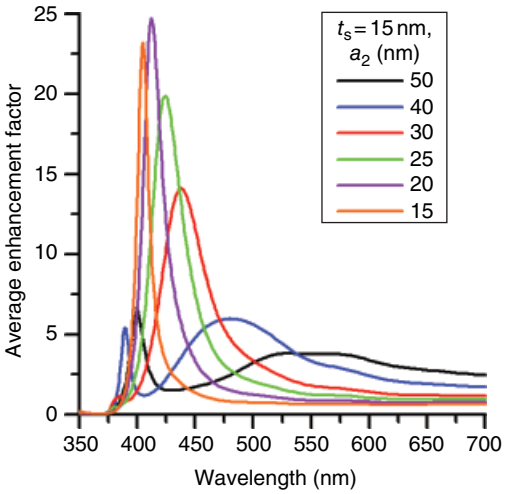

Figure 3.16 AEF versus wavelengths for Ag@SiO_2 of $t_s = 15$ nm with different core radii a_2 [124].

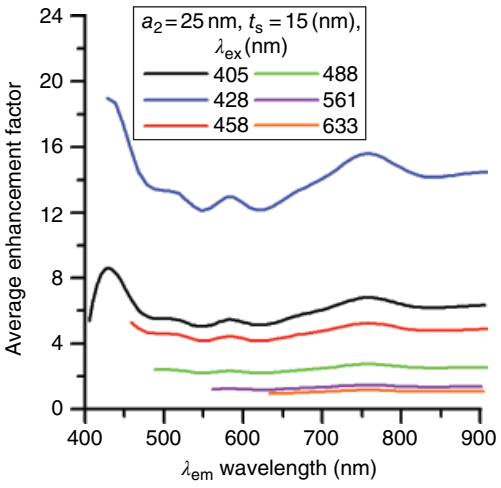

Figure 3.17 AEF versus emission wavelengths λ_{em} for a molecule-doped Ag@SiO_2 of $a_2 = 25$ nm, $t_s = 15$ nm excited by different lasers (λ_{ex} = 405, 428, 458, 488, 561, and 633 nm) [124].

To illustrate the Stokes-shift effect ($\lambda_{em} \geq \lambda_{ex}$), each curve of AEF versus the emission wavelength is plotted corresponding to a given excitation wavelength, where the starting point of the emission wavelength λ_{em} is from λ_{ex}. Moreover, the Stokes-shift effect of molecular fluorescence spectra on the AEF is significant only when the molecular excitation spectrum overlaps the SPR band of the Ag NP. Therefore, due to the narrowband AEF, a molecule-doped Ag@SiO_2 is a highly molecule-selective enhancer for fluorescence. For those molecules, whose excitation spectrum is redshifted from the SPR band of the Ag NP, a larger Ag core is needed to provide a broadband AEF to cover their excitation spectrum for enhancing the fluorescence. Otherwise, a quenching, rather than an enhancement, could be obtained for the molecular fluorescence by using Ag@SiO_2. For example, a larger Ag@SiO_2 ($[t_s, a_2] = [11,65]$ nm) still can provide a 2.85-fold AEF for Alexa 647 dye at $[\lambda_{ex}, \lambda_{em}] = [645,685]$ nm, which is stronger than the 1.02-fold AEF of a smaller one ($[t_s, a_2] = [15,25]$ nm).

Subsequently, the Stokes-shift effect of molecular fluorescence on the AEF will be discussed. The AEF versus the emission wavelengths λ_{em} for Ag@SiO_2 of $[t_s, a_2] = [15,25]$ nm irradiated by different excitation-wavelength lasers (λ_{ex} = 405, 428, 458, 488, 561, and 633 nm) is shown in Figure 3.17. It is easy to see that the AEF of $\lambda_{ex} = 428$ nm is much higher than the others. This is because $\lambda_{ex} = 428$ nm is near the wavelength of SPR mode (420 nm) of the Ag@SiO_2, which is the dipole mode. Therefore, Ag@SiO_2 has a high selectivity for enhancing molecular fluorescence. For example, for Alexa 430 dye-doped Ag@SiO_2, the AEF is 12.34 at $[\lambda_{ex}, \lambda_{em}] = [428,538]$ nm, whereas for CYe-doped one, the AEF is 5.046 at $[\lambda_{ex}, \lambda_{em}] = [405,550]$ nm. For FITC-doped Ag@SiO_2, AEF is 2.406 at $[\lambda_{ex}, \lambda_{em}] = [488,518]$ nm.

To verify the model of AEF, the numerical data are compared with the experimental data of Ag–Au@SiO_2 [29] on the fluorescence of a specific molecule, $Ru(dpp)_3^{2+}$. In Ref. [29], Ag–Au (4:1) alloy was synthesized as the core and then coated with a 5 nm silica layer. After that, a monolayer of molecule was attached on the outer surface of silica. The molecule $Ru(dpp)_3^{2+}$ has a large Stokes shift with an excitation peak at 450 nm and an emission peak at 620 nm. Since the frequency-dependent permittivity of the Ag–Au alloy is not known, the permittivity of Ag [131] is adopted instead for simulation. Figure 3.18 shows the theoretical AEF of $d = 5$ nm compared to the experimental data for various a_2. Roughly, the theoretical AEF is in

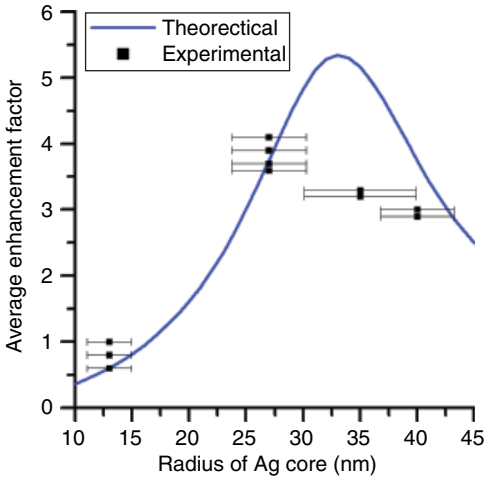

Figure 3.18 AEF of Ag@SiO_2 of a 5 nm silica layer with molecules attached on the outer surface excited by a laser of $\lambda_{ex} = 450$ nm for emission of $\lambda_{em} = 620$ nm compared to the experimental data of Ref. [29, 124].

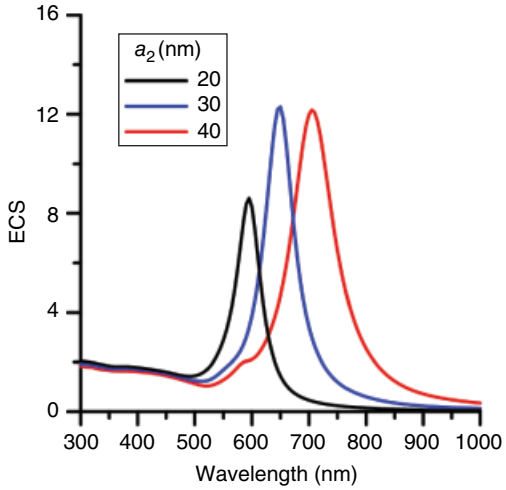

Figure 3.19 ECSs of Au NS of $t_s = 10$ nm with different radii a_2 (20, 30, 40 nm).

accordance with the experimental data. The error bars of the experiment result from the size uniformity of Ag core, which the discrepancy between the theoretical and experimental data is attributed to.

3.3.2 Nanoshelled Nanocavity

In this section, the AEF of NS on the fluorescence of an encapsulated molecule will be analyzed. The major works are referred to Ref. [125]. For this problem, an important theoretical work was reported in Refs. [46, 47]. The configuration of NS is shown in Figure 3.2. The thickness of the metal shell is denoted by t_s ($t_s = a_1 - a_2$), where a_1 and a_2 are the outer radii of the metal shell and the silica core, respectively. When an NS is irradiated by an incident wave at SPR mode, the electric field in the core can be amplified. Therefore, NS can be utilized to raise the excitation rate of an encapsulated molecule (or a quantum dot). However, once the molecule is excited, a part of its fluorescence will be dissipated by the metallic shell due to Ohm's loss. Therefore the overall effect of NS should be evaluated carefully in order not to overestimate its performance. Recently, the Mie theory and finite element method [112] have been also utilized to analyze the interaction of a dipole with Ag NS, and a quasi-static approximation [119] solved by the finite difference time domain (FDTD) method has been used to simulate the plasmonic enhancement on the emission of an emitter at the center of NS.

3.3.2.1 Au NS

Consider Au NS submerged in water irradiated by a polarized plane wave. The ECSs of Au NS of $t_s = 10$ nm with different core radii a_2 (20, 30, 40 nm) irradiated by a plane wave are shown in Figure 3.19. The major SPR band of ECS belongs to the dipole mode. The peaks of these bands are at 600 nm, 650 nm, and 705 nm corresponding to $a_2 = 20$ nm, 30 nm, and 40 nm, respectively. The quadrupole mode is not obvious; for example, there is a shoulder at 585 nm for the case of $a_2 = 40$ nm.

Further, the AEFs of Au NS of $t_s = 10$ nm on the fluorescence of a single molecule doped in the silica core with different radii a_2 (20, 30, 40, 50 nm) are shown in Figure 3.20a. It indicates that the AEF for a molecule located at the center of the core is larger than that for a molecule randomly located in the core. Moreover, the larger the silica core, the more redshifted the SPR band of Au NS and the larger the bandwidth. In addition, the optimal radius of the core is about 30 nm to obtain the maxima of AEF for $t_s = 10$ nm. It is tradeoff that the apparent quantum yield increases as the core size increases, while the excitation rate is reduced. Therefore there is an optimal size for maximizing AEF. This behavior is frequency dependent. Moreover, the results of Au NS of $a_2 = 30$ nm with different thicknesses of Au shell ($t_s = 5$, 10, and 20 nm) are shown in Figure 3.20b. These curves show that Au NS with a thinner shell has a stronger AEF, and the SPR band becomes narrower as well as more redshifted. Therefore, Au NS with a thinner shell possesses a higher selectivity for enhancing the fluorescence of a specific molecule. For a bigger Au NS (e.g., $a_2 = 40$ or 50 nm), there is an unobvious shoulder in the AEF curve, which corresponds to the quadrupole mode.

If the Stokes-shift effect of the molecular fluorescence is further considered, the frequency-dependent AEF becomes more complicated; that is, AEF depends

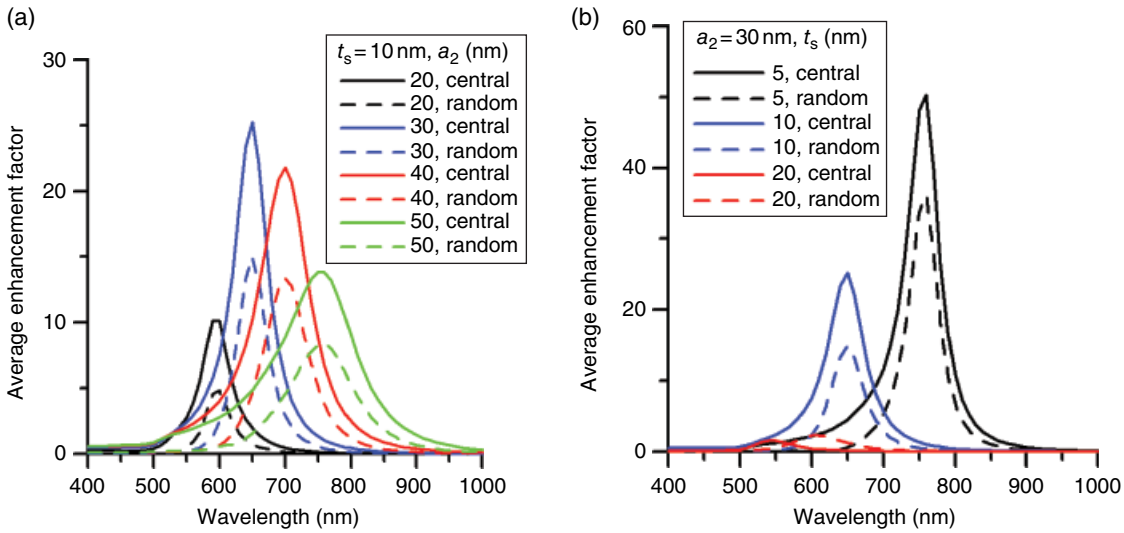

Figure 3.20 (a) AEF versus wavelengths for Au NS of $t_s = 10$ nm with different radii a_2 (20, 30, 40, 50 nm) of silica core. (b) AEF versus wavelengths for Au NS of $a_2 = 30$ nm with different thicknesses of Au shell t_s (5, 10, 20 nm). Solid line: molecule is at the center of core. Dashed line: molecule is randomly located in core [125].

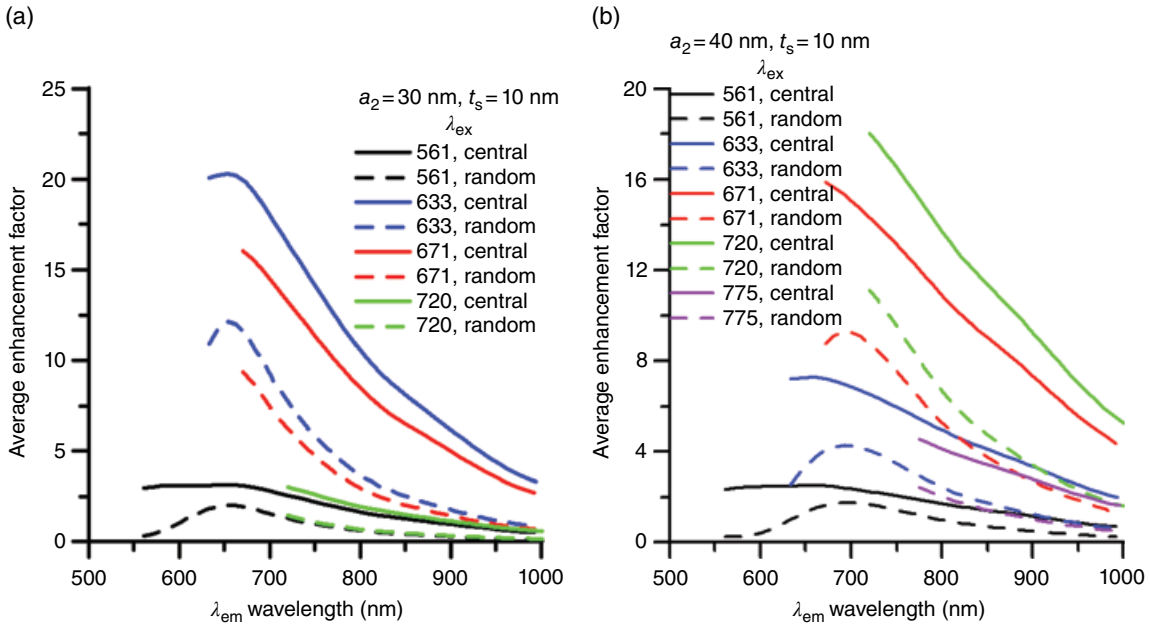

Figure 3.21 (a) AEF versus emission wavelengths for Au NS of $[t_s, a_2] = [10,30]$ nm excited by lasers of different wavelengths (561, 633, 671, and 720 nm). (b) AEF of $[t_s, a_2] = [10,40]$ nm excited by lasers of different wavelengths (561, 633, 671, 720, and 775 nm). Solid line: molecule is at the center of core. Dashed line: molecule is randomly located in core [125].

both on the excitation and emission wavelengths. Figure 3.21a shows the curves of AEF versus λ_{ex} for Au NS of $[t_s, a_2] = [10,30]$ nm excited by different lasers ($\lambda_{ex} = 561$, 633, 671, and 720 nm). For comparison, the results of a bigger Au NS of $[t_S, a_2] = [10,40]$ nm excited by different lasers (λ_{ex} = 561, 633, 671, 720, and 775 nm) are shown in Figure 3.21b. Again, these curves show that AEF of the molecule located at the core center is always stronger than that of the one randomly located in the core. The optimal λ_{ex} is 633 nm to obtain a maximum AEF curve for $a_2 = 30$ nm. This finding is in agreement with the results of Figure 3.20a for the non-Stokes shift; a maximum AEF occurs at 650 nm for $a_2 = 30$ nm. In contrast to a larger one of $a_2 = 40$ nm, the optimal λ_{ex} is 720 nm to obtain a maximum AEF. The result demonstrates that the

frequency-selective enhancement on the fluorescence is also dependent on the core size. In addition, the AEF of Au NS decreases as the Stokes shift (the wavelength difference of $\lambda_{em} - \lambda_{ex}$) increases.

3.3.2.2 Ag NS

Consider Ag NS submerged in water irradiated by a polarized plane wave. The ECSs of Ag NS of $t_s = 10$ nm with different radii of core, $a_2 = 20$, 30, and 40 nm, are plotted in Figure 3.22 to show the SPR modes. The dipole mode of $a_2 = 20$ nm is at 495 nm, and the quadrupole mode is at 405 nm. The dipole and quadrupole modes of $a_2 = 30$ nm are at 560 nm and 440 nm, respectively, and those of $a_2 = 40$ nm are at 630 nm and 475 nm. In addition, there is a small peak at 410 nm for the case of $a_2 = 40$ nm, which is the sextupole mode of Ag NS. The common peak of these cases of different sizes at 335 nm is the absorption band of Ag, not related to any SPR mode.

Furthermore, the AEFs of Ag NS of $t_s = 10$ nm with different radii a_2 (20, 30, 40, and 50 nm) on the fluorescence of an encapsulated molecule are plotted against the wavelength in Figure 3.23a. Here, we assume that there is no Stokes shift between the excitation and emission spectra of fluorescence, that is, $\lambda_{em} = \lambda_{ex}$. The results of a molecule located at the core center and randomly located in the core are plotted with solid line and dashed line, respectively. These curves show that AEF of the latter is always weaker than that of the former; for example, for $a_2 = 20$ nm and $t_s = 10$ nm, the peak value of AEF for a randomly located molecule is 58 at 495 nm, which is smaller than the value (88) for a molecule at the center. Moreover, the AEF of Ag NS decreases as the core size increases. For example, the peak of AEF of $a_2 = 30$ nm is 35 at 560 nm for a molecule located at the core center, while the peak value of $a_2 = 40$ nm is 18 at 630 nm. All these peaks of AEFs correspond to the dipole modes of Ag NS, as shown in Figure 3.22. For the quadrupole mode, the peaks are at 440 nm, 475 nm, and 510nm for the cases of $a_2 = 30$ nm, 40 nm, and 50 nm, respectively. In comparison with the dipole mode, the AEF at the quadrupole mode is relatively small. To illustrate the effect of the shell thickness on AEF, the results of $a_2 = 20$ nm with different thicknesses of Ag shell ($t_s = 5$, 10, and 20 nm) are shown in Figure 3.23b. This figure indicates that the thinner the shell, the more redshifted the SPR band and the larger the AEF. For example, the peaks of AEFs for the randomly located molecule are 180 at 590 nm for $t_s = 5$ nm and 57 at 490 nm for $t_s = 10$ nm. Moreover, the bandwidth becomes relatively narrower as the shell thickness and the core size decrease. These properties show that Ag NS is a tunable narrowband enhancer with a high selectivity to enhance photoluminescence.

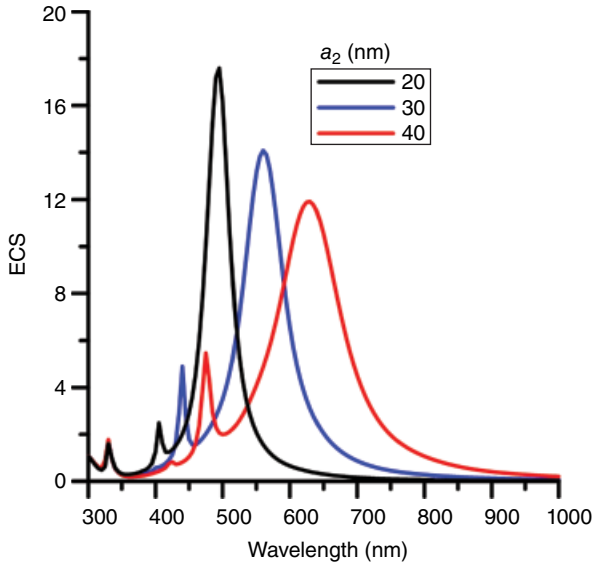

Figure 3.22 ECSs of Ag NS of $t_s = 10$ nm with different radii a_2 (20, 30, 40 nm).

Moreover, the effect of Stokes shift on AEF will be discussed in the following: Figure 3.24a shows the results of a smaller Ag NS of $[t_s, a_2] = [10, 20]$ nm excited by different lasers (λ_{ex} =458, 488, 514, 532, and 561 nm). The AEF of a molecule located at the core center is plotted as a solid line, and the data of a molecule randomly located in core as a dashed line. The AEFs of a bigger Ag NS with $[t_s, a_2] = [10, 30]$ nm excited by different lasers (λ_{ex} =488, 514, 532, 561, and 633 nm) against the emission wavelength are provided in Figure 3.24b for comparison. Again, AEF of the molecule located at the center of the core is always stronger than that of the one randomly located in the core. For the smaller Ag NS of $a_2 = 20$ nm, the maximum AEF curve is obtained at λ_{ex} =488 nm, while for the bigger Ag NS ($a_2 = 30$ nm), the maximum AEF occurs at λ_{ex} =561 nm. The behavior indicates that Ag NS is a frequency-selective enhancer, where the optimum excitation wavelength depends on the core size. Moreover, Figure 3.24a and b shows that the AEF decreases as the Stokes shift (the wavelength difference of $\lambda_{em} - \lambda_{ex}$) increases.

In summary, our results show that the AEF of Au or Ag NS on the fluorescence of a molecule randomly embedded in the silica core is lower than that at the core center. This nanoshelled nanocavity is a tunable enhancer. The major SPR band of NS for AEF is the dipole mode. In contrast, the minor SPR band of the quadrupole mode exhibits a weaker enhancement on fluorescence, particularly for Au NS. The SPR band of Au NS is in the

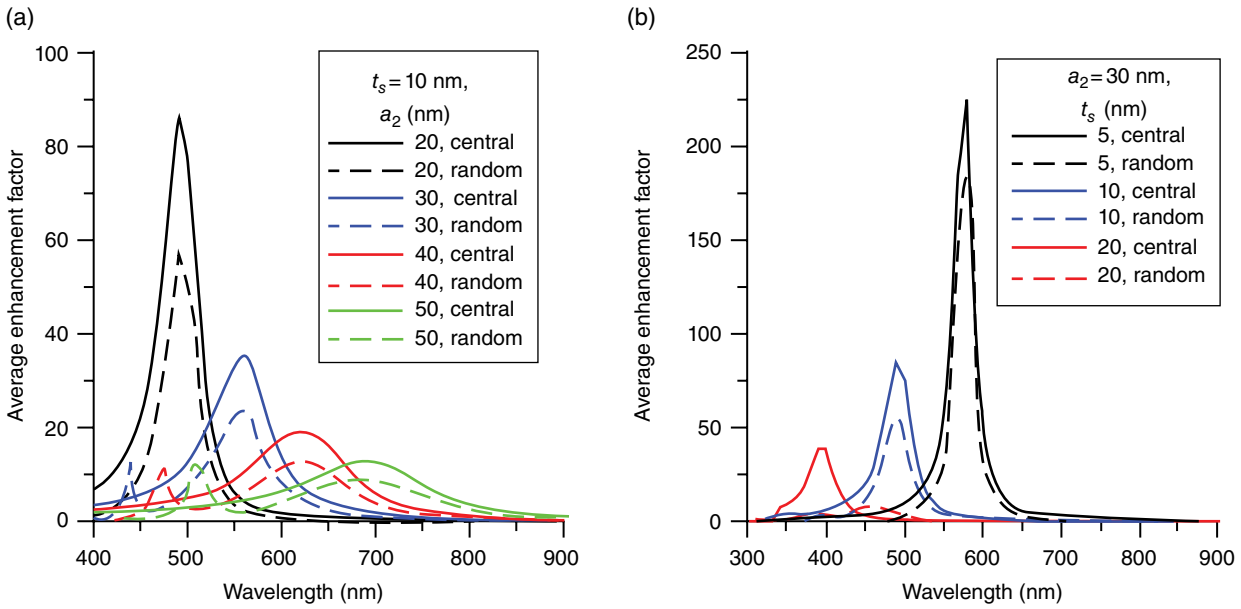

Figure 3.23 (a) AEF versus wavelengths for Ag NS of t_s = 10 nm with different radii a_2 (20, 30, 40, 50 nm) of silica core. (b) AEF versus wavelengths for Ag NS of a_2 = 20 nm with different thicknesses of Ag shell t_s (5, 10, 20 nm). Solid line: molecule is at the center of core. Dashed line: molecule is randomly located in core [125].

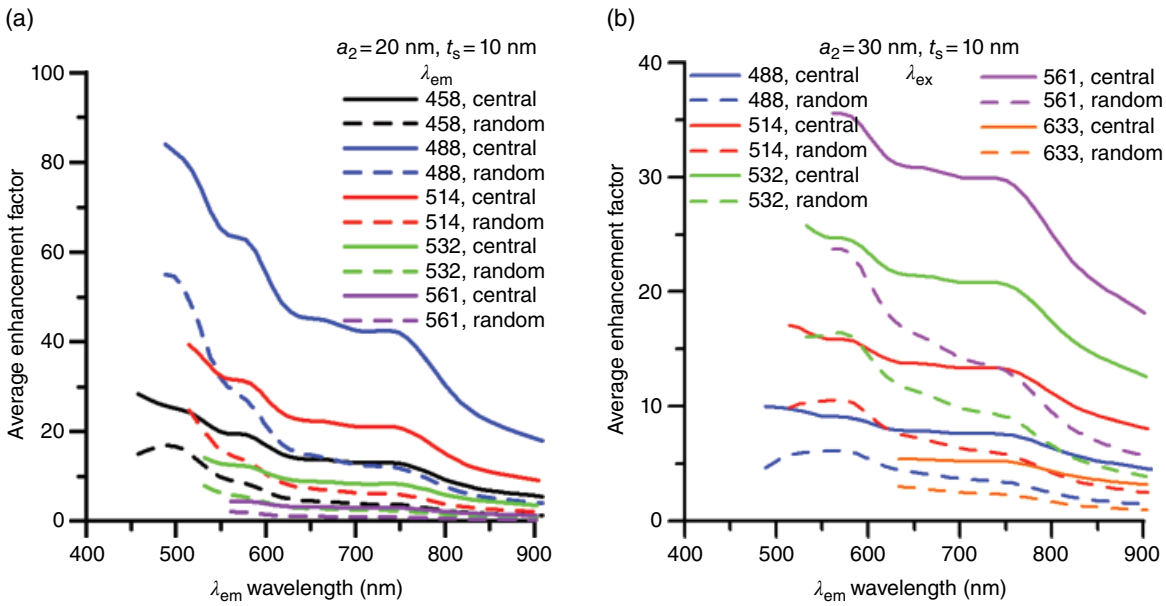

Figure 3.24 (a) AEF versus emission wavelengths for Ag NS of $[t_s,a_2]$ = [10,20] nm excited by lasers of different wavelengths (458, 488, 514, 532, and 561 nm). (b) AEF of $[t_s,a_2]$ = [10,30] nm excited by lasers of different wavelengths (488, 514, 532, 561, and 633 nm). Solid line: molecule is at the center of core. Dashed line: molecule is randomly located in core [125].

longer-wavelength regime and the bandwidth is broader, in comparison with Ag NS; for example, for Au NS of $[t_s,a_2]$ = [10,30] nm, the peak of AEF is at 650 nm, while the peak is at 560 nm for Ag NS with the same size. Moreover, the AEF of Au NS is lower than that of Ag NS. In addition, the thinner the metal shell, the more redshifted the SPR band and the larger the AEF.

3.3.3 NS@SiO_2

The other application of metal NS for SEF is to enhance the fluorescence of the molecule embedded in the outer silica layer, which attaches on NS. The configuration of NS@SiO_2 is shown in Figure 3.3. The thicknesses of the outer silica layer and metal shell are denoted by t_1 and t_2, respectively, where $t_1 = a_1 - a_2$

and $t_2 = a_2 - a_3$. Here a_1, a_2, and a_3 are the outer radii of the silica shell, NS, and the silica core, respectively. In this section, the far-field (e.g., SCS) and the near-field (excitation rate) optical responses of Au or Ag NS@SiO_2 irradiated by a plane wave are studied. The excitation rate and EF for a molecule embedded in the middle of the outer silica layer at four typical locations (points A, B, C, and D) will be discussed, as shown in Figure 3.3. Moreover, the AEF on a molecule embedded in the silica layer is investigated. In addition, the roles of the SPR modes of these NSs, particularly the dipole and quadrupole modes, playing on SEF will be discussed. The surrounding medium is water. The major works are referred to Refs. [126, 127].

3.3.3.1 Au NS@SiO_2

Consider Au NS@SiO_2 of $[t_1,t_2,a_3] = [25,15,50]$ nm submerged in water irradiated by a polarized plane wave [126]. The SCS, ACS, and ECS are shown in Figure 3.25. There are two SPR bands corresponding to the dipole mode and the quadrupole mode. The peak of the former is at 730 nm within the NIR regime, and that of the latter is at 580 nm. For comparison, the results of core–shell Au@SiO_2 of $[t_s,a_2] = [25,65]$ nm are also depicted in Figure 3.25 by the dashed line. The dipole mode of core–shell Au@SiO_2 is at 640 nm, but the quadrupole mode is not obvious. To verify the patterns of these SPR modes, the near-field distribution of the electric field around Au NS@SiO_2 of $[t_1,t_2,a_3] = [25,15,50]$ nm irradiated by a plane wave is studied. The cross sections of $|\mathbf{E}_r|$ and $|\mathbf{E}_\theta|$ in the

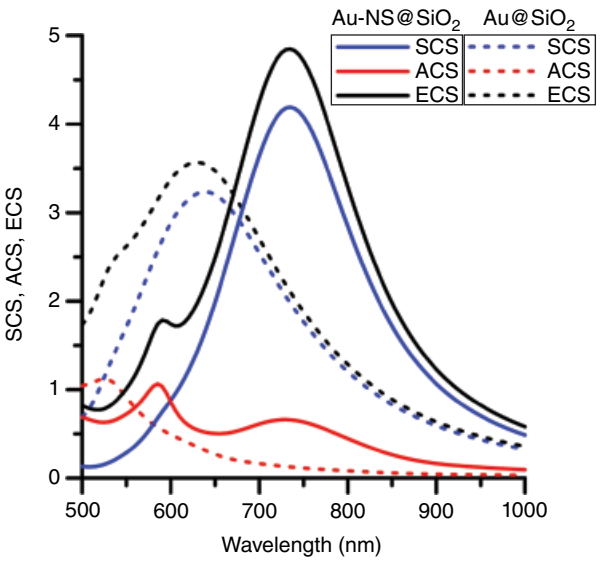

Figure 3.25 SCS, ACS, and ECS of Au NS@SiO_2 of $[t_1,t_2,a_3] = [25,15,50]$ nm irradiated by a plane wave (solid line). The results of core–shell Au@SiO_2 of $[t_s,a_2] = [25,65]$ nm (dashed line).

xz-plane are plotted in Figure 3.26 for the dipole modes at 730 nm, and the results of the quadrupole mode at 580 nm are shown in Figure 3.27.

First, we assume there is no Stokes shift for the fluorescence, that is, $\lambda_{em} = \lambda_{ex}$. We further discuss the EFs at four typical molecular points (A, B, C, and D) in the silica layer at a typical wavelength $\lambda_{ex} = 775$ nm, where $d = 12.5$ nm. This wavelength is in the NIR regime and close to the dipole mode. If the molecule is located at point A on the lateral side of Au NS for illumination, the 3D spherical plot of EF versus the dipole orientations looks like a dumbbell, as shown in Figure 3.28a. The distance of each point on this profile to the center represents the magnitude of EF for the corresponding orientation. The xz-plane cross section of Figure 3.28a is shown in Figure 3.28b. The optimal orientation at point A should be in the x-direction, which is the polarization direction of the incident plane wave. This is because for this wavelength, the major SPR behavior of the electron collective oscillation is the dipole mode of NS. If the molecule is located at point B on the front side of Au NS, the 3D spherical plot of EF becomes a butterfly shape, as depicted in Figure 3.28c, and the xz-plane cross section of this profile is plotted in Figure 3.28d. If the molecule is at point C, also on the same equator of the spherical Au NS (lateral side) as point A, the EF becomes much smaller than that of point A. The spherical plot of EF at point C is shown in Figure 3.28e and the xz-plane cross section in Figure 3.28f. The EF at point D is shown in Figure 3.28g, and the xz-plane cross section in Figure 3.28h. Figure 3.28 illustrates that EF depends on the molecular orientation and location sensitively. Furthermore, the spherical plot of EEF for molecule at various locations with the same distance ($d = 12.5$ nm) from the surface of Au NS at 775 nm is shown in Figure 3.29a. For the EEF, the molecular orientation effect has been averaged. In this spherical plot, the distance of each point of the profile to the center represents the magnitude of EEF for the position vector. The xz-, yz-, and xy-plane cross sections of the EEF are shown in Figure 3.29b, c, and d, respectively. This 3D profile illustrates that EEF is sensitive to the relative position of molecule not only to the Au NS but also to the direction and polarization of the incident wave. The minimum EEF (0.36) occurs at point D on the back side of the irradiated Au NS, and the maximum EEF (17.27) occurs at point A′, 14° away from point A, as shown in Figure 3.29b. The EEF of point B is 1.26, and the EEF of point C is 0.57, much less than that of point A (16.09). This is because the x-polarized incident light makes the SPR oscillation of the dipole mode along the x-direction, so the excitation rate at point

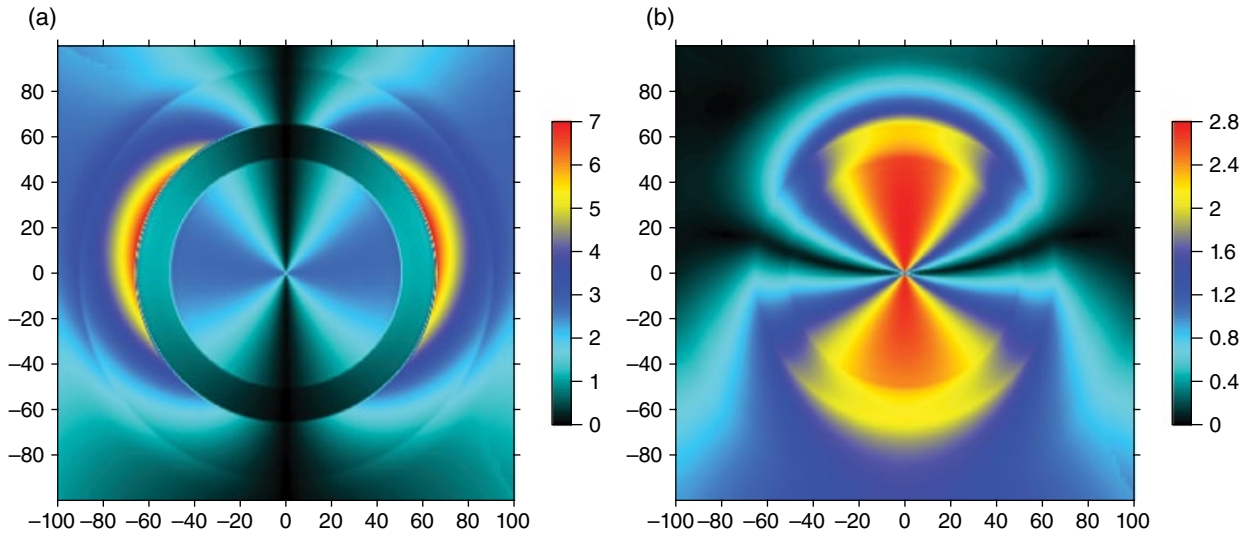

Figure 3.26 The cross sections of (a) $|\mathbf{E}_r|$ and (b) $|\mathbf{E}_\theta|$ in the *xz*-plane of Au NS@SiO_2 in water irradiated by a plane wave of 730 nm at the dipole mode, where $[t_1,t_2,a_3]=[25,15,50]$ nm.

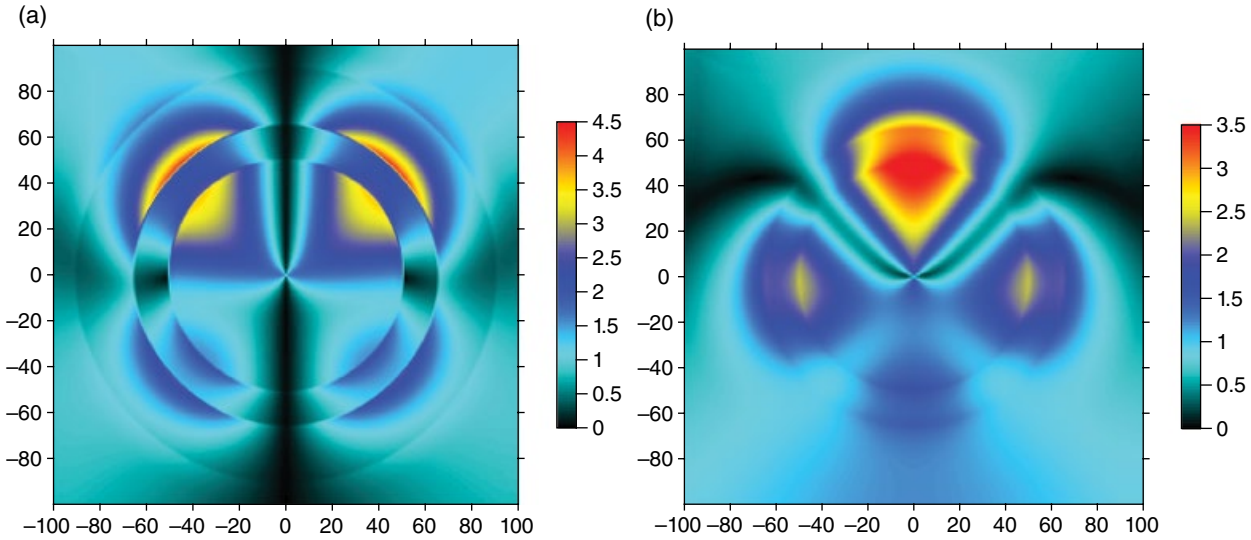

Figure 3.27 The cross sections of (a) $|\mathbf{E}_r|$ and (b) $|\mathbf{E}_\theta|$ in the *xz*-plane of Au NS@SiO_2 in water irradiated by a plane wave of 580 nm at the quadrupole mode, where $[t_1,t_2,a_3]=[25,15,50]$nm.

A is much stronger than that at point C. The AEF of Au NS@SiO_2 on the fluorescence of a monolayer of molecules embedded at $d=12.5$ nm is 5.82.

Subsequently, the distribution of AEF versus distance d between the monolayer of molecules and Au NS of $[t_1,t_2,a_3]=[25,15,50]$ nm at $\lambda_{ex}=\lambda_{em}=775$ nm is shown in Figure 3.30. Figure 3.30 indicates that the maximum AEF (6.45) is obtained if a monolayer of molecules is embedded at $d=8.5$ nm. In addition, when these molecules are too close to Au NS (say $d<2$ nm), AEF is less than unit one; that is, a quenching phenomenon is induced, if these molecules are too close to the Au NS. The AEF of the entire silica shell is 4.73. Moreover, the AEF versus wavelength for Au NS@SiO_2 of $t_2=15$ nm, $t_1=25$ nm with different a_3 is shown in Figure 3.31a. These curves of AEF show that Au NS@SiO_2 is a broadband enhancer. The range is dependent on the core size; for example, the enhancement range of $a_3=50$ nm covers 700–950 nm. The larger the silica core, the more broadened and redshifted the AEF spectrum. In addition, the peak value of AEF decreases as the core size increases. For example, the peak value of AEF for $a_3=35$ nm is 6.0 at 690 nm, while the peak value for $a_3=50$ nm is 4.6 at 775 nm. Moreover, the AEFs for Au NS@SiO_2 ($a_3=50$ nm, $t_1=25$ nm) with different

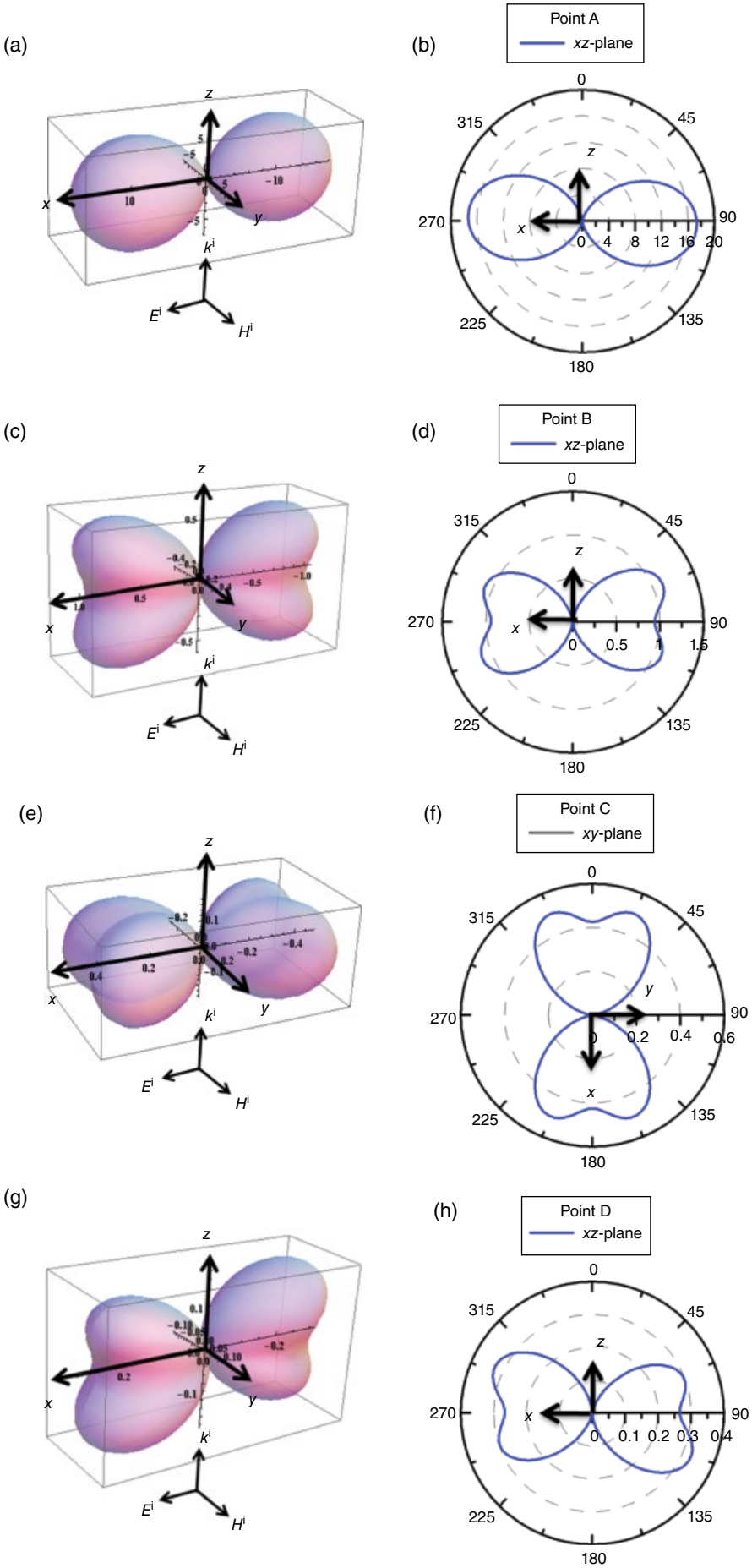

Figure 3.28 (a) Spherical plot of the 3D profile of EF versus dipole orientations at $\lambda_{ex} = \lambda_{em} = 775\,nm$ for Au NS@SiO_2 ($[t_1,t_2,a_3] = [25,15,50]\,nm$) containing a molecule located at point A. (b) The *xz*-plane cross section of (a), (c), (e), and (g) is an EF at points B, C, and D. (d), (f), and (h) are the *xz*-plane or *xy*-plane cross section of (c), (e), and (g), respectively [126].

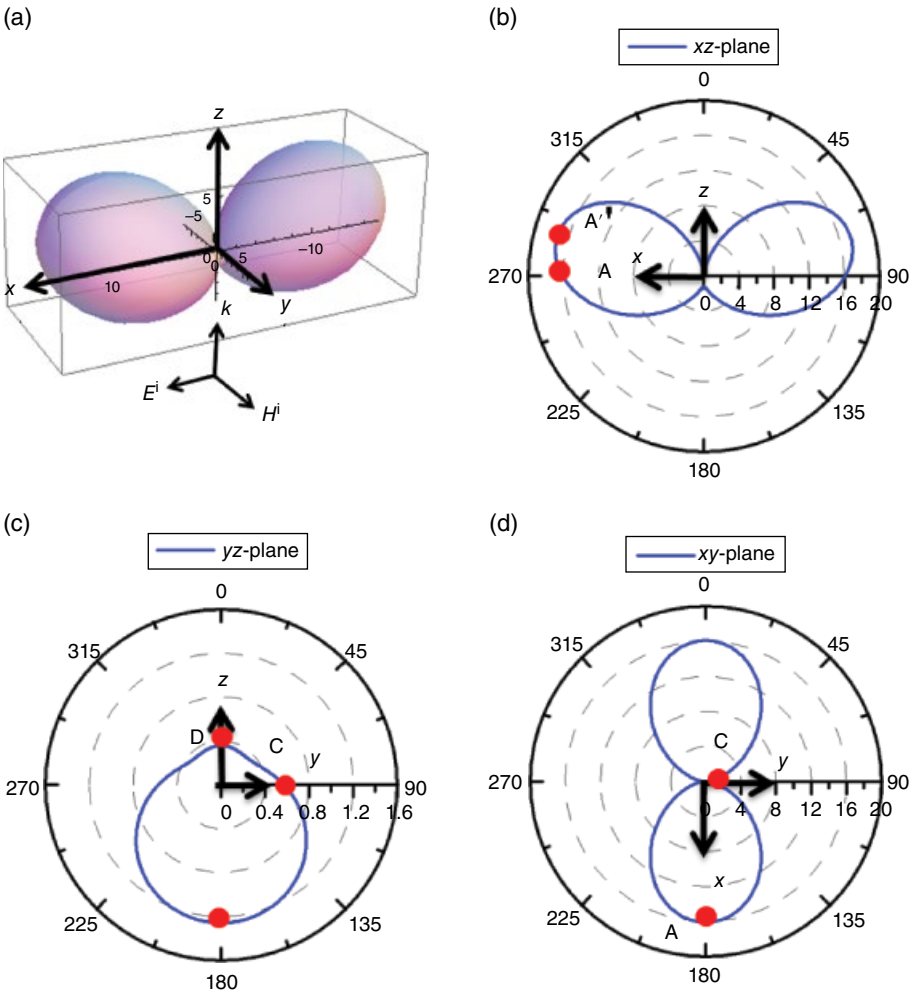

Figure 3.29 (a) Spherical plot of the 3D profile of EEF versus molecular positions for Au NS@SiO_2 ($[t_1,t_2,a_3]=[25,15,50]$ nm) at $\lambda_{ex}=\lambda_{em}=775$ nm, where these molecules are embedded in the middle layer of the silica shell ($d=12.5$ nm). (b) The *xz*-plane, (c) the *yz*-plane, and (d) the *xy*-plane cross sections of (a) [126].

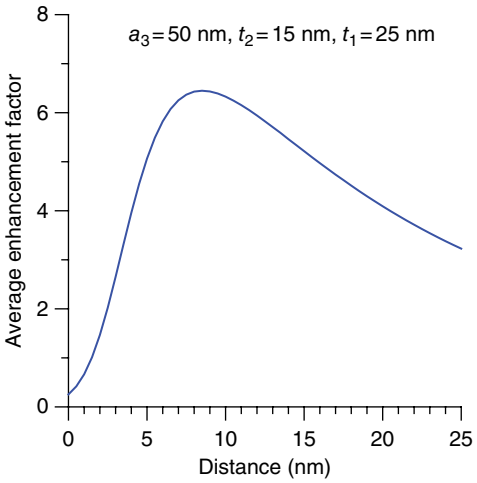

Figure 3.30 Distribution of AEF versus distances *d* between the molecule-doped layer and Au shell of Au NS@SiO_2 of $[t_1,t_2,a_3]=[25,15,50]$ nm at $\lambda_{ex}=\lambda_{em}=775$ nm. The maximum AEF (6.45) is at $d=8.5$ nm. The AEF of the entire shell is 4.73 [126].

t_2 are shown in Figure 3.31b. It shows that the thinner the Au shell, the more redshifted the peak of AEF is. These results of Figure 3.31 are in agreement with the finding of Ref. [7]; the SPR band redshifts as the ratio of the radius of the core to the thickness of the shell increases. The peak value of AEF increases as the thickness of Au shell decreases, particularly when $t_2 \leq 15$ nm. Moreover, the thickness effect of the outer silica on AEF is also studied, as shown in Figure 3.32 for Au NS@SiO_2 ($a_3=50$ nm, $t_2=15$ nm). Figure 3.32 indicates that the optimal thickness of the outer silica layer is about 25 nm.

Subsequently, we further discuss the Stokes-shift effect between the molecular excitation and emission spectra on AEF, that is, $\lambda_{em} \geq \lambda_{ex}$. Two different sizes of Au NS@SiO_2 ($a_3=35$ and 50 nm) with $t_2=15$ nm and $t_1=25$ nm are studied. The curves of AEF versus the emission wavelength λ_{em} for Au NS@SiO_2 irradiated by different lasers ($\lambda_{ex}=561$, 633, 671, 720, 775,

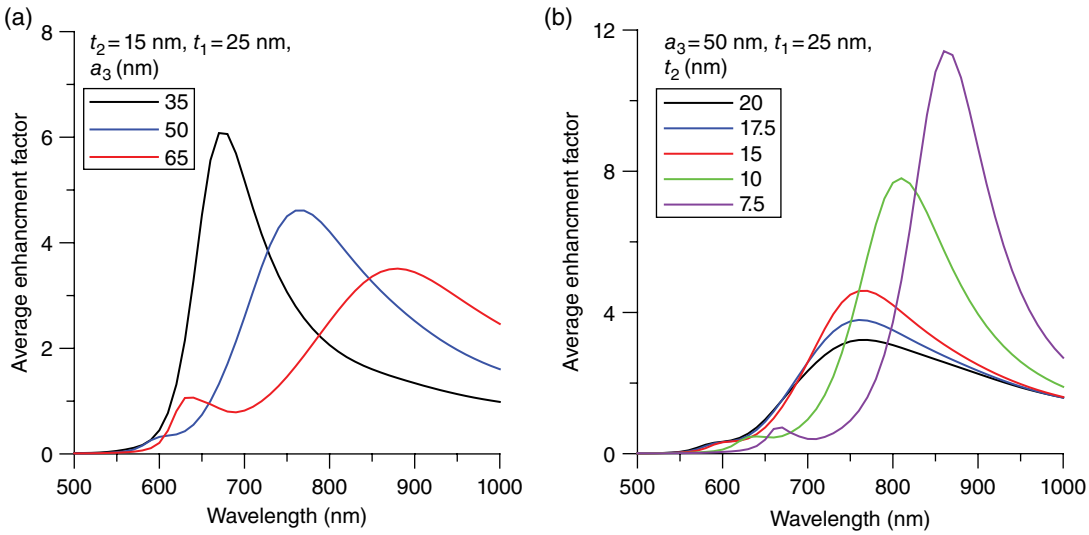

Figure 3.31 (a) AEF versus wavelength for Au NS@SiO_2 of t_2 = 15 nm, t_1 = 25 nm with different radii a_3 of the silica core. (b) AEF versus wavelength for Au NS@SiO_2 with different thicknesses t_2 of Au NS [126].

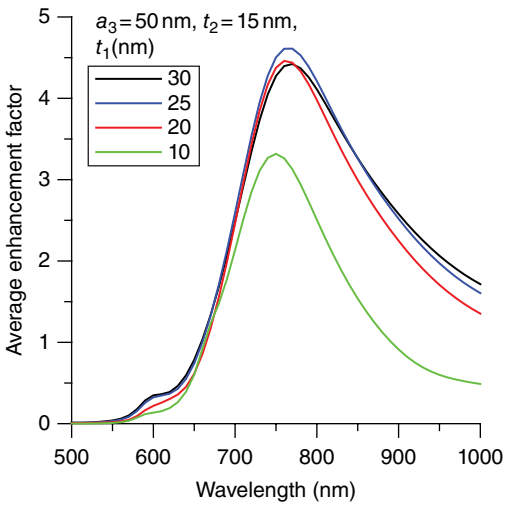

Figure 3.32 AEF versus wavelengths for Au NS@SiO_2 (a_3 = 50 nm, t_2 = 15 nm) with different thicknesses of the outer silica layer t_1 [126].

800, or 900 nm) are calculated. The results of a_3 = 35 nm and 50 nm are depicted in Figure 3.33a and b, respectively. Figure 3.33 illustrates that Au NS@SiO_2 is a molecule-selective fluorescence enhancer. The SPR band of Au NS is tunable and dependent on the core size. The larger the silica core, the more the redshift of the peak of AEF. For example, the maximum AEF is obtained for the case of a_3 = 35 nm excited by a 671-nm laser, and the maximum AEF curve is obtained for a_3 = 50 nm excited by a NIR laser of 775 nm. In other words, the optimum dimension of Au NS@SiO_2 is adjustable to match the molecular excitation and emission spectra for obtaining a maximum enhancement on a specific type of molecule. For example, for Cy 5.5-doped, a smaller Au NS@SiO_2 ($[t_1,t_2,a_3]$ = [25,15,35] nm) is preferred to obtain a maximum AEF (6.16) at $[\lambda_{ex},\lambda_{em}]$ = [671,691] nm. However, if a larger one of a_3 = 50 nm is used for Cy 5.5, AEF is 1.90, which is less than that of a_3 = 35 nm. In contrast, for the ICG-dye, a larger Au NS@SiO_2 of a_3 = 50 nm can be used to obtain a maximum AEF (4.54) at $[\lambda_{ex},\lambda_{em}]$ = [780,820] nm, while AEF is 2.38, if a smaller one of a_3 = 35 nm is used.

3.3.3.2 Ag NS@SiO_2

Consider Ag NS@SiO_2 submerged in water irradiated by a polarized plane wave [127]. The SCS, ACS, and ECS are shown in Figure 3.34a, where $[t_1,t_2,a_3]$ = [25,15,40] nm. For comparison, the results of core–shell Ag@SiO_2 of $[t_s,a_2]$ = [25,55] nm are also depicted in Figure 3.34a by the dashed line, and the results of bare Ag NS of $[t_s,a_2]$ = [15,40] nm are shown in Figure 3.34b. The SCS and ACS indicate that there are two SPR bands for Ag NS@SiO_2, Ag NS, and core–shell: one is a narrow shorter-wavelength band, which is the quadrupole mode, and the other is a broad longer-wavelength band, the dipole mode. For Ag NS@SiO_2, the former band is at 460 nm and that of the latter is at 610–650 nm. Moreover, there is another small peak at 410 nm, which corresponds to the sextupole mode of Ag NS@SiO_2. For the bare Ag NS, the sextupole mode is at 400 nm, the quadrupole mode is at 440 nm, and the broadband dipole mode is at 590 nm. Because the permittivity of the outer silica layer is higher than that of the surrounding medium (water), the corresponding SPR modes of Ag NS@SiO_2 are slightly redshifted from those of Ag NS of the

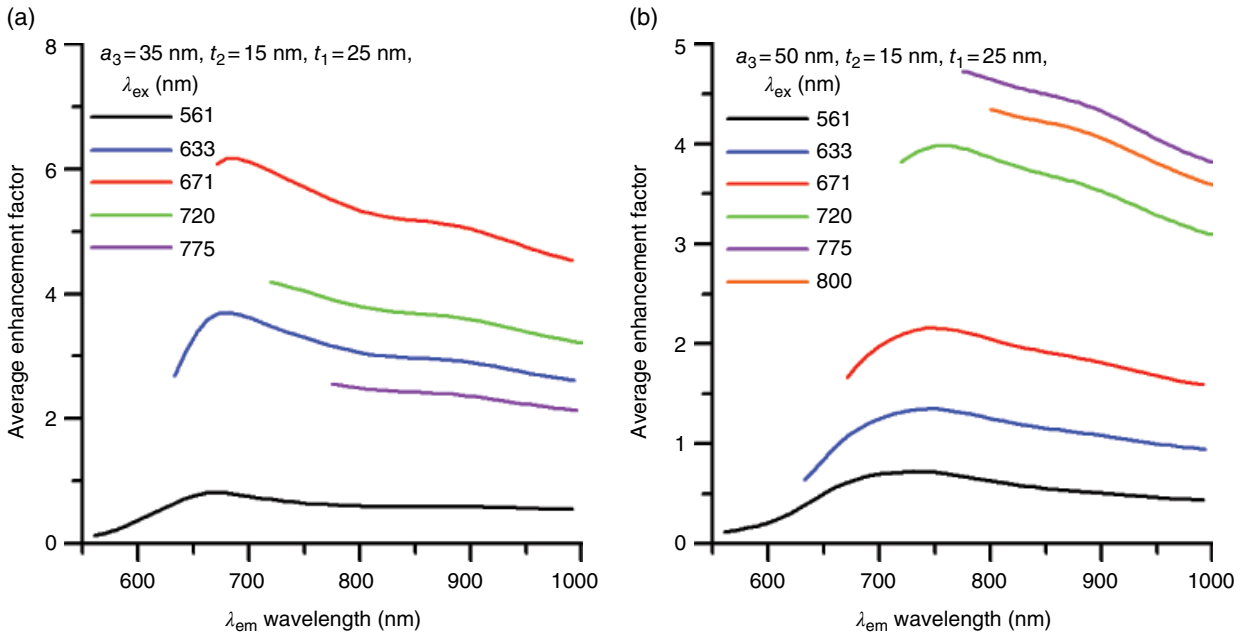

Figure 3.33 (a) AEF versus emission wavelengths λ_{em} for a molecule-doped Au NS@SiO_2 of $[t_1,t_2,a_3]$ = [25,15,35] nm excited at λ_{ex} = 561, 633, 671, 720, and 775 nm. (b) AEF of $[t_1,t_2,a_3]$ = [25,15,50] nm excited at λ_{ex} = 561, 633, 671, 720, 775, and 800 nm [126].

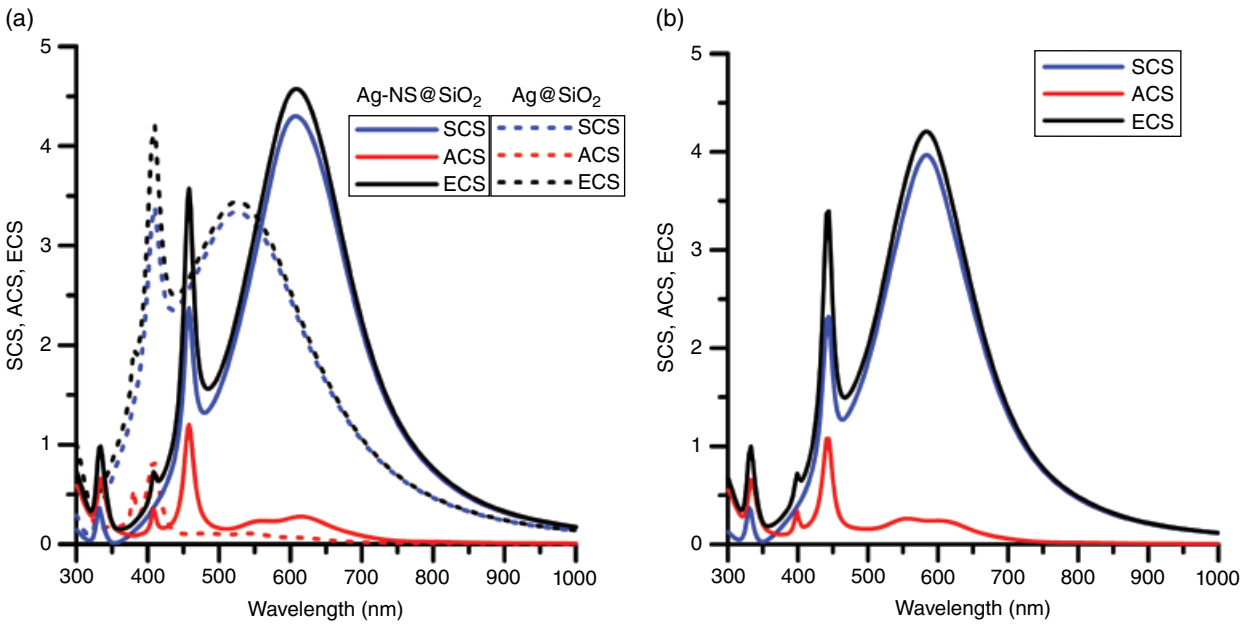

Figure 3.34 (a) SCS, ACS, and ECS of Ag NS@SiO_2 of $[t_1,t_2,a_3]$ = [25,15,40] nm irradiated by a plane wave (solid line). The results of core–shell Ag@SiO_2 of $[t_s,a_2]$ = [25,55] nm (dashed line). (b) SCS, ACS, and ECS of bare Ag NS of $[t_s,a_2]$ = [15,40] nm.

same size. In addition, for the core–shell Ag@SiO_2, the narrowband quadrupole mode is at 410 nm, and the broadband dipole mode is at 520 nm. In general, the corresponding SPR modes of Ag NS are redshifted from those of Ag NP of the same size. Moreover, the thinner the shell, the larger the redshift. To verify the patterns of these SPR modes, the near-field distribution of the electric field around Ag NS@SiO_2 of $[t_1,t_2,a_3]$ = [25,15,40] nm irradiated by a plane wave is studied. The cross sections of $|\mathbf{E}_r|$ and $|\mathbf{E}_\theta|$ in the *xz*-plane are plotted in Figure 3.35 for the dipole modes at 610 nm. The results of the quadrupole mode at 460 nm and the sextupole mode at 410 nm are shown in Figures 3.36 and 3.37, respectively.

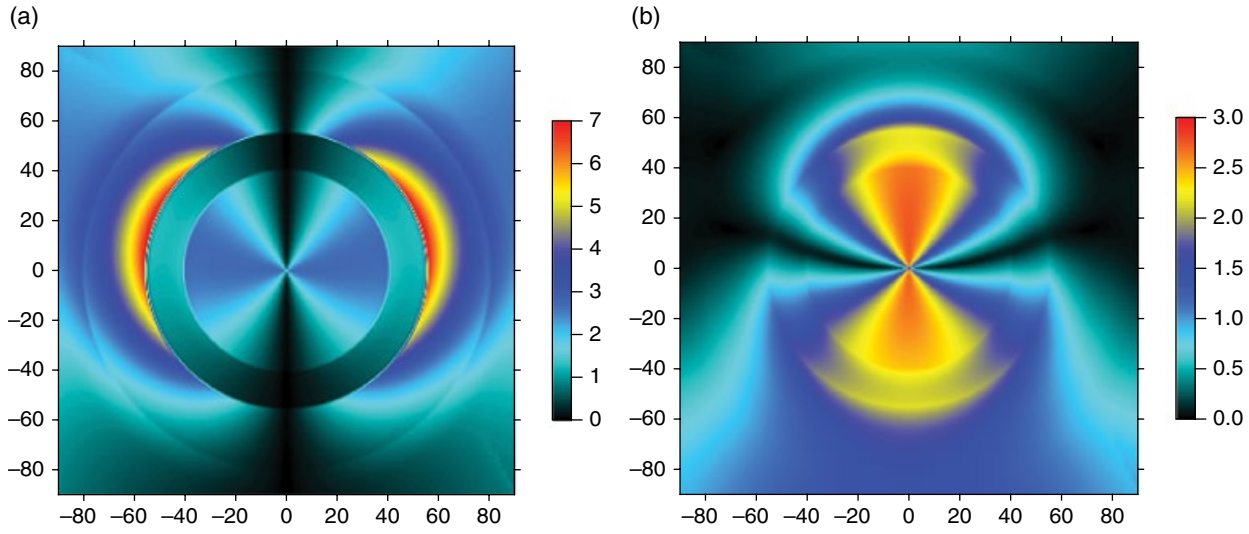

Figure 3.35 The cross sections of (a) $|\mathbf{E}_r|$ and (b) $|\mathbf{E}_\theta|$ in the *xz*-plane for Ag NS@SiO_2 in water irradiated by a plane wave of 610 nm at the dipole mode, where $[t_1,t_2,a_3]=[25,15,40]$ nm.

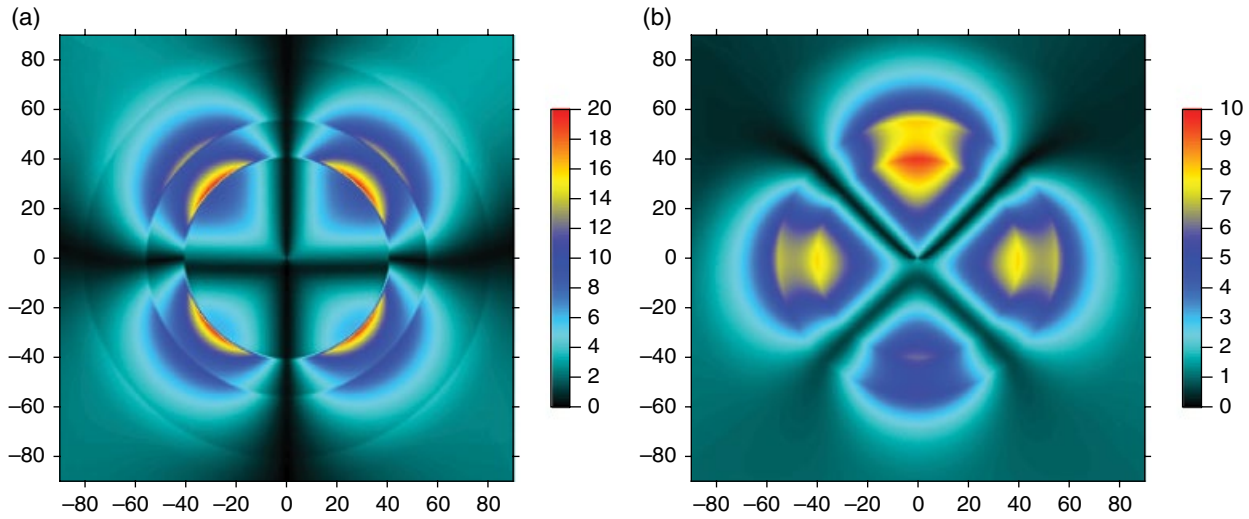

Figure 3.36 The cross sections of (a) $|\mathbf{E}_r|$ and (b) $|\mathbf{E}_\theta|$ in the *xz*-plane for Ag NS@SiO_2 in water irradiated by a plane wave of 460 nm at the quadrupole mode, where $[t_1,t_2,a_3]=[25,15,40]$ nm.

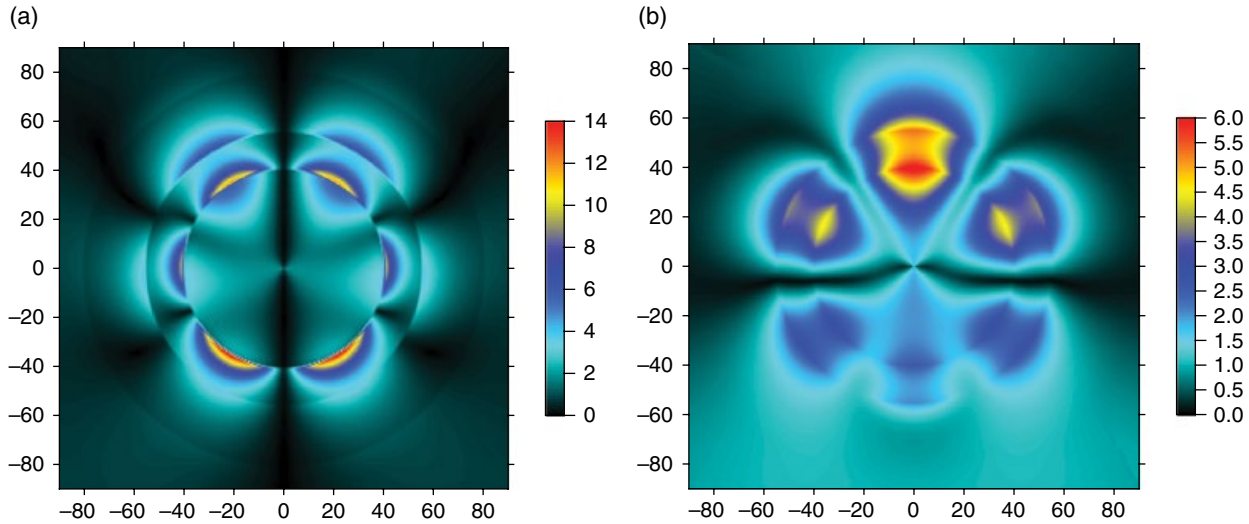

Figure 3.37 The cross sections of (a) $|\mathbf{E}_r|$ and (b) $|\mathbf{E}_\theta|$ in the *xz*-plane for Ag NS@SiO_2 in water irradiated by a plane wave of 410 nm at the sextupole mode, where $[t_1,t_2,a_3]=[25,15,40]$ nm.

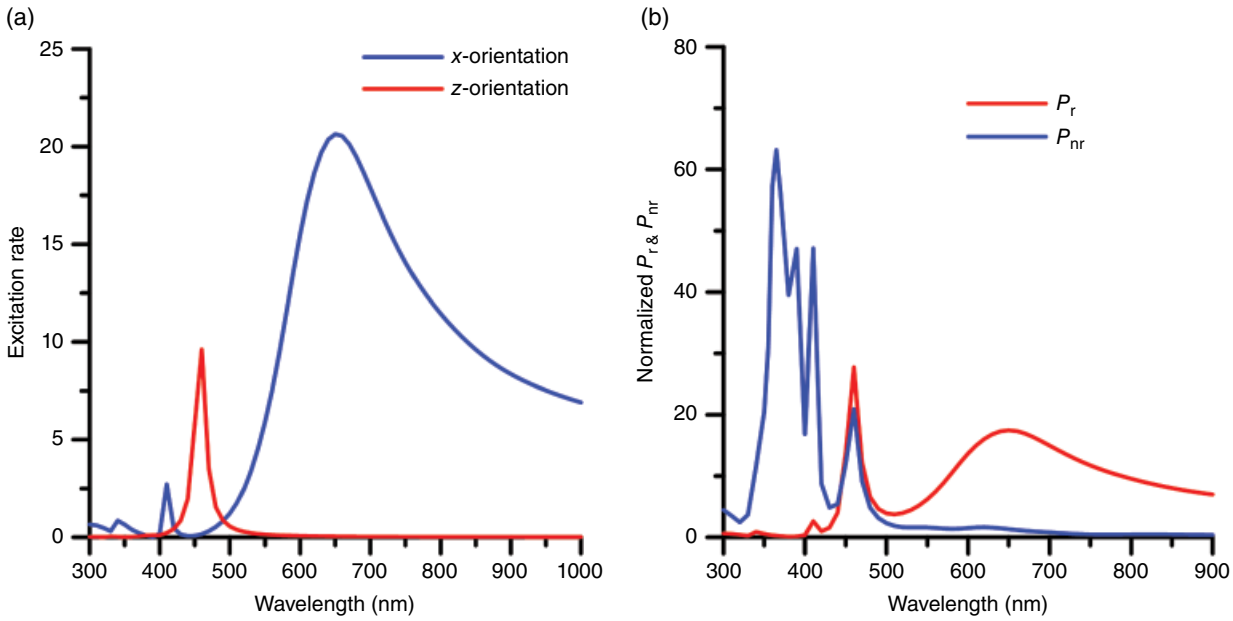

Figure 3.38 (a) Excitation rates of Ag NS@SiO_2 of $[t_1,t_2,a_3]=[25,15,40]$ nm on a molecule at point A with *x*-orientation or *z*-orientation. (b) Radiative and nonradiative powers of an electric dipole at point A with *x*-orientation [127].

Furthermore, consider a molecule with *x*-oriented or *z*-oriented dipole moment at point A embedded in the silica layer of Ag NS@SiO_2. The normalized excitation rates on the molecule irradiated by a plane wave in the presence of Ag NS are plotted in Figure 3.38a. These curves indicate that an *x*-oriented molecule at point A can easily be excited by an *x*-polarized plane wave, propagating along the *z*-axis, at the dipole mode (650 nm) and the sextupole mode (410 nm) of Ag NS@SiO_2. In contrast, a *z*-oriented molecule at point A can easily be excited by the *x*-polarized plane wave at the quadrupole mode (460 nm). The radiative and nonradiative powers of an *x*-oriented dipole at point A are also plotted in Figure 3.38b. For the quadrupole mode (460 nm) and sextupole mode (410 nm), the peaks of SCS, the excitation rate, the radiative power, and the nonradiative power are in agreement. For the dipole mode, there is a 40-nm difference between the peak of ECS (610 nm) and those of the excitation rate and the radiative power (650 nm). This is because the dipole mode is broadband. Notice that the dependency of the excitation rate and the radiative power on the molecular location and orientation is sensitive to the excitation wavelength. This is because that for different SPR modes of NS, this dependency varies.

In fact, the EF of Ag NS@SiO_2 on a molecule is also dependent on the molecular location and orientation sensitively. First, we assume there is no Stokes shift for the molecular fluorescence, $\lambda_{em}=\lambda_{ex}$. For example, the EF at a typical wavelength $\lambda_{ex}=\lambda_{em}=671$ nm versus the dipole orientation in a 3D spherical plot at points A, B, C, and D is shown in Figure 3.39a, c, e, and g, respectively, where $[t_1,t_2,a_3]=[25,15,40]$ nm. The corresponding cross sections in the *xz*-plane or *xy*-plane are shown in Figure 3.39b, d, f, and h, respectively. At this wavelength of 671 nm, the major SPR behavior of Ag NS is close to the dipole mode. Since EF is sensitive to the molecular orientation, EEF is used to present the plasmonic effect of Ag NS@SiO_2 on a molecular fluorescence. Figure 3.40 shows the EEF in the 3D spherical plot against the molecular location with $d=12.5$ nm. In this 3D profile, the maximum EEF (19.32) is at the point A′, and the minimum EEF (0.34) at the point D. The values of EEF at point A, B, and C are 18.38, 1.21, and 0.37, respectively. The point A′ is 12° away from the point A. Furthermore, the AEF of Ag NS@SiO_2 of Figure 3.40 on the fluorescence of a monolayer of molecules embedded at the middle of the silica layer is 6.46 at 671 nm for $d=12.5$ nm. It is interesting to find that Figures 3.39 and 3.40 are similar to Figures 3.28 and 3.29. This is because both are at the dipole mode. Furthermore, the distribution of AEF versus distance *d* between the monolayer of molecule and Ag NS at $\lambda_{ex}=\lambda_{em}=671$ nm is shown in Figure 3.41, where $[t_1,t_2,a_3]=[25,15,40]$ nm. The maximum AEF (8.96) is at $d=6$ nm. This curve indicates that the optimal distance is 6 nm between the molecule and Ag NS. Moreover, the AEF of the entire silica shell is 5.67 at 671 nm.

Notice that the location dependence of EEF really depends on the excitation wavelength. For example,

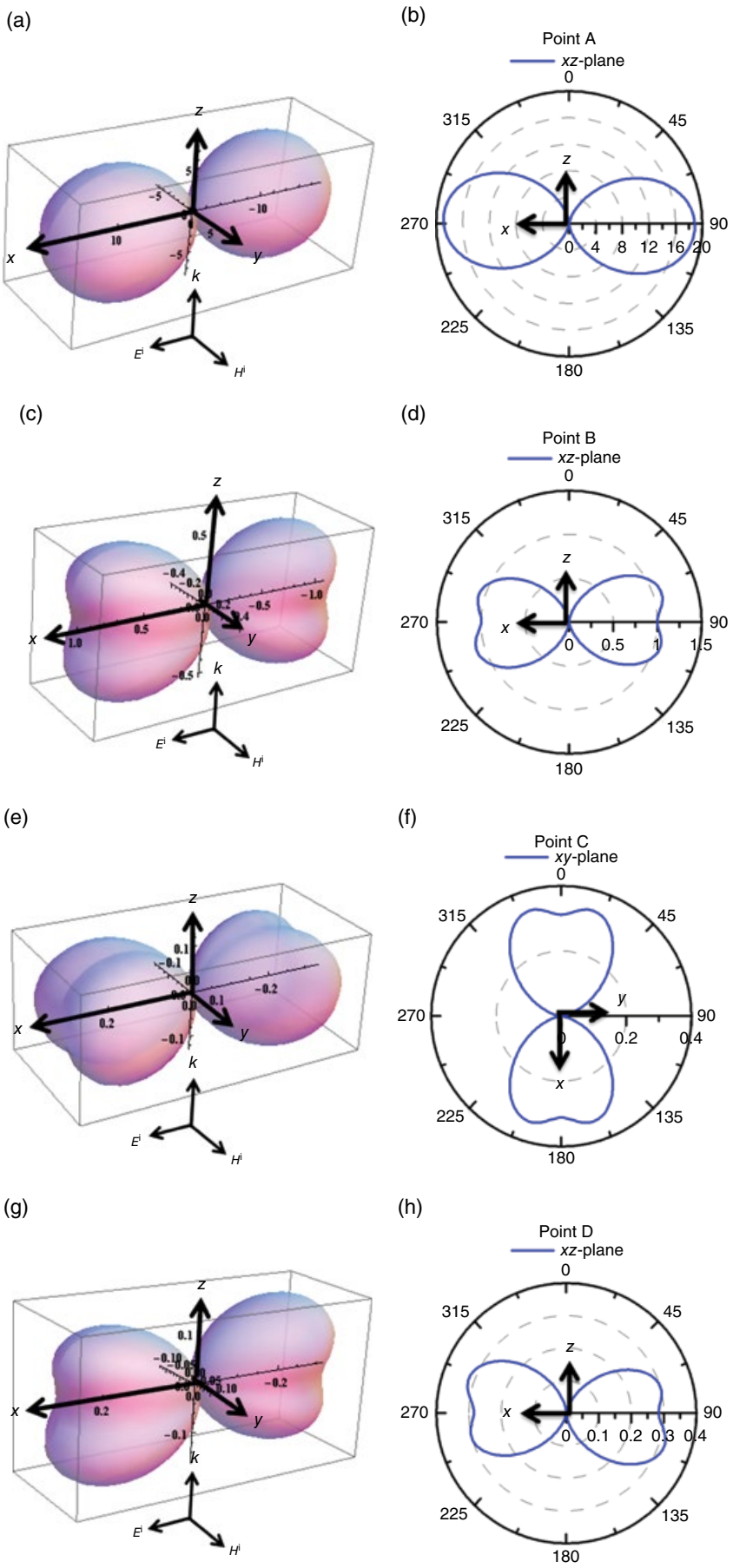

Figure 3.39 (a) Spherical plot of the 3D profile of EF versus dipole orientations for Ag NS@SiO_2, $[t_1,t_2,a_3]=[25,15,50]$ nm at $\lambda_{ex}=\lambda_{em}=671$ nm, containing a molecule located at the point A. (b) The *xz*-plane cross section of (a), (c), (e), and (g) is an EF at points B, C, and D. (d), (f), and (h) are the *xz*-plane or *xy*-plane cross section of (c), (e), and (g), respectively [127].

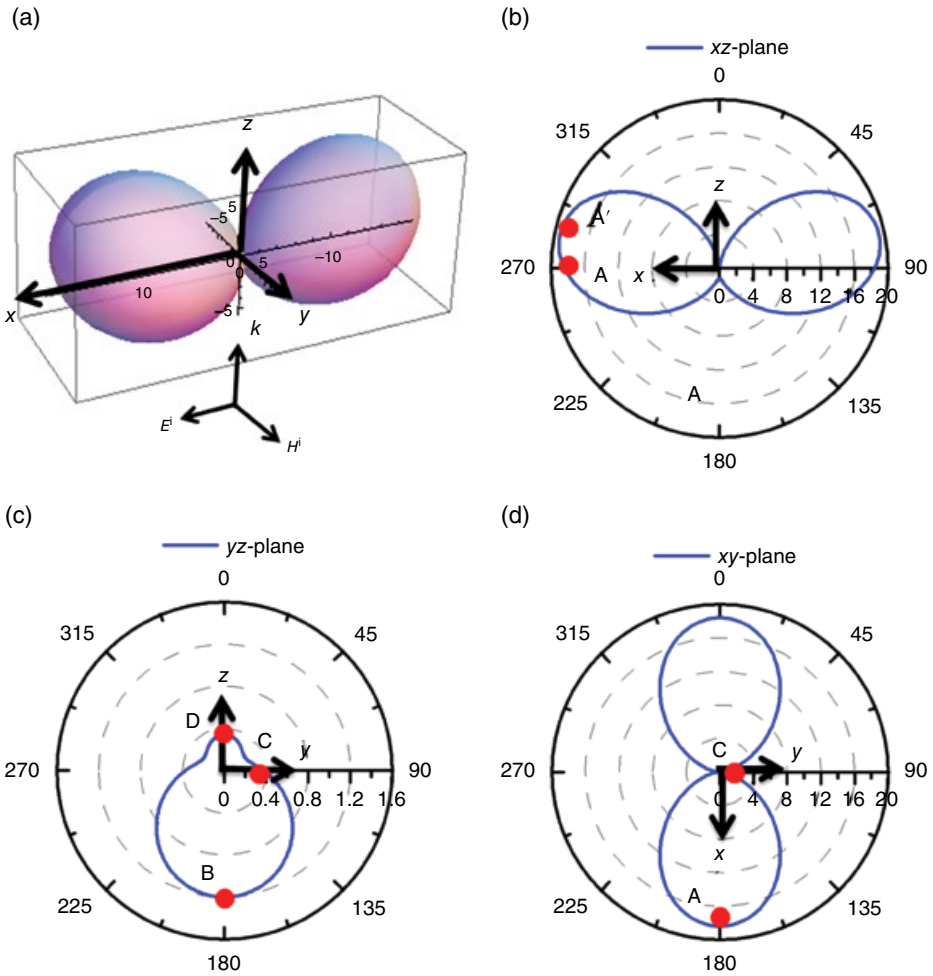

Figure 3.40 (a) Spherical plot of the 3D profile of EEF versus molecular positions for Ag NS@SiO_2, $[t_1,t_2,a_3]=[25,15,50]$ nm at $\lambda_{ex}=\lambda_{em}=671$ nm, where these molecules are embedded in the middle layer of the silica shell ($d=12.5$ nm). (b) The *xz*-plane, (c) the *yz*-plane, and (d) the *xy*-plane cross sections of (a) [127].

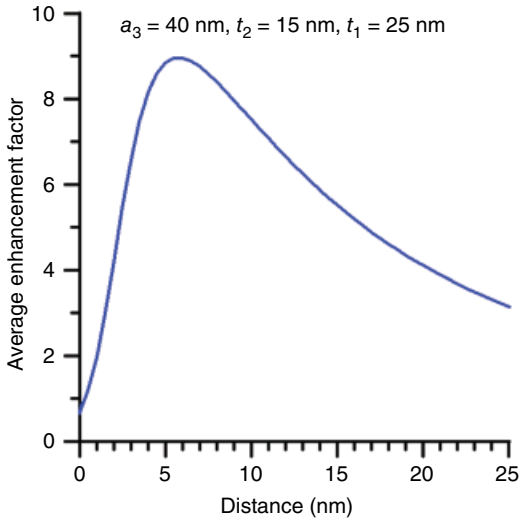

Figure 3.41 Distribution of AEF versus distances *d* between the molecule-doped layer and Ag shell of Ag NS@SiO_2 of $[t_1,t_2,a_3]=[25,15,50]$ nm at $\lambda_{ex}=\lambda_{em}=671$ nm.

when Ag NS@SiO_2 of $[t_1,t_2,a_3]=[25,15,40]$ nm is irradiated by a plane wave at 460 nm, the quadrupole mode can be excited. The 3D spherical plot of EEF is shown in Figure 3.42 for $d=12.5$ nm at 460 nm (quadrupole mode), which looks like a butterfly but quite different from the profile of Figure 3.40 at 671 nm (dipole mode). This profile is due to the pattern of the electric field of Ag NS@SiO_2 irradiated by a plane wave at the quadrupole mode, as shown in Figure 3.36. The maximum EEF (28.173) occurs at the position of $(67.5/\sqrt{2}\,\text{nm}, 0, 67.5/\sqrt{2}\,\text{nm})$, which is point A″, rather than point A′, as shown in Figure 3.42b, at 460 nm. The point A″ is 45° away from the point A. The orientation-dependent EF at point A″ is shown in Figure 3.43, which is like a dumbbell. The AEF of Figure 3.42 at 460 nm is 8.72 for $d=12.5$ nm, larger than the AEF (6.46) at 671 nm.

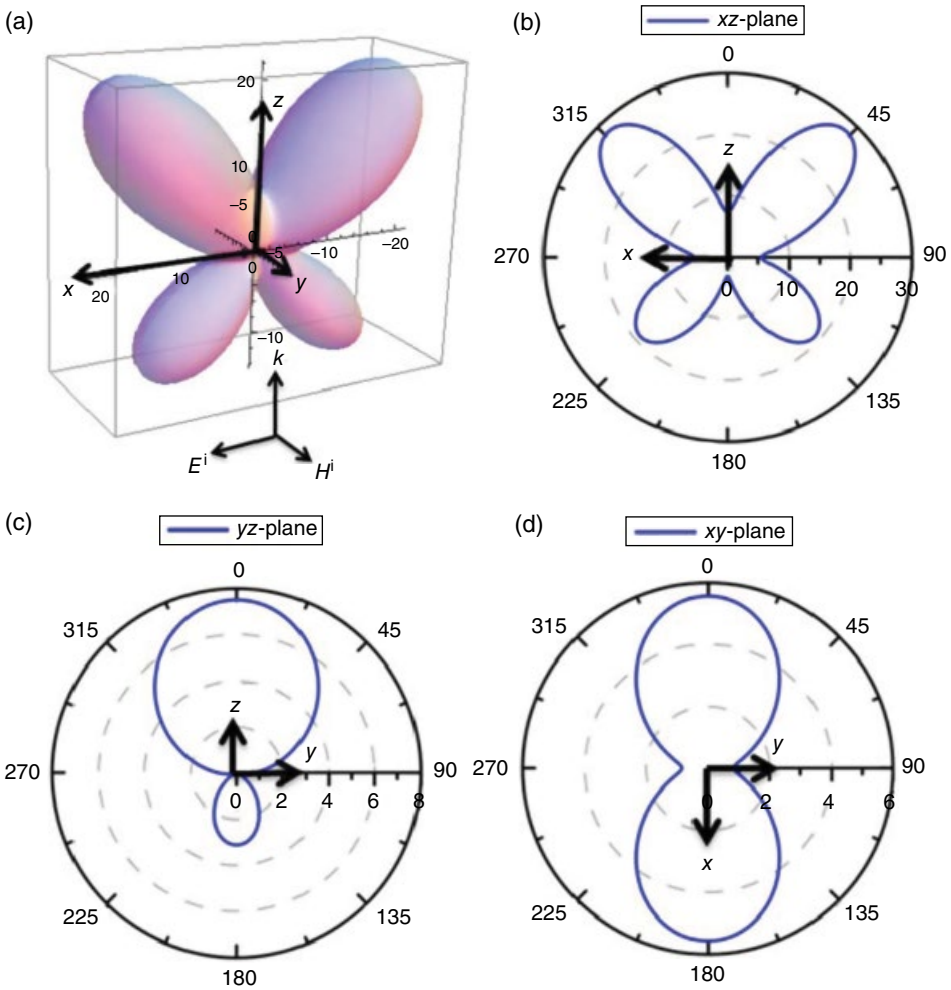

Figure 3.42 (a) Spherical plot of the 3D profile of EEF versus molecular positions for Ag NS@SiO_2, $[t_1,t_2,a_3]=[25,15,40]$ nm at $\lambda_{ex}=\lambda_{em}=460$ nm (quadrupole mode), where these molecules are embedded in the middle layer of the silica shell ($d=12.5$ nm). (b) The *xz*-plane, (c) the *yz*-plane, and (d) the *xy*-plane cross sections of (a).

Moreover, the AEF versus wavelengths for Ag NS@SiO_2 with different a_3 (30, 40, 50 nm) is shown in Figure 3.44a to demonstrate the size effect of the silica core, where $[t_1,t_2]=[25,15]$ nm. These results illustrate that Ag NS@SiO_2 is a dual-band enhancer for fluorescence: a narrow shorter-wavelength band (quadrupole mode), and a broad longer-wavelength band (dipole mode). For example, the peaks of the AEF of $a_3=40$ nm occur at 460 and 650 nm, respectively, caused by the quadrupole and the dipole modes. Both peaks are redshifted, as the core size increases; the dual bands of Ag NS@SiO_2 are tunable. For example, the second peak of a larger Ag NS@SiO_2 (say $a_3>40$ nm) is more significant to enhance the red color and NIR fluorescence. However, the AEF decreases as the size of silica core increases. Moreover, the AEF of Ag NS@SiO_2 with different thicknesses of Ag shell t_2 is shown in Figure 3.44b, where $[t_1,a_3]=[25,40]$ nm. Figure 3.44b indicates that the thinner the Ag NS, the more redshifted the peaks of the AEF of both bands. Additionally, the peak of AEF of the second band (dipole mode) increases as the thickness of the Ag shell decreases. For Ag NS@SiO_2, the AEF is dominated by the dipole and quadrupole modes. In contrast, the sextupole mode is useless to enhance the fluorescence, because apparent quantum yield of emission is too low. Thinning the Ag shell or enlarging the silica core will redshift these two bands and increase the AEF.

Subsequently, we discuss the Stokes-shift effect between the molecular excitation and emission spectra on AEF, $\lambda_{em}\geq\lambda_{ex}$. The AEF versus the emission wavelength λ_{em} excited by lasers of different excitation wavelengths ($\lambda_{ex}=428$, 458, 488, 561, 633, and 671 nm) is calculated for Ag NS@SiO_2 of different core sizes $a_3=30,40$ nm with $[t_1,t_2]=[25,15]$ nm. The AEFs are shown in Figure 3.45a and b, respectively. For example,

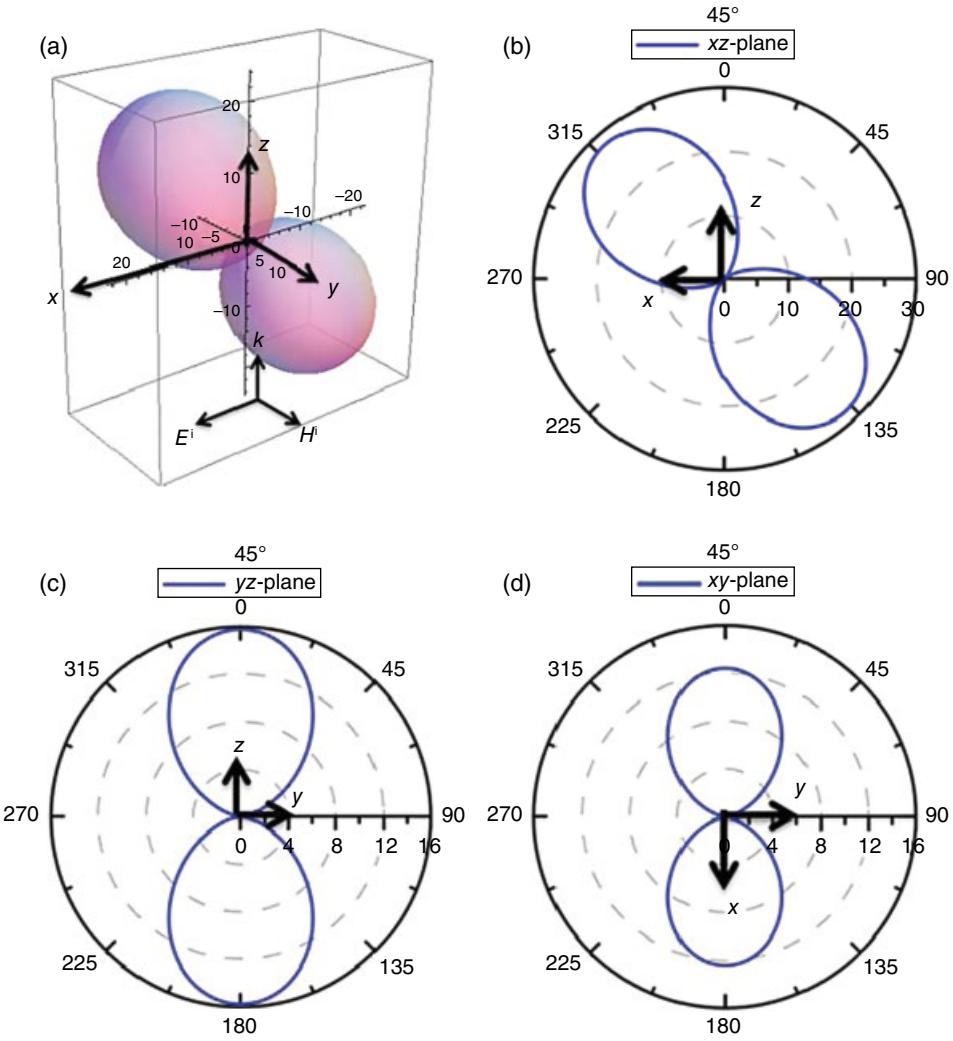

Figure 3.43 (a) Spherical plot of the 3D profile of EF versus dipole orientations for Ag NS@SiO_2, $[t_1,t_2,a_3]=[25,15,40]$ nm at $\lambda_{ex}=\lambda_{em}=460$ nm, containing a molecule located at point A″. (b) The *xz*-plane, *yz*-plane, and *xy*-plane cross sections of (a).

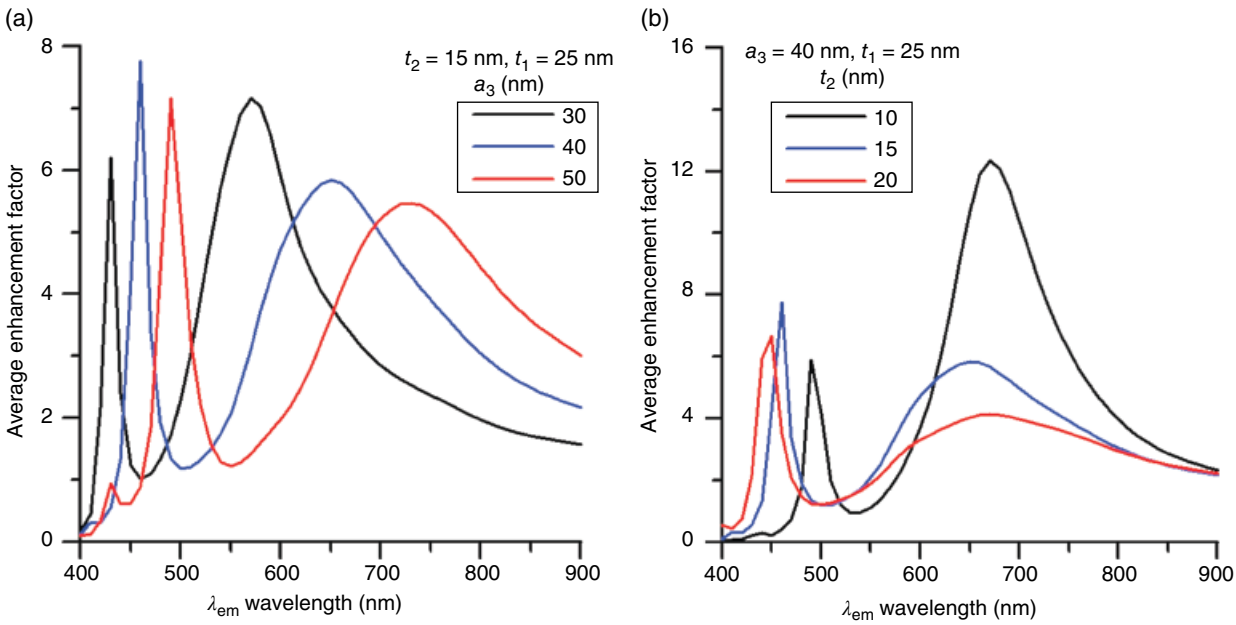

Figure 3.44 (a) AEF versus wavelengths for Ag NS@SiO_2, $[t_1,t_2]=[25,15]$ nm, with different radii a_3 (30, 40, 50 nm) of the silica core. (b) AEF versus wavelengths for Ag NS@SiO_2, $[t_1,a_3]=[25,40]$ nm, with different thicknesses t_2 (10, 15, 20 nm) of the Ag NS [127].

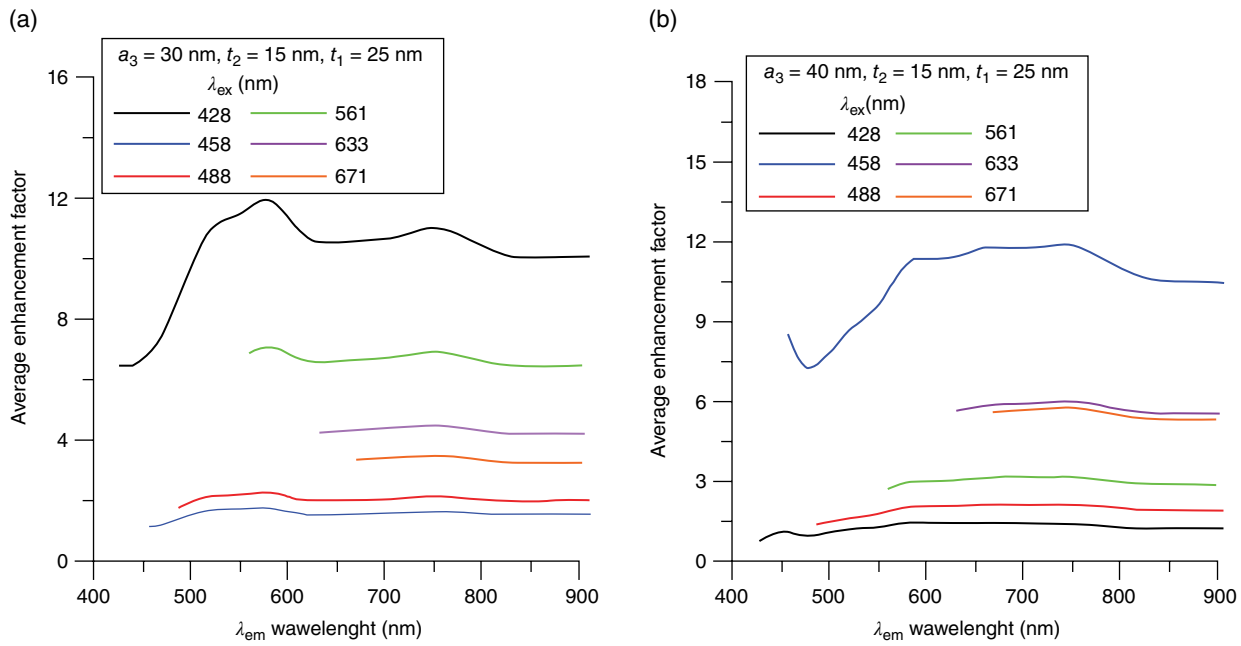

Figure 3.45 (a) AEF versus emission wavelengths λ_{em} for Ag NS@SiO_2, irradiated by different wavelengths λ_{ex} (428, 458, 488, 561, 633, and 671 nm), $[t_1,t_2,a_3]=[25,15,30]$ nm. (b) AEF for $[t_1,t_2,a_3]=[25,15,40]$ nm [127].

the maximum AEFs of $a_3 = 30$ nm are obtained by the excitations of 428-nm and 561-nm lasers. In contrast, for the case of $a_3 = 40$ nm, the maximum ones are obtained by 458-nm and 633-nm lasers. These results indicate that Ag NS@SiO_2 is a dual-band enhancer for those molecules with excitation and emission wavelengths overlapping the SPR modes of the Ag NS. In addition, Figure 3.45a and b shows that the AEF of Ag NS@SiO_2 depends on the size of silica core. This is because the dipole and quadrupole modes are dependent on the ratio of the core size to the shell thickness.

In summary, the aforementioned data indicate that Ag NS@SiO_2 is a dual-band enhancer for the fluorescence of an embedded molecule. The first one is a narrowband in a shorter-wavelength regime corresponding to the quadrupole mode, and the other a wideband in a longer-wavelength regime to the dipole mode. Moreover, the first band is sensitive to the Stokes shift, while the second one is rather insensitive. The detailed comparisons between SEFs of Au NS and Ag NS on a nearby dye were given in Ref. [132]. The results of NS without the outer silica layer are similar with those mentioned in this section.

3.4 Conclusion

The concept of AEF has been used to evaluate the overall performances of a molecule-doped core–shell, NS, or NS@SiO_2 on molecular fluorescence. Using the Mie theory, the SCS and ACS of these NPs interacting with a plane wave as well as the near-field excitation rate at a given molecular position can be calculated analytically for a specific excitation wavelength. The formers are useful to identify the SPR modes, and the latter is used to evaluate the near-field amplification, particularly for the excitation of a molecule. Our analysis shows that the major SPR mode of core–shell and NS is the dipole mode, which is broadband. However, for Ag NS, the quadrupole mode is also significant, which is narrowband. Subsequently, the radiative and nonradiative powers of an excited molecule, which is modeled as an electric dipole, in the presence of the NP can be calculated for a specific emission wavelength by using the dyadic Green's functions. Using the two powers, the apparent quantum yield is obtained. Combining the excitation rate and apparent quantum yield, the EF is then calculated. The EF is a function of the excitation and emission wavelengths. The numerical results show that EF is dependent on the molecular location and orientation. Therefore, AEF is further used, instead of EF, to present the average performance of a large number of core–shells or NSs without overestimating their performance. The peaks of AEF always correspond to the dipole and quadrupole modes of these nanostructures. Moreover, the AEF depends not only on the excitation wavelength but also on the emission wavelength of a specific molecular fluorescence. Therefore, a proper design of core–shell or NS is needed to obtain the maximum enhancement for a specific

molecular fluorescence. According to our analysis, if the proper conditions are not met, a quenching could be obtained, rather than an enhancement, by using core–shell or NS. For the other newly proposed multilayered nanostructure, "nanomatryoshka" [8], for example, Au–SiO_2–Au NP [104, 133], the AEF might be also useful to evaluate the overall performance on SEF. Using the dyadic Green's functions, the plasmon-mediated FRET between a donor and an acceptor via Ag NS can be studied [134]. In addition, the bi-dipole emission of a pair of radial-oriented emitters (e.g., quantum dots) via the plasmon modes (the dipole and quadrupole modes) of Au/Ag NS can be investigated theoretically using the dyadic Green's functions [135]. For the other plasmonic nanostructures, for example, nanorod (NR), there is no analytical solution available. However using semi-analytical methods, for example, the multiple multipole (MMP) method, the plasmonic enhancement or quenching effects of a silica-coated Au NR on the fluorescence of a molecule doped in the outer silica layer can be studied numerically [136, 137]. Moreover, the SEF of a plasmonic dimer can also be studied by MMP method [65, 66].

Acknowledgement

The research was supported by the Ministry of Science and Technology, Taiwan (99-2221-E-182-030-MY3, 102-2221-E-002-056-MY3) and Chang Gung Memorial Hospital (CMRPD290041).

References

1 H. Tamaru, H. Kuwata, H. T. Miyazaki, and K. Miyano, "Resonant light scattering from individual Ag nanoparticles and particle pairs," *Appl. Phys. Lett. 80*, 1826–1828, **2002**.

2 S.-S. Chang, C.-W. Shih, C.-D. Chen, W.-C. Lai, and C. R. C. Wang, "The shape transition of gold nanorods," *Langmuir 15*, 701–709, **1999**.

3 C. J. Murphy and N. R. Jana, "Controlling the aspect ratio of inorganic nanorods and nanowires," *Adv. Mater. 14*, 80–82, **2002**.

4 S. Eustis and M. A. El-Sayed, "Determination of the aspect ratio statistical distribution of gold nanorods in solution from a theoretical fit of the observed inhomogeneously broadened longitudinal plasmon resonance absorption spectrum," *J. Appl. Phys. 100*, 044324, **2006**.

5 Y. Sun, and Y. Xia, "Shape-controlled synthesis of gold and silver nanoparticles," *Science 298*, 2176–2178, **2002**.

6 I. Pastoriza-Santos, D. S. Koktysh, A. A. Mamedov, M. Giersig, N. A. Kotov, and L. M. Liz-Marzan, "One-pot synthesis of Ag@TiO_2 core–shell nanoparticles and their layer-by-layer assembly," *Langmuir 16*, 2731–2735, **2000**.

7 S. J. Oldenburg, R. D. Averitt, S. L. Westcott, and N. J. Halas, "Nanoengineering of optical resonances," *Chem. Phys. Lett. 288*, 243–247, **1998**.

8 R. Bardhan, S. Mukherjee, N. A. Mirin, S. D. Levit, P. Nordlander, and N. J. Halas, "Nanosphere-in-a-nanoshell: a simple nanomatryushka," *J. Phys. Chem. C 114*, 7378–7383, **2010**.

9 H. Xu, J. Aizpurua, M. Käll, and P. Apell, "Electromagnetic contributions to single-molecule sensitivity in surface-enhanced Raman scattering," *Phys. Rev. E 62*(3), 4318–4324, **2000**.

10 J. B. Jackson, S. L. Westcott, L. R. Hirsch, J. L. West, and N. J. Halas "Controlling the surface enhanced Raman effect via the nanoshell geometry," *Appl. Phys. Lett. 82*, 257–259, **2003**.

11 W. Wang, Z. Li, B. Gu, Z. Zhang, and H. Xu, "Ag@SiO_2 core–shell nanoparticles for probing spatial distribution of electromagnetic field enhancement *via* surface-enhanced Raman scattering," *ACS Nano 3*(11), 3493–3496, **2009**.

12 C. Fernandez-Lopez, C. Mateo-Mateo, R. A. Alvarez-Puebla, J. Perez-Juste, I. Pastoriza-Santos, and L. M. Liz-Marzan, "Highly controlled silica coating of PEG-capped metal nanoparticles and preparation of SERS-encoded particles," *Langmuir 25*(24), 13894–13899, **2009**.

13 P. Zhang and Y. Guo, "Surface-enhanced Raman scattering inside metal nanoshells," *J. Am. Chem. Soc. 131*, 3808–3809, **2009**.

14 J. F. Li, Y.F. Huang, Y. Ding, Z. L. Yang, S. B. Li, X. S. Zhou, F. R. Fan, W. Zhang, Z. Y. Zhou, D. Y. Wu, B. Ren, Z. L. Wang, and Z. Q. Tian, "Shell-isolated nanoparticle-enhanced Raman spectroscopy," *Nature 464*, 08907, **2010**.

15 E. Fort and S. Gresillon, "Surface enhanced fluorescence," *J. Phys. D 41*, 013001, **2008**.

16 J. R. Lakowicz, "Radiative decay engineering 5: metal-enhanced fluorescence and plasmon emission," *Anal. Biochem. 337*, 171–194, **2005**.

17 S. Kuhn, U. Hakanson, L. Rogobete, and V. Sandoghdar, "Enhancement of single-molecule fluorescence using a gold nanoparticle," *Phys. Rev. Lett. 97*, 017402, **2006**.

18 P. Anger, P. Bharadwaj, and L. Novotny, "Enhancement and quenching of single-molecule fluorescence," *Phys. Rev. Lett. 96*, 113002, **2006**.

19 P. Bharadwaj and L. Novotny, "Spectral dependence of single molecule fluorescence enhancement," *Opt. Express 15*(21), 14266–14274, **2007**.

20 T. Nakamura and S. Hayashi, "Enhancement of dye fluorescence by gold nanoparticles: analysis of particle size dependence," *Jpn. J. Appl. Phys. 44*, 6833–6837, **2005**.

21 J. N. Farahani, D.W. Pohl, H.-J. Eisler, and B. Hecht, "Single quantum dot coupled to a scanning antenna: a tunable super emitter," *Phys. Rev. Lett. 95*, 017402, **2005**.

22 H. Mertens, J. S. Biteen, H. A. Atwater, and A. Polman, "Polarization-selective plasmon-enhanced silicon quantum-dot luminescence," *Nano Lett. 6*, 2622–2625, **2006**.

23 T. Ming, L. Zhao, Z. Yang, H. Chen, L. Sun, J. Wang, and C. Yan, "Strong polarization dependence of plasmon-enhanced fluorescence on single gold nanorods," *Nano Lett. 9*(11), 3896–3903, **2009**.

24 Y. Fu, J. Zhang, and J. R. Lakowicz, "Plasmon-enhanced fluorescence from single fluorophores end-linked to gold nanorods," *J. Am. Chem. Soc. 132*, 5540–5541, **2010**.

25 O. G. Tovmachenko, C. Graf, D. J. van den Heuvel, A. van Blaaderen, and H. C. Gerritsen, "Fluorescence enhancement by metal-core/silica-shell nanoparticles," *Adv. Mater. 18*, 91–95, **2006**.

26 K. Aslan, M. Wu, J. R. Lakowicz, and C. D. Geddes, "Fluorescent core–shell Ag@SiO_2 nanocomposites for metal-enhanced fluorescence and single nanoparticle sensing platforms," *J. Am. Chem. Soc. 129*, 1524–1525, **2007**.

27 K. Aslan, M. Wu, J. R. Lakowicz, and C. D. Geddes, "Metal enhanced fluorescence solution-based sensing platform 2: fluorescent core–shell Ag@SiO_2 nanoballs," *J. Fluores. 17*, 127–131, **2007**.

28 D. Cheng and Q.-H. Xu, "Separation distance dependent fluorescence enhancement of fluorescein isothiocyanate by silver nanoparticles," *Chem. Comm.*, 248–250, **2007**.

29 O. Stranik, R. Nooney, C. McDonagh, and B. D. MacCraith, "Optimization of nanoparticle size for plasmonic enhancement of fluorescence," *Plasmonics 2*, 15–22, **2007**.

30 F. Tam, G. P. Goodrich, B. R. Johnson, and N. J. Halas, "Plasmonic enhancement of molecular fluorescence," *Nano Lett. 7*, 496–501, **2007**.

31 R. Bardhan, N. K. Grady, J. R. Cole, A. Joshi, and N. J. Halas, "Fluorescence enhancement by Au nanostructures: nanoshells and nanorods," *ACS Nano 3*(3), 744–752, **2009**.

32 R. Bardhan, N. K. Grady, and N. J. Halas, "Nanoscale control of near-Infrared fluorescence enhancement using Au nanoshells," *Small 4*(10), 1716–1722, **2008**.

33 S. Xu, S. Hartvickson, and J. X. Zhao, "Engineering of SiO_2-Au-SiO_2 sandwich nanoaggregates using a building block: single, double, and triple cores for enhancement of near infrared fluorescence," *Langmuir 24*, 7492–7499, **2008**.

34 E. Dulkeith, A. C. Morteani, T. Niedereichholz, T. A. Klar, J. Feldmann, S. A. Levi, F. C. J. M. van Veggel, D. N. Reinhoudt, M. Moller, and D. I. Gittins, "Fluorescence quenching of dye molecules near gold nanoparticles: radiative and nonradiative effects," *Phys. Rev. Lett. 89*, 203002, **2002**.

35 E. Dulkeith, M. Ringler, T. A. Klar, J. Feldmann, A. M. Javier, and W. J. Parak, "Gold nanoparticles quench fluorescence by phase induced radiative rate suppression," *Nano Lett. 5*, 585–589, **2005**.

36 C. Sönnichsen, T. Franzl, T. Wilk, G. von Plessen, and J. Feldmann, "Drastic reduction of plasmon damping in gold nanorods," *Phys. Rev. Lett. 88*, 077402, **2002**.

37 K. Aslan and V. H. Perez-Luna, "Quenched emission of fluorescence by ligand functionalized gold nanoparticles," *J. Fluores. 14*(4), 401–405, **2004**.

38 X. Li, J. Qian, L. Jiang, and S. He, "Fluorescence quenching of quantum dots by gold nanorods and its application to DNA detection," *Appl. Phys. Lett. 94*, 063111, **2009**.

39 E. Prodan, C. Radloff, N. J. Halas, and P. Nordlander, "A hybridization model for the plasmon response of complex nanostructures," *Science 302*, 419–422, **2003**.

40 H. Wang, K. Fu, R. A. Drezek, and N. J. Halas, "Light scattering from spherical plasmonic nanoantennas: effects of nanoscale roughness," *Appl. Phys. B 84*, 191–195, **2006**.

41 F. Tam and N. Halas, "Plasmon response of nanoshell dopants in organic films: a simulation study," *Prog. Org. Coatings 47*, 275–278, **2003**.

42 S. J. Oldenburg, G. D. Hale, J. B. Jackson, and N. J. Halas, "Light scattering from dipole and quadrupole nanoshell antennas," *Appl. Phys. Lett. 75*, 1063–1065, **1999**.

43 M. Shopa, K. Kolwas, A. Derkachova, and G. Derkachov, "Dipole and quadrupole surface plasmon resonance contributions in formation of near-field images of a gold nanosphere," *OptoElectronics Rev. 18*(4), 421–428, **2010**.

44 F. Zhou, Z.-Y. Li, and Y. Liu, "Quantitative analysis of dipole and quadrupole excitation in the surface plasmon resonance of metal nanoparticles," *J. Phys. Chem. C 112*(51), 20233–20240, **2008**.

45 D. Wu and X. Liu, "Optimization of the bimetallic gold and silver alloy nanoshell for biomedical applications *in vivo*," *Appl. Phys. Lett. 97*, 061904, **2010**.

46 J. Enderlein, "Spectral properties of a fluorescing molecule within a spherical metallic cavity," *Phys. Chem. Chem. Phys. 4*, 2780–2786, **2002**.

47 J. Enderlein, "Theoretical study of single molecule fluorescence in a metallic nanocavity," *Appl. Phys. Lett. 80*, 315–317, **2002**.

48 J. Zhang, Y. Fu, F. Jiang, and J. R. Lakowicz, "Dye-labeled silver nanoshell-bright particle," *J. Phys. Chem. B 110*, 8986–8991, **2006**.

49 J. Zhang, Y. Fu, and J. R. Lakowicz, "Luminescent silica core/silver shell encapsulated with Eu(III) complex," *J. Phys. Chem. C 113*, 19404–19410, **2009**.

50 Y. Jin and X. Gao, "Plasmonic fluorescent quantum dots," *Nat. Nanotechnol. 4*, 571–576, **2009**.

51 F. Reil, U. Hohenester, J. R. Krenn, and A. Leitner, "Förster-type resonant energy transfer influenced by metal nanoparticles," *Nano Lett. 8*(12), 4128–4133, **2008**.

52 R. M. Bakker, V. P. Drachev, Z. Liu, H.-K. Yuan, R. H. Pedersen, A. Boltasseva, J. Chen, J. Irudayaraj, A. V. Kildishev, and V. M. Shalaev, "Nanoantenna array-induced fluorescence enhancement and reduced lifetimes," *New J. Phys. 10*, 125022, **2008**.

53 C. Oubre and P. Nordlander, "Finite-difference time-domain studies of the optical properties of nanoshell dimers," *J. Phys. Chem. B 109*, 10042–10051, **2005**.

54 M. H. Chowdhury, J. Pond, S. K. Gray, J. R. Lakowicz, "Systematic computational study of the effect of silver nanoparticle dimers on the coupled emission from nearby fluorophores," *J. Phys. Chem. C 112*, 11236–11249, **2008**.

55 C. G. Khoury, S. J. Norton, and T. Vo-Dinh, "Plasmonics of 3-D nanoshell dimers using multipole expansion and finite element method," *ACS Nano 3*(9), 2776–2788, **2009**.

56 L. V. Brown, H. Sobhani, J. B. Lassiter, P. Nordlander, and N. J. Halas, "Heterodimers: plasmonic properties of mismatched nanoparticle pairs, *ACS Nano 4*(2), 819–832, **2010**.

57 J. B. Lassiter, J. Aizpurua, L. I. Hernandez, D. W. Brandl, I. Romero, S. Lal, J. H. Hafner, P. Nordlander, and N. J. Halas. "Close encounters between two nanoshells," *Nano Lett. 8*(4), 1212–1218, **2008**.

58 S. Savasta, R. Saija, A. Ridolfo, O. D. Stefano, P. Denti, and F. Borghes, "Nanopolaritons: vacuum Rabi splitting with a single quantum dot in the center of a dimer nanoantenna," *ACS Nano 4*(11), 6369–6376, **2010**.

59 B. Deutsch, R. Hillenbrand, and L. Novotny, "Visualizing the optical interaction tensor of a gold nanoparticle pair," *Nano Lett. 10*, 652–656, **2010**.

60 Mohammadi, A., V. Sandoghdar, and M. Agio, "Gold nanorods and nanospheroids for enhancing spontaneous emission," *New J. Phys. 10*, 105015, **2008**.

61 J.-W. Liaw, "New surface integral equations for the light scattering of multi-metallic nanoscatterers," *Eng. Anal. Boundary Elem. 31*(4), 299–310, **2007**.

62 J.-W. Liaw, "The quantum yield of a metallic nanoantenna," *Appl. Phys. A 89*, 357–362, **2007**.

63 J.-W. Liaw, "Analysis of a bowtie nanoantenna for the enhancement of spontaneous emission," *IEEE J. Sel. Top. Quant. El. 14*(6), 1441–1447, **2008**.

64 J.-W. Liaw, "Local field enhancement and quantum yield of metallic dimer," *Jpn. J. Appl. Phys. 46*(8A), 5373–5378, **2007**.

65 J.-W. Liaw, C.-S. Chen, J.-H. Chen, and M.-K. Kuo, "Purcell effect of nanoshell dimer on single molecule's fluorescence", *Opt. Express 17*(16), 13532–13540, **2009**.

66 J.-W. Liaw, J.-H. Chen, and C.-S. Chen, "Enhancement or quenching effect of metallic nanodimer on spontaneous emission," *J. Quant. Spectrosc. Radiat. Transfer 111*, 454–465, **2010**.

67 J.-W. Liaw, H.-C. Chen, B.-R. Chen, and M.-K. Kuo, "Metal enhanced fluorescence of Ag-nanoshell dimer," *Appl. Phys. A 115*, 45–52, **2014**.

68 H. Fischer and O. J. F. Martin, "Engineering the optical response of plasmonic nanoantennas," *Opt. Express 16*(12), 9144–9154, **2008**.

69 H. Szmacinski, K. Ray, and J. R. Lakowicz, "Effect of plasmonic nanostructures and nanofilms on fluorescence resonance energy transfer," *J. Biophotonics. 2*(4): 243–252, **2009**.

70 E. Giorgetti, S. Cicchi, M. Muniz-Miranda, G. Margheri, T. Del Rosso, A. Giusti, A. Rindi, G. Ghini, S. Sottini, A. Marcelli, and P. Foggi, "Förster resonance energy transfer (FRET) with a donor–acceptor system adsorbed on silver or gold nanoisland films," *Phys. Chem. Chem. Phys. 11*(42), 9798–9803, **2009**.

71 M. Lessard-Viger, M. Rioux, Lu. Rainville, and D. Boudreau, "FRET enhancement in multilayer core–shell nanoparticles," *Nano Lett. 9*(8), 3066–3071, **2009**.

72 H. Y. Xie, H. Y. Chung, P. T. Leung, and D. P. Tsai, "Plasmonic enhancement of Förster energy transfer between two molecules in the vicinity of a metallic nanoparticle: nonlocal optical effects," *Phys. Rev. B 80*, 155448, **2009**.

73 M. I. Stockman, "Spasers explained," *Nature Photonics 2*, 327–329, **2008**.

74 D. J. Bergman and M. I. Stockman, "Surface plasmon amplification by stimulated emission of radiation: quantum generation of coherent surface plasmons in nanosystems," *Phys. Rev. Lett. 90*, 027402, **2003**.

75 M. I. Stockman, "The spaser as a nanoscale quantum generator and ultrafast amplifier," *J. Opt. 12*, 024004, **2010**.

76 M. A. Noginov, G. Zhu, A. M. Belgrave, R. Bakker, V. M. Shalaev, E. E. Narimanov, S. Stout, E. Herz, T. Suteewong, and U. Wiesner, "Demonstration of a spaser-based nanolaser," *Nature 460*, 1110–1113, **2009**.

77 C. Loo, A. Lin, L. Hirsch, M.-H. Lee, J. Barton, N. J. Halas, J. West, and R. Drezek, "Nanoshell-enabled photonics-based imaging and therapy of cancer," *Technol. Cancer Res. Treatm. 3*(1), 33–40, **2004**.

78 D. Lapotko, "Plasmonic nanoparticle-generated photothermal bubbles and their biomedical applications," *Nanomedicine 4*(7), 813–845, **2009**.

79 C. Ungureanu, R. Kroes, W. Petersen, T. A. M. Groothuis, F. Ungureanu, H. Janssen, F. W. B. van Leeuwen, R. P. H. Kooyman, S. Manohar, and T. G. van Leeuwen, "Light interactions with gold nanorods and cells: implications for photothermal nanotherapeutics," *Nano Lett. 11*, 1887–1894, **2011**.

80 M. G. González, X. Liu, R. Niessner, and C. Haisch, "Strong size-dependent photoacoustic effect on gold nanoparticles by laser-induced nanobubbles," *Appl. Phys. Lett. 96*, 174104, **2010**.

81 Y.-S. Chen, W. Frey, S. Kim, K. Homan, P. Kruizinga, K. Sokolov, and S. Emelianov, "Enhanced thermal stability of silica-coated gold nanorods for photoacoustic imaging and image-guided therapy," *Opt. Express 18*(9), 8867–8878, **2010**.

82 Y.-S. Chen, W. Frey, S. Kim, P. Kruizinga, K. Homan, and S. Emelianov, "Silica-coated gold nanorods as photoacoustic signal nanoamplifiers," *Nano Lett. 11*, 348–354, **2011**.

83 E. Y. Lukianova-Hleb, E. Y. Hanna, J. H. Hafner, and D. O. Lapotko, "Tunable plasmonic nanobubbles for cell theranostics," *Nanotechnology 21*, 085102, **2010**.

84 L.-C. Chen, C.-W. Wei, J. S. Souris, S.-H. Cheng, C.-T. Chen, C.-S. Yang, P.-C. Li, and L.-W. Lo, "Enhanced photoacoustic stability of gold nanorods by silica matrix confinement," *J. Biomed. Opt. 15*(1), 016010, **2010**.

85 H. Wang, T. B. Huff, D. A. Zweifel, W. He, P. S. Low, A. Wei, and J.-X. Cheng, "In vitro and in vivo two-photon luminescence imaging of single gold nanorods," *Proc. Natl. Acad. Sci. USA 102*, 15752–15756, **2005**.

86 K. Imura, T. Nagahara, and H. Okamoto, "Plasmon mode imaging of single gold nanorods," *J. Am. Chem. Soc. 126*, 12730–12731, **2004**.

87 Y. Jiang, N. N. Horimoto, K. Imura, H. Okamoto, K. Matsui, and R. Shigemoto, "Bioimaging with two-photon-induced luminescence from triangular nanoplates and nanoparticle aggregates of gold," *Adv. Mater. 21*, 2309–2313, **2009**.

88 J.-W. Liaw, S.-W. Tsai, K.-L. Chen, and F.-Y. Hsu, "Single-photon and two-photon cellular imagings of gold nanorods and dye," *J. Nanosci. Nanotechnol. 10*(1), 467–473, **2010**.

89 X.-W. Chen, W. C.-H. Choy, S. He, and P. C. Chui, "Highly efficient fluorescence of a fluorescing nanoparticle with a silver shell," *Opt. Express 15*, 7083–7094, **2007**.

90 X.-W. Chen, S. He, and W. C. H. Choy, "Highly efficient and tunable fluorescence of a nanofluorophore in silica/metal dual shells with plasmonic resonance," *J. Appl. Phys. 103*, 024301, **2008**.

91 T. V. Teperik, V. V. Popov, and F. J. Garcia de Abajo, "Radiative decay of plasmons in a metallic nanoshell," *Phys. Rev. B 69*, 155402, **2004**.

92 J.-W. Liaw, C.-S. Chen, and J.-H. Chen, "Plasmonic effect of gold nanospheroid on spontaneous emission," *PIER B 31*, 283–296, **2011**.

93 P. Johansson, H. Xu, and M. Käll, "Surface-enhanced Raman scattering and fluorescence near metal nanoparticles," *Phys. Rev. B 72*, 035427, **2005**.

94 V. V. Klimov, M. Ducloy, and V. S. Letokhov, "Spontaneous emission of an atom placed near a prolate nanospheroid," *Eur. Phys. J. D 20*, 133–148, **2002**.

95 M. Thomas, J.-J. Greffet, R. Carminati, and J. R. Arias-Gonzalez, "Single-molecule spontaneous emission close to absorbing nanostructures," *Appl. Phys. Lett. 85*, 3863–3865, **2004**.

96 J. Azoulay, A. debarred, A. Richard, and P. Tchenio, "Quenching and enhancement of single-molecule fluorescence under metallic and dielectric tips," *Europhys. Lett. 51*, 374–380, **2000**.

97 R. Carminati, J. J. Greffet, C. Henkel, and J. M. Vigonreux, "Radiative and non-radiative decay of a single molecule close to a metallic nanoparticle," *Opt. Comm. 261*, 368–375, **2006**.

98 L. B. Blanco and F. J. Garcia de Abajo, "Spontaneous emission enhancement near nanoparticles," *J. Quant. Spectrosc. Radiat. Transfer 89*, 37–42, **2004**.

99 G. Colas des Francs, A. Bouhelier, E. Finot, J. C. Weeber, A. Dereux, C. Girard, and E. Dujardin, "Fluorescence relaxation in the near–field of a mesoscopic metallic particle: distance dependence and role of plasmon modes," *Opt. Express 16*, 17654–17666, **2008**.

100 U. Hohenester and A. Trügler, "Interaction of single molecules with metallic nanoparticles," *IEEE J. Sel. Top. Quant. Electron., 14*, 1430–1440, **2008**.

101 M. H. Chowdhury, S. K. Gray, J. Pond, C. D. Geddes, K. Aslan, and J. R. Lakowicz, "Computational study of fluorescence scattering by silver nanoparticles," *J. Opt. Soc. Am. B 24*, 2259–2267, **2007**.

102 T. Hartling, P. Reichenbach, and L. M. Eng, "Near-field coupling of a single fluorescent molecule and a spherical gold nanoparticle," *Opt. Express 15*, 12806–12817, **2007**.

103 R. Ruppin, "Decay of an excited molecule near a small metal sphere," *J. Chem. Phys. 76*, 1681–1684, **1982**.

104 Y. Hu, R. C. Fleming, and R. A. Drezek, "Optical properties of gold–silica–gold multilayer nanoshells," *Opt. Express 16*(24), 19579–19591, **2008**.

105 P. Viste, J. Plain, R. Jaffiol, A. Vial, P. M. Adam, and P. Royer, "Enhancement and quenching regimes in metal-semiconductor hybrid optical nanosources," *ACS Nano 4*(2), 759–764, **2010**.

106 P. K. Jain, K. S. Lee, I. H. El-Sayed, and M. A. El-Sayed, "Calculated absorption and scattering properties of gold nanoparticles of different size, shape, and composition: applications in biological imaging and biomedicine," *J. Phys. Chem. B 110*, 7238–7248, **2006**.

107 P.C. Das and A. Puli, "Energy flow and fluorescence near a small metal particle," *Phys. Rev. B 65*, 155416, **2002**.

108 W. Sun, N. G. Loeb, and Q. Fu, "Light scattering by coated sphere immersed in absorbing medium: a comparison between the FDTD and analytic solutions," *J. Quant. Spectrosc. Radiat. Transfer 83*, 483–492, **2004**.

109 Y. S. Kim, P.T. Leung, and T. F. George, "Classical decay rates for molecules in the presence of a spherical surface: a complete treatment," *Surface Sci. 195*, 1–14, **1988**.

110 B. J. Messinger, K. Ulrich von Raben, and R. K. Chang, "Local fields at the surface of noble-metal microspheres," *Phys. Rev. B 24*, 649–657, **1981**.

111 H. Mertens, A. F. Koenderink, and A. Polman, "Plasmon-enhanced luminescence near noble-metal nanospheres: comparison of exact theory and an improved Gersten and Nitzan model," *Phys. Rev. B 76*, 115123, **2007**.

112 C. G. Khoury, S.J. Norton, and T. Vo-Dinh, "Investigating the plasmonics of a dipole-excited silver nanoshell: Mie theory versus finite element method nanotechnology," *Nanotechnology 21*(31), 315203, **2010**.

113 J. J. Penninkhof, L. A. Sweatlock, A. Moroz, H. A. Atwater, A. van Blaaderen, and A. Polman, "Optical cavity modes in gold shell colloids," *J. Appl. Phys. 103*, 123105, **2008**.

114 H. Xu, "Multilayered metal core–shell nanostructures for inducing a large and tunable local optical field," *Phys. Rev. B 72*, 073405, **2005**.

115 J. L.-W. Li, Z.-C. Li, H.-Y. She, S. Zouhdi, J. R. Mosig, and O. J. F. Martin , "A new closed-form solution to light scattering by spherical nanoshells," *IEEE T. Nanotechnol. 8*(5), 617–626, **2009**.

116 A. Moroz, "A recursive transfer-matrix solution for a dipole radiating inside and outside a stratified sphere," *Ann. Phys. 315*, 352–418, **2005**.

117 A. Moroz, "Spectroscopic properties of a two-level atom interacting with a complex spherical nanoshell," *Chem. Phys. 317*, 1–15, **2005**.

118 A. Moroz, "Electron mean-free path in a spherical shell geometry," *J. Phys. Chem. C 112*(29), 10641, **2008**.

119 X. Miao, I. Brener, and T. S. Luk, "Nanocomposite plasmonic fluorescence emitters with core/shell configurations," *J. Opt. Soc. Am. B 27*(8), 1561–1570, **2010**.

120 J.-W. Liaw, M.-K. Kuo, and C.-N. Liao, "Plasmon resonance of spherical and ellipsoidal nanoparticles," *J. Electromagn. Waves Appl. 19*(13), 1787–1794, **2005**.

121 J.-W. Liaw, "Analysis of the surface plasmon resonance of a single core-shelled nanocomposite by surface integral equations," *Eng. Anal. Boundary Elem. 30*(9), 734–745, **2006**.

122 J.-W. Liaw, "Simulation of surface plasmon resonance of metallic nanoparticles by boundary-element method," *J. Opt. Soc. Am. A 23*(1), 108–116, **2006**.

123 J.-W. Liaw, C.-L. Liu, W.-M. Tu, and C.-S. Sun, "Plasmonic enhancement of coreshell ($Au@SiO_2$) on molecular fluorescence," *J. Quant. Spectrosc. Radiat. Transfer 112*(5), 893–900, **2011**.

124 J.-W. Liaw, C.-L. Liu, W.-M. Tu, C.-S. Sun, and M.-K. Kuo, "Average enhancement factor of molecules-doped coreshell ($Ag@SiO_2$) on fluorescence," *Opt. Express 18*(12), 12788–12797, **2010**.

125 J.-W. Liaw and C.-L. Liu, "Plasmonic effect of nanoshelled nanocavity on encapsulated emitter's spontaneous emission", *J. Quant. Spectrosc. Radiat. Transfer 112*, 2480–2485, **2011**.

126 J.-W. Liaw and C.-L. Liu, "Average plasmonic enhancement of molecules-doped Au-$NS@SiO_2$ on fluorescence," *J. Nanosci. Nanotechnol. 11*(9), 7687–7692, **2011**.

127 J.-W. Liaw, C.-L. Liu, and M.-K. Kuo, "Dual-band plasmonic enhancement of Ag-$NS@SiO_2$ on gain medium's spontaneous emission", *Plasmonics 6*, 673–680, **2011**.

128 L. Novotny and B. Hecht, *Principles of Nano-Optics*, Cambridge University Press, Cambridge, UK, **2006**.

129 C.T. Tai, *Dyadic Green's Functions in Electromagnetic Theory*, IEEE, Piscataway, NJ, **1971**.

130 C. T. Tai, "On the eigenfunction expansion of dyadic Green's functions," *Proc. IEEE 61*, 480–481, **1973**.

131 P. B. Johnson and R.W. Christy, "Optical constants of the noble metals," *Phys. Rev. B 6*, 4370–4379, **1972**.

132 J.-W. Liaw, H.-C. Chen, and M.-K. Kuo, "Comparison of Au and Ag nanoshells' metal-enhanced fluorescence", *J. Quant. Spectrosc. Radiat. Transfer 146*, 321–330, **2014**.

133 J.-W. Liaw, H.-C. Chen, and M.-K. Kuo, "Plasmonic Fano resonance and dip of Au-SiO_2-Au nanomatryoshka," *Nanoscale Res. Lett. 8*, 468, **2013**.

134 J.-W. Liaw, B.-R. Chen, and M.-K. Kuo, "Plasmon-mediated excitation modulation of FRET by silver nanoshell," *Microelectron. Eng. 138*, 122–127, **2015**.

135 J.-W. Liaw and C.-Y. Jiang, "Bi-dipole emission via plasmon modes of Au/Ag nanoshell," *J. Quant. Spectrosc. Radiat. Transfer 114*, 56–64, **2013**.

136 J.-W. Liaw, and H.-Y. Tsai, "Theoretical investigation of plasmonic enhancement of silica-coated gold nanorod on molecular fluorescence," *J. Quant. Spectrosc. Radiat. Transfer 113*, 470–479, **2012**.

137 J.-W. Liaw, H.-Y. Tsai, and C.-H. Huang, "Size-dependent surface enhanced fluorescence of gold nanorod: enhancement or quenching," *Plasmonics 7*(3), 543–553, **2012**.

4

Controlling Metal-Enhanced Fluorescence Using Bimetallic Nanoparticles

Debosruti Dutta, Sanchari Chowdhury, Chi Ta Yang, Venkat R. Bhethanabotla, and Babu Joseph

Department of Chemical & Biomedical Engineering, University of South Florida, Tampa, FL, USA

4.1 Introduction

Metal-enhanced fluorescence (MEF) is the enhancement of photoluminescence by the presence of vicinal metallic particles [1]. Metals such as gold and silver are typically used since nanoparticles (NPs) made from these metals exhibit very narrow and intense surface plasmon resonance (SPR) peaks that in turn are responsible for the fluorescence enhancement. Recently, other metals such as copper [2], aluminum [3], chromium [4], and zinc [5] have been reported to enhance fluorescence. The wavelength corresponding to the SPR peak and the scattering efficiency of the NP are the most important factors that dictate the enhancement/quenching effect on the fluorophore molecules [6]. These properties can be manipulated by controlling the particle composition, size, aspect ratio, shape, particle-to-particle distance, and surrounding dielectric medium [7]. Thus, alloying NPs can be an attractive option in manipulating the fluorophore signal as it offers additional degrees of freedom for tuning their optical properties by altering atomic composition and atomic arrangement [8]. The ability to tune the position of the SPR peak of the NPs over a wide range of wavelengths will allow for the extension of the MEF phenomenon to a wide range of fluorophores. Using NP platforms, it is possible to increase the quantum yield of weakly luminescent probes by modifying their radiative decay rate to increase their emission efficiency or by coupling the emission with far-field scattering. Thus we can develop specifically tailored NP platforms for MEF suited to specific applications.

Both enhancement and quenching of fluorescence due to the proximity of NPs are efficiently utilized for many different applications. Enhanced signal and photostability of fluorophores, improved surface immunoassay and DNA detection, enhanced wavelength ratiometric sensing, and amplified assay detection are few examples of the applications of MEF. On the other hand, quenching resulting from metallic NPs has been successfully utilized for the improvement of homogeneous and competitive fluorescence immunoassay [9, 10], optical detection of DNA hybridization [11], competitive hybridization assay [12], and optoelectronics [13].

Light intensity of NPs at near field is strongly dependent on the SPR wavelength of the metal nanostructures. Spectral overlap between the absorption and emission spectra of fluorophore and the SPR spectra of metal NPs is necessary for optimum fluorescence enhancement [6, 14, 15]. Theoretical and experimental studies have suggested that fluorescence enhancement is largest when the emission wavelength is slightly redshifted from that of the SPR [16, 17]. Cheng *et al*. [17] suggested that the optimal location of the SPR peak of NPs is between the excitation and emission peaks of fluorophores for maximum enhancement, as both excitation and emission rates can be enhanced in such a situation.

In our previous works [18, 19], we have demonstrated that Ag–Cu NPs can serve as excellent candidates for MEF, due to their interesting optical properties [6, 15]. The imaginary component of the dielectric constant of copper is significantly larger (more than twice) than that of silver in the wavelength range of 300 nm–600 nm. As expected in this wavelength range, due to higher ohmic losses, Cu NPs mostly quench the fluorescence at close proximity [2]. We have demonstrated a simple technique to tune the brightness of a luminophore by changing the composition of Ag–Cu alloy NPs. It was observed

Surface Plasmon Enhanced, Coupled and Controlled Fluorescence, First Edition. Edited by Chris D. Geddes.
© 2017 John Wiley & Sons, Inc. Published 2017 by John Wiley & Sons, Inc.

that pure Ag NPs in the vicinity of fluorophores have the highest fluorescence enhancement and the enhancement factor keeps decreasing with the addition of more % Cu in the Ag–Cu NPs. More interestingly in another case, Ag–Cu NPs were observed to show even better enhancement than pure Ag NPs when the SPR spectrum was tuned to result in maximum spectral overlap with dye [18]. The SPR spectrum of pure Ag is more intense and narrower than that of Cu NPs. The absorption peak attributed to SPR occurs at shorter wavelengths for Ag. Hence, by modifying the composition and atomic arrangement, we can tune both breadth and location of the peak of the SPR spectrum of Ag–Cu alloy NPs [20]. SPR peak wavelengths of Ag–Cu alloy NPs can easily be tuned in the visible and near-infrared regions by changing only one experimental condition, the annealing temperature [7]. We observed enhanced fluorescence emission from two thiol-reactive dyes, Alexa Fluor 594 and Alexa Fluor 488, at the proximity of these Ag–Cu alloy NPs.

In the following sections, we provide experimental details of the synthesis and characterization techniques for preparing the Ag–Cu bimetallic NPs and also elucidate the fluorescence spectroscopy techniques to measure the fluorescence enhancements of vicinal fluorophores. Also, details for modeling the fluorescence enhancement analytically are provided along with a comparison of the experimental results. The theoretical calculations provide deep insights in understanding the influence that the various geometries of Ag–Cu NPs have on their SPR spectra. A better understanding of the principles that govern fluorescence enhancement can lead to designing an optimum fluorescence enhancement platform for commonly utilized fluorophores.

4.2 Experimental Methods

In the following subsections, we describe the synthesis methods used in making the bimetallic NPs and the various particle characterization techniques used in establishing the size, shape, and composition of these NPs and, finally, discuss the fluorescence spectroscopy methods used to study the fluorescence enhancements in the vicinity of the bimetallic NPs.

4.2.1 Synthesis

In this work, we have used two different techniques to synthesize the Ag–Cu bimetallic NPs, namely, (i) *sputtering and annealing* process and (ii) *polyol* synthesis process. Each synthesis technique has its own distinct advantages in controlling a parameter that governs the SPR peak and in turn the fluorescence enhancement.

4.2.1.1 NP Synthesis by Sputtering and Annealing

The *sputtering and annealing* technique is a relatively easy technique to synthesize bimetallic Ag–Cu NPs. However, there is little control on the size and composition of the NPs. The subsequent annealing of the NPs after sputtering changes the atomic arrangement of the constituent atoms in the NP, and this changes the plasmonic properties of the NP. In this work, DC magnetron sputtering is used to deposit Ag or Ag–Cu NPs on 22 mm× 22 mm glass cover. Annealing was done in an electrical furnace in vacuum (30 inch Hg vacuum) to minimize oxidation of the NPs. Annealing temperature ranged from 298 to 523 K and the annealing time was 5 min. These annealed particles were used to study the fluorescence enhancement effects of fluorophores in proximity of Ag–Cu alloy NPs. Mouse immunoglobulin G (IgG), labeled with fluorophores Alexa Fluor 488 and Alexa Fluor 594, was coated on the samples using known methods. As the fluorophores were coated following the same procedure for all samples, the separation distance between fluorophore molecules and NPs and the coverage of the fluorophore molecules on NPs are assumed to be the same for all samples.

4.2.1.2 Nanoparticle Synthesis by the Polyol Process

Using the *polyol* synthesis process, Ag_xCu_{100-x} NPs of five different compositions, $x = 100$, 67, 50, 30, and 0, were synthesized as described in Hongjin's work [21]. Silver nitrate (>99%), copper(II) acetate hydrate (98%), and polyvinylpyrrolidone (PVP, 55 000 molecular weight (MW)) were obtained from Sigma-Aldrich Co., MO. Reducing agent, ascorbic acid, was used instead of the silver nitrate solution to synthesis copper NPs following the same procedure mentioned. Silver NPs were synthesized using the well-known Tollens reaction [22]. Glass substrates were silanized to immobilize silver–copper NPs on them [23]. Fluorophore coatings on the NPs and glass substrates were accomplished by dispersing Cy3-labeled streptavidin in 0.25% poly(vinyl alcohol) (PVA, 15 000 MW) aqueous solution by sonicating and then coating the solution on the substrates by spin coating (1500 rpm speed). The resulting polymer thickness was ~26 nm. Hence, the average distance between the substrate and a fluorophore molecule was approximated by 13 nm. As the fluorophores were coated following the same procedure for all

samples, the separation distance between fluorophore molecules and NPs and the coverage of the fluorophore molecules on NPs are assumed to be the same for all samples.

4.2.2 Particle Characterization

For the Ag–Cu NPs synthesized by the sputtering and annealing technique, the TEM data shows that the average size of Ag–Cu NPs is 15 nm ± 5 nm (derived from a population of 100 particles) (Figure 4.1a), and after annealing these NPs at 448 K, the average size is 14 nm, whereas the average size of Ag NPs was 14 ± 3 nm. From the HRTEM image (Figure 4.1b), the lattice spacing was measured to be 0.21–0.24 nm. In the {111} lattice plane, silver has lattice spacing of 0.24 nm, whereas the lattice spacing of Cu is 0.21 nm [25]. A confirmation is made from Figure 4.1b and STEM-EDS data (Figure 4.1c) that the NPs are comprised of both Ag and Cu and possessing a ratio of Ag–Cu to be 1 : 1.

For the particles synthesized using the polyol synthesis process, TEM data (Figure 4.2a and b) of the colloidal Ag–Cu alloy NPs indicated the particle size to be in the range of 130–200 nm (derived from a population of 100 particles). The STEM-EDS data (Figure 4.2c) confirms that the NPs comprise both Ag and Cu. The sizes of different compositions of Ag–Cu NPs coated on glass slides were also found to be approximately the same. The sizes of NPs and particle density were measured using ImageJ software. From the SEM images of the Ag–Cu NPs (Figure 4.3b and c), the average size of these NPs on the glass slides was measured to be ~150 nm (derived from a population of 800 NPs). SEM images of the Ag NPs (Figure 4.3a) indicate their average size to be ~80 nm. AFM images of the Ag and Ag–Cu NPs on glass slides

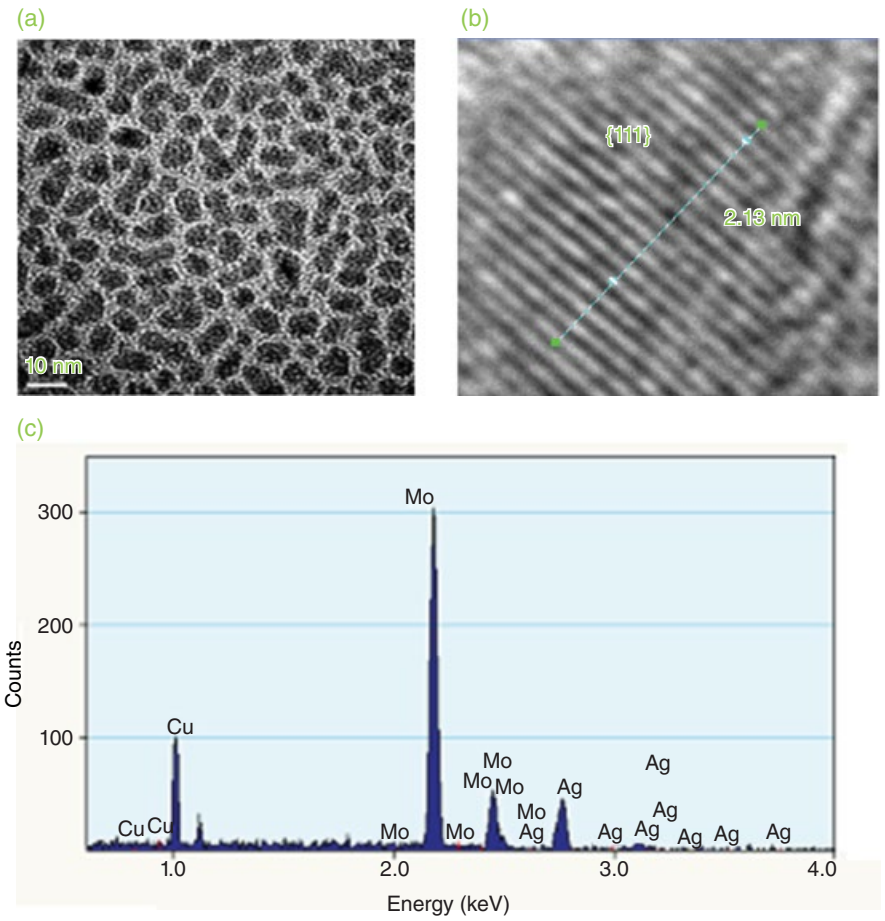

Figure 4.1 (a and b) High-resolution transmission electron micrograph and (c) STEM-EDS spectra, for the Ag–Cu alloy nanoparticles as synthesized using the sputtering technique. Jeremie *et al*. [24]. Reproduced with the permission of Hindawi Publication Corporation. (*See insert for color representation of this figure*.)

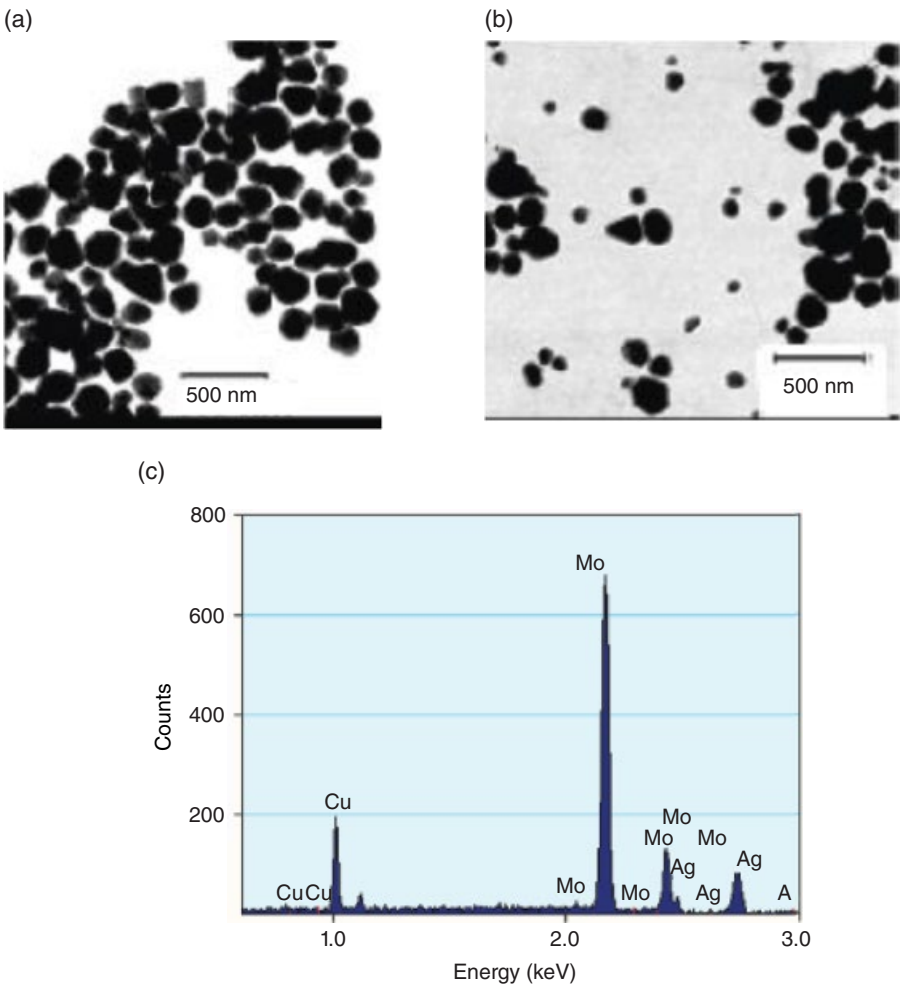

Figure 4.2 Transmission electron microscopy image of (a) 1 : 1 Ag–Cu nanoparticles, (b) 3 : 7 Ag–Cu nanoparticles, and (c) STEM-EDS spectra for 1 : 1 Ag–Cu alloy nanoparticles. Jeremie *et al*. [24]. Reproduced with the permission of Hindawi Publication Corporation.

are given in Figure 4.3d–f. The particle density for Ag NPs was estimated to be 38 particles/μm^2. Particle density for Ag–Cu NPs was estimated to be 20 particles/μm^2. It is difficult to obtain the same size and particle density for silver and silver–copper NPs due to limitations of the synthesis techniques.

4.2.3 Fluorescence Spectroscopy

The Leica DMI4000b inverted fluorescence microscope equipped with Leica DFC340 FX charge-coupled device camera was utilized for MEF measurements. Fluorescence intensity of each sample was determined by measuring the mean intensity of an image of sample and subtracting the mean value of the background image. Fluorescence intensities for each sample were obtained by analyzing a 1.64 mm × 2.19 mm image section of each substrate.

4.2.3.1 On Sputtered and Annealed Ag–Cu NPs

The UV–VIS extinction spectra attributed to SPR of colloidal Ag–Cu NPs show a single peak in the visible range. For the sputtered and annealed Ag–Cu NPs, the SPR peak blueshifts upon increasing the annealing temperature from 298 K to 523 K (Figure 4.4). Cu atoms segregate to the surface with increasing annealing temperature, thereby increasing the concentration of Ag in the NP core as a result, and the SPR peak gradually moves nearer to the SPR peak of pure Ag NPs (Figure 4.4a). This can be explained as follows: for the core–shell structure, the effective dielectric constant is a function of the dielectric constant of both core and shell materials and also the volume fraction of shell layer. The SPR extinction spectrum peak, which can be calculated from the imaginary part of polarizability, a function of effective dielectric

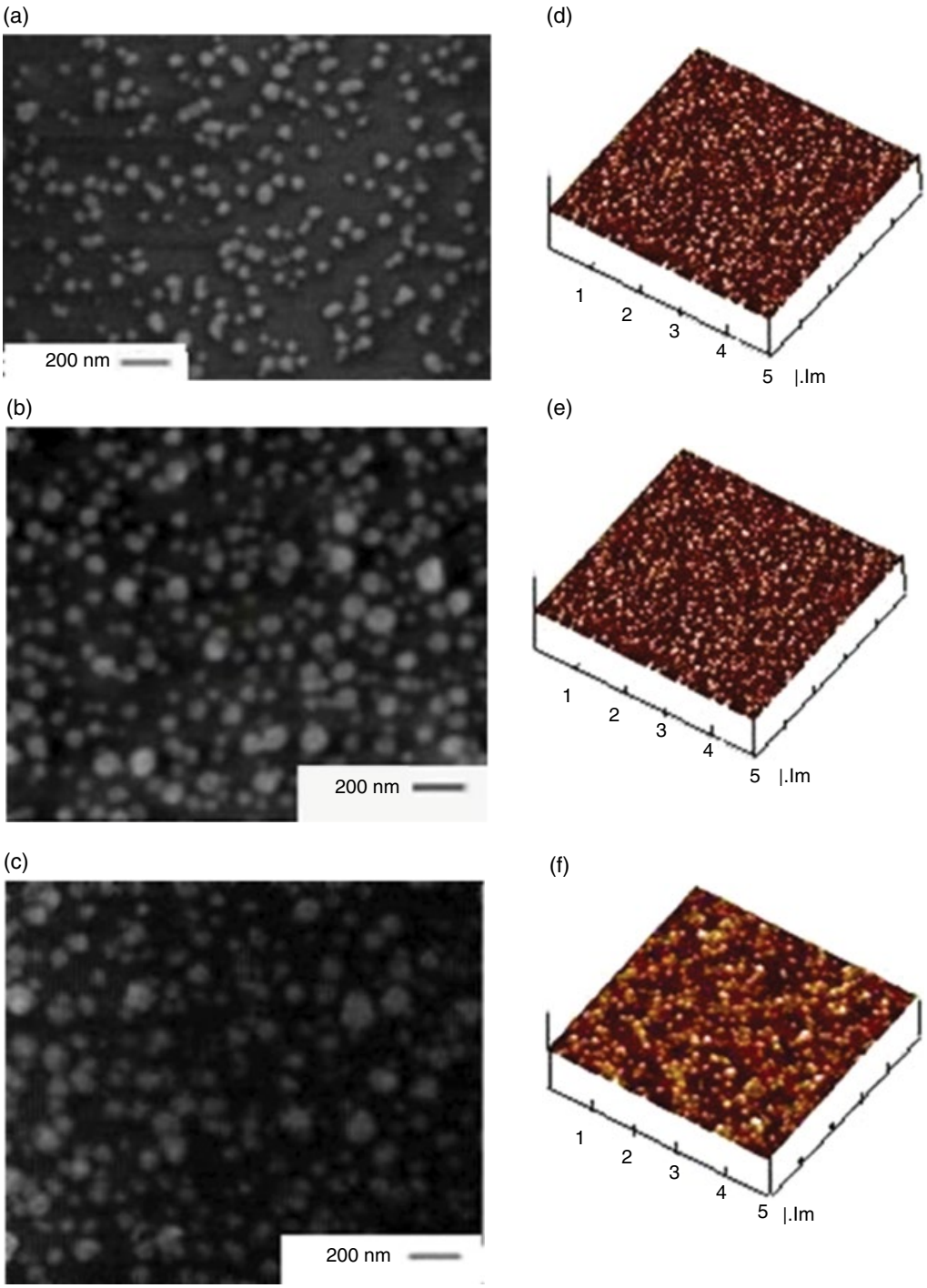

Figure 4.3 SEM images of (a) Ag nanoparticles (average size 78.81 ± 11.44 nm and particle density 38/μm^2), (b) 2 : 1 Ag–Cu nanoparticles (average size 157 ± 38 nm and particles density 19/μm^2), and (c) 1 : 1 Ag–Cu nanoparticles coated on glass substrates (average size 144 ± 12 nm and particles density 21/μm^2). AFM images of (d) Ag nanoparticles, (e) 2 : 1 Ag–Cu nanoparticles, and (f) 1 : 1 Ag–Cu nanoparticles coated on glass substrates. Jeremie *et al*. [24]. Reproduced with the permission of Hindawi Publication Corporation.

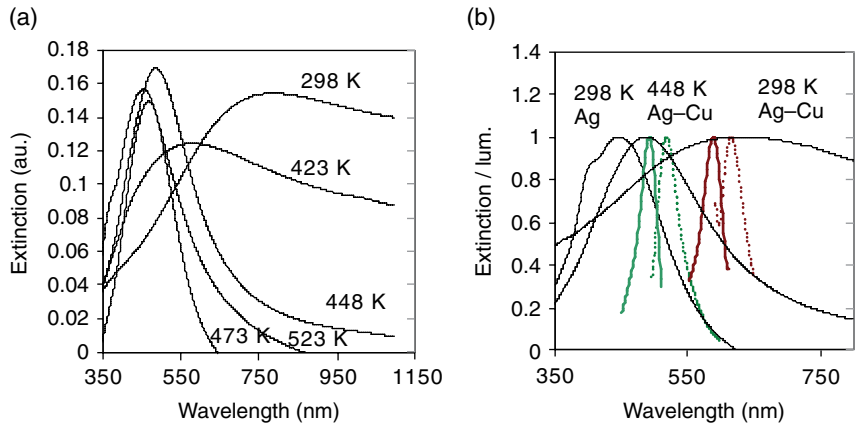

Figure 4.4 (a) Extinction spectra of annealed Ag–Cu nanoparticles and (b) extinction spectra of Ag–Cu nanoparticles and Ag nanoparticles used for MEF experiments and the excitation and emission spectra of Alexa Fluor 594 (dotted line with peak at 617 nm peak-emission spectrum, solid line with peak at 590 nm excitation spectrum) and Alexa Fluor 488 (dotted line with peak at 525 nm peak-emission spectrum, solid line with peak at 480 nm excitation spectrum). All spectra were normalized for comparison. Jeremie *et al*. [24]. Reproduced with the permission of Hindawi Publication Corporation.

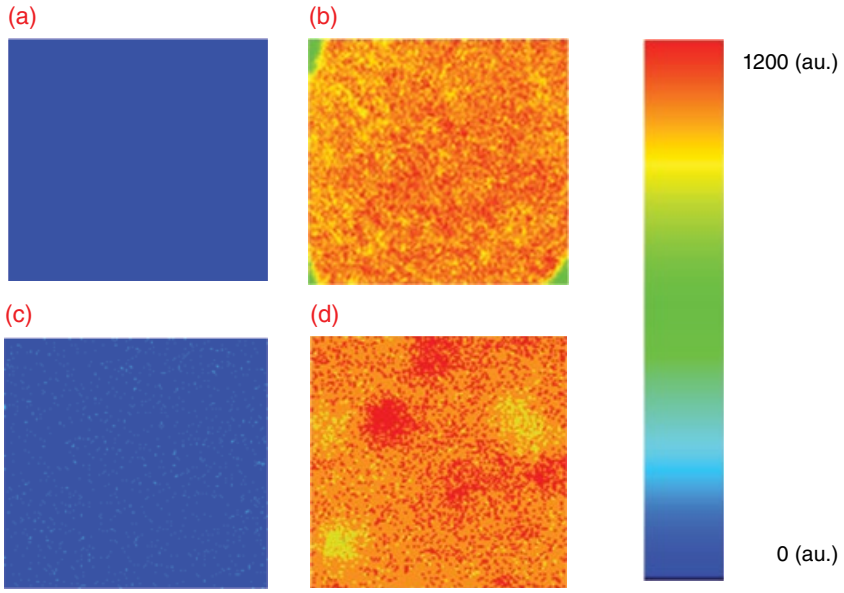

Figure 4.5 Pseudo-colored image of fluorophores coated on glass and Ag–Cu nanoparticles. (a) Alexa Fluor 488 coated on glass, (b) Alexa Fluor 488 coated on 448 K annealed silver–copper alloy nanoparticles, (c) Alexa Fluor 594 coated on glass, and (d) Alexa Fluor 594 coated on room-temperature (298 K) silver–copper alloy nanoparticles. Jeremie *et al*. [24]. Reproduced with the permission of Hindawi Publication Corporation.

constant, will be nearer to that of core material for shell layer volume fraction up to ~0.6 [26].

Fluorescence intensity of both Alexa Fluor 594 and Alexa Fluor 488 was observed to increase significantly in the vicinity of these Ag–Cu NPs (Figure 4.5b and d). Enhancement ratio was calculated by comparing fluorescence intensity of the sample with the fluorescence intensity of the fluorophore coated on a glass cover slip. As shown in Figure 4.4b, the SPR spectrum of the Ag–Cu NPs annealed at 448 K nicely overlaps both the excitation and emission spectra of Alexa Fluor 488. This annealed Ag–Cu NP platform results in a very strong enhancement (141 ± 19 times) of fluorescence of Alexa Fluor 488 (Figure 4.5a and b). The Ag–Cu NPs annealed at 298 K, which show less spectral overlap, also result in substantial enhancement (100 ± 10 times). The lowest enhancement (50 ± 10) was observed at the proximity of pure Ag NPs (deposited at the same conditions as Ag–Cu NPs), for which the spectral overlap is least.

The effect of spectral overlap on fluorescence enhancement is also pronounced for Alexa Fluor 594. We found 23 ± 12 times enhancement of emission from Alexa Fluor 594 at the proximity of room-temperature grown Ag–Cu NPs (Figure 4.5c and d). On the other hand, both pure Ag NPs and the 448 K annealed Ag–Cu NPs grown at similar conditions result in lower enhancements (9 ± 0.9 times for 448 K annealed Ag–Cu NPs and 6 ± 3 times for Ag particles) because of less spectral overlap. The best case Ag–Cu studied was 2.8 times better than pure Ag for Alexa Fluor 488 and ~3 times better for Alexa Fluor 594. In both cases, the spectral overlap was largest when maximum enhancement was seen. It is possible to achieve this enhancement for the alloy particles because the breadth of the peak can also be tuned.

4.2.3.2 On Ag–Cu NPs Synthesized with the Polyol Process

For the Ag–Cu NPs synthesized using the polyol synthesis process, Figure 4.6 shows the normalized extinction spectra for Ag–Cu alloy NPs at different percentages of copper as synthesized by the polyol technique. With increasing copper percentage, this SPR peak shifts to longer wavelengths. Indeed, the SPR peak is shifted from 380 nm (pure Ag) to 480 nm ($Ag_{0.30}Cu_{0.70}$) with increase in the percentage of Cu in the bimetallic NP. The redshifts of the SPR peak with increasing copper concentrations are attributed to the decrease in conductivity [7].

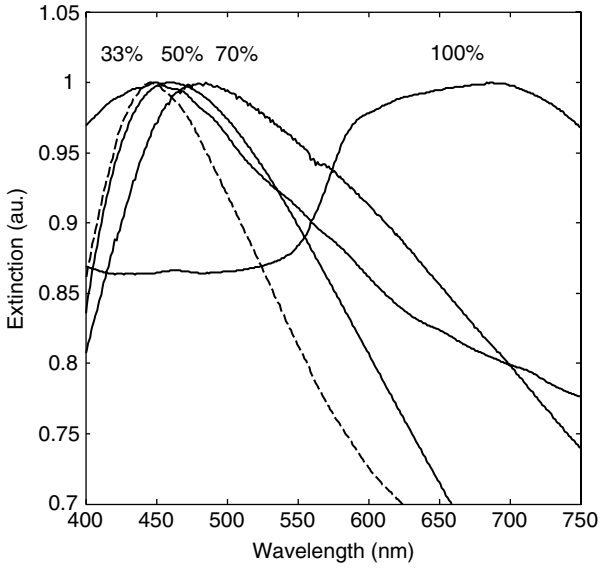

Figure 4.6 Normalized extinction spectra for Ag–Cu alloy nanoparticles at different percentages of copper as synthesized by the polyol technique. Solid lines show the extinction spectra of Ag–Cu nanoparticles in solution. Dotted line shows the extinction spectra of Ag–Cu nanoparticles with 33% Cu on APS-coated glass slides. Jeremie *et al.* [24]. Reproduced with the permission of Hindawi Publication Corporation.

The fluorescence intensity of Cy3 was observed to increase significantly in the vicinity of both Ag and Ag–Cu NPs (Figure 4.7). The enhancement ratio for Ag and Ag–Cu NPs was calculated by comparing fluorescence intensity of the sample with the fluorescence intensity of the fluorophore coated on an APS-coated glass substrate. In the case of copper NPs, the enhancement ratio was calculated comparing the fluorescence intensity with fluorophore coated on PDDA-coated glass slides. The Ag NPs platform resulted in a very strong enhancement (90 ± 20 times) for Cy3 (Figure 4.7b). As the quantum efficiency of dye Cy3 is very small, the enhancement effect is high. The Ag–Cu NPs (Figure 4.7c) also showed enhancement (55 ± 15 times for 2 : 1 Ag–Cu, 30 ± 6 times for 1 : 1 Ag–Cu), but as the copper percentage in NPs increased, the enhancement decreased. Finally, instead of enhancing, the Cu NPs quenched (8 ± 5 times) the fluorescence of Cy3 (Figure 4.7d). This may be because, in the vicinity of metal NPs, both the radiative decay rate and the non-radiative decay rates increase, and as percentage of Cu increases, the non-radiative decay rate also increases, eventually surpassing the radiative decay rate.

4.3 Theoretical Modeling

The theoretical modeling of the emission enhancements of the fluorophore coupled to an NP is based on the numerical solution of the Maxwell's equations. In the following sections, we discuss about the modeling theory and present results for the following: (i) SPR of metallic NPs using Mie theory, (ii) the analytical solution for fluorescence excitation and emission in the presence of NPs using modified Gersten–Nitzan [27, 28] (G–N) model, and (iii) the numerical solution of the fluorescence emission process using finite-difference time-domain (FDTD) calculations.

4.3.1 Modeling SPR Using Mie Theory

The earliest model to calculate the SPR of spherical metallic particles was presented by Mie in 1908 [29]. Mie theory calculates the absorption spectra of spherical particles by providing an exact solution of the Maxwell's equations. Mie's theory is valid for any size particles but is limited to system where interparticle

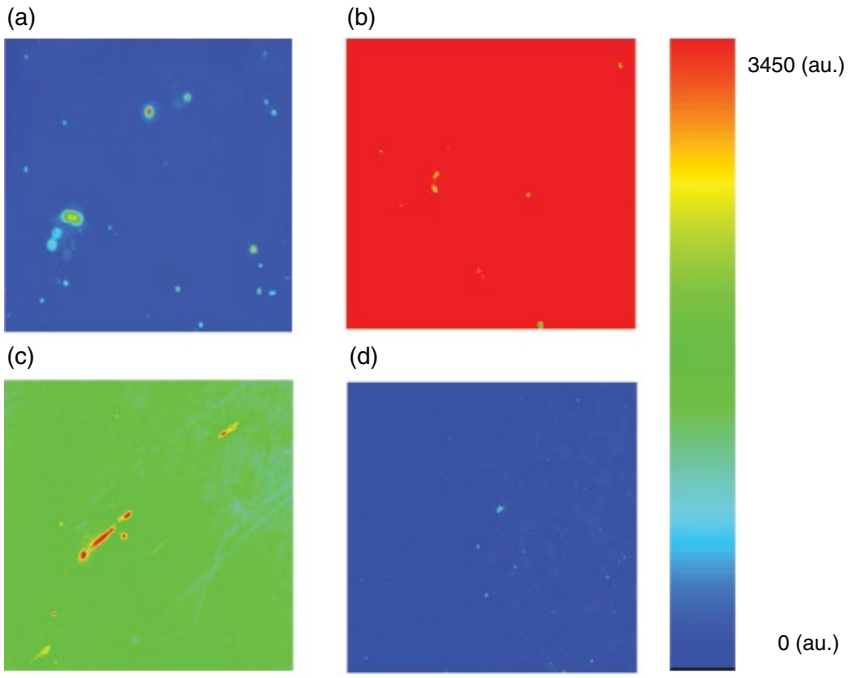

Figure 4.7 Pseudo-colored image (intensity increases from dark to bright) of Cy3 coated on (a) glass, (b) Ag nanoparticles, (c) 1 : 1 Ag–Cu nanoparticles, and (d) Cu nanoparticles. Jeremie *et al*. [24]. Reproduced with the permission of Hindawi Publication Corporation.

separation distance is much larger than the wavelength of incident light. According to Mie's theory, the total transmittance through films containing spherical metal particles is

$$T_{\text{tot}} = \exp\left(-N\pi a^2 Q_{\text{ext}} d\right)$$

where N is the number concentration of spheres per unit volume, a is sphere radius, and d is film thickness. The extinction coefficient is given as

$$Q_{\text{ext}} = \left(\frac{2}{x^2}\right)\sum_{n=1}(2n+1)\,\text{Re}(a_n + b_n)$$

where $x = 2\pi n a_0/\lambda$, n_0 is refractive index of the host medium, and λ is wavelength of the incident light in vacuum. a_n and b_n are Mie scattering coefficients.

For calculating absorption spectra for spherical particles using Mie's theory, one needs to know the effective refractive index or dielectric constant for the system. The complex dielectric constant of metals can be calculated using a combination of Drude theory and Lorentz theory. The combined effects of the free electrons (Drude model) and the bound d-electrons (Lorentz model) influence the reflectance properties of the metal. So, for most metals, the dielectric constant can be calculated by the formula

$$\varepsilon_{\text{r}} = \varepsilon_{\text{f}} + \varepsilon_{\text{b}}$$

where ε_{f} is described by the Drude model ($\omega_0 = 0$) and ε_{b} is described by the Lorentz model ($\omega_0 = [E_{\text{F}} - E_{\text{D}}]/\hbar$) as follows:

$$\varepsilon'_{\text{f}}(\omega) = 1 - \frac{\omega_p^2\tau^2}{1+\omega^2\tau^2}$$

$$\varepsilon''_{\text{f}}(\omega) = \frac{\omega_p^2\tau}{\omega\left(1+\omega^2\tau^2\right)}$$

$$\varepsilon'_{\text{b}}(\omega) = 1 + \frac{4\pi n\text{e}^2}{m}\frac{\left(\omega_0^2-\omega^2\right)}{\left(\omega_0^2-\omega^2\right)^2+\omega^2/\tau^2}$$

$$\varepsilon''_{\text{b}}(\omega) = \frac{4\pi n\text{e}^2}{m}\frac{\omega/\tau}{\left(\omega_0^2-\omega^2\right)^2+\omega^2/\tau^2}$$

where the single and double dashes denote the real and imaginary part of the dielectric constant and e is the electronic charge.

There are many studies devoted to calculating effective dielectric constants for composite materials [30–35]. Maxwell Garnett (MG) and Bergman

theories have been mostly used to calculate effective dielectric constant for metal-dielectric composite [30, 31, 36]. These theories are valid for only spherical or ellipsoidal metal NPs in dielectric media. These theories are developed considering the interaction of the external electric field with metal particles acting as interacting dipoles, with an effective polarizability given by the Drude relation, while the dielectric constant of the composite material was obtained through the Clausius–Mossotti relation [36]. MG theory is based on the assumptions that the percentage of metal (f_a) in dielectric media is very small and interparticle separation is very small compared to the wavelength of light.

For a random mixture of two dissimilar materials, the effective dielectric constant can be calculated using Bergman's theory [30]. According to this theory,

$$\frac{1}{\varepsilon} = \frac{f_a}{a} + \frac{f_h}{h} - \frac{2}{3}\frac{f_a f_h \left(1/h - 1/a\right)^2}{\left[\gamma/\varepsilon_a + \left(1-\gamma\right)/\varepsilon_h\right]}$$

where ε is the effective permittivity in the vacuum of the alloy NP, f_a and f_h are the volume fractions of the constituent materials with relative permittivity ε_a and ε_h, respectively, and

$$f_a + f_h = 1$$

γ is a parameter that is related to the volume fraction f_a and, for a homogeneously mixed alloy, they are related by the MG mixing rule as follows:

$$\gamma = 1 - \frac{2f_a}{3}$$

Gao *et al.* [33] incorporated shape distribution of the components in both MG and Bergman theories. Garcia *et al.* [34] developed a self-consistent technique based on mixing rules to predict the effective dielectric constants, and thus SPR spectra, for multicomponent mixtures.

Dielectric constants for alloy NPs of different compositions are not available and have to be calculated using semiempirical models such as those based on Drude theory and experimental data for pure bulk metals. In the work done by Bruzzone *et al.* [37], semiempirical models are developed based on the assumption of homogeneous distribution of metallic atoms in their alloys. For the core–shell structure, the dielectric constant is given as follows:

$$\varepsilon_{\text{core}}(\omega,R) = \varepsilon_{\text{exp}}(\omega) + \frac{\omega_p^2}{\omega^2 + i\omega\Gamma_\infty} - \frac{\omega_p^2}{\omega^2 + i\omega\left(\Gamma_\infty + \Gamma_{\text{core}}\right)}$$

$$\varepsilon_{\text{shell}}(\omega,R) = \varepsilon_{\text{exp}}(\omega) + \frac{\omega_p^2}{\omega^2 + i\omega\Gamma_\infty} - \frac{\omega_p^2}{\omega^2 + i\omega\left(\Gamma_\infty + \Gamma_{\text{shell}}\right)}$$

where Γ_{core} and Γ_{shell} are surface-induced contributions to the damping.

4.3.2 Modeling of Metal-Enhanced Fluorescence Modified Gersten–Nitzan Model

The first attempt to model the surface plasmon-enhanced fluorescence of fluorophores was done by Gersten and Nitzan [27]. Using the G–N model, the modifications to the radiative decay rate and the total decay rate of fluorophore in proximity to metal NPs can be calculated. According to this model, the excited state decay rate is calculated in two steps. First the quasi-static approximation is used to analyze the electromagnetic interaction between source dipole and metal sphere. The analysis is done based on electrostatics, as the retardation effect is neglected assuming the sizes of NPs to be much smaller than the wavelength. Electrostatic potential is derived from the superposition of the source dipole potential and the induced multipoles of sphere. In the second step, radiative power is calculated from the effective dipole moment comprised of a vectorial superposition of the source dipole moment and the induced dipole moment. Radiative rate modification is obtained by normalizing to the power radiated by an uncoupled source with identical dipole moment. The non-radiative decay rate is calculated by calculating the power dissipated in the metal sphere by the Joule heating law. This model does not consider multipole radiation, and the interference between source dipole and induced dipole is neglected. The key advantage of model over exact electrodynamical theory is that model can be generalized to spheroidally shaped particles. Mertens *et al.* [38] introduced a correction factor for radiative reaction and dynamic depolarization in the G–N model to modify the quasi-static polarizability of the NPs to account for the retardation effect. For the radial dipole orientation, the expressions for the fluorophore molecule are positioned at distance d from the surface of sphere with radius a and dielectric constant located in its medium. This corrected model can accurately describe decay rate enhancement near larger NPs (several 100 nm). In this model, the fluorophore is modeled as a classical dipole with dipole moment μ. For the radial dipole orientation, the expressions for Γ_R and Γ_{tot} for the fluorophore

molecule positioned at a distance d from the surface of sphere with radius a and dielectric constant $\varepsilon = \varepsilon' + i\varepsilon''$ located in its medium ε_m are given as follows:

$$\frac{\Gamma_{tot}^{\perp}}{\Gamma_R^{ref}} = 1 + \frac{3}{4(ka)^3}\sum_l l(l+1) \operatorname{Im}\left\{ C_l \frac{\varepsilon - \varepsilon_m}{\varepsilon + ((l+1)/l)\varepsilon_m} \left(\frac{a}{a+d} \right)^{2l+4} \right\}$$

$$\frac{\Gamma_R^{\perp}}{\Gamma_R^{ref}} = \left| 1 + 2C_1 \frac{\varepsilon - \varepsilon_m}{\varepsilon + 2\varepsilon_m} \left(\frac{a}{a+d} \right)^3 \right|^2$$

where a is the radius of the nanoparticle; $k = \varepsilon(\mathrm{m}) \times (2\omega/\mathrm{c})$, where ω is the optical frequency (radian per second), $\varepsilon(\mathrm{m})$ is the dielectric constant of the media, and c is the velocity of light in vacuum.

For the tangential dipole orientation, the expressions for Γ_{tot} and Γ_R are

$$\frac{\Gamma_{tot}^{\parallel}}{\Gamma_R^{ref}} = 1 + \frac{3}{2(ka)^3}\sum_l (l+1)^2 \operatorname{Im}\left\{ C_l \frac{\varepsilon - \varepsilon_m}{\varepsilon + ((l+1)/l)\varepsilon_m} \left(\frac{a}{a+d} \right)^{2l+4} \right\}$$

$$\frac{\Gamma_R^{\parallel}}{\Gamma_R^{ref}} = \left| 1 - C_1 \frac{\varepsilon - \varepsilon_m}{\varepsilon + 2\varepsilon_m} \left(\frac{a}{a+d} \right)^3 \right|^2$$

In the previous expressions, l is the angular mode number and Γ_R^{ref} is the radiative decay rate of fluorophore in the absence of NPs. C_1 is the correction factor for radiation dumping and dynamic depolarization:

$$C_1 = \frac{1}{1 - (ik^3\alpha/6\pi) - (k^2\alpha/4\pi a)}$$

α is the quasi-static polarizability:

$$\alpha = 4\pi a^3 \frac{\varepsilon - \varepsilon_m}{\varepsilon + 2\varepsilon_m}$$

For $l \neq 1$, C_l is assumed to be 1.

A fluorophore emits fluorescence by absorbing incident light at a particular frequency ω_{abs} and then by emitting light at the emission frequency ω_{flu}. The intensity of the fluorophore at the proximity of metal NPs can be written as [16, 39]

$$I = C\,\eta(\omega_{flu})\,\sigma_{abs}(\omega_{abs})\left|K(\omega_{abs})\right|^2 I_{exc}(\omega_{abs})\,T$$

Here, $\eta(\omega_{flu})$ is quantum yield of emission measured at ω_{flu}, $\sigma_{abs}(\omega_{abs})$ is absorption cross section of the molecule in vacuum, $I_{exc}(\omega_{abs})$ is excitation intensity in vacuum, C is a constant, T is the integration time of the detector, and $K(\omega_{abs})$ is local field vector.

From the previous expression, it can be seen that by changing the local field for absorption and/or quantum yield, we can change the intensity of fluorescence. The absorption rate of the fluorophore can be enhanced by increasing both the absorption coefficient of the fluorophore itself and the local field intensity. On the other hand, the quantum yield of the fluorophore can be influenced by varying the radiative and non-radiative decay rates.

Kümmerlen *et al.* [40] suggested that the quantum efficiency enhancement factor Y (ratio of quantum efficiencies in the presence of metal NPs and without NPs) can be calculated using the following equation:

$$Y = \left|L(\omega_{abs})\right|^2 Z(\omega_{flu})$$

The first term represents the enhancement of local electric field at the excitation frequency. The second term describes the change in quantum efficiency due to radiative and non-radiative decay rate enhancements at the emission frequency. In the following sections, calculation of both excitation enhancement factor and quantum efficiency enhancement factor are discussed.

We used the model proposed by Kümmerlen *et al.* [40] for calculating the overall quantum efficiency enhancement factor in the proximity of metal NPs. This model includes both the excitation enhancement factor by local field effects and the emission enhancement factor due to radiative and non-radiative decay rates. The corrected G–N model proposed by Mertens *et al.* [38] is applied for calculating the emission enhancement factor. These theoretical calculations help in providing insights into the experimental findings.

Here, we present theoretical calculations for modeling the phenomenon of MEF and compare them with our experimental results to study the composition effect as well as the annealing effect. The model suggested by Kümmerlen *et al.* [40] that includes both excitation and emission enhancement factors is used for calculating the overall quantum efficiency enhancement factors. Exact representation of experimental conditions is not possible in theoretical calculations due to the differences in experimental geometry (NPs are not in a homogeneous dielectric environment, all the NPs are not of spherical shape and not of the same size, fluorophore–nanostructures separation distance is not uniformly the same). Furthermore, accurate dielectric constants of room temperature and annealed Ag–Cu NPs are not known, or evaluable, as they remain phase separated. However, these calculations provide some insights into the experimental findings.

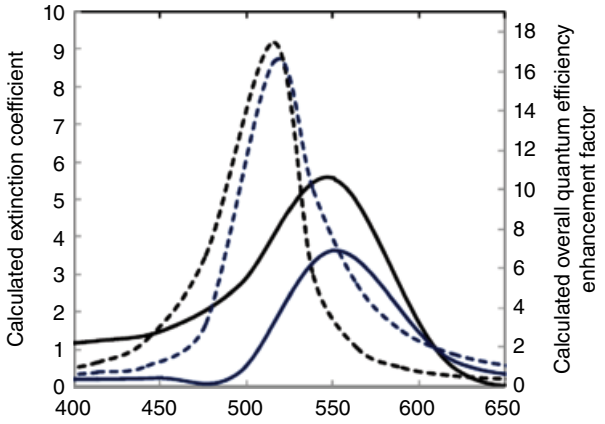

Figure 4.8 Theoretically calculated extinction coefficient (black) and theoretically calculated overall quantum efficiency enhancement ratio (gray) for Ag (dotted line) and 1 : 1 Ag–Cu nanospheres (solid line) (size 20 nm, surrounding dielectric media silica glass, separation distance 15 nm, dipole orientation averaged over all solid angles). Jeremie *et al.* [24]. Reproduced with the permission of Hindawi Publication Corporation.

Figure 4.8 shows the theoretically calculated extinction coefficient (using Mie theory) and the overall quantum efficiency enhancement factor for pure Ag and 1 : 1 bimetallic Ag–Cu NPs. From Figure 4.4, the effect of spectral overlap is clearly evident. In the wavelength range of 450–555 nm, as the extinction spectrum for the Ag NPs is more pronounced, overall quantum efficiency enhancement in the proximity of the Ag is better than that of the Ag–Cu NPs. Most importantly, in the wavelength range of 555–605 nm, the Ag–Cu NPs show better overall quantum efficiency enhancement than pure Ag as the spectral overlap is better for the Ag–Cu NPs. For both Ag NPs and Ag–Cu NPs, the maximum overall quantum efficiency enhancement wavelengths are slightly red-shifted with respect to the extinction coefficient peaks. As the calculations were done for the high quantum yield (0.5) fluorophore, the excitation enhancement effect is more pronounced than the emission enhancement effect.

Figure 4.9a and b shows the theoretically calculated modified overall quantum efficiency and the experimentally observed fluorescence enhancement ratio of fluorophore Cy3 in the vicinity of different compositions of Ag–Cu NPs. The calculations were done assuming the size of NPs to be 150 nm and the separation distance between NPs and fluorophore molecules to be 13 nm to compare with experimental results. The surrounding dielectric medium was assumed to be PVA. The enhancement of local electric field amplitude ($|L(\omega_{abs})|^2$) was calculated at the absorption frequency of Cy3 (550 nm). The quantum efficiency change ($Z(\omega_{flu})$) due to radiative and non-radiative decay rate enhancement was calculated at 570 nm emission wavelength, which is the emission peak for Cy3. The quantum efficiency was calculated taking into account all multipole modes up to $l = 100$. Dipole orientation was assumed to be averaged over all solid angles. For better representation of experimental conditions, the source dipole orientation was averaged over all solid angles. This was achieved by averaging the results for decay rates obtained for radial and tangential orientations. Dielectric constants for Ag–Cu NPs of different compositions were calculated following the procedure described by Bruzzone *et al.* [37]. The dielectric function was calculated using the semiempirical model based on Drude theory and experimental data. The experimental data used for this calculation were obtained by averaging the values for pure metals over the volume. Drude contributions for nanostructure and bulk were calculated using the values of pure metal averaged over volumes.

It can be seen from Figure 4.9a that both the experimental and theoretical (inset) results show the same trend that with the increase in copper percentage in NPs, the enhancement effect decreases, with pure copper quenching fluorescence. The theoretically calculated emission enhancement factor and excitation enhancement factor are separately shown in Figure 4.9b and c, respectively. We can see that both emission and excitation have comparable effects on overall quantum efficiency change. Some reasons for the discrepancy in numerical values between theoretical and experimental results are the differences in experimental geometry (NPs are not in a homogeneous dielectric environment, all the NPs were not of spherical shape and not of same size, fluorophore nanostructure separation distance is not precise) with respect to theoretical calculations, which assumed uniformity in these parameters. It can be also because we observed the fluorescence intensity of the image over the entire bandwidth of filters used for fluorescence microscopy not at any particular wavelength.

It is known that quantum efficiency enhancement depends on the size of spherical NPs. Figure 4.10 shows the dependencies of quantum efficiency enhancement on the size of Ag–Cu NPs at the fluorophore–NPs separation distance of 13 nm. The calculation for Figure 4.10 was done considering the same dipole–NP orientation and surrounding conditions as for Figure 4.8. It can be seen from Figure 4.10 that there is an optimum size of NPs for which quantum efficiency enhancement is maximum. The coupling between the emission of the fluorophore and the plasmon mode increases as the size of the NPs decreases, and coupling efficiency of emission at far field through

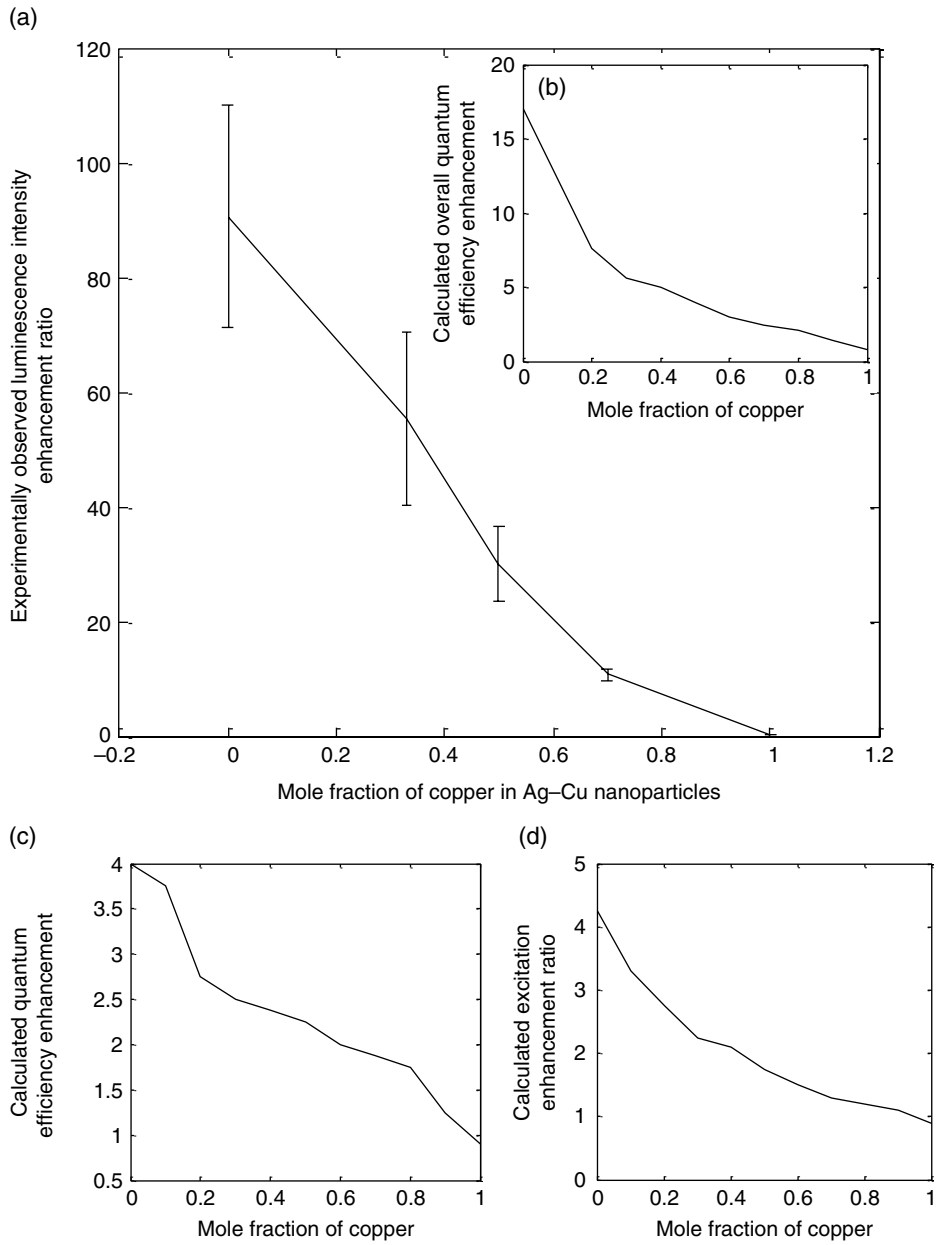

Figure 4.9 (a) Experimentally observed luminescence enhancement ratio of Cy3 in the proximity of different compositions of Ag–Cu nanoparticles. (b) Inset shows theoretically calculated overall luminescence quantum efficiency enhancement ratio. (c) Calculated quantum efficiency enhancement factor due to emission enhancement. (d) Calculated excitation rate enhancement factor as a function of composition of Ag–Cu nanoparticles. Jeremie *et al*. [24]. Reproduced with the permission of Hindawi Publication Corporation.

NP scattering increases as the size of NPs increases. Both of these coupling phenomena are responsible for the enhancement of quantum efficiency. Spectral overlap between the absorption and emission spectra of fluorophore and SPR spectra of metal NPs is very important for optimum fluorescence enhancement. Some theoretical and experimental studies have suggested that fluorescence enhancement is largest when the emission wavelength is slightly redshifted from that of the SPR. When the size of the particle increases, the SPR is shifted to longer and broadened wavelength and decreases in magnitude due to dynamic polarization. So, there exists an optimum diameter. We can see from Figure 4.10 that the optimum radius for Ag, Ag–Cu, and Cu NPs is ~60 nm. At this optimum diameter, even Cu NPs show enhancement instead of

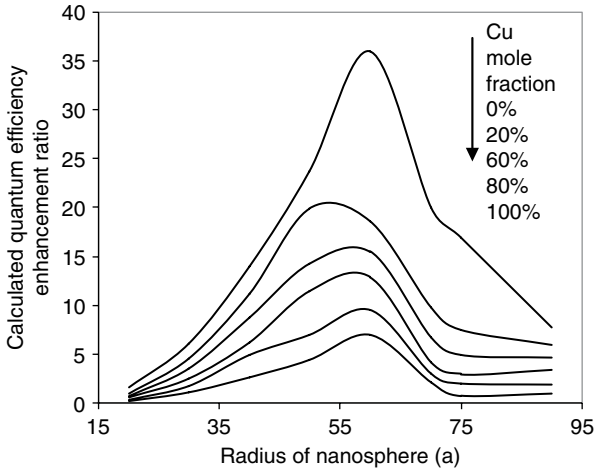

Figure 4.10 Quantum efficiency enhancement ratio of Cy3 in the proximity of different diameter Ag–Cu nanoparticles at different compositions embedded in a dielectric medium of poly(vinyl alcohol). Fluorophore–nanoparticle separation distance is assumed to be 13 nm. Jeremie *et al*. [24]. Reproduced with the permission of Hindawi Publication Corporation.

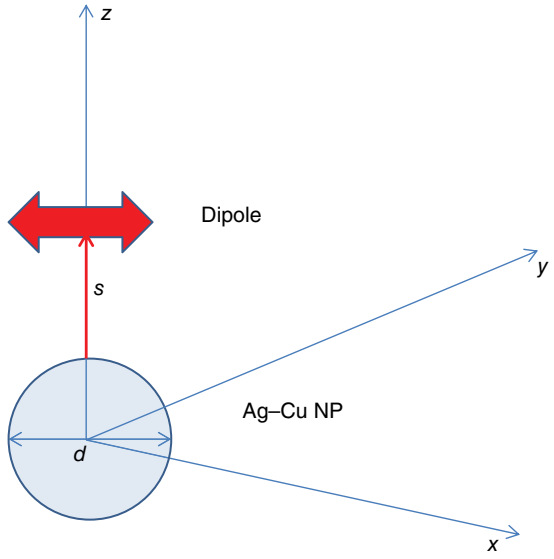

Figure 4.11 Schematic diagram for the FDTD calculation of the Ag–Cu bimetallic nanoparticle placed near the fluorophore, which is modeled as an oscillating dipole. The diameter of the NP is represented as *d* and the dipole–NP separation distance is represented as *s*. Jeremie *et al*. [24]. Reproduced with the permission of Hindawi Publication Corporation.

quenching. So it can be inferred that if we can synthesize alloy NPs of optimum diameter using advanced methods like electron-beam lithography, we can elucidate the effect of composition on MEF better.

4.3.3 Modeling MEF Using Finite-Difference Time-Domain (FDTD) Calculations

The analytical model of Gersten and Nitzan is only valid for spherical or oblate spheroid geometries [27]. However, it has been shown in recent years that NPs with geometries like cubes or prisms have much well-defined, intense, and narrow SPR peaks and, hence, are likely to do much better fluorescence enhancements than spherical NPs (refs). In order to study the optical properties of these intricate geometries in a detailed and accurate way, the state-of-the-art FDTD calculations has been established as a powerful engineering tool for integrated and diffractive optics device simulations. The FDTD approach is based on a direct numerical solution of the time-dependent Maxwell's curl equations. Here, we show the compositional effects of a spherical Ag–Cu bimetallic NP on the fluorescence enhancement factor. A time-windowed dipole source, radiating at a fixed wavelength of 570 nm, was used to mimic the emission of a commercially available fluorophore, Cy3. It is assumed that the excitation stage of fluorescence has occurred and the fluorophore is now emitting dipole radiation.

Three-dimensional FDTD simulations were performed using the program FDTD solutions (version 7.5.2) from Lumerical Solutions, Inc. (Vancouver, Canada). The methodology of the FDTD calculations for calculating the fluorescence enhancements is based on similar work done by Chowdhury *et al*. [41] on fluorophores placed in the vicinity of silver NP dimers. The theory involved in doing the FDTD calculation has been discussed in detail by Bharadwaj *et al*. [42] Figure 4.11 is a schematic illustration of the system studied, where d is the diameter of the Ag–Cu bimetallic NP, s is the distance between the NP surface and the dipole, θ is the polar angle from the z-axis where $0 < \theta < \pi$, and Φ is the azimuthal angle in the x–y plane from the x-axis with $0 < \Phi < 2\pi$. The center of the spherical Ag–Cu bimetallic NP is placed at the origin and the dipole is placed nearby along the z-axis. The z orientation of the dipole is perpendicular to the NP surface, and the x and y orientations of the dipole are parallel to the NP surface.

Results are shown for Ag–Cu bimetallic NP of average diameter $d = 150$ nm as this is the average size observed in our TEM micrographs. Assuming a uniform distribution of the fluorophore around the NPs, we set $s = 13$ nm for the dipole–NP separation distance. We considered a homogeneously mixed alloy for the Ag–Cu bimetallic NP. The experimentally determined relative permittivity of Ag and Cu for small NPs (<2 μm) as obtained by Palik *et al*. [43] was used as input parameters for the calculations. For the alloy, the effective relative permittivity ε_{eff} of the

Ag–Cu bimetallic NP is calculated using a volume-weighted average of ε of the individual metals.

We employed a grid spacing of 1 nm for discretization of the spatial domain and, the simulation time duration was 400 fs, corresponding to an excess of 1 00 000 time propagation steps for each calculation. The FDTD package employed has frequency-domain monitors that perform discrete Fourier transforms of the time-domain fields while the simulation is running. In this manner, continuous wave information is obtained at any pre-specified wavelengths for the various electric and magnetic field components. All of the calculations were done by assuming a background relative dielectric constant of 1.5 corresponding to a glass substrate.

The fluorescence emission is a quantum mechanical phenomenon involving excited electronic states, whereas we have modeled this phenomenon using a classical mechanical model. This correspondence between quantum and classical theory is valid if normalized quantities are considered and is given by

$$\frac{\Gamma_r}{\Gamma_0} = \frac{P_r}{P_0}$$

where Γ_0 and Γ_r are the radiative decay rate of an isolated classical dipole in a homogeneous background like air and the radiative decay rate of the dipole in proximity of the metal NPs. Again, P_r is the total power radiated by the dipole–NP system, and P_0 is the total power radiated by the isolated dipole. In our calculations, since we use a radiating dipole source to model the excited fluorophore, P_0 is well known. For obtaining the radiated power P_r from our FDTD calculations, we used a set of six frequency-domain surface monitors to create a box around the system and measured the total power radiated by the system by integrating the real part of the Poynting vector over all six surfaces. The power was normalized to the analytic expression for the power radiated by a dipole in a homogeneous dielectric (air) to get the relative change in power radiated. In the absence of the metallic NP, the ratio of P_r to P_0 can be calculated and the expected result is 1. Once the values of P_r/P_0 are computed, we can make inferences on changes in the radiative decay rate of the dipole system when compared to the isolated dipole.

Table 4.1 lists the overall emission enhancements of the fluorophores placed in the vicinity of various compositions of bimetallic Ag–Cu spherical NPs for both the perpendicular and parallel orientations of the fluorophore with respect to the NP surface. We observe that for the perpendicular orientation of the dipole, there is a considerable emission enhancement of the fluorophore. However, for all the parallel orientations of the dipole, the fluorescence emission is essentially quenched irrespective of the composition of the bimetallic NP. In order to calculate the overall enhancement averaged over all the orientations, we follow the following procedure. In a mutually orthogonal coordinate system, there are two orientations of the dipole: one that is parallel and one that is perpendicular to the surface. Hence, the overall emission enhancement of the fluorophore is a weighted average of the parallel and perpendicular orientations.

Figure 4.12 shows the plot of overall fluorescence emission enhancement as a function of the % Cu in the Ag–Cu bimetallic NPs. We observe that the magnitude of the fluorescence enhancement is highest for the pure silver NP and it monotonically decreases with increase in the fraction of copper in the Ag–Cu bimetallic NP. In fact, for the pure copper NP, we observe a quenching of the fluorescence instead of the enhancement. These results are in close agreement with our calculations from the modified G–N model as shown in Figure 4.9c. The close agreements between

Table 4.1 Table for the fluorescence enhancements of the Ag–Cu bimetallic nanoparticles for the dipoles oriented as perpendicular and parallel to the surface of the nanoparticle.

% Cu in the Ag–Cu NP	Dipole orientation perpendicular	Dipole orientation parallel	Overall emission enhancement
0	10.74	0.81	4.00
20	7.19	0.65	2.83
40	6.06	0.51	2.36
60	5.09	0.38	1.95
80	4.46	0.23	1.64
100	2.83	0.04	0.97

Jeremie *et al.* [24]. Reproduced with the permission of Hindawi Publication Corporation.

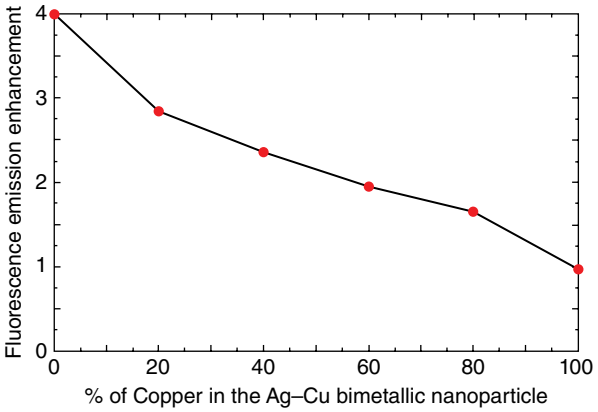

Figure 4.12 Calculated quantum efficiency obtained from FDTD calculations as a function of the % of copper in the Ag–Cu bimetallic nanoparticles. The size of the spherical nanoparticle is 150 nm and the fluorophore–nanoparticle separation distance is 13 nm. Jeremie *et al*. [24]. Reproduced with the permission of Hindawi Publication Corporation.

the results obtained from the FDTD calculations and the modified G–N model give credibility to our method of performing the FDTD calculations. In future, using the FDTD calculations we intend to study the fluorescence enhancements of various shapes and sizes of the bimetallic NPs.

4.4 Conclusion and Future Directions

MEF has been described by many researchers as the next-generation technique for fluorescence spectroscopy. However, most of the previous work has been limited to noble monometallic particles like gold and silver. In this work, using an example of Ag–Cu bimetallic NPs, we have demonstrated that the width and the location of the SPR peak can be modified by changing either the composition or the atomic arrangement of the bimetallic NPs.

This has implications for use of a large variety of fluorophores with different emission wavelengths. However, we have observed that the fluorescence enhancement of the bimetallic NP is significantly lower than the pure silver NP. The magnitude of the fluorescence enhancement of the bimetallic NP can be increased by optimizing the size, shape, and separation distance between the fluorophore and the NP. The FDTD method is a powerful technique to calculate and predict these optimized geometrical structures and can serve as an excellent guiding tool for synthesizing these NPs that can have maximum fluorescence enhancements. Again, major advances are being made on the synthesis aspects of these NPs with precise control on these geometrical parameters of the NPs. Thus, going forward, controlling MEF with bimetallic NPS seems to be an attractive option in advancing the detection limits of the fluorescence spectroscopy technique.

References

1 Geddes, C. D.; Lakowicz, J. R., Metal-enhanced fluorescence. *Journal of Fluorescence* **2002**, *12* (2), 122–129.
2 Zhang, Y.; Aslan, K.; Previte, M. J. R.; Geddes, C. D., Metal-enhanced fluorescence from copper substrates. *Applied Physics Letters* **2007**, *90* (17), 173116.
3 Ray, K.; Chowdhury, M. H.; Lakowicz, J. R., Aluminum nanostructured films as substrates for enhanced fluorescence in the ultraviolet-blue spectral region. *Analytical Chemistry* **2007**, *79* (17), 6480–6487.
4 Pribik, R.; Aslan, K.; Zhang, Y.; Geddes, C. D., Metal-enhanced fluorescence from chromium nanodeposits. *The Journal of Physical Chemistry C* **2008**, *112* (46), 17969–17973.
5 Aslan, K.; Previte, M. J. R.; Zhang, Y.; Geddes, C. D., Metal-enhanced fluorescence from nanoparticulate zinc films. *The Journal of Physical Chemistry C* **2008**, *112* (47), 18368–18375.
6 Tam, F.; Goodrich, G. P.; Johnson, B. R.; Halas, N. J., Plasmonic enhancement of molecular fluorescence. *Nano Letters* **2007**, *7* (2), 496–501.
7 Hirai, M.; Kumar, A., Wavelength tuning of surface plasmon resonance by annealing silver–copper nanoparticles. *Journal of Applied Physics* **2006**, *100* (1), 014309–014309-4.
8 Li, Z. Y.; Wilcoxon, J. P.; Yin, F.; Chen, Y.; Palmer, R. E.; Johnston, R. L., Structures and optical properties of 4–5 nm bimetallic AgAu nanoparticles. *Faraday Discussions* **2008**, *138* 363–373.
9 Ao, L.; Gao, F.; Pan, B.; He, R.; Cui, D., Fluoroimmunoassay for antigen based on fluorescence quenching signal of gold nanoparticles. *Analytical Chemistry* **2006**, *78* (4), 1104–1106.
10 Kato, N.; Caruso, F., Homogeneous, competitive fluorescence quenching immunoassay based on gold nanoparticle/polyelectrolyte coated latex particles. *The Journal of Physical Chemistry B* **2005**, *109* (42), 19604–19612.
11 Wu, Z.-S.; Jiang, J.-H.; Fu, L.; Shen, G.-L.; Yu, R.-Q., Optical detection of DNA hybridization based on fluorescence quenching of tagged oligonucleotide probes by gold nanoparticles. *Analytical Biochemistry* **2006**, *353* (1), 22–29.

12 Dubertret, B.; Calame, M.; Libchaber, A. J., Single-mismatch detection using gold-quenched fluorescent oligonucleotides. *Nature Biotechnology* **2001**, *19* (4), 365–370.

13 Imahori, H.; Fukuzumi, S., Porphyrin monolayer-modified gold clusters as photoactive materials. *Advanced Materials* **2001**, *13* (15), 1197–1199.

14 Yeechi, C.; Keiko, M.; Ilan Jen-La, P.; Andrea, M. M.; Sara, E. S.; Younan, X.; David, S. G., Excitation enhancement of CdSe quantum dots by single metal nanoparticles. *Applied Physics Letters* **2008**, *93* (5), 053106.

15 Chen, Y.; Munechika, K.; Ginger, D. S., Dependence of fluorescence Intensity on the spectral overlap between fluorophores and plasmon resonant single silver nanoparticles. *Nano Letters*. **2007**, *7* (3), 690–696.

16 Thomas, M.; Greffet, J. J.; Carminati, R.; Arias-Gonzalez, J. R., Single-molecule spontaneous emission close to absorbing nanostructures. *Applied Physics Letters* **2004**, *85* (17), 3863–3865.

17 Cheng, D.; Xu, Q.-H., Separation distance dependent fluorescence enhancement of fluorescein isothiocyanate by silver nanoparticles. *Chemical Communications* **2007**, (*3*), 248–250.

18 Chowdhury, S.; Bhethanabotla, V. R.; Sen, R., Silver–copper alloy nanoparticles for metal enhanced luminescence. *Applied Physics Letters* **2009**, *95* (13), 13115.

19 Chowdhury, S.; Bhethanabotla, V. R.; Sen, R., Effect of Ag–Cu alloy nanoparticle composition on luminescence enhancement/quenching. *Journal of Physical Chemistry C* **2009**, *113* (30), 13016–13022.

20 Zhang, J.; Liu, H.; Wang, Z.; Ming, N., Preparation and optical properties of silica Ag–Cu alloy core-shell composite colloids. *Journal of Solid State Chemistry* **2007**, *180* (4), 1291–1297.

21 Hongjin, J.; Kyoung-Sik, M.; Wong, C. P. Synthesis of Ag–Cu alloy nanoparticles for lead-free interconnect materials, Proceedings. International Symposium on Advanced Packaging Materials: Processes, Properties and Interfaces, IEEE, Boston, **2005**; pp. 173–177.

22 Pan, S.; Rothberg, L. J., Enhancement of platinum octaethyl porphyrin phosphorescence near nanotextured silver surfaces. *Journal of the American Chemical Society* **2005**, *127* (16), 6087–6094.

23 Aslan, K.; Lakowicz, J. R.; Geddes, C. D., Metal-enhanced fluorescence using anisotropic silver nanostructures: critical progress to date. *Analytical and Bioanalytical Chemistry* **2005**, *382* (4), 926–933.

24 Asselin, J., Viger, M.L., and Boudreau, D., "Metal-enhanced fluorescence and FRET in multilayer core–shell nanoparticles," *Advances in Chemistry*, **2014**, *2014*, 1–16.

25 Haverkamp, R.; Marshall, A.; van Agterveld, D., Pick your carats: nanoparticles of gold–silver–copper alloy produced in vivo. *Journal of Nanoparticle Research* **2007**, *9* (4), 697–700.

26 Moskovits, M.; Srnová-Šloufová, I.; Vlčková, B., Bimetallic Ag–Au nanoparticles: extracting meaningful optical constants from the surface-plasmon extinction spectrum. *The Journal of Chemical Physics* **2002**, *116*, 10435–10446.

27 Gersten, J. I.; Nitzan, A., Spectroscopic properties of molecules interacting with small dielectric particles. *The Journal of Chemical Physics*. **1981**, *75* (3), 1139.

28 Gersten, J. I.; Nitzan, A., Resonance optical response of small dielectric clusters. *Physical Review B* **1984**, *29* (7), 3852.

29 Mie, G., Beiträge zur Optik trüber Medien, speziell kolloidaler Metallösungen. *Annals of Physics* **1908**, *330* (3), 377–445.

30 Bergman, D. J., Exactly solvable microscopic geometries and rigorous bounds for the complex dielectric constant of a two-component composite material. *Physical Review Letters* **1980**, *44* (19), 1285.

31 Milton, G. W., Bounds on the complex permittivity of a 2-component composite-material. *Journal of Applied Physics* **1981**, *52* (8), 5286–5293.

32 Mondio, G.; Neri, F., The dielectric constant of Pd–Ni alloys. *Physica Scripta* **1992**, *1992* (T41), 153–159.

33 Gao, L.; Gu, J. Z., Effective dielectric constant of a two-component material with shape distribution. *Journal of Physics D* **2002**, *35* (3), 267–271.

34 Garcia, H.; Trice, J.; Kalyanaraman, R.; Sureshkumar, R., Self-consistent determination of plasmonic resonances in ternary nanocomposites. *Physical Review B* **2007**, *75* (4), 045439–045442.

35 Shaoli, Z.; Xiangang, L., Hybrid metallic nanoparticles for excitation of surface plasmon resonance. *Journal of Applied Physics* **2007**, *101*, 064701.

36 Maxwell-Garnett, J. C., Colours in metal glasses and in metallic films. *Philosophical Transactions of the Royal Society of London. Series A* **1904**, *203*, 385–420.

37 Bruzzone, S.; Malvaldi, M.; Arrighini, G. P.; Guidotti, C., Near-field and far-field scattering by bimetallic nanoshell systems. *The Journal of Physical Chemistry B* **2006**, *110* (23), 11050–11054.

38 Mertens, H.; Koenderink, A. F.; Polman, A., Plasmon-enhanced luminescence near noble-metal nanospheres: comparison of exact theory and an improved Gersten and Nitzan model. *Physical Review B* **2007**, *76* (11), 115123.

39 Azoulay, J.; Debarre, A.; Richard, A.; Tchenio, P., Quenching and enhancement of single-molecule

fluorescence under metallic and dielectric tips. *Europhysics Letters* **2000**, *51* (4), 374–380.

40 Kummerlen, J.; Leitner, A.; Brunner, H.; Aussenegg, F. R.; Wokaun, A., Enhanced dye fluorescence over silver island films: analysis of the distance dependence. *Molecular Physics* **1993**, *80* (5), 1031–1046.

41 Chowdhury, M. H.; Pond, J.; Gray, S. K.; Lakowicz, J. R., Systematic computational study of the effect of silver nanoparticle dimers on the coupled emission from nearby fluorophores. *The Journal of Physical Chemistry C* **2008**, *112* (30), 11236–11249.

42 Bharadwaj, P.; Novotny, L., Spectral dependence of single molecule fluorescence enhancement. *Optics Express* **2007**, *15* (21), 14266–14274.

43 Palik, E. D., *Handbook of Optical Constants of Solids, 1st Edition*. Academic Press, Inc., Orlando **1985**.

5

Roles of Surface Plasmon Polaritons in Fluorescence Enhancement

K. F. Chan, K. C. Hui, J. Li, C. H. Fok, and H. C. Ong

Department of Physics, The Chinese University of Hong Kong, Sha Tin, Hong Kong

5.1 Introduction

Surface plasmon polaritons (SPPs) arising from metal–interface have recently been capturing considerable attention because of their potential applications in bio- and nano-photonics [1, 2]. In particular, in nano-photonics, owing to their strongly localized electromagnetic field, SPPs can interact with light-emitting material (LEM) by increasing both its electronic absorption and decay rates, thus leading to enhancement in emission efficiency [3]. As a result, it is expected that SPPs can evolve as an effective means to improve the performance of light-emitting diodes (LEDs), laser diodes (LDs), solar cells, and so on. In fact, numerous studies to date have been reported in these aspects [4]. Most of these studies are focused on fabrication and characterization of various plasmonic systems in different dimensionalities so that desired electromagnetic modes can be generated [5].

5.1.1 Surface Plasmon-Mediated Emission

In general, resonant photoluminescence (PL) enhancement mediated by SPPs involves five sequential steps as shown in Figure 5.1. Assume a layer of LEM is in close contact with a metal surface. (i) When under appropriate resonant excitation, part of the energy from the incident field at λ_{exe} is coupled to the metal surface and produces SPP_{exe}s. (ii) The strong electric field arising from these ingoing SPP_{exe}s then increases the absorption–excitation rate of the nearby LEM and gives rise to absorption enhancement. (iii) The excited electrons relax and decay back into the ground states, subsequently coupling their emission energy either directly into far field at wavelength λ_{em} or into outgoing SPP_{em}s. (iv) The coupling of energy into SPP_{em}s possibly modifies the electronic decay rate, resulting in the increase of spontaneous emission rate [6]. (v) Finally, when SPP_{em}s radiatively decay, they couple energy back into far field at λ_{em}, yielding surface plasmon-mediated emission (SPME) [7, 8]. From this model, it is expected that two SPPs, SPP_{exe}s and SPP_{em}s, both take part sequentially in controlling the absorption and decay enhancements, and the overall enhancement factor (EF) can be expressed as

$$\mathrm{EF} = \mathrm{Abs}\left(\lambda_{exe}\right) \times \mathrm{De}\left(\lambda_{em}\right), \tag{5.1}$$

where Abs and De are absorption and decay EFs, respectively.

In fact, it is possible to consider the prementioned scenario in steady state within the framework of conservation of energy. Figure 5.2 schematically shows the process of SPME that involves SPP_{exe}s and SPP_{em}s. Considering the LEM can be excited either directly by an incident field with power I_o or via SPP_{exe}s, the power being input to the LEM thus is given as

$$\alpha\varepsilon I_o + \beta I_o = \left(\alpha\varepsilon + \beta\right) I_o \tag{5.2}$$

where α and β are the coupling efficiencies to SPP_{exe}s and LEM, respectively. ε is given as $\Gamma_A/\Gamma_1 + \gamma_1 + \Gamma_A$, where Γ_A is the coupling rate from SPP_{exe}s to LEM, whereas Γ_1 and γ_1 are radiative and nonradiative decay rates of SPP_{exe}s. From Eq. (5.2), we know that $(1-\alpha-\beta)I_o$ is reflected off the metal surface without being involved in any kind of excitation, and $\alpha(1-\varepsilon)I_o$ is lost through the total decay of SPP_{exe}s. As a result, we see from Eq. (5.2) that additional absorption is possible by exciting SPP_{exe}s, provided that both α and Γ_A are sufficiently large. Once the LEM is excited, it decays via two channels. While the direct decay gives

Surface Plasmon Enhanced, Coupled and Controlled Fluorescence, First Edition. Edited by Chris D. Geddes.
© 2017 John Wiley & Sons, Inc. Published 2017 by John Wiley & Sons, Inc.

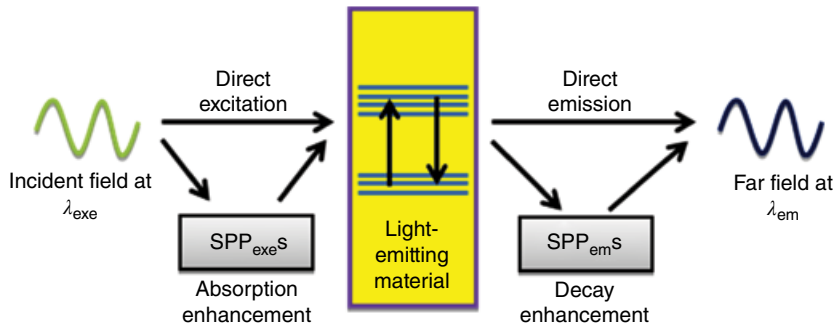

Figure 5.1 The mechanism of the resonant photoluminescence enhancement mediated by SPPs.

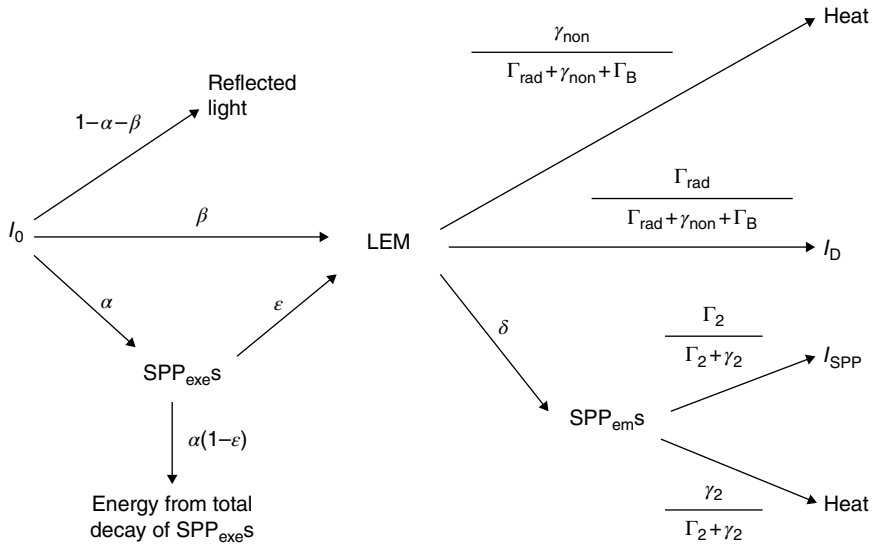

Figure 5.2 The process of SPME that involves $SPP_{exe}s$ and $SPP_{em}s$ in steady state within the framework of conservation of energy.

rise to direct emission I_D, the other decay channel yields SPP-related I_{SPP}. For LEM with low radiative efficiency, that is, $\Gamma_{rad}/\Gamma_{rad}+\gamma_{non}<<1$, where Γ_{rad} and γ_{non} are the radiative and nonradiative decay rates of the LEM, the second SPP decay channel thus increases the total emission given as

$$I_{SPP}+I_D=\delta\frac{\Gamma_2}{\Gamma_2+\gamma_2}(\alpha\varepsilon+\beta)I_o+(1-\delta)\frac{\Gamma_{rad}}{\Gamma_{rad}+\gamma_{non}}(\alpha\varepsilon+\beta)I_o, \quad (5.3)$$

where δ is the coupling efficiency to $SPP_{em}s$ and Γ_2 and γ_2 are the radiative and nonradiative decay rates of $SPP_{em}s$. Similar to ε, δ can be written as $\Gamma_B/\Gamma_{rad}+\gamma_{non}+\Gamma_B$, where Γ_B is the coupling rate from LEM to $SPP_{em}s$. Explicitly, I_{SPP} can be expressed as

$$I_{SPP}=\frac{I_o\Gamma_B\Gamma_2}{(\Gamma_{rad}+\gamma_{non}+\Gamma_B)(\Gamma_2+\gamma_2)}\left(\frac{\alpha\Gamma_A}{\Gamma_1+\gamma_1+\Gamma_A}+\beta\right). \quad (5.4)$$

One can see from Eq. (5.4) that I_{SPP} is proportional to the radiative decay rate of outgoing $SPP_{em}s$, the coupling rates Γ_A and Γ_B and the quality (Q) factors of $SPP_{exe}s$ and $SPP_{em}s$, which are related to the inverse of the total decay rates or $1/\Gamma_1+\gamma_1$ and $1/\Gamma_2+\gamma_2$. From Eq. (5.4), one would expect that $SPP_{exe}s$ with high Q-factor should facilitate stronger I_{SPP}, whereas, for $SPP_{em}s$, I_{SPP} increases with Γ_2 when $\gamma_2>\Gamma_2$ but is weakly dependent on the decay process when $\Gamma_2>\gamma_2$. Both coupling rates are strongly dependent on the local field strength and the density of states (DOS) arising from the corresponding SPPs, which is well described by the Purcell effect [6]. As a result, we conclude that the absorption and decay enhancements are strongly dependent on the generation and decay processes of corresponding SPPs.

Although the connection between SPME and SPPs is established in Eq. (5.4), how to effectively produce strong I_{SPP} remains a challenge. In other words, how to develop a bottom-up approach for any given LEM so that both absorption and decay enhancements can be systematically maximized is of great importance.

To achieve such a task is not trivial since many parameters are involved in determining the ultimate enhancement. In particular, it is known that the generation and decay processes of SPPs are so strongly geometry dependent that slight modification of the system's structure can lead to large variation in outcome. Thus, the dependence of fundamental properties of SPPs on geometry has to be understood properly prior to the emission optimization [9]. Two major types of SPPs, namely, the propagating and the localized [8], can be present in the plasmonic system, and they could have very different plasmonic properties, which have different impacts on emission enhancement. For propagating SPPs, they travel freely on metal surface and thus have a well-defined momentum. As a result, an incident light with an equally well-defined momentum is necessary to excite these SPPs [7]. However, as given by the dispersion relation in Figure 5.3, due to the evanescent nature of SPPs, the momentum of SPPs is larger than that of light so that direct excitation is impossible. To facilitate such a phase-matching condition, propagating SPPs are usually realized in thin film form under the attenuated total reflection geometry [7] or in periodic array [9] where the momentum of light can be altered. On the other hand, SPPs are localized if the electric fields are strongly pinned spatially. Since the propagating length is now much shorter than the SPP wavelength, the localized SPPs contain a wide range of momentum so that direct excitation is possible even under different incident angles [10] (Figure 5.3). Nanostructures such as nanosphere [11], nanorods [12], and so on are examples where localized SPPs are usually found.

Here, we focus mainly on periodic metallic arrays because both propagating and localized SPPs can be excited [9]. In fact, metallic arrays have attracted considerable attention recently. In particular, extraordinary transmission from two-dimensional (2D) hole arrays has revitalized the field of plasmonics since its first discovery in 1998 [13]. The transmittance observed from the hole arrays is found to be order of magnitude stronger than that predicted by Beth's diffraction theory. Numerous experimental and theoretical studies have been conducted in attempt to understand the underlying mechanism [9, 14]. The interplay between localized and propagating SPPs is believed to play a major role in extraordinary transmission [15]. On other hand, the strongly localized field associated with SPPs is also found useful in both linear and nonlinear photonics. Extending the application of periodic arrays from transmission to fluorescence [16], surface enhanced Raman scattering [17], second harmonic generation [18], surface plasmon (SP) resonance sensing [19], optical trapping [20], and so on have been widely reported in these few years, demonstrating the flexibility and versatility of periodic arrays. Other than a wide range of applications, another advantage that periodic arrays offer is their strong controllability and high reproducibility. Compared with other plasmonic counterparts such as nanoparticles in which their size, shape, and nearest neighbor distance are difficult to control, the geometry of periodic arrays can be fabricated precisely by using currently available state-of-the-art lithographic methods. The well-defined geometry thus provides more stable and controllable generation and decay processes of SPPs, resulting in a simpler platform for us to understand the plasmonic effects both experimentally and theoretically.

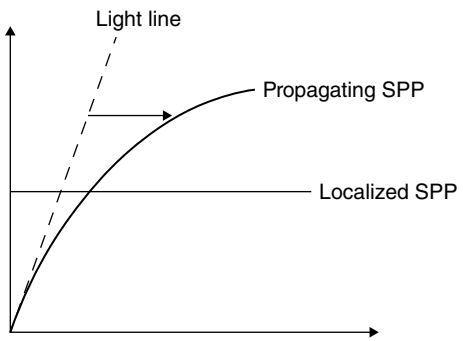

Figure 5.3 The dispersion relation of propagating SPPs and localized SPPs. Propagating SPPs are realized by altering the momentum of light line by attenuated total reflection geometry or in periodic array. On the other hand, the localized SPPs contain a wide range of momentum so that direct excitation is possible even under different incident angles.

5.1.2 Excitation of Propagating and Localized Surface Plasmon Polaritons in Periodic Metallic Arrays

In order to excite propagating SPPs in periodic arrays, matching the phase between SPPs and light is necessary. To fulfill such condition, the incident light is diffracted from the metal surface crafted with periodic corrugation so that weak Bragg scattering can occur to alter the momentum of light [7]. For example, for one-dimensional (1D) metallic grating, propagating SPPs can be excited when the following phase-matching equation given by [7]:

$$\vec{k}_{\mathrm{SPP}} = \vec{k}\hat{u} \pm n\vec{G}, \tag{5.5}$$

is fulfilled. $\vec{k}_{\mathrm{SPP}}$ and $\vec{k}$ are the wave vectors of the SPPs and the in-plane component of the incident field along the direction defined by unit vector $\hat{u}$. The magnitude of $\vec{k}_{\mathrm{SPP}}$ is given as $2\pi/\lambda\sqrt{\varepsilon_{\mathrm{m}}\varepsilon_{\mathrm{d}}/\varepsilon_{\mathrm{m}}+\varepsilon_{\mathrm{d}}}$, where λ is the free-space wavelength and ε_{m} and ε_{d}

are the dielectric functions of metal and dielectric, respectively, while $\bar{k}$ is equal to $2\pi/\lambda \sin\theta$, where θ is the angle of incidence. $\bar{G}$ is the reciprocal unit vector, which is equal to $2\pi/P$, where P is the period of the grating and n is the integer. One can see that Eq. (5.5) has a similar form as the phase-matching equations for electronic [21] and photonic [22] crystals. The dispersion relation of light therefore folds itself for every $\pm\bar{G}$, yielding the one shown in Figure 5.4. From the Figure, it is clear that some of the light lines are now intersected with the SPP modes and Bloch-like propagating SPPs can be excited. These modes are dispersive and thus have high group velocity and small DOS. In addition, for a given wavelength, well-defined incident angle is necessary to excite the SPPs. The prementioned formalism can also be extended to 2D periodic arrays simply by modifying Eq. (5.5) into [23]

$$\bar{k}_{\mathrm{SPP}} = \bar{k}\hat{u} \pm \frac{2\pi n_x}{P_x}\hat{x} \pm \frac{2\pi n_y}{P_y}\hat{y}, \tag{5.6}$$

where P_x and P_y are the periods in x- and y-directions and n_x and n_y are integers. $\hat{x}$ and $\hat{y}$ are the unit vectors.

Other than Bloch-like SPPs, localized SPPs can also be found in periodic arrays [9, 24]. Unlike the dispersive propagating SPPs, localized modes are nondispersive, and their properties rely primarily on the detailed structure of the individual basis rather than the lattice [9, 25]. Thus, localized SPPs have small group velocity but large DOS (Figure 5.4). More importantly, the electric field profile generated by these modes is strongly concentrated around the bases and do not extend much over the metal surface. Thus, interaction between bases is usually neglected when the period is larger than the SPP wavelength. For example, waveguide (WG)-like localized SPPs can be excited within 1D groove array roughly given by [26]:

$$\lambda_{\mathrm{WG}} = \frac{2H}{N}, \tag{5.7}$$

where λ_{WG} is the resonant wavelength, H is the height of groove, and N is the mode order. On the other hand, for 2D perfect-conducting cylindrical hole array, the fundamental TE_{11} mode (λ_{TE}) excited within the holes can be qualitatively estimated as [27]

$$\lambda_{\mathrm{TE}} = \frac{2\pi}{\sqrt{(b/R)^2 + (\pi/2H)^2}}, \tag{5.8}$$

where R is the radius of hole and b is the first-order Bessel constant, which is equal to 1.841.

Finally, it is also noted that different SPPs can interact together to form new coupled modes when their energy and momentum are identical [28]. A plasmonic gap is formed at the same time due to the energy splitting between two new coupled states, signifying the strong coupling regime [29]. For example, as shown in Figure 5.4, the localized SPPs can interact with the Bloch SPPs at the cross point, leading to the formation of new coupled modes separated by an energy gap. In fact, this mode coupling can be understood from a classical perspective in which energy splitting can be readily shown within the framework of a coupled harmonic oscillator model [28]. In addition to such a propagating-localized coupling, coupling between different localized modes arising from nanoparticle assemblies has also been widely studied theoretically and experimentally [30, 31]. The coupling leads to hybridization of different modes in analogy to atomic and molecular interaction models [32]. Interaction between different Bloch SPP modes has also been reported in 1D and 2D arrays [33, 34]. Nevertheless, the coupling is shown to generate new states inheriting the characters of original modes while at the same time creating new properties that could be useful in different applications.

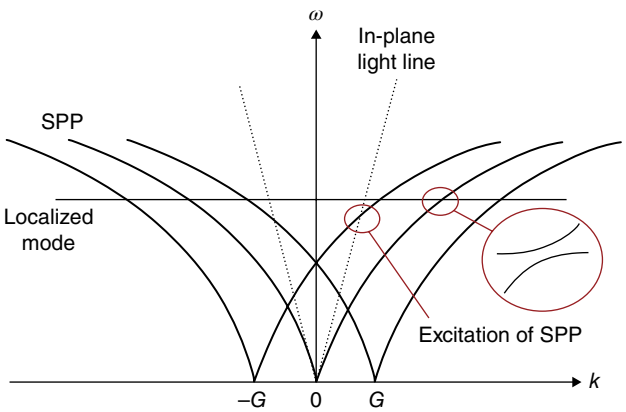

Figure 5.4 In periodic arrays, the dispersion relation of SPPs folds for every $\pm\bar{G}$. Bloch-like propagating SPPs are excited when the light lines intersect with the SPP modes at well-defined incident angle for a given wavelength. These modes are dispersive and thus have high group velocity and small DOS. Nondispersive localized SPPs whose properties rely primarily on the detailed structure of the individual basis rather than the lattice can also be found. These modes have small group velocity but large DOS. When the Bloch SPPs and the localized SPPs having the same energy and momentum interacts each other, new coupled modes separated by an energy gap are found.

5.1.3 Surface Plasmon-Mediated Emission from Periodic Arrays

To realize SPP from periodic array, a general scheme is laid out in Figure 5.5. In principle, absorption and decay enhancements are realized when both absorption and emission wavelengths are matched with the SPP resonances so that both SPP_{exe}s and SPP_{em}s can be generated [3]. For example, for a 2D Ag square array with P_x and $P_y = 600$ nm, its dispersion relation in Γ–X direction can be constructed following Eq. (5.6) in Figure 5.5, illustrating the excitation of ($n_x = -1$, $n_y = 0$), (1,0) and (0,±1) Bloch-like SPPs [23, 35]. Assuming the LEM with absorption and emission spectra given in Figure 5.5 is placed near the array, we then expect absorption enhancement is realized when an excitation laser at $\lambda_{exe} = 514$ nm is incident on the sample at $\theta_{exe} = 10.6°$ for generating the ingoing SPP_{exe}s. For decay enhancement, one then expects emission enhancements are observed at different emission angles θ_{em} across the entire emission spectrum whenever the momentum of far-field emission matches with that of outgoing SPP_{em}s. Finally, it is also anticipated that the degree of emission enhancement should vary depending on the generation and decay processes of SPPs, as indicated in Eq. (5.4), and geometry thus is expected to play a major role in governing the basic properties of SPPs.

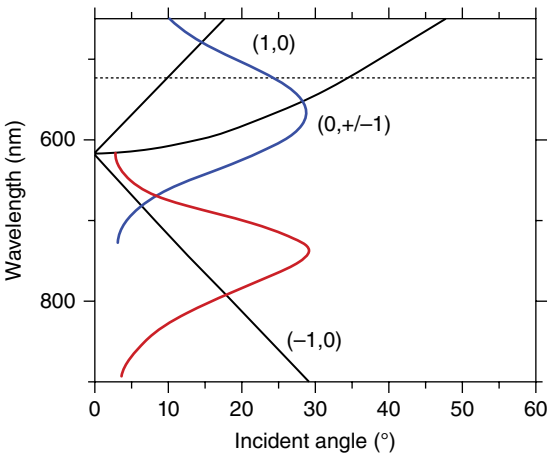

Figure 5.5 The dispersion relation of a 2D Ag square array with P_x and $P_y = 600$ nm constructed from Eq. (5.6) and the LEM's absorption and emission spectrum. The absorption enhancement is realized by the ingoing SPP_{exe}s excited by an excitation laser at $\lambda_{exe} = 514$ nm (dotted line) incident on the sample at $\theta_{exe} = 10.6°$. Emission enhancements are expected at different emission angles θ_{em} across the entire emission spectrum once the momentum of far-field emission matches with that of outgoing SPP_{em}s.

5.2 Experimental

5.2.1 Sample Preparation

A number of lithographic methods have been used to fabricate periodic arrays with different geometries. Electron-beam lithography [36], nanoimprint lithography [37], nanosphere lithography [38], focused ion beam [13], interference lithography (IL) [23, 35], and so on are few examples. While electron-beam lithography, focused ion beam, and nanoimprinting offer high precision, stability, and reproducibility, they suffer from high instrumentation cost and moderate productivity. We use IL as our routine sample preparation method as it is more cost effective and has higher throughput than others.

Basically, IL crosses two identical laser beams with expanded beam size to spatially create an interference pattern for exposing photoresist [39]. The dimensionality of the arrays can be controlled by controlling the number of exposure; one exposure produces 1D pattern whereas two exposures create 2D pattern. In addition, for 2D pattern, negative photoresist yields well-like structure, whereas positive photoresist creates dot-like pattern. As a result, dimple- or protrusion-based arrays can be fabricated by using different types of photoresist. In our study, a Lloyd's mirror configuration is used and its schematic is shown in Figure 5.6a [23, 35]. This setup consists of a HeCd laser at $\lambda = 325$ nm as the light source and a spatial filter for producing a uniform and clean Gaussian beam. The beam then passes a beam expander and an iris so that the central part of the Gaussian beam is collected to mimic a plane wavelike beam. At the sample stage, a flat mirror is mounted perpendicular to the sample on a rotation stage. As part of the laser beam is reflected by the mirror, it interferes with the nonreflected part to form an interference pattern on the photoresist. A wide range of geometrical parameters such as groove width, hole size, disk size, periodicity, and so on can be controlled independently by changing the incident angle, the exposure time, and the thickness of photoresist (see a few scanning electron microscopy (SEM) images of fabricated samples in Figure 5.6b). For example, the period P is given as $P = \lambda/2\sin\theta$, where θ is the incident angle [39] and the hole or groove depth can be varied by using different photoresist thicknesses. After lithography and baking, dielectric templates are obtained for metallization. The templates are transferred into either an electron-beam or a thermal evaporation thin film deposition system for depositing 20–50 nm thick Ag or Au thin film. We will focus only on 2D circular hole arrays here.

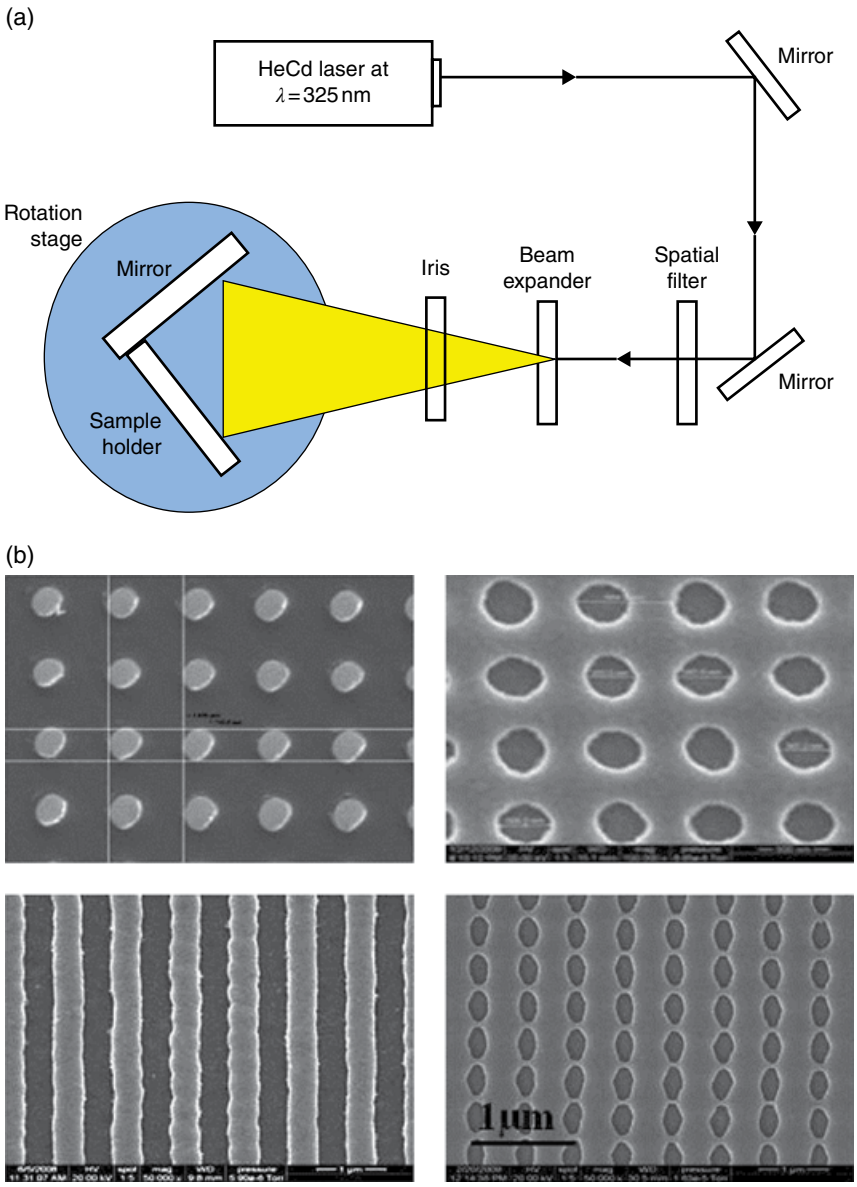

Figure 5.6 (a) Lloyd's mirror configuration used in interference lithography. (b) The scanning electron microscopy (SEM) images of different fabricated samples with periodic arrays.

Two types of LEMs are used and they are LDS 751 (Styryl 8) laser dyes [40] and CdSe-based quantum dots (QDs) [41]. Their absorption and emission spectra are given in Figure 5.7 for reference. For LDS, two configurations are used. For the first configuration, it is dissolved into water-soluble polyvinyl alcohol (PVA) and then directly spin-coated on the array surface. For the second configuration, on the other hand, it is first dissolved in propylene carbonate (PC) and then is mixed with SU8 before spin-coated on glass substrates. It is then solidified by UV illumination and hard baking at 95°C to form a 350 nm thick thin film. Metallic hole arrays are then fabricated on top of LDS by IL [42]. For QDs, they are diluted by toluene and then directly spin-coated on the arrays followed by air dry.

5.2.2 Optical Characterizations

We use several angle-resolved measurements to characterize the samples. A home-built computer-controlled goniometer is used, and angle-dependent reflectivity and PL spectroscopy, as shown in Figure 5.8a, are performed. For the reflectivity measurements, the specular reflection is collected from the sample by using a collimated white light output from a quartz lamp as the excitation source (Figure 5.8a)

[43]. The reflection spectra are then obtained by normalizing the raw spectra with respect to that of the incident light. By contour plotting the reflectivity as a function of wavelength and angle, reflectivity mappings, also known as dispersion relations, are obtained. The dispersion relations not only identify all electromagnetic resonances in the metallic arrays but also allow us to extract the decay rates and Q-factors of SPPs, as we will show later. For PL measurements, two types of emission scans, which are detection and incident scans, are carried out and they are shown in Figure 5.8b and c [42]. For detection scan, the incident angle is fixed, while the detection angle is varied. Likewise, for incident scan, the incident angle is scanned at a fixed detection angle. All the optical signals are collected by a CCD-detection system attached on a 0.25 m spectrograph. Two cube-type polarizers are placed after the light sources and the sample for selecting desired excitation and detection polarizations. Therefore, in the following, p-p is defined as both incidence and detection are oriented in p-polarization, while s-s refers to the s-polarization. Specifically for PL measurements, a notch filter is used to remove the unwanted Rayleigh laser line from the spectra. The PL mappings will then be compared with the corresponding dispersion relations so that the roles of different SPP play in emission enhancement can be determined accordingly.

Time-resolved fluorescence imaging is also performed by using Leica TCS SP5 confocal fluorescence lifetime microscope [44]. The microscope is equipped with high-power femtosecond laser and several CW lasers for excitation. For lifetime determination, time-correlated single-photon counting method is used by using an avalanche photodiode [44].

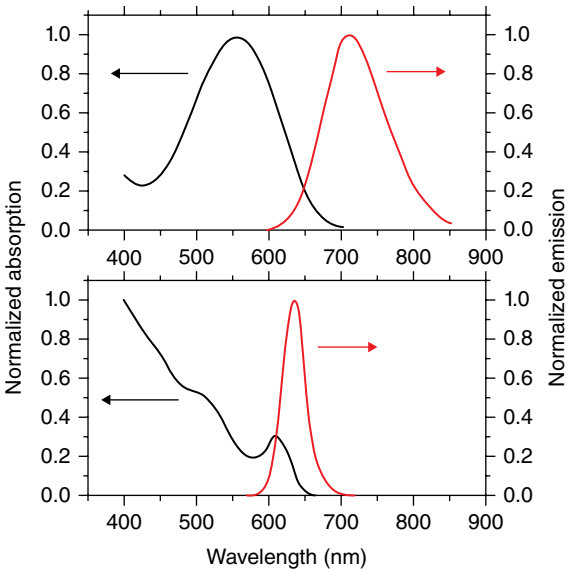

Figure 5.7 The absorption and emission spectra of two different LEMs: LDS 751 (Styryl 8) laser dyes (top) and CdSe-based quantum dots (QDs) (bottom).

5.3 Result and Discussion

5.3.1 The Decay Lifetimes of Metallic Hole Arrays

Studying the fundamental properties of SPPs is the first step toward the understanding of SPME. As indicated in Eq. (5.4), one would agree that the SPP generation and decay processes play a major role in controlling the resulting emission enhancement. Therefore, how to extract the Q-factor and radiative decay rate for any particular SPP mode is essential to properly understand how SPP_{exe}s and SPP_{em}s take part in SPME. In principle, the total SPP decay lifetime can be measured either in time or frequency domains as they are connected by the Fourier transformation [45]. In time domain, an ultrashort laser pulse, usually in femtosecond, first excites the SPP mode resonantly, and its decay profile is then measured by a time-resolved technique [34]. In contrast, in frequency domain, the

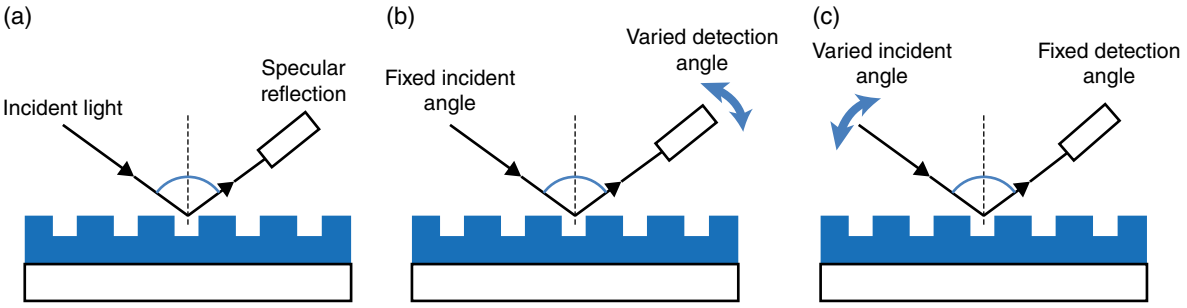

Figure 5.8 The experimental configurations for different angle-resolved measurements: (a) angle-dependent reflectivity measurement, (b) photoluminescence detection scan, and (c) photoluminescence incident scan.

resonance mode is measured spectrally as a line shape function, and its linewidth reflects the decay lifetime [46]. Since the full width at half maximum (FWHM) of the function is governed by the lifetime of the resonance mode given as $\tau = \hbar/\Gamma$, where τ is the lifetime and Γ is the FWHM, it is possible to deduce the SPP lifetime τ_{SPP} by fitting the spectrum by appropriate function. We have determined τ_{SPP} and resonant wavelength λ_{res} of the SPP resonances from the reflectivity spectra by fitting the reflection spectra with a Fano function given as [47]

$$R = R_0 + \frac{A(\xi + q)^2}{1 + \xi^2}, \tag{5.9}$$

where $\xi = 2(E - E_{res})/\Gamma$ and E and E_{res} are the photon energy and the resonant energy, respectively. R_o is the offset function to take into account of the reflectivity background, and A is a coefficient describing the contribution of the zero-order continuum state coupled to the discrete resonant state. q is the Breit–Wigner–Fano coupling coefficient and is related to $2\delta/\Gamma$, where δ defines the ratio between the resonant transition amplitude and the direct transition amplitude [48]. The Fano characteristic of SPP reflection is due to the interference that occurs between SPP discrete resonance and the continuum diffraction background [47, 48]. Once τ_{SPP} is obtained, the radiative decay or scattering rate, Γ_{scatt}, can be determined by subtracting the nonradiative absorption rate, γ_{abs}, given as $1/\tau_{SPP} = \Gamma_{SPP} = \Gamma_{scatt} + \gamma_{abs}$.

5.3.2 Dependence of Decay Lifetime on Hole Size

We first examine the lifetime dependence on hole radius R and depth H [49]. Circular hole arrays with R and H ranging from 101 to 166 nm and from 200 to 480 nm, respectively, have been prepared by IL. Some of their SEM images are shown in the insets of Figure 5.9. From the Figures, we see all samples have cubic lattice with period = 550 nm. Figure 5.9 shows the p-p reflectivity mappings (dispersion relations) of the corresponding arrays taken in the Γ–X direction. For shallow hole depth H = 200 nm (Figure 5.9a–c), all arrays displaying several reflection bands that are dispersive with angle are clearly visible, and they can be identified as Bloch-like propagating SPPs using the phase-matching equation given by Eq. (5.6). The solid lines deduced from Eq. (5.6) are superimposed on the mappings revealing that (–1,0), (1,0), $(0,\pm 1)_s$ and $(-1,\pm 1)_s$ SPP modes are excited. Other than Bloch SPPs, Wood's anomalies are also observed as bright bands, and they can be traced by replacing $\sqrt{\varepsilon_m\varepsilon_d/\varepsilon_m + \varepsilon_d}$ in Eq. (5.6) with $\sqrt{\varepsilon_d}$, indicated as dashed lines. Nevertheless, one can see that the spectral positions of all SPP modes are primarily governed by period rather than hole radius. However, for a given SPP mode, particularly (1,0) and (–1,0) SPPs, the reflection dips become broader when the hole radius increases. As the linewidth of the reflection dip is inversely proportional to lifetime, larger hole radius facilitates shorter SPP lifetime.

It is also noted that the $(0,\pm 1)_s$ SPP mode for all samples is barely visible because of its extremely low coupling efficiency compared with other modes [50]. In fact, the excitation of $(0,\pm 1)_s$ (and $(-1,\pm 1)_s$) SPPs is a direct consequence of strong coupling between the degenerate (0,1) and (0,–1) (and (–1,1) and (–1,–1)) SPPs at all incident angles. Once the degenerate modes are coupled, two new states $(0,\pm 1)_s$ and $(0,\pm 1)_a$ (and $(-1,\pm 1)_s$ and $(-1,\pm 1)_a$) with distinctive field symmetries are excited under p- or s-polarization. Since the $(0,\pm 1)_s$ mode is symmetric with respect to the plane of incidence, it appears in the p-polarized mapping. In contrast, the $(0,\pm 1)_a$ mode has asymmetric field profile and thus is only excited in the s-polarized mapping (not shown). In addition, as a result of coupling, $(0,\pm 1)_s$ mode is found to have longer decay lifetime compared with the $(0,\pm 1)_s$ mode, thus giving rise to very low coupling efficiency [51].

We then examine the reflectivity mappings for thicker hole arrays in Figure 5.9d–j. When H increases to 300 and 480 nm, even though the mappings for small radius (Figure 5.9f and i) are similar to those of the shallow counterparts, a broad and low reflectivity band slowly evolves at larger hole radius, and the SPP bands become blurred (Figure 5.9d and g). The broad band can be attributed to the evolution of localized SPPs [52], causing the coupling between localized and propagating SPP modes. However, no plasmonic gaps are formed resulting from the coupling because both propagating and localized SPPs have strong radiative damping rates, which "smear out" the SPPs. In fact, the dissipation in each mode needs to be smaller than the coupling strength in order to observe the plasmonic gaps. By using Eq. (5.8) as a guideline for the spectral position of the localized mode, we determine λ_{TE} for R = 166 nm, 123 nm, and 101 nm, respectively, to be 507 nm, 396 nm, and 331 nm when H = 300 nm, and 543 nm, 423 nm, and 346 nm when H = 480 nm, which confirm the presence of localized SPPs.

Once all the modes have been identified, we then move on to study the effects of hole radius and depth on $\tau_{SPP} \cdot \tau_{SPP}$ of all samples are determined by Fano fitting and are plotted in Figure 5.10 for λ_{res} = 750 nm. Only the modes that are not coupled with the localized mode are

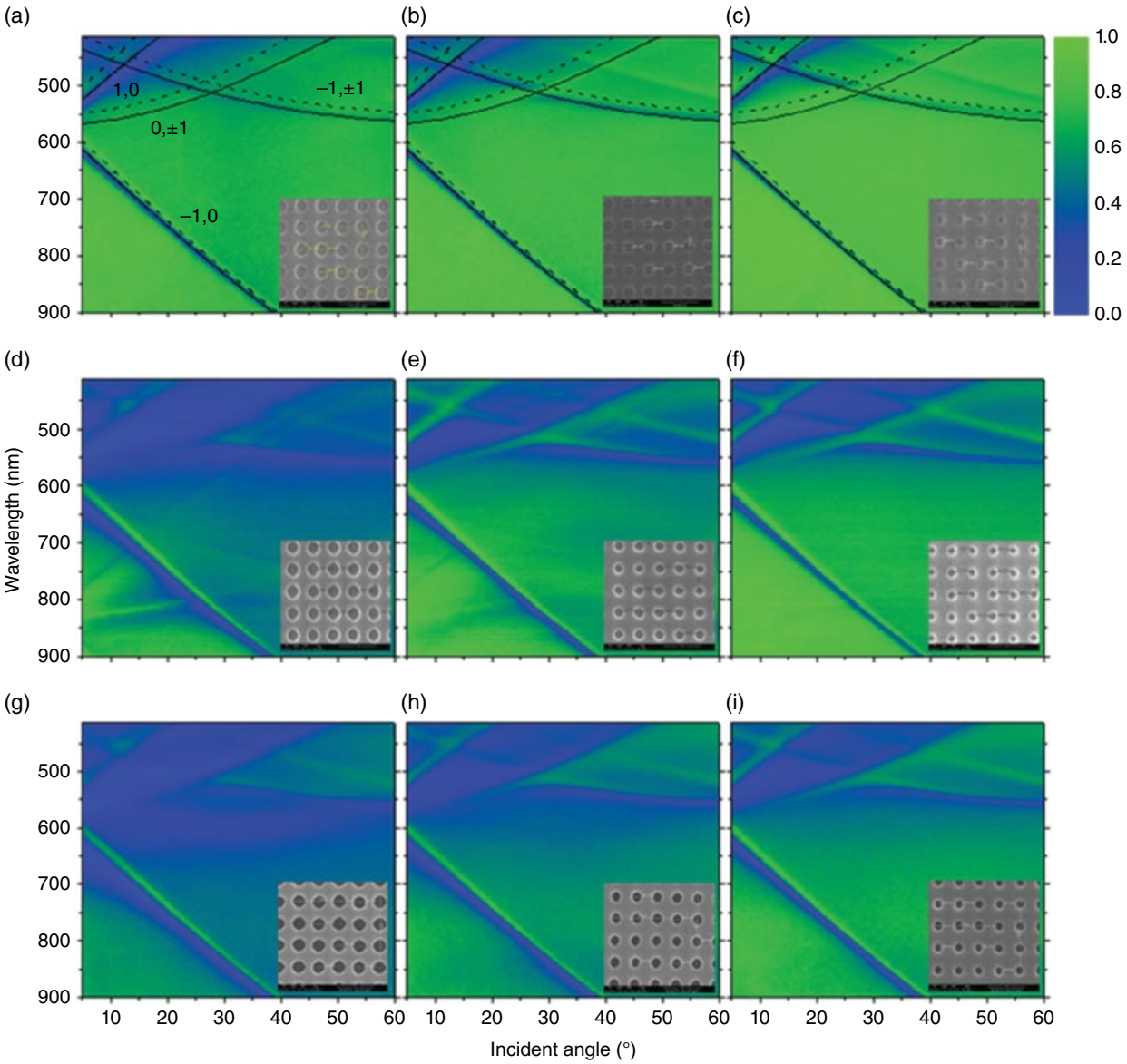

Figure 5.9 The p-p angle-dependent reflectivity mapping (dispersion relations) of each 2D grating was measured in Γ–*X* direction. The SEM images of the circular hole arrays having cubic lattice with period = 550 nm are shown in the insets of Figure 5.9. The height *H* of the grooves are (a)–(c) 200 nm, (d)–(f) 300 nm, and (g)–(i) 480 nm, respectively, for shallow, medium depth, and thick holes. The radius *R* of the holes for different *H* range from (a), (d), and (g) 101 nm to (c), (f), and (i) 166 nm. The solid lines deduced from Eq. (5.6) indicate the excitation of (−1,0), (1,0), $(0,\pm 1)_s$, and $(-1,\pm 1)_s$ Bloch-like propagating SPPs modes. Wood's anomalies (dashed lines) deduced from replacing $\sqrt{\varepsilon_m\varepsilon_d/\varepsilon_m+\varepsilon_d}$ with $\sqrt{\varepsilon_d}$ in Eq. (5.6) are also observed as bright bands. (*See insert for color representation of this figure.*)

considered here for simplification. Apparently, τ_{SPP} remains almost the same at small *R* and *H* but decreases nonlinearly with increasing hole size. To account for these dependences, we determine the intrinsic nonradiative absorption and radiative scattering lifetimes, τ_{abs} and τ_{scatt}, analytically [49]. For τ_{abs}, we assume the hole sizes are small compared with the wavelength being considered; the propagation length is written as $l_{SPP}=v_{SPP}\tau_{abs}=\lambda\left(\mathrm{Re}\left(\varepsilon_m\right)^2/2\pi\mathrm{Im}\left(\varepsilon_m\right)\right)$, where v_{SPP} is the group velocity. Consider ε_m is given by the Drude model: $\varepsilon_m(\omega)=1-\left(\omega_p^2/\omega(\omega-i\gamma)\right)$; we then can express $\mathrm{Re}\left(\varepsilon_m\right)=1-\left(\lambda/\lambda_p\right)^2\approx-\left(\lambda/\lambda_p\right)^2$ and $\mathrm{Im}\left(\varepsilon_m\right)\approx-\lambda\left(\gamma/2\pi c\right)\left(\lambda/\lambda_p\right)^2$, where λ_p is the plasma wavelength, *c* is the speed of light, and γ is the damping loss. As a result, τ_{abs} can be approximated as

$$\tau_{abs}=\frac{\lambda^2}{\lambda_p^2\gamma\left(1-\pi R^2/P^2\right)}, \tag{5.10}$$

which depends on P and R but not on H. On the other hand, within the framework of Mie scattering, the scattering loss τ_{scatt} is proportional to P/σ, where σ is the SPP scattering cross section and is given as

$$\sigma = \frac{72\pi^5}{3}\left[\frac{R^4H^2}{\lambda^4}\left(\frac{(\varepsilon_m-1)}{(\varepsilon_m+2)}\right)^2 - 5\pi^4\frac{R^{20/3}H^{10/3}}{\lambda^8}\left(\frac{(\varepsilon_m-2)(\varepsilon_m-1)}{(\varepsilon_m+2)^2}\right)^2\right], \tag{5.11}$$

after the inclusion of the quadrupolar corrections in cylindrical hole [49]. From the prementioned equation, we see the first component indicates the dipolar, or Rayleigh, scattering with $(R/\lambda)^4$ dependence, whereas the second one represents the quadrupolar counterpart. Therefore, $\tau_{scatt} \propto \left(P/\left(\left(R^4H^2/\lambda^4\right)-\left(R^{\sim 6.7}H^{\sim 3.3}/\lambda^8\right)\right)\right)$, which exhibits strong dependence on all geometrical parameters.

From prementioned formulations, one can see that for all depth H and small radius R, τ_{abs} dominates the total decay lifetime, which shows a weak dependence on R, as evident in Figure 5.10 in which τ_{SPP} is plotted against R for different depths. However, when hole size increases, the radiative decay begins to take over nonradiative absorption, and stronger R dependences emerge. As a result, at $R > 150$ nm, we see from Figure 5.10 that $\tau_{SPP} \propto R^{-m}$, where m varies from −0.3 to −2.4, signifying the emergence of radiative scattering loss. Overall, the interplay between the intrinsic absorption and radiative scattering of SPPs by single isolated holes dominates the entire SPP decay process, and these simple analytical formulations should assist us in extracting the Q-factor and radiative decay rate of propagating SPPs.

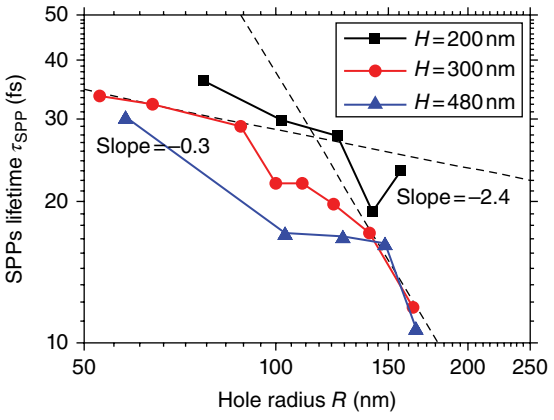

Figure 5.10 Plot of the SPPs lifetime τ_{SPP} against hole radius R for H = 200 nm (square), 300 nm (circle), and 480 nm (triangle) at λ_{res} = 750 nm. At $R > 150$ nm, m varies from −0.3 to −2.4, where m is given by $\tau_{SPP} \propto R^{-m}$, signifying the emergence of radiative scattering loss.

5.3.3 Comparison between Dispersion Relation and PL Mapping

The combination of angle-resolved reflectivity and PL spectroscopy is an effective means to study the underlying mechanism of SPME. In the following, we shall first establish the connection between emission enhancement and SPPs by comparing the dispersion relation with PL mapping of an Ag array-coated LDS array. In fact, a one-to-one correspondence between two mappings will be demonstrated to verify the role of SPPs plays in SPME. From comparison, we also illustrate the usefulness of using dispersion relations as a guideline to find the conditions for realizing absorption and decay enhancements separately. Enhanced emission is observed whenever the excitation laser and/or PL emission coincide with the ingoing and outgoing SPPs, leading to a strong angular dependence of SPME.

Figure 5.11a shows the p-p dispersion relation of the array taken in Γ–X direction. As shown in the inset, the array has period = 550 nm, R = 53 nm, and H = 300 nm. We see from the dispersion relation that only propagating Ag/air (1,0) and (−1,0) SPPs prevail without any localized mode. Then, the corresponding p-p PL detection scan taken at an incident angle = 10° is shown in Figure 5.11b. This angle is chosen so that the 514 nm Ar^+ laser does not match with any of the SPP mode to avoid absorption enhancement. As a result, the SPME being observed is due entirely to decay enhancement. Apparently, a rough comparison immediately shows that a close correlation exists between reflectivity and PL mappings in which strong emission always arises from Ag/air (−1,0) SPPs. To examine this closer, several PL spectra extracted from different detection angles are displayed in Figure 5.12a. We see sharp and narrow emission peaks are superimposed on the broad emission background. While the sharp peaks redshift to longer wavelength at larger detection angles, the background is only weakly dependent on angle. As a result, we conclude the peaks are due to SPP mediation but the background arises from direct emission of LDS. In fact, the emission profile of the background is almost identical to that of bare LDS, which is given as the dashed line in Figure 5.12a and b compares the cuts extracted from the reflectivity with PL mappings at emission wavelength = 700, 735 and 770 nm, and we surely confirm that strong emissions are always observed at the reflectivity dips, complementing the importance of SPP_{em}s for decay enhancement. Therefore, the directional

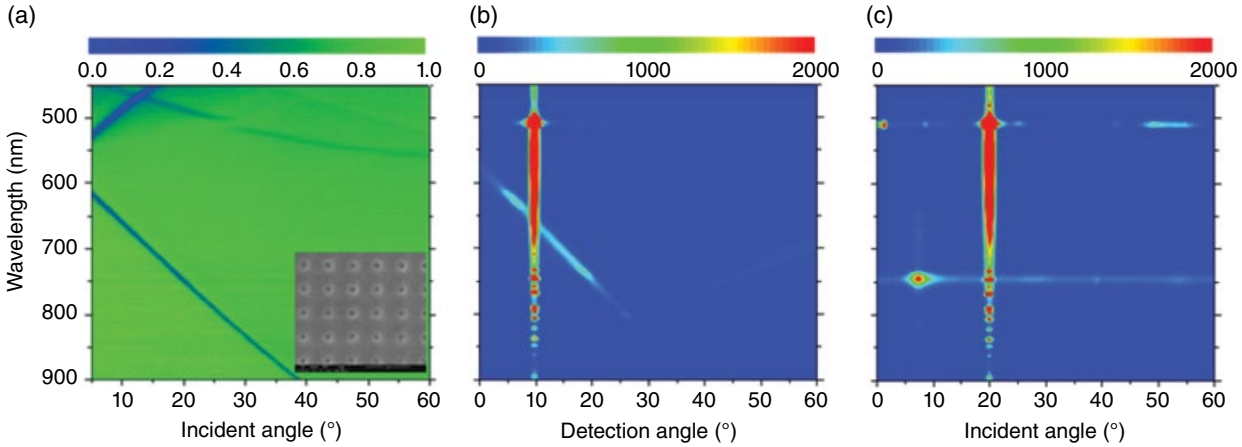

Figure 5.11 (a) The p-p dispersion relation of the array taken in Γ–*X* direction. The inset shows the SEM image of the array having period = 550 nm, *R* = 53 nm, and *H* = 300 nm. (b) The p-p PL detection scan taken at fixed incident angle = 10° with no absorption enhancement. A close correlation exists between reflectivity and PL mappings in which strong emission always arises from Ag/air (–1,0) SPPs. (c) The p-p incident scan taken by at a fixed detection angle at 20° so that the decay enhancement at 750 nm is maximized. The increases in PL emission at incident angles = 7° correspond the absorption enhancement by (1,0) SPP_{exe}s at 514 nm.

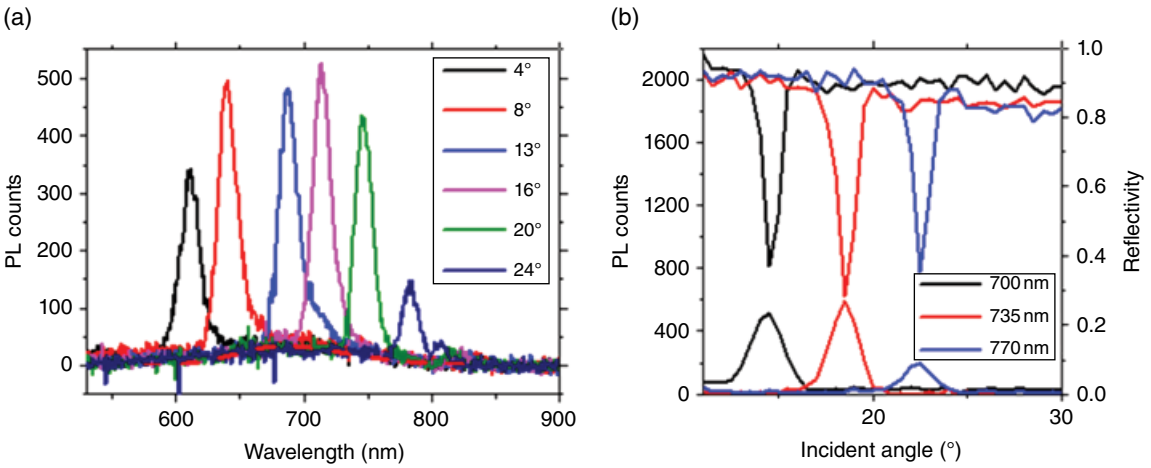

Figure 5.12 (a) Different PL spectra (solid line) extracted from detection angles equal 4°, 8°, 13°, 16°, 20°, and 24° (from left to right). Sharp and narrow emission peaks due to the SPP mediation are superimposed on the broad emission background arises from the direct emission of LDS, which is almost identical to the emission profile of bare LDS (dashed line). (b) Comparisons of the cuts extracted from the reflectivity with detection scan at emission wavelength = 700 nm, 735 nm, and 770 nm (from left to right).

PL emission mainly arises from the decay enhancement when the energy emitted from the LDS molecules are first coupled to the (–1,0) SPP_{em}s and then subsequently radiatively decay into free space. We also have performed the p-p incident scan in Figure 5.11c by fixing the detection angle at 20° so that the decay enhancement at 750 nm is maximized. From the incident mapping, we see that PL emission increases at incident angles = 7°, corresponding to the excitation of (1,0) SPP_{exe}s at 514 nm for producing absorption enhancement. The intensity cuts at $\lambda = 650$, 700, and 770 nm are plotted in Figure 5.13, and they match very well with the reflectivity taken at 514 nm. From Figure 5.13, we evaluate the absorption enhancement can reach 10 times for (1,0) SPPs by comparing the resonant enhancements at 7° with the nonresonant region at 50°. As a result, both incident and detection scans unambiguously indicate a close connection between emission enhancements and SPPs.

We then qualitatively study the relationship between the emission enhancement ratio and the SPP radiative decay rate. First, by using τ_{abs} given in Eq. (5.10) and Fano fitting, we have determined the radiative decay rate of (–1,0) SPPs as a function of resonant wavelength in Figure 5.14. The enhancement ratio is determined by deconvoluting the PL spectra at different

detection angles in Figure 5.11b with two Lorentzian peaks representing the SPP-mediated emission peak and the direct LDS emission background. The ratios are then plotted in Figure 5.14. Apparently, at long resonant wavelength, EF increases gradually from 0.29 to 4.33 with increasing decay rate confirming that faster Γ_2 indeed facilitates stronger emission enhancement when $\gamma_2 > \Gamma_2$. However, at short wavelength where the radiative decay rate begin to speed up, the ratio falls to 0.68 because of the reduction in the Q-factor, which reduces the effect of Γ_2 as well as the coupling efficiency of emission energy to the (−1,0) SPPs. In fact, the coupling efficiency, Γ_B in this case, is determined by the Fermi's golden rule given as $\Gamma_B(\omega) = 2\pi/\hbar d \cdot E_{SPP}{}^2 \rho(\hbar\omega)$, where d is the electron–hole pair dipole moment, E_{SPP} is the local electric field strength produced by(−1,0) SPPs, and $\rho(\hbar\omega)$ is the plasmonic DOS [6]. For an SPP with high decay rate and low Q-factor, it is expected that the field strength is not sufficiently strong to sustain a high coupling rate, thus lowering the enhancement ratio.

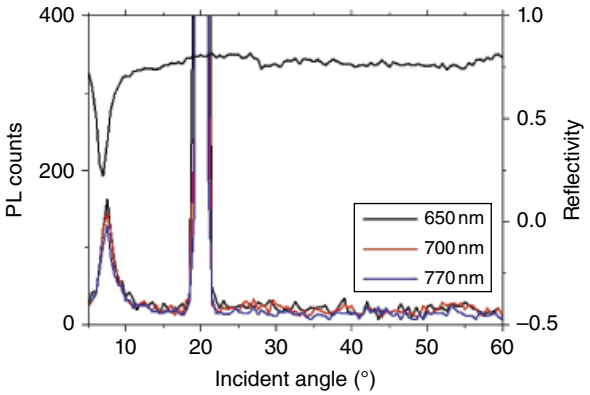

Figure 5.13 Comparisons of the cuts extracted from the reflectivity at 514 nm with the incident scan at $\lambda = 650$ nm, 700 nm, and 770 nm. The strong PL counts at 20° come from the specular reflection of the 514 nm laser. The absorption enhancement can reach 10 times for (1,0) SPPs by comparing the resonant enhancements at 7° with the nonresonant region at 50°.

5.3.4 Comparison of the Coupling Rate Γ_B of Different SPP Modes

To further elucidate the role of SPPs in decay enhancement, we attempt to determine the coupling efficiency Γ_B. By taking the ratio of I_{SPP} to I_D given in Eq. (5.3), we have

$$\frac{I_{SPP}}{I_D} = \frac{\Gamma_B}{\Gamma_{rad}} \frac{\Gamma_2}{\Gamma_2 + \gamma_2} \tag{5.12}$$

As a result, for a given wavelength, by measuring I_{SPP} for a particular SPP modes and I_D across all space, $\Gamma_B(\omega)$ can be determined accordingly, provided that $\Gamma_{rad}(\omega)$ is known. From the phase-matching equation (5.5), the propagating SPP modes are found to lie on a three-dimensional (3D) space as shown in Figure 5.15 for a particular wavelength. The Γ–X dispersion relation is obtained at $\varphi = 0°$, which is along the positive x-axis. It is also noticed that the angular position of SPPs shows an 8-fold spatial symmetry, which means all the information about the SPP modes are contained in the region spanned from $\varphi = 0°$ to $\varphi = 45°$. More importantly, the (1,0), (0,1), (−1,0), and (0,−1) modes are all expected to exhibit the same behavior, such as the generation and decay processes. They should have the same $\Gamma_{B(1,0)}$ for all wavelengths. Hence, from now on, we shall name these four modes to be the (1,0) SPP set. Similarly, for another set, the (1,1) SPP set includes (1,1), (1,−1), (−1,1), and (−1,−1) SPP modes, eventually yielding $\Gamma_{B(1,1)}$. We then measure the dispersion relations and the corresponding PL detection scans at different θ from $\varphi = 0°$ to $\varphi = 45°$. The unpolarized excitation laser is kept at normal incidence to the sample so that absorption enhancement is constant. By extrapolating all reflectivity dips from the dispersion relations and the SPP enhanced emission peaks from

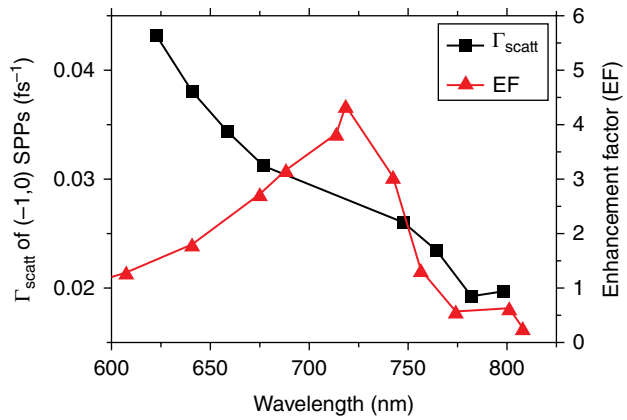

Figure 5.14 The plot of the radiative decay rate Γ_{scatt} square) of (−1,0) SPPs and the enhancement factor (EF) (triangle) against the resonant wavelength.

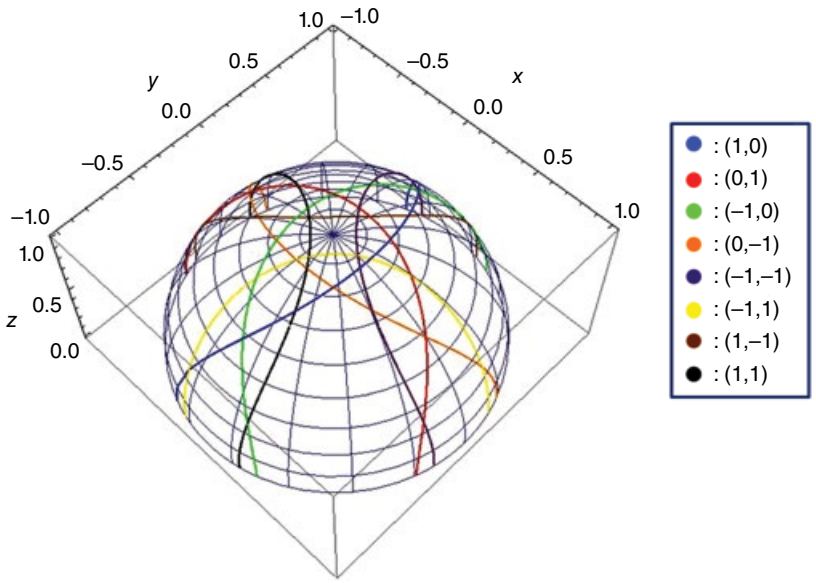

Figure 5.15 The angular position, derived from the phase-matching equation, in 3D space at which SPPs scatter into far field for a particular wavelength. Only the (1,0) (blue), (−1,0) (green), (0,1) (red), (0,−1) (orange), (−1,−1) (purple), (−1,1) (yellow), (1,−1) (brown), and (1,1) (black) SPPs modes are shown here.

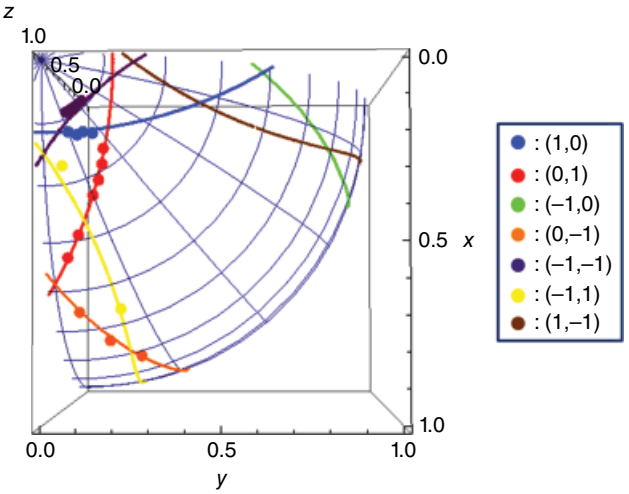

Figure 5.16 Matching between the angular position at which SPPs out-couple and the data points extrapolated at the reflectivity dip in the band structure and the SPP enhanced emission peaks in the PL scan.

the PL scans for (1,0) and (1,1) SPP sets for $\lambda = 700$ nm, they are all found to match with the angular position of SPPs deduced from the phase-matching equation given in Eq. (5.5), and the results are shown in Figure 5.16. Thus, SPME is confirmed in a 3D space.

To extract $\Gamma_{B(1,0)}$ and $\Gamma_{B(1,1)}$ in Eq. (5.12), the PL intensity and the SPP decay rates for two sets have to be determined. The total decay rates of (1,0) and (1,1) sets are fitted with the Fano expression at different angular positions, and they are found to be ~0.052 and 0.051 fs^{-1} at 700 nm. This agrees with the expectation from Mie scattering in which the decay process of the SPPs modes only depends on the hole geometry as depicted in Eq. (5.11). The nonradiative and radiative SPP decay rates are then determined to be 0.004 and 0.048 fs^{-1} for (1,0) set and 0.004 and 0.047 fs^{-1} for (1,1) set, respectively. On the other hand, for $I_{SPP(1,0)}$ and $I_{SPP(1,1)}$, the SPP-related emissions along the angular resonant positions of the modes are collected. For example, the PL emission for SPP (1,0) set is found by folding (0,1) and (0,−1) modes given in Figure 5.16 due to the 8-fold symmetry. The variation of SPP intensity for (1,0) and (1,1) sets are plotted as a function of φ in Figure 5.17. In order to determine the coupling rates for only uncoupled SPP mode, all the points where coupling of propagating SPP modes occur are avoided. The integrated areas, which are proportional to $I_{SPP(1,0)}$ and $I_{SPP(1,1)}$, are found to be 27 868 and 10 043. As a result, the ratio of $\Gamma_{B(1,0)}/\Gamma_{B(1,1)} = I_{SPP(1,0)}/I_{SPP(1,1)}$ was found to be 2.77, indicating coupling of emission into (1,0) SPP modes are more effective than (1,1) modes.

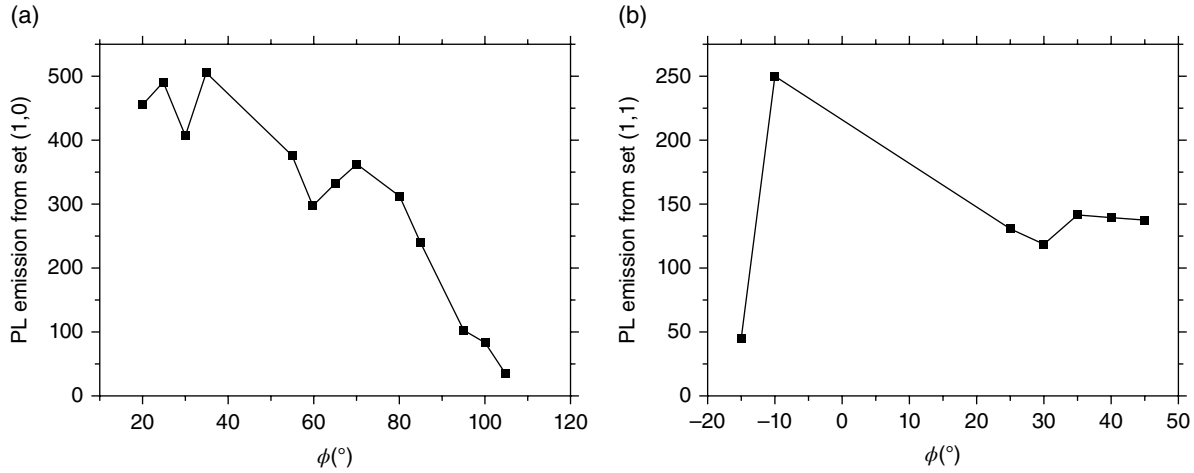

Figure 5.17 The PL emission from the uncoupled (a) (1,0) mode and (b) (−1,−1) mode against φ found by folding (a) (0,1) and (0,−1) modes and (b) (−1,1) mode according to the spatial symmetry.

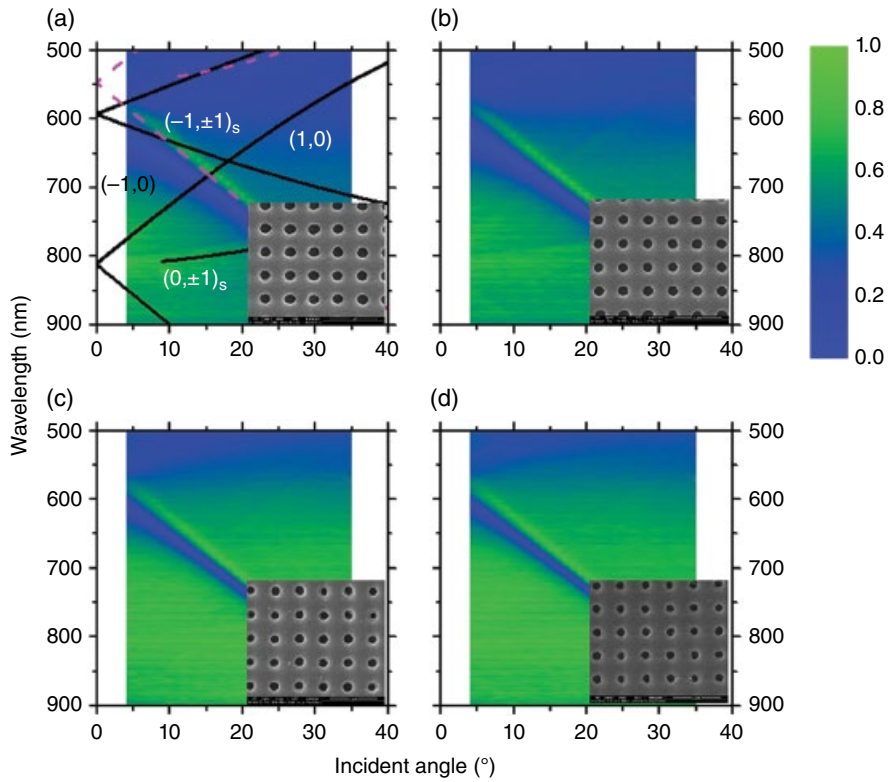

Figure 5.18 The p-p dispersion relations of arrays for R = a) 116, b) 105, c) 90, and d) 84 nm and their SEM images are shown in the insets. The period and hole depth are determined to be 539 and 290 nm, respectively. The solid and dash lines are the dispersion relations for Au/air and Au/SU8, respectively.

5.3.5 Photoluminescence Dependence on Hole Size

To illustrate the dependence of SPME on hole size, we have studied the emission from Au-coated LDS arrays with different hole radii [42]. Figure 5.18 displays the p-p dispersion relations of arrays for R = 116, 105, 90, and 84 nm, and their SEM images are shown in the insets. The period and hole depth are determined to be 539 and 290 nm, respectively. From the Figures, we see only propagating (−1,0) Au/air SPP mode is prominent although several weak (1,0), $(0,\pm1)_s$, and $(-1,\pm1)_s$ Au–SU8 SPPs are also present, particularly when the hole size is large. Their corresponding p-p PL detection mappings taken at incident angle = 10° are shown

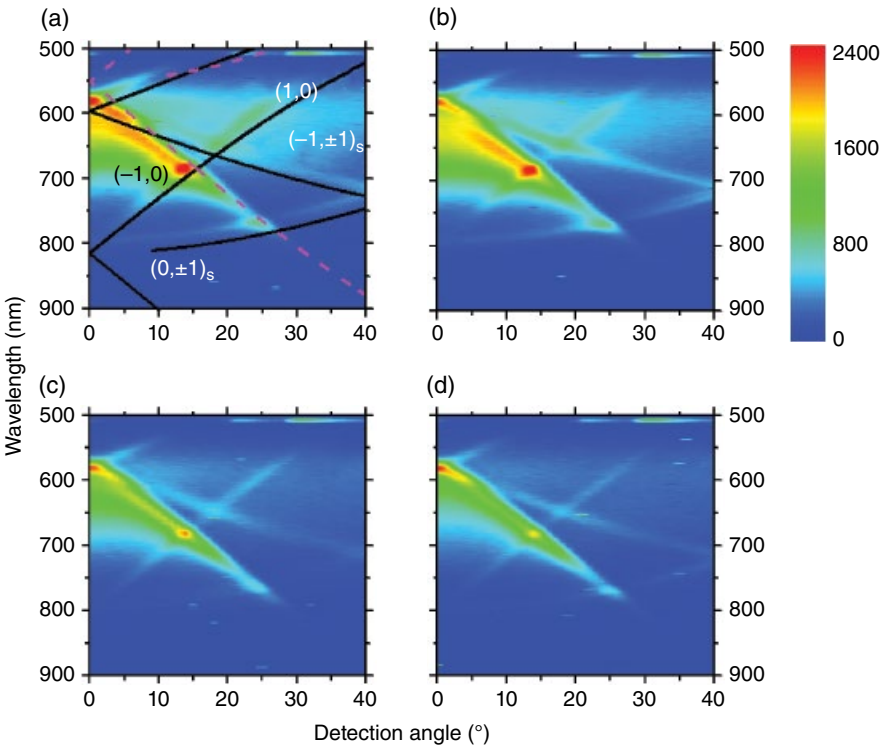

Figure 5.19 The p-p PL detection mappings measured from the forward emission at the metal side for R = a) 116 nm, b) 105 nm, c) 90 nm and d) 84 nm when the 514 nm laser source illuminate at the incident angle = 10° on the glass side.

in Figure 5.19. The laser is illuminated from the glass side, while the forward emission is collected from the metal side. Again, no absorption enhancement is expected from this case as the excitation wavelength of 514 nm is shorter than the absorption of Au film at ~550 nm. Although the SPP-mediated emission peaks follow very well with all SPP resonances, they behave differently with hole radius; the emission intensity increases with hole radius for all SPPs. To further understand the dependence of forward emission on radius, we focus on the (−1,0) Au/air SPP mode. We note that the (−1,0) reflectivity bands become darker and broader when radius increases, indicating both SPP decay rate and radiation coupling efficiency increase. Therefore, it is necessary to examine the connection between emission enhancement and these two parameters. The SPP decay rate and coupling efficiency, which is defined as $\left(R_{\text{base}} - R_{\text{res}}\right)/R_{\text{base}}$, where R_{base} is the reflectivity taken at $\lambda = 1000$ nm in which resonance is far off and R_{res} is the reflectivity at (−1,0) SP resonance, at angle = 7° have been determined and are plotted in Figure 5.20 together with the integrated emission intensities [42]. One can see a strong correlation exits between the decay rate, the coupling efficiency, and the emission intensity confirming the role of SPP damping plays in determining the SPP-mediated emission.

5.3.6 Dependence of Fluorescence Decay Lifetime on Hole Size

To confirm that SPP-mediated emission increases the emission decay rate of LEM, we have studied the dependence of decay lifetime of CdSe-based QDs on hole radius [53]. QDs are deposited directly on Au arrays with period and depth = 800 and 200 nm and R = 60, 70, 120, and 170 nm by spin coating method, and their corresponding p-p dispersion relations and PL detection mappings are then measured in Γ–X direction. For the PL scans, the 514 nm laser is incident on metal surface at 40°. As shown in Figure 5.21a and b for R = 70 and 120 nm, one can see that at 600–700 nm, indicated by the red lines, several SPP modes such as (1,0), (−2,0), and $(-1,\pm1)_s$ are seen. Their features are blurred because a localized SPP is present at ~700 nm in small hole and slightly redshifts to ~750 nm in large hole array. The coupling of propagating and localized SPPs smears out the sharp reflection bands, as evident in the regions between (1,0) and $(0,\pm1)_s$ SPPs where very low reflectivity is observed. Nevertheless, the PL detection mappings still capture the influence of SPPs on decay enhancement. By comparing the dispersion relations with the PL scans illustrated in Figure 5.21c and d, one can see stronger emissions are observed at detection angles = 5–10° and

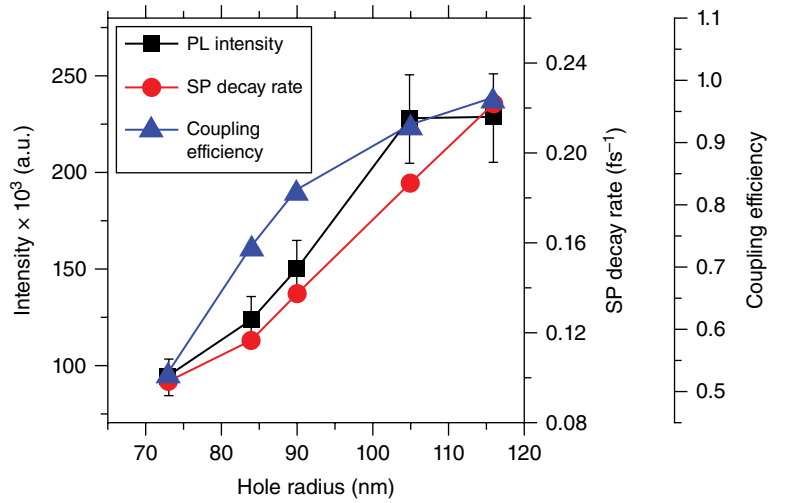

Figure 5.20 The plot of the SPP decay rate (circle); the coupling efficiency (triangle), which is defined as $(R_{base} - R_{res})/R_{base}$, where R_{base} is the reflectivity taken at $\lambda = 1000$ nm in which resonance is far off and R_{res} is the reflectivity at (−1,0) SP resonance at incident angle = 7°; and the integrated emission intensities (square) against hole radius.

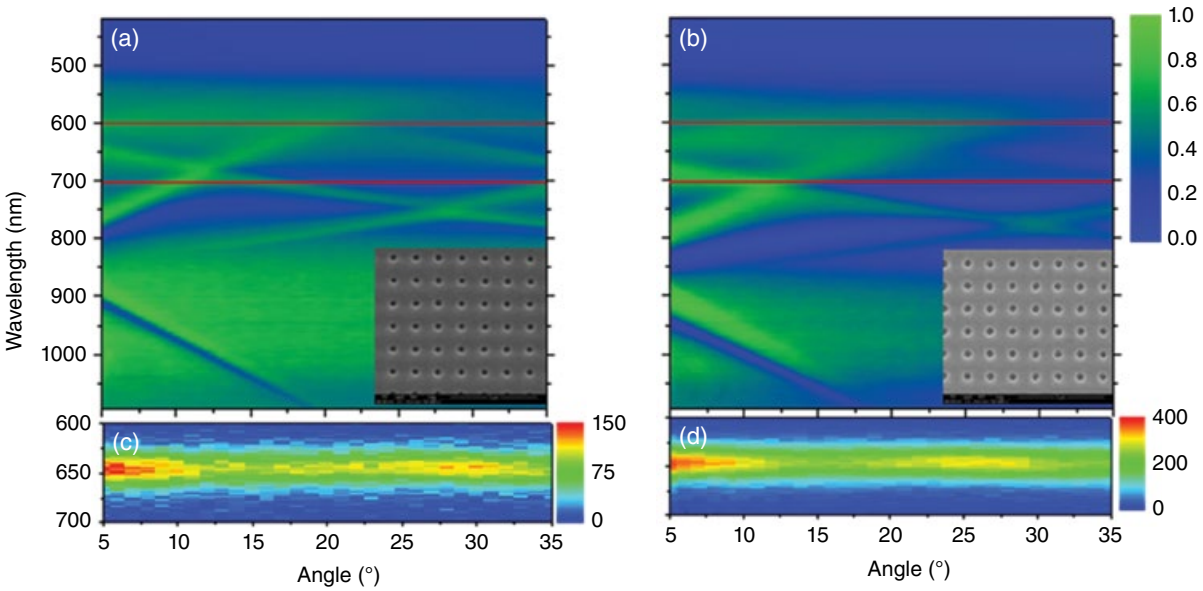

Figure 5.21 The p-p dispersion relations in Γ–*X* direction for (a) $R = 70$ nm and (b) 120 nm. Several SPP modes such as (1,0), (−2,0), and $(-1,\pm1)_s$ are seen at the region of 600–700 nm, indicated by the solid lines. The corresponding PL detection mappings in Γ–*X* direction for (c) $R = 70$ nm and (d) 120 nm are measured when the 514 nm laser is incident on metal surface at 40°. (*See insert for color representation of this figure.*)

25–30° that match with the dispersion relations, indicating that the emission of QDs is indeed enhanced by SPPs. However, due to the coupling, it is difficult to differentiate the localized and propagating modes and their contribution to the SPME.

The spontaneous emission rate of QDs is then studied by using fluorescence lifetime imaging confocal microscope. A water immersion 64 × objective lens is used for excitation and signal collection. The confocal reflection and lifetime images of the arrays with different radii are shown in Figure 5.22. The reflection images show clear array pattern with circular holes although the sizes of the holes appear almost the same due to the resolution limit of the confocal microscope that cannot resolve image smaller than 300 nm. Nevertheless, they serve as a good reference when comparing with the emission images. To examine closer the dependence of lifetime on morphology, we extract and compare the reflectivity with lifetime cuts in Figure 5.22c, f, i, and l and see that high reflection regions (i.e., array surfaces) always give longer lifetime although the reason remains unclear. Finally, the lifetime distributions for different arrays are shown in Figure 5.23. The distributions exhibit Gaussian-like distribution with the peaks located at 2.0, 2.2, 2.4, and 2.8 ns when hole size decreases. As larger hole size induces shorter SPP lifetime due to stronger scattering at the hole edge, it is expected that the plasmonic field increases with hole size, leading to shorter lifetime.

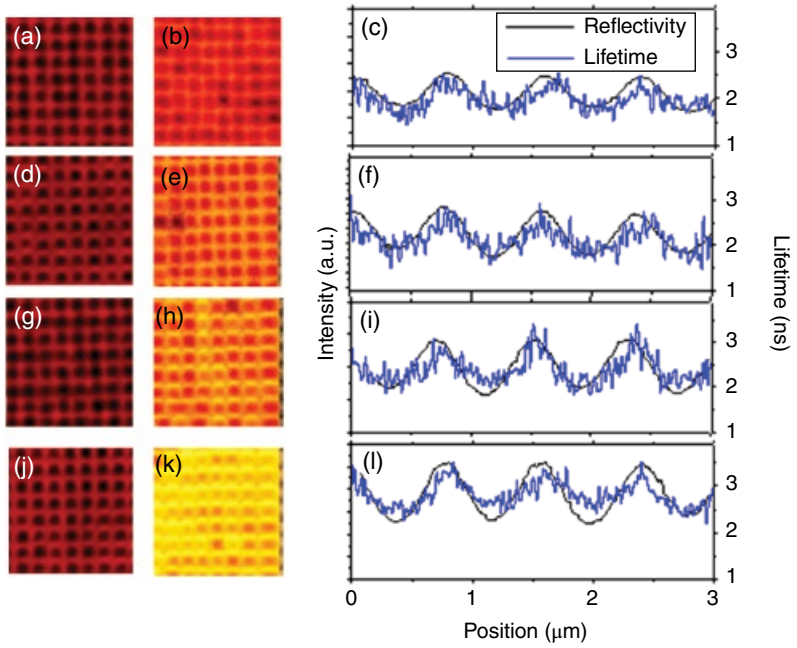

Figure 5.22 The confocal reflection and lifetime images of the arrays with (a, b) $R = 170$ nm, (d, e) 120 nm, (g, h) 70 nm, and (j, k) 60 nm. Their corresponding cuts in reflectivity (black) and lifetime (blue) shown in (c), (f), (i), and (l), respectively, reveal that high reflection regions (i.e., array surfaces) always give longer lifetime. (*See insert for color representation of this figure.*)

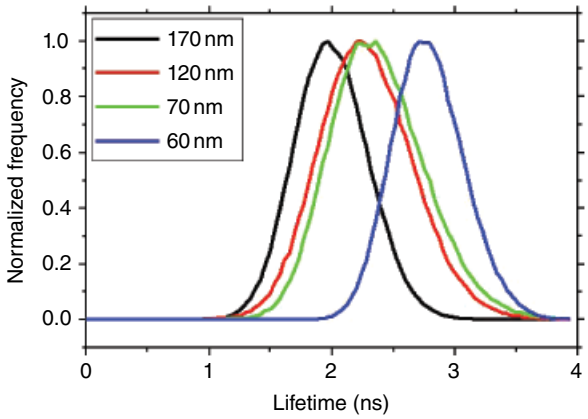

Figure 5.23 The Gaussian-like lifetime distributions with peaks located at 2.8, 2.4, 2.2, and 2.0 ns for $R = 60$, 70, 120, and 170 nm, respectively, in fluorescence lifetime imaging.

5.4 Conclusions

Various 2D periodic metallic arrays have been fabricated by IL, and their optical properties have been studied by angle-resolved reflectivity and PL spectroscopy. The combination of these two techniques has been proven to be an effective tool in understanding the underlying mechanism of SPME. In particular, the reflectivity mapping unambiguously discerns SPP modes individually so that both absorption and decay enhancements can be studied individually and quantitatively. It has been demonstrated that both absorption and decay enhancements contribute to the overall emission enhancement, and each exhibits different wavelength and angle dependences, which can be traced by using the reflectivity mappings. In addition, we also find the decay process of SPPs has a great influence on SPME. We have carried out an extensive study to understand the dependence of SPP decay on array geometry and argue that the decay rate is basically controlled by scattering at single hole. By using Mie formalism, we see the dependence of decay lifetime on hole radius and depth results from the interplay between the intrinsic absorption and radiative scattering.

Acknowledgments

This research was supported by the Chinese University of Hong Kong (CUHK) through the RGC Competitive Earmarked Research Grants (402807, 402908, and 403310), Innovative Technology Fund (ITS_053_09), and UGC special equipment grant (SEG_CUHK07). The authors thank D.Y. Lei, A.I. Fernández-Domínguez and S.A. Maier from Imperial College, London, and J.T.K. Wan and P.M. Hui from CUHK for valuable discussions.

References

1 J.N. Anker, W.P. Hall, O. Lyandres, N.C. Shah, J. Zhao, and R.P. Van Duyne, *Nat. Mater.* *7*, 442 (**2008**).
2 D.K. Gramotnev and S.I. Bozhevolnyi, *Nat. Photonics* *4*, 83 (**2010**).

3 *Radiative decay engineering*, Topics in fluorescence spectroscopy, vol. *8* Ed. C.D. Geddes and J.R. Lakowicz, (Springer, New York, **2005**). J.R. Lakowicz, *Principle of fluorescence spectroscopy* (Springer, Berlin, **2006**).

4 K. Okamoto, I. Niki, A. Shvartser, Y. Narukawa, T. Mukai, and A. Scherer, *Nat. Mater. 3*, 601 (**2004**). H.A. Atwater and A. Polman, *Nat. Mater. 9*, 205 (**2010**). A.I. Zhmakin, *Phys. Rep. 498*, 189 (**2011**).

5 P. Zijlstra and M. Orrit, *Rep. Prog. Phys. 74*, 106401 (**2011**). T.W. Odom and G.C. Schatz Ed, *Chem. Rev. 111*, 3667 (**2011**) and reference therein.

6 I. Gontijo M. Boroditsky, E. Yablonovitch, S. Keller, U.K. Mishra, and S.P. DenBaars, *Phys. Rev. B 60*, 11564 (**1999**). A. Neogi, C.W. Lee, H.O. Everitt, T. Kuroda, A. Tackeuchi, and E. Yablonovitch, *Phys. Rev. B 66*, 153305 (**2002**).

7 H. Raether, *Surface plasmons on smooth and rough surfaces and on gratings*, Tracts in modern physics (Springer, Berlin, **1988**).

8 W.L. Barnes, A. Dereux, and T.W. Ebbesen, *Nature 424*, 824 (**2003**).

9 F. J. García de Abajo, *Rev. Mod. Phys. 79*, 1267 (**2007**).

10 S.A. Maier and H.A. Atwater, *J. Appl. Phys. 98*, 0111101 (**2005**) E. Hutter and J.H. Fendler, *Adv. Mater. 16*, 1685 (**2004**).

11 L. Rogach, F. Jckel, T.A. Klar, and J. Feldmann, *Adv. Mater. 22*, 1805 (**2010**).

12 X.H. Huang, S. Neretina, and M.A. El-Sayed, *Adv. Mater. 21*, 4880 (**2009**).

13 T.W. Ebbesen, H.J. Lezec, H.F. Ghaemi, T. Thio, and P.A. Wolff, *Nature 391*, 667 (**1998**).

14 R. Gordon, A.G. Brolo, D. Sinton, and K. L. Kavanagh, *Laser Photonics Rev. 4*, 311 (**2010**).

15 L. Martín-Moreno, F.J. García-Vidal, H.J. Lezec, K.M. Pellerin, T. Thio, J.B. Pendry, and T. W. Ebbesen, *Phys. Rev. Lett. 86*, 1114 (**2001**).

16 T.D. Corrigan, S.H. Guo, H. Szmacinski, and R.J. Phaneuf, *Appl. Phys. Lett. 88*, 101112 (**2006**). A.G. Brolo, S.C. Kwok, M.D. Cooper, M.G. Moffitt, C.W. Wang, R. Gordon, J. Riordon, and K.L. Kavanagh, *J. Phys. Chem. B 110*, 8307 (**2006**). J.Y. Zhang, Y.H. Ye, X.Y. Wang, P. Rochon, and M. Xiao, *Phys. Rev. B 72*, 201306 (**2005**).

17 A.G. Brolo, E. Arctander, R. Gordon, B. Leathem, and K.L. Kavanagh, *Nano Lett. 4*, 2015 (**2004**).

18 M. Airola, Y. Liu, and S. Blair, *J. Opt. A Pure Appl. Opt. 7*, S118 (**2005**).

19 R. Gordon, D. Sinton, K.L. Kavanagh, and A.G. Brolo, *Acc. Chem. Res. 41*, 1049 (**2008**).

20 A.N. Grigorenko, N.W. Roberts, M.R. Dickinson, and Y. Zhang, *Nat. Photonics 2*, 365 (**2008**).

21 C. Kittel, *Introduction to solid state physics* (Wiley, New York, **2004**).

22 J.D. Joannopoulos, S.G. Johnson, J.N. Winn, and R.D. Meade, *Photonic crystals: molding the flow of light* (Princeton University Press, Princeton, **2008**).

23 J. Li, H. Iu, W. C. Luk, J. T. K. Wan, and H. C. Ong, *Appl. Phys. Lett. 92*, 213106 (**2008**).

24 P.B. Catrysse, H. Shin, and S.H. Fan, *J. Vac. Sci. Technol. 23*, 2675 (**2005**).

25 F. J. Garcia-Vidal, L. Martin-Moreno, T. W. Ebbesen, and L. Kuipers Rev. *Mod. Phys. 82*, 729 (**2010**).

26 A.P. Hibbins, M.J. Lockyear, and J.R. Sambles, *J. Appl. Phys. 99*, 124903 (**2006**).

27 E. Laux, C. Genet, and T.W. Ebbesen, *Opt. Express 17*, 6920 (**2009**).

28 L. Novotny, *Am. J. Phys. 78*, 1199 (**2010**).

29 W. L. Barnes, T. W. Preist, S. C. Kitson, J. R. Sambles, N. P. K. Cotter, and D. J. Nash, *Phys. Rev. B 51*, 11164 (**1995**).

30 Y. Chu and K.B. Crozier, *Opt. Lett. 34*, 244 (**2009**).

31 A. Ghoshal, I. Divliansky, and P.G. Kik, *Appl. Phys. Lett. 94*, 171108 (**2009**).

32 H. Wang, D. Brandl, P. Nordlander, and H.J. Halas, *Acc. Chem. Res. 40*, 53 (**2006**). E. Prodan, C. Radloff, N. J. Halas, and P. Nordlander, *Science 302*, 419 (**2003**).

33 J.A. Porto, F.J. García-Vidal, and J.B. Pendry, *Phys. Rev. Lett. 83*, 2845 (**1999**).

34 C. Ropers, D.J. Park, G. Stibenz, G. Steinmeyer, J. Kim, D.S. Kim, and C. Lienau, *Phys. Rev. Lett. 94*, 113901 (**2005**).

35 K.C. Hui, J.T.K. Wan, J.B. Xu, and H.C. Ong, *Appl. Phys. Lett. 95*, 063110 (**2009**).

36 G. Laurent, N. Félidj, J. Grand, J. Aubard, G. Lévi, A. Hohenau, F. R. Aussenegg, and J. R. Krenn, *Phys. Rev. B 73*, 245417 (**2006**). N. Félidj, S.L. Truong, J. Aubard, G. Levi, J.R. Krenn, A. Hohenau, A. Leitner, and F.R. Aussenegg, *J. Chem. Phys. 120*, 7141 (**2004**).

37 B.D. Lucas, J.S. Kim, C. Chin, and L.J. Guo, *Adv. Mater. 20*, 1129 (**2008**). R. Alvarez-Puebla, B. Cui, J. Bravo-Vasquez, T. Veres, and H. Fenniri, *J. Phys. Chem. C 111*, 6720 (**2007**).

38 J.P. Camden, J. Dieringer, J. Zhao, and R.P. Van Duyne, *Acc. Chem. Res. 41*, 1653 (**2008**). P. Stiles, J. Dieringer, N. C. Shah, and R. P. Van Duyne, *Annu. Rev. Anal. Chem. 1*, 601 (**2008**).

39 M. Maldovan and E.L. Thomas, *Periodic materials and interference lithography for photonics, phononics and mechanics* (Wiley-VCH, Weinheim, **2008**).

40 www.exciton.com/pdfs/lds751.pdf (accessed on October 7, 2016).

41 http://www.sigmaaldrich.com/catalog/product/aldrich/694606.

42 J. Li, J.B. Xu, H.C. Ong, *Appl. Phys. Lett. 94*, 241114 (**2009**).

43 J. Li, H. Iu, D.Y. Lei, J.T. K. Wan, J.B. Xu, H.P. Ho, M.Y. Waye, and H.C. Ong, *Appl. Phys. Lett. 94*, 183112 (**2009**).

44 Lecia TCS SMD FLIM http://www.leica-microsystems.com/products/confocal-microscopes/ (accessed on October 7, 2016).

45 C. Sönnichsen, T. Franzl, T. Wilk, G. von Plessen, J. Feldmann, O. Wilson and P. Mulvaney, *Phys. Rev. Lett. 88*, 077402 (**2002**).

46 D. S. Kim, S. C. Hohng, V. Malyarchuk, Y. C. Yoon, Y. H. Ahn, K. J. Yee, J.W. Park, J. Kim, Q. H. Park, and C. Lienau, *Phys. Rev. Lett. 91* 143901 (**2003**).

47 C. Genet, M.P. van Exter, J.P. Woerdman, *Opt. Commun 225*, 331 (**2003**).

48 J. Braun, B. Gompf, G. Kobiela, and M. Dressel, *Phys. Rev. Lett. 103*, 203901 (**2009**).

49 D.Y. Lei, J. Li, A.I. Fernández-Domínguez, H.C. Ong, and S.A. Maier, *ACS Nano 4*, 432 (**2010**).

50 S. Collin, C. Sauvan, C. Billaudeau, F. Pardo, J.C. Rodier, J.L. Pelouard, and P. Lalanne, *Phys. Rev. B 79*, 165405 (**2009**).

51 H. Iu, J. Li, H. C. Ong, and J.T.K. Wan, *Opt. Express 16* 10294 (**2008**). J. Li, H. Iu, J.T.K. Wan, and H.C. Ong, *Appl. Phys. Lett. 94* 033101 (**2009**).

52 T.A. Kelf, Y. Sugawara, J.J. Baumberg, M. Abdelsalam, and P.N. Bartlett, *Phys. Rev. Lett. 95*, 116802 (**2005**).

53 C.H. Fok, H.Y. Lo, K.F. Chan, and H.C. Ong (in preparation).

6

Fluorescence Excitation, Decay, and Energy Transfer in the Vicinity of Thin Dielectric/Metal/Dielectric Layers near Their Surface Plasmon Polariton Cutoff Frequency

Kareem Elsayad[1] *and Katrin G. Heinze*[2]

[1] *Advanced Microscopy, Vienna Biocenter Core Facilities (VBCF), Vienna, Austria*
[2] *Rudolf Virchow Center, DFG Research Center for Experimental Biomedicine, University of Wüerzburg, Wüerzburg, Germany*

6.1 Introduction

The interactions of fluorescent molecules with metallic structures has attracted a great deal of attention over the last few decades, motivated largely by the near-field coupling that can be realized between electric-dipole-like emitters and surface plasmon polaritons (SPPs)/surface plasmons (SPs) and driven by the promise of active nano-photonic components and sensors. There has also been much work and progress in exploiting these effects for life-science applications, for example, utilizing the strong localized fields near plasmonic structures to enhance the fluorescence intensities and decay rates and allowing for sub-diffraction limit resolution mapping of molecules in the vicinity of the metal. Numerous approaches have been undertaken in this regard, which include exploiting the coupling of fluorophores to SPPs/SPs on metallic nanoparticles , metallic tips, and planar structures, with potential applications range from improved drug delivery techniques to ultrafast subwavelength-scale sensors and high throughput molecular imaging/sensing platforms.

In this chapter we take a closer look at the interactions of fluorescent molecules with smooth and continuous planar metallic structures—in particular a thin smooth silver film clad between two different dielectric layers. We model the fluorophores beyond the conventionally used two-level electric-dipole emitter model by assuming a (more realistic) broad emission and excitation spectrum—from the first electronic excited state to different vibrational levels in the ground electronic state and from the ground electronic state to various vibrational excited levels in the first electronic excited state, respectively. We also consider the broadening of spectra as a result of the reduced excited-state lifetime near the structure. We find that for a dense collection of fluorophores, the radiative fluorescence emission can be enhanced near certain metal/dielectric structures by a process where the fluorophores excite plasmonic modes in the structure that can subsequently excite other fluorophores from the ground state. In other words, fluorophores can serve as a means of coupling the applied free-space radiation to the SPPs, which subsequently can enhance the excitation rate of other fluorophores.

Unlike the cases of metal-enhanced fluorescence (MEF) [1] or surface plasmon-coupled emission (SPCE) [2], the smooth metal structures we consider will not enhance the fluorescence through an "out-coupling" mechanism (which can consist of subwavelength surface features for the case of MEF or a higher refractive index material in SPCE) i.e. the measurable radiative enhancement in the case we consider here will originate from the fluorophores themselves (as opposed to the metal or metal-fluorophore-coupled system), which may lead to potential benefits for single-molecule imaging/sensing.

6.2 Background

It is well known that measurable (radiative) fluorescence in the immediate vicinity of a smooth semi-infinite metal slab or a metallic film supporting no "leaky" radiative modes will usually be quenched as a result of coupling to dissipative and non-radiative excitations associated with the metal interface(s) and the bulk of the metal. The interactions of fluorophores with single- and layered-metallic films supporting non-radiative modes has been extensively studied since the 1960s—see, for example, a nice review by Barnes [3]. A robust and easily measurable (using time-resolved techniques) quantity often of interest is the total excited-state lifetime of the fluorophore, which will depend on the fluorophore emission spectrum and its distance from the

Surface Plasmon Enhanced, Coupled and Controlled Fluorescence, First Edition. Edited by Chris D. Geddes.
© 2017 John Wiley & Sons, Inc. Published 2017 by John Wiley & Sons, Inc.

interface, and can directly be used to infer the coupling strength to the different excitations in the metal. A two-level semiclassical framework—as first introduced by Sommerfeld (for point-dipole emitters near "conducting" planar surfaces) [4]—describes experimental observations surprisingly well at not too small distances for which nonlocal effects are negligible. A comprehensive summary of the semiclassical treatment for the case of chromophores near smooth metal/dielectric layers was given by Chance, Prock and Sibley [5]. Aside from the spectral shift in the dipole frequency, full quantum mechanical calculations yield identical results [6]. Indeed in most cases (in the linear regime), it is sufficient to know the (complex) frequency and wavevector-dependent reflection and transmission coefficients of the structure in order to characterize their interactions with fluorophores at not too small separations.

There has also been renewed interest in studying the coupling of fluorophores to smooth metal films, in regard to realizing structures where the fluorophores serve as a gain medium for compensating the losses of the SPPs and increasing their in-plane propagation distance (active plasmonic waveguides). In this scenario the fluorophores emission spectrum coincides with the excited SPP frequency so that pumping the fluorophores while simultaneously launching an SPP can result in large increases in the SPP propagation distance [7]. Potential applications of such devices could include plasmonic interconnects where it is the propagation distance of the SPPs that is often the limiting feature. Furthermore, when the fluorophore density is large enough, that is, so that one overcompensates the SPP loses [8], stimulated SPP generation can ensue [9], which opens up the door for many potential applications in nano-optical circuitry and processing.

It is also understood that energy from an excited fluorophore can be effectively transferred through a thin low loss smooth metallic film via the coupled SPP modes at the two metal/dielectric interfaces [10]. This has been receiving attention in regard to the so-called perfect lens proposed by Pendry [11], which can be realized to a certain extent in the form of (plasmonic) superlenses [12]. The problem with metal-based superlenses is in general the dissipative nature of the metals that leads to often detrimental loses in the transmitted field amplitude and phase. It has been proposed [13] and shown [14] that including an active layer of fluorophores can compensate for this. The use of multilayered smooth metallic/dielectric structures, with layer thicknesses much smaller than the wavelength, has also been receiving much interest in this regard on account of their often nontrivial optical reflection/transmission properties. These may support various resonant and non-resonant modes depending on the parameters of the individual layers, which can provide significant non-active loss reduction for near-field superlensing applications by, for example, concentrating the energy density in the low loss dielectric layers [15]. Such structures lead to large modifications in the decay rates of nearby fluorophores [16]. One such structure that has been receiving much attention is the so-called hyperlens, which can be used for sub-diffraction-limit imaging (when fabricated in a nonplanar geometry) and greatly enhance the decay rate of nearby fluorophores [16,19].

6.3 Theory

In this chapter we will focus exclusively on dielectric/metal/dielectric planar structures that support an SPP mode close to the low frequency mode cutoff (ω_c)—that is, where the SPP transitions from being bound to being propagating. The reason this is of interest is that for appropriate material and thickness parameters, this weakly bound SPP mode can be made to extend far into the sample medium such that fluorophores over a macroscopically large range of distances can couple to it. We see that the combination of several factors including the short lifetimes of the SPPs and of the excited-state fluorophores with a small Stokes shift positioned close to the substrate can result in a significant increased overlap between the SPP field and the fluorophore absorption spectrum in the vicinity of the substrate. This in turn can give rise to a fraction of the fluorophores over a wide range of distances "pumping" those close to the substrate, even to the extent that the decrease in the radiative quantum yield is compensated by the increase in their excitation rate. In Figure 6.1 we show a simplified sketch of the effect described where a fluorophore (left) excites an SPP (middle), which subsequently excites a second fluorophore (right). In the top figure the second fluorophore is close to the metallic structure and has a shorter excited-state lifetime and hence also a broader absorption spectrum that extends to lower frequencies. As will be seen this results in stronger coupling of the SPP to the absorption transition. In the lower figure the fluorophore is further from the substrate and has a longer lifetime and resulting in the absorption spectrum not being broadened to the same extent and a reduced overlap between the fluorophore absorption spectrum and the SPP field.

Let us start by considering a simplified fluorophore energy diagram as shown in Figure 6.2. For simplicity we will neglect contributions from triplet state

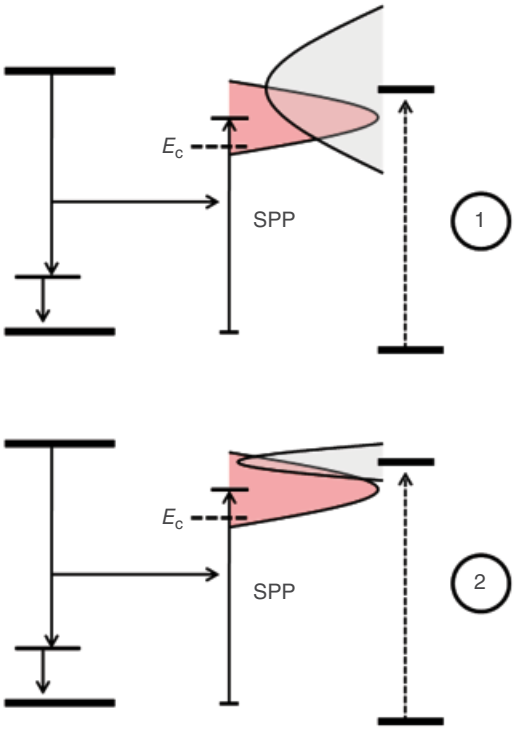

Figure 6.1 Sketch of the origin of the additional excitation field. SPPs excited by fluorophores in the sample can couple effectively with fluorophores close to the substrate (1) but less effectively with those far away whose effective absorption spectrum is not as broad.

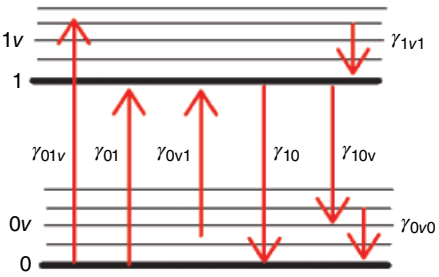

Figure 6.2 Simplified energy diagram of a fluorophore showing the considered transitions.

dynamic[1] and assume at equilibrium all molecules are in the lowest ground state (i.e., $\exp(-\hbar\omega/k_BT) \sim 0$). For simplicity we have grouped together all the vibrational/rotational excited states of each of the two levels and called them 0ν and 1ν. Including the distribution of discrete levels may be obtained by inserting summations over these levels at the appropriate positions in the rate equations. Furthermore we will assume that decay from higher energy states in the first excited state (designated 1ν) to the lowest first excited state (1) is much faster than all other rates (i.e., $\gamma_{1\nu1}$ is large), which is a reasonable assumption when the fluorophore is not too strongly coupled to any system. The fluorophore can be excited from the ground state by an incident radiative or non-radiative field harmonic in the absorption spectrum at a rate determined by the frequency (ω) -dependent extinction coefficients $\varepsilon(\omega)$ (or equivalently the absorption cross-section $\sigma_\alpha(\omega)$). In particular, the excitation rate from the ground state $\gamma_{ex} = \gamma_{01} + \gamma_{01\nu}$ will be given by

$$\gamma_{ex} = \int d\omega \frac{\sigma_\alpha(\omega) I(\omega)}{\hbar\omega} = \int d\omega \frac{\Re\{\eta(\omega)\}}{\eta(\omega)} \frac{\sigma_\alpha(\omega)|E(\omega)|^2}{\hbar\omega} \tag{6.1}$$

where $E(\omega)$ and $I(\omega)$ are the electric field and intensity at the position of the molecule and $\eta_s(\omega) = [\mu_s(\omega)/\varepsilon_s(\omega)]^{1/2}$ is the characteristic impedance of the medium that the molecule is in.

By solving the steady-state rate equations for Figure 6.2, one obtains the relative population of the first excited state as:

$$\hat{n}_1 = \gamma_{ex}\left[\left(1 + \frac{\gamma_{10\nu}}{\gamma_{1\nu0} + \gamma_{0\nu0}}\right)\gamma_{ex} + \left(\frac{\gamma_{0\nu0}}{\gamma_{10}}\frac{\gamma_{10\nu}}{\gamma_{0\nu1} + \gamma_{0\nu0}}\right)\gamma_{10}\right]^{1}. \tag{6.2}$$

The measurable "fluorescence" at a distance much larger than the wavelength ($\gg hc(\varepsilon_1 - \varepsilon_0)^{-1}$) from the molecule will then be given by

$$I(\omega_{1i}) \quad \gamma_{1i}\hat{n}_1 \tag{6.3}$$

where γ_{1i}^r is the decay rate via radiative transitions (those emitting a propagating photon) into the solid angle defined by the detector and the index $i = 0$ or 0ν. This may be extended to a continuous or quasi-continuous emission/absorption spectrum, in which case the measurable fluorescence at a frequency ω can be described by

$$I(\omega) \approx \hat{\gamma}_r(\omega) f(\omega) \frac{\gamma_{ex}}{(1 + a_\omega)\gamma_{ex} + \int d\omega' (1 + a_{\omega'}) f(\omega') \hat{\gamma}_t(\omega')}. \tag{6.4}$$

Here the coefficient $f(\omega)$ describes the decay probability associated with a change in energy of $\hbar\omega$ intrinsic to the transition (as can be estimated by the unperturbed and the normalized radiative emission spectrum for a high quantum yield fluorophore). $\hat{\gamma}_r(\omega) = \gamma_r(\omega)/\gamma_0(\omega)$ and $\hat{\gamma}_t(\omega) = \gamma_t(\omega)/\gamma_0(\omega)$ are the measurable radiative and total (= radiative + non-radiative) decay rates

1 The triplet decay path can be argued to have a reduced significance on account of the comparatively slow intersystem crossing rate compared with the total decay rates of the excited states.

normalized to the theoretical unmodified decay rate at the same frequency $[\gamma_0(\omega)=(2/3)e^2c^{-3}m^{-1}\varepsilon_s^{1/2}\omega^2]$. The quantity $a_\omega=\gamma_t[\gamma_{v1}(\omega)+\gamma_v]^{-1}$ (where γ_v is the decay rate of a vibrationally/rotationally excited ground state and $\gamma_{v1}(\omega)$ is the rate at which it is excited into the first excited state) is harder to calculate[2] but can be considered negligible since γ_v is assumed large. For the case of a weak excitation field ($\gamma_{ex}\ll\gamma_t$), Eq. 6.4 simplifies to the standard equation for the fluorescence intensity, namely, $I(\omega)\sim\gamma_{ex}\gamma_r(\omega)/\gamma_t$

The modification to the decay rate in the vicinity of a planar structure is most easily investigated by looking at the power transferred to the structure as a function of wavevector parallel to the interface, which is given in the semiclassical point electric-dipole approximation by

$$\frac{dP}{dk_{||}}=\frac{3}{4}\Re\left\{\left[2\alpha_\perp\left(\frac{k_{||}}{k_S}\right)^2 r_p-\alpha_{||}\left(\frac{k_{\perp S}}{k_S}\right)^2 r_p-\alpha_{||}r_S\right]\right\}\frac{k_{||}}{k_{\perp S}}e^{2ik_{\perp S}z}. \tag{6.5}$$

Here $k_S=\sqrt{\mu_S}\sqrt{\varepsilon_S}\,\omega/c$, where μ_S (ε_S) are the permeability (permittivity) of the sample medium and c is the vacuum light speed. $k_{||}$ and $k_{\perp S}=(k_S^2-k_{||}^2)^{1/2}$ are the parallel and perpendicular wavevector components to the interface in the sample medium. $r_p(r_s)$ are the transverse magnetic (transverse electric) reflection coefficients of the structure, and z is the distance of the fluorophore from the structure. We assume the emission and excitation dipole are and remain in the same direction, which is often a reasonable first approximation for immobilized molecules, and the coefficients $\alpha_{||}(\alpha_\perp)$ define the dipole-moment orientation (such that $\alpha_{||}=2\alpha_\perp=2/3$) for an isotropically orientated excitation/emission dipole distribution.

The modified field at a distance z' above the structure from an electric-dipole transition at a position z can be written as

$$E_r(\omega,z,z')=\frac{\mu}{2i\varepsilon_s}\int_0^{2.2k_F}dk_{||}\frac{k_{||}}{k_{\perp S}}\left[\left(2\alpha_\perp+\alpha_{||}\right)k_{||}^2r_p-\alpha_{||}k_s^2\left(r_s+r_p\right)\right]e^{2ik_{\perp S}(z+z')} \tag{6.6}$$

where k_F is the Fermi wavevector of the metal ($\approx 12\ \mathrm{nm}^{-1}$ for silver). For the case of the field at the fluorophores position (the so-called back-reacted field), $E_r(\omega,z'=z,z)=E_r(\omega,z)$, the change in the total decay rate is given by

$$\hat{\gamma}t(\omega,z)=1+\frac{3\varepsilon_s}{2\mu k_s^3}\Im\left\{E_r(\omega,z)\right\}. \tag{6.7}$$

The total measurable radiative decay rate that constitutes a part of this will also be modified and is given by [5]

$$\begin{aligned}\hat{\gamma}_r(\omega,z)=1+\frac{3}{8}\Re\int_0^{N.k_s}dk_{||}\frac{2k_{||}}{k_{\perp,s}k_s^3}\Big\{&2\alpha_\perp k_{||}^2+\alpha_{||}\left(1+|r_s|^2\right)k_s^2\\&+\ldots\left(2\alpha_\perp k_{||}^2+\alpha_{||}k_\perp^2\right)|r_p|^2+\alpha_{||}\left(k_\perp^2-2k_s^2r_s\right)\\&+\left(4\alpha_\perp k_s^2-2\alpha_{||}k_\perp^2\right)r_pe^{2ik_{\perp S}z}\Big\}\end{aligned} \tag{6.8}$$

where N is the numerical aperture of the detector.

It should be noted that the structure will in a typical experimental configuration also modify the fluorescence excitation rate. The modified excitation rate will be for a single emitter and at a single frequency due to an externally applied applied excitation field will be given by

$$\begin{aligned}\gamma_{ex}(z)&=\frac{1}{2}\int d\omega\frac{\sigma_a(\omega)}{\hbar\omega}\frac{\Re\{\eta(\omega)\}}{|\eta(\omega)|}\left|E_{ex}^0(\omega,z)\right|^2\\E_{ex}^0(\omega,z)&=\int dk_{||}\left(1+r(\omega,k_{||})e^{-2ik_{\perp s}z}\right)I_0^{1/2}(\omega,k_{||})\end{aligned} \tag{6.9}$$

where $I_0(\omega,k_{||})$ is the applied excitation intensity, which will be modeled as having a normal frequency distribution about the laser emission peak and an angular distribution defined by the objective (for collimated/wide-field illumination $I_0(\omega,k_{||})\to\delta(k_{||})I_0(\omega,k_{||})$ and the wavevector integral disappears). $r=r(\omega,k_{||})$ is the complex reflection coefficient of the structure, which for an unpolarized source would be $(r_p+r_s)/2$ (r_p and r_s being the P- and S- polarization components respectively).

Eq.'s (6.1)–(6.9) constitute the standard semiclassical treatment of the modified emission intensity of a fluorophore modeled as a point dipole as a result of its own back-reacted field (Eq. 6.8) and the modified excitation rate from the applied field reflected from the structure (Eq. 6.9), which when inserted into Eq. 6.4 can be used to calculate the measurable fluorescence intensity.

There also exists a contribution to the total excitation rate of fluorophores from excitations in the structure that have been excited by other fluorophores. This is somewhat analogous to conventional Förster resonant energy transfer (FRET), except that the energy transfer is mediated by a resonance in the structure. Also important to note is that one would not necessarily expect an additional modification to the decay rate of the donor as a result of the acceptors

2 It will depend on the Franck–Condon coefficients between the vibrational/rotational ground states and those of the first excited state.

presence. There has recently been some controversy surrounding the issue of SP/SPP-mediated FRET, which in some cases it appears stems from how FRET has been defined (i.e., the reduced donor lifetime due to the presence of a nearby acceptor or the enhanced excitation rate of an acceptor due to the presence of a nearby donor). Either way, energy transfer has been shown to be significant over very large distances for donor/acceptor pairs separated by a thin symmetric-clad silver film [10]. In an analogous manner to conventional FRET, the energy transfer efficiency depends on the overlap between the SPP spectrum and the fluorophores absorption spectrum both of which may be modified in a manner dependent on the nearby metallic structure.[3] It can qualitatively be seen that for a generic planar metallic structure, the latter should be *broader* when fluorophores are *closer to the structure,* where the excited-state lifetime is smaller. To estimate this effect we firstly consider the finite energy width of the SPP field (excited with a frequency ω), which will have a half width given by the inverse SPP lifetime:

$$\tau_{spp}^{-1} = \Gamma_{spp}(\omega) = -\left[\varepsilon''(\omega) + \frac{4\varepsilon'(\omega)^2}{1-\varepsilon'(\omega)} \Im\left\{r_p \exp\left(2ik_{\perp,z} z_m\right)\right\}\right] \left(\frac{d\varepsilon'(\omega)}{d\omega}\right)^{-1} \tag{6.10}$$

where $\varepsilon(\omega) = \varepsilon'(\omega) + i\varepsilon''(\omega)$ is the permittivity of the metal. The second term here accounts for the radiative damping of the SPP where r_p is the reflection coefficient of the structure and z_m is the thickness of the metal film. For a fluorophore density in the z direction given by $\rho(z')$, we can estimate the field generated by the SPPs at a given location z as

$$E_{spp}(\omega,z) = \iint \rho(z') f(\omega') L\left[\omega', \Gamma_{spp}(\omega'), \omega\right] E_{spp}(\omega', z', z)\, d\omega' dz' \tag{6.11}$$

Here $E_{spp}(\omega, z, z')$ is the electric field due to an excited SPP given by Eq. 6.6 but with the upper and lower integration limits set at $k'_{spp} + k''_{spp}$ and $k'_{spp} - k''_{spp}$, where $k_{spp} = k'_{spp} - ik''_{spp}$ is the complex wavevector[4] associated with the SPP for which τ_{spp}^{-1} was defined. (L) is the Lorentzian defined as

$$L(\omega_0, \Delta, \omega) = \frac{1}{4\pi} \frac{\Delta}{(\omega_0 - \omega_2)^2 + (\Delta/2)^2} \tag{6.12}$$

The total excitation field will now become

$$E_{ex} = E_{ex}^0 + E_{spp} \tag{6.13}$$

where $E_{ex}^0 = E_{ex}^0(\omega, z)$ is given by Eq. 6.9.

Finally to calculate the modified excitation rate, we should also consider the homogeneous broadening of absorption spectrum of the molecule at z, which will have a half width given by $\gamma_t(\omega, z)$. The modified excitation rate, $\gamma_{ex}(z)$, will be given by:

$$\gamma_{ex}(z) = \frac{1}{2} \int \frac{\Re\{\eta(\omega)\}}{\hbar\omega |\eta(\omega)|^2} |E_{ex}(\omega, z)|^2 \int \sigma(\omega') L\left[\omega', \gamma_t(\omega', z), \omega\right] d\omega' d\omega \tag{6.14}$$

The emission intensity spectrum as a function of distance can now readily be calculated for a given fluorophore density distribution $\rho(z)$ from Eqs. 6.4 and 6.8–6.14.

The effect described previously, may be realized for a structure that supports a weakly bound SPP mode that extends far into the sample medium. In this regard long-range surface plasmon polariton modes (LRSPPs) [20] in slightly asymmetric structures [21] are appealing. To make the structure versatile, the supported SPPs should ideally not be too strongly dependent on the dielectric properties of the sample medium at the interface. For thin metal films the SPP modes may be appreciably perturbed by the sample medium. Furthermore, since the lowest loss simple metal at the optical frequencies of interest is silver, it is also desirable the sample not be in direct contact with the metal for toxicity issues. A thin dielectric "buffer" layer is therefore desirable between the sample and the metal. The SPP (and SPP-coupled waveguiding) modes supported by different structures composed of metal films with thin dielectric coatings have been studied quite extensively, often with the intention of achieving simultaneously strong mode confinement and low propagation loss (as would be desirable for plasmonic waveguides), - e.g. [22].

Based on these considerations we will consider a structure consisting of (i) a low permittivity dielectric, (ii) a thin metal film, (iii) a high permittivity dielectric thin film, and (iv) the sample medium with the fluorophores that has a permittivity larger than the lower dielectric layer. The motivation for choosing this design is that the SPP mode associated with the (i)–(ii) interface can be made to be weakly localized in the sample

3 The homogeneous broadening of an emitter's excitation/absorption spectra due to the finite lifetime of the excited/ground state may for very fast process become significant [17], as may be the energy broadening of the SPP spectrum (which has been studied mainly in regard to the SPR sensitivity [18]).

4 k_{spp} can be determined from the dispersion relation of the structure.

medium if the layers are thin enough, whereas the lower frequency SPP mode (associated with the (ii)–(iii) interface) is strongly localized and thus only be able to couple to fluorophores very nearby.

We consider the specific structure where layer (1) is a quartz substrate, layer (2) a smooth continuous silver film of thickness d_{Ag}, and layer (3) a Si_3N_4 film of thickness d_{SiN}. The sample medium above the Si_3N_4 film containing the fluorophores will be taken to have the consistency of oil. The choice of Si_3N_4 is for fabrication reasons (high quality thin films can be easily fabricated using physical vapor deposition).

To model the structure we assume frequency-independent permittivities of 2.13, 2.3, and 4.15 for the quartz, oil, and Si_3N_4, respectively. The permittivity of the silver is described by a simple Drude model[5]: $\varepsilon(\omega) = \varepsilon_\infty - \omega_p^2[\omega(\omega + i\Gamma)]^{-1}$, with $\varepsilon_\infty = 5$, $\omega_p = 9$ eV, and $\Gamma = 0.02$ eV. This setup in general supports two bound SPP modes, one associated predominantly with each interface. We choose thicknesses $d_{Ag} = 10$ nm and $d_{SiN} = 15$ nm, as this assures that the mode associated with the quartz–silver interface is close to the cutoff in the sample medium. Decreasing the thickness of the dielectric layer results in the mode having a higher cut of frequency and becoming unbound (radiative in the sample medium) at the frequencies of interest (~500 nm). On the other hand increasing the thickness results in the mode becoming more strongly localized.

We proceed by calculating reflection coefficients for the structure. The P-polarization Fresnel coefficient for the four-layer system is given by

$$r_p^{(1234)} = \frac{r_p^{(12)} + r_p^{(234)} e^{2ik_{\perp 2} d_2}}{1 + r_p^{(234)} r_p^{(12)} e^{2ik_{\perp 2} d_2}}$$

where

$$r_p^{(234)} = \frac{r_p^{(23)} + r_p^{(34)} e^{2ik_{\perp 3} d_3}}{1 + r_p^{(23)} r_p^{(34)} e^{2ik_{\perp 3} d_3}} \text{ and } r_p^{(ij)} = \frac{\varepsilon_j k_{\perp,i} - \varepsilon_i k_{\perp,j}}{\varepsilon_j k_{\perp,i} + \varepsilon_i k_{\perp,j}}$$

where the ω and $k_{||}$ dependence of the reflection coefficients is implied. The S-polarization coefficient can be obtained by substituting $\varepsilon \leftrightarrow \mu = 1$. The absolute value of these (r_s and r_p) are plotted as a function of transverse wavevector and frequency in Figure 6.3. The two SPP modes are clearly visible in the P-polarization case, whereas for the S-polarization there are no bound modes apparent. In Figure 6.4 the P-polarization reflection coefficient is plotted for different thicknesses of the Si_3N_4 layer at wavelengths around ~500 nm, where it can be seen that if the Si_3N_4 layer is made thinner, the cutoff frequency increases (and the second SPP mode shifts to smaller in-plane wavevectors), whereas if it is made thicker, it moves away from the light line and becomes more strongly localized.

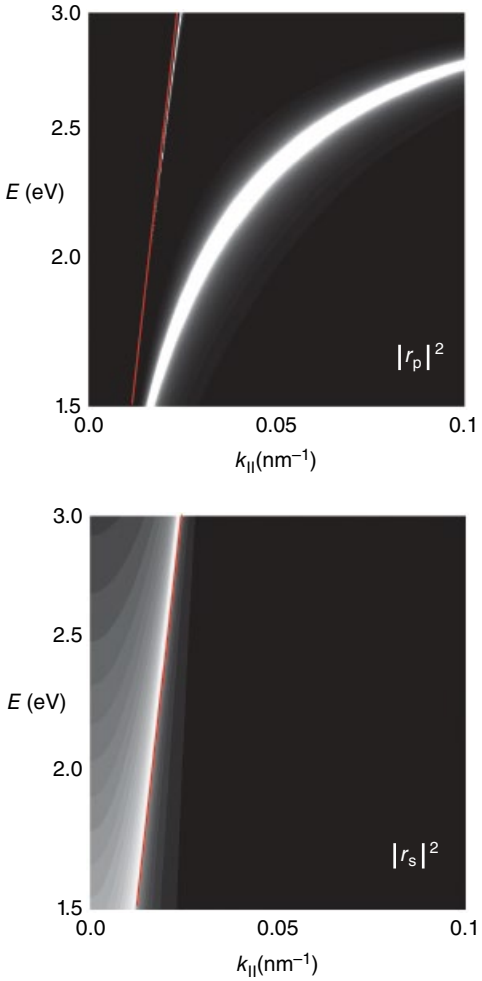

Figure 6.3 Absolute value of the P- and S-polarization reflection as a function of in-plan wavevector and frequency for the metal/dielectric structure discussed in text.

The dispersion relation can be explicitly calculated by writing the fields in each layer, imposing the boundary condition ($\Delta E_{||}, \Delta B_\perp = 0$) and solving a matrix constructed from the field amplitude coefficients as outlined in, for example, [23]. For the weakly localized mode, this is plotted in Figure 6.5a for the case when the Si_3N_4 layer is 0, 5, 8, 10, 12, and 15 nm thick. As can be seen the frequency at which the "bound" SPP becomes "unbound" (i.e., where the dispersion curve crosses the sample light line) decreases with increasing Si_3N_4 layer thickness. This is shown more clearly in Figure 6.5b where we plot the penetration depth into

5 For very thin films (<10 nm), a correction to the imaginary component of the permittivity [21] should be included.

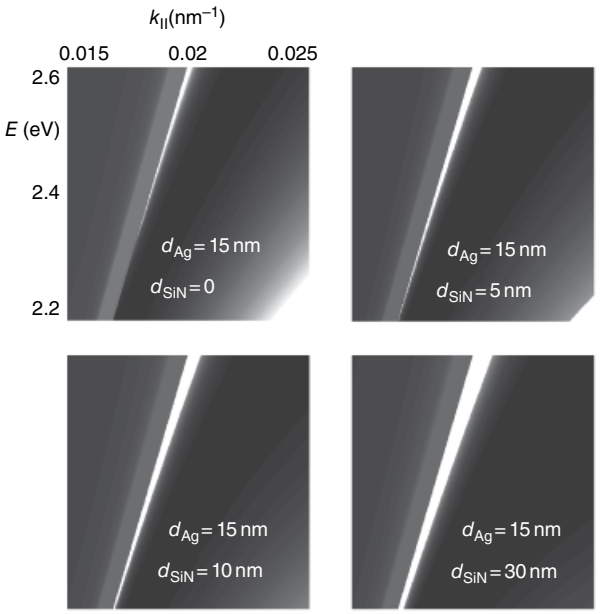

Figure 6.4 Absolute value of P-polarization reflection coefficient for different thickness of the Si_3N_4 dielectric coating layers, showing the weakly bound SPP in the vicinity of the cutoff.

the sample space on a linear (left) and logarithmic scale (right).

The power dissipated to this structure as a function of in-plane wavevector and frequency for a (isotropically averaged) dipole emitter at distances of 15 nm–5 μm from the Si_3N_4/sample interface is shown in Figure 6.6. It can be seen that energy will be transferred predominantly to the strongly localized SPP, the weakly localized SPP, and the leaky modes as the fluorophore is progressively brought away from the substrate.

For the fluorophores we will consider the dye Alexa488 which has a high quantum efficiency ($q \approx 0.9$) and an absorption/emission spectra presented by symbols in Figure 6.7. To simplify calculations we will use a fitted Gaussian distribution for these spectra shown by the solid lines in Figure 6.6 labeled $g_{ex}(\omega)$ and $g_{em}(\omega)$. We then set $f(\omega) = g_{em}(\omega)$ and $\sigma(\omega) = \varepsilon g_{ex}(\omega)$, where ε is the extinction coefficient. The SPP spectrum excited by an (isotropically averaged) fluorophore concentration at a distance z from the sample can be extracted from Eqs. 6.6, 6.7, and 6.11 as:

$$f_{spp}(\omega,z) \approx \sum_{i=1,2} \int f(\omega') L\left[\omega', \Gamma_{spp}^{(i)}(\omega'), \omega\right] \gamma_{spp}^{(i)}(\omega', z) d\omega' \tag{6.15}$$

where

$$\gamma_{spp}^{(i)}(\omega,z) = \Im \int_{k_{spp}^{r(i)} - k_{spp}^{r(i)}}^{k_{spp}^{r(i)} + k_{spp}^{r(i)}} dk_{||} \frac{k_{||}}{k_s^3 k_{\perp,s}} \left[k_s^2 (r_s + r_p)\right] e^{2ik_{\perp,s}z}$$

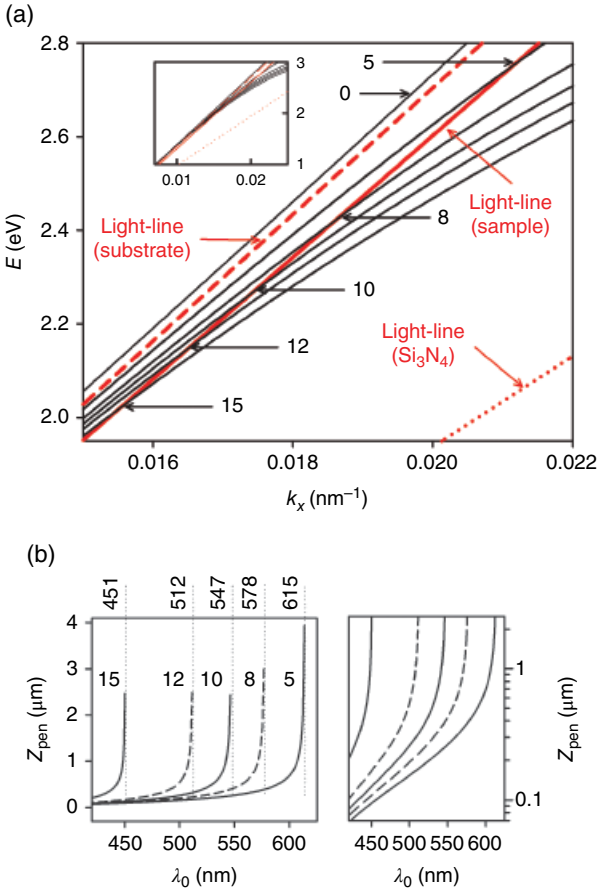

Figure 6.5 (a) Dispersion relation of the weakly bound SPP mode for the structure discussed in the text with different thicknesses of the Si_3N_4 layer (labeled on graph in nm). As can be seen the curve intersects the sample light line at higher frequencies when the layer is made thinner (inset: same plot over a larger energy/in-plane-wavevector range). (b) Penetration depth into the sample space for the same five Si_3N_4 thicknesses as a function of free-space wavelength ($\lambda_0 = \omega/c$) plotted on linear (*left*) and logarithmic (*right*) scales. Cutoff wavelength is labeled on the top horizontal axis.

$k_{spp}^{(i)}$ are the complex wavevectors of the two SPP modes ($i = 1,2$) and $\Gamma_{spp}^{(i)}(\omega)$ their respective decay rates given by Eq. 6.10. Equation 6.15 is plotted for different z in Figures 6.8 and 6.9. In each case the light (dark) gray lines represent the free-space emission (absorption) spectra of the fluorophores, and in Figure 6.7 the dashed dark gray line is the absorption spectrum plotted on a linear scale (right vertical axis) to more clearly illustrate the position of the absorption peak. As can be seen $f_{spp}(\omega, z)$ shows significantly more broadening near the sample (Figure 6.8) as may be expected; however the broadening is also significant for distances on the order of the wavelength (Figure 6.9a and b) - note logarithmic scale. There is also a clear shift to shorter wavelengths (Figure 6.9c) at larger distances, which can be

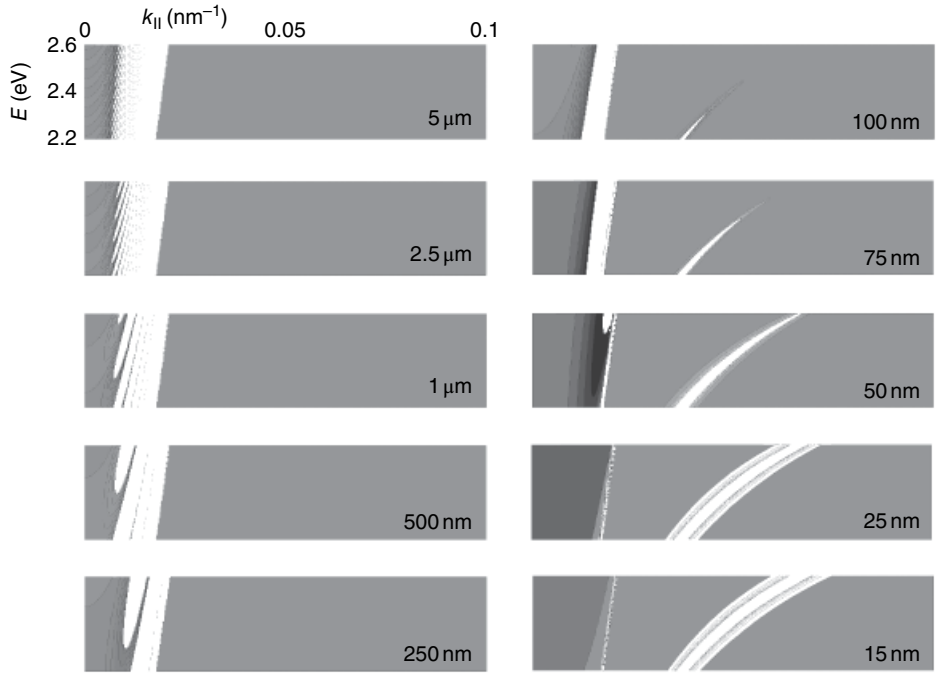

Figure 6.6 Dissipated power in the structure as a function of in-plane wavevector and frequency (calculated from Eq. 6.5) for a dipole-like emitter at different distances from the substrate. The color scale is linear and the same in each plot, with white corresponding to values $dp / dk_{||} \geq 0.5$. The transition from the dominant coupling being to the strongly bound SPP, then to the weakly bound SPP, and then to the dissipation via radiative losses can be seen as the distance (z) is increased.

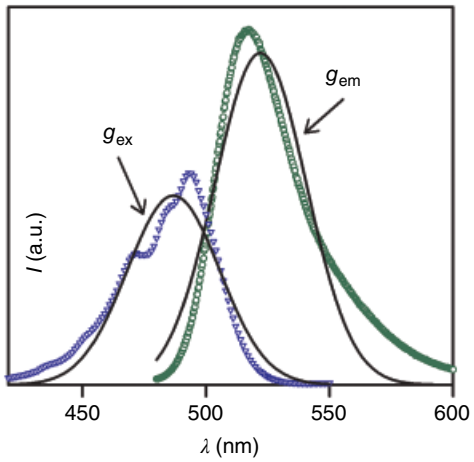

Figure 6.7 The absorption and emission spectra of Alexa488 and the corresponding normal curves ($g_{ab}(\omega)$ and $g_{em}(\omega)$) used for the calculations.

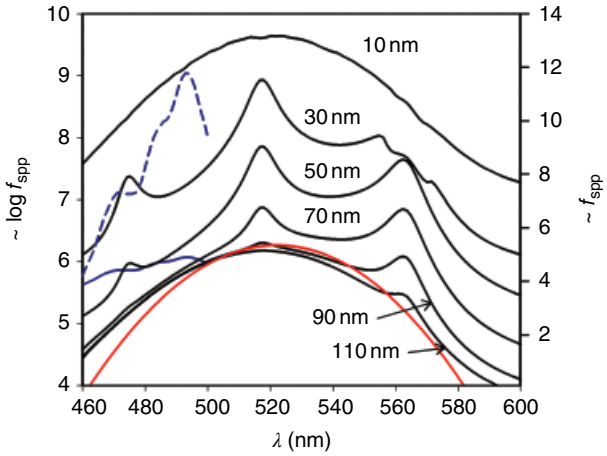

Figure 6.8 The coupling spectrum to SPPs as described in the function $f_{spp}(\omega)$ (see text) for fluorophores at different distances close to the substrate. The solid light gray line is the free-space emission spectrum of the dye used for calculations. Solid and dashed dark gray lines are the actual free-space absorption spectrum (plotted on linear and logarithmic vertical axes respectively). Dashed line should be read from right vertical (linear) axis, whereas all solid lines should be read from the left (log) axis.

explained by the shift in the SPP frequency [11]. The narrowing of the peak that is visible in Figure 6.9c is a consequence of the frequemcy dependence of the SPP lifetime.[6]

The absorption spectra of fluorophores are also modified in a distance-dependent manner (due to the increased total decay rate). This will be described by the second integral in Eq. 6.14 and is comparatively

6 τ_{spp}^{-1} is governed largely by the imaginary component of the metal permittivity, which decreases with increasing frequency over this range.

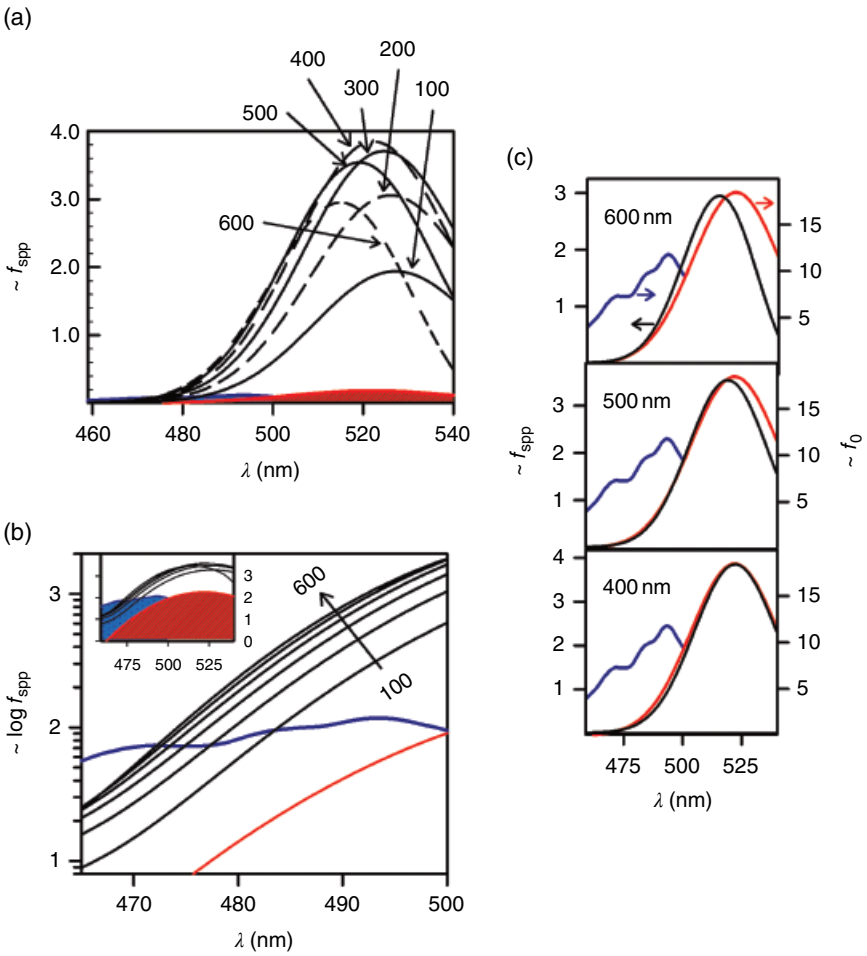

Figure 6.9 Same as Figure 6.8 but for larger distances from the substrate. (Numbers on plots are the distances in nm.) (a) On linear axis, (b) on log axis showing the short wavelength region overlap with the absorption spectrum. (c) Same as (a) but on separate plots and scales so that peak coincides with free-space emission spectrum used for calculation [red line]. (*See insert for color representation of this figure.*)

straightforward to calculate. Since the total decay rate increases (in a monotonous fashion) with deceasing distance, so will the width of the fluorophore absorption spectrum. The broadening will be larger for larger frequencies closer to the substrate where the total decay rate is larger. This causes more significant broadening at higher frequencies, resulting in a reduced absorption peak at these frequencies, and an effective redshift in the total absorption spectrum. As a result the overlap between the excited SPP spectra and the fluorophore absorption spectrum will become larger closer to the substrate.

The total increased excitation rate for the structure as a function of distance will be governed by the "spectral overlap" and given by Eq. 6.14. For illustrative purposes we will take the excitation field to be unpolarized narrow bandwidth 488 nm wide-field coherent illumination with a power of $I = 20\text{mW}$. Using all the parameters listed previously and Eqs. 6.6, 6.7, and 6.9–6.14, the distance-dependent excitation rate increase $\hat{\gamma}_{ex} = \gamma_{ex}/\gamma_{ex}^{(0)}$ (where $\gamma_{ex}^{(0)}$ is obtained from Eq. 6.9) is calculated and plotted in Figure 6.10a as a function of distance from the substrate. The total expected fluorescence intensity enhancement as a function of distance and wavelength is evaluated using Eq. 6.4 (where $\hat{\gamma}_r$ is given by Eq. 6.8). This is plotted for different wavelength ratios in Figure 6.10b. It can be seen that a relative enhancement occurs for short wavelength and the total enhancement peaks between 50 and 100 nm. This may be interpreted by noting that coupling to the strongly localized SPP mode ceases to be dominant at this distance (see also Figure 6.6). Below about 100 nm there is a monotonic dependence of the relative enhancement with respect to distance.

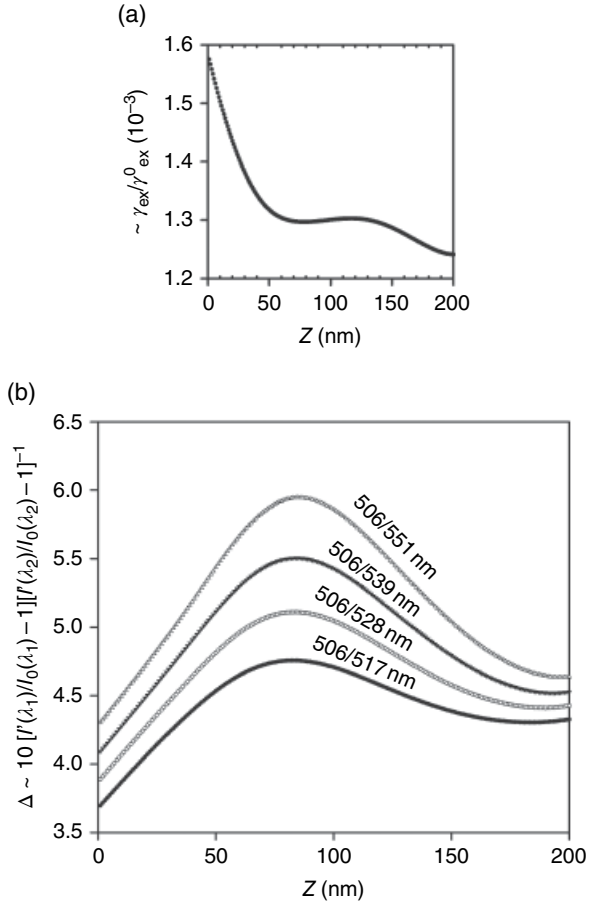

Figure 6.10 (a) Fractional increase in excitation rate as a function of distance from the substrate (see text). (b) Modified emission spectrum plotted as the ratio of emission intensities at different wavelengths.

6.4 Summary

In summary, we have shown how an additional "type" of metal-enhanced surface fluorescence can be realized near certain metal/dielectric thin films that support weakly localized SPP modes. In particular it was shown that a type of FRET effect can be realized where fluorophores of the same type over a relatively large region above the sample (several hundred nanometers) can contribute to increasing the excitation rate of those closer. The effect is amplified by the finite (energy) width of the SPPs generated and the increased width of the absorption closer to the substrate. As with MEF the spectral emission is dependent on the radiative transition (for not too strong coupling to the scattered SPPs) [24].

The effective coupling of (dipole-like) emitters to resonant modes near the cutoff has also recently been proposed as an efficient means of launching SPPs [25], and there are likely to be more applications that will be revealed by studying the collective coupling of emitters to resonant structures in the vicinity of their cutoff frequencies. One particular case not considered here is the possibility of using higher fluorophore concentrations and applied excitation fields to achieve a significant stimulated emission contribution from fluorophores at certain distances from the substrate.

References

1 K Aslan *et al.*, *Curr Opin Biotechnol 16*:55 (**2005**).
2 JR Lakowicz *et al.*, *Biochem Biophys Res Commun 307*:435 (**2003**).
3 WL Barnes, *J Mod Opt*, *45*:661 (**1998**).
4 A Sommerfeld, *Ann Phys 28*:665 (**1909**).
5 RR Chance *et al.*, *Adv Chem Phys*, *37*:1 (**1978**).
6 MS Yeung & TK Gustafson, *Phys Rev A 54*:**1996** (1996).
7 (a) I De Leon & P. Berini, *Nat Photonics 4*:382 (**2010**). (b) M Gather *et al.*, *Nat Photonics 4*:457 (**2010**). (c) I De Leon & P Berini, *Phys Rev B 78*:161401(R) (**2008**).
8 MI Stockman, *Phys Rev Lett 106*:156802 (**2011**).
9 MA Noginov *et al.*, *Phys Rev Lett 101*:226806 (**2008**).
10 P Andrew & WL Barnes, *Science 306*:1002 (**2004**).
11 JB Pendry, *Phys Rev Lett 85*:3966 (**2000**).
12 (a) N Fang *et al.*, *Science 308*:534 (**2005**). (b) DOS Melville & RJ Blaikie, *Opt Exp 13*:2127 (**2005**).
13 SA Ramakrishna & JB Pendry, *Phys Rev B 67*:201101(R) (**2003**).
14 S Xiao *et al.*, *Nature 466*:735 (**2010**).
15 (a) SA Ramakrishna *et al.*, *J Mod Opt 50*:1419 (**2003**). (b) PA Belov & Y Hao, *Phys Rev B 73*:113110 (**2006**). (c) K Elsayad & KG Heinze, *Phys Rev A 81*:053840 (**2010**).
16 X Ni *et al.*, *Appl Phys B 103*:553 (**2011**).
17 (a) W Rhodes, *Chem Phys Lett 11*:179 (**1971**). (b) W Rhodes *et al.*, *Proc Nat Acad Sci USA 63*:31 (**1969**).
18 H Raether, *Surface Plasmons on Smooth and Rough Surfaces and on Gratings*, Berlin: Springer-Verlag (**1986**).
19 O Kiwai *et al.*, *Opt Lett*, *36*:2530 (**2011**).
20 D Sarid, *Phys Rev Lett 47*:1927 (**1981**).
21 (a) L Wendler & R Haupt, *J Appl Phys 59*:3289 (**1986**). (b) MN Zervas, *Opt Lett 16*:720 (**1991**).
22 (a) R Adato & J Guo, Opt Exp *15*:5008 (**2007**). (b) CG Durfee *et al.*, *J Appl Phys 103*:113106 (**2008**).
23 JA Dionne *et al.*, *Opt Express 16*:19001 (**2008**).
24 (a) Y Zhang *et al.*, *J Phys Chem C 113*:12095 (**2009**). (b) EC Le Ru & PG Etchegoin, *J Phys Chem C, 111*:16076 (**2007**).
25 A. Alù & N. Engheta, *Phys Rev Lett 103*:043902 (**2009**).

7

Metal-Enhanced Fluorescence in Biosensing Applications

Ruoyun Lin[1], Chenxi Li[2], Yang Chen[3], Feng Liu[4], and Na Li[4]

[1] *Beijing National Laboratory for Molecular Sciences (BNLMS), Peking University, Beijing, China*
[2] *Key Laboratory of Bioorganic Chemistry and Molecular Engineering of Ministry of Education, Peking University, Beijing, China*
[3] *Institute of Analytical Chemistry, Peking University, Beijing, China*
[4] *College of Chemistry and Molecular Engineering, Peking University, Beijing, China*

7.1 Introduction

Metal-enhanced fluorescence (MEF) has made a profound impact on biosensor developments, since the pioneer work of Lakowicz and Geddes [1–4]. Through the near-field interaction between the metallic surface and excited fluorophores in close proximity, the emission efficiency and the photostability of fluorophores can be substantially modified for favorable fluorescence biosensing applications with improved sensitivity and robustness of the assay platform [2, 5, 6]. With proper experimental design, weak signals that cannot be measured in the free-space condition can even be captured and quantitatively measured with the metal surface enhancement effect.

Despite the different underlying mechanisms for interpreting the MEF effects, it is generally agreed that factors that can alter optical properties of the metallic nanoparticles (NPs) or nanostructures, including size, shape, and surface morphology, will have strong influence on the performance of the enhancement effects. In addition, spectral properties of the fluorophores, including the emission wavelength, the lifetime of the excited state, and the quantum yield, as well as the distance between the fluorophore and the metallic substrate, will also have influence on the enhancement effect [2, 3, 5, 7].Continuous efforts have been made to evaluate the diversified metallic nanomaterials with different sizes, compositions, and morphologies to achieve the optimal enhancement effects; on the other hand, experimental designs toward distance control have been explored in order to maximize the signal enhancement effects for sensitive sensing method development.

This chapter is intended to provide a brief overview on MEF applications in the biosensing area in recent years. The enhancing substrates, the approaches to control the metal–fluorophore distance, and challenges in quantification of fluorescence enhancement have been addressed.

7.2 Substrates

A variety of metallic materials have been evaluated for their fluorescence enhancement performance for analytical applications. Noble metal nanomaterials, such as gold and silver, are most frequently adopted as the enhancing substrates, because the spectral signature of their plamon resonance has long been studied and recognized for surface-enhanced spectroscopies [6–13]. In this regard, this chapter concerns the MEF biosensing applications involving noble metal nanomaterials (primarily silver and gold), although other metals may impart a new functionality to the substrate [13, 14]. On the other hand, the size and morphology of the metallic substrate, as they influence the surface electromagnetic field and plasmon resonance spectra of the metallic NPs/structures, are also of great importance on fluorescence enhancement. Therefore, a great deal of effort has been put on improving fluorescence enhancement performance of metallic materials through fabricating novel metallic nanocomposites or nanostructures.

Silver nanomaterials are the most favorable class of widely applied substrates for metal-enhanced fluorescence. According to the radiating plasmon model, the plasmon absorption of silver nanostructures is located at short wavelength region of the visible light (~400 nm), permitting applications of a wide range of fluorophores without significant fluorescence quenching;

Surface Plasmon Enhanced, Coupled and Controlled Fluorescence, First Edition. Edited by Chris D. Geddes.
© 2017 John Wiley & Sons, Inc. Published 2017 by John Wiley & Sons, Inc.

the scattering component of the extinction spectrum is located at around 500 nm and the longer wavelength, overlapping with the emission band of most visible-light-emitting fluorophores to facilitate radiating plasmon enhancement [6]. Together with the easy silver-thiol chemistry, diversified sizes and morphologies of silver nanostructures offer convenience in experimental operations and a variety of options in experimental designs.

Silver island films (SIFs) are one of the earliest nanostructures studied [15, 16]. In 2006, Lakowicz's group for the first time carried out a single-molecule analysis of cyanine (Cy5)-labeled DNA tethered to SIFs, and the study revealed that fluorophores in close proximity to SIFs emitted photons 10 times more than free fluorophores on the control glass substrate (Figure 7.1) [17]. It was also revealed that fluorescence lifetimes of molecules in the vicinity of the SIF surface were modified substantially, resulting in enhanced photostability and accelerated emission rate of fluorophores. A fluoroimmunoassay was performed with metal mirror-supported SIFs, and up to 50-fold enhancement was obtained [18]. SIFs have also been used to evaluate the enhancement effects on the intrinsic fluorescence of biomolecules, such as DNA [19] and proteins [20]. With SIFs for fluorescence enhancement, the optimal detection limit for avidin was found to be <2 ng/cm^2, indicating the possibility of a label-free protein sensing of tryptophan residues in protein [20]. In 2009, Geddes's group reported a sonication-accelerated MEF-based bioassay to study the protein–ligand interaction, using biotin and fluorescein isothiocyanate (FITC)-labeled avidin as the model. The fluorescent signal obtained with SIFs was about 6-fold larger than that with the control glass substrate [21].

SIF-enhanced fluorescence-based DNA and RNA detection methods were also developed. Geddes and coworkers developed an MEF-based RNA and DNA sensing platform using SIFs as the substrate, TAMRA-labeled oligonucleotide as the fluorescent sensing probe, and thiolated oligonucleotide as the capture

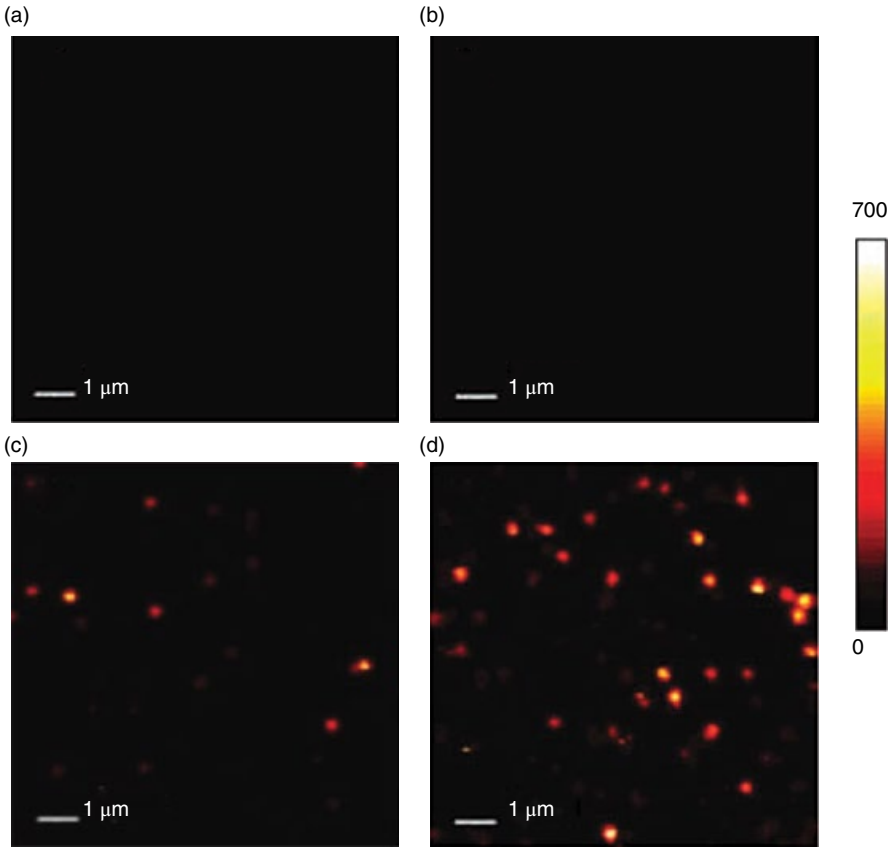

Figure 7.1 Typical 10 μm× 10 μm fluorescence images. The fluorescence intensity is displayed in a colorized scale, ranging from dark to light. (a) Cy5-labeled dsDNA molecules spin dispersed on a glass coverslip, (b) silver island film (SIF) deposited on a glass coverslip, (c) Cy5-labeled dsDNA-SH molecules tethered to SIF deposited on a glass coverslip with an incubation concentration of 0.5 nM, AND (d) Cy5-labeled dsDNA-SH molecules tethered to SIF deposited on a glass coverslip with incubation concentration of 1.5 nM. Copyright from 2006 the American Chemical Society.

probe [22, 23]. A detection limit of 25 fM was achieved for a 484-mer RNA sequence [22]. Baillie and Geddes *et al*. reported a rapid and accurate assay of toxins A and B gene sequences from the human pathogen *Clostridium difficile* using SIFs as the enhancing substrate and fluorophore-labeled DNA as the capture probe. With the combination of microwave acceleration and metal-enhanced fluorescence, the direct pathogen detection can be carried out in unprocessed human feces with a detection limit of 10 bacteria within 40 s [24]. Employing fluorophores of different colors, the detection of multiple DNA sequences within one sample well has also been achieved [25, 26]. A label-free aptasensor for highly sensitive detection of adenosine triphosphate (ATP) and thrombin based on SIF-enhanced fluorescence was reported [27]. Despite the favorable enhancement properties of SIFs, this material still suffers from the particle size and spatial heterogeneity, which often results in undesirable nonuniformity of fluorescence enhancement on different spots of the metallic surface [17].

Core–shell Ag@SiO_2 NPs are one of the most frequently applied nanomaterials for fluorescence enhancement because of their easiness in size control and surface functionalization. In 2007, Geddes's group reported the development of fluorescent core–shell Ag@SiO_2 nanocomposites for two platform technologies: metal-enhanced fluorescence and single NP sensing. This silica over silver nanocomposite can incorporate any fluorophore into the silica shell by either simple doping or covalent attachment. This work demonstrated up to 20-fold (with Rh800) enhancement of the fluorescent signal and a potentially 200-fold increase in particle detectability [28]. Using the core–shell Ag@SiO_2 NPs, Boudreau's group reported an MEF-based biosensor for rapid identification of the *SRY* gene from the unamplified human genomic DNA [29]. Huang's group reported a promising MEF and dual-aptamer-based strategy to achieve solution prion protein and intracellular protein imaging [30]. Assays for ATP [31], metal ions [32], small-molecule drugs [32], the H5N1 virus [33], and the enzyme activity [34] have also been reported. In addition to silica-coated silver NPs (AgNPs), polymer-coated AgNPs were also reported to be capable of enhancing the fluorescence signal [35].

Silver nanoparticles are a class of widely applied material because of the easiness in synthesis and surface functionalization. Ozaki and coworkers reported a protocol for detection of protein–protein and protein–ligand interactions via surface-enhanced Raman scattering (SERS) and MEF properties of Ag colloids. With occurrence of the protein–ligand interaction on the functionalized glass slide, the complex was stained by deposition of silver colloids to provide remarkable Raman and fluorescence signal enhancement. Results from this study revealed that significant enhancement of Raman scattering occurred at spot where fluorophores were in close contact with the metallic surface, and MEF was observed at longer distance (~10 nm) where fluorescence quenching was minimal [36].

Li's group developed an MEF sensing platform based on the molecule beacon design, and demonstrated the feasibility of the design with quantitative detection of mercuric ions [37]. Silver NPs were functionalized with the thymine-rich molecular beacon via silver-thiol chemistry. The fluorescence signal of the beacon was quenched, because the fluorophore (fluorescein) was brought in the quenching distance by the closed hairpin conformation. The presence of mercuric ions could mediate the formation of the T–Hg^{2+}–T structure between the hairpin and the noncomplementary strand; thus, the hairpin was opened and the fluorescence signal was recovered and enhanced. The enhancement effect was found to be dependent on the size of the AgNPs with the enhancement factor of 3-fold for 36-nm AgNPs, and 6–8-fold for both 89-nm and 199-nm AgNPs. A 5-fold sensitivity improvement was achieved for mercuric ion detection (Figure 7.2). Based on the Ag NP substrate, Li's group also demonstrated a dual amplification strategy for DNA detection by combining the bio-barcode amplification and the metal-enhanced fluorescence modality [38]. In this design, magnetic NPs seeded with AgNPs were modified with the capture DNA, and AgNPs for enhancement purpose were modified with the binding ssDNA and the fluorescently labeled barcode dsDNA. Upon the introduction of the target DNA, a sandwich structure formed by the hybridization reaction, which was readily measured with simple magnetic separation without the need for a further step to liberate barcode DNAs, endowing the method with simplicity and high sensitivity with a 1 pM detection limit (Figure 7.3).

Xu's group took efforts on cell imaging based on AgNPs-enhanced fluorescence [39–41]. They reported a decahedral AgNPs-enhanced fluorescence resonance energy transfer (FRET) sensor for sensitive and specific leukemia cell imaging. Silver NPs were functionalized with the fluorescent, thiolated target cell aptamer (Sgc8-FITC) and a quencher-carrying DNA strand hybridized with the immobilized Sgc8 aptamer strand to form a dim Ag_{10}NP-based FRET sensor. The presence of leukemia cell bound with the fluorescent aptamer to release the quencher DNA strand, such that leukemia cells were fluorescently labeled on the Ag NP surface [40]. The authors also reported fluorescently labeled aptamer functionalized

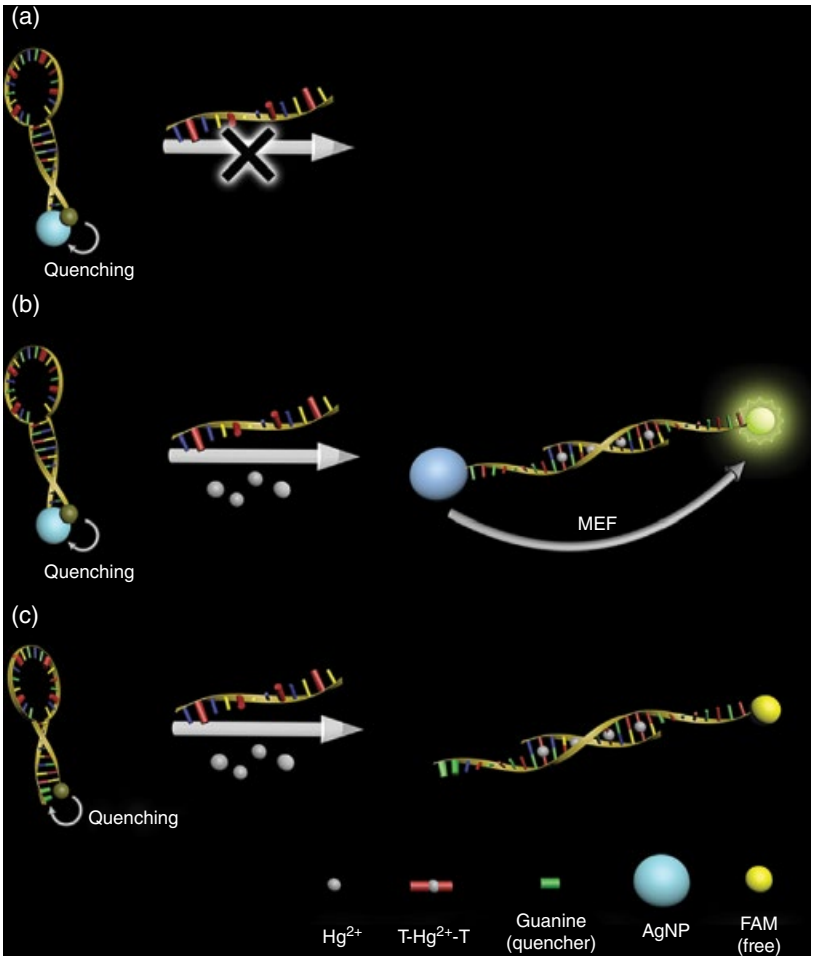

Figure 7.2 A schematic illustration of the principle of the quantitative Hg^{2+} detection method based on MEF and molecule beacon design. (a) The beacon remained the closed hairpin conformation with the presence of T-mismatch strand and absence of Hg^{2+}, thus the fluorescence of the FAM was quenched by silver NP. (b) The hairpin beacon was opened in the presence of both T-mismatch strand and Hg^{2+}, and the fluorescence of the FAM was enhanced by silver NP. (c) The silver NP attached to the beacon was displaced by guanine, which quenched the fluorescence of the FAM when the hairpin was closed. In the presence of both T-mismatch strand and Hg^{2+}, the hairpin conformation was opened and the fluorescence of the FAM recovered, but was weaker than that with silver NP enhancement. Copyright from 2014 Elsevier.

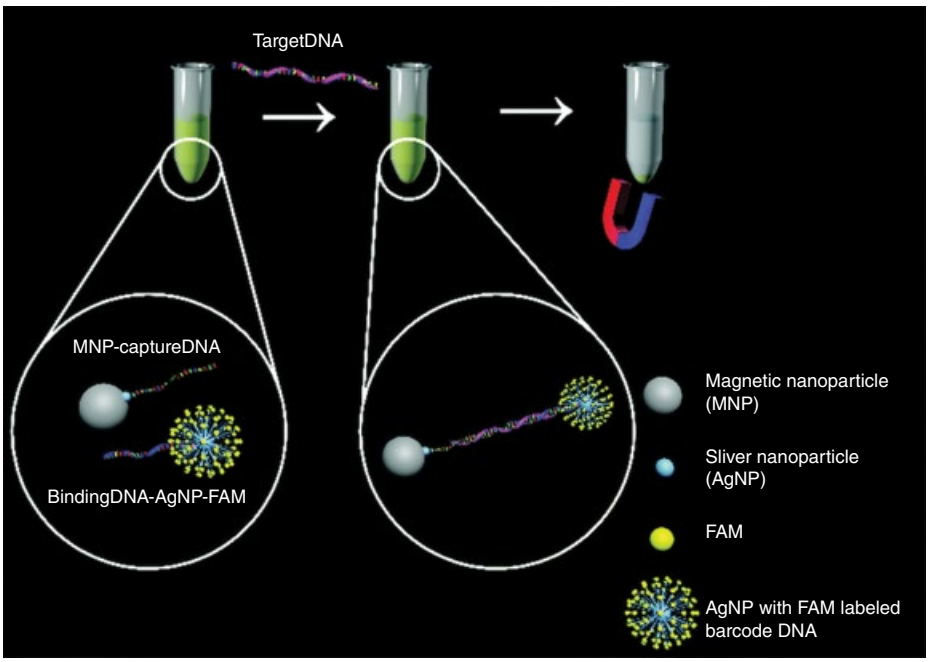

Figure 7.3 Schematic illustration of the assay rationale of the dual amplification strategy for DNA detection. Copyright from 2014 the Royal Society of Chemistry. (*See insert for color representation of this figure.*)

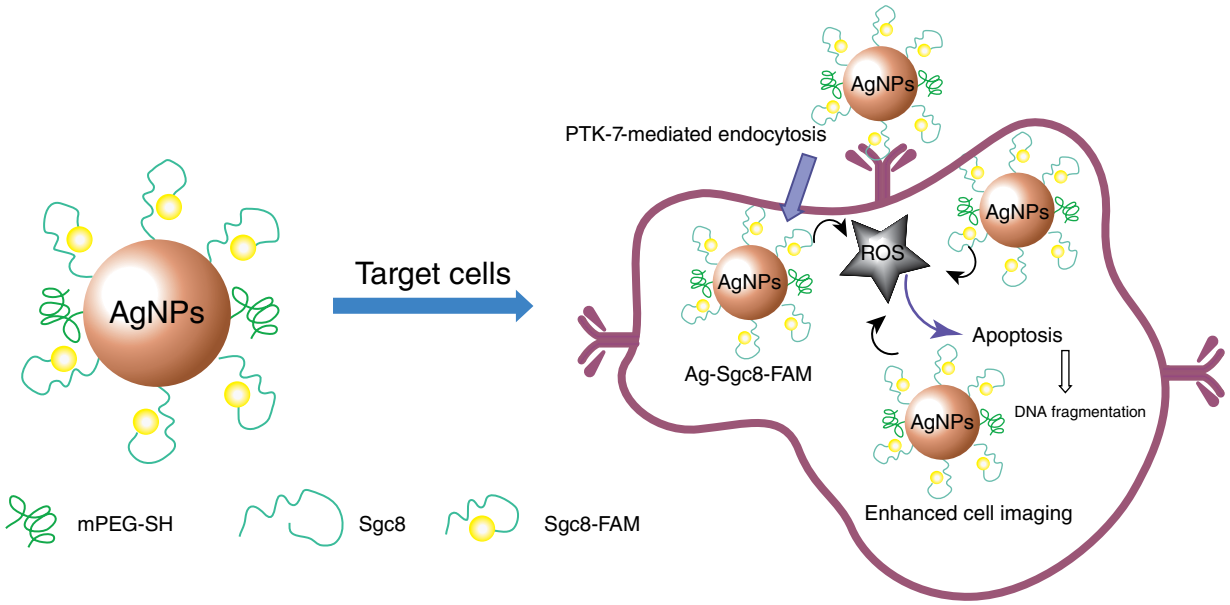

Figure 7.4 Aptamer–silver conjugate induced apoptosis for specific cancer therapy and fluorescence-enhanced cell imaging. Copyright from 2015 the American Chemical Society.

AgNPs as theragnostic agents for specific cancer cell therapy and fluorescence-enhanced cell imaging (Figure 7.4) [41].

Metal-enhanced fluorescence studies of AgNPs with different shapes have been explored. Geddes's group first reported the fluorescence enhancement performance of silver nanorods (Ag NRs) and triangular silver nanoplates deposited planar film [42, 43]. Fifty-fold or even greater enhancement was obtained reproducibly for indocyanine green with the high loading density of Ag NRs on the glass substrate [43], and 16-fold enhancement was observed for protein-immobilized indocyanine green with the silver triangle-loaded glass substrate [42]. Silver nanocubes were proved to be a potential enhancing substrate for single-molecule fluorescence (Figure 7.5). The emission of individual polymer poly(3-hexylthiophene) (P3HT) was enhanced by 7-fold with 150-nm silver nanocubes deposited on the glass substrate [44]. Unalan and Aslan *et al*. demonstrated both theoretically and experimentally the potential of high aspect ratio silver nanowires on fluorescence enhancement. Fluorescence enhancement factors larger than 14 were observed for FITC, and the fluorescence lifetime of the fluorophore was significantly reduced, which greatly enhanced the photostability of fluorophore [45]. Bozio and coworkers developed a sensitive chip sensor of ochratoxin A (OTA) in food and drinks based on silver film over nanosphere (AgFON)-enhanced fluorescence. The AgFON was fabricated through Ag deposition on the polystyrene nanosphere assembly, and this chip sensor was found to be notably superior to commercial chip sensor for quantitative OTA onsite detection with the detection limit of 3.3 ng/kg [46].

Silver aggregates were considered as a promising MEF substrate, because the "hotspots" generated from close coupling of AgNPs can significantly improve the fluorescence efficiency [47–49]. Xu and coworkers demonstrated that highly sensitive protein detection could be achieved with enhanced fluorescence by silver aggregates [50]. Pal and coworkers reported 250-fold fluorescence enhancement of the in situ produced quinone by Ag (0) aggregates in situ generated with the phenol-to-quinone conversion process [51].

The fluorescence enhancement feature of gold nanomaterials has been commonly recognized in recent years, which brought a rise in the number of biosensing applications based on the gold-enhanced fluorescence [7]. The longitudinal surface plasmon resonance wavelength of gold NRs (Au NRs) can be tuned via the aspect ratio, and AuNRs with larger aspect ratio display a dominant scattering component over an absorption component above 600 nm, which is advantageous for fluorescence enhancement of fluorophores with 600 nm and longer emission wavelengths [52, 53]. Wang's group reported fluorescence enhancement effects of AuNRs coated with the mesostructured silica thin film [52]. Lakowicz's group reported the phenomenon of plasmon-enhanced fluorescence with single fluorophores controllably linked

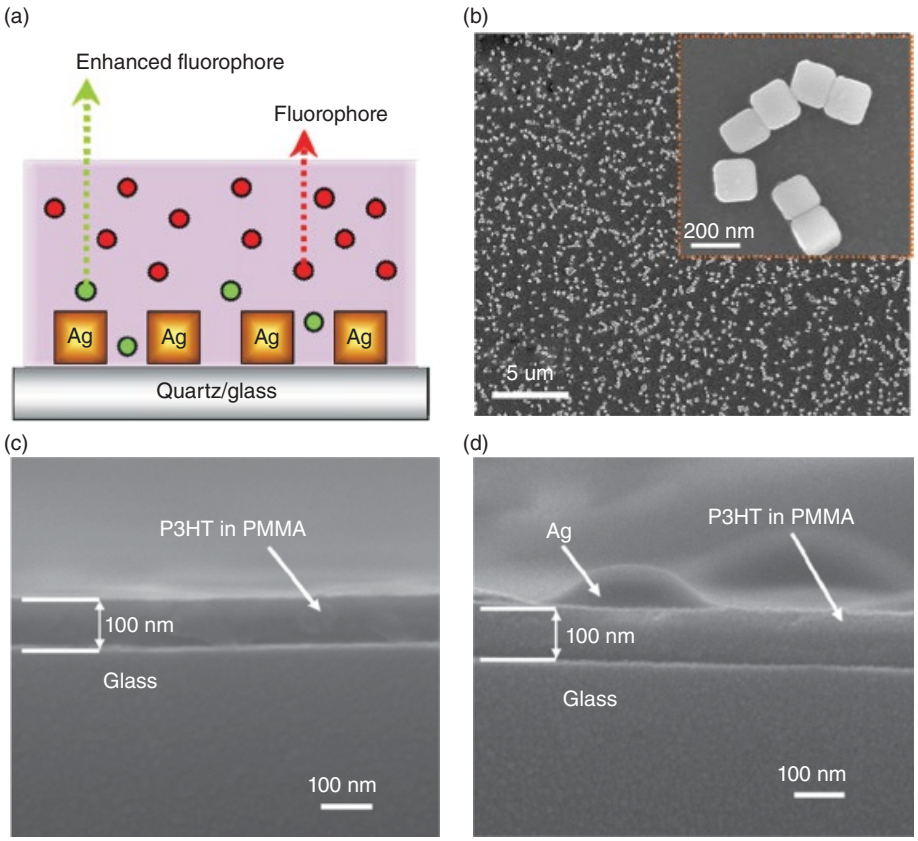

Figure 7.5 (a) Scheme of metal-enhanced fluorescence with silver nanocubes, (b) scanning electron microscopy (SEM) image of synthesized silver nanocubes, (c) cross-sectional SEM image of poly(3-hexylthiophene) P3HT in poly(methyl methacrylate (PMMA) on the glass substrate, and (d) cross-sectional SEM image of P3HT in PMMA on the silver nanocube substrate. Copyright from 2014 Elsevier.

to the ends of AuNRs. The strong coupling between localized surface plasmon of AuNRs and the fluorophore led to a 40-fold fluorescence enhancement and a decrease in fluorescence lifetime from 2.51 to 0.33 ns, demonstrating the great potential of AuNRs in MEF-based single-fluorophore imaging [53]. Wacogne and coworkers studied the MEF performance of the gold/silica thin film to amplify the fluorescence signal without a complex nanostructuration of the surface. Their work revealed that in addition to the distance between the fluorophore and the substrate surface, surface periodicity and surface roughness of the gold film also affected the enhancement of fluorescence [54]. Mooney and coworkers proposed a bacterial adhesion quantification method based on gold film-enhanced intrinsic bacterial fluorescence. A planar 35-nm-thick gold surface prepared by a standard electron beam lithographic technique was used as the basic substrate. Because of the distance-dependent feature of MEF, only the intrinsic fluorophore of bacteria close to the substrate surface could be enhanced. This technique provided a new way to acquire precise information on the three-dimensional (3D) distribution of bacteria and to monitor individual bacterial adhesion [55]. Lee's group developed a nanoporous gold leaf (NPGL)-enhanced fluorescence platform for the rapid and sensitive virus detection. The hybrid structure of quantum dots (QDs) and NPGLs was prepared by dealloying bimetallic film, with which the surface morphology and roughness were fairly controlled. The virus assay presented a detection limit (50 PFU/mL) for the influenza A virus isolated from a clinical sample, which was two orders of magnitude more sensitive than a commercially available rapid influenza diagnostic test [56]. Chen and coworkers studied the fluorescence enhancement of aluminum phthalocyanines (AlPcS), a photosensitizer for photodynamic therapy of cancers, by gold nanocubes. Gold nanocubes were found to produce better enhancement of the fluorescence signal than AuNRs with the enhancement factor of 150 in water and 300 in tumor cell imaging, respectively, while AuNRs only produced 2–6-fold enhancement for AlPcS, demonstrating that gold nanocubes were a type of extremely promising fluorescence enhancement material for biological researches. The higher enhancement in tumor cell imaging compared with enhancement in solution was attributed to the fact

that positively charged AlPcS–gold nanocube conjugates were more apt to be taken up by cells than negatively charged AlPcS molecules [57]. Chou and coworkers demonstrated a 3D plasmonic nano-antenna dot array as the fluorescence-enhancing substrate for immunoassay. The structure of the nano-antenna, named "disk-coupled dots-on-pillar antenna-array" (D2PA), is an array of dense 3D-resonant cavity nano-antennas with dense plasmonic nanodots inside and the nanogaps that couple the metallic components (Figure 7.6). The 3D nano-antennas greatly increased the efficiency in receiving and radiating light; the metallic nanodots and the nanogaps further "focused" the light to small regions to increase the local electric field. The high density of the nano-antennas increased the average enhancement and improved the uniformity of the substrate. With D2PA, the fluorescent signal of the immunoassay for Protein A and human immunoglobulin G (IgG) (scheme of the immunoassay, Figure 7.6b) was enhanced by over 7400-fold, and the detection limit was improved from 0.9 nM to 300 aM, compared with the flat glass plate control [58].

The hybrid metallic materials were studied in efforts to explore the MEF potential of rationally designed, well-studied SERS substrates and novel nanomaterials for biosensing purpose. Wu's group designed noble hybrid magnetic NP/nanogold clusters (HMNCs) (Figure 7.7) and demonstrated the potential of HMNCs in specific DNA sequence detection [59]. The HMNCs were fabricated by covalently linking 20-nm gold NPs (AuNPs) to the Fe_3O_4 NP core, and fluorophores (FITC) was attached to the gold surface via hybridization reaction. The local electric field intensity was considerably higher than the single AuNP due to the coupling effect of satellite AuNPs in HMNC according to the finite-difference time-domain (FDTD) simulation. Furthermore, using magnetic Fe_3O_4 NPs as the core of the HMNCs, the "hotspots" region was confined at the junction between satellite AuNPs; while in the case of AuNP core, the "hotspots" region displayed at both the core–satellite and the satellite–satellite junctions. According to the FDTD simulation, more "hotspots" dilute the entire local electric field intensity enhancement. By contrast, less "hotspots" in the case of HMNCs led to greater local electric field enhancement, which consequently produced larger fluorescence enhancement. The overall enhanced electric field intensity of the HMNCs resulted in great

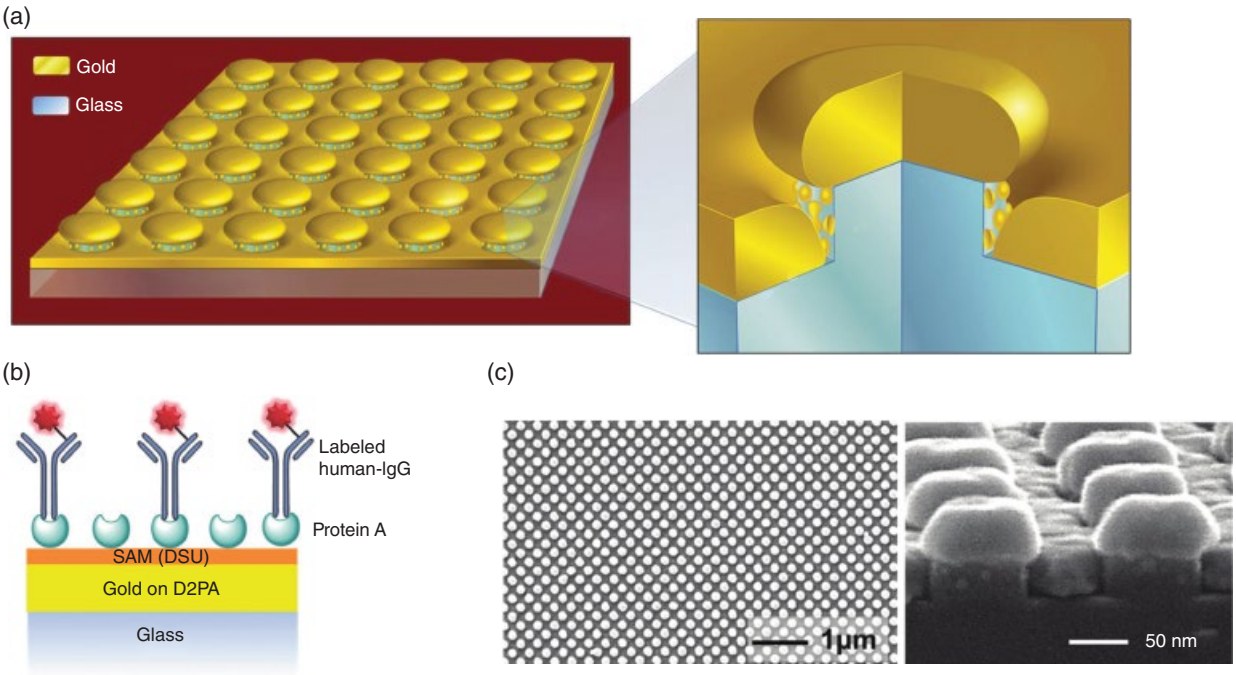

Figure 7.6 Disk-coupled dots-on-pillar antenna-array (D2PA) plate and immunoassay. (a) Schematic (overview and cross section) of D2PA plate without an immunoassay. D2PA has an array of dense 3D-resonant cavity nano-antennas (formed by the gold disks on top of periodic nonmetallic pillars and the gold backplane on the pillar foot) with dense plasmonic nanodots inside and couples the metallic components through nanogaps. (b) Schematic of the immunoassay on the D2PA, consisting of a self-assembled monolayer of adhesion layer, Protein-A (as capture layer) and human-IgG prelabeled with IRDye-800cw (as prelabeled biomarker). (c) Scanning electron micrograph of D2PA with 200 nm period (overview and cross section). The gold nanodots rested on the silica nanopillar sidewalls are clearly observed. Copyright from 2012 the American Chemical Society.

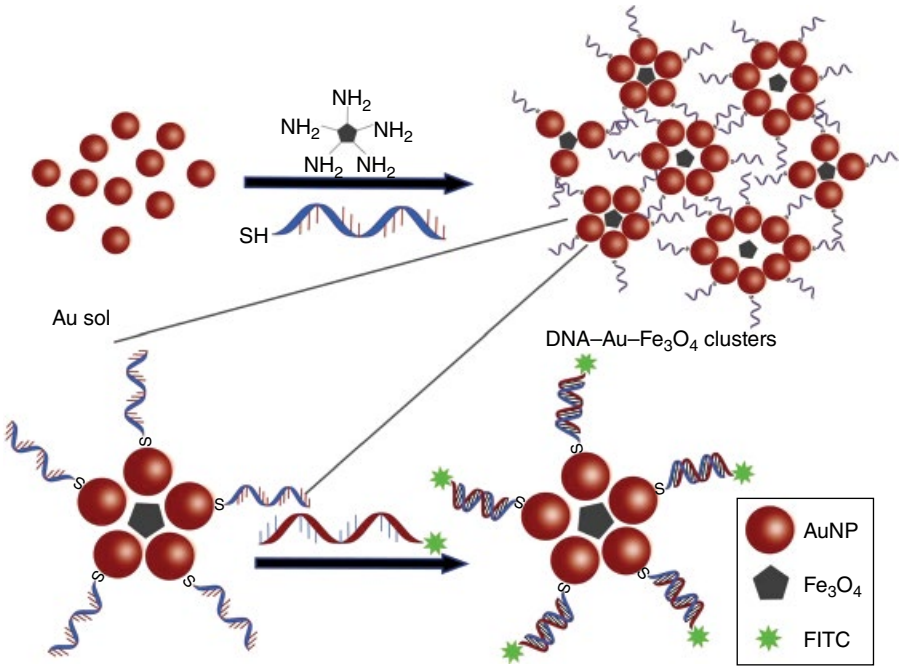

Figure 7.7 Schematic representation of the fabrication process of hybrid magnetic NP/nanogold clusters (HMNCs) and their dye-tagged DNA modified conjugates. Copyright from 2014 the Royal Society of Chemistry.

fluorescence enhancement for FITC with a maximum factor of 10.4. In addition, the authors proved the potency of HMNCs as contrast agents for magnetic resonance imaging (MRI), indicating that HMNCs was promising multimodal bio-imaging agents with MRI/computed tomography/MEF imaging effects in further studies. MacCraith and coworkers studied the dependence of the fluorescence enhancement on diameters of silica-coated Au/Ag alloy NPs [60]. Som and Karmakar fabricated core–shell bimetallic (Au^0–Ag^0) NPs embedded glasses, which exhibited 2-fold up-conversion fluorescence enhancement [61]. Lakowicz and coworkers built the silver–gold nanocomposite structure by a one-step galvanic replacement reaction from thin silver films coated on glass slides. Fifteen-fold fluorescence enhancement was observed with Atto655, accompanied with a reduction in fluorescence lifetime. The single-molecule spectroscopic study revealed ~50-fold maximum enhancement with fluorophores in close proximity to the "hotspots" regions, which were often nanoscale clefts, gaps, and fissures in the nanostructure of the substrate [62].

7.3 Distance Control

It has been well recognized that the effect of MEF strongly depends on the distance between the metallic surface and fluorophores. On the one hand, the fluorophore needs to be placed in close proximity to the metallic surface; on the other hand, the fluorophore needs to be at a distance where quenching by energy transfer near the metallic surface (<5 nm) is minimal [6]. Therefore, MEF-based biosensing method requires a fine distance control for the desirable enhancement performance. Additionally, the effective enhancement distance may also be associated with the dimension of the substrate. For instance, the decay length of the surface electromagnetic field is generally ~200 nm for planar film characterized by the surface plasmon resonance [63, 64], and 5–15 nm for NPs characterized by the localized surface plasmon resonance. As a result, the distance dependency of the enhancement may be different for these two types of substrates. The optimal enhancement may occur at the larger distance for the planar substrate than for metallic colloids, although more dramatic enhancement is generally observed with the latter.

The simplest and most desirable way of controlling the distance between the enhancing substrate and fluorophores is to use molecules or polymers, which can play roles of spacing as well as recognition and even facilitating immobilization of recognition moieties for sensing events. The approaches applied to the development of MEF-based biosensing methods in the past decade include the protein–protein interaction [18, 20, 36, 46, 50, 56, 62, 65], the nucleic acid hybridization [31, 33, 37, 38, 59, 66], the aptamer-based

recognition [31, 33], the silica [28, 30–33, 54, 67, 68], and polymer coating [12, 69]. The spacing strategy based on the protein–protein interaction benefits from the strong binding interaction and the easiness of metallic surface modification. Antigen–antibody and biotin–avidin interactions are often adopted for the MEF sensor development, as these two high specific interactions have been very well understood and the very high binding affinity makes it easy to facilitate the surface construction for spacing and recognition purposes [18, 20, 36, 46, 50, 56, 62, 65].

Both the competitive/noncompetitive direct assay and the sandwich assay modes have been used for development metal-enhanced fluoroimmunoassays, in which the fluorophore was brought in the vicinity of the metallic surface via the antibody–antigen binding [18, 36, 46, 65, 66]. The experimental design based on biotin–avidin interaction uses the same strategy as that of immunoassays to bring the fluorphores to the metallic surface [20, 50, 62]. In addition, the multiligand binding mode of the biotin–avidin interaction made it possible to build multiprotein layers and facilitate distance control by varying the number of layers. Lakowicz and coworkers have investigated the effect of number of (BSA-biotin–avidin)$_n$ layers on the SIF-enhanced intrinsic fluorescence of tryptophan, finding that the best MEF performance of SIFs was obtained with three layers of the protein complex (Figure 7.8), which was estimated to be approximately 30 nm [20].

Silica-coated NPs are one of the most adopted choices of the fluorescence enhancement substrate, because (i) the silica shell prevents NPs from aggregation, maintaining the good dispersity and uniformity of colloids; (ii) the thickness of the silica shell can be simply tuned by adjusting the experimental condition, easily providing the proper distance for optimal fluorescence enhancement; (iii) the silica shell is easy to be functionalized for developing biosensing platforms; (iv) potential cytotoxicity of NPs can be reduced by the silica shell mask for cell imaging [67]. The distance-dependent feature of MEF has been well studied using the thickness of silica shell as the measure of the distance between the fluorophore and metallic surface [28, 31–33, 68]. Wang and coworkers developed an aptasensor for the H5N1 influenza virus based on the fluorescence enhancement of 55-nm Ag@SiO_2 NPs. As the silica shell thickness increased, the fluorescence signal was found to increase first and decrease afterward with the best enhancement occurring at the 30 nm thickness (Figure 7.9) [33]. Huang and coworkers prepared aptamer-functionalized core–shell Ag@SiO_2 NPs for the prion detection. The maximum enhancement factor (over 3-fold) was achieved

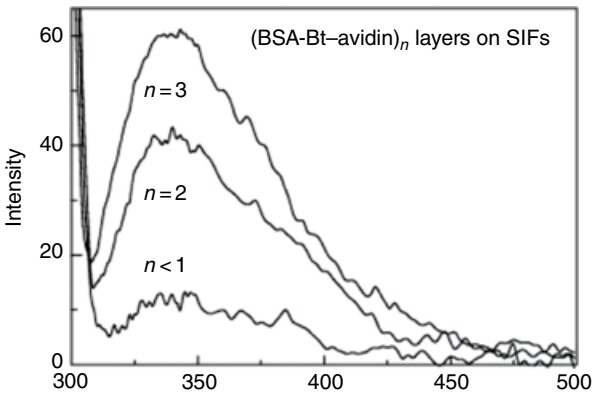

Figure 7.8 Emission spectra of (BSA-Bt–avidin)$_n$ layers deposited on SIFs. Number of layers (n) = <1 (less than a full layer of avidin), 2, or 3. Copyright from 2009 Elsevier.

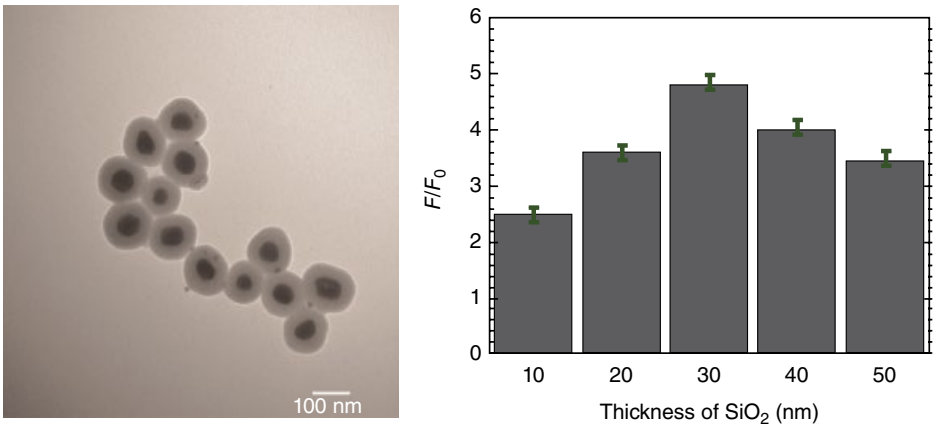

Figure 7.9 Transmission electron microscopy (TEM) image of core–shell 55-nm Ag@SiO_2 NPs with 30 nm shell thickness (*left*) and the fluorescence intensity response F/F_0 of the system solution to a series of silica shell thickness (*right*). Copyright from 2015 Elsevier.

with around 15-nm silica thickness [30]. A study by Wacogne and coworkers revealed that for gold–silica thin film, the maximum of enhancement factor (~9 for Cy5), was obtained with 90-nm silica layer over the gold film deposition through electron beam evaporation [54]. Guerrero and Aroca investigated the SERS and MEF performance of silica shell-isolated AuNPs (SHINs), finding that the enhancement factor of SERS and MEF using SHINs could be tuned by adjusting the thickness of coating silica. About 10-nm or more coating thickness was recommended to maximize fluorescence enhancement and avoid SERS for practical applications [68].

Since DNA exhibits promising potentials as a programmable and engineerable biomaterial, efforts have been made by using DNA oligomers for both the spacer and the molecular recognition moiety to tether the fluorophore to the close proximity of the metallic surface and also to produce recognition events for signal transduction. DNA as the distance controlling unit presents the following features: (i) DNA oligomers can be easily attached to the noble metal substrate via the thiol chemistry, and fluorophores can be placed in the vicinity of metallic surface by chemically labeling on the immobilized DNA strand or by hybridization of the fluorescently labeled DNA with the immobilized DNA; (ii) the DNA helix with Watson–Crick hydrogen bonding enables simple and fine length adjustment by simply changing the number of base pairs; (iii) some DNA oligomers can form conformations different from the classical double helix, such as G-quadruplex and i-motif, or undergo conformational changes via aptamer–target recognition, and thus can also act as the signal transducer. In recent years, DNA, as a multifunctional unit, has been extensively applied to the investigation of MEF distance dependency and the development of MEF-based biosensing platforms [31, 33, 37, 38, 59, 66]. Zhao and coworkers studied the distance dependence of metal-enhanced fluorescence of QDs by changing the length of linker dsDNA formed via hybridization. The number of base pairs provided the measure of the distance between QDs and AuNPs. It was found that the quenching effect of AuNPs on fluorescence of QDs dominated at the distance of 3.4–11.9 nm, while the enhancing effect dominated at the distance of 11.9–18.7 nm with 2.3-fold maximum enhancement occurred at 11.9 nm [66]. Xu's group developed an AgNP-enhanced fluorescence method for IgE detection. The distance effect was evaluated by adjusting the length of the linker DNA between silver surface and the fluorophore, Cy5, and the optimal enhancement distance was found to be 8 nm with 20-nm AgNPs [39]. Using the DNA-modified DNA-HMNCs, which consisted of 20-nm Fe_3O_4 particle core and 19-nm satellite AuNPs, as the fluorescence-enhancing substrate, Wu's group found that the suitable distance of the MEF effect was about 4 nm [59]. Li's group investigated systemically the distance effect on MEF performance of different-sized AgNPs by adjusting the base pair number of dye-labeled dsDNA. The maximum enhancement factor was observed at a distance of 10 nm for 36-nm AgNPs, 13 nm for 89-nm AgNPs, and 7.5 nm for 199-nm AgNPs, respectively (Figure 7.10). Experimental results also showed that the enhancement factor followed a d^6-dependency at short distances, which was in agreement with the quenching by AgNPs based on the FRET mechanism; while above the maximum enhancement distance, the enhancement factor followed a d^3-dependency, which was in agreement with the plasmonic enhancement mechanism [37].

In recent years, the potential of DNA aptamer has drawn great attention in biosensing applications. With the presence of the target molecule, highly specific target–aptamer complex forms to bring forth the conformational change of the aptamer strand, which induces an abrupt change in distance between two terminal ends of the strand. This target-responsive distance control feature can also be used in MEF-based biosensing as a fluorescent signal transducer [31]. Zhang's group developed core–shell Ag@SiO_2 nanoflares for affinity biosensing via target-induced structural switching of the aptamer. The nanoflare consisted of a 50-nm spherical AgNP core with an 8-nm silica shell, and Cy5-labeled aptamer immobilized onto the shell surface via hybridization; thus, the fluorophore was confined to the NP surface. The presence of target molecules replaced the complementary strands, leading to a decrease in fluorescence intensity to provide the rationale of the "signal-off" design [31, 33]. Xiao and Wang *et al*. also used aptamer-modified Ag@SiO_2 NPs to build an MEF sensing platform for the detection of the recombinant hemagglutinin (rHA) protein of the H5N1 influenza virus (Figure 7.11). Following the formation of the G-quadruplex structure with target binding, the dark thiazole orange (TO) was inserted into the quartet structure to produce enhanced fluorescence [33].

The potential of layer-by-layer (LbL) assembly of polyelectrolyte by electrostatic adsorption has been applied to MEF studies in the past few years. The spacing layers fabricated via LbL assembly are well defined and easy to control [12, 69]. Ray and coworkers developed a label-free protein detection method based on aluminum NP-enhanced intrinsic protein fluorescence. The distance between the protein and the aluminum particle surface was adjusted by the number of alternate layers of poly(styrene sulfonate) and poly(allylamine hydrochloride) formed via LbL

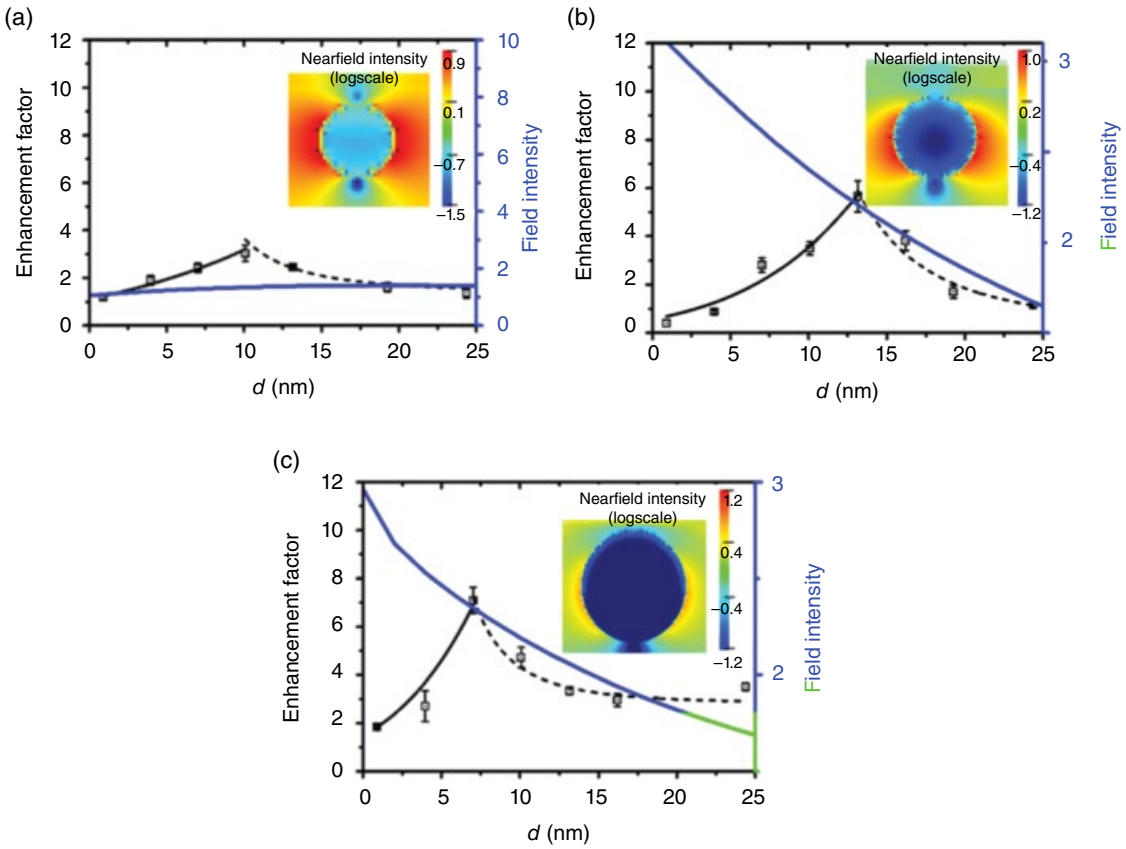

Figure 7.10 The enhancement factor and the finite-difference time-domain (FDTD) simulation result of electric field as a function of the distance between the fluorophore and the surface of 36-nm (a), 89-nm (b), and 199-nm (c) AgNPs. The black solid line is the enhancement factor fitted to d^6, the black dashed line is the enhancement factor fitted to d^3, and the blue solid line is the field intensity decay by FDTD simulation. Copyright from 2014 Elsevier.

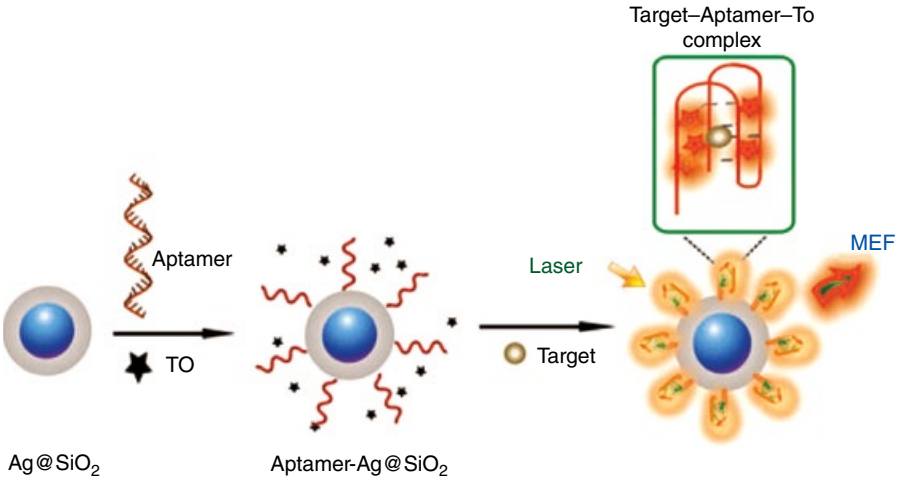

Figure 7.11 Schematic illustration of the preparation of aptamer–Ag@SiO_2 sensor and the determination of recombinant hemagglutinin (rHA) protein of H5N1. Copyright from 2015 Elsevier.

assembly (Figure 7.12). A maximum of ~9-fold increase in fluorescence intensity was observed with BSA at a distance of ~9 nm from the aluminum nanostructured surface; the 6- and 7-fold enhancement were observed with goat and rabbit IgG at a distance of ~8 nm, respectively [12]. Koh's group built a metal-enhanced QD fluorescence immunoassay using AgNPs-containing hybrid polymer film as the enhancing substrate

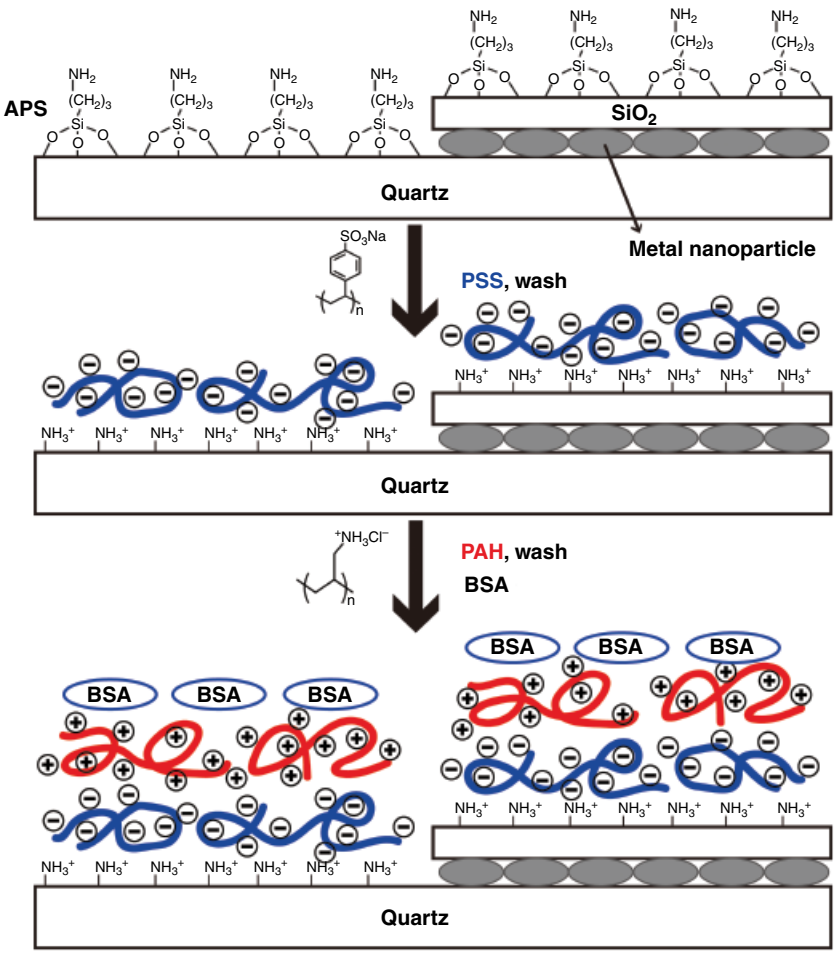

Figure 7.12 Schematic representation of metallic nanostructured surfaces and layer-by-layer (LbL) assembly. Copyright from 2012 the American Chemical Society.

which was fabricated through in situ photoreduction of Ag^+ inside a multilayer film consisting of polyethyleneimine (PEI) and hyaluronic acid (HA). A 6.2-fold enhancement was obtained with 41.2-nm-thick AgNP-$(PEI/HA)_{40}$ [69].

7.4 Summary and Outlook

MEF phenomenon provides a new way of developing highly sensitive and highly stable sensing probes for bio-related researches, intriguing researchers to explore the potential of metal–fluorophore interactions. Remarkable progresses on enhancing substrate fabrication and MEF biosensing applications have already been achieved in the past decade. MEF-based sensing methods have been proved to be advantageous for highly sensitive DNA sequencing [23–26, 38, 70], protein and small-molecule detections [12, 20, 27, 30, 37, 50, 51, 71], and cell recognition and imaging [40, 57].

Despite making numerous efforts in MEF-based biosensing applications and achieving promising analytical performances, there are still problems remaining to be solved for sensing applications. The fluorescence enhancement factor is an index of the enhancement performance of the metal substrate; thus, it is highly desirable that a reproducible enhancement factor can be obtained in practical applications. In this regard, the heterogeneity of the metallic substrate in size, morphology, and coating thickness may result in varied enhancement effect [72], and single fluorophores would exhibit different optical properties from ensemble signals [17]. Studies on silver nanowire-enhanced fluorescence revealed that the fluorescence intensity of fluorescein-labeled protein absorbed on the silver nanowire-loaded glass substrate was varied depending on the location [45]. Extremely high fluorescence enhancement for fluorophores in "hotspots" regions was reported using nano-antennas [47, 58] and nanocomposites [62]. In case of enhancing substrate with heterogeneous

surface morphology, the average ensemble enhancement factor would not reflect the actual enhancement performance of the metallic substrate. On the other hand, the density of fluorophores on the metallic surface is not easy to quantify or match the amount of fluorophores in experimental control; thus, biased quantification result of the enhancement factor may be obtained.

There is still room to improve the enhancement efficiency. Compared with the theoretical prediction by computer simulations, most of enhancing materials showed only moderate fluorescence enhancement with an enhancement factor less than one order of magnitude, which is far from anticipated. Furthermore, most of the current studies are for proof-of-concept demonstration, though metallic NP-coated microplates and microarray slides could be commercially available. Vast efforts are urgently needed to make this new and promising signal enhancement strategy more applicable to practical samples with high sensitivity, desirable reproducibility and simplicity.

Acknowledgment

This work was supported by the National Natural Science Foundation of China (No. 21275011, No. 21475004, and No. 21535006).

References

1 Geddes, C. D. & Lakowicz, J. R. (**2002**). Editorial: Metal-enhanced fluorescence. *Journal of Fluorescence*, *12*(2), 121–129.

2 Lakowicz, J. R., Shen, Y., D'Auria, S., Malicka, J., Fang, J., Gryczynski, Z., & Gryczynski, I. (**2002**). Radiative decay engineering: 2. Effects of silver island films on fluorescence intensity, lifetimes, and resonance energy transfer. *Analytical Biochemistry*, *301*(2), 261–277.

3 Gryczynski, I., Malicka, J., Gryczynski, Z., & Lakowicz, J. R. (**2004**). Radiative decay engineering 4. Experimental studies of surface plasmon-coupled directional emission. *Analytical Biochemistry*, *324*(2), 170–182.

4 Lakowicz, J. R. (**2004**). Radiative decay engineering 3. Surface plasmon-coupled directional emission. *Analytical Biochemistry*, *324*(2), 153–169.

5 Lakowicz, J. R. (**2001**). Radiative decay engineering: biophysical and biomedical applications. *Analytical Biochemistry*, *298*(1), 1–24.

6 Lakowicz, J. R. (**2005**). Radiative decay engineering: 5: Metal-enhanced fluorescence and plasmon emission. *Analytical Biochemistry*, *337*(2), 171–194.

7 Larguinho, M. & Baptista, P. V. (**2012**). Gold and silver nanoparticles for clinical diagnostics—from genomics to proteomics. *Journal of Proteomics*, *75*(10), 2811–2823.

8 Stiles, P. L., Dieringer, J. A., Shah, N. C., & Van Duyne, R. P. (**2008**). Surface-enhanced Raman spectroscopy. *Annual Review of Analytical Chemistry*, *1*, 601–626.

9 Willets, K. A., & Van Duyne, R. P. (**2007**). Localized surface plasmon resonance spectroscopy and sensing. *Annual Review of Physical Chemistry*, *58*, 267–297.

10 Sugawa, K., Tamura, T., Tahara, H., Yamaguchi, D., Akiyama, T., Otsuki, J., Kusaka, Y., Fukuda, N., & Ushijima, H. (**2013**). Metal-enhanced fluorescence platforms based on plasmonic ordered copper arrays: wavelength dependence of quenching and enhancement effects. *ACS Nano*, *7*(11), 9997–10010.

11 Zhang, Y., Aslan, K., Previte, M. J., & Geddes, C. D. (**2007**). Metal-enhanced fluorescence from copper substrates. *Applied Physics Letters*, *90*(17), 173116.

12 Akbay, N., Lakowicz, J. R., & Ray, K. (**2012**). Distance-dependent metal-enhanced intrinsic fluorescence of proteins using polyelectrolyte layer-by-layer assembly and aluminum nanoparticles. *The Journal of Physical Chemistry C*, *116*(19), 10766–10773.

13 Chowdhury, M. H., Ray, K., Gray, S. K., Pond, J., & Lakowicz, J. R. (**2009**). Aluminum nanoparticles as substrates for metal-enhanced fluorescence in the ultraviolet for the label-free detection of biomolecules. *Analytical Chemistry*, *81*(4), 1397–1403.

14 Zhang, X., Zhao, J., Whitney, A. V., Elam, J. W., & Van Duyne, R. P. (**2006**). Ultrastable substrates for surface-enhanced Raman spectroscopy: Al_2O_3 overlayers fabricated by atomic layer deposition yield improved anthrax biomarker detection. *Journal of the American Chemical Society*, *128*(31), 10304–10309.

15 Sokolov, K., Chumanov, G., & Cotton, T. M. (**1998**). Enhancement of molecular fluorescence near the surface of colloidal metal films. *Analytical Chemistry*, *70*(18), 3898–3905.

16 Pribik, R., Dragan, A. I., Zhang, Y., Gaydos, C., & Geddes, C. D. (**2009**). Metal-enhanced fluorescence (MEF): physical characterization of silver-island films and exploring sample geometries. *Chemical Physics Letters*, *478*(1–3), 70–74.

17 Fu, Y. & Lakowicz, J. R. (**2006**). Enhanced fluorescence of Cy5-labeled DNA tethered to silver island films: fluorescence images and time-resolved studies using single-molecule spectroscopy. *Analytical Chemistry*, *78*(17), 6238–6245.

18 Matveeva, E. G., Gryczynski, I., Barnett, A., Leonenko, Z., Lakowicz, J. R., & Gryczynski, Z. (**2007**).

Metal particle-enhanced fluorescent immunoassays on metal mirrors. *Analytical Biochemistry*, *363*(2), 239–245.

19 Lakowicz, J. R., Shen, B., Gryczynski, Z., D'Auria, S., & Gryczynski, I. (**2001**). Intrinsic fluorescence from DNA can be enhanced by metallic particles. *Biochemical and Biophysical Research Communications*, *286*(5), 875–879.

20 Szmacinski, H., Ray, K., & Lakowicz, J. R. (**2009**). Metal-enhanced fluorescence of tryptophan residues in proteins: application toward label-free bioassays. *Analytical Biochemistry*, *385*(2), 358–364.

21 Aslan, K., Zhang, Y., & Geddes, C. D. (**2009**). Sonication-assisted metal-enhanced fluorescence-based bioassays. *Analytical Chemistry*, *81*(12), 4713–4719.

22 Aslan, K., Huang, J., Wilson, G. M., & Geddes, C. D. (**2006**). Metal-enhanced fluorescence-based RNA sensing. *Journal of the American Chemical Society*, *128*(13), 4206–4207.

23 Aslan, K., Zhang, Y., Hibbs, S., Baillie, L., Previte, M. J. R., & Geddes, C. D. (**2007**). Microwave-accelerated metal-enhanced fluorescence: application to detection of genomic and exosporium anthrax DNA in <30 seconds. *Analyst*, *132*(11), 1130–1138.

24 Joshi, L. T., Mali, B. L., Geddes, C. D., & Baillie, L. (**2014**). Extraction and sensitive detection of toxins A and B from the human pathogen *Clostridium difficile* in 40 seconds using microwave-accelerated metal-enhanced fluorescence. *PLoS One*, *9*(8), e104334.

25 Dragan, A., & Geddes, C. D. (**2014**). 5-Color multiplexed microwave-accelerated metal-enhanced fluorescence: detection and analysis of multiple DNA sequences from within one sample well within a few seconds. *Journal of Fluorescence*, *24*(6), 1715–1722.

26 Dragan, A., Pavlovic, R., & Geddes, C. D. (**2014**). Rapid catch and signal (RCS) technology platform: multiplexed three-color, 30 s microwave-accelerated metal-enhanced fluorescence DNA assays. *Plasmonics*, *9*(6), 1501–1510.

27 Wang, K., Liao, J., Yang, X., Zhao, M., Chen, M., Yao, W., Tan, W., & Lan, X. (**2015**). A label-free aptasensor for highly sensitive detection of ATP and thrombin based on metal-enhanced PicoGreen fluorescence. *Biosensors and Bioelectronics*, *63*, 172–177.

28 Aslan, K., Wu, M., Lakowicz, J. R., & Geddes, C. D. (**2007**). Fluorescent core-shell Ag@SiO_2 nanocomposites for metal-enhanced fluorescence and single nanoparticle sensing platforms. *Journal of the American Chemical Society*, *129*(6), 1524–1525.

29 Brouard, D., Ratelle, O., Bracamonte, A. G., St-Louis, M., & Boudreau, D. (**2013**). Direct molecular detection of SRY gene from unamplified genomic DNA by metal-enhanced fluorescence and FRET. *Analytical Methods*, *5*(24), 6896–6899.

30 Hu, P. P., Zheng, L. L., Zhan, L., Li, J. Y., Zhen, S. J., Liu, H., Luo, L. F., Xiao, G. F., & Huang, C. Z. (**2013**). Metal-enhanced fluorescence of nano-core–shell structure used for sensitive detection of prion protein with a dual-aptamer strategy. *Analytica Chimica Acta*, *787*, 239–245.

31 Lu, L., Qian, Y., Wang, L., Ma, K., & Zhang, Y. (**2014**). Metal-enhanced fluorescence-based core–shell Ag@SiO_2 nanoflares for affinity biosensing via target-induced structure switching of aptamer. *ACS Applied Materials & Interfaces*, *6*(3), 1944–1950.

32 Sui, N., Wang, L., Yan, T., Liu, F., Sui, J., Jiang, Y., Wan, J., Liu, M., & William, W. Y. (**2014**). Selective and sensitive biosensors based on metal-enhanced fluorescence. *Sensors and Actuators B: Chemical*, *202*, 1148–1153.

33 Pang, Y., Rong, Z., Wang, J., Xiao, R., & Wang, S. (**2015**). A fluorescent aptasensor for H5N1 influenza virus detection based-on the core–shell nanoparticles metal-enhanced fluorescence (MEF). *Biosensors and Bioelectronics*, *66*, 527–532.

34 Ma, K., Lu, L., Qi, Z., Feng, J., Zhuo, C., & Zhang, Y. (**2015**). In situ induced metal-enhanced fluorescence: a new strategy for biosensing the total acetylcholinesterase activity in sub-microliter human whole blood. *Biosensors and Bioelectronics*, *68*, 648–653.

35 Kim, K., Lee, J. W., & Shin, K. S. (**2012**). Polyethylenimine-capped Ag nanoparticle film as a platform for detecting charged dye molecules by surface-enhanced Raman scattering and metal-enhanced fluorescence. *ACS Applied Materials & Interfaces*, *4*(10), 5498–5504.

36 Han, X. X., Kitahama, Y., Tanaka, Y., Guo, J., Xu, W. Q., Zhao, B., & Ozaki, Y. (**2008**). Simplified protocol for detection of protein–ligand interactions via surface-enhanced resonance Raman scattering and surface-enhanced fluorescence. *Analytical Chemistry*, *80*(17), 6567–6572.

37 Zhou, Z., Huang, H., Chen, Y., Liu, F., Huang, C. Z., & Li, N. (**2014**). A distance-dependent metal-enhanced fluorescence sensing platform based on molecular beacon design. *Biosensors and Bioelectronics*, *52*, 367–373.

38 Zhou, Z., Li, T., Huang, H., Chen, Y., Liu, F., Huang, C., & Li, N. (**2014**). A dual amplification strategy for DNA detection combining bio-barcode assay and metal-enhanced fluorescence modality. *Chemical Communications*, *50*(87), 13373–13376.

39 Wei, X., Li, H., Li, Z., Vuki, M., Fan, Y., Zhong, W., & Xu, D. (**2012**). Metal-enhanced fluorescent probes based on silver nanoparticles and its application in IgE detection. *Analytical and Bioanalytical Chemistry*, *402*(3), 1057–1063.

40 Li, H., Hu, H., & Xu, D. (**2015**). Silver decahedral nanoparticles-enhanced fluorescence resonance energy transfer sensor for specific cell imaging. *Analytical Chemistry*, *87*(7), 3826–3833.

41 Li, H., Hu, H., Zhao, Y., Chen, X., Li, W., Qiang, W., & Xu, D. (**2015**). Multifunctional aptamer–silver conjugates as theragnostic agents for specific cancer cell therapy and fluorescence-enhanced cell imaging. *Analytical Chemistry*, *87*(7), 3736–3745.

42 Aslan, K., Lakowicz, J. R., & Geddes, C. D. (**2005**). Rapid deposition of triangular silver nanoplates on planar surfaces: application to metal-enhanced fluorescence. *The Journal of Physical Chemistry B*, *109*(13), 6247–6251.

43 Aslan, K., Leonenko, Z., Lakowicz, J. R., & Geddes, C. D. (**2005**). Fast and slow deposition of silver nanorods on planar surfaces: application to metal-enhanced fluorescence. *The Journal of Physical Chemistry B*, *109*(8), 3157–3162.

44 Ou, J., Yang, Y., Yuan, Z., Zhang, Y., Gan, L., & Chen, X. (**2014**). Enhanced single molecule fluorescence of conjugated polymer poly(3-hexylthiophene) on silver-nanocubes. *Synthetic Metals*, *195*, 9–15.

45 Abel, B., Coskun, S., Mohammed, M., Williams, R., Unalan, H. E., & Aslan, K. (**2014**). Metal-enhanced fluorescence from silver nanowires with high aspect ratio on glass slides for biosensing applications. *The Journal of Physical Chemistry C*, *119*(1), 675–684.

46 Todescato, F., Antognoli, A., Meneghello, A., Cretaio, E., Signorini, R., & Bozio, R. (**2014**). Sensitive detection of Ochratoxin A in food and drinks using metal-enhanced fluorescence. *Biosensors and Bioelectronics*, *57*, 125–132.

47 Gill, R., Tian, L., Somerville, W. R., Le Ru, E. C., van Amerongen, H., & Subramaniam, V. (**2012**). Silver nanoparticle aggregates as highly efficient plasmonic antennas for fluorescence enhancement. *The Journal of Physical Chemistry C*, *116*(31), 16687–16693.

48 Gill, R. & Le Ru, E. C. (**2011**). Fluorescence enhancement at hot-spots: the case of Ag nanoparticle aggregates. *Physical Chemistry Chemical Physics*, *13*, 16366–16372.

49 Moskovits, M. (**2011**). Imaging: spot the hotspot. *Nature*, *469*(7330), 307–308.

50 Li, H., Chen, C.-Y., Wei, X., Qiang, W., Li, Z., Cheng, Q., & Xu, D. (**2012**). Highly sensitive detection of proteins based on metal-enhanced fluorescence with novel silver nanostructures. *Analytical Chemistry*, *84*(20), 8656–8662.

51 Ganguly, M., Pal, J., Mondal, C., Pal, A., & Pal, T. (**2014**). Intriguing manipulation of metal-enhanced fluorescence for the detection of CuII and cysteine. *Chemistry-A European Journal*, *20*(39), 12470–12476.

52 Yang, Z., Ni, W., Kou, X., Zhang, S., Sun, Z., Sun, L.-D., Wang, J., & Yan, C.-H. (**2008**). Incorporation of gold nanorods and their enhancement of fluorescence in mesostructured silica thin films. *The Journal of Physical Chemistry C*, *112*(48), 18895–18903.

53 Fu, Y., Zhang, J., & Lakowicz, J. R. (**2010**). Plasmon-enhanced fluorescence from single fluorophores end-linked to gold nanorods. *Journal of the American Chemical Society*, *132*(16), 5540–5541.

54 Renier, A., Mangeat, T., Benalia, H., Elie-Caille, C., Pieralli, C., & Wacogne, B. (**2010**). Gold/silica thin film for biosensors applications: metal enhanced fluorescence. *Laser Physics*, *20*(3), 591–595.

55 Lee, K., Hahn, L. D., Yuen, W. W., Vlamakis, H., Kolter, R., & Mooney, D. J. (**2011**). Metal-enhanced fluorescence to quantify bacterial adhesion. *Advanced Materials*, *23*(12), H101–H104.

56 Ahmed, S. R., Hossain, M. A., Park, J. Y., Kim, S.-H., Lee, D., Suzuki, T., Lee, J., & Park, E. Y. (**2014**). Metal enhanced fluorescence on nanoporous gold leaf-based assay platform for virus detection. *Biosensors and Bioelectronics*, *58*, 33–39.

57 Xu, Y.-K., Hwang, S., Kim, S., & Chen, J.-Y. (**2014**). Two orders of magnitude fluorescence enhancement of aluminum phthalocyanines by gold nanocubes: a remarkable improvement for cancer cell imaging and detection. *ACS Applied Materials & Interfaces*, *6*(8), 5619–5628.

58 Zhou, L., Ding, F., Chen, H., Ding, W., Zhang, W., & Chou, S. Y. (**2012**). Enhancement of immunoassay's fluorescence and detection sensitivity using three-dimensional plasmonic nano-antenna-dots array. *Analytical Chemistry*, *84*(10), 4489–4495.

59 Gu, X., Wu, Y., Zhang, L., Liu, Y., Li, Y., Yan, Y., & Wu, D. (**2014**). Hybrid magnetic nanoparticle/nanogold clusters and their distance-dependent metal-enhanced fluorescence effect via DNA hybridization. *Nanoscale*, *6*(15), 8681–8693.

60 Stranik, O., Nooney, R., McDonagh, C., & MacCraith, B. D. (**2007**). Optimization of nanoparticle size for plasmonic enhancement of fluorescence. *Plasmonics*, *2*(1), 15–22.

61 Som, T. & Karmakar, B. (**2009**). Core–shell Au–Ag nanoparticles in dielectric nanocomposites with plasmon-enhanced fluorescence: a new paradigm in antimony glasses. *Nano Research*, *2*(8), 607–616.

62 Choudhury, S. D., Badugu, R., Ray, K., & Lakowicz, J. R. (**2012**). Silver–gold nanocomposite substrates

for metal-enhanced fluorescence: ensemble and single-molecule spectroscopic studies. *The Journal of Physical Chemistry C*, *116*(8), 5042–5048.

63 Jung, L. S., Campbell, C. T., Chinowsky, T. M., Mar, M. N., & Yee, S. S. (**1998**). Quantitative interpretation of the response of surface plasmon resonance sensors to adsorbed films. *Langmuir*, *14*(19), 5636–5648.

64 Haes, A. J., & Duyne, R. P. V. (**2004**). Preliminary studies and potential applications of localized surface plasmon resonance spectroscopy in medical diagnostics. *Expert Review of Molecular Diagnostics*, *4*(4), 527–537.

65 Matveeva, E. G., Gryczynski, Z., Malicka, J., Gryczynski, I., & Lakowicz, J. R. (**2004**). Metal-enhanced fluorescence immunoassays using total internal reflection and silver island-coated surfaces. *Analytical Biochemistry*, *334*(2), 303–311.

66 Li, Y.-Q., Guan, L.-Y., Zhang, H.-L., Chen, J., Lin, S., Ma, Z.-Y., & Zhao, Y.-D. (**2011**). Distance-dependent metal-enhanced quantum dots fluorescence analysis in solution by capillary electrophoresis and its application to DNA detection. *Analytical Chemistry*, *83*(11), 4103–4109.

67 Fang, P.-P., Lu, X., Liu, H., & Tong, Y. (**2015**). Applications of shell-isolated nanoparticles in surface-enhanced Raman spectroscopy and fluorescence. *TrAC Trends in Analytical Chemistry*, *66*, 103–117.

68 Guerrero, A. R. & Aroca, R. F. (**2011**). Surface-enhanced fluorescence with shell-isolated nanoparticles (SHINEF). *Angewandte Chemie International Edition*, *50*(3), 665–668.

69 Jang, E., Son, K. J., & Koh, W.-G. (**2014**). Metal-enhanced fluorescence using silver nanoparticles-embedded polyelectrolyte multilayer films for microarray-based immunoassays. *Colloid and Polymer Science*, *292*(6), 1355–1364.

70 Mao, K., Liu, Y., Xiao, H., Chen, Y., Wu, Z., Zhou, X., Shen, A., & Hu, J. (**2015**). A novel platform for detection of protooncogene based on Au nanocluster enhanced fluorescence. *Analytical Methods*, *7*(1), 40–44.

71 Zhang, Y., Mali, B. L., Aitken, C., & Geddes, C. D. (**2013**). Highly sensitive quantitation of human serum albumin in clinical samples for hypoproteinemia using metal-enhanced fluorescence. *Journal of Fluorescence*, *23*(1), 187–192.

72 Geddes, C. D., Cao, H., Gryczynski, I., Gryczynski, Z., Fang, J., & Lakowicz, J. R. (**2003**). Metal-enhanced fluorescence (MEF) due to silver colloids on a planar surface: potential applications of indocyanine green to in vivo imaging. *The Journal of Physical Chemistry A*, *107*(18), 3443–3449.

8

Long-Range Metal-Enhanced Fluorescence

Ofer Kedem

Center for Bio-Inspired Energy Science, Northwestern University, Evanston, IL, USA

8.1 Introduction

When a luminescent species is in proximity to a discontinuity in the dielectric function, such as that created by a metal or dielectric film, or a metallic nanoparticle (NP), its luminescence properties can be drastically altered. The emission intensity, lifetime, peak wavelength, and linewidth [1–4] of such diverse emitters as organic dyes, metal complexes, or quantum dots are all subject to these interactions, and this field has been extensively studied [2, 3, 5–7]. While most studies focus on fluorescence (photoluminescence), the interaction is general, and is observed for other types of emitters, such as chemiluminescent [8] and phosphorescent [9, 10] species. When the discontinuity is caused by plasmonically active metal NPs, the interaction is commonly termed *metal-enhanced fluorescence* (MEF), although the interaction can also result in quenching of the emission. Alternative, somewhat distinct terms are *surface plasmon-coupled emission* (SPCE), and *plasmon-controlled fluorescence* (PCF) [11]. When discussing metal NPs, the exact effect of the NPs on the emission depends on multiple factors, among them the exact composition of the metal [12], the size and shape of the NPs [13, 14], the spectral overlap of the fluorophore excitation and emission bands with the NPs' localized plasmon band [15–17], the fluorophore's quantum yield [18], and the distance between the fluorophore and the NP [19–21]. In this chapter, we narrow our discussion to the effect of this last parameter—the metal–fluorophore distance.

Let us begin by defining the relevant parameters. The rates of a fluorophore's decay to the ground state determine its quantum efficiency [2],

$$\eta = \frac{\Gamma_r}{\Gamma_r + \Gamma_{nr}^0 + \Gamma_{ET}} \tag{8.1}$$

where η is the quantum efficiency, Γ_r is the radiative decay rate, Γ_{nr}^0 is the intrinsic nonradiative decay rate, and Γ_{ET} is the rate of radiationless energy transfer to the metal. The observed lifetime is

$$\tau = \frac{1}{\Gamma_r + \Gamma_{nr}^0 + \Gamma_{ET}} \tag{8.2}$$

The transition rates are typically described by Fermi's golden rule [22, 23],

$$\Gamma_{ij} \propto \left|M_{ij}\right|^2 \rho\left(\nu_{ij}\right) \tag{8.3}$$

where Γ_{ij} is the transition rate between states i and j; M_{ij} is a measure of the coupling between the states, specifically the matrix element connecting the states; and $\rho(\nu_{ij})$ is the density of states at the transition frequency (also known as the *photonic mode density*). A change to either the coupling strength between the states, or to their density can modify the transition rate and, ultimately, the fluorescence quantum yield.

The quantum yield, however, paints an incomplete picture, as it does not take into account the efficiency of the excitation process. Incorporating the latter results in the total fluorescence yield [2],

$$F\left(\lambda_{ex},\lambda_{em}\right) = \frac{\lambda_{ex} I\left(\lambda_{ex}\right)}{hc} \sigma_{abs}^{eff}\left(\lambda_{ex}\right) \eta\left(\lambda_{em}\right) \tag{8.4}$$

where λ_{ex} and λ_{em} are the excitation and emission wavelengths, respectively; $I(\lambda_{ex})$ is the intensity of the excitation beam; and $\sigma_{abs}^{eff}(\lambda_{ex})$ is the effective absorption cross section,

$$\sigma_{abs}^{eff}\left(\lambda_{ex}\right) = \frac{\left|\vec{p}\cdot\vec{E}\left(\lambda_{ex}\right)\right|^2}{\left|\vec{p}\cdot\vec{E}^0\left(\lambda_{ex}\right)\right|^2} \sigma_{abs}^0\left(\lambda_{ex}\right) \tag{8.5}$$

Surface Plasmon Enhanced, Coupled and Controlled Fluorescence, First Edition. Edited by Chris D. Geddes.
© 2017 John Wiley & Sons, Inc. Published 2017 by John Wiley & Sons, Inc.

where $\vec{p}$ is the molecular dipole moment, $\vec{E}(\lambda_{ex})$ and $\vec{E}^0(\lambda_{ex})$ are the electric fields in the presence and absence of a metallic nanostructure, respectively, and $\sigma^0_{abs}(\lambda_{ex})$ is the intrinsic absorption cross section of an unperturbed fluorophore. $\vec{E}(\lambda_{ex})$ can be increased, decreased, or reoriented with respect to $\vec{E}^0(\lambda_{ex})$ [2]. Note that the orientation of the dipole relative to the field has a strong effect on the interaction. However, as the dipole orientation is only rarely determined experimentally, we will not discuss this parameter.

The vast majority of published works examining the distance dependence of MEF focus on a range spanning, at most, tens of nanometers, and typically show little-to-no interaction between the metal and the fluorophore at longer ranges [12, 20, 24–28]. However, when discussing NP *films*, rather than single NPs, longer range interactions manifest themselves [29]. The interactions are largely similar to those of fluorophores with continuous metal films, a topic which was explored in multiple theoretical and experimental works [2, 4, 11, 30–34]. A highly detailed 1998 review by Barnes, analyzing MEF in terms of photonic mode density modification, is an excellent source of information for this topic [23].

8.2 Collective Effects in NP Films

It may not be immediately apparent that NP films can be treated as mirrors, but dense NP films can, in fact, behave as partially reflective mirrors, through far-field interaction [29, 35]. In the context of MEF, Corrigan *et al*. noted that while sparse NP films produce enhancements consistent with a single-NP model, denser films deviate from those predictions [36]. I, with coworkers Alexander Vaskevich and Israel Rubinstein, along with theory collaborator Takumi Sannomiya, have previously investigated the collective behavior of NP films for plasmonic Au nanoisland substrates, coated with dielectric spacers of controllable thickness [37]. We found an oscillation in the plasmonic absorption and scattering wavelengths and intensities, brought about by interference between waves reflected by the AuNP/dielectric and dielectric/air interfaces. Modeling this interaction as an asymmetric etalon (Fabry–Pérot interferometer), we found that the NP films played the part of a partially reflective mirror, with one important distinction—the phase shift upon reflection was different from that of smooth films, and has a strong wavelength dependence, with an inflection point around the plasmon resonance wavelength, a typical feature for resonant systems.

8.3 Investigations of Metal–Fluorophore Interactions at Long Separations

In the pages that follow, we will discuss the long-range interactions of metal mirrors and metal NP films with fluorophores. We will divide our discussion by the different aspects of fluorescence—lifetime, intensity, and emission wavelength and linewidth. Though this categorization is artificial, as these aspects are all modified by the same, or interconnected, mechanisms, they are often measured and discussed separately, and so this is a convenient scheme. For each topic, we will examine some notable theoretical and experimental works, as well as a study we recently conducted on the topic, introduced in the following section.

8.3.1 Distance-Dependent Fluorescence of Tris(bipyridine)ruthenium(II) on Supported Plasmonic Gold NP Ensembles

Recently, my collaborators, Israel Rubinstein and Wendel Wohlleben, and I explored the effect of MEF for plasmonic gold NP films [38]. Our original motivation was to explore a possible connection between the distance-dependence profile of MEF, and the decay length of plasmonic sensing, previously measured for these same gold NP films [39]. In the plasmonic decay length work, we measured the shifts in the peak extinction wavelength and intensity of the NP films in response to step-wise adsorption of dielectric layers and obtained an exponential decay profile. The characteristic decay length of the response is strongly correlated with the NP size, and so for our subsequent MEF study, we selected two very different NP sizes, of ~20 and 100 nm mean diameter (the particles are not spheres, but rather flattened ellipsoids; the diameters are those of the in-plane primary axis), with plasmonic exponential decay lengths of 3 and 20 nm, respectively (Figure 8.1).

We found that films of either NP size result in similar fluorescence emission distance-dependent profiles (though of different emission intensity, see detailed discussion later), thus refuting the original hypothesis. However, we observed other interesting phenomena, chiefly a long-range modification of the intensity and lifetime, as well as oscillations in the emission wavelength and linewidth.

Full experimental details are available in the original publication [38]; what follows is a brief summary. The plasmonic substrates were produced by thermally evaporating gold to subpercolation thickness on glass substrates [40–42]. The evaporation is followed by high-temperature annealing, 580°C for 10 h; in the

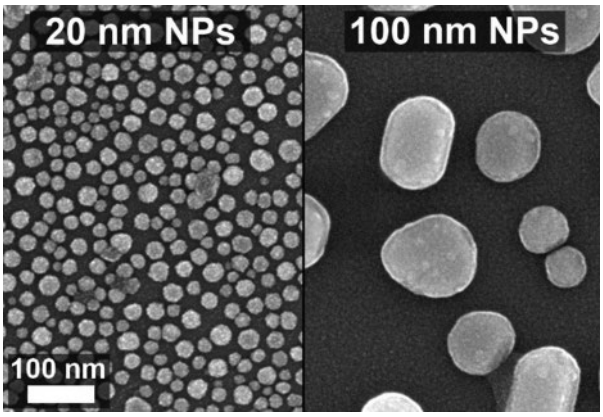

Figure 8.1 Scanning electron microscopy (SEM) images of pristine 20 and 100 nm mean major axis AuNP samples (15 kV accelerating voltage). Samples were coated with 2 nm (20 nm NPs) and 3 nm (100 nm NPs) of Cr for improved conductivity during imaging. Images were recorded using the in-lens secondary electron detector. Kedem *et al*. [38]. Reproduced with the permission of Royal Society of Chemistry.

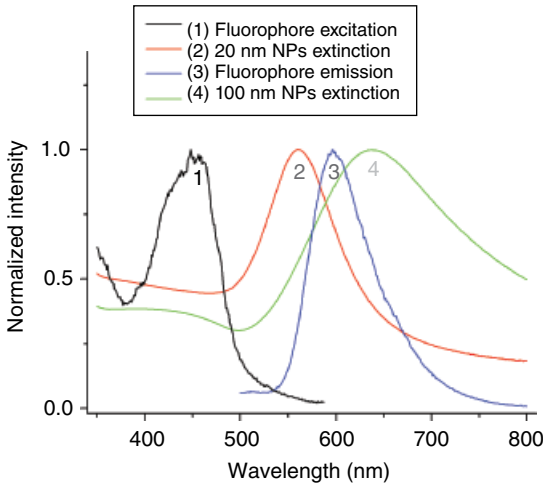

Figure 8.2 Normalized fluorescence excitation (1) and emission (3) spectra for $[Ru(bpy)_3]^{2+}$ on a glass control slide. The excitation spectrum was determined by measuring the emission at 605 nm and scanning over different excitation wavelengths; for the emission spectrum, the sample was excited at 454 nm. Also shown are extinction spectra of 20 nm (2) and 100 nm (4) AuNP films on glass, coated with a 21 nm thick polyelectrolyte multilayer. Kedem *et al*. [38]. Reproduced with the permission of Royal Society of Chemistry.

annealing process, the gold de-wets the surface, forming nanosized islands, which are partially embedded in the surface and firmly attached to it without using an adhesion layer. The evaporated nominal (mass) thickness of the gold determines the final particle size. The substrates were then coated with a transparent dielectric spacer—a polyelectrolyte multilayer (PAH/PSS—poly(allylamine hydrochloride)/poly(styrene sulfonate), sodium salt), for thicknesses up to 72 nm, or a SiO_x layer ($x \leq 2$, as no oxygen is added during the physical vapor deposition process) of up to 348 nm thickness, followed by a PAH/PSS bilayer, to facilitate fluorophore deposition by providing a negatively charged surface. The fluorophore used was $[Ru(bpy)_3]^{2+}$ (tris(bipyridine)ruthenium[II] oxalate), which easily adsorbs to the top PSS layer via electrostatic interactions. In water, $[Ru(bpy)_3]^{2+}$ has a broad absorption band, with a peak at 454 nm, and a corresponding emission band centered around 605 nm. This large Stokes shift (difference between absorption and emission wavelengths) enables us to focus on the effect of the spectral overlap between the emission and plasmonic extinction peaks (Figure 8.2), and it, alongside excellent stability, are two key advantages of $[Ru(bpy)_3]^{2+}$ compared to organic dyes. The samples were illuminated by light at 454 nm hitting the sample at 30° from the normal, with the light sensor positioned at 60° off the normal to the other side. We measured the emission spectrum and lifetime for fluorophore monolayers deposited on a variety of spacer thicknesses, from 2 to 348 nm. The measured values were compared to those of control samples—glass slides coated with several bilayers of PAH/PSS and a $[Ru(bpy)_3]^{2+}$ monolayer.

8.3.2 Lifetime

Some of the very earliest studies of MEF involved the modification of the fluorescence lifetime of Eu^{3+} ions in front of an interface, carried out by Kuhn and Drexhage in the late 1960s and early 1970s [43–45]. In those studies, a layer of Eu^{3+} complexes was separated from a metal or dielectric interface by a spacer of controllable thickness, prepared using the Langmuir–Blodgett method for monolayer and multilayer deposition. Drexhage and Kuhn found an oscillation of the lifetime as a function of metal–fluorophore separation and explained the results using an interference formalism. This approach produced good agreement between theory and experiment (Figure 8.3a), except for close separations (on the order of 10 nm), as it excludes the possibility of energy transfer between the fluorophore and the metal. Thus, the approach describes the metal's effect only on the radiative component of the lifetime [46]. Energy transfer was added to the interference model, but the results were still not fully satisfactory [43]. In 1975, Chance *et al*. analyzed results from Drexhage and others, for multiple experimental configurations of single- and double-mirror systems, and demonstrated that a more complete classical description accurately matches the experimental results (Figure 8.3b) [46]. A highly detailed classical treatment of the problem was presented in 1978 by Chance, Prock, and Silbey (CPS), and in it coupling to surface plasmon polariton (SPP)

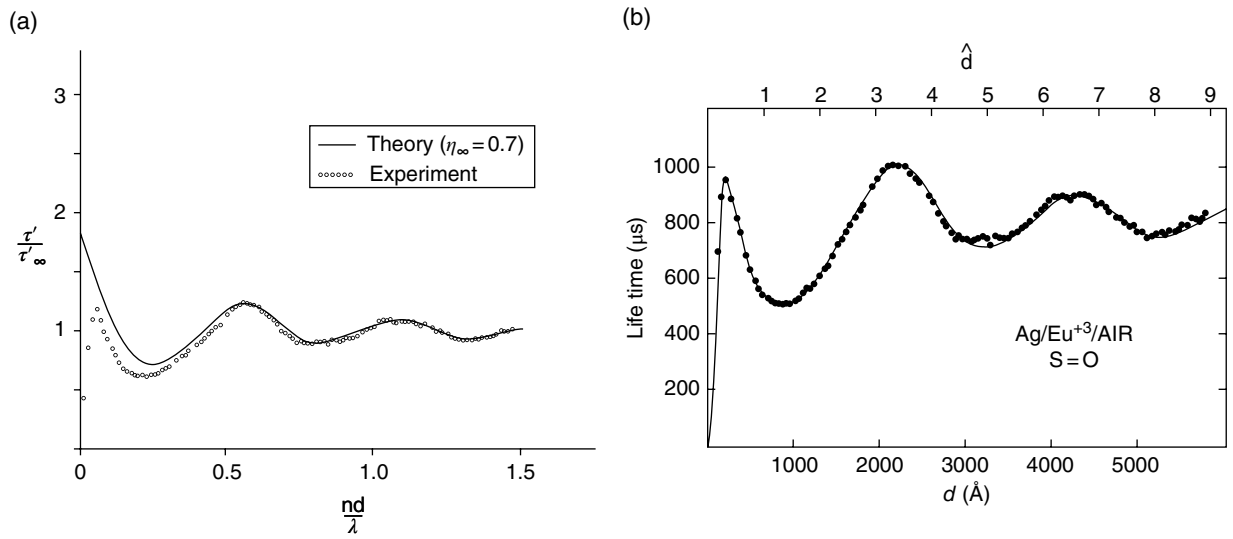

Figure 8.3 (a) Distance-dependent fluorescence lifetime of Eu^{3+} ions in front of an Ag mirror. The simple interference model works well for larger distances, but fails for close proximity. Drexhage *et al*. [44]. Reproduced with the permission of Elsevier. (b) Chance *et al*.'s fit (line) for Drexhage's experimental data (dots), incorporating energy transfer; note the good agreement at close ranges. Chance *et al*. [46]. Reproduced with the permission of AIP Publishing LLC.

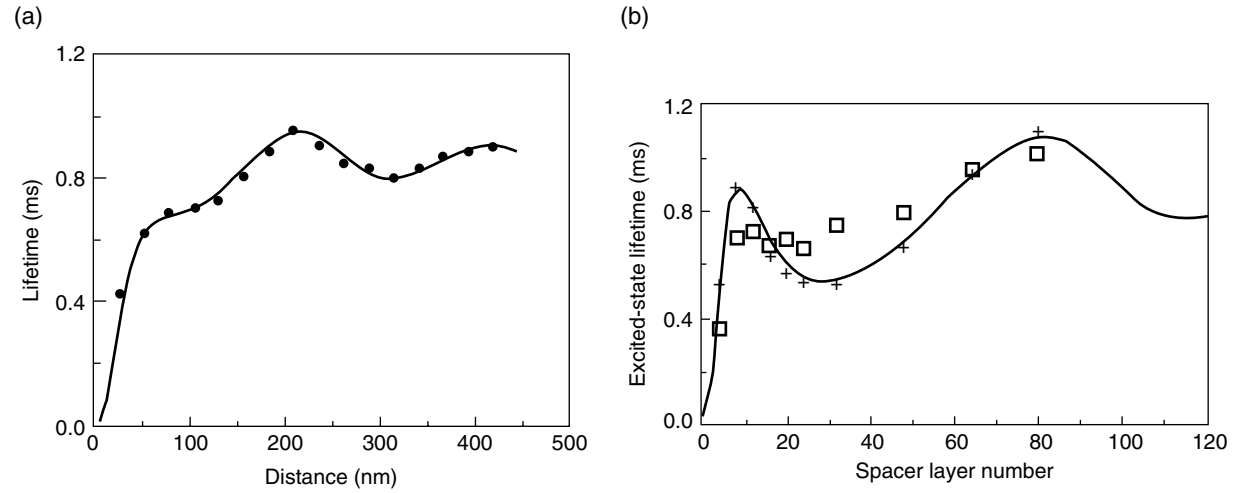

Figure 8.4 (a) Distance-dependent fluorescence lifetime of Eu^{3+} ions in front of a 14 nm thick Ag mirror; a classical dipole model (line) fits well to the experimental data (circles). Amos *et al*. [48]. Reproduced with the permission of American Physical Society. (b) Fluorescence lifetime of Eu^{3+} (squares) above a corrugated Ag film, with a pitch of 408 nm and amplitude of 68 ± 4 nm; the line is a theoretical prediction for a planar film. Amos *et al*. [49]. Reproduced with the permission of American Physical Society.

modes arises as a natural result of the complex dielectric permittivity of the metal [47].

Following the successful explanation of the lifetime modification effected by thick mirrors, research turned to more complex cases. In 1997, Amos *et al*. measured the fluorescence lifetime of Eu^{3+} ions close to a thin (<100 nm) metal mirror and found that the lifetime is further modified compared to the thick mirror case (Figure 8.4a, contrast with Figure 8.3) [48]. The results confirm a theoretical prediction made by CPS in 1978 [47], and show coupling between the emitter and the SPP mode on the far side of the metal film. The work showed a gradual intensification of the SPP coupling route with a decrease in Ag film thickness. In a later work, Amos *et al*. examined the effect of a corrugated Ag film on the measured lifetime, for several corrugation periods; it was found that while for periods longer than the emission wavelength there was virtually no difference from planar mirrors, there was a significant deviation in the case of short corrugation periods

(Figure 8.4b) [49]. The deviation was not fully explained at that time, but the authors proposed that it arose due to diffraction of the dipole far field, which would reduce the field intensity, thus damping the oscillations in lifetime. In 2001, Andrew and Barnes further investigated the coupling of emitters with Bragg gratings, measuring both the lifetime and angular distribution of the emitted radiation; [50]. In 2012, Toma *et al*. studied a similar system and demonstrated the ability to modify the amount of light emitted in certain directions, by tuning the refractive indices at the interfaces [51].

In our study, we measured the samples' fluorescence emission lifetime using a custom-built instrument, comprising an Nd:YAG 355 nm third-harmonic laser as the excitation source, and a multichannel scaling (MCS) detector. An MCS detector provides a better signal/noise ratio for a relatively slow emitter like $[Ru(bpy)_3]^{2+}$ (1 μs range), compared to a time-correlated single-photon counter (TCSPC), which better serves faster emitters (1 ns range). We found the decay plots (Figure 8.5a) can be fit to a biexponential model,

$$I = I_0 + A_1 \exp\left(-\frac{t}{\tau_1}\right) + A_2 \exp\left(-\frac{t}{\tau_2}\right) \tag{8.6}$$

where I is the fluorescence intensity, I_0 is the baseline intensity, A_1 and A_2 are the amplitudes of the two exponentials (ratios plotted in Figure 8.5e), t is the time, and τ_1 and τ_2 are the fast and slow lifetimes, respectively (Figure 8.5b, c). We use the definition from Zhang *et al*. for the mean lifetime [10],

$$\bar{\tau} = \frac{A_1\tau_1^2 + A_2\tau_2^2}{A_1\tau_1 + A_2\tau_2} \tag{8.7}$$

plotted in Figure 8.5d. In addition, after Zhang *et al*., we define the fractional contribution of each component to the steady-state emission intensity,

$$f_i = \frac{A_i\tau_i}{\sum_i A_i\tau_i} \tag{8.8}$$

with the relative contribution of the faster (τ_1) mode plotted in Figure 8.5f. From these plots, we note several interesting observations: (i) The mean lifetime is dominated by τ_2, which exhibits two peaks in the thickness range studied—around 50 nm and 200 nm; these peaks do not correspond to a minimum or maximum of emission intensity (Figure 8.8b). In fact, the fluorescence lifetime appears to be completely uncorrelated with the measured intensity (Figure 8.9). (ii) τ_1 for the 20 nm NPs appears to be almost unaffected by the change in spacer thickness. (iii) The slower exponential term (τ_2) is responsible for most of the measured emission at all spacer thicknesses, but the exact distribution between the exponential terms varies with spacer thickness. The observed oscillation in lifetime is very similar to that observed for the Eu^{3+}/Ag mirror system, discussed earlier.

8.3.3 Intensity

Though most early work exploring long-range MEF only examined the effect on the fluorescence lifetime, some studies also measured the changes in the emission intensity. A notable example is a 1993 study by Kümmerlen *et al*., in which a layer of the dye Rhodamine 6G (R6G), at several different surfaces coverages, was separated from a silver nanoisland film by deposited SiO_2 layers in the thickness range 0–100 nm [29]. For R6G, higher coverage results in lower quantum yield, and so this method allowed the authors to examine the influence of quantum yield on MEF, while still using a single dye. This study is one of the earliest, perhaps the very earliest, exploring the distance dependence of MEF for NP films, as opposed to flat mirrors or isolated NPs. For the three R6G coverages used (10^{-3}, 10^{-2}, and full monolayer), the authors found two enhancement peaks, at ~8 and 60 nm spacer thickness (Figure 8.6). The relative intensities of the two peaks varied with the coverage, but their positions, as a function of spacer thickness, remained relatively unchanged. As noted in the work, a distance of 60–70 nm is far beyond the range of a single NP's local field enhancement; fluorescence enhancement at that range indicates collective action by the nanoislands. The total measured intensity depends on both the excitation and emission, and both are modified by the presence of the AgNP film. The authors analyze the effect of the film on the excitation intensity in terms of stratified medium theory, recursively calculating Fresnel coefficients at each interface, and for the entire assembly as a whole. The analysis predicts a maximal enhancement of ~3.0 around 60 nm, matching the experimental results. The effect on the emission lifetime is treated by modeling the film as an effective medium, adapting the earlier procedure developed by Kuhn [43] and Drexhage [44, 45] for smooth silver films; the authors find the greatest shortening of the lifetime, to a factor of ~0.55, at a distance of 52 nm. The short-range enhancement is treated in terms of single-particle localized surface plasmon resonance [52, 53]. The results largely match the experimental observations (Figure 8.6).

In 1997, Becker *et al*., as part of a larger study, positioned conjugated polymer films at controlled distances from Al mirrors and measured their

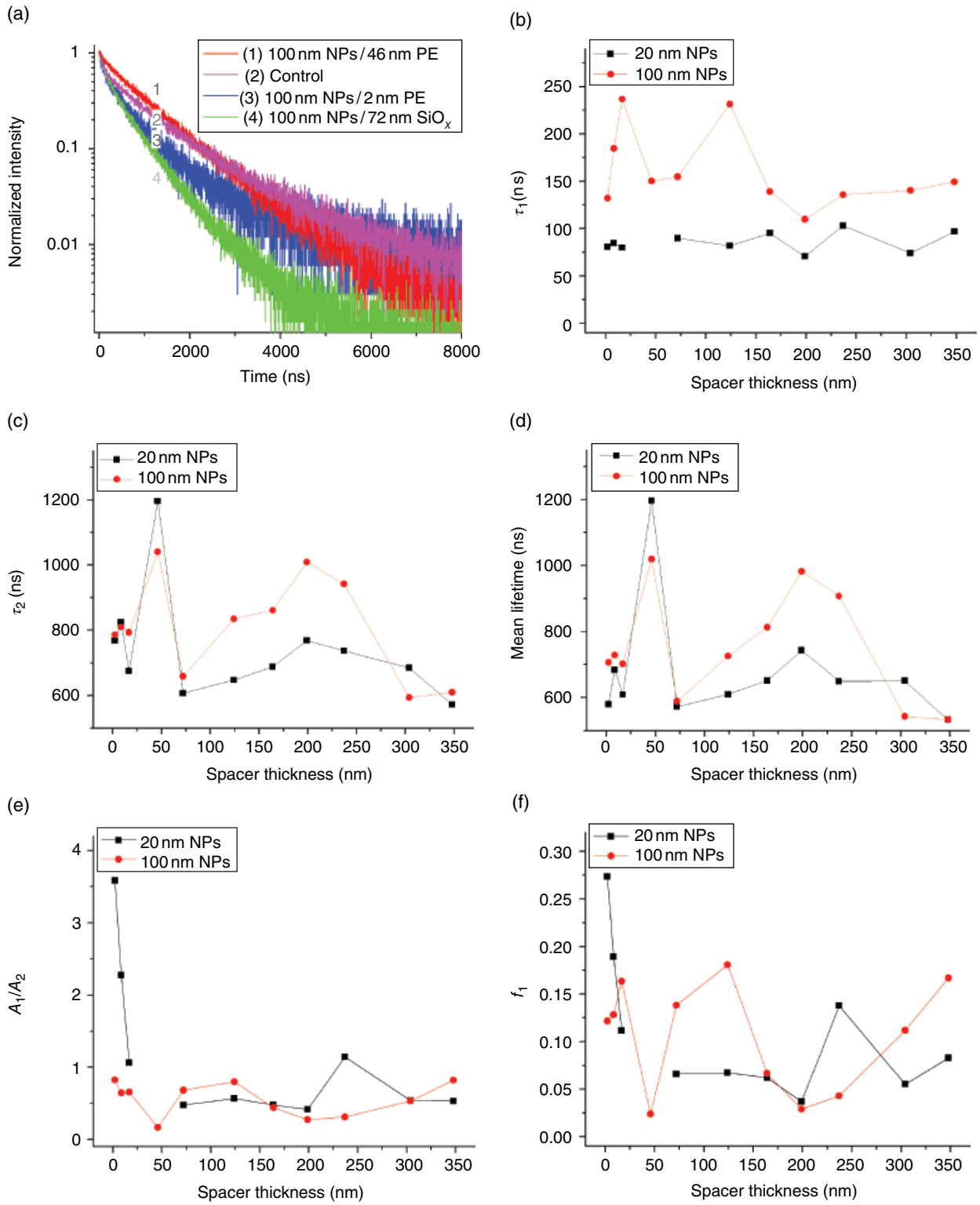

Figure 8.5 (a) Fluorescence decay curves for a control slide and three 100 nm AuNP samples, coated with spacers of different thicknesses (indicated) and $[Ru(bpy)_3]^{2+}$, excited at a wavelength of 355 nm (*See insert for color representation of this figure*); (b–d) the fast decay component lifetime τ_1, slow decay component lifetime τ_2, and mean fluorescence lifetime $\overline{\tau}$, respectively (see text) versus spacer thickness; (e) ratios of the exponential prefactors; (f) the relative contribution of the first exponential term, per Eq. 8.8. The 20 nm NP curve in panels b, e, and f is missing a data point, because the fit for that decay plot produced only a single exponential component, in the τ_2 range of values, and was thus assigned to τ_2. Kedem *et al*. [38]. Reproduced with the permission of Royal Society of Chemistry.

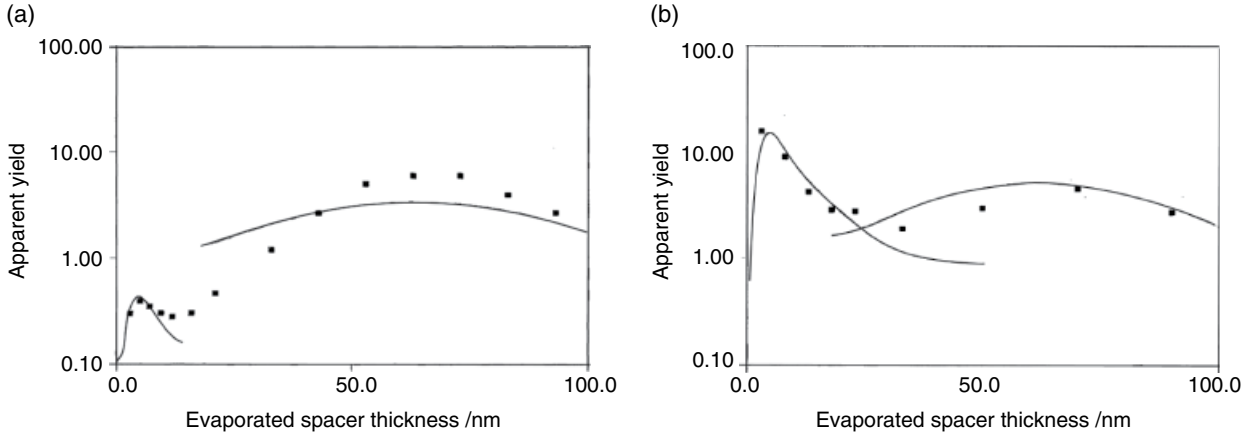

Figure 8.6 Distance-dependent enhancement of the apparent quantum yield of a layer of Rhodamine 6G at (a) 10^{-3} monolayer coverage or (b) full monolayer coverage, separated from a layer of AgNPs by an SiO_2 spacer of varying thickness. Points are the measured experimental results; solid lines are the calculated enhancement (see text). Kummerlen *et al*. [29]. Reproduced with the permission of Taylor & Francis.

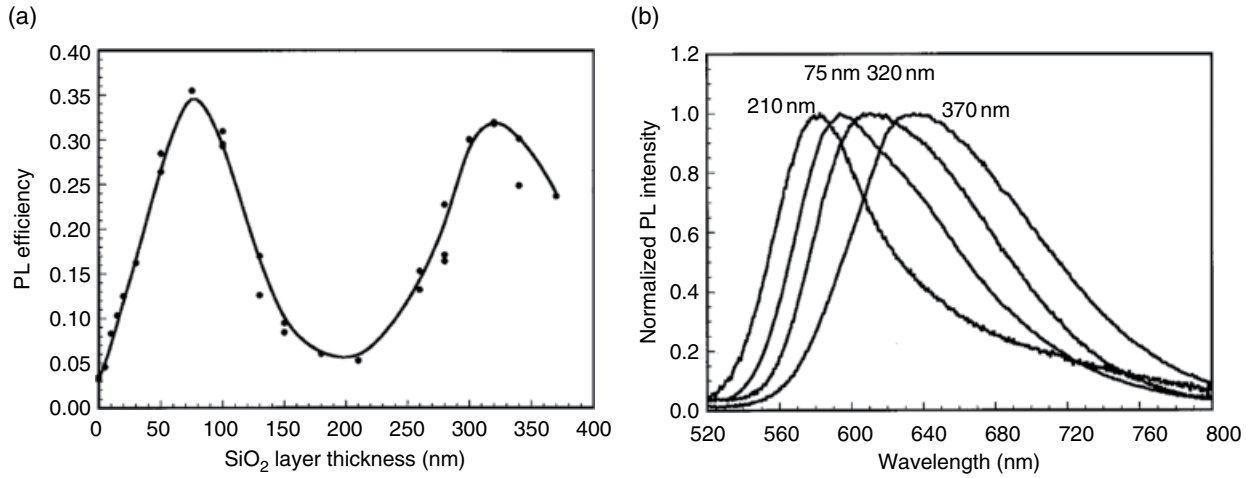

Figure 8.7 Photoluminescence (a) quantum efficiency and (b) spectra of a 15–20 nm thick film of MEH–CN–PPV separated from a 35 nm Al film by SiO_2 spacers of varying thickness. Becker *et al*. [34]. Reproduced with the permission of American Physical Society.

photoluminescence efficiency. They observed a strong oscillation with spacer thickness (Figure 8.7a), which they assigned to interference. They also observed large changes in the emission wavelength (Figure 8.7b), a topic we further discuss in Section 8.3.4.

In our work, we found a similar distance dependence for the two NP sizes used, but with different fluorescence intensities (Figure 8.8b). The fluorescence is strongly quenched at very short separations (~2 nm), increases to a maximum at 60–70 nm separation, and then slowly decreases to the level of the control samples after ~300 nm. For the 100 nm NPs, the peak emission intensity is slightly under five times that of the controls. For the smaller, 20 nm diameter NPs, the whole intensity curve is shifted downward (toward lower emission intensities) compared to the 100 nm NPs, by a factor of about 3.5—even at the maximal separation, the measured emission intensity is only about 0.5 that of the controls. The reason for this across-the-board quenching is unclear. As mentioned earlier, the intensity appears completely uncorrelated with the lifetime (Figure 8.9). Note that even in the absence of any metal–fluorophore interaction, the fluorescence intensity from the Au nanoisland samples is expected to be higher than the controls (glass slides coated with a spacer and fluorophore layer), due to the AuNP film's higher roughness, which leads to correspondingly higher surface coverage.

8.3.4 Emission Wavelength and Linewidth

The emission not only changes in lifetime and intensity with varying emitter–surface separation, but the emission wavelength and linewidth can be affected as well.

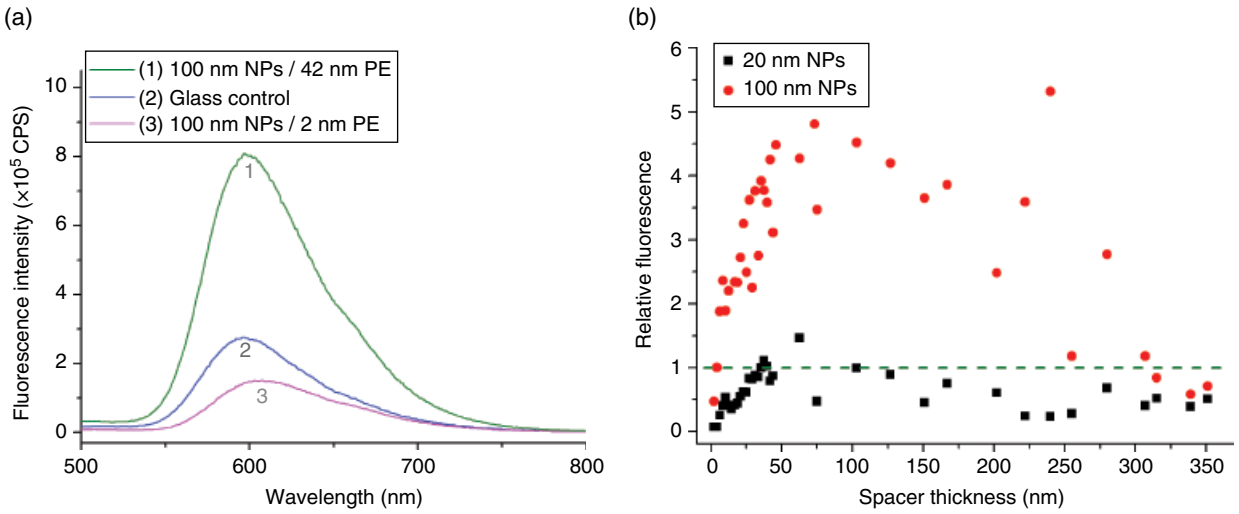

Figure 8.8 (a) Emission spectra for a glass control sample and for 100 nm AuNP samples coated with $[Ru(bpy)_3]^{2+}$ fluorophore on 2 nm and 42 nm polyelectrolyte (PE) spacers; (b) fluorescence intensity, relative to control samples without Au islands (dashed line), for 20 and 100 nm NP samples, coated with various thicknesses of PE (≤72 nm) or SiO_x (≥70 nm). Kedem *et al.* [38]. Reproduced with the permission of Royal Society of Chemistry.

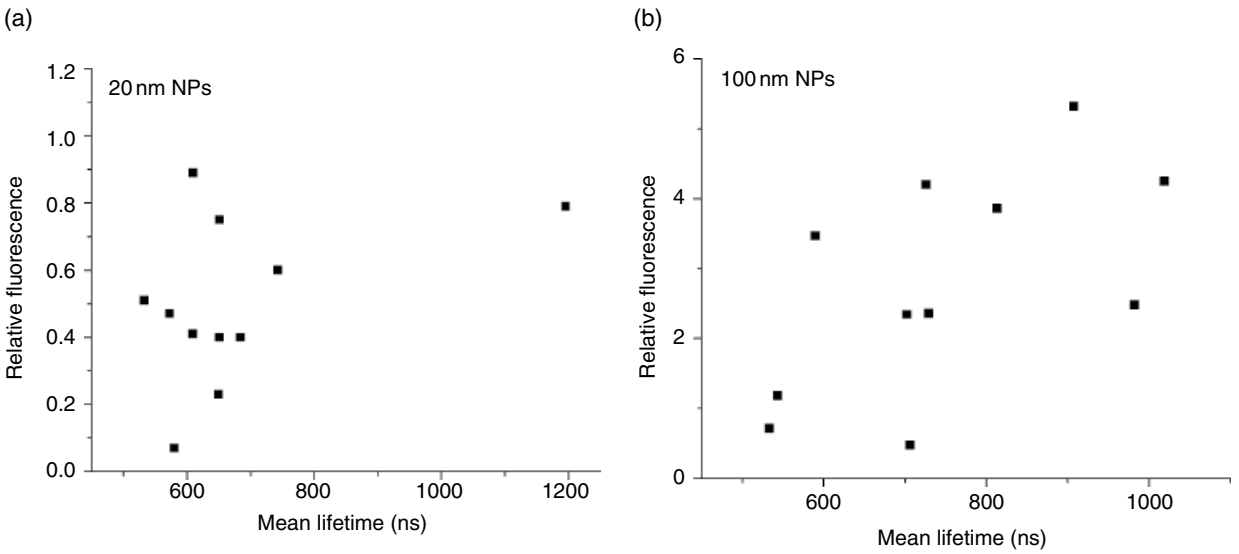

Figure 8.9 Fluorescence intensity (relative to controls), as a function of mean fluorescence lifetime, for $[Ru(bpy)_3]^{2+}$ monolayers on a dielectric spacer of various thicknesses, on (a) 20 nm and (b) 100 nm mean diameter AuNPs, showing the two factors are not correlated. Kedem *et al.* [38]. Reproduced with the permission of Royal Society of Chemistry.

In 1969, Morawitz discussed the self-coupling of a two-level system in front of a mirror and mentioned a shift of the resonant frequency, not observed in experiments, but possibly observable for "sufficiently small distances" [54]. The interaction is explored classically using image theory, which involves considering the retardation of the dipole's reflected radiation field. In 1970, Kuhn developed expressions for both the changes in radiative lifetime, and the shift in emission frequency, stemming from interaction with a reflective boundary, based on image theory with the addition of energy transfer [43]. From his expressions, the predicted shift is completely negligible for any molecule not directly at the boundary. Later, CPS developed a different formulation to Kuhn's for the case of partially reflective surfaces and obtained better agreement with lifetime measurement for short dipole–surface separations [55]. They, too, note that the frequency shift is "negligible for all cases of physical significance." The following

year, Chance *et al*. revisited the issue of frequency shifts in detail and concluded that for partially reflective surfaces, the shift might be significantly larger than for fully reflective surfaces [56]. However, in their treatment, the shift is still subject to a strong monotonic relationship with distance, decaying as d^{-3}, where d is the dipole–surface separation distance.

In 1984 Garoff *et al*. observed large shifts in the emission peak of an Ru complex layer on different surfaces, but were unable to measure the distance relationship, or to pin the source of the observed shift [57]. Kümmerlen *et al*. noted some distance-dependent shifts of the emission maximum, but they were unable to account for them using their proposed model [29]; the shifts were only mentioned in passing, and not presented in the paper. In 1997, Balzer *et al*. measured the fluorescence lifetime and frequency of Na atoms 2–4 nm from Au and Pt surfaces [58]. The measured lifetimes were a factor of two smaller than predicted by a CPS-type model, and the frequency shifts were two orders of magnitude smaller. When they included roughness in the model, using a selvedge region, the predictions approached the measurements, though the fits are still very poor. The image dipole approach predicts the frequency shifts to be larger for emitters with shorter lifetimes [23]. This is strengthened by the observation of large (~10%) shifts in the resonant frequency of Ag nanoislands above an Ag mirror by Holland *et al*. in 1984, as such plasmonic NPs have very short lifetimes [59]. In this type of approach, it can be said that it is the *in-phase* component of the reflected field which changes the emission frequency of the fluorophore, and the *out-of-phase* component which modifies the decay rate (and thus the linewidth) [23].

An especially interesting case was reported in 1997 by Becker *et al*. (mentioned earlier), where the emission band of the conjugated polymer MEH–CN–PPV shifted dramatically as a function of the thickness of a dielectric spacer separating it from an Al mirror (Figure 8.7b) [34]. The authors explore this effect in detail, assigning it to the strong wavelength dependence of the correction factor of the radiative rate, which changes drastically with spacer thickness. They define the modified emission spectrum,

$$S'(\lambda) \propto \frac{g(\lambda)k_R(\lambda)}{\int g(\lambda)k_R(\lambda)d\lambda + K_{NR}} \tag{8.9}$$

where k_R and K_{NR} are the radiative and nonradiative decay rates, respectively; $g(\lambda)$ is a wavelength dependent correction factor to the radiative decay rate, arising from the interaction with the reflective surface. Thus, any change in the wavelength dependence of $g(\lambda)$ with spacer thickness would shift the emission peak. The wavelength dependence of $g(\lambda)$ was extracted from the measured spectra, and matched simulated values.

In our work, we also observed variations in the peak emission wavelength and linewidth of the $[Ru(bpy)_3]^{2+}$ monolayers with distance (Figure 8.10). The peak wavelength and linewidth oscillate with metal–fluorophore separation distance, the wavelength ranging approximately from 600 to 615 nm, and the linewidth (as full width at half maximum, FWHM) from 70 to 100 nm. The values for both the peak wavelength and the linewidth appear similar for both NP sizes, though the values for the 20 nm NPs are much noisier and harder to interpret, whereas those for the 100 nm NPs are more clearly sinusoidal in nature. The oscillation period is ~200 nm, or about 300 nm in optical thickness (as the spacer has a refractive index of about 1.5), half the emission wavelength, as expected for an interference-based phenomenon. The entire emission peak shifts, rather than changing shape asymmetrically (Figure 8.11a).

The amplitude of the observed oscillations in peak wavelength, on the order of 10 nm peak to peak (about 8 THz in this wavelength range) is far larger than predicted by the models discussed by Chance *et al*. [55, 56] or Barnes [23]. The fluorophore in our system has a fairly long lifetime (on the order of 1 μs), which should result in very small shifts. In addition, most predictions are for any appreciable shift to occur only in the immediate vicinity of the metal mirror, and certainly not beyond a few nanometers of separation. However, the shifts are very similar to those discussed and explained by Becker *et al*. [34] and most likely share a common origin.

A possible complication in our study is the variation in the plasmon resonance itself. The plasmon resonance peak wavelength and intensity oscillate with increasing spacer thickness, an effect we have studied in the past, as mentioned earlier [37]. The amplitudes of the oscillations in the plasmon resonance peak are very large, at about 30 nm and 0.15 A.U., for wavelength and intensity, respectively (Figure 8.11b). The oscillation in the emission peak, coupled with those of the plasmonic extinction peak, results in a significant variation in the spectral overlap between the two (Figure 8.11c, d). It could well be that the varying overlap between the plasmon resonance and the fluorophore emission band is partially responsible for the observed oscillation of the emission band.

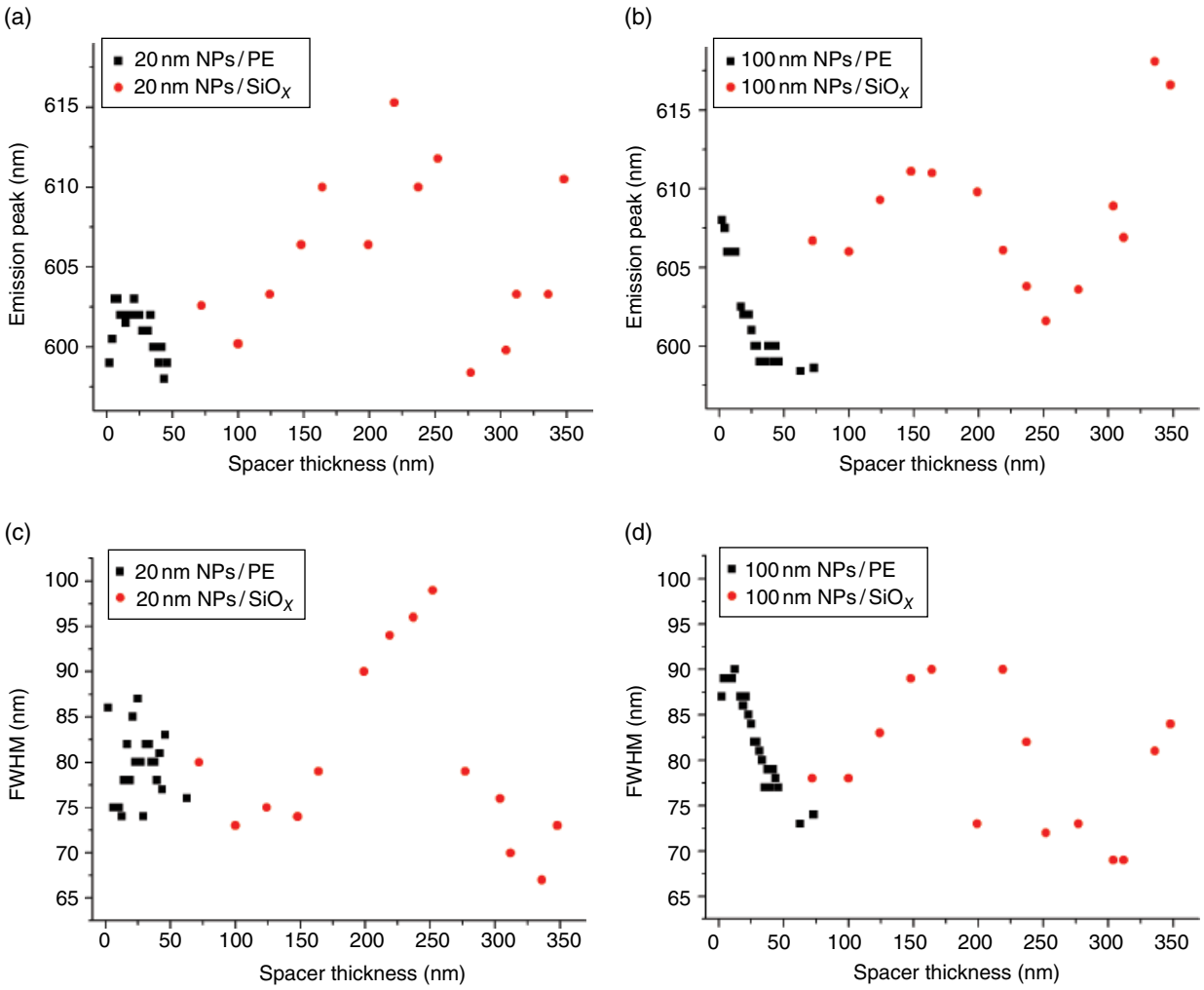

Figure 8.10 Fluorescence emission peak (a, b) wavelength and (c, d) linewidth, as full width at half maximum (FWHM), for (a, c) 20 nm AuNP samples and (b, d) 100 nm NP samples, coated with various thicknesses of PE or SiO_x spacers (indicated). Kedem *et al.* [38]. Reproduced with the permission of Royal Society of Chemistry.

8.4 Conclusions

In this chapter, we explored the effect a continuous or discontinuous metallic film has on luminescent species, at metal–fluorophore separations in the range of hundreds of nanometers. At such distances, the metal film modifies all aspects of the luminescent emission, with a distance-dependent oscillation, arising from the interference of incident and reflected waves. The simple interference picture gives a reasonable approximation of the results at long-range separations, but must be corrected for near-field effects—energy transfer from the excited fluorophores to the radiating or nonradiating states in the metal.

While experiments in the MEF field often treat NP films as composed of isolated NPs, we have seen that collective effects arise in dense films, where the entire film acts, in some aspects at least, as a mirror via far-field interactions. In these cases, interference effects modify the distance-dependent profile of MEF effects, leading to deviations from the expected single NP interaction profile. Thus, it is advantageous to be aware of the existence of such effects and take them into account in the experimental design stage (using films sparse enough to minimize these interactions), or in the analysis stage of the study.

The modification of fluorescent lifetime and intensity at long ranges has been explored in a multitude of experimental systems, and is explained satisfactorily by the models developed over the past few decades. The modification of the shape of emission spectrum, however, is far less well-developed, with contradictory models. This author feels that this aspect of long-range MEF would especially benefit from further work, both experimental and theoretical.

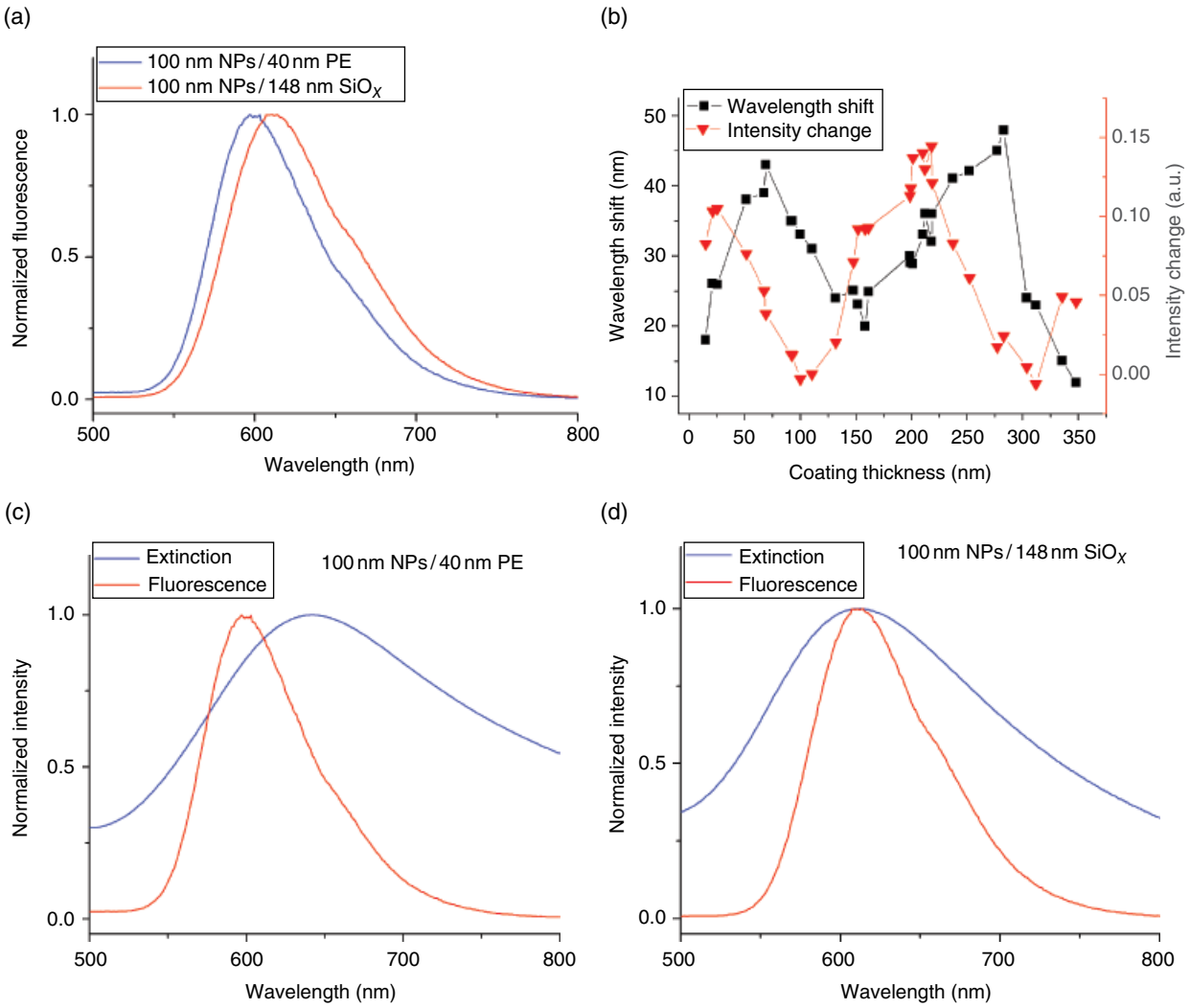

Figure 8.11 (a) Normalized emission spectra for 100 nm NP samples, on two spacer thicknesses; the original, nonnormalized, intensities are very similar. (b) The shift in plasmon resonance wavelength and extinction intensity of 100 nm AuNPs coated with 2–348 nm of SiO_x. The resonance wavelength of pristine 100 nm NPs in extinction mode is 575 nm, and the extinction intensity is about 0.5 absorption units. (c, d) Normalized emission and extinction spectra for two 100 nm NP samples, with a (c) 40 nm PE spacer and (d) 148 nm SiO_x spacer. Kedem *et al.* [37]. Reproduced with the permission of American Chemical Society.

Acknowledgments

The author would like to express his gratitude to his coauthors in the main study presented here (Ref. [38]), Prof. Israel Rubinstein and Dr. Wendel Wohlleben, and to Dr. Gerhard Wagenblast, T. Altenbeck, and Th. Ohmer (BASF SE, Ludwigshafen, Germany) for assisting with the fluorescence lifetime measurements. Support of the work by the Israel Science Foundation, grant No. 1251/11, and by the Gerhardt M. J. Schmidt Minerva Center of Supramolecular Architectures, is gratefully acknowledged.

References

1 Zhao, L.; Ming, T.; Chen, H.; Liang, Y.; Wang, J., Plasmon-Induced Modulation of the Emission Spectra of the Fluorescent Molecules near Gold Nanorods. *Nanoscale* **2011**, *3*, 3849–3859.

2 Klar, T. A.; Feldmann, J., Fluorophore, Metal Nanoparticle Interactions and Their Applications in Biosensing. In *Complex-Shaped Metal Nanoparticles: Bottom-up Syntheses and Applications*, 1st ed.; Sau, T. K.; Rogach, A. L., Eds. Wiley-VCH: Weinheim, **2012**; pp 395–427.

3 Ray, K.; Chowdhury, M. H.; Zhang, J.; Fu, Y.; Szmacinski, H.; Nowaczyk, K.; Lakowicz, J. R., Plasmon-Controlled Fluorescence Towards High-Sensitivity Optical Sensing. In *Optical Sensor Systems in Biotechnology*, Rao, G., Ed. Springer-Verlag Berlin Heidelberg, **2010**; pp 29–72.

4 Fort, E.; Grésillon, S., Surface Enhanced Fluorescence. *J. Phys. D Appl. Phys.* **2008**, *41*, 013001.

5 Lakowicz, J. R.; Geddes, C. D.; Gryczynski, I.; Malicka, J.; Gryczynski, Z.; Aslan, K.; Lukomska, J.; Matveeva, E.; Zhang, J.; Badugu, R.; Huang, J., Advances in Surface-Enhanced Fluorescence. *J. Fluoresc.* **2004**, *14*, 425–441.

6 Ming, T.; Chen, H.; Jiang, R.; Li, Q.; Wang, J., Plasmon-Controlled Fluorescence: Beyond the Intensity Enhancement. *J. Phys. Chem. Lett.* **2012**, *3*, 191–202.

7 Biteen, J. S.; Lewis, N. S.; Atwater, H. A.; Mertens, H.; Polman, A., Spectral Tuning of Plasmon-Enhanced Silicon Quantum Dot Luminescence. *Appl. Phys. Lett.* **2006**, *88*, 131109.

8 Aslan, K.; Geddes, C. D., Metal-Enhanced Chemiluminescence: Advanced Chemiluminescence Concepts for the 21st Century. *Chem. Soc. Rev.* **2009**, *38*, 2556–2564.

9 Zhang, Y.; Aslan, K.; Malyn, S.; Geddes, C. D., Metal-Enhanced Phosphorescence (MEP). *Chem. Phys. Lett.* **2006**, *427*, 432–437.

10 Zhang, Y.; Aslan, K.; Previte, M. J. R.; Malyn, S. N.; Geddes, C. D., Metal-Enhanced Phosphorescence: Interpretation in Terms of Triplet-Coupled Radiating Plasmons. *J. Phys. Chem. B* **2006**, *110*, 25108–25114.

11 Lakowicz, J. R.; Ray, K.; Chowdhury, M.; Szmacinski, H.; Fu, Y.; Zhang, J.; Nowaczyk, K., Plasmon-Controlled Fluorescence: A New Paradigm in Fluorescence Spectroscopy. *Analyst* **2008**, *133*, 1308–1346.

12 Tanaka, H.; Mitsuishi, M.; Miyashita, T., Luminescence Enhancement of Ruthenium Complexes in Polymer Nanosheet by Surface Plasmon Resonance of Metal Nanoparticle. *Chem. Lett.* **2005**, *34*, 1246–1247.

13 Pompa, P. P.; Martiradonna, L.; Torre, A. D.; Sala, F. D.; Manna, L.; De Vittorio, M.; Calabi, F.; Cingolani, R.; Rinaldi, R., Metal-Enhanced Fluorescence of Colloidal Nanocrystals with Nanoscale Control. *Nat. Nanotechnol.* **2006**, *1*, 126–130.

14 Stranik, O.; Nooney, R. I.; McDonagh, C.; MacCraith, B. D., Optimization of Nanoparticle Size for Plasmonic Enhancement of Fluorescence. *Plasmonics* **2007**, *2*, 15–22.

15 Zhang, Y.; Dragan, A.; Geddes, C. D., Wavelength Dependence of Metal-Enhanced Fluorescence. *J. Phys. Chem. C* **2009**, *113*, 12095–12100.

16 Singh, M. P.; Strouse, G. F., Involvement of the LSPR Spectral Overlap for Energy Transfer between a Dye and Au Nanoparticle. *J. Am. Chem. Soc.* **2010**, *132*, 9383–9391.

17 Chen, Y.; Munechika, K.; Ginger, D. S., Dependence of Fluorescence Intensity on the Spectral Overlap between Fluorophores and Plasmon Resonant Single Silver Nanoparticles. *Nano Lett.* **2007**, *7*, 690–696.

18 Lakowicz, J. R.; Shen, Y.; D'Auria, S.; Malicka, J.; Fang, J.; Gryczynski, Z.; Gryczynski, I., Radiative Decay Engineering. 2. Effects of Silver Island Films on Fluorescence Intensity, Lifetimes, and Resonance Energy Transfer. *Anal. Biochem.* **2002**, *301*, 261–277.

19 Chan, Y.-H.; Chen, J.; Wark, S. E.; Skiles, S. L.; Son, D. H.; Batteas, J. D., Using Patterned Arrays of Metal Nanoparticles to Probe Plasmon Enhanced Luminescence of Cdse Quantum Dots. *ACS Nano* **2009**, *3*, 1735–1744.

20 Ray, K.; Badugu, R.; Lakowicz, J. R., Polyelectrolyte Layer-by-Layer Assembly to Control the Distance between Fluorophores and Plasmonic Nanostructures. *Chem. Mater.* **2007**, *19*, 5902–5909.

21 Gu, X.; Wu, Y.; Zhang, L.; Liu, Y.; Li, Y.; Yan, Y.; Wu, D., Hybrid Magnetic Nanoparticle/Nanogold Clusters and Their Distance-Dependent Metal-Enhanced Fluorescence Effect Via DNA Hybridization. *Nanoscale* **2014**, *6*, 8681–8693.

22 Fermi, E., Quantum Theory of Radiation. *Rev. Mod. Phys.* **1932**, *4*, 87–132.

23 Barnes, W. L., Fluorescence near Interfaces: The Role of Photonic Mode Density. *J. Mod. Opt.* **1998**, *45*, 661–699.

24 Malicka, J.; Gryczynski, I.; Gryczynski, Z.; Lakowicz, J. R., Effects of Fluorophore-to-Silver Distance on the Emission of Cyanine-Dye-Labeled Oligonucleotides. *Anal. Biochem.* **2003**, *315*, 57–66.

25 Akbay, N.; Lakowicz, J. R.; Ray, K., Distance-Dependent Metal-Enhanced Intrinsic Fluorescence of Proteins Using Polyelectrolyte Layer-by-Layer Assembly and Aluminum Nanoparticles. *J. Phys. Chem. C* **2012**, *116*, 10766–10773.

26 Nooney, R. I.; Stranik, O.; McDonagh, C.; MacCraith, B. D., Optimization of Plasmonic Enhancement of Fluorescence on Plastic Substrates. *Langmuir* **2008**, *24*, 11261–11267.

27 Wokaun, A.; Lutz, H.-P.; King, A. P.; Wild, U. P.; Ernst, R. R., Energy Transfer in Surface Enhanced Luminescence. *J. Chem. Phys.* **1983**, *79*, 509–514.

28 Teng, Y.; Ueno, K.; Shi, X.; Aoyo, D.; Qiu, J.; Misawa, H., Surface Plasmon-Enhanced Molecular Fluorescence Induced by Gold Nanostructures. *Ann. Phys.* **2012**, *524*, 733–740.

29 Kümmerlen, J.; Leitner, A.; Brunner, H.; Aussenegg, F. R.; Wokaun, A., Enhanced Dye

Fluorescence over Silver Island Films: Analysis of the Distance Dependence. *Mol. Phys.* **1993**, *80*, 1031–1046.

30 Klimov, V. V.; Ducloy, M.; Letokhov, V. S., Spontaneous Emission of an Atom in the Presence of Nanobodies. *Quantum Electron.* **2001**, *31*, 569–586.

31 Lakowicz, J. R., Radiative Decay Engineering: Biophysical and Biomedical Applications. *Anal. Biochem.* **2001**, *298*, 1–24.

32 Lakowicz, J. R., Radiative Decay Engineering 5: Metal-Enhanced Fluorescence and Plasmon Emission. *Anal. Biochem.* **2005**, *337*, 171–194.

33 Lakowicz, J. R.; Malicka, J.; Gryczynski, I.; Gryczynski, Z.; Geddes, C. D., Radiative Decay Engineering: The Role of Photonic Mode Density in Biotechnology. *J. Phys. D Appl. Phys.* **2003**, *36*, R240–R249.

34 Becker, H.; Burns, S.; Friend, R., Effect of Metal Films on the Photoluminescence and Electroluminescence of Conjugated Polymers. *Phys. Rev. B* **1997**, *56*, 1893–1905.

35 Sannomiya, T.; Balmer, T. E.; Hafner, C.; Heuberger, M.; Vörös, J., Optical Sensing and Determination of Complex Reflection Coefficients of Plasmonic Structures Using Transmission Interferometric Plasmonic Sensor. *Rev. Sci. Instrum.* **2010**, *81*, 053102.

36 Corrigan, T. D.; Guo, S.; Szmacinski, H.; Phaneuf, R. J., Enhanced Fluorescence from Periodic Arrays of Silver Nanoparticles. *J. Fluoresc.* **2005**, *15*, 777–784.

37 Kedem, O.; Sannomiya, T.; Vaskevich, A.; Rubinstein, I., Oscillatory Behavior of the Long-Range Response of Localized Surface Plasmon Resonance Transducers. *J. Phys. Chem. C* **2012**, *116*, 26865–26873.

38 Kedem, O.; Wohlleben, W.; Rubinstein, I., Distance-Dependent Fluorescence of Tris(Bipyridine) Ruthenium(II) on Supported Plasmonic Gold Nanoparticle Ensembles. *Nanoscale* **2014**, *6*, 15134–15143.

39 Kedem, O.; Tesler, A. B.; Vaskevich, A.; Rubinstein, I., Sensitivity and Optimization of Localized Surface Plasmon Resonance Transducers. *ACS Nano* **2011**, *5*, 748–760.

40 Karakouz, T.; Tesler, A. B.; Bendikov, T. A.; Vaskevich, A.; Rubinstein, I., Highly Stable Localized Plasmon Transducers Obtained by Thermal Embedding of Gold Island Films on Glass. *Adv. Mater.* **2008**, *20*, 3893–3899.

41 Karakouz, T.; Tesler, A. B.; Sannomiya, T.; Feldman, Y.; Vaskevich, A.; Rubinstein, I., Mechanism of Morphology Transformation During Annealing of Nanostructured Gold Films on Glass. *Phys. Chem. Chem. Phys.* **2013**, *15*, 4656–4665.

42 Tesler, A. B.; Chuntonov, L.; Karakouz, T.; Bendikov, T. A.; Haran, G.; Vaskevich, A.; Rubinstein, I., Tunable Localized Plasmon Transducers Prepared by Thermal Dewetting of Percolated Evaporated Gold Films. *J. Phys. Chem. C* **2011**, *115*, 24642–24652.

43 Kuhn, H., Classical Aspects of Energy Transfer in Molecular Systems. *J. Chem. Phys.* **1970**, *53*, 101–108.

44 Drexhage, K. H., Influence of a Dielectric Interface on Fluorescence Decay Time. *J. Lumin.* **1970**, *1–2*, 693–701.

45 Drexhage, K. H., Interaction of Light with Monomolecular Dye Layers. In *Progress in Optics XII*, Wolf, E., Ed. North-Holland, Amsterdam, **1974**; pp 163–232.

46 Chance, R. R.; Miller, A. H.; Prock, A.; Silbey, R., Fluorescence and Energy Transfer near Interfaces: The Complete and Quantitative Description of the Eu^{+3}/Mirror Systems. *J. Chem. Phys.* **1975**, *63*, 1589–1595.

47 Chance, R. R.; Prock, A.; Silbey, R., Molecular Fluorescence and Energy Transfer near Interfaces. In *Advances in Chemical Phyics*, Prigogine, I.; Rice, S. A., Eds. John Wiley & Sons, Hoboken, NJ, USA: **1978**; Vol. *37*, pp 1–65.

48 Amos, R. M.; Barnes, W. L., Modification of the Spontaneous Emission Rate of Eu^{3+} Ions Close to a Thin Metal Mirror. *Phys. Rev. B* **1997**, *55*, 7249–7254.

49 Amos, R.; Barnes, W., Modification of Spontaneous Emission Lifetimes in the Presence of Corrugated Metallic Surfaces. *Phys. Rev. B* **1999**, *59*, 7708–7714.

50 Andrew, P.; Barnes, W. L., Molecular Fluorescence above Metallic Gratings. *Phys. Rev. B* **2001**, *64*, 125405.

51 Toma, M.; Toma, K.; Adam, P.; Homola, J.; Knoll, W.; Dostálek, J., Surface Plasmon-Coupled Emission on Plasmonic Bragg Gratings. *Opt. Express* **2012**, *20*, 14042.

52 Gersten, J.; Nitzan, A., Spectroscopic Properties of Molecules Interacting with Small Dielectric Particles. *J. Chem. Phys.* **1981**, *75*, 1139.

53 Gersten, J. I.; Nitzan, A., Photophysics and Photochemistry near Surfaces and Small Particles. *Surf. Sci.* **1985**, *158*, 165–189.

54 Morawitz, H., Self-Coupling of a Two-Level System by a Mirror. *Phys. Rev.* **1969**, *187*, 1792–1796.

55 Chance, R. R.; Prock, A.; Silbey, R., Lifetime of an Emitting Molecule near a Partially Reflecting Surface. *J. Chem. Phys.* **1974**, *60*, 2744.

56 Chance, R.; Prock, A.; Silbey, R., Frequency Shifts of an Electric-Dipole Transition near a Partially Reflecting Surface. *Phys. Rev. A* **1975**, *12*, 1448–1452.

57 Garoff, S.; Weitz, D. A.; Alvarez, M. S.; Gersten, J. I., Electrodynamics at Rough Metal Surfaces: Photochemistry and Luminescence of Adsorbates near Metal-Island Films. *J. Chem. Phys.* **1984**, *81*, 5189.

58 Balzer, F.; Bordo, V. G.; Rubahn, H. G., Frequency Shifts and Lifetime Changes of Sodium Atoms near Rough Metal Surfaces. *Opt. Lett.* **1997**, *22*, 1262–1264.

59 Holland, W. R.; Hall, D. G., Frequency Shifts of an Electric-Dipole Resonance near a Conducting Surface. *Phys. Rev. Lett.* **1984**, *52*, 1041–1044.

9

Evolution, Stabilization, and Tuning of Metal-Enhanced Fluorescence in Aqueous Solution

Jayasmita Jana[1], Mainak Ganguly[2], and Tarasankar Pal[1]

[1] *Department of Chemistry, Indian Institute of Technology, Kharagpur, India*
[2] *Department of Chemistry, Furman University, Greenville, SC, USA*

9.1 Introduction

Fluorescence quantification is a spectroscopic technique that is used widely for recording various molecular events [1–3]. The emission of light at a longer wavelength by an excited molecule provides lots of information about the molecule. Exceptionally higher sensitivity of the fluorescence spectroscopy than other common spectroscopic techniques is inherited by high signal to noise ratio. The limit of detection (LOD) in this technique can easily be manipulated by changing the physical conditions of the fluorescing molecule [4]. Fluorescent materials are widely used in sensing, optical imaging, cell imaging, optical device making, signaling, ink, pigment, drug delivery, and biomarker. In biological research including single molecule detection, cellular imaging, gene profiling, proteomics, drug discovery, and disease diagnostic, the fluorescence technique has become a popular vocabulary. Fluorescent markers are very efficiently introduced for labeling and cell imaging. However, this technique is applicable only for molecules with inherent fluorescence that often suffers from two major drawbacks: weak fluorescence signal from low concentration of fluorophores and low photostability of molecular fluorophores [5]. The quantum yield of the materials can be improved by bringing foreign materials like electron-rich metals near the fluorescing system. The enhancement of fluorescence intensity of a weak fluorophore in conjugation of a metal surface is termed as metal-enhanced fluorescence (MEF). The term MEF was first introduced by Geddes in 2002 [6]. Metal nanoparticles (MNPs) work as nanoantennas that frequently manipulate light and light–matter interactions at the nanoscale [7]. Metal particles possess free electrons that resonate with the incidence of light of appropriate wavelength. When the frequency of the incident light matches with the oscillation of the electrons of metal against the restoring force of nucleus of the metal, there arises a resonance condition. This phenomenon is termed as surface plasmon resonance (Figure 9.1). The resonance condition, determined from absorption and scattering spectroscopy, depends on the morphology, size, and dielectric constants of both the metal and the adjacent materials. With the change in shape or size of the nanoparticle, the geometry of the surface alters, causing a shift in the electric field density on the metal surface. In the presence of metal surface, the excitation as well as emission characteristics of fluorophore can be changed in terms of modification in molecular cross section. Again it is well established that the nearby surface alters the "free-space" condition of a fluorophore and follows the modified Maxwell's equation from their free-space counterparts [8–10]. It is clear from the Jablonski diagram (Figure 9.2a), where a fluorophore is excited from the ground state S_0 to the first excited state S_1 considered it may emit a photon at the rate of Γ. Again non-radiative decay at a rate of k_{nr} or quenching process with a rate k_q after a time τ_0 may occur. Then the quantum yield, Q_0, and lifetime τ_0 will be

$$Q_0 = \frac{\Gamma}{\Gamma + k_q + k_{nr}},$$

and

$$\tau_0 = \frac{1}{\Gamma + k_q + k_{nr}}.$$

However when an MNP is present at a suitable distance from the fluorophore, the decay rate changes to $(\Gamma + \Gamma_M)$ (Γ_M corresponds to the decay from MNP). Then there occurs an increase in quantum yield, Q_M, and decrease in lifetime, τ_M, listed as follows:

Surface Plasmon Enhanced, Coupled and Controlled Fluorescence, First Edition. Edited by Chris D. Geddes.
© 2017 John Wiley & Sons, Inc. Published 2017 by John Wiley & Sons, Inc.

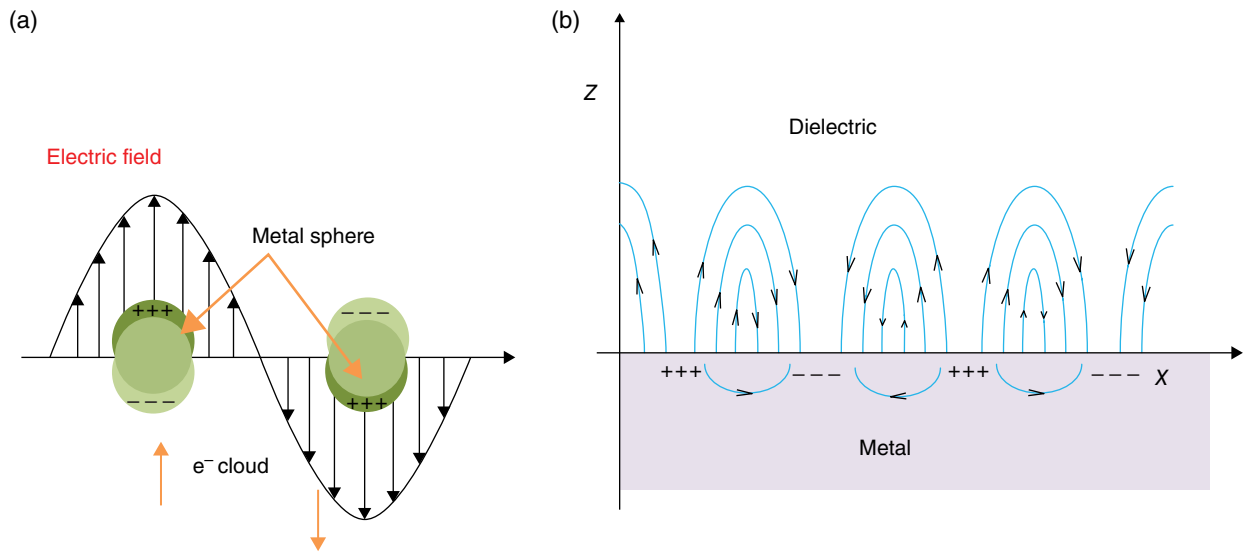

Figure 9.1 Pictorial depiction of SPR. (a) Localized surface plasmon resonance. (b) Surface plasmon polariton.

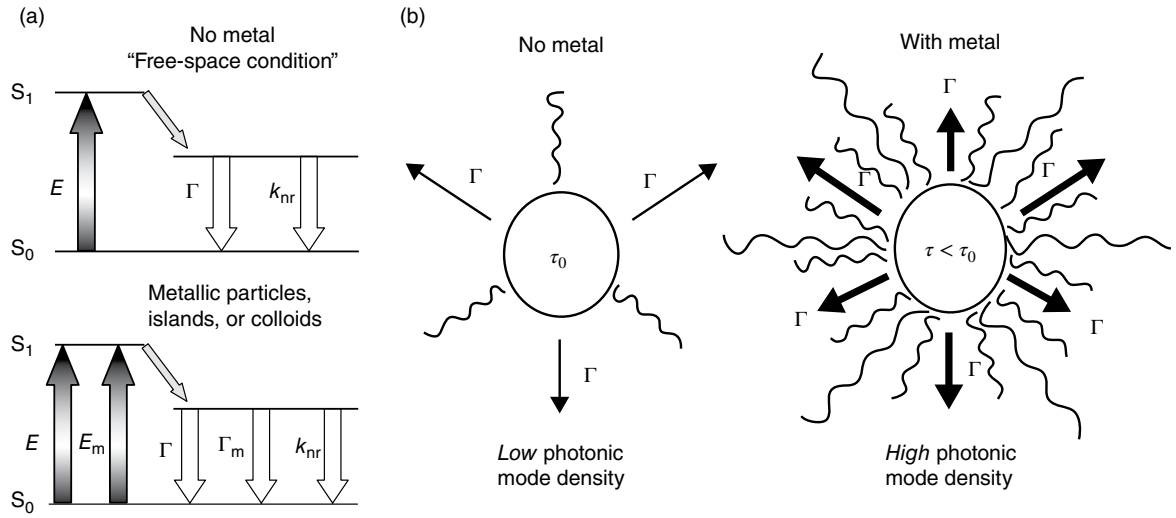

Figure 9.2 (a) Classical Jablonski diagram for the free-space condition and the modified form in the presence of metallic particles, islands or colloids. E-excitation, Em-metal enhanced excitation rate, and Γm-radiative rate in the presence of metal. (b) Low- and high-photonic mode densities in the absence and presence of metal, respectively. Geddes and Lakowicz [6]. Reproduced with the permission of Springer.

$$Q_M = \frac{\Gamma + \Gamma_M}{\Gamma + \Gamma_M + k_q + k_{nr}},$$

and

$$\tau_M = \frac{1}{\Gamma + \Gamma_M + k_q + k_{nr}}.$$

Conducting MNPs can manipulate free-space conditions by [7] altering the incident electric field on the fluorophore and changing the radiative decay [11–13]. These effects can be elucidated by the variation of photonic mode density. Large photonic density is associated with the radiative decay rates and increasing the number of pathways available to discharge the excited energy [6]. Figure 9.2b shows the photonic mode densities of a fluorophore in absence and in presence of a metal. In the absence of metal, the fluorophore possesses higher radiative lifetime (τ_0) and lower photonic density, whereas the presence of metal decreases the radiative lifetime (τ_m) and enhances the photonic mode density. A fluorophore is considered as an oscillating dipole, just like a radiating antenna. Proximate metal surfaces very often respond to the oscillating dipole, resulting in the modification of the emission rate and the spatial distribution of the radiated energy. Interactions between the metal surface and the incident light as well as oscillating dipole of the fluorophore affect the electric field. This can be sensed by a fluorophore. Besides, the oscillating dipoles of fluorophores induce a field on the metal. Such

interactions can manipulate the incident field on the fluorophore and also the radiative decay rate. In short, two complementary effects are found in literature [14] in the context of MEF: (i) enhanced absorption assisted enhanced emission ("lightening rod effect") and (ii) surface plasmons can radiate coupled fluorescence efficiently. The emission directionality in the prism and its exceptional polarization properties imply that the radiation occurs from surface plasmons that are induced in the metal by the closely situated excited fluorophores. However, the wavelength distribution of the emission matches accurately with the normal emission spectra. This phenomenon is called as surface plasmon–coupled emission (SPCE) [15]. The radiating plasmon (RP) model suggests the far-field radiation originated from scattering to be responsible for the observed fluorescence intensity [15]. The extent of the enhancement lies in the geometry of the metallic nanostructures. The size and shape contribute to different surface plasmonic modes with drastic enhancement of the fluorescence signals at "hotspots" [16]. At very close proximity (<20 nm), the lifetime of the fluorophore drops dramatically and the emission intensity is strongly reduced. This quenching effect in the proximity of MNPs has been attributed to lossy surface waves (LSWs), dissipated losses, ohmic losses, and such similar phenomena, all of which are examples of non-radiative dissipation of energy within metals [16]. MEF can be enhanced by increasing the near field around the fluorophore and emission efficiency through nanoparticle scattering and improvement of the radiative decay rate of close fluorophores along with a change in the fluorescence quantum yield and lifetime [17].

9.1.1 Coinage Metal Nanoparticles in Metal-Enhanced Fluorescence

Fluorescence measurement in bulk samples is a very common practice where the solutions are typically transparent to the emitted radiation, and isotropic emission of the fluorophore in the free space is observed in the far field. An alteration of refractive index is the main consequence of it. Free-space spectral properties of the fluorophore are very minutely influenced with the change of refractive index [6]. To explain the huge change of fluorescence near metallic surface, modifications of free-space conditions of the fluorophore have come into the field since a decade. Intense narrow surface plasmon band (SPB) has provoked researchers to study silver and gold nanoparticles (AuNPs) in the context of MEF. The free electrons present in the metal (d electrons in silver and gold) freely travel through the material. As the mean free path in gold and silver is 50 nm, the particles, smaller than this, show no scattering like the bulk. When the wavelength of light is much longer than the size of the nanoparticle, it can establish standing resonance condition [18].

Lakowicz *et al.* considered the silver island films (SIFs) as interesting candidates for escalating the intensities and photostability of fluorophores with low quantum yields [19]. SIFs can cause quenching, increased rates of excitation, and/or increased quantum yields depending upon the way of interaction with the fluorophore [6]. Not only SIFs but also other various silver surfaces like silver colloids [20], silver nanotriangles [21], silver nanorods [22], and fractal-like silver surfaces [23] are found to be active in the context of MEF. The MEF for silver can be explained in terms of RP model [24] (Figure 9.3).

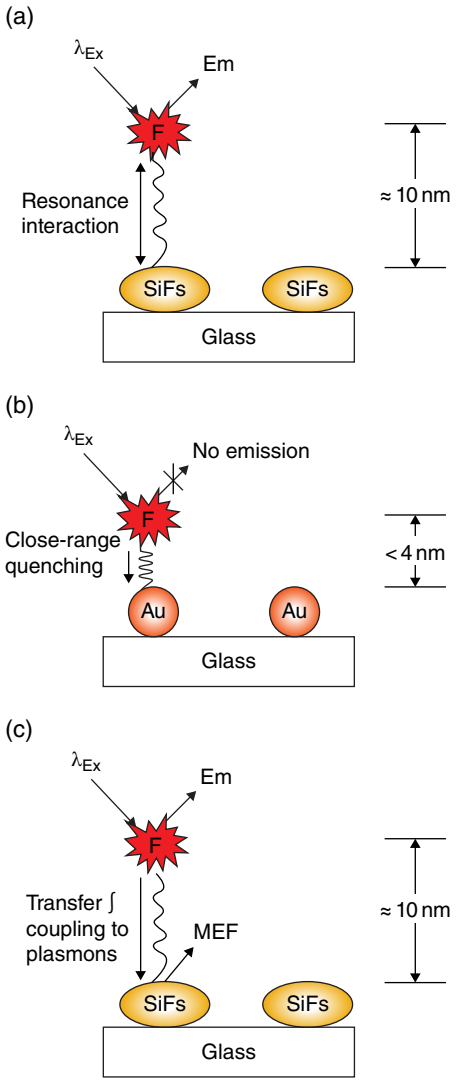

Figure 9.3 Graphical representation of original interpretation of metal enhanced fluorescence (a), close range metal quenching of fluorescence (b) and current interpretation for metal-enhanced fluorescence (c). F Fluorophore, MEF metal-enhanced fluorescence, Au small gold nanoparticles, SiFs Silver Island Films. Zhang *et al.* [24]. Reproduced with the permission of Springer.

Colloidal suspension over films has an advantage that it has a homogeneous distribution of metals and their possible promising impregnation for medical imaging. But a lot of interactions in solution phase make the study complicated. Moreover, to position the metals at a right distance in the solution phase is very difficult to maintain. An interesting report by Aslan *et al*. [25] to produce MEF in solution has been found to be a potential sensing platform. Again, the Tb^{3+} complex of salicylic-based open-chain crown ether possesses enhanced fluorescence in silver chloride collosol [26]. A study by Gill *et al*. demonstrates that dye-DNA composite becomes extremely fluorescent with silver nanoaggregates [27].

Not only silver (Ag) but also gold (Au) and copper (Cu) are known to exhibit MEF. However there are more reports on silver-enhanced fluorescence (SEF) [19–23, 28] as Ag has a more favorable imaginary component in the dielectric function than Au and Cu. The absorption cross section relies on the imaginary component of the metal and it is higher for Cu than Au or Ag. So, close proximity of the fluorophore will cause mostly quenching by the copper nanoparticles (CuNPs). Again, copper also has a scattering component responsible for the MEF effect [29].

However AuNPs can enhance or quench fluorescence depending on the fluorophore–particle separation distance, molecular dipole orientation with respect to particle surface, and size of the nanoparticle [30–33]. It is found that comparatively smaller (<30 nm) AuNPs quench the fluorescence emission due to the non-radiative transfer from the excited states of luminophores to the AuNPs [31, 32]. The scattering efficiency of the nanoparticles is increased with particle size resulting in improved fluorescence [30–34]. Further conformation for the fact that larger aggregated colloids enhance the fluorescence to a larger extent than the smaller ones came from Lukomska *et al*. [35].

Cu possesses a very large value of the imaginary component of dielectric constant (more than twice) than that of noble metals in the wavelength range of 300–600 nm. Hence, it is expected that in this wavelength range CuNPs have a tendency to quench the luminescence at their close proximity owing to greater ohmic losses [28]. However, for large nanoparticles (>100 nm) with high aspect ratio, the increase of coupling efficiency of the fluorescence emission to the far field through nanoparticle scattering excels MEF. In this case, as effect of ohmic losses on MEF is decreased, less expensive metals such as Al and Cu, which are more lossy than Ag and Au, can be considered as promising candidates for fluorescence enhancement [36].

9.2 Metal-Enhanced Fluorescence in Solution Phase

Generally MEF is obtained in solid phase. Most of them are reported for metals on solid support kept at a certain distance from the fluorophore using suitable experimental setup [19–23, 25–36]. However MEF in solution phase is quite rare. In solution it is difficult to maintain the exact distance from the fluorophore surface. There are only few reports of MEF in solution phase. Some of them report about silicon oxide-coated AgNPs for the enhancement of fluorescence of dye [37]. To attain MEF in solution phase, the selection of spacers in fluorophore is important. The spacers maintain suitable distance between MNPs and fluorophore. Zhang *et al*. found ~90-fold fluorescence enhancement by doping dye molecules into a ZnO nanomatrix [38]. DNA sequences can also be applied as the spacer to adjust the distance between dye molecules and the metal core [39]. However, DNA spacers require strict experimental conditions, such as pH and temperature. Sometimes silica layers are also useful [37].

9.2.1 Metal-Enhanced Fluorescence from Metal(0) in Solution

9.2.1.1 Silver- and Gold-Enhanced Fluorescence

Salicylaldehyde (SL) is a small organic moiety that shows fluorescence with low intensity. Again, alkaline SL solution shows weaker fluorescence with an emission maximum at 509 nm. When SL is mixed with $AgNO_3$ and irradiated under 365 nm ultraviolet (UV) light for an hour (concentration ratio $[SL]/[Ag^+] = 1$), followed by 2 days of aging, an intensely strong fluorescent solution (AgSQSL) is generated with an emission maximum at ~424 nm (Figure 9.4). In the solution, SL is oxidized quantitatively to quinone (SQSL) through the semiquinone pathway by losing an electron [17, 40] and eventually generates Ag(0) particles from Ag(I) (Figure 9.5). Formation of Ag(0) particles is confirmed by the X-ray photoelectron spectroscopy (XPS), selected area electron diffraction (SAED), and lattice fringe data [41, 42] (Figure 9.4). The as-synthesized silver nanoparticles (AgNPs) become highly aggregated. Such increment in the fluorescence intensity in the presence of *in situ*-produced AgNPs is denoted as SEF. SQSL behaves as a plasmophore that irradiates at the far field with intriguingly increased fluorescence in the presence of proximal Ag(0). However, when Ag(I) remains absent during exposure of alkaline SL under UV light, the solution exhibits fluorescence quenching (in comparison with unexposed alkaline SL) with a blueshifted emission band at 430 nm (due to SQSL) along with the original emission band at ~509 nm (due to phenolate) (Figure 9.4). Thus it has been assumed that Ag(I) causes quantitative conversion of SL into

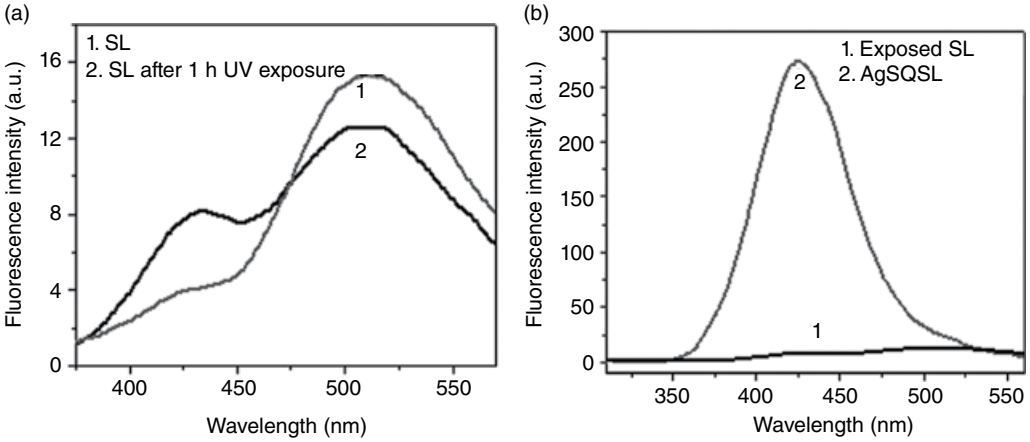

Figure 9.4 Fluorescence spectral profile of (a) SL and SL after 1 h UV exposure and (b) AgSQSL and SL after 1 h UV exposure in alkaline medium. Conditions: [SL] = 1.4×10^{-4}M, [Ag^{I}] = 1.4×10^{-4}M, λ_{ex} = 290 nm. Ganguly *et al.* [17]. Reproduced with the permission of John Wiley & Sons, Inc.

SQSL along with a very large fluorescence enhancement and hypsochromic shift (~6 nm) of the emission band of SQSL (Figure 9.5). This is due to *in situ*-produced Ag(0) at the proximity of Ag(0). SL is the smallest molecule reported so far for SEF or rather MEF. The gold-enhanced fluorescence (GEF) is also observed for SL as the SEF. Upon UV exposure of the alkaline mixture of $HAuCl_4$ and SL for an hour followed by a 2-day aging results in an excellent GEF phenomenon (highly fluorescent solution has been termed as AuSQSL with an emission maximum at 418 nm). However for the same condition along with same concentration ratio of SL and metal, where metal is either Au or Ag (i.e., ratio = 1), Au shows higher enhancement in fluorescence intensity. The possible reduction of Au(III) to Au(0), via quinone (SQSL) formation pathway, is similar to that for Ag(I). The XPS analysis confirms the presence of Au(0) (Figure 9.4). In both the cases, the substantial binding energy shift toward lower energy site (~1.8 eV) in the XPS spectra indicated the efficient capping property of SQSL. Fringe spacings of 0.235 nm and 0.236 nm indicate (111) plane for Ag(0) and Au(0), respectively. It may be apprehended that the increment in fluorescence is due to chelate-enhanced fluorescence (CHEF), but the zero oxidation state of metals (Au/Ag) rules out the idea [43, 44].

However, no characteristic plasmonic band is obtained for the as-synthesized Ag(0)/Au(0). Hence, there arose a doubt whether this enhanced fluorescence is due to the ultrasmall silver clusters admixed with aggregated particles, as ultrasmall clusters are highly fluorescent [45, 46]. However, positively charged surface is known to stabilize noble metal clusters [47, 48]. In strongly alkaline solution, fluorescent cluster formation is quite unlikely, as they get aggregated forming non-fluorescent nanocrystals [49]. Thiolate groups are usually important during the synthesis of the fluorescent clusters [49, 50]. Furthermore, emission maximum of such clusters appears at >550 nm [48]. Thus, in this case, MEF plays the pivotal role and no cluster formation takes place.

SEF and GEF are strongly dependent on the proximity of phenolate and aldehyde functionalities in the fluorophore, SL. 3-Hydoxybenzaldehyde also shows efficient SEF- and GEF-like SL. However, SL shows higher efficiency than 3-hydoxybenzaldehyde because of the proximity effect. On the other hand, insignificant change in fluorescence intensity is noticed for 4-hydoxybenzaldehyde after the treatment of Au(III) and Ag(I). Alkaline SL, with phenolate and aldehyde groups at the *ortho* position, offers a perfect scaffold to bring Au(0) or Ag(0) in aggregation with the most intense GEF and SEF. Again no such SEF or GEF is observed for phenol or benzaldehyde.

Now, two complementary effects are found in literature in the context of MEF [14]: (i) enhanced absorption assisted enhanced emission (lightening rod effect) and (ii) surface plasmon–coupled fluorescence. The possibility of the second factor can be ruled out due to the absence of plasmon band. Besides, radiative decay rate of the oxidized SL does not improve in the presence of Au(0)/Ag(0), as the lifetime of the oxidized SL is not decreased due to metal(0) [6]. However, the first effect, that is, lightening rod effect, is the main reason behind the fluorescence enhancement. A very sturdy absorption effect due to the localized enhanced electromagnetic field of the incident excitation field is obtained when the fluorophore is positioned near a metalized surface. In other words, in the presence of metal surface, the electromagnetic field gets concentrated around the fluorophore. Thus, conducting metallic particles adjust the free-space absorption condition. Consequently, the photonic mode density as well as incident electric field, felt by a fluorophore,

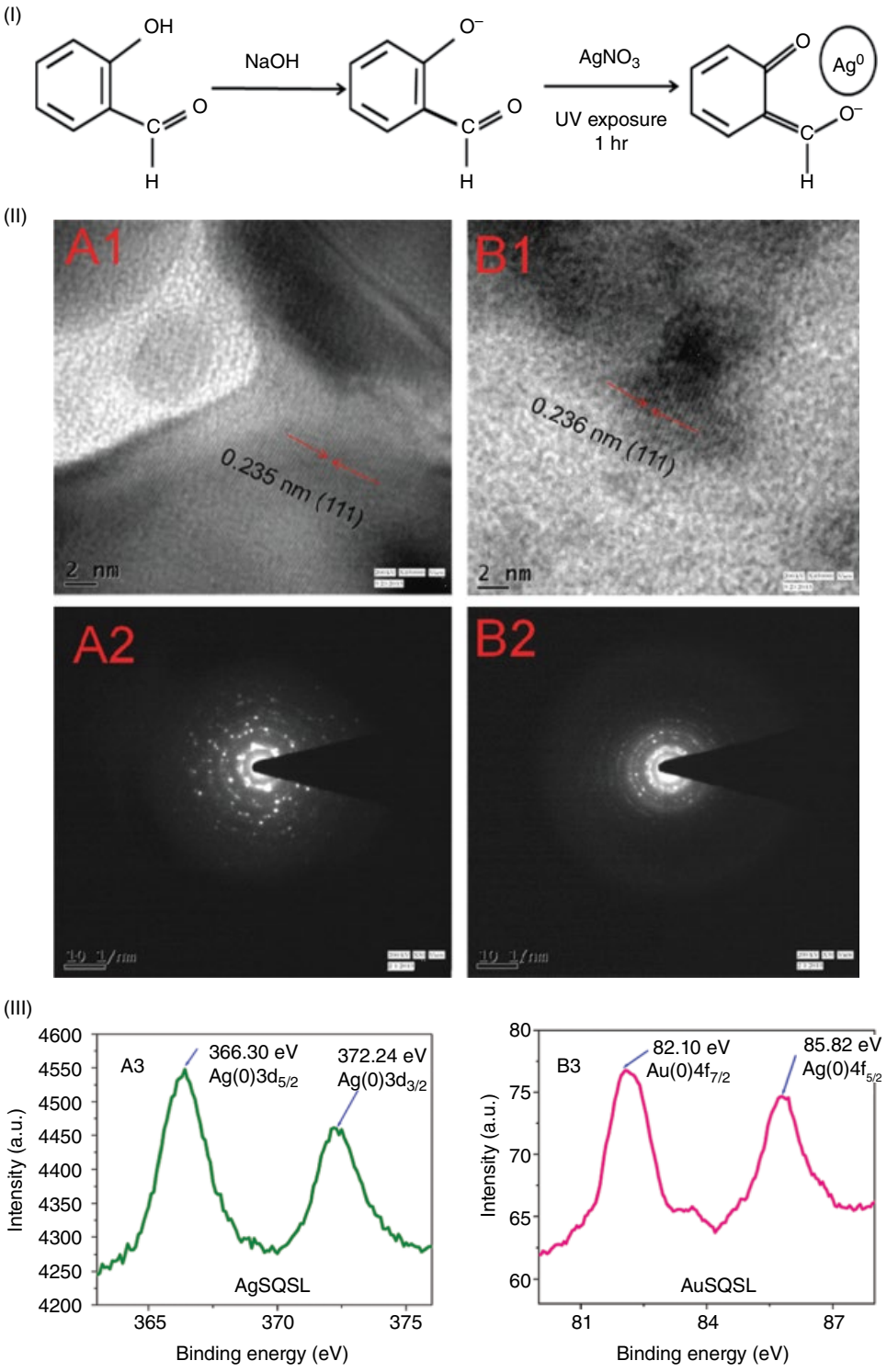

Figure 9.5 (I) Schematic route for Ag(0) synthesis. (II) Lattice fringe of (A1) Ag(0) and (B1) Au(0) from the solution AgSQSL and AuSQSL, respectively. SAED images of (A2) Ag(0) and (B2) Au(0) from the solution AgSQSL and AuSQSL, respectively. XPS spectra of (A3) Ag and (B3) Au from the solution AgSQSL and AuSQSL under freeze drying. Ganguly *et al.* [4]. Reproduced with the permission of Royal Society of Chemistry.

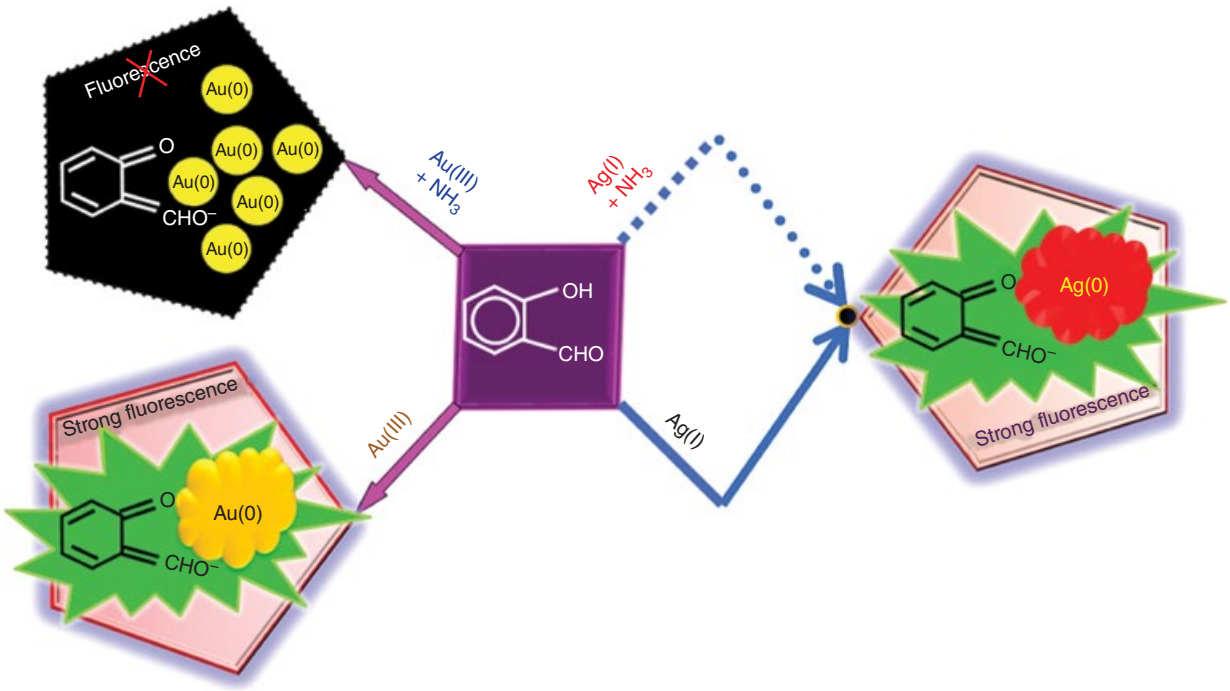

Figure 9.6 Intriguing gold- and silver-enhanced fluorescence from SL. Introduction of ammonia destroys gold-enhanced fluorescence selectively. Ganguly *et al*. [4]. Reproduced with the permission of Royal Society of Chemistry. (*See insert for color representation of this figure*.)

is increased [14]. Higher rate of excitation causes such strong emission. Again the aggregated nature of the Ag(0)/Au(0) particles favors MEF. Lakowicz *et al*. showed that aggregated particles with larger cross sections show higher tendency for MEF [8].

9.2.1.2 Selectivity for Silver-Enhanced Fluorescence

Now, both Au and Ag show enhanced fluorescence, where the fluorophore is SL. However, to attain selectivity in SEF, ammonia/amine compounds were used (Figure 9.6). It has been reported that the introduction of ammonia/amine before the formation of Au(0) from Au(III) hinders GEF [51]. Primary amine or ammonia produces imine (>C═N) with SL by the condensation reaction between aldehyde and amine. Different condensation products (CPs) are produced from the condensation between SL and different monoamines (ammonia (1N0), methyl amine (1N1), etc.), diamines (ethylene diamine (2N2)), 1,3-diaminopropane (2N3), 1,4-diaminobutane (2N4), *o*-phenylenediamine (2N2A), *m*-phenylenediamine (2N3A), *p*-phenylenediamine (2N4A)), and triamine (triethylenetetramine (3N2)) (Figure 9.7). In all cases only SEF and no GEF has been achieved. This is not affected by presence of other metal ions. The deciding factor for this selectivity is the iminic bond present in the SL-based Schiff bases (SBs) (where –CH═O is converted to –CH═N), prepared from SL involving the condensation reaction with different amines (SBs 1SB0, 1SB1, 2SB2, 2SB3, 2SB4, 2SB2A, 2SB3A, 2SB4A, and 3SB2A have been synthesized using 1N0, 1N1, 2N2, 2N3, 2N4, 2N2A, 2N3A, 2N4A, and 3N2, respectively) [4]. Thus employment of preformed SBs shows selective SEF.

Again addition of NH_3 to alkaline SL (NSL) containing Au(III) causes quenching of fluorescence. This quenching is dependent on the NH_3 concentration and complete destruction of GEF can be attained for a unique molar ratio of SL and NH_3. This supports the hypothesis that the quenching effect is due to the imine bond formation. In this context, it is important to note that ammonia does not stop GEF for *meta*-hydroxybenzaldehyde unlike SL. Thus, phenolate group and iminic bond at the mutual *ortho* position make the surface wave lossy for gold without any enhancement of fluorescence. But the same experiment with Ag(I) instead of Au(III) shows prominent SEF. (The fluorescent solution showing SEF has been termed as NAgSQSL and the non-fluorescent solution with gold has been termed as NAuSQSL.) In this case also, the reaction progressed via semiquinone formation. For further investigation of the mechanism of fluorescence enhancement, lifetime measurements have been carried out by Ganguly *et al*. Lifetime measurement shows that all the molecules of SL are converted to the quinone form. Also the increase of lifetime in the presence of

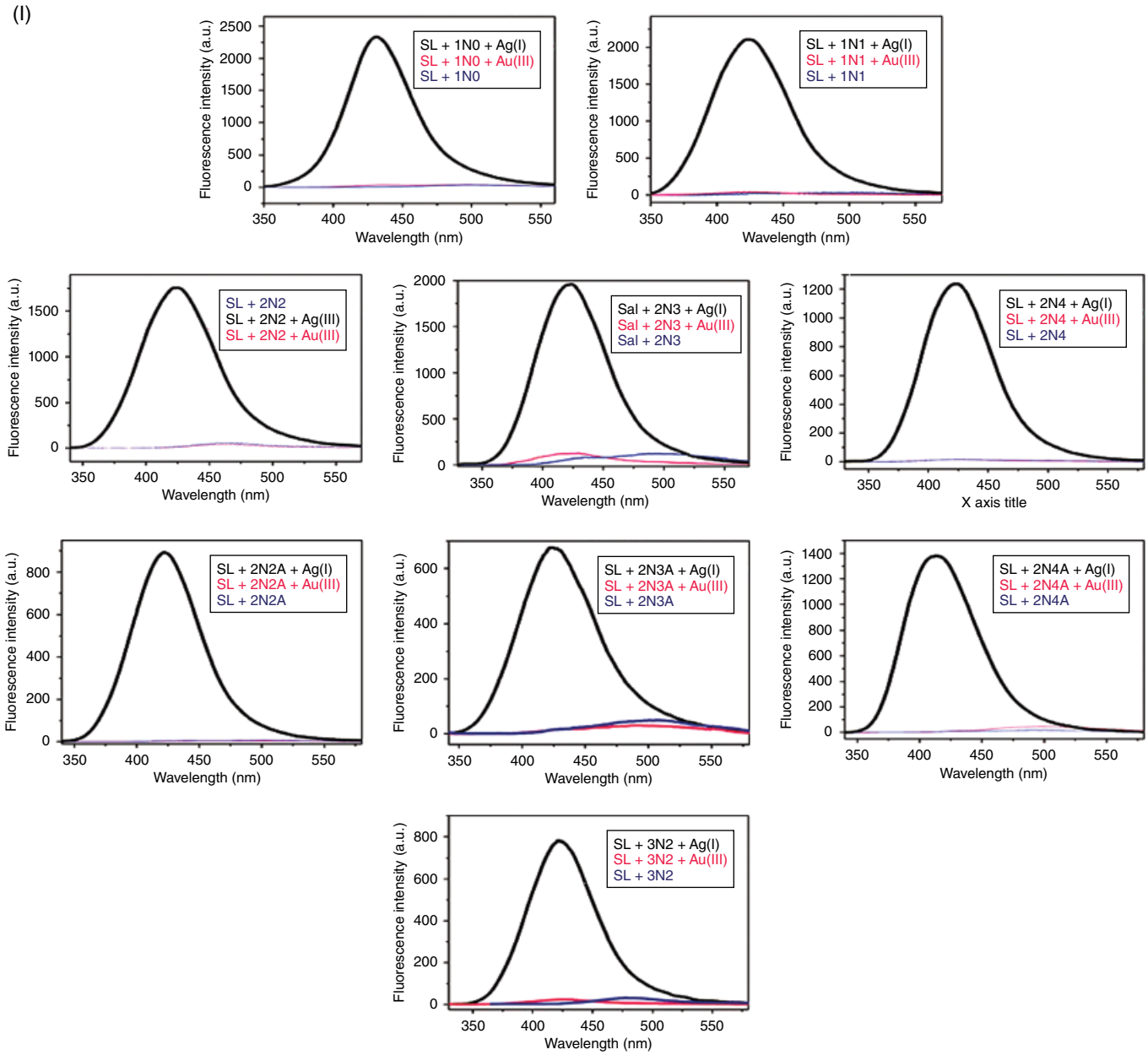
(I)
Fluorescence intensity (a.u.)
Wavelength (nm)
SL + 1N0 + Ag(I)
SL + 1N0 + Au(III)
SL + 1N0
SL + 1N1 + Ag(I)
SL + 1N1 + Au(III)
SL + 1N1
SL + 2N2
SL + 2N2 + Ag(III)
SL + 2N2 + Au(III)
Sal + 2N3 + Ag(I)
Sal + 2N3 + Au(III)
Sal + 2N3
SL + 2N4 + Ag(I)
SL + 2N4 + Au(III)
SL + 2N4
X axis title
SL + 2N2A + Ag(I)
SL + 2N2A + Au(III)
SL + 2N2A
SL + 2N3A + Ag(I)
SL + 2N3A + Au(III)
SL + 2N3A
SL + 2N4A + Ag(I)
SL + 2N4A + Au(III)
SL + 2N4A
SL + 3N2 + Ag(I)
SL + 3N2 + Au(III)
SL + 3N2

Figure 9.7 (I) Fluorescence spectral profile showing the effect of different amines on SL-based gold- and silver-stimulated fluorescence. (II) Fluorescence spectral profile showing gold- and silver-stimulated fluorescence of different SL-based Schiff bases. (III) Comparative account to show the effect of (A) different amines on SL-based SEF and GEF and (B) Schiff bases (SL-based) on SEF and GEF. Conditions: $[SL] = 1.4 \times 10^{-4}$ M; $[Amine] = 1.4 \times 10^{-4}$ M; $[SB] = 1.4 \times 10^{-4}$ M; $[Ag(I)]/[Au(III)] = 1.4 \times 10^{-4}$ M; aging = 2 days; $\lambda_{ex} = 300$ nm. Ganguly *et al.* [4]. Reproduced with the permission of Royal Society of Chemistry.

(II)

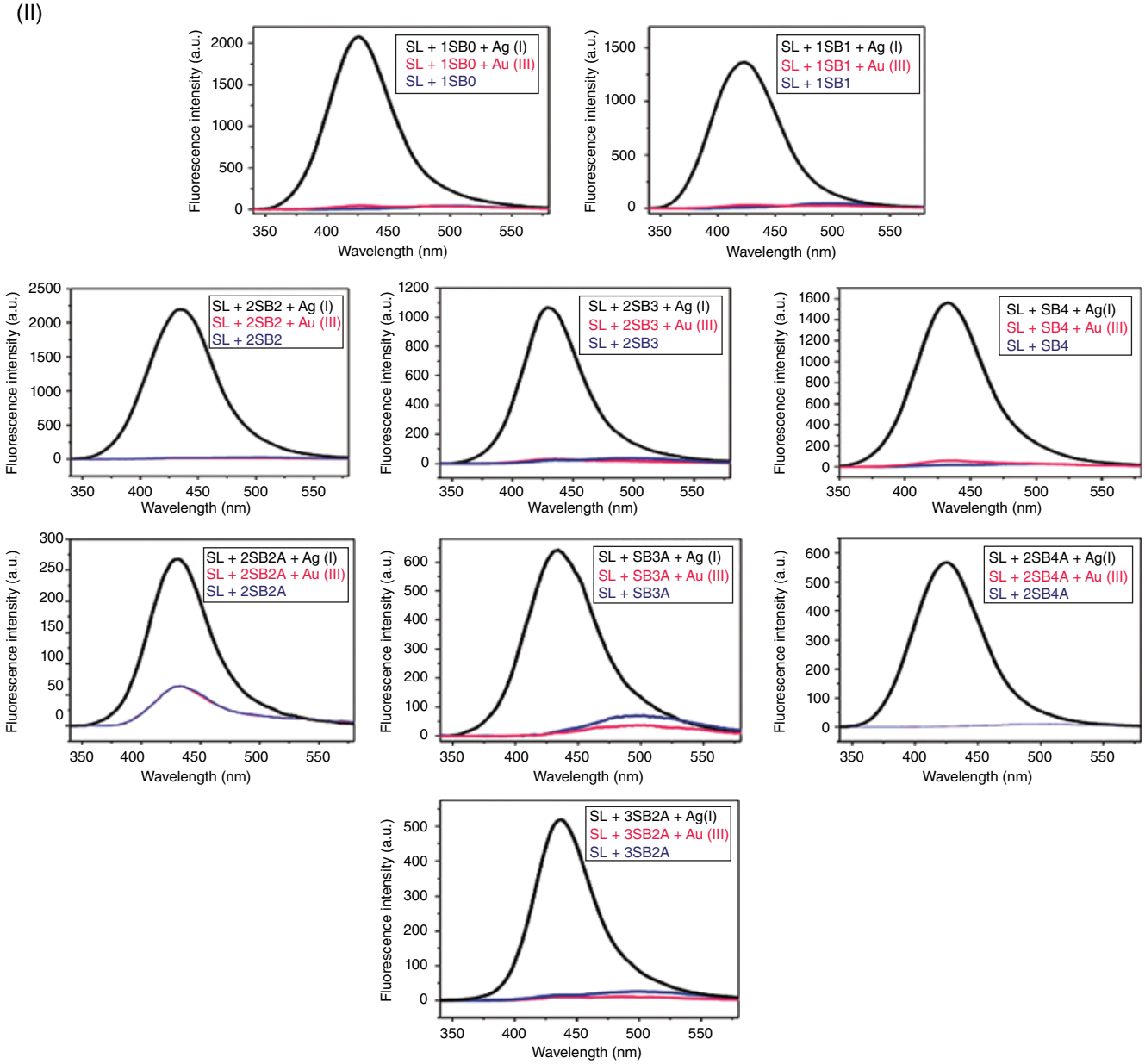
SL + 1SB0 + Ag (I)
SL + 1SB0 + Au (III)
SL + 1SB0
SL + 1SB1 + Ag (I)
SL + 1SB1 + Au (III)
SL + 1SB1
SL + 2SB2 + Ag (I)
SL + 2SB2 + Au (III)
SL + 2SB2
SL + 2SB3 + Ag (I)
SL + 2SB3 + Au (III)
SL + 2SB3
SL + SB4 + Ag(I)
SL + SB4 + Au (III)
SL + SB4
SL + 2SB2A + Ag (I)
SL + 2SB2A + Au (III)
SL + 2SB2A
SL + SB3A + Ag (I)
SL + SB3A + Au (III)
SL + SB3A
SL + 2SB4A + Ag(I)
SL + 2SB4A + Au (III)
SL + 2SB4A
SL + 3SB2A + Ag(I)
SL + 3SB2A + Au (III)
SL + 3SB2A
Fluorescence intensity (a.u.)
Wavelength (nm)

Figure 9.7 (*Continued*)

(III)

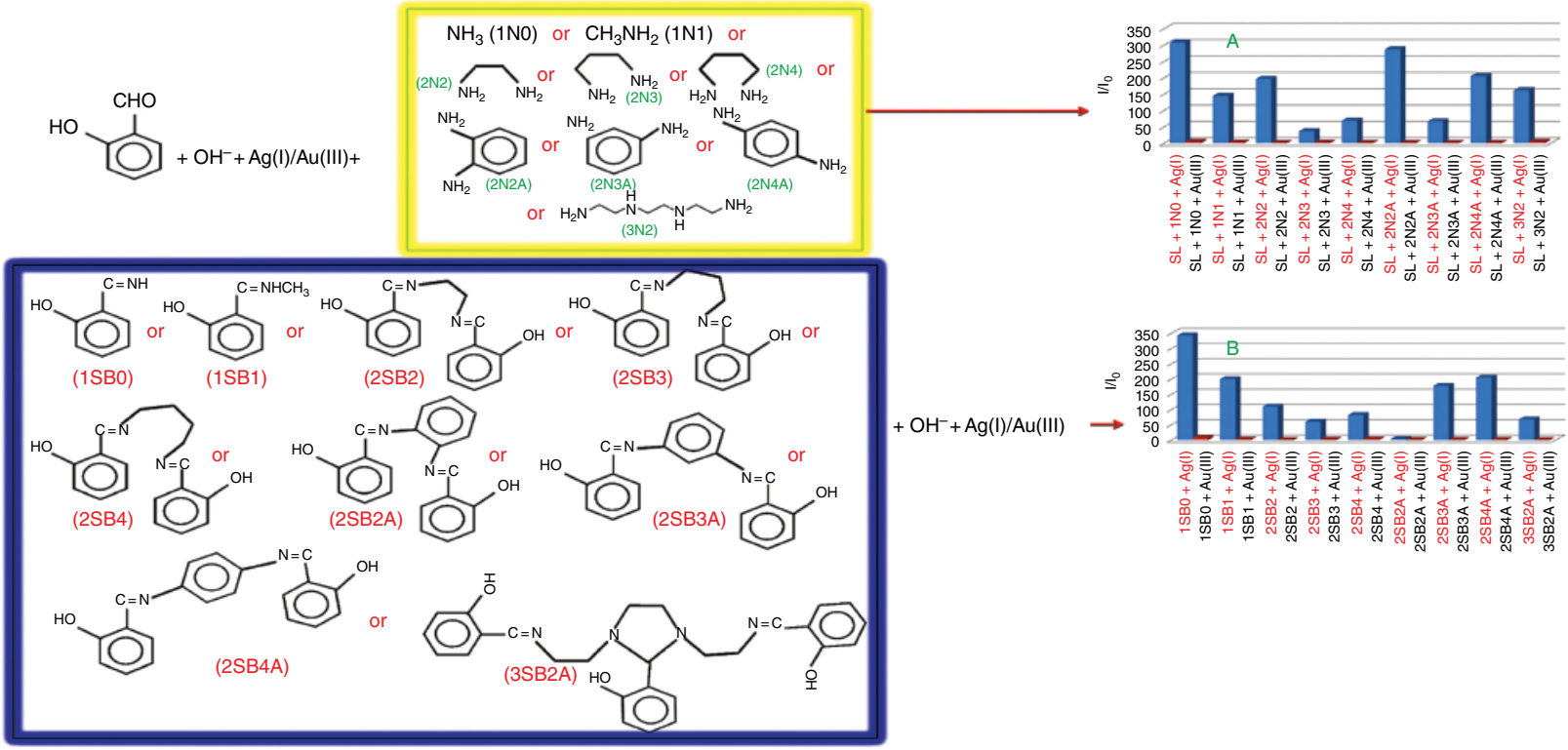

Figure 9.7 (*Continued*)

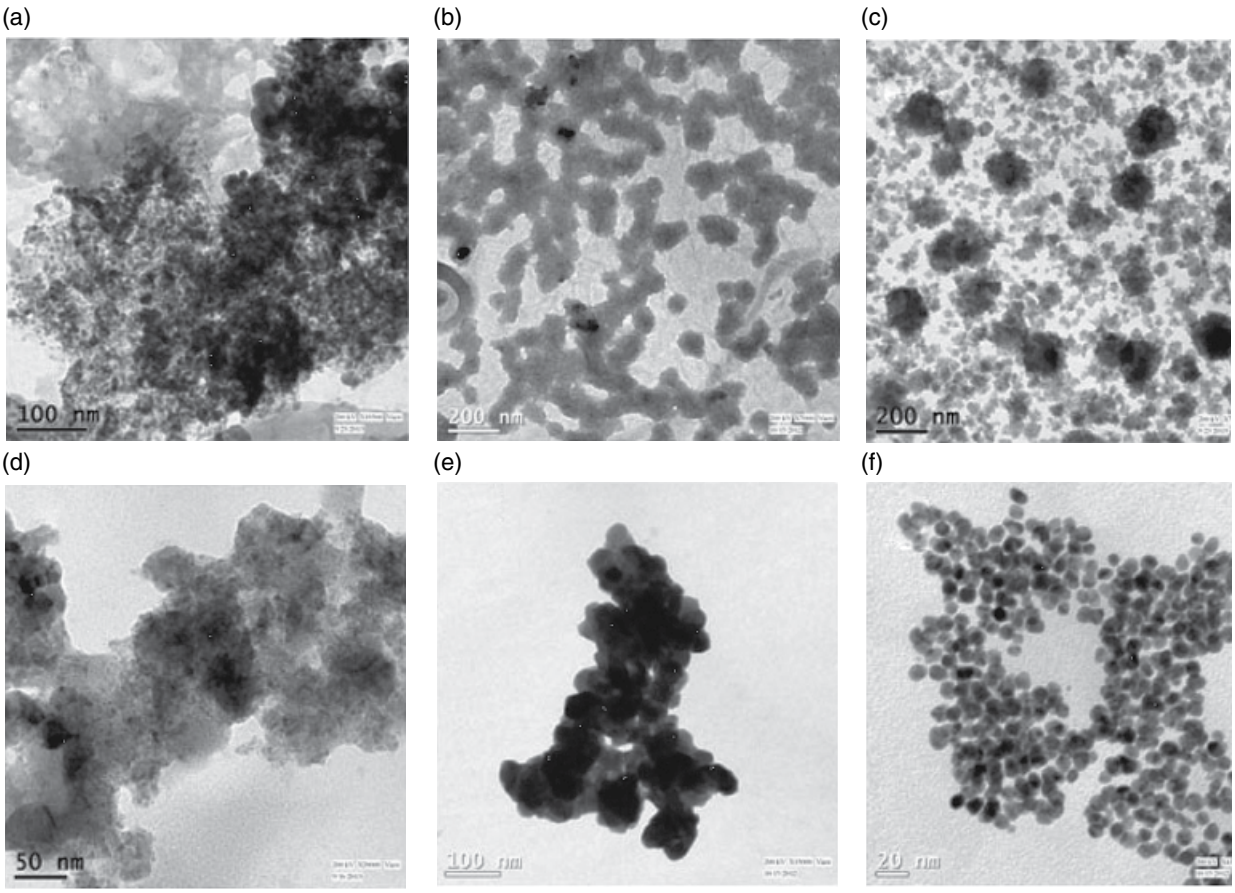

Figure 9.8 TEM image for (a) AgSQSL, (b) AuSQSL, (c) NAgSQSL, and (d) NAuSQSL. Conditions: AgSQSL = [SL] 1.4×10^{-4} M, [Ag(I)] 1.4×10^{-4} M; AuSQSL = [SL] 1.4×10^{-4} M, [Au(III)] 1.4×10^{-4} M; NAgSQSL = [SL] 1.4×10^{-4} M, [Ag(I)] 1.4×10^{-4} M, [NH_3] 1.4×10^{-4} M; NAuSQSL = [SL] 1.4×10^{-4} M, [Au(III)] 1.4×10^{-4} M, [NH_3] 1.4×10^{-4} M. (e) and (f) represent TEM images for [3SB2A + Ag(I)] and [3SB2A + Au(III)] after 2 days of aging. Conditions: [3SB2A] 1.4×10^{-4} M, [Ag(I)] 1.4×10^{-4} M, [Au(III)] 1.4×10^{-4} M. Ganguly *et al*. [4]. Reproduced with the permission of Royal Society of Chemistry.

Ag rules out the probability of enhancement of radiative decay rate [8, 52–54].

As stated before, the high scattering and poor absorption cross section of metals in AgSQSL and AuSQSL solution (particles have highly aggregated morphology) support the mentioned mechanism of fluorescence enhancement (evident from Mie theory [42, 55]). Again, aggregated Ag(0) for NAgSQSL with SEF and Au(0) particles of small, ill-defined shapes for NAuSQSL with no GEF also corroborated the fact (Figure 9.8).

9.2.1.3 Silver-Enhanced Fluorescence in Diiminic Schiff Bases

SL undergoes condensation reaction with diimines with different chain lengths to form diiminic Schiff bases (DSBs). Chemistry of salen (a CP of SL and ethylenediamine) has drawn high attention of the scientists because of the multifaceted applications since Pfeiffer reported this phenomenon for the first time in 1933 [56]. Diehl and Hach [57] demonstrated that cobalt complex of salen is a potential oxygen carrier. Chiral salarg ligand was synthesized following the similar route of achiral salen. A thorough fluorescence study of both the ligands and their metal complexes confirmed that salen-like ligands are potential fluorophore and eventually become probe molecule [58]. Liu *et al*. [59] reported that Mn-salen is a promising probe molecule to detect traces of DNA in solution because of the prominent alteration of fluorescence property of the molecule. They noticed a remarkable decrement of fluorescence intensity for Mn-SBs bound to DNA with a blue shift of excitation and emission peaks. This observation relates to the observed hypochromic shift in the UV absorption spectra. Salicylideneaniline-based organogelator with very high fluorescence quantum yield was synthesized employing J aggregation of the molecule and inhibition of intramolecular rotation in gel state by Chen *et al*. [60]. Deda *et al*. [61] reported the metal-perturbed

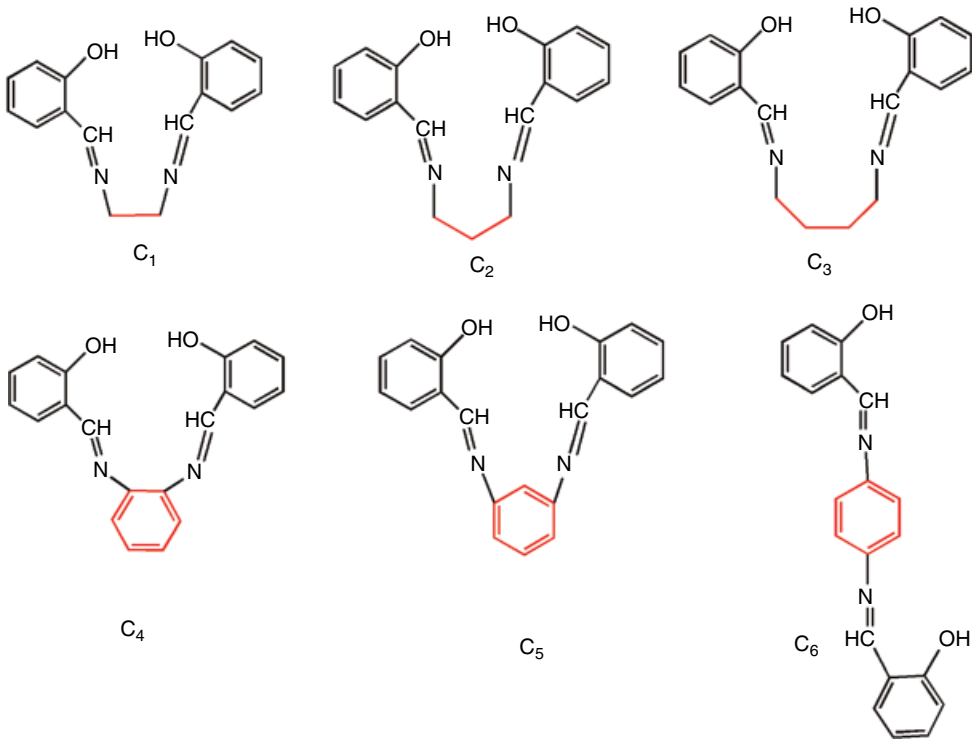

Figure 9.9 Structures of the six DSBs with different spacers in between the two imine bonds.

ligand-centered state of a novel salen-like compound with 12 carbon atom bridges between iminic nitrogen atoms. There are other reports where the fluorescence property of salen/salen derivatives and their metal complexes are exploited for the determination of trace amount of hazardous and useful substances like Mg [62], H_2O_2, triacetone organic peroxides [63], cyanide [64], and others. Aoki *et al.* [65] determined aliphatic primary amines by flow injection fluorometry using beryllium–SB complexes.

The salen or salen derivatives have been used for MEF by Ganguly *et al.* [41]. Actually this phenomenon of MEF arises during the synthesis of AgNPs. It is very interesting to synthesize AgNPs with the help of such compounds. They have reported a novel photochemical strategy to synthesize both AgNPs with salen and salen-like molecules having different spacers between the two iminic bonds. For this purpose different diamines like ethylenediamine, 1,3-propylenediamine, 1,4-butanediamine, *o*-phenylenediamine, *m*-phenylenediamine, and *p*-phenylenediamine have been used. The produced salens with different spacers have been named as C_1, C_2, C_3, C_4, C_5, and C_6, respectively (Figure 9.9). Then capping capability of different salen-like DSBs, due to varied chain length, for AgNPs has been explored. The salen and salen-like molecules possess self-quenching fluorescence property. In general, UV irradiation for more than 2 h causes excimer formation from the quinone form of salen and salen-like molecules (Figure 9.10, the excimer formation and self quenching under UV irradiation is shown for C_2). The fluorescence quenching by fluorescence resonance energy transfer (FRET) [41, 66] mechanism is very common in the presence of MNPs. Also the resonance energy transfer (RET) is very important in the context of self-quenching [6]. Under the UV light irradiation, the emission maxima of the DSB solutions get blueshifted with the decrease in intensity (Figure 9.10). However, after UV irradiation, it is observed that its fluorescence intensity increased with blue shift that increased upon dilution, indicating the formation of excimer. Probably, conversion of quinone from phenolate ion helps the double bonds to be somewhat localized, facilitating excited state dimer formation, that is, excimer formation. When the excimer returns to the ground state, its components dissociate and often repel each other, causing low fluorescence quantum yield and red shift of emission maxima [6].

However, AgNPs synthesized by similar photoactivation reaction increase the fluorescence intensity dramatically. The mixture of alkaline DSB (C_n, $n=1$–6) and $AgNO_3$ under UV irradiation generated AgNPs (Figure 9.11). This *in situ*-generated AgNPs cause the phenomenon of SEF for oxidized salen–salen-like compounds. The stability of the *in situ*-generated AgNPs depends on the UV irradiation time and the C_n ($n=1$–6)

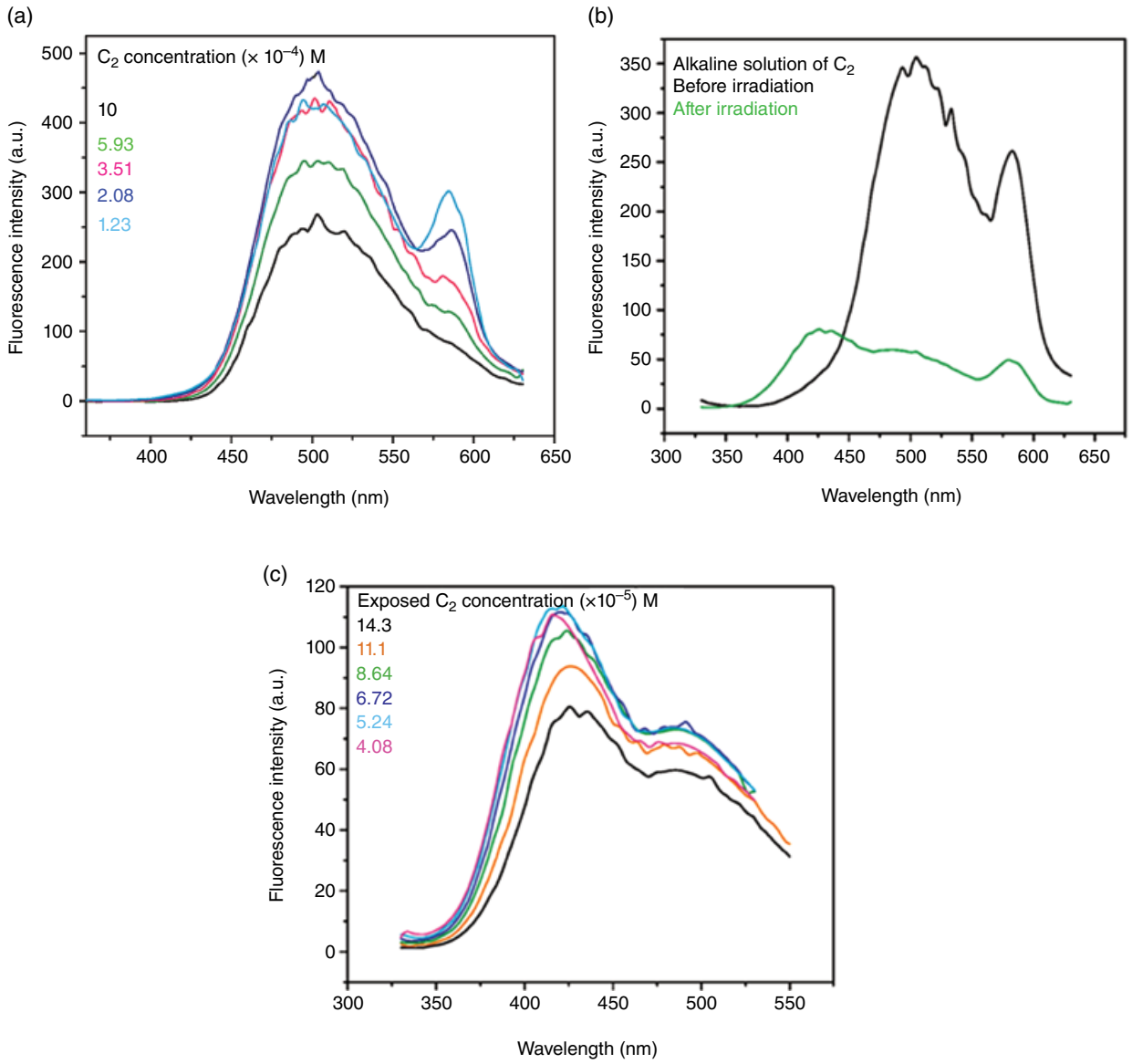

Figure 9.10 (a) Fluorescence study involving C_2. Conditions for self-quenching $>2.08\times10^{-4}$ M and for normal fluorescence $<2.08\times10^{-4}$ M, excitation wavelength 290 nm. (b) Fluorescence intensity of alkaline solution of C_2 before and after 365 nm light irradiation. Condition: concentration of C_2, 1.42×10^{-4} M; excitation wavelength, 290 nm; irradiation time, 3 h. (c) Excimer formation of alkaline C_2 solution after UV irradiation, excitation wavelength, 290 nm.

versus $AgNO_3$ concentration ratio and more importantly on the spacers. (Figure 9.11) The maximum enhancement of fluorescence has been obtained for C_3. Much interestingly for C_5, quenching occurs. Three hours of irradiation time and C_n:$AgNO_3$ = 1:2 molar ratio show maximum enhancement for the DSBs except for C_5.

The same experiments with the salen compounds have been performed using Au(III) salt as well. Although in that case also metal (0) nanoparticle, that is, Au(0) nanoparticle is produced and there is no GEF.

The dramatic enhancement of fluorescence by the AgNPs is due to "lightening rod effect." In the presence of AgNP the local electromagnetic field gets concentrated on the fluorophore causing the increase of the rate of excitation. The silver metal can also modify the rate at which a fluorophore emits photon, that is, intrinsic radiative decay rate of the fluorophore. The coupling between molecular dipole of fluorophore and SPB of the metal leads to an enhancement of the radiative decay rate that results in a stronger fluorescence emission with high quantum yield, a phenomenon known as radiative decay engineering (RDE) [67]. The size of the NPs has a very close relationship with fluorescence intensity of the capping agent. Lakowicz

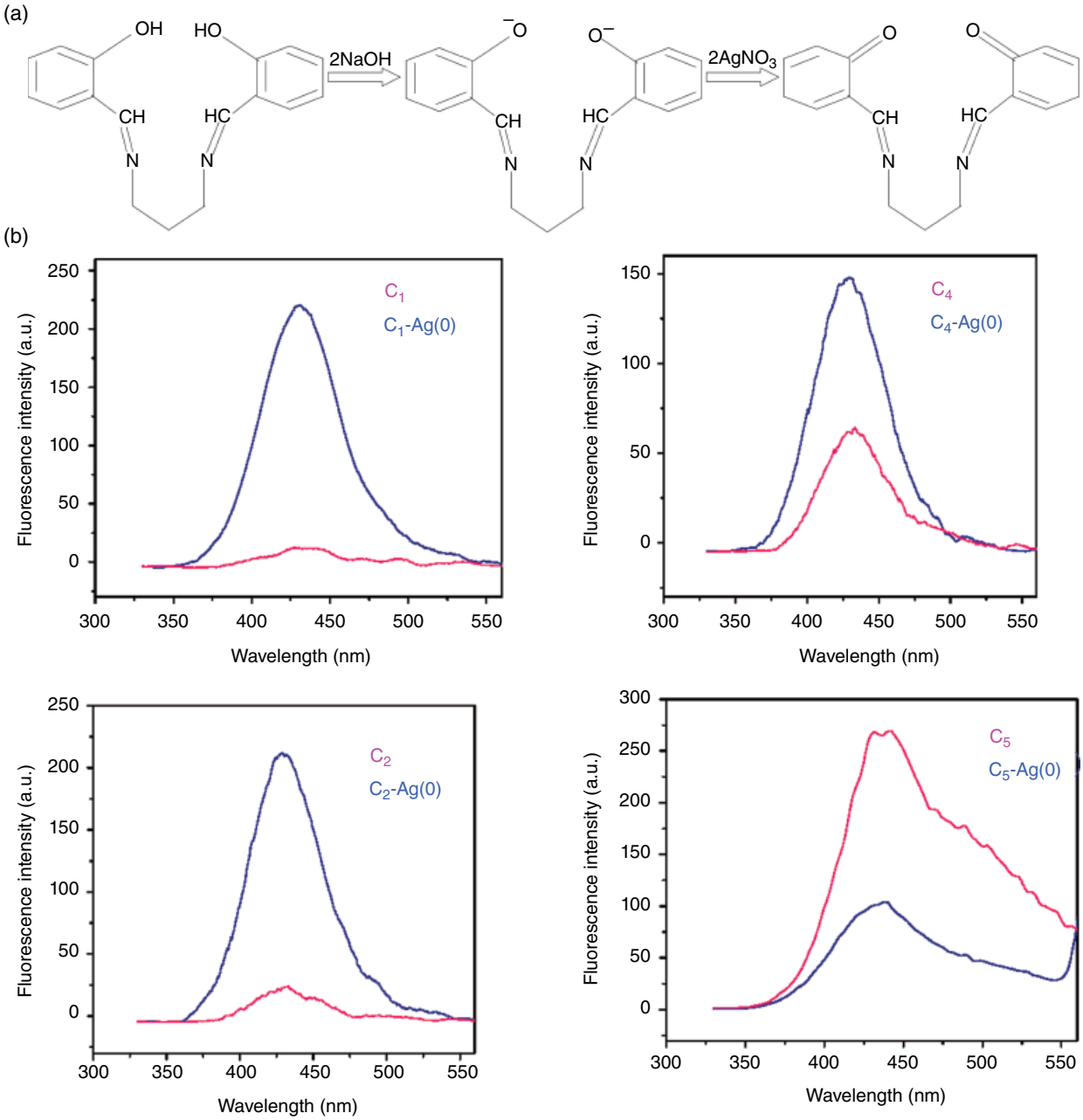

Figure 9.11 (a) Mechanism of formation of nanoparticles in the presence of DSBs. (b) Fluorescence enhancement of all the DSBs in the presence of AgNPs (photoproduced *in situ*) and quenching for C_5 only. Condition : ratio of $C_2 : AgNO_3 = 1 : 2$, irradiation time, 3 h; excitation wavelength, 290 nm. (c) Bar diagram displaying different fluorescence intensities of DSBs in the presence of *in situ*-generated AgNPs. Ganguly *et al.* [32]. Reproduced with the permission of American Chemical Society.

et al. [68] reported that the surfaces of uniform colloids are not as effective as the aggregates for MEF. In close proximity, up to ~50 Å fluorophore emission is strongly damped by metallic surfaces. Maximum enhancement occurs for the probe while its distance is ~100 Å from the metallic surface. But there was a report by Sokolov *et al.* [69] demonstrating distance to be ~600 Å. Quinone form of C_5, the nanoparticles probably lie in a very close proximity (~50 Å), which is reflected in fluorescence quenching in presence of AgNPs. The different degrees of fluorescence enhancement of the other irradiated DSBs are related to local incident field and the coupling between molecular dipole of fluorophore and SPB of the Ag(0), which in turn is dependent on the proximity of the capping agent and photoproduced Ag(0). Astonishingly GEF is not observed for the DSBs due to size effect and also the close proximity of the as-synthesized Au(0) particles.

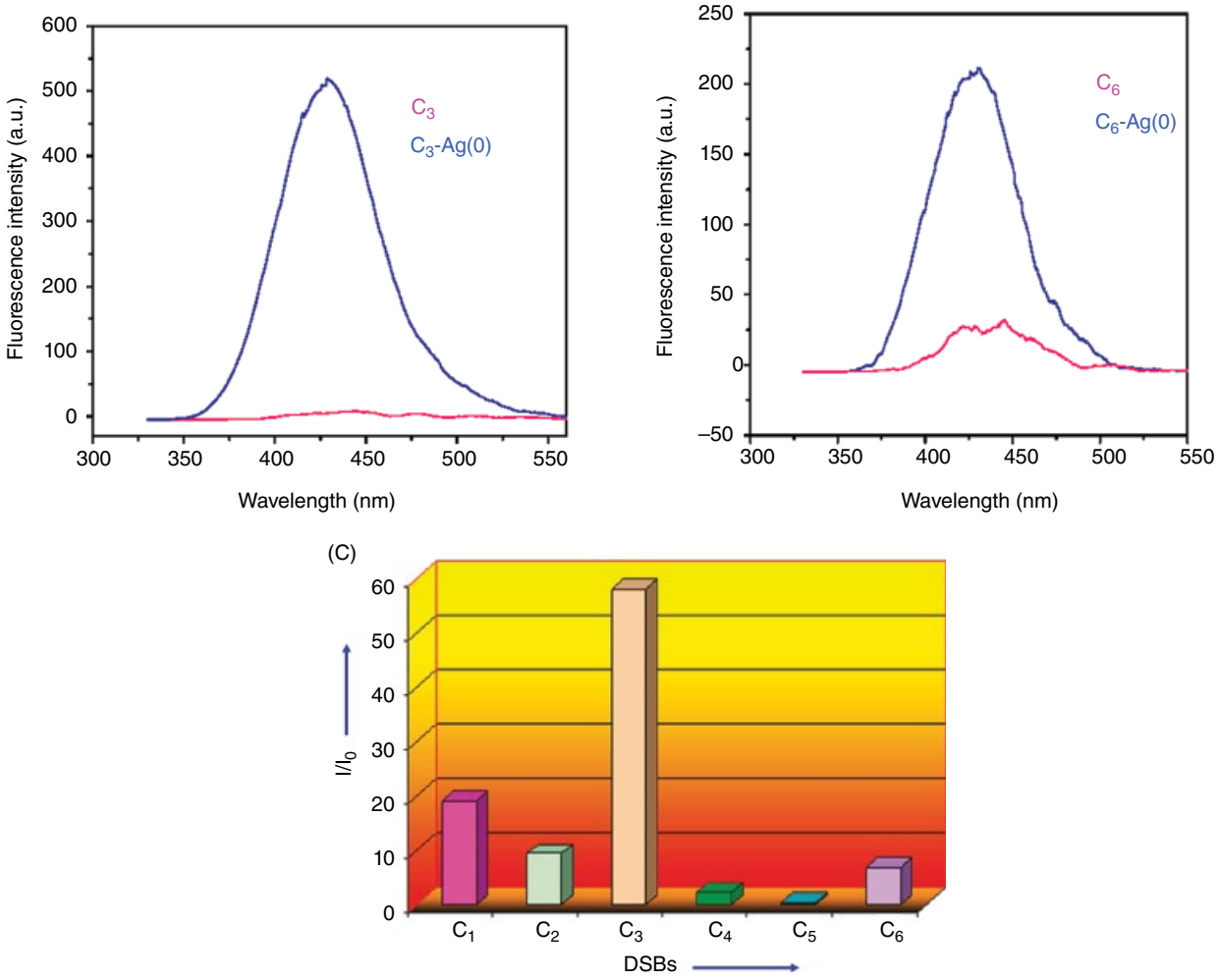

Figure 9.11 (*Continued*)

9.2.1.4 Copper-Enhanced Fluorescence

Copper-enhanced fluorescence (CEF) in solution is rarely reported. Ganguly *et al.* [7] have reported the CEF for the DSBs, synthesized using different diamines and SL. The evolution strategy for CuNPs has been endowed with high fluorescence enhancement as well as quenching of the fluorescence of the exposed reaction mixtures. They have shown that the contrast of the luminescence behavior depends upon the spacers (in between the two iminic bonds) of the DSBs. Nine hours of irradiation of an alkaline reaction mixture of a copper salt in the presence of DSBs causes the formation of CuNPs under UV light. The *in situ*-generated CuNPs exhibited strikingly different fluorescence behavior out of the exposed reaction mixture. An irradiation time of more than 9 h gives a constant fluorescence intensity of the reaction mixture, that is, the fluorescence property does not change further. In this case also quinone formation from the phenolic OH group through the same mechanism (as proposed by Selvakannan *et al.* [40]) for nanoparticle synthesis in the presence of DSB has been proposed. In this mechanism, phenolate ions lose electrons and Cu(II) is reduced to Cu(0) by accepting electrons. UV light provides the necessary activation energy for the productive photoactivation process. Without UV irradiation, quenching of fluorescence occurs due to the formation of cupric hydroxide in the alkaline medium. Visible light of variable wavelengths, for example, 450, 550, and 650 nm, shows a similar type of quenching. However, only UV irradiation (~365 nm) causes a drastic change in fluorescence. After 365 nm UV light exposure, the 501 nm peak of alkaline DSB decreases and a new peak at 449 nm arises. Formation of quinone as a result of UV irradiation causes a loss of resonance in the fluorophore system, which results in a higher energy emission (blue shift of the emission maxima)

but with lower intensity [70]. If DSB solution is exposed under UV light with copper salt, the *in situ*-generated Cu(0) produces a dramatic enhancement of the fluorescence ($\lambda_{em} = 429$ nm) for the individual exposed reaction mixtures for the cases of C_1, C_2, C_3, and C_4. Interestingly, for C_5 and C_6 the quenching occurs. When the two iminic bonds are separated by aliphatic groups (C_1–C_3), a huge enhancement of the emission intensity is observed. On the contrary, an aromatic group between the two iminic bonds exhibits a low enhancement of the fluorescence (C_4) and sometimes quenching (C_5 and C_6) in the presence of photoproduced Cu(0). So, the spacer in between the iminic bonds dramatically tunes the fluorescence behavior of the exposed DSBs in the presence of CuNPs, produced *in situ* in the reaction mixture as a consequence of UV light irradiation (Figure 9.12). For maximum enhancement in the fluorescence intensity of salen/salen-like compounds, the DSB : Cu(II) concentration should be 2 : 1 and the 9 h irradiation time is needed. To prove that the fluorescence is only from the Cu(0), authors have used disodium ethylenediaminetetraacetate (Na_2-EDTA) along with Cu(II) salt instead of lone Cu(II) salt. This resulted in fluorescence quenching. However, the use of preformed cuproammonium complex and Cu(II)-EDTA shows an insignificant amount of the enhancement under UV irradiation. Both the Na_2-EDTA and ammonia form highly stable complexes with Cu(II). DSBs cannot at all reduce Cu(II) to Cu(0) from such stable complexes. Phenomena of quenching is due to the effect (spin–orbit coupling effect) of Cu(II) [71]. Interestingly, introduction of individual complexing agent, Na_2-EDTA or ammonia, to the already exposed reaction mixtures, that is, the reaction mixtures with preformed CuNPs, shows no effect of these complexing agents on the CEF.

The high fluorescence enhancement of the fluorophore in the presence of MNPs is due to an increased rate of excitation and radiative decay rate. MNPs concentrate the local field on the fluorophore, which increases the rate of excitation (the phenomenon known as the "lightening rod effect") [70, 72]. MNPs can also modify the rate at which a fluorophore emits a photon [73]. According to the RP model, instead of the fluorophore, it is the metal that radiates after energy transfer from fluorophore. Far-field radiation from fluorophore-induced plasmons and trapped plasmons are accountable for enhancement and quenching of fluorescence.

Usually, the scattering efficiency is smaller for Cu and CuNPs having an especially smaller size are known for quenching of fluorescence. For larger nanoparticles, CEF is found in the literature [36]. Again there are some reports where the CuNPs are used to attain CEF but those are not in solution phase [74, 75]. Sugawa *et al.* [76] have fabricated and modified the ordered arrays of Cu nanostructures with porphyrin molecules in order to evaluate fluorescence enhancement due to the localized surface plasmon resonance. The nanostructures have been prepared by thermally depositing Cu on the upper hemispheres of two-dimensional silica colloidal crystals. In this case not only the enhancement of the fluorescence of porphyrin but also the quenching has been reported within the interband transition region. Geddes *et al.* [28] observed an enhanced fluorescence emission, 2.5-fold brighter from acridine orange near CuNPs as compared with a glass control substrate containing no nanoparticles.

9.2.1.5 Tuning of Metal-Enhanced Fluorescence

The MEF from AuNP, AgNP, and CuNPs can be tuned by simply changing the experimental conditions. Ganguly *et al.* [42] employed the CP of SL and triethylenetetramine (termed as 3SB2) for this purpose (Figure 9.13). They have showed that although AuNP and AgNP evolution in the alkaline solution of 3SB2 needs no UV exposure, CuNP formation demands UV irradiation. However, AuNP and AgNP formation kinetics was accelerated by UV exposure. Thus the ease of evolution of MNPs relates to the nobility of the coinage metals in use and the resulting solutions show fluorescence contrast behavior (fluorescence enhancement by Cu and Ag and quenching by Au) due to match and mismatch of wave vectors. The electric field evident from finite-difference time-domain (FDTD) (Figure 9.14) simulation abreast of the scattering cross section of the particles governed from Mie theory as a consequence of SPCE and lightening rod effect concentrating the electric field around the fluorophore is an important factor. These two effects are responsible for CuNP and AgNP stimulated fluorescence. The SEF and CEF can be differentiated with respect to the irradiation time. One hour of UV irradiation time is enough to attain SEF where ~11 h of irradiation is essential to observe CEF. Long-term exposure kills observed SEF, donating selectivity toward CEF. Again, LSWs are anticipated for efficient quenching by AuNPs even after prolong exposure. The electromagnetic field around Ag(0) is higher than Cu(0) NP, thus the enhancement in fluorescence happens to be greater for Ag than Cu. It has also been reported that substitution of Au(0) or Cu(0) from Au or Cu hydrosol by Ag(0) (when Ag(I) is introduced in Au/Cu hydrosol) in solution has been made possible. Addition of Au(III) to the preformed alkaline solution

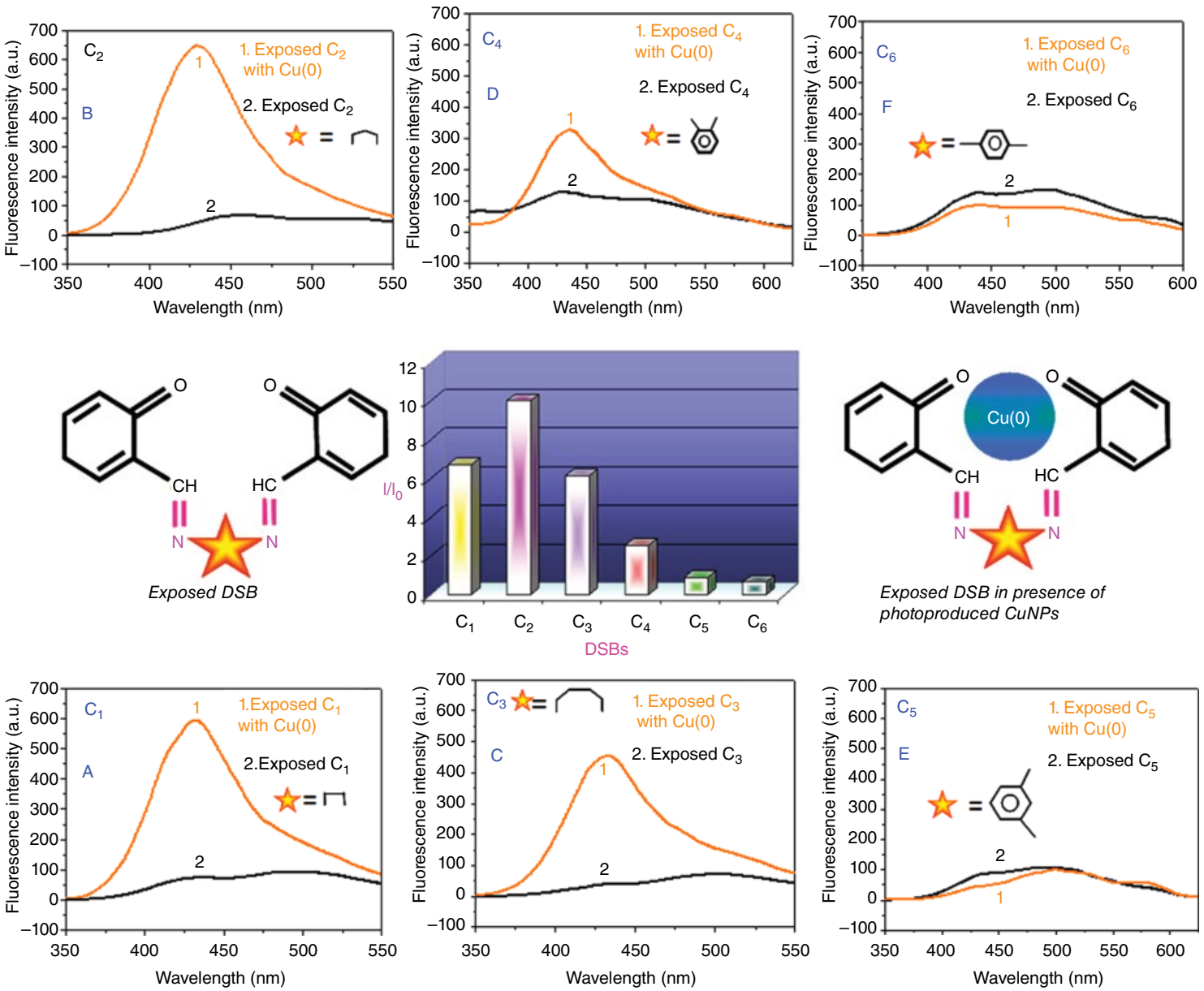

Figure 9.12 Fluorescence spectra (a–f) showing enhancement/quenching of exposed DSBs in the presence of photoproduced CuNPs. The bar diagram represents different degrees of enhancement from the exposed DSBs in the presence of photoproduced CuNPs (I = fluorescence intensity of exposed C_2 in the presence of photogenerated CuNPs; I_0 = fluorescence intensity of exposed C_2 solution without copper). Conditions: C_2 concentration = 1.66×10^{-4} M; $CuSO_4$ concentration = 83×10^{-6} M; λ_{ex} = 290 nm.

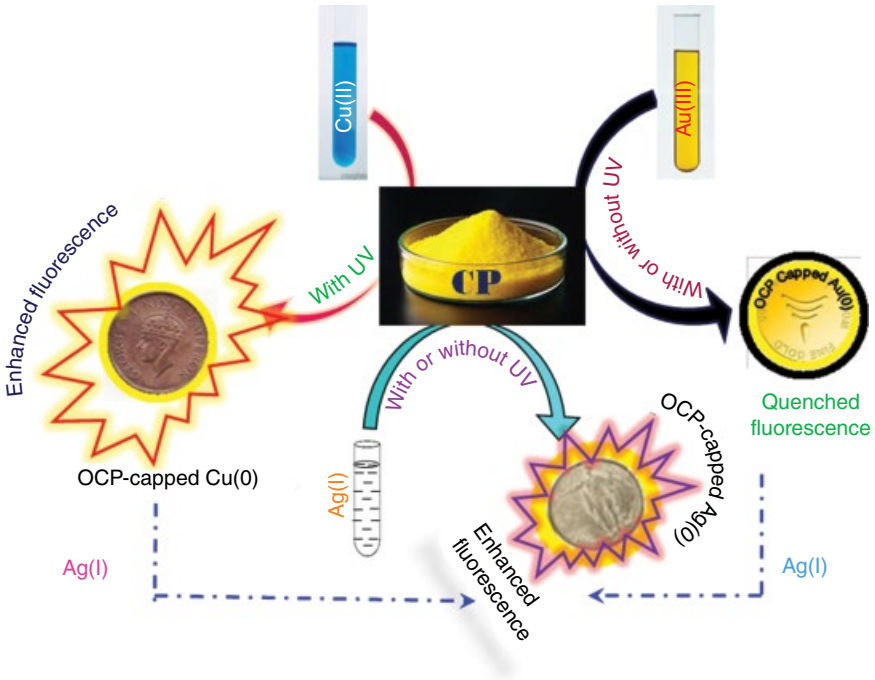

Figure 9.13 Exploitation of a Schiff base compound (CP) for photochemical evolution and stabilization of coinage metal nanoparticles in solution is presented. The process stimulates metal-enhanced fluorescence activity to the solution that offers selective sensing of metals well below the EPA permissible level.

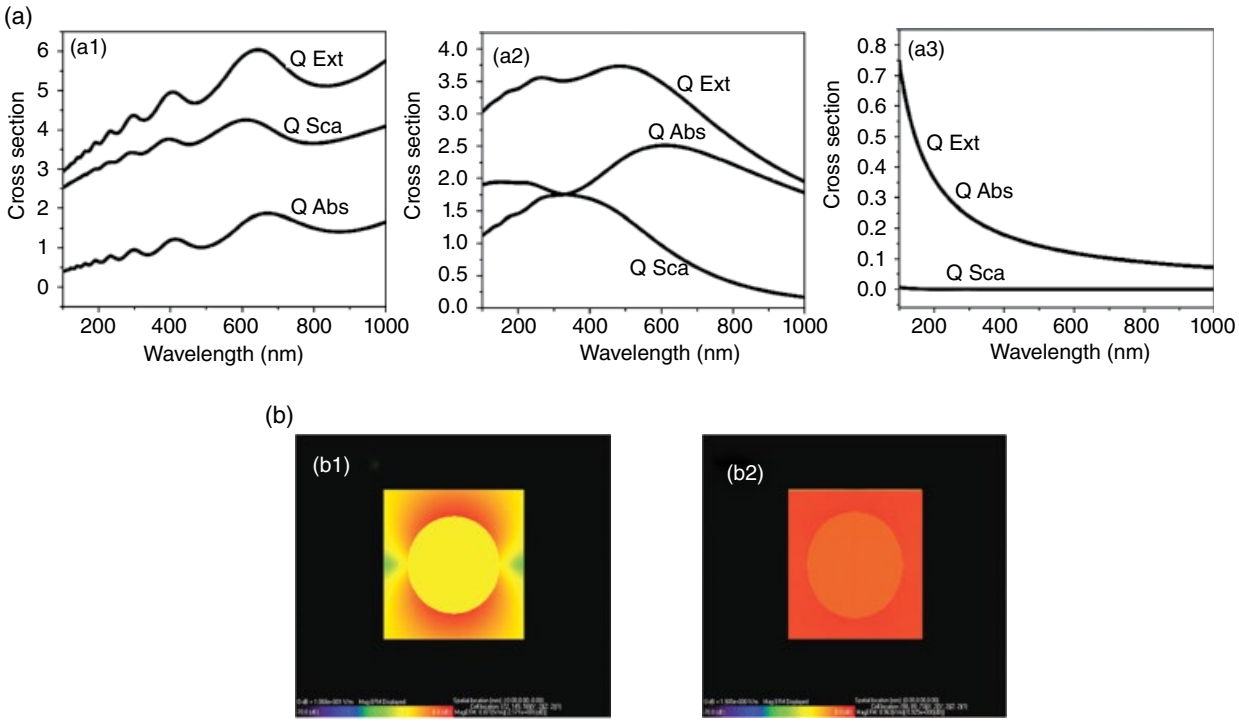

Figure 9.14 (a) The extinction, scattering, and absorption cross section of (a1) 200 nm silver, (a2) 100 nm copper, and (a3) 5 nm gold sphere. (b) Snapshots indicating the near-field distribution around (b1) 200 nm silver sphere and (b2) 100 nm copper sphere obtained from a 3D FDTD simulation. Ganguly *et al.* [42]. Reproduced with the permission of Royal Society of Chemistry.

of DSB results in a non-fluorescent gold hydrosol (wine red colored) with or without UV exposure. Interestingly, addition of $AgNO_3$ from outside to the non-fluorescent Au(0)-containing solution shows dramatic SEF, keeping Au out of the solution as a precipitate. Thus, red solution turns yellow. This has been also proved to be the same, while Cu(0) is considered in lieu of Au(0). In either case, "Turn On" fluorescence from "Turn Off" Au(0)/Cu(0) case results in serving a platform for selective determination of Ag(I) and Cu(II) separately.

9.3 Applications of Metal-Enhanced Fluorescence

The huge amount of the enhance fluorescence by noble metals can be successfully utilized in sensing of different biocompounds, heavy metals, and so on. The sensing technique works via the fluorescence "Turn Off/On" phenomenon. There are certain compounds that cause selective quenching/enhancement depending on the physical parameters, thus paves the way of selective and sensitive quenching. Among the spectroscopic techniques, fluorescence spectroscopy is considered as one of the most sensitive technique due to high signal to noise ratio.

9.3.1 Sensing of Biomolecules

Dopamine (DA) is an important neurotransmitter present in the mammalian central nervous system [77–80]. Imbalances in the DA concentration cause severe diseases including Parkinson's disease [79, 80]. Hence sensing of DA remains an important quest for the scientists. Although the most widely used techniques involve electrochemical methods, but the close redox potential of the coexisting biocompounds uric acid (UA) and ascorbic acid (AcA) cause interference. Again DA oxidation at the solid electrode surface also causes hazard. To improve the detection technique, several methods with chemically and physically modified electrodes have also been tried [81, 82]. Interestingly, the fluorometric technique has become appealing in the field of DA sensing with higher order of sensitivity [83, 84]. The intriguing fluorescence due to SEF for the DSBs remains unaltered in the presence of common metal ions like, Na(I), K(I), Zn(II), and certain biocompounds like AcA, amino acids (AAs), glucose, and lactose. However, this fluorescence is quenched drastically by DA (the quenched solution was termed as Ag-QLDA) paving the way of selective DA sensing [83]. Ganguly *et al.* have used a DSB, *N,N′-bis*(salicylidene)-1,3-propanediamine (L), CP of SL, and 1,3 propylenediamine for DA sensing. In this method the use of suitable excitation wavelength is important to eliminate UA interference (Figure 9.15I). The lower detection limit has been obtained to be 16 nM and a good linear correlation of $(I_0 - I)/I_0$ with DA concentration has been attained over the concentration range from 0 to 300 nM (Figure 9.15II). This technique has been applied in determining the DA contents in four types of banana peels (pachabale, elakkibale, nendra bale, and plantain). First three are ripe (yellow) and plantain is green. Per 100 g peel, they contain 9.2, 10.1, 8.9, and 1.8 mg of DA, respectively. The prescribed method utilizing the MEF is proved to show better sensitivity than a report by Yu *et al.* [85]. They have employed mesoporous silica particle for fluorometric determination of DA.

The quenching phenomenon has been described in the light of trapping of plasmon (LSWs) that radiates heat. The quinine form of L (QL) works as a radiating plasmophore [86, 87] and near-field radiation of AgQL association causes enhanced fluorescence in presence of Ag(0) due to the coupling of metal plasmons with QL. However in the presence of DA, plasmon is trapped and the particles become discrete from the aggregated form. Thus due to the reduction of scattering cross section, efficient quenching occurs. Further confirmation of this proposition comes from the measurement of fluorescence decay time. A slight increase in the lifetime of AgQL solution after DA addition indicates a very small decrease in the radiative decay rate although the quenching is drastic. Hence the decrease in the radiative decay rate has not been considered as the quenching factor.

SEF has been utilized in sensing of another bio-molecule cysteine (Cys) [17]. Cys is an important AA that is used as potential neurotoxin, biomarker, and so on. Imbalance of Cys causes different problems like edema, lethargy, liver damage, muscle and fat loss, and so on. While sensing of Cys, SEF from SL is utilized. In addition of different AAs to the alkaline SL in the presence of Ag(I) solution under UV exposure for an hour, the photoproduced SEF remains virtually unaffected except for Cys, histidine, arginine, tryptophan, and methionine. The phenomenon of "FRET" is facilitated for the prementioned three AAs (Cys, histidine, and arginine) producing surface waves lossy [15, 32]. Again, these three AAs, responsible for quenching, disintegrate the aggregated Ag(0) into tiny (~10 nm) particles presenting plasmon band (~400 nm). Thus, with the decrement in size, absorption cross section is increased according to Mie theory and scattering cross section associated with fluorescence intensity is decreased [42, 55]. To design a Cys sensor by the

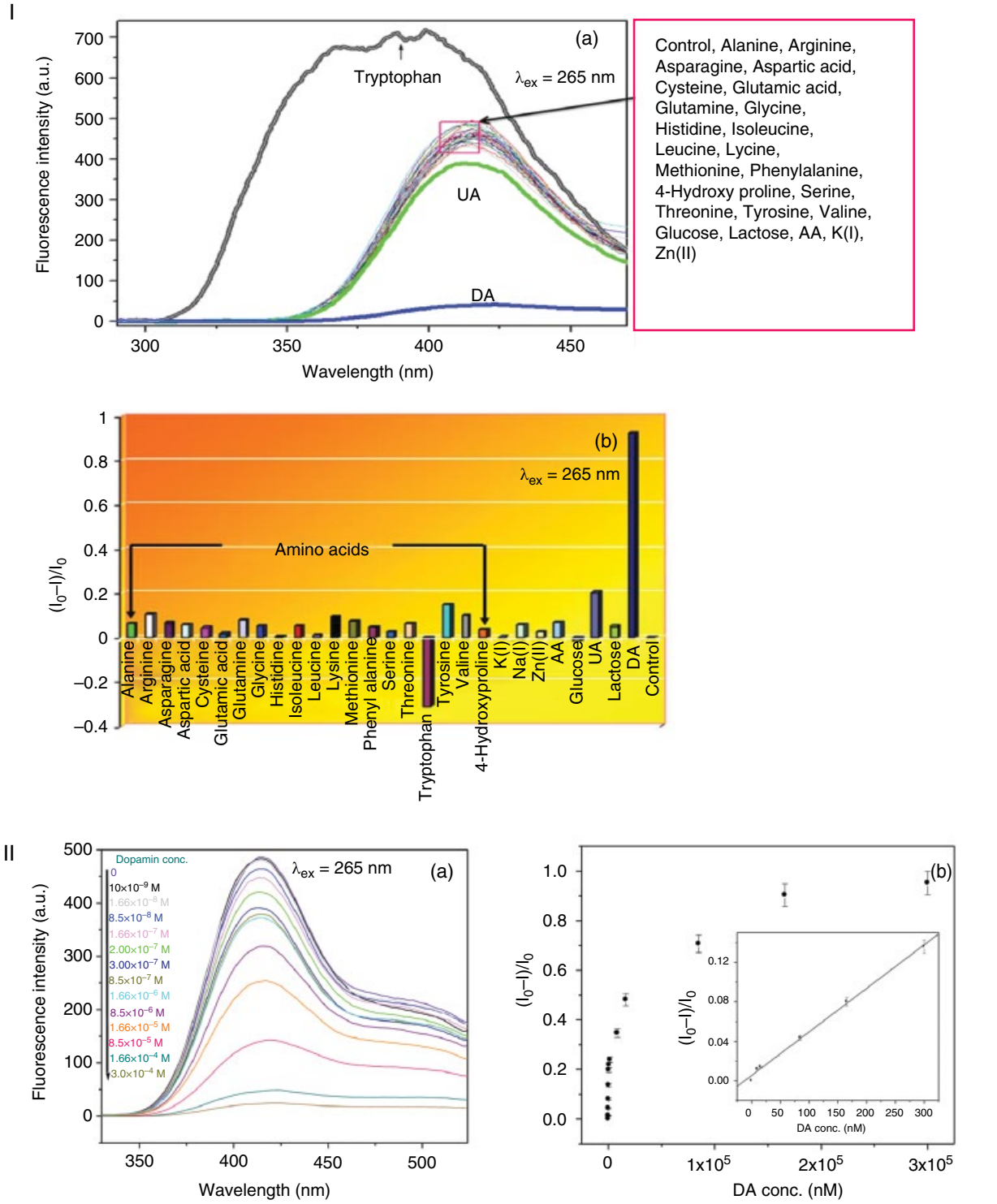

Figure 9.15 (I) (a) Fluorescence spectral profile and (b) bar diagram indicating the selectivity of DA regarding the fluorescence quenching of **AgQL** (3 mL) solutions; [DA/competitor] = 3.0×10^{-4} M. (II) (a) Fluorescence spectral profile and (b) degree of fluorescence quenching of **AgQL**–DA solution with the variation of DA concentration. Inset of (b) represents linear detection limit. Ganguly *et al*. [83]. Reproduced with the permission of American Chemical Society.

prementioned photoactivation tactic, histidine, arginine, tryptophan, and methionine are dominant interferants as they are also quenchers like Cys. That problem of interference during Cys sensing has been removed by aging the photoactivated solution for one day. After aging of the irradiated solution with individual quencher AAs, the regeneration of fluorescence occurs for histidine, arginine, tryptophan, and methionine excepting Cys. Thus the intriguing strategy for selective Cys recognition has been successfully achieved (Figure 9.16). The fluorescence intensity of the Cys-containing solution decreased gradually with the increased Cys concentration and lower detection limit for Cys was 50 nM (Figure 9.16).

9.3.2 Sensing of Toxic Metals

SEF has been used in sensing of toxic metals like Hg(II) and Cu(II). Both Hg(II) and Cu(II) are highly toxic. Hg(II) causes severe health hazards like breakdown of nervous system, muscle weakness, paralysis, damage of hearing and vision, and so on. It is exposed in environment mostly as factory wastage and it easily dissolves in water. Thus mercury poisoning mostly occurs from water-related foods like fish, shellfish, and so on. In 1956 the first report of mercury-assisted deadly disease, Minamata, was reported. Since then detection of mercury has become a severe concern of the scientists. There are many methods for

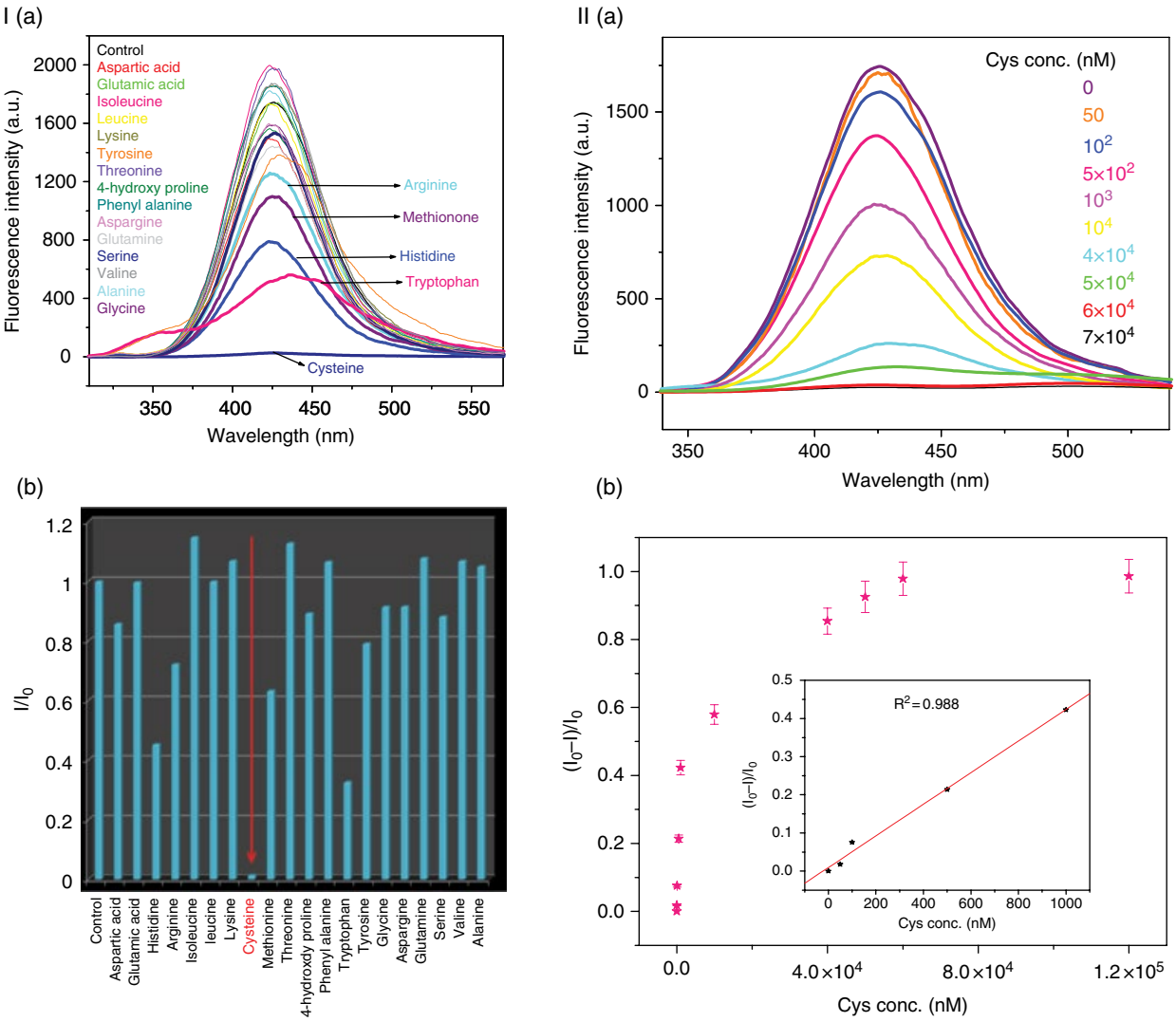

Figure 9.16 (I) (a) Fluorescence spectral profile and (b) bar diagram showing the effect of different AAs on the fluorescence of AgSQSL after 1 day of aging. Condition: [SL] = 1.4×10^{-4} M, [Ag(I)] = 1.4×10^{-4} M, [AA] = 7×10^{-5} M, λ_{ex} = 290 nm. (II) (a) Fluorescence spectral profile and (b) degree of fluorescence quenching of AgSQSL with the variation of Cys concentration. Inset of (b) represents range of linear detection (I and I_0 are fluorescence intensity of AgSQSL with and without Cys). Condition: [SL] = 1.4×10^{-4} M, [Ag(I)] = 1.4×10^{-4} M, λ_{ex} = 290 nm. Ganguly *et al.* [17]. Reproduced with the permission of American Chemical Society.

Hg detection [88–90]. However fluorometric technique is one of the suitable methods. Cu helps in human growth and development, but imbalance of Cu in the body causes serious neurodegenerative diseases such as Alzheimer's disease, Menkes and Wilson's diseases, amyotrophic lateral sclerosis, prion diseases [91], and so on. Fluorometric technique is one of the selective and sensitive ways for Cu(II) sensing leaving aside several other techniques [92, 93].

Hg(II) sensing has been performed by simply regeneration of quenched fluorescence of the Ag-QLDA solution (Figure 9.17). This method is interference free and effective. As Hg(II) has been found not to cause any alteration of the fluorescence of L, the enhancement is attributed to complex formation of DA with Hg(II). However, the extent of Hg(II)-induced rebirth of fluorescence is not exactly same as SEF (before addition of DA) because of the permanent change of the size and morphology of Ag(0) particle. Hg(II) causes further aggregation of Ag(0), which became discrete in presence of DA, enhancing the scattering efficiency along with complexation with DA. This enhances the fluorescence intensity. Introduction of Na2-EDTA to the Ag-QLDA–Hg(II) solution again lowers the fluorescence. This is due to the formation of Hg(II)-EDTA complex (formation constant, $K = 21.5$) resulting in free AgQDA that quenches the fluorescence again as before.

Cu(II) sensing has been done using the Cys-induced quenching of SEF. On aging of the quenched solution with different cationic salts for 3 days, only the solution with Cu(II) selectively regenerates the quenched fluorescence (Figure 9.18I). This process resulted in the formation of Cu(0). To this fluorescent solution,

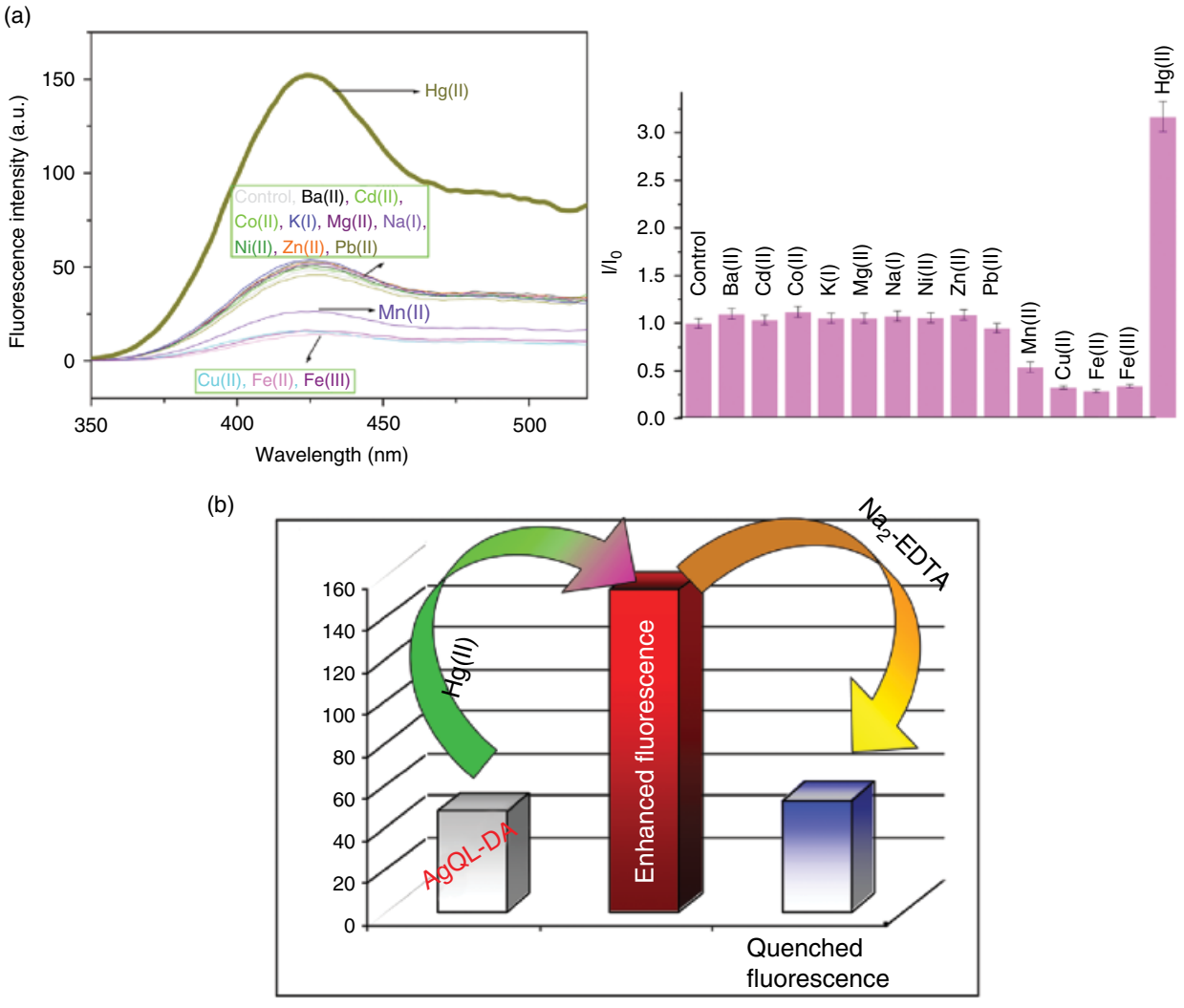

Figure 9.17 (a) Fluorescence spectral profile and bar diagram showing the effect of different metal ions on **AgQL**–DA solution; $[DA] = 3 \times 10^{-4}$ M, $[M^{n+}] = 3.0 \times 10^{-4}$ M. (b) Effect of Na_2-EDTA on **AgQL**–DA–Hg(II) solution. Ganguly *et al*. [83]. Reproduced with the permission of American Chemical Society.

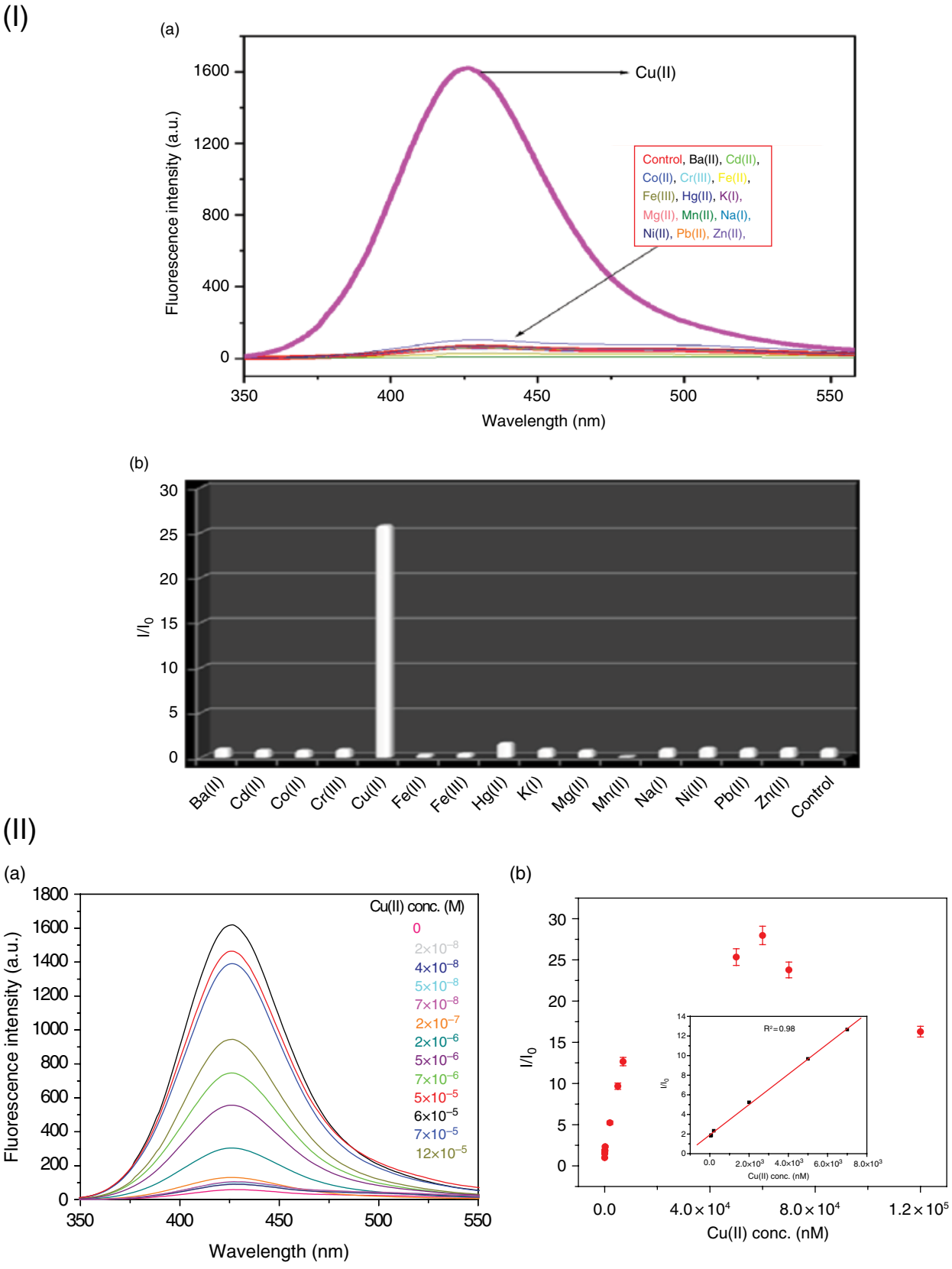

Figure 9.18 (I) (a) Fluorescence spectral profile and (b) bar diagram showing the effect of different metal ions on CyAgSQSL. Condition: $[SL] = 0.4 \times 10^{-4}$ M, $[Ag(I)] = 0.4 \times 10^{-4}$ M, $[Cys] = 2 \times 10^{-5}$ M, $[M^{n+}] = 6 \times 10^{-5}$ M, $\lambda_{ex} = 290$ nm. (II) (a) Fluorescence spectral profile ($\lambda_{ex} = 290$ nm) and (b) degree of fluorescence enhancement of CyAgSQSL with the variation of Cu(II) concentration. Inset of (b) represents linear detection limit (I and I_0 are fluorescence intensity of CyAgSQSL with and without Cu(II)). Condition: $[SL] = 0.4 \times 10^{-4}$ M, $[Ag(I)] = 0.4 \times 10^{-4}$ M, $[Cys] = 2 \times 10^{-5}$ M. Ganguly *et al.* [17]. Reproduced with the permission of John Wiley & Sons.

introduction of Na_2-EDTA could not change CEF, indicating the absence of Cu(II) in solution. XPS and lattice fringe measurements ratified that the formation of Cu(0) [7] was responsible for CEF. The lower detection limit was obtained to be 50 nM, and a good linear correlation of I/I_0 with Cu(II) concentration in the range from 50 nM to 7 μM was obtained (Figure 9.18II). A three-times higher concentration of Cu(II) than Cys concentration showed maximum (~190 times) fluorescence enhancement and further increase of [Cu(II)] caused quenching due to spin–orbit coupling [7]. Copper might get engaged [94] in Cys making Ag(0) free to enhance the fluorescence of oxidized SL (i.e., the rebirth of SEF) in solution. Again the enhancement of the fluorescence intensity might be due to concentrating the electric field around fluorophore in the presence of LSPR of Cu(0) [55, 71] along with the increased scattering cross section of the aggregated particles.

9.4 Conclusion

The *in situ*-produced M(0) nanoparticles have been successfully utilized in enhancing the fluorescence of well-known organic compounds. Unique property of the small molecule SL has been explored in the presence of Au(0) and Ag(0). The obtained SEF and GEF has been found to be admirably high in solution phase. The substitution of oxygen by nitrogen in the aldehyde functionality, that is, –CH═O to –CH═N–, selectively ceases GEF causing selective SEF. Such condensation reaction, involving iminic bond formation, made the way to design a highly sensitive Ag(I) sensor due to selective and mammoth SEF. Thus, one simple requirement of a suitable fluorophore with the "–CH═O" and phenolate group at the mutual *ortho*/*meta* position of an aromatic ring for silver and gold metal particle-mediated fluorescence enhancement is understood. Again, selective SEF, as a result of suitable wave vector matching, requires imine (–CH═N–) functionality instead of a carbonyl at the *ortho* position of the phenolate. Thus, the interference due to gold is nullified quantitatively due to the formation of LSWs. The proposed strategy may be a promising route for *in vivo* and *in vitro* detection of Ag(I) present at trace levels. Again the DSB produced out of condensation reaction shows CEF but at different experimental conditions. Thus by tuning the experimental condition, selective MEF is attained in solution phase. These MEF phenomena are also successfully applied in sensing of different biomolecules and heavy metals. Also such MEF can be successfully applied in bioimaging, chemical sensing and biosensing, single molecule studies, possibly catalysis, and other fields of science.

References

1 Deng, W.; Xie, F.; Baltar, H. T. M. C. M.; Goldys, E. M. Metal-Enhanced Fluorescence in the Life Sciences: Here, Now and Beyond. *Phys. Chem. Chem. Phys.* **2013**, *15*, 15695–15708.

2 Ganguly, M.; Mondal, C.; Jana, J; Pal, A.; Pal, T. Photoproduced Fluorescent Au(I)@(Ag_2/Ag_3)-Thiolate Giant Cluster: An Intriguing Sensing Platform for DMSO and Pb(II). *Langmuir* **2014**, *30*, 348–357.

3 Aslan, K.; Lakowicz, J. R.; Szmacinski, H.; Geddes, C. D. Metal-Enhanced Fluorescence Solution-Based Sensing Platform. *J. Fluoresc.* **2004**, *14*, 677–679.

4 Ganguly, M.; Pal, J.; Mondal, C.; Pal, A.; Pal, T. Imine (–CH═N–) brings selectivity for silver enhanced fluorescence. *Dalton Trans.* **2015**, *44*, 4370–4379.

5 Moal, E. L.; Fort, E.; Lévêque-Fort, S.; Cordelieres, F. P.; Fontaine-Aupart, M. P.; Ricolleau, C. Enhanced Fluorescence Cell Imaging with Metal-Coated Slides. *Biophys. J.* **2007**, *92*, 2150–2161.

6 Geddes, C. D.; Lakowicz, J. R. Metal Enhanced Fluorescence. *J. Fluoresc.* **2002**, *12*, 121–129.

7 Ganguly, M.; Pal, A.; Negishi, Y.; Pal, T. Diiminic Schiff Bases: An Intriguing Class of Compounds for a Copper-Nanoparticle-Induced Fluorescence Study. *Chem. Eur. J.* **2012**, *18*, 15845–15855.

8 Lakowicz, J. R. Radiative Decay Engineering 3. Surface Plasmon Coupled Directional Emission. *Anal. Biochem.* **2004**, *324*, 153–169.

9 Ford, G. W.; Weber, W. H. Electromagnetic Interactions of Molecules with Metal Surfaces. *Phys. Rep.* **1984**, *113*, 195–287.

10 Chance, R. R.; Prock, A.; Silbey, R. Molecular Fluorescence and Energy Transfer Near Interfaces. *Adv. Chem. Phys.* **1978**, *37*, 1–65.

11 Aslan, K.; Huang, J.; Wilson, G. M.; Geddes, C. D. Metal-Enhanced Fluorescence Based RNA Sensing. *J. Am. Chem. Soc.* **2006**, *128*, 4206–4207.

12 Song, J. H.; Atay, T.; Shi, S.; Urabe, H.; Nurmikko, A. V. Large Enhancement of Fluorescence Efficiency from CdSe/ZnS Quantum Dots Induced by Resonant Coupling to Spatially Controlled Surface Plasmons. *Nano Lett.* **2005**, *5*, 1557–1561.

13 Lakowicz, J. R.; Chowdhury, M. H.; Ray, K.; Zhang, J.; Fu, Y.; Badugu, R.; Sabanayagam, C. R.; Nowaczyk, K.; Szmacinski, H.; Aslan, K.; *et al.* Plasmon-Controlled Fluorescence: A New Detection Technology. *Proc. SPIE* **2006**, *6099*, 609909/1–609909/15.

14 Zhang, Y.; Dragan, A.; Geddes, C. D. Wavelength Dependence of Metal-Enhanced Fluorescence. *J. Phys. Chem. C* **2009**, *113*, 12095–12100.

15 Lakowicz, J. R. Radiative Decay Engineering 5: Metal-Enhanced Fluorescence and Plasmon Emission. *Anal. Biochem.* **2005**, *337*, 171–194.

16 Bek, A.; Jansen, R.; Ringler, M.; Mayilo, S.; Klar, T. A.; Feldmann, J. Fluorescence Enhancement in Hot Spots of AFM-Designed Gold Nanoparticle Sandwiches. *Nano Lett.* **2008**, *8*, 485–490.

17 Ganguly, M.; Pal, J.; Mondal, C.; Pal, A.; Pal, T. Intriguing Manipulation of Metal-Enhanced Fluorescence for the Detection of Cu(II) and Cysteine. *Chem. Eur. J.* **2014**, *20*, 12470–12476.

18 Susie, E.; El-Sayed, M. A. Why Gold Nanoparticles are more Precious than Pretty Gold: Noble Metal Surface Plasmon Resonance and its Enhancement of the Radiative and Nonradiative Properties of Nanocrystals of Different Shapes. *Chem. Soc. Rev.* **2006**, *35*, 209–217.

19 Lakowicz, J. R. Radiative Decay Engineering: Biophysical and Biomedical Applications. *Anal. Biochem.* **2001**, *298*, 1–24.

20 Geddes, C. D.; Cao, H.; Gryczynski, I.; Gryczynski, I. Z.; Fang, J.; Lakowicz, J. R. Metal-Enhanced Fluorescence (MEF) Due to Silver Colloids on a Planar Surface: Potential Applications of Indocyanine Green to In Vivo Imaging. *J. Phys. Chem. A* **2003**, *107*, 3443–3449.

21 Aslan, K.; Lakowicz, J. R.; Geddes, C. D. Rapid Deposition of Triangular Silver Nanoplates on Planar Surfaces: Application to Metal-Enhanced Fluorescence. *J. Phys. Chem. B* **2005**, *109*, 6247–6251.

22 Aslan, K.; Leonenko, Z.; Lakowicz, J. R.; Geddes, C. D. Fast and Slow Deposition of Silver Nanorods on Planar Surfaces: Application to Metal-Enhanced Fluorescence. *J. Phys. Chem. B* **2005**, *109*, 3157–3162.

23 Parfenov, A.; Gryczynski, I.; Malicka, J.; Geddes, C. D.; Lakowicz, J. R. Enhanced Fluorescence from Fluorophores on Fractal Silver Surfaces. *J. Phys. Chem. B* **2003**, *107*, 8829–8833.

24 Zhang, Y.; Aslan, K.; Previte, M. J. R.; Geddes, C. D. Low Temperature Metal-Enhanced Fluorescence. *J. Fluoresc.* **2007**, *17*(6), 627–631.

25 Aslan, K.; Wu, M.; Lakowicz, J. R.; Geddes, C. D. Metal Enhanced Fluorescence Solution-Based Sensing Platform 2: Fluorescent Core-Shell Ag@ SiO_2 Nanoballs. *J. Fluoresc.* **2007**, *17*, 127–131.

26 Qin, W.; Liu, W.; Tan, M. Study on the New Fluorescence Enhancement System of Tb-1,10-bis(2′-Carboxyphenyl)-1,4,7,10-Tetraoxadecane in Silver Chloride Collosol and its Analytical Application. *Anal. Chim. Acta* **2002**, *468*, 287–292.

27 Gill, R.; Tian, L.; Somerville, W. R. C.; Ru, E. C. L.; Amerongen, H. v.; Subramaniam, V. Silver Nanoparticle Aggregates as Highly Efficient Plasmonic Antennas for Fluorescence Enhancement. *J. Phys. Chem. C* **2012**, *116*, 16687–16693.

28 Zhang, Y.; Aslan, K.; Previte, M. J. R.; Geddes, C. D. Metal-Enhanced Fluorescence from Copper Substrates. *Appl. Phys. Lett.* **2007**, *90*, 173116-1–173116-3.

29 Aslan, K.; Leonenko, Z.; Lakowicz, J. R.; Geddes, C. D. Annealed Silver-Island Films for Applications in Metal-Enhanced Fluorescence: Interpretation in Terms of Radiating Plasmons. *J. Fluoresc.* **2005**, *15*, 643–654.

30 Pompa, P. P.; Martiradonna, L.; Della Torre, A.; Della Sala, F.; Manna, L.; De Vittorio, M.; Calabi, F.; Cingolani, R.; Rinaldi, R. Metal-Enhanced Fluorescence of Colloidal Nanocrystals with Nanoscale Control. *Nat. Nanotechnol.* **2006**, *1*, 126–130.

31 Dulkeith, E.; Ringler, M.; Klar, T. A.; Feldmann, J.; Munoz, J. A.; Parak, W. J. Gold Nanoparticles Quench Fluorescence by Phase Induced Radiative Rate Suppression. *Nano Lett.* **2005**, *5*, 585–589.

32 Ganguly, M.; Pal, A.; Pal, T. Intriguing Fluorescence Behavior of Diiminic Schiff Bases in the Presence of in situ Produced Noble Metal Nanoparticles. *J. Phys. Chem. C* **2012**, *116*, 9265–9273.

33 Aslan, K.; Malyn, S. N.; Geddes, C. D. Metal-Enhanced Fluorescence from Gold Surfaces: Angular Dependent Emission. *J. Fluoresc.* **2007**, *17*, 7–13.

34 Aslan, K.; Malyn, S. N.; Geddes, C. D. Angular-Dependent Metal-Enhanced Fluorescence from Silver Island Films. *Chem. Phys. Lett.* **2008**, *453*, 222–228.

35 Lukomska, J.; Malicka, J.; Gryczynski, Z.; Leonenko, Z.; Lakowicz, J. R. Fluorescence Enhancement of Fluorophores Tethered to Different Sized Silver Colloids Deposited on Glass Substrate. *Biopolymers* **2005**, *77*, 31–37.

36 Mertens, H.; Polman, A., in *ArXiv* e-prints. **2007**, 711.

37 Chen, J.; Jin, Y.; Fahruddin, N.; Zhao, J. X. Development of Gold Nanoparticle-Enhanced Fluorescent Nanocomposites. *Langmuir* **2013**, *29*, 1584–1591.

38 Zhang, J.; Thurber, A.; Tenne, D. A.; Rasmussen, J. W.; Wingett, D.; Hanna, C.; Punnoose, A. Enhanced Dye Fluorescence in Novel Dye–ZnO Nanocomposites. *Adv. Funct. Mater.* **2010**, *20*, 4358–4363.

39 Malicka, J.; Gryczynski, I.; Kusba, J.; Lakowicz, J. R. Effects of Metallic Silver Island Films on Resonance Energy Transfer Between *N*,*N*′-(Dipropyl)-tetramethyl-indocarbocyanine(Cy3)- and *N*,*N*′-(Dipropyl)-tetramethyl-indodicarbocyanine(Cy5)-Labeled DNA. *Biopolymers* **2003**, *70*, 595–603.

40 Selvakannan, P. R.; Swami, A.; Srisathiyanarayanan, D.; Shirude, P. S.; Pasricha, R.; Mandale, A. B.; Sastry, M. Synthesis of Aqueous Au Core–Ag Shell Nanoparticles Using Tyrosine as a pH-Dependent Reducing Agent and Assembling Phase-Transferred Silver Nanoparticles at the Air–Water Interface. *Langmuir* **2004**, *20*, 7825–7836.

41 Ganguly, M.; Pal, A.; Pal, T. Intriguing Fluorescence Behavior of Diiminic Schiff Bases in the Presence of in situ Produced Noble Metal Nanoparticles. *J. Phys. Chem. C* **2011**, *115*, 22138–22147.

42 Ganguly, M.; Mondal, C.; Chowdhury, J.; Pal, J.; Pal, A.; Pal, T. The Tuning of Metal Enhanced Fluorescence for Sensing Applications. *Dalton Trans.* **2014**, *43*, 1032–1047.

43 Al-Kady, A. S.; Gaber, M.; Hussein, M. M.; Ebeid, E. Fluorescence Enhancement of Coumarin Thiourea Derivatives by Hg^{2+}, Ag^{+}, and Silver Nanoparticles. *J. Phys. Chem. A* **2009**, *113*, 9474–9484.

44 Zhang, J. F.; Zhou, Y.; Yoon, J. Kim, J. S. Recent progress in fluorescent and colorimetric chemosensors for detection of precious metal ions (silver, gold and platinum ions). *Chem. Soc. Rev.* **2011**, *40*, 3416–3429.

45 Yuan, X.; Luuuo, Z.; Zhang, Q.; Zhang, X.; Zheng, Y.; Lee, J. Y.; Xie, J. Synthesis of Highly Fluorescent Metal (Ag, Au, Pt, and Cu) Nanoclusters by Electrostatically Induced Reversible Phase Transfer. *ACS Nano* **2011**, *5*, 8800–8808.

46 Yuan, X.; Tay, Y.; Dou, X.; Luo, Z.; Leong, D. T.; Xie, J. Glutathione-Protected Silver Nanoclusters as Cysteine-Selective Fluorometric and Colorimetric Probe. *Anal. Chem.* **2013**, *85*, 1913–1919.

47 Ganguly, M.; Pal, J.; Das, S.; Mondal, C.; Pal, A.; Negishi, Y.; Pal, T. Green Synthesis and Reversible Dispersion of a Giant Fluorescent Cluster in Solid and Liquid Phase. *Langmuir* **2013**, *29*, 10945–10958.

48 Maretti, L.; Billone, P. S.; Liu, Y.; Scaiano, J. C. Facile Photochemical Synthesis and Characterization of Highly Fluorescent Silver Nanoparticles. *J. Am. Chem. Soc.* **2009**, *131*, 13972–13980.

49 Ganguly, M.; Pal, A.; Negishi, Y.; Pal, T. Synthesis of Highly Fluorescent Silver Clusters on Gold(I) Surface. *Langmuir* **2013**, *29*, 2033–2043.

50 Luo, Z.; Zheng, K.; Xie, J. Engineering Ultrasmall Water-Soluble Gold and Silver Nanoclusters for Biomedical Applications. *Chem. Commun.* **2014**, *50*, 5143–5155.

51 Ray, P. C.; Darbha, G. K.; Ray, A.; Hardy, W.; Walker, J. A Gold-Nanoparticle-Based Fluorescence Resonance Energy Transfer Probe for Multiplexed Hybridization Detection: Accurate Identification of Bio-Agents DNA. *Nanotechnology* **2007**, *18*, 375504–375510.

52 Chowdhury, M. H.; Lakowicz, J. R.; Ray, K. Ensemble and Single Molecule Studies on the Use of Metallic Nanostructures to Enhance the Intrinsic Emission of Enzyme Cofactors. *J. Phys. Chem. C* **2011**, *115*, 7298–7308.

53 Chowdhury, M. H.; Chakraborty, S.; Lakowicz, J. R.; Ray, K. Feasibility of Using Bimetallic Plasmonic Nanostructures to Enhance the Intrinsic Emission of Biomolecules. *J. Phys. Chem. C* **2011**, *115*, 16879–16891.

54 Ray, K.; Chowdhury, M. H.; Lakowicz, J. R. Single-Molecule Spectroscopic Study of Enhanced Intrinsic Phycoerythrin Fluorescence on Silver Nanostructured Surfaces. *Anal. Chem.* **2008**, *80*, 6942–6942.

55 G. Mie, Beiträge zur Optik trüber Medien, speziell kolloidaler Metallösungen. *Ann. Physik.* **1908**, *330*, 377–445.

56 Pfeiffer, P.; Breith, E.; Lübbe, E.; Tsumaki, T. Tricyclische orthokondensierte Nebenvalenzringe. *Justus Liebig's Ann. Chem.* **1933**, *503*, 84–130.

57 Diehl, H.; Hach, C. C. Bis(*N,N′*-Disalicylalethylenediamine)-μ – Aquodicobalt(II). *Inorg. Synth.* **1950**, *3*, 196–201.

58 Roy, G. B. Synthesis and Study of Physico-Chemical Properties of a New Chiral Schiff Base Ligand and its Metal Complex. *Inorg. Chim. Acta* **2009**, *362*, 1709–1714.

59 Liu, G. D.; Liao, J. P.; Huang, S. S.; Shen, G. L.; Yu, R. Q. Fluorescence Spectral Study of Interaction of Water-Soluble Metal Complexes of Schiff-Base and DNA. *Anal. Sci.* **2001**, *17*, 1031–1036.

60 Chen, P.; Lu, R.; Xue, P.; Xu, T.; Chen, G.; Zhao, Y. Emission Enhancement and Chromism in a Salen-Based Gel System. *Langmuir* **2009**, *25*, 8395–8399.

61 Deda, M. L.; Ghedini, M.; Aiello, I.; Grisolia, A. A New Blue Photoluminescent Salen-like Zinc Complex with Excellent Emission Quantum Yield. *Chem. Lett.* **2004**, *33*, 1060–1061.

62 White, C. E.; Cuttitta, F. Fluorometric Study of Magnesium-Bissalicylidene–Ethylenediamine System. *Anal. Chem.* **1959**, *31*, 2083–2087.

63 Germain, M. E.; Knapp, M. J. Turn-On Fluorescence Detection of H_2O_2 and TATP. *Inorg. Chem.* **2008**, *47*, 9748–9750.

64 Lee, J. H.; Jeong, A. R.; Shin, I. S.; Kim, H. J.; Hong, J. I. Fluorescence Turn-On Sensor for Cyanide Based on a Cobalt(II)–Coumarinylsalen Complex. *Org. Lett.* **2010**, *12*, 764–767.

65 Aoki, I.; Takahashi, A.; Watanabe, K. Determination of aliphatic primary amines by flow injection fluorometry using beryllium–Schiff base complexes. *Anal. Sci.* **1992**, *8*, 323–327.

66 Ray, P. C.; Darbha, G. K.; Ray, A.; Walker, J.; Hardy, W. Gold Nanoparticle Based FRET for DNA Detection. *Plasmonics* **2007**, *2*, 173–183.

67 Lakowicz, J. R.; Shen, Y.; Auria, S.; Malicka, J.; Fang, J.; Gryczynski, Z.; Gryczynski, I. Radiative Decay Engineering: 2. Effects of Silver Island Films on Fluorescence Intensity, Lifetimes, and Resonance Energy Transfer. *Anal. Biochem*. **2002**, *301*, 261–277.

68 Lakowicz, J. R.; Geddes, C. D.; Gryczynski, I.; Malicka, J.; Gryczynski, Z.; Aslan, K.; Lukomska, J.; Matveeva, E.; Zhang, J.; Badugu, R.; *et al*. Advances in Surface-Enhanced Fluorescence. *J. Fluoresc.* **2004**, *14*, 425–441.

69 Sokolov, K.; Chumanov, G.; Cotton, T. M. Enhancement of Molecular Fluorescence near the Surface of Colloidal Metal Films. *Anal. Chem.* **1998**, *70*, 3898–3905.

70 Malshet, V. G.; Tappel, A. L. Fluorescent Products of Lipid Peroxidation: I. Structural Requirement for Fluorescence in Conjugated Schiff Bases. *Lipids* **1973**, *8*, 194–198.

71 Rahimi,Y.; Goulding, A.; Shrestha, S.; Mirpuri, S.; Deo, S. K. Mechanism of Copper Induced Fluorescence Quenching of Red Fluorescent Protein, DsRed. *Biochem. Biophys. Res. Commun.* **2008**, *370*, 57–61.

72 Selvan, S. T.; Hayakawa, T.; Nogami, M. Remarkable Influence of Silver Islands on the Enhancement of Fluorescence from Eu^{3+} Ion-Doped Silica Gels. *J. Phys. Chem. B* **1999**, *103*, 7064–7067.

73 Kinkhabwala, A.; Yu, Z.; Fan, S.; Avlasevich, Y.; Muellen, K.; Moerner, W. E. Large Single-Molecule Fluorescence Enhancements Produced by a Bowtie Nanoantenna. *Nat. Photonics* **2009**, *3*, 654–657.

74 Darugar, Q.; Qian, W.; El-Sayed, M. A. Size-Dependent Ultrafast Electronic Energy Relaxation and Enhanced Fluorescence of Copper Nanoparticles. *J. Phys. Chem. B* **2006**, *110*, 143–149.

75 Volpati, D.; Spada, E. R.; Pla Cid, C. C.; Sartorelli, M. L.; Aroca, R. F.; Constantino, C. J. L. Exploring copper nanostructures as highly uniform and reproducible substrates for plasmon-enhanced fluorescence. *Analyst*, **2015**, *140*, 476–482.

76 Sugawa, K.; Tamura, T.; Tahara, H.; Yamaguchi, D.; Akiyama,T.;Otsuki,J.;Kusaka,Y.;Fukuda,N.;Ushijima,H. Metal-Enhanced Fluorescence Platforms Based on Plasmonic Ordered Copper Arrays: Wavelength Dependence of Quenching and Enhancement Effects. *ACS Nano* **2013**, *7*, 9997–10010.

77 Wightman, R. M.; May, L. J.; Michael, A. C. Detection of Dopamine Dynamics in the Brain. *Anal. Chem.* **1988**, *60*, 769A–779A.

78 Zhang, A.; Neumeyer, J. L.; Baldessarini, R. J. Recent Progress in Development of Dopamine Receptor Subtype-Selective Agents: Potential Therapeutics for Neurological and Psychiatric Disorders. *Chem. Rev.* **2007**, *107*, 274–302.

79 Damier, P.; Hirsch, E. C.; Agid, Y.; Graybiel, A. M. The Substantia Nigra of the Human Brain. II. Patterns of Loss of Dopamine-Containing Neurons in Parkinson's Disease. *Brain* **1999**, *122*, 1437–1448.

80 Dawson, T. M.; Dawson, V. L. Molecular Pathways of Neurodegeneration in Parkinson's Disease. *Science* **2003**, *302*, 819–822.

81 Arrigan, D. W. M.; Ghita, M.; Beni, V. Selective Voltammetric Detection of Dopamine in the Presence of Ascorbate. *Chem. Commun.* **2004**, 732–733.

82 Fragoso, A.; Almirall, E.; Cao, R.; Echegoyen, L.; Gonzalez-Jonte, R. A Supramolecular Approach to the Selective Detection of Dopamine in the Presence of Ascorbate. *Chem. Commun.* **2004**, 2230–2232.

83 Ganguly, M.; Mondal, C.; Jana, J.; Pal, A.; Pal, T. Selective Dopamine Chemosensing Using Silver-Enhanced Fluorescence. *Langmuir* **2014**, *30*, 4120–4128.

84 Lin, Y.; Chen, C.; Wang, C.; Pu, F.; Ren, J.; Qu., X. Silver Nanoprobe for Sensitive and Selective Colorimetric Detection of Dopamine via Robust Ag–Catechol Interaction. *Chem. Commun.* **2011**, *47*, 1181–1183.

85 Yu, C.; Luo, M.; Zeng, F.; Zheng, F.; Wu, S. Mesoporous Silica Particles for Selective Detection of Dopamine with β-Cyclodextrin as the Selective Barricade. *Chem. Commun.* **2011**, *47*, 9086–9088.

86 Choudhury, S. D.; Badugu, R.; Ray, K.; Lakowicz, J. R. Silver-Gold Nanocomposite Substrates for Metal-Enhanced Fluorescence: Ensemble and Single-Molecule Spectroscopic Studies. *J. Phys. Chem. C* **2012**, *116*, 5042–5048.

87 Ming, T.; Zhao, L.; Chen, H.; Woo, K. C.; Wang, J.; Lin, H. Q. Experimental Evidence of Plasmophores: Plasmon-Directed Polarized Emission from Gold Nanorod-Fluorophore Hybrid Nanostructures. *Nano Lett.* **2011**, *11*, 2296–2303.

88 Ono, A.; Togashi, H. Highly Selective Oligonucleotide-Based Sensor for Mercury(II) in Aqueous Solutions. *Angew. Chem. Int. Ed.* **2004**, *43*, 4300–4302.

89 Madhu, S.; Sharma, D. K.; Basu, S. K.; Jadhav, S.; Chowdhury, A.; Ravikanth, M. Sensing Hg(II) *in Vitro* and *in Vivo* Using a Benzimidazole Substituted BODIPY. *Inorg. Chem.* **2013**, *52*, 11136–11145.

90 Huanga, C.-C.; Chang, H.-T. Parameters for Selective Colorimetric Sensing of Mercury(II) in Aqueous Solutions Using Mercaptopropionic

Acid-Modified Gold Nanoparticles. *Chem. Commun.* **2007**, 1215–1217.

91 Que, E. L.; Chang, C. J. A Smart Magnetic Resonance Contrast Agent for Selective Copper Sensing. *J. Am. Chem. Soc.* **2006**, *128*, 15942–15943.

92 Royzen, M.; Dai, Z.; Canary, J. W. Ratiometric Displacement Approach to Cu(II) Sensing by Fluorescence. *J. Am. Chem. Soc.* **2005**, *127*, 1612–1613.

93 Yin, K.; Li, B.; Wang, X.; Zhang, W.; Chen, L. Ultrasensitive Colorimetric Detection of Cu^{2+} Ion based on Catalytic Oxidation of L-Cysteine. *Biosens. Bioelectron.* **2015**, *64*, 81–87.

94 Rigo, A.; Corazza, A.; di Paolo, M. L.; Rossetto, M.; Ugolini, R.; Scarpa, M. Interaction of Copper with Cysteine: Stability of Cuprous Complexes and Catalytic Role of Cupric Ions in Anaerobic Thiol Oxidation. *J. Inorg. Biochem.* **2004**, *98*, 1495–501.

10

Distance and Location-Dependent Surface Plasmon Resonance-Enhanced Photoluminescence in Tailored Nanostructures

Saji Thomas Kochuveedu[1,2] *and Dong Ha Kim*[2*]

[1] *Institute of Applied Physics, Johannes Kepler University, Altenbergerstraße, Austria*
[2] *Department of Chemistry and Nano Science, School of Natural Sciences, Ewha Womans University, Seoul, Korea*

10.1 Introduction

The interaction of light with materials such as fluorophores, metals, and semiconductors helps us to analyze and understand their fundamental physiochemical features, and the extent of optical analysis contributes a lot to the applications of them. Absorption of light followed by emission is difEferent for each light-emitting material. The specific wavelength at which the material absorbs and emits light is the fingerprint of various energy levels existing in them. The wavelength of absorption of light by a semiconductor is dependent on the band gap, which is the void region, between the top of the filled valence band (VB) and the bottom of the vacant conduction band (CB). Upon illumination, absorption of photons followed by generation of excited ones occurred, and the energy of excited state is released mainly through emission of light, called as photoluminescence (PL) (Scheme 10.1) [1] and is characteristic of each material [2, 3]. The mechanism of light emission is similar in the case of fluorophores such as dyes. Following light absorption, fluorophore is excited from the ground state (S_0) to a higher level S_1 or S_2. Through a process called internal conversion (IC), the fluorophores relax to lower vibrational level. Fluorophores may come back to S_0 by the emission of light called fluorescence or undergo a spin conversion called intersystem crossing (ISC), which causes a spin conversion from the singlet (S_1) to the triplet (T1) state. Decay from T1 to ground state is termed as phosphorescence. The whole process can be explained using Jablonski diagram (Scheme 10.2) [1, 4, 5].

Low-dimensional material called "quantum dots (QDs)" represent a class of quantum confined system and have profound impact in semiconductor physics. The ease to tune the wavelength of emission of light by altering the size of semiconductor nanoparticles (NPs) makes them an apt material for applications in areas such as optoelectronics [6, 7] and medical diagnosis/theranostics [8, 9]. For example, CdSe nanocrystals of 2 nm size emit light in the blue region, whereas those of 6 nm give red emission [10]. Despite of all the merits QDs have, the quantum yield (QY) achieved is always less than the theoretical predictions due to the issues related to surface defects and stability of QDs. Thus, adopting appropriate measures to improve the QY of QDs in reproducible manner has become an attractive topic of research. Similarly, fluorescence is considered as highly sensitive technique, but detection of single molecule demands high level of sensitivity, which is often hindered by poor QY and background signals from the sample. Improvement of brightness of the fluorophore enhances the sensitivity of fluorescence-based applications in the fields such as optics [11, 12], medicine [13–15], and photonics [16, 17].

Good control over absorption and emission of light is highly required for most of the fluorophore-based techniques. For example, light-emitting devices demand high emission output, whereas optical sensing and imaging need high excitation and emission for deep penetration into the tissue for detecting traces of target. Moreover, the brightness or emission rate decides the quality of observability of fluorophores. Therefore, finding an appropriate strategy to enhance emission has been a critical challenge to the researchers. Ability of noble metals to alter the light emission of vicinal fluorophores is an attractive approach to amply the light emission since noble metal NPs show extraordinary optical sensitivity toward light of wide range of wavelength. The unique optical property of noble metal NPs is due to the phenomenon called surface plasmon resonance (SPR), which occurred when

* corresponding author

Surface Plasmon Enhanced, Coupled and Controlled Fluorescence, First Edition. Edited by Chris D. Geddes.
© 2017 John Wiley & Sons, Inc. Published 2017 by John Wiley & Sons, Inc.

the oscillation propagating waves along the surface of the metal, known as surface plasmons (SPs), resonate with the wave vector of the incident light (Scheme 10.3) [18]. When the SPs are confined to a nanostructure, it is called localized SPs, whereas propagating surface plasmons (PSPs) are obtained when the propagating electromagnetic waves couple with the oscillation of the electron plasma of the metal film (Scheme 10.4) [19]. Plasmonic nanostructures can concentrate light into localized field around the nanostructures, and the intensity of the field is influenced by the size, shape, organization, and environment of the nanostructures [19–22]. Therefore, by altering any of the depending factors, the intensity and distribution of the field can be modified. Following the enhanced local field of the irradiated metal NPs, absorption efficiency, radiative rate, and QY of vicinal fluorophores can be influenced [23]. Enhancement or quenching of emission of fluorophores is strongly affected by the metal-emitter separation and geometry of nanostructures. When the emission of light is directly absorbed by the metal, quenching is observed, while a few nanometer of separation between metal and emitter can lead to the enhancement of emission [1, 24]. The enhancement of emission in the presence metal is broadly termed as metal-enhanced fluorescence (MEF).

Noble metals such as gold (Au) and silver (Ag) are recognized for their size and shape-dependent SP absorption wavelength ranging from UV to near infrared (IR), which gives the advantage to use wide range of fluorophores in combination with metal to explore MEF and their specific applications. The mechanisms playing role in MEF can be many, but a few which draw more attention are resonance energy

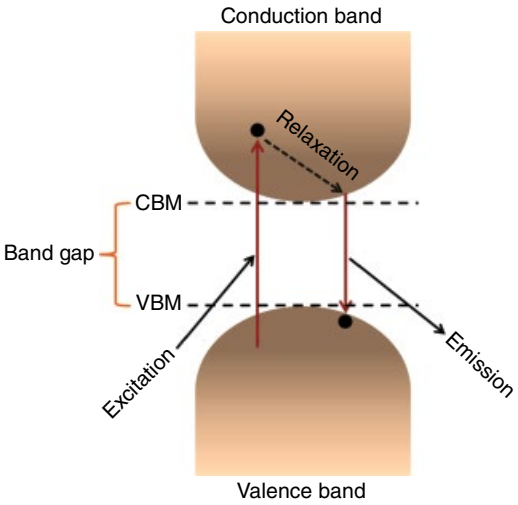

Scheme 10.1 Schematic representation of the photoluminescence process in semiconductors. CBM and VBM represent conduction band minimum and valence band maximum, respectively. The distance between VBM and CBM is called the band gap. Kochuveedu and Kim [1]. Reproduced with the permission of Royal Society of Chemistry.

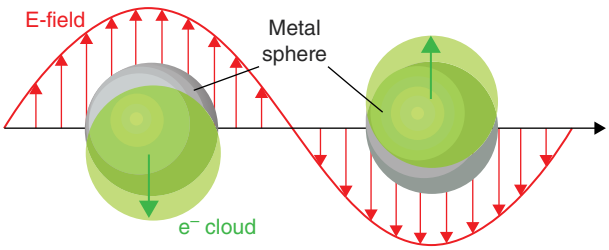

Scheme 10.3 Schematic of plasmon oscillation for a sphere, showing the displacement of the conduction electron charge cloud relative to the nuclei. Kelly *et al*. [18]. Reproduced with the permission of American Chemical Society. (*See insert for color representation of this figure*.)

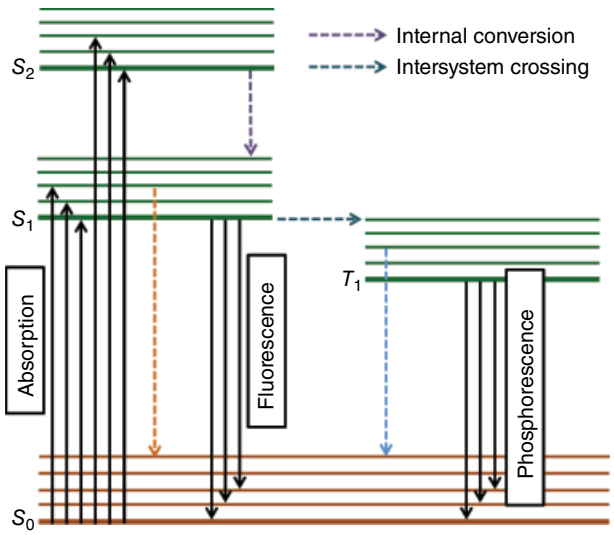

Scheme 10.2 Jablonski diagram showing the various steps involved in fluorescence and phosphorescence. S_0 denotes the singlet ground state, and S_1 and S_2 are the excited singlet states. T represents triplet states. IC and ISC are nonradiative processes. Intersystem crossings are accompanied by a forbidden change in the spin state, which later leads to phosphorescence. Kochuveedu and Kim [1]. Reproduced with the permission of Royal Society of Chemistry.

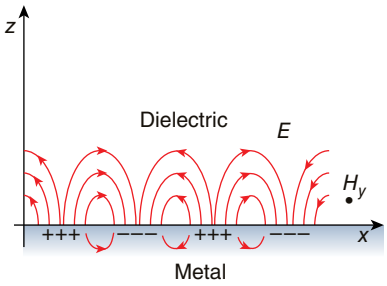

Scheme 10.4 SPP showing a collective excitation at a metal-dielectric interface. The electromagnetic field (electric field, *E*, plotted in the *z*–*x* plane; magnetic field, H_y, sketched in the *y*-direction) is drastically enhanced. SPs at the interface between a metal and a dielectric material have a combined character of electromagnetic wave and surface charge. Barnes *et al*. [19]. Reproduced with the Nature Publishing Group.

transfer (RET) and near-field enhancement (NFE), while quenching of fluorescence is mainly ruled by direct energy transfer (DET). By fine-tuning of distance between emitter and metal, quenching or enhancement of emission can be controlled [1, 18].

The advantage of MEF can be further extended to three-component systems, especially in Förster resonance energy transfer (FRET). FRET is the nonradiative energy transfer from an excited donor fluorophore to the ground-state acceptor fluorophore via dipole–dipole interaction. Spectral overlap of emission of donor and absorbance of acceptor, relative orientation of the dipoles of the donor–acceptor pair, and distance between donor and acceptor is the essential requisite for FRET [4, 5]. Due to the significant importance of FRET in the study of various biological phenomena, such as protein–protein interactions [25, 26] and conformational changes of biomolecules [27, 28], considerable amount of efforts has been devoted to improve the efficiency of FRET. Inclusion of plasmonic metal at an appropriate place in a FRET pair is a useful strategy to improve the energy transfer between donor and acceptor since most of the FRET pairs suffer from poor QY and low photostability [29–32].

In this chapter we will introduce various mechanisms involved in the energy transfer between metal and fluorophores leading to enhancement or quenching of emission. The discussions are mainly based on binary and tertiary components of metal-fluorophore systems.

10.2 Effect of SPR in PL

10.2.1 Photoluminescence

The energy of the excited electrons is decayed mainly through two pathways, radiative decay and nonradiative decay. Spontaneous emission of photons after the excitation of electrons is known as radiative decays, which is observed as PL [1]. The mechanism of generation of PL in semiconductors and fluorophores is discussed in the introduction. When the energy is released as photons, it is known as nonradiative decay. Mostly heat is released as nonradiative decay. The quantum efficiency of the emitter is the combinational effect of radiative and nonradiative decay and is calculated as [33]

$$\mathrm{QY} = \frac{\Gamma_{\mathrm{rad}}}{\Gamma_{\mathrm{rad}} + \Gamma_{\mathrm{non-rad}}} \tag{10.1}$$

where Γ_{rad} and $\Gamma_{\mathrm{non-rad}}$ are radiative and nonradiative decay rates.

The presence of metal NPs in the vicinity of fluorophore affects the radiative and nonradiative decays, thereby the emission properties. The rate of both radiative and nonradiative decay depends on the size and shape of metal NPs, distance between the NPs and emitter, and overlap of emission of fluorophore with the absorption of metal NPs [4, 34]. Therefore the QY is modified in the presence of metal. The rate of emission $\left(\Gamma'_{\mathrm{emiss}}\right)$ of fluorophore near the metal is expressed as

$$\Gamma'_{\mathrm{emiss}} = \Gamma'_{\mathrm{exc}} \cdot \frac{\Gamma'_{\mathrm{rad}}}{\Gamma'_{\mathrm{rad}} + \Gamma'_{\mathrm{non-rad}}} \tag{10.2}$$

where Γ'_{exc} is the rate of excitation and Γ'_{rad} and $\Gamma'_{\mathrm{non-rad}}$ are radiative and nonradiative decay rate of fluorophore in the presence of metal, respectively [33, 35].

10.2.1.1 Radiative Decay in MEF

The energy difference between the excited state and empty ground state is released mostly as light, during the transition of electrons from higher energy to lower energy state. The ratio between number of photons absorbed and number of photons emitted is defined as the yield. Metals are known for their richness of conducting electrons. The emission property of fluorophores can be influenced by the presence of metal due to the correspondence between the excitation and emission wavelength of fluorophores and SPR of the metal [36]. The changes in the absorption and emission intensity in the presence of metal are strongly influenced by the distance between the metal and fluorophore. It is observed mostly that quenching of emission is strong at short distances, but the radiative decay is increased as the distance between fluorophore and metal increases [37]. When excited fluorophores are located near the metal, the oscillating near field of the decaying molecules excites the SPs in the metal provided their respective frequencies are close. In such resonant cases, the emission energy

from the emitter is transferred to the metal and radiated off, which increases the radiative decay rate [38]. Fluorophores in the vicinity of metal may experience increased emission intensity and quantum efficiency, decreased lifetime due to the increased rate in the excitation, and radiative decay of fluorophores. The increased excitation is due to the enhanced near field around the metal [37]. Another concept to explain quenching and enhancement of emission is radiating plasmons (RPs). According to RP model fluorescence quenching is caused by absorption by the NPs, whereas scattering leads to enhancement of fluorescence. The incident light can induce oscillating charge in the metal NPs. The oscillating charges radiate the energy to far field, and the scattering component decides the extension of radiation into far field by plasmons. In the case of smaller metallic NPs, the extinction coefficient is dominated by absorption than by scattering, leading to mostly quenching of emission. Larger particles show dominant scattering, resulting in the enhancement of emission. The extinction spectra shift toward longer wavelength when NPs are at interacting distance, due to the coupling of plasmons. Normally the increased extinction at longer wavelength is due to cluster of NPs. Therefore, MEF is more vivid in the case of interacting NPs. The scattering intensity is further increased in the case of elongated particles [23]. The RP model provides information for the use of desirable metallic nanostructures to collect and direct the energy from the fluorophores. It is therefore desirable to couple the energy fluorophore with the radiative energy of plasmon to extract the maximum benefit of MEF.

The orientation of fluorophore with respect to the metal affects the radiative decay dramatically. The radiative decay is enhanced by a factor of 1000 or more when a fluorophore is oriented perpendicular to the surface of spheroid, whereas it was much smaller for a sphere and for an elongated spheroid [39]. In the perpendicular orientation, the dipole of fluorophore and that of metal is synergetic and increases the radiative decay rate. In the parallel orientation the dipole in the fluorophore cancels the dipole in the metal, slowing the radiative decay.

10.2.1.2 Nonradiative Decay in MEF

It is often observed that the emission energy is quenched when the fluorophore is very close to the metal, mainly due to the nonradiative dissipation of energy within the metal such as dissipated losses and ohmic losses [23, 40]. When the fluorophore is far from the metal, the interaction between them is through far-field radiation, inducing the same charge distribution on the metal and for the incident light. This results in the lifetime of oscillation as a function of distance between metal and fluorophore. While near field is active if the fluorophore is close to the metal, the plasmons cannot radiate since the charges are closely distributed. When the plasmons are trapped because of the optical restrictions at the interface, they decay as heat. If the induced charge on the metal is not radiated, then quenching of emission is observed [40].

10.2.2 Enhancement of Emission by SPR

The emission of fluorophores can be modified by tuning their photonic environment, leading to the new opportunities in bio and optoelectronic applications. Owing to the chemical stability and to the size and shape-dependent absorption wavelength, Au and Ag nanostructures are considered suitable candidates for MEF. An overlap of absorption wavelength of plasmonic metal and emission wavelength of fluorophore offers feasible excitation and energy transfer between metal and fluorophore [41–43]. Influence of near and far field of metal NPs on the emission of fluorophores is a topic of extensive study. The alterations in the emission are not only dependent on the optical properties of the components but also on the position and orientation of emitters with respect to the metal nanostructures. Appropriate control over the distance between fluorophore and metal and knowing the various mechanisms involved in the quenching and enhancement of emission are primary requisites for obtaining enhancement of emission [44, 45].

10.2.2.1 Resonance Energy Transfer

Emission of fluorophores in the vicinity of metal nanostructures is contributed by two competing mechanisms: enhancement due to the energy transfer from an excited dipole to the SP, called as RET, and quenching due to the energy transfer to the optically inactive excitations in the metal, resulting in nonradiative decay. The energy transfer between the dipoles and SP is mutual, and thus the emission light is a cooperative process of all the dipoles. This cooperative emission is called as Dicke effect [46]. The cooperative event can be described as follows: when a number of dipoles in the vicinity of metal nanostructures are confined into a volume with specific size, which is smaller than the wavelength of radiation, the radiation of the ensemble is due to the virtual photon exchange between individual emitters and SPs [47]. The plasmon-enhanced radiative coupling can be obtained by incorporating SP local field into the radiation field. This coupling gives rise to plasmonic superradiant states, which enhances the emission of

photon. The SPs of metal nanostructure extends through the structure and act as a hub, which couples nearby and remote dipoles. The uniform distribution of SP dipole coupling leads to efficient cooperative emission [47]. RET is mainly arisen from the electromagnetic interactions between the dipole of the emitter and plasmons of the metal nanostructure and can be controlled by tuning the size and shape of the nanostructures since they alter the intensity of near field around the metal nanostructure. Another influencing factor is the distance between the emitter and metal. When the emitter is close to the metal, the emission energy is transferred to the optically inactive excitations in the metal and leads to Ohmic losses [47, 48].

10.2.2.2 NFE Mechanism

The resonant SPs oscillation in the metal nanostructure generates a local field around the nanostructure, and the strength of the field exceeds the strength of the incident light field. Enhancement of emission by NFE is due to the interaction of excited-state fluorophore within the near field of metal [49, 50]. The metal nanostructures act as optical antenna and concentrate the incident light, whereas excited fluorophore acts as transmitter and fluorophore in ground state as receiver. The strength of the field decreases exponentially with distance from the metal nanostructure. The advantages of NFE can be further extracted when the metal NPs are uniformly distributed, and they are at an interacting distance. The radiative efficiency and NFE is high between two interactive particles. The emitters located in near-field experiences an increase in the excitation intensity followed by enhancement in the emission rate [40]. This interaction reduces the lifetime of the emitters, resulting in faster recombination of excitons. Such significant enhancement in emission may amplify the emission signals of weak fluorophores. The emission enhancement is greater in the case of bigger metal NPs since magnitude and distribution of NFE is larger in the case of larger NPs compared with the near-field distribution in smaller NPs [1]. Even though the strength of the field is maximal on the surface of the metal, emission of the fluorophores in direct contact with metal is mostly quenched since the excited states of the fluorophores may undergo nonradiative decay through energy or charge transfer from fluorophores to the metal [51]. A different instance where quenching observed is at high concentration of Au NPs. At higher concentration the distance between fluorophore and metal is reduced, which leads to the tunneling of electrons and holes to the metal through nonradiative relaxation [52]. In order to reduce the quenching effect, spacers such as polyelectrolytes and silica are employed to separate the fluorophores a few nanometers away from the metal.

Activating SPP, which is seen continuously in metallic nanostructures, is another mode of enhancing the radiative decay and thus increasing the emission of fluorophores. Lithography is a technique, which can place well-ordered metal nanostructures at an interactive distance. SPP resonance of the lithography pattern can be tuned by varying geometrical parameters of the array (Figure 10.1) [53]. The fluorophores present on the patterned area experience larger enhancement in emission compared with those that are on the unpatterned surface, and the enhancement is maximal when the SPP features are tuned to resonance with the emission energy of the fluorophores. The patterned metal nanostructures exhibit local and propagating SPs. Each metal nanostructure can receive energy from all the neighboring components, and coupling of these energies enhances the radiative and scattering efficiency. When there is no continuous pattern, the dipole–dipole interaction between the metal NPs is weak, and absorptive component exceeds the radiative scattering, resulting in lesser enhancement in the emission. The SPs and SPPs of interacting metal NPs become highly active when light is incident on the coupled system, inducing strong local fields around the interacting region. Therefore, the fluorophores located at the interacting area experience enhanced quantum efficiency [53].

Another interesting feature of interacting nanostructures is the generation of "hot spots." Since each nanostructure acts as an optical antenna to concentrate incident light, thereby generating the local field, the strength of the field between two interactive NPs is several folds larger than that exist between two noninteracting NPs. Such spots where intensified field exist between two metal NPs are called hot spot. Though the simplest system, which can be used for the representation of hot spot is a dimer, any junction within interacting distance, available in pairs, clusters, patterns, or even aggregates can also generate hot spots when light of appropriate wavelength and polarization is incident on them (Figure 10.2) [50]. Enhancement of 270% of the original value was observed when a fluorophore is placed between two Au NPs, and the enhancement was weakened when the fluorescent sphere is not located on the connecting axis of the two Au NPs. The enhancement was only 150% of the original value when the fluorophore is closer to a single NP (Figure 10.3) [54]. When two Au nanorods (NRs) of

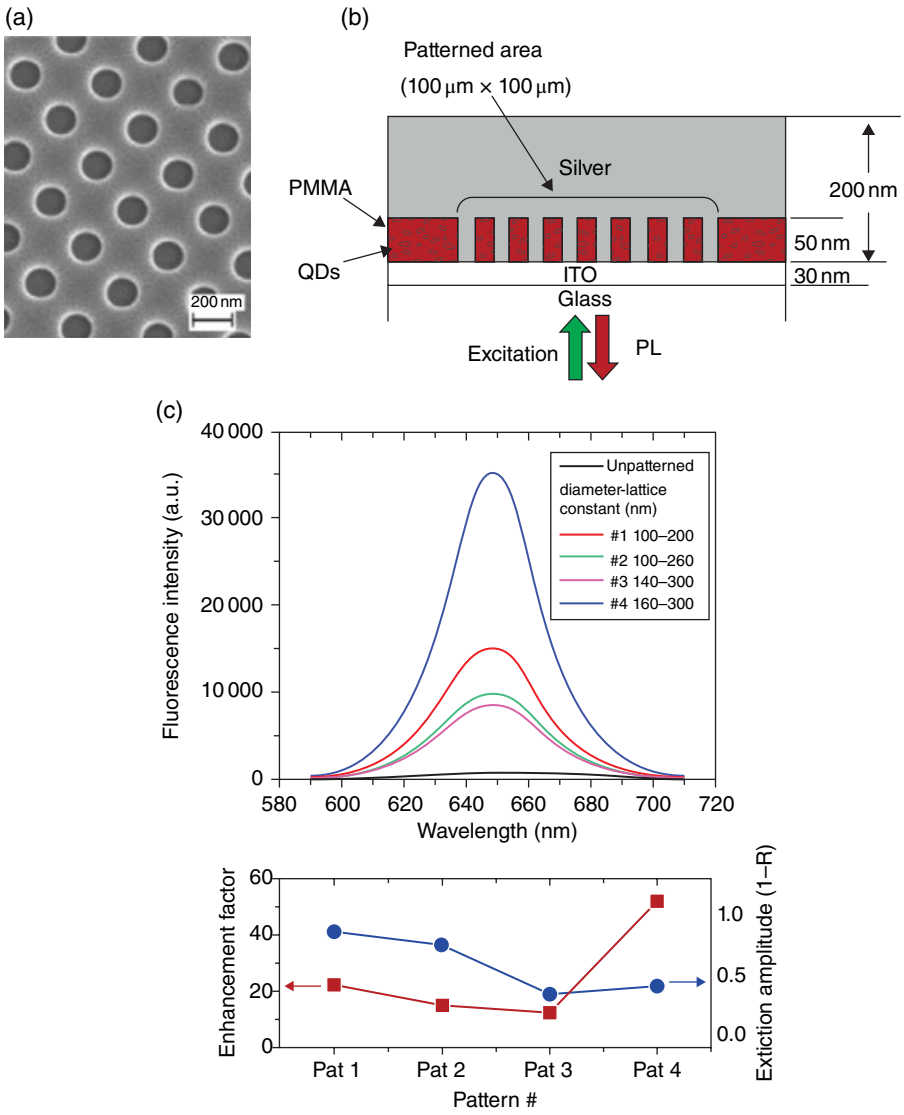

Figure 10.1 (a) SEM image of a square array of holes in PMMA after developing. (Thin Au/Pd film was sputtered to avoid the charging effect in imaging.) The particle diameter is 160 nm, and the lattice constant is 300 nm. (b) Schematic of a typical finished sample structure. Fluorescence is excited by a 532 nm laser line incident on the glass substrate side and detected at normal incident angle. (c) Fluorescence spectra (top panel) and enhancement factors (bottom panel, black trace) from the given arrays. Inset shows the Ag disk diameter and the lattice constant (in nanometers) of the corresponding array. The enhancement factors were obtained by dividing the PL intensity from QDs in a particular pattern by the PL peak intensity from QDs in an unpatterned area with a Ag layer atop. The amplitude of extinction at 532 nm is also shown (gray trace) in the bottom panel. Song *et al*. [53]. Reproduced with the permission of American Chemical Society.

extended size are placed at an interacting distance, they act as standing-wave resonators for SPPs, and resonant dimer antennas with strongly coupled arms yield a larger enhancement of emission of fluorophores than uncoupled antennas (Figure 10.4) [44]. Metallic nanostructures with sharp edges are also able to produce a concentrated enhanced field at the edges, and the largest enhancement of emission at hot spot is reported for two metallic triangles, separated by a small gap, facing tip to tip, called as "bowtie." An enhancement of 1340 times of original value of emission was reported for a single fluorophore placed at the hot spot of bowtie antenna [55].

10.2.3 Quenching of Emission by SPR

Due to their unique tunable optical properties, plasmonic metals have proven to be very effective, but they act as quenchers too, particularly when they are very close to the fluorophore. At closer distance, the quenching is mainly due to two effects: first, radiative decay rate is decreased because of out-of-phase orientation of

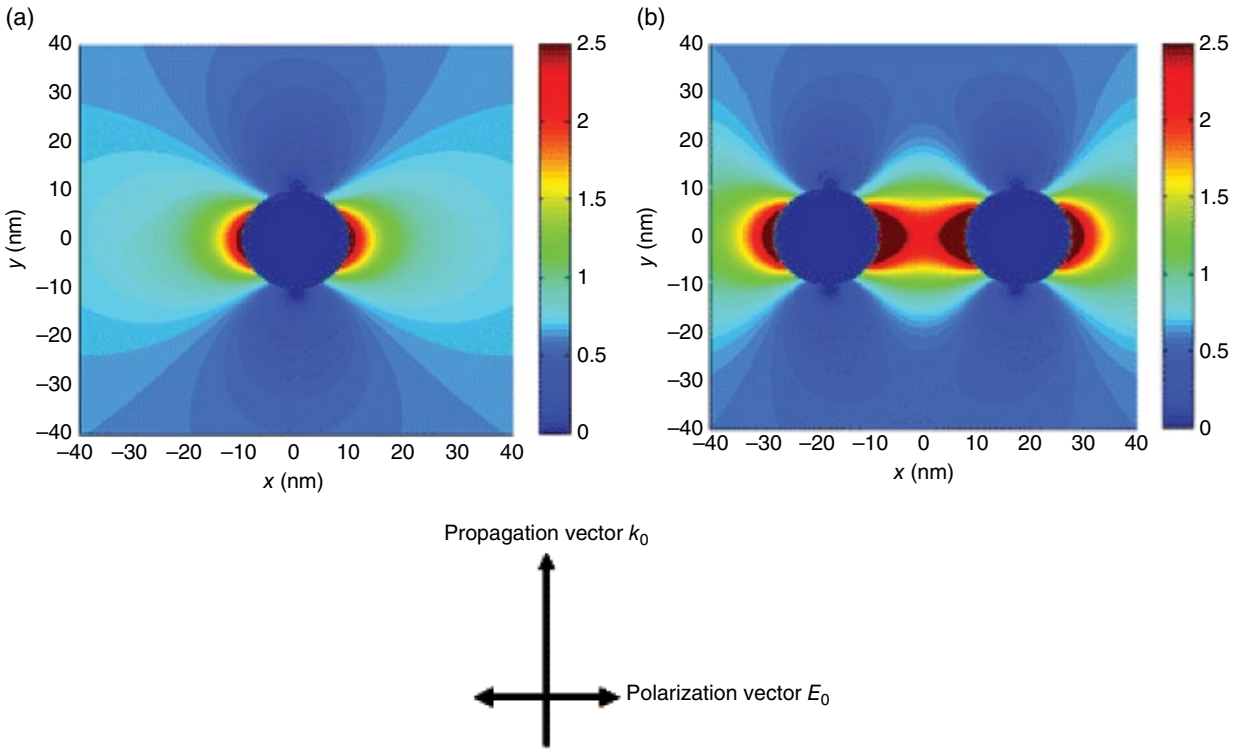

Figure 10.2 Electric fields near silver (a) monomer and (b) dimer were calculated by FDTD model under an incident light of 635 nm. Note that the incident light is propagating along the *y*-axis and is polarized along the *x*-axis. Zhang *et al.* [50]. Reproduced with the permission of American Chemical Society.

dipoles of fluorophores and metal NPs, and second, increase in nonradiative decay rate energy dissipation such as heat or collision of photons with the metal surface [1, 56]. Another reason for quenching is charge transfer from fluorophores to metal NPs. In the case of QDs, when the CB edge is above the Fermi level of metal, the excited electrons from QDs are transferred to the metal, and the distance between QDs and metal dictates the efficiency of electron transfer. Therefore, when QDs and metal are in close contact, the electrons from QDs are easily transferred to metal, resulting in quenching of emission (Figure 10.5) [52]. Further, chemical interface damping where the delocalized CB electrons of metal occupy the energy levels of nearby molecules electronic levels also results in quenching of emission [57, 58]. Quenching is observed in case of fluorophores too, when there is charge repulsion between fluorophores and metal NPs or when they are directly adsorbed on the surface of metal NPs. This issue is partially resolved by using spacers between metal and fluorophores/QDs. Oligonucleotides are used as the linker between fluorophores and metal in biosensing and molecular engineering [59]. Efficiency of quenching is larger when there is sufficient overlap between emission spectrum of fluorophores and absorption spectrum of metal NPs, and they are located close to each other, since this spectral overlap leads to the transfer of energy from fluorophores to metal [60]. Another explored mechanism explaining the quenching process is nanometal surface energy transfer mechanism (NSET). The origin for NSET is the interaction of the electromagnetic field of the fluorophore dipole interacting with the nearly free conduction electrons of the accepting metal, and they behave as acceptors. These electrons interact most strongly with the oscillating dipole if they travel near and perpendicular to the metal surface. This leads to the nonradiative energy transfer from electrons at energies close to the metals' Fermi level in the CB, which increases the total nonradiative rate of the fluorophores and reduces the lifetime of excited state and the QY [57, 61]. The quenching efficiency is decreased when the distance between fluorophores and metal is increased (Figure 10.6) [61].

10.3 Effect of SPR in FRET

10.3.1 FRET

The process of FRET involves the nonradiative energy transfer from an excited-state fluorophore to ground-state fluorophore via long-range dipole–dipole interactions [4].

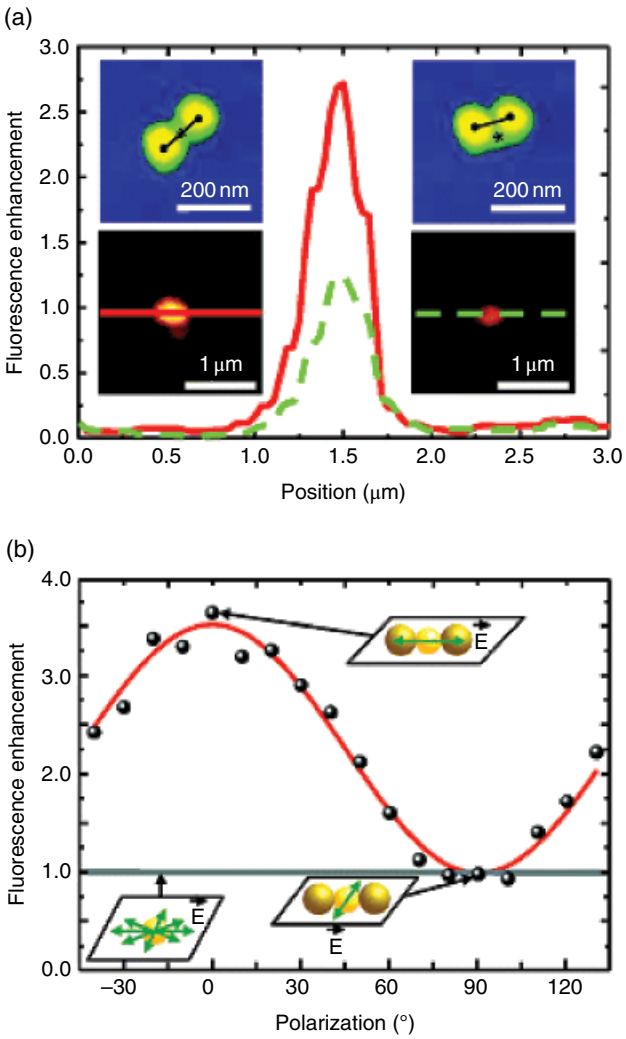

Figure 10.3 (a) The fluorescence enhancement is very sensitive to the exact placement of the FS between the AuNPs. The graph shows fluorescence intensities obtained with two different FS positions. The AFM height images are shown in the upper two insets, and the corresponding fluorescence images are shown in the lower two insets. The exact positions of the AuNPs and the FS are indicated by solid black dots and asterisks, respectively. The axis connecting the two AuNP centers is also indicated. In the left column, the FS is sandwiched in the hot spot right between the two AuNPs, which leads to a strong fluorescence enhancement (solid gray line). In the right column, the FS is not in the hot spot and, consequently, the fluorescence enhancement is less pronounced (dashed gray line). (b) The polarization of the excitation laser is rotated through 180°. The fluorescence intensity is enhanced when the laser is polarized parallel to the axis of the sandwich, whereas the fluorescence is decreased when the laser is polarized perpendicular to it. The gray horizontal line shows that the fluorescence level of the FS before the AuNPs has been approached (using unpolarized excitation). The red curve is a sin2 fit to the data. Bek *et al*. [54]. Reproduced with the permission of American Chemical Society.

The emission energy of the donor is absorbed by the acceptor, which requires a spectral overlap between the emission wavelength of the donor and absorption wavelength of the acceptor. The efficiency of FRET is decided by other factor too, such as the relative orientation of the dipoles of the donor and acceptor and the distance between the donor and acceptor molecules (Scheme 10.5) [62]. The energy transfer between the donor and acceptor is dependent on the distance between them and is expressed in terms of the Förster radius (R_0). R_0 is the distance between donor and acceptor at which 50% of the excited energy of the donor is decayed through energy transfer, and the other half is decayed through radiative and nonradiative channels [63]. In the case of most of the FRET pairs, R_0 lies between 1 and 10 nm, which is calculated using the equation:

$$R_0 = 9.78 \times 10^3 [\kappa^2 n^{-4} Q_D J(\lambda)]^{1/6} \tag{10.3}$$

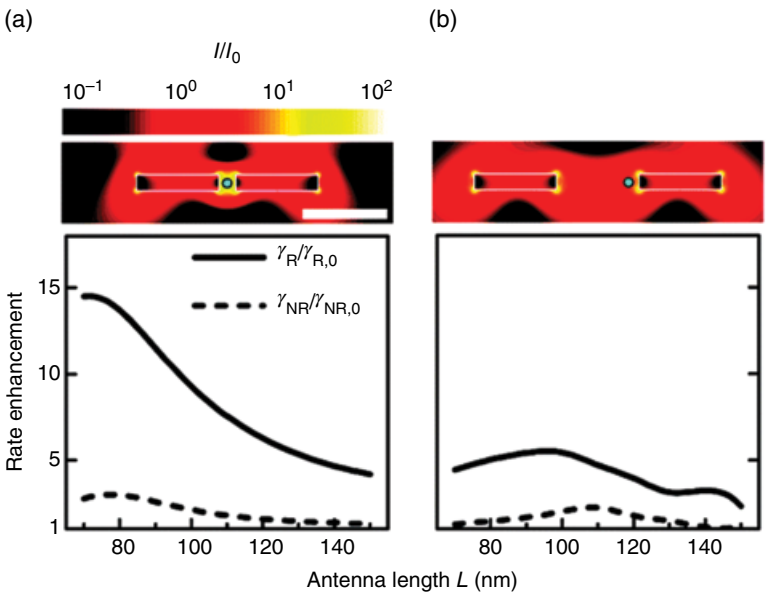

Figure 10.4 Modified spontaneous emission calculated for a dipole emitter at 730 nm wavelength, positioned at the location of maximum coupling to the antenna and oriented parallel to the antenna axis. Radiative and nonradiative decay rates γ_R and γ_{NR} are shown versus antenna arm length L for the two cases of (a) strongly coupled antenna arms ($\Delta = 20$ nm) and (b) uncoupled antenna arms ($\Delta = 80$ nm). (Top graphs) Calculated near-field intensities around two resonant antennas for plane-wave illumination, with spots (black open circle) indicating the location of the emitter in the calculations (scale bar denotes 100 nm). Muskens *et al*. [44]. Reproduced with the permission of American Chemical Society.

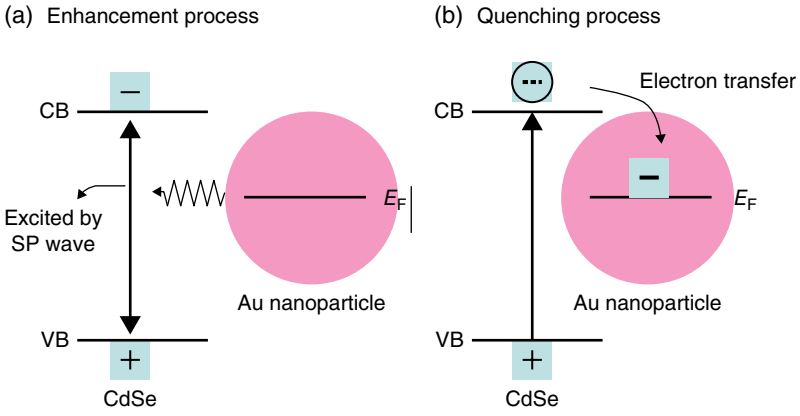

Figure 10.5 A schematic diagram showing the PL (a) enhancement and (b) quenching processes from CdSe/Au nanocomposites with the variation of CdSe–Au distance. Hsieh *et al*. [52]. Reproduced with the permission of IOP Publishing.

where κ^2 is the donor–acceptor transition dipole orientation and has range from 0 to 4. In most of the biological FRET pairs, κ^2 is reported as 2/3; n is the refractive index of the medium, which is 1.4 for bio moieties in aqueous medium; Q_D is the QY of the donor in the absence of the acceptor; and $J(\lambda)$ is the overlap integral. The value of overlap integral is decided by the extent of spectral overlap between the emission of the donor and the absorbance of the acceptor. Greater value for $J(\lambda)$ and R_0 indicates better spectral overlap between donor and acceptor and efficient energy transfer from the donor to the acceptor, respectively. The efficiency of energy transfer is calculated from either steady-state or time-resolved spectral measurements:

$$E = 1 - \frac{F_{DA}}{F_D} \quad \text{steady-state analysis} \qquad (10.4)$$

$$E = 1 - \frac{\tau_{DA}}{\tau_D} \quad \text{time-resolved analysis} \qquad (10.5)$$

F_D and F_{DA} are the fluorescence intensity of the donor in the absence and presence of the acceptor, and τ_D and τ_{DA} are the lifetime of the donor in the absence and presence of acceptor, respectively [4, 63]. In conventional FRET system, organic dyes are used as donor and acceptor, but using QDs as either donor or acceptor or both has drawn considerable interest since the absorption and emission wavelengths can be finely tuned by altering the size of QDs. Significant amount of efforts has been given to FRET-based study in many biological phenomena such as protein–protein interactions [4, 25, 26] and conformational changes of biomolecules [27, 28]. FRET-based imaging has been used as a successful analytical tool to study the spatial orientation between fluorophore-labeled biomolecules and to investigate the molecular interactions in living organisms [1]. Though the advantages of using FRET in biological application is advanced, the decrease in efficiency of FRET when R_0 is above 5 nm limits its use since the range of biomolecular interactions is longer than this range [64, 65].

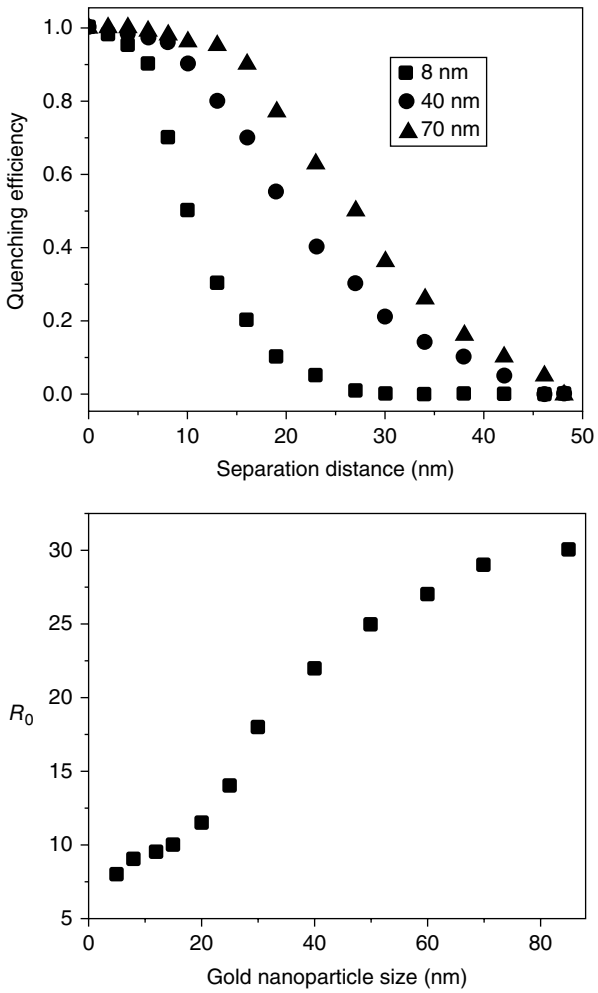

Figure 10.6 Top: variation of the quenching efficiency with distance between gold nanoparticle of sizes 8, 40, and 70 nm and Cy3 dye. Bottom: variation of R0 with the size of gold nanoparticle. Griffin *et al*. [61]. Reproduced with the permission of John Wiley & Sons.

MEF-induced enhanced FRET is a recent topic of interest since the presence of plasmonic metal improves the emission of donor or acceptor or both the FRET pairs and increases the Förster range. Increasing the QY of any of the components of FRET improves quality of imaging and the detection range. However, proper engineering is required to utilize the benefits of including SPs in FRET since inappropriate control over the distance between fluorophores and metals may lead to the quenching of emission, which is discussed in Section 10.2.3.

10.3.2 SPR-Induced Enhanced FRET

At an appropriate distance between plasmonic metal and fluorophore, the emission intensity is increased and lifetime of fluorophore is decreased. These changes in radiative properties of fluorophores can be extended to enhance the efficiency of FRET. The intensity of the emission of the fluorophore can be varied in two ways: first, increase in the excitation rate by the local electric field induced by LSPR, and second, increase in decaying of the energy through the nonradiative pathway. The presence of plasmonic metal influences various decay channels, such as energy transfer from the donor to acceptor, energy transfer between SPs and flourophores, radiative decay to the far field, and nonradiative decay [66]. When the excitation emission of donor or acceptor is altered by SPs, the excitation and de-excitation of the FRET pair is also subsequently changed [55, 66, 67]. Considering all the plasmon-induced changes in the optical properties of donor and acceptor, advantageous results can be obtained by including plasmonic metal in FRET pair.

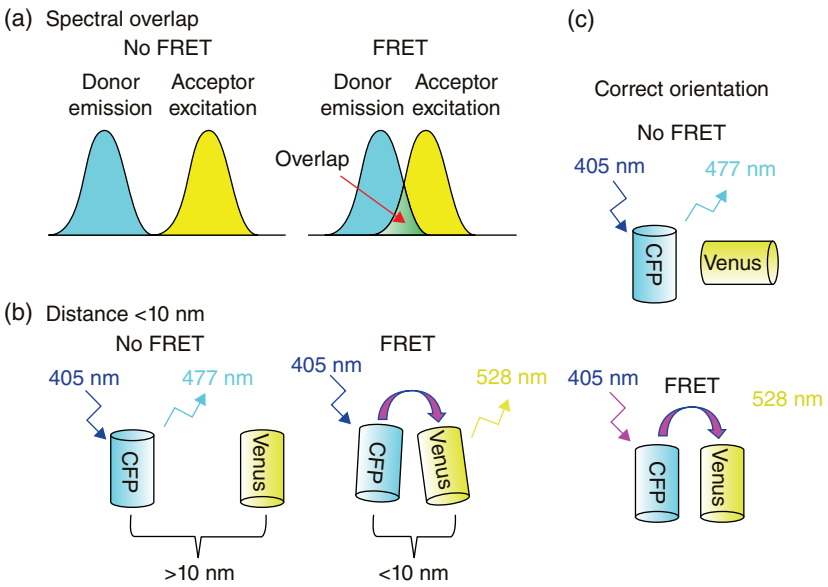

Scheme 10.5 Schematic diagrams depicting the three conditions that must be met for efficient FRET. (a) The energy of donor emission must be an energy that the acceptor can absorb. In other words, the emission spectrum from the donor fluorophore must overlap with the excitation spectrum of the acceptor fluorophore. (b) If the FRET donor and acceptor are more than 10 nm apart, then no FRET occurs and the donor emits fluorescence. If the donor and acceptor are within ~10 nm of one another, then energy transfer can occur from the donor (CFP) to the acceptor (Venus). (c) If the donor and acceptor fluorophore dipoles are perpendicular to one another, then the donor molecule will emit fluorescence. However, if the dipoles are parallel to each other, FRET will occur. Broussard *et al*. [62]. Nature Publishing Group.

The efficiency of energy transfer is calculated according to

$$E = \frac{k_{ET}}{k_D + k_{ET}} \tag{10.6}$$

where k_{ET} is the energy transfer rate and k_D is the sum of the radiative and nonradiative decay rates of the donor.

Since the inclusion of plasmonic metal can enhance both k_{ET} and k_D, the overall change in E may not be significant. The efficiency of energy transfer from donor to plasmonic metal is increased when there is a spectral between the emission spectrum of donor and absorption spectrum of plasmonic metal. This energy transfer results in an increase in k_D, resulting in a decrease in E. k_D can be effectively tuned by altering the distance between metal and donor. k_{ET} is increased when the plasmonic energy is in between the emission energy of the donor and the absorption energy of the acceptor. The changes in the PL decay of the donor in FRET pair in combination with metal indicate the direction of energy transfer among the components of plasmonic FRET. A slower PL decay of the donor in the presence of metal compared to that in the absence of metal evidence the energy transfer from the donor to the acceptor [1, 32, 66]. When there is spectral overlap of Au NP absorption with the donor emission and acceptor absorption spectra, the emitting and absorbing transition dipoles resonate the SP dipole fields of Au NPs. Since SP dipole fields are intense than the fluorophore exciton dipole fields, SP dipole fields interact with exciton dipoles efficiently. This coupled exciton and SP field may extend spatially beyond their neighbors, thus enhancing the FRET process [68].

Inclusion of metal into FRET not only increases the energy transfer but also the distance over, which FRET occurs. Using polyelectrolyte as spacer between the components of plasmonic FRET pair, doubling of Förster radius from 3.9 nm to 7.9 nm, and distance between donor and acceptor over 20 nm were reported for plasmonic FRET pair compared with FRET pair without metal (Figure 10.7) [32]. The distance between components can be tuned by using silica shell around metal nanostructure as spacer. The distance between metal and donor/acceptor can be varied by changing the thickness of silica shell, and the optimum thickness of shell for efficient energy transfer varies with size and shape of the nanostructure [69, 70].

10.3.3 Effect of the Position, Concentration, and Size of Plasmonic Nanostructures in FRET System

General study on enhancement of FRET in the presence of plasmonic metal has been reported well, but influence of spatial location plasmonic metal and consequent changes in the optical properties of

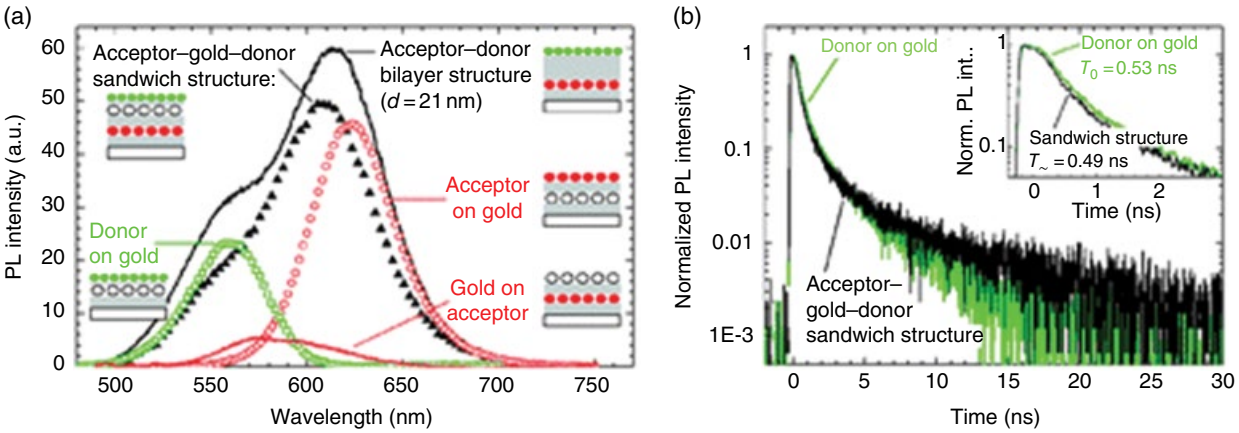

Figure 10.7 (a) PL spectrum of an acceptor–gold–donor sandwich structure (black triangles) with gold. The PL spectrum of the sandwich structure prior to the deposition of the final polyelectrolyte and donor QD monolayer is also shown (gray line). For comparison the PL spectra of donor monolayers (open gray square) and acceptor monolayers (open red circles) deposited on top of a gold nanoparticle layer as well as a donor–acceptor bilayer structure without gold s (black line) are also included. The acceptor PL in the gold on acceptor structure is lower than that measured from the acceptor on gold reference structure due to absorption of the incident excitation light and the acceptor emission by both the PE layers and gold nanoparticles on top of the buried acceptor QD monolayer. The schematics show the layer structures of the different samples prepared on quartz (white rectangle). The polyelectrolyte spacer layers are indicated in gray; the red, white, and green spheres represent the acceptor QDs, gold nanoparticles, and donor QDs, respectively. (b) Time-resolved donor PL decays for the donor on gold reference (gray line) and the acceptor–gold–donor sandwich structure (black line). The inset shows a close-up of these two donor PL decays over the first 3 ns. Lunz *et al*. [32]. Reproduced with the permission of American Chemical Society.

donor or acceptor also demands thorough investigation. LSPR may not only affect FRET between acceptor and donor but also the individual optical properties of donor and acceptor by quenching or enhancing the PL emission. Enhancement of FRET by placing metal nanostructures between the donor and the acceptor was demonstrated by a few groups [29–32]. Using polyelectrolytes as spacer, when a monolayer of Au NPs was introduced between layers of donor and acceptor, 13% reduction in donor emission and 24% increase in acceptor emission were noted with the donor to acceptor distance of 23 nm, indicating the successful transfer of energy from the donor to the acceptor via SPR. FRET was found absent when the similar structure is devoid of Au NPs because the distance between the donor and acceptor is too large for efficient energy transfer [32]. Coupling SPR only to either donor or acceptor shows different results compared with coupling SPR to both donor and acceptor. Enhancement in the emission of acceptor was observed even when SPR is coupled with the donor in the FRET pair, but the enhancement in the emission of acceptor is larger for acceptor-coupled SPR than for donor-coupled SPR (Figure. 10.8) [30]. Again, placing plasmonic metal closer to the acceptor is helpful when the QY of acceptor is low. Same as SPR-FRET pair included in multilayer thin film, multilayer core–shell nanostructures, where each layer is separated by silica shell, also show SPR-induced enhanced FRET. Again, placing Au NP closer to the acceptor is helpful especially when the QY of the acceptor is low [64, 71, 72]. Au NP closer to donor improves the emission of donor by MEF and by NFE, and the enhanced emission energy can then be transferred to the acceptor via FRET. The optimum distance between the donor and acceptor can be tuned by changing the thickness of silica shell. If the distribution of near field extends till the acceptor (Figure 10.9), the emission of acceptor can be enhanced by NFE and FRET (Scheme 10.6) [72].

Concentration and size of plasmonic metal is also as important as the position of plasmonic metal. Low to intermediate level of Au concentration has shown helping the FRET, and efficiency of FRET is decreased at higher concentration of Au NPs due to the quenching effect of metal [29]. Bigger NPs increase the range of near-field distribution, thus fluorophores present within the range of near-field experience enhanced optical properties and scattering component too contribute to the enhancement of emission of fluorophores when the emission wavelength fluorophore is larger than the scattering wavelength of metal [23]. When the absorption or emission band of the fluorophore overlaps with the scattering wavelength of metal NPs, MEF is further enhanced due to the RPs, as discussed in Section 10.2.2.2 [73].

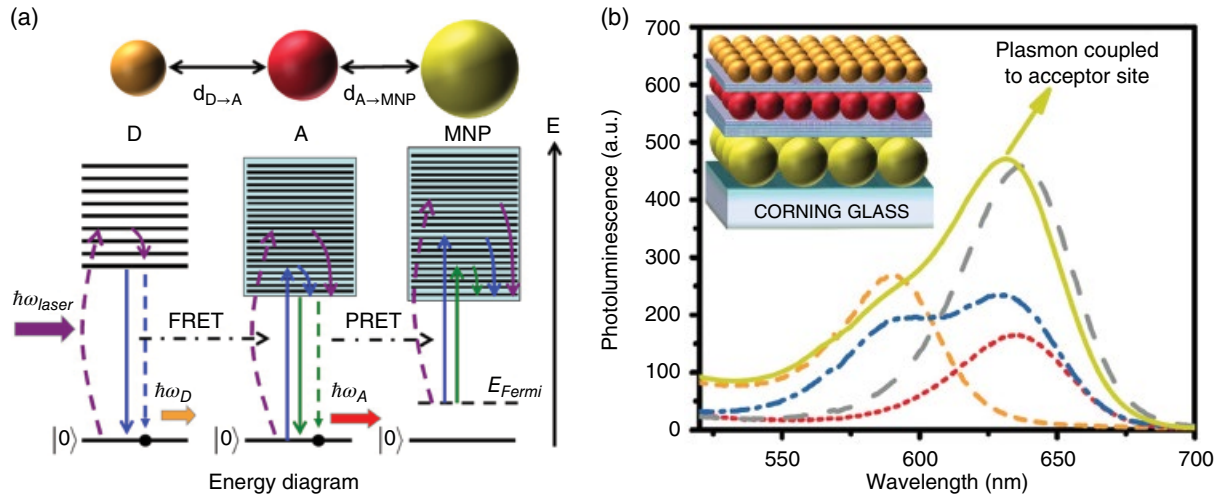

Figure 10.8 (a) Schematic representation of a donor–acceptor (D–A) energy transfer pair in the case of plasmon coupling to only acceptor QD along with an energy band diagram with the absorption process of the MNP/donorQD/acceptorQD, fast relaxation process, light emission process, energy transfer from the donor to the acceptor, and the Coulomb interaction between the donor and acceptor pairs are shown. In the energy diagram, the discrete energy levels for the QDs are depicted, as well as the energy level for the localized plasmons within the continuous energy band of the MNP. (b) PL spectra of the D (dashed light gray), A (dotted gray), D–A QD pair (dashed black) under Förster-type energy transfer, plasmon-coupled A (dashed dark gray), and FRET for the D–A QD pair when only the acceptor QD is coupled to MNP (solid gray). Ozel *et al.* [30]. Reproduced with the permission of American Chemical Society.

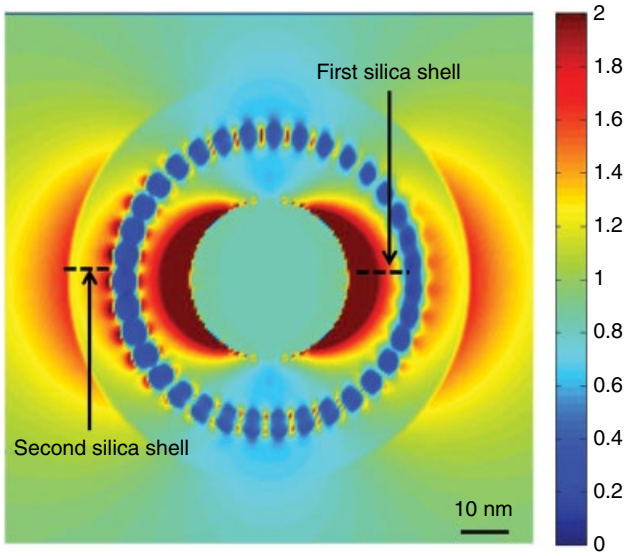

Figure 10.9 Electric field intensity distribution created by the addition of the second silica shell is calculated by FDTD. NFE due to second silica shell is clearly observed. Kochuveedu *et al*. [72]. Reproduced with the permission of Macmillan Publishers Limited.

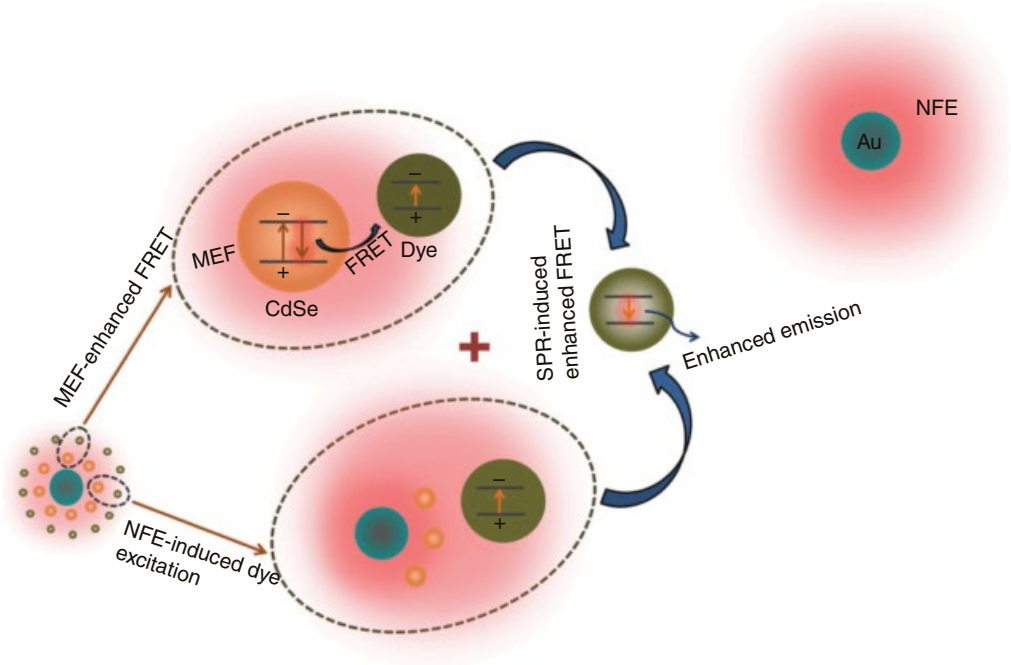

Scheme 10.6 Schematic representation of mechanisms playing role in the SPR-induced enhanced FRET. Two pathways can be involved in SPR-induced enhanced FRET. The major contribution is made by MEF. The emission of CdSe is significantly enhanced by the NFE around the Au NP. The enhanced emission energy is transferred to S101 through FRET, thereby leading to enhanced emission of S101. The extension of the near field to the second silica shell also constitutes a considerable portion. As confirmed in Figure 10.9, the plasmonic field around the Au NP is stretched to the second silica shell. Therefore, dye molecules on the surface of the second silica shell can be directly excited by the near field extended to the second shell. Concisely it can be assumed that the SPR-enhanced FRET is due to the concurrent near-field interaction between the metal and the acceptor as well as the metal and the donor. Kochuveedu *et al*. [72]. Reproduced with the permission of Macmillan Publishers Limited.

10.4 Conclusions and Outlook

The essence of this chapter is the comprehensive overview on various factors, which play role in the MEF. When metal-emitter configuration is suitably designed and engineered, enhanced radiative decay and consequently enhanced QY are obtained. Proper tuning of the distance between metal and emitter is considered as the most important criterion to enhance the emission; adverse result, that is, quenching, is

observed when the fluorophores are very close to the metal due to the increase in nonradiative decay and due to the prevalent transfer of emission from the fluorophores to the metal. RET and NFE are two major mechanisms we used to discuss the MEF. Coupling between SPs and molecular dipoles generates RET, and fluorophores experience enhanced excitation rate when they are at the near field around plasmonic structure. Quenching of FRET driven by the presence of plasmonic metals is mainly due to NSET and due to electron tunneling from QDs to metal when the energy bands between QDs and metal are aligned in such a way that electrons from the CB of QDs can be transferred to the Fermi level of metal. Incorporation of bigger metal NPs contribute to scattering component, and thus emission is further enhanced. The MEF can be extended to FRET if plasmonic nanostructures are placed appropriately in the FRET system. How the magnitude of enhancement of emission is varied depends on the position of metal NPs in the FRET system.

Though significant success is achieved in MEF and MEF-based applications, many issues regarding the architectural control over the metal-emitter configuration still remain unresolved. Improved understanding on the interaction between plasmonic metal and flourophores may make it possible to design suitable metal-fluorophore system that shows enhanced emission properties. Though many challenges must be met to make practical use of these optical phenomena, in brief, we believe that understanding the mechanisms behind SP-coupled emission provides new insights to design many fluorophore-based devices for sensing, biotechnology, and medical applications.

References

1 Kochuveedu, S. T.; Kim, D. H., Surface plasmon resonance mediated photoluminescence properties of nanostructured multicomponent fluorophore systems. *Nanoscale* **2014**, *6*, 4966–4984.

2 Shinde, K. N.; Dhoble, S.J.; Swart, H.C.; Park, K., *Phosphate Phosphors for Solid-State Lighting*. Springer Series in Materials Science, Vol. 174. Berlin: Springer Science & Business Media: **2012**.

3 Ropp, R. C., *Luminescence and the Solid State*. Burlington, MA: Elsevier: **2013**.

4 Lakowicz, J. R., *Principles of Fluorescence Spectroscopy*. New York: Springer Science & Business Media: **2007**.

5 Valeur, B.; Berberan-Santos, M. N., *Molecular Fluorescence: Principles and Applications*. Weinheim: John Wiley & Sons: **2012**.

6 Yanover, D.; Vaxenburg, R.; Tilchin, J.; Rubin-Brusilovski, A.; Zaiats, G.; Capek, R. K.; Sashchiuk, A.; Lifshitz, E., Significance of small-sized PbSe/PbS core/shell colloidal quantum dots for optoelectronic applications. *J. Phys. Chem. C* **2014**, *118*, 17001–17009.

7 Stokes, E. B.; Stiff-Roberts, A. D.; Dameron, C. T., Quantum dots in semiconductor optoelectronic devices. *Electrochem. Soc. Interface* **2006**, *15*, 23–27.

8 Jamieson, T.; Bakhshi, R.; Petrova, D.; Pocock, R.; Imani, M.; Seifalian, A. M., Biological applications of quantum dots. *Biomaterials* **2007**, *28*, 4717–4732.

9 Michalet, X.; Pinaud, F. F.; Bentolila, L. A.; Tsay, J. M.; Doose, S.; Li, J. J.; Sundaresan, G.; Wu, A. M.; Gambhir, S. S.; Weiss, S., Quantum dots for live cells, in vivo imaging, and diagnostics. *Science* **2005**, *307*, 538–544.

10 Rogach, A. L., *Semiconductor Nanocrystal Quantum Dots*. Wien/New York: Springer: **2008**.

11 Kwon, M. K.; Kim, J. Y.; Kim, B. H.; Park, I. K.; Cho, C. Y.; Byeon, C. C.; Park, S. J., Surface-plasmon-enhanced light-emitting diodes. *Adv. Mater.* **2008**, *20*, 1253–1257.

12 Cho, C.-Y.; Kwon, M.-K.; Lee, S.-J.; Han, S.-H.; Kang, J.-W.; Kang, S.-E.; Lee, D.-Y.; Park, S.-J., Surface plasmon-enhanced light-emitting diodes using silver nanoparticles embedded in p-GaN. *Nanotechnology* **2010**, *21*, 205201.

13 Ji, X.; Zheng, J.; Xu, J.; Rastogi, V. K.; Cheng, T.-C.; DeFrank, J. J.; Leblanc, R. M., (CdSe) ZnS quantum dots and organophosphorus hydrolase bioconjugate as biosensors for detection of paraoxon. *J. Phys. Chem. B* **2005**, *109*, 3793–3799.

14 Freeman, R.; Gill, R.; Shweky, I.; Kotler, M.; Banin, U.; Willner, I., Biosensing and probing of intracellular metabolic pathways by NADH-sensitive quantum dots. *Angew. Chem.* **2009**, *121*, 315–319.

15 Samia, A. C.; Chen, X.; Burda, C., Semiconductor quantum dots for photodynamic therapy. *J. Am. Chem. Soc.* **2003**, *125*, 15736–15737.

16 Block, I. D.; Mathias, P. C.; Ganesh, N.; Jones, S. I.; Dorvel, B. R.; Chaudhery, V.; Vodkin, L. O.; Bashir, R.; Cunningham, B. T., A detection instrument for enhanced-fluorescence and label-free imaging on photonic crystal surfaces. *Opt. Express* **2009**, *17*, 13222–13235.

17 Tam, F.; Goodrich, G. P.; Johnson, B. R.; Halas, N. J., Plasmonic enhancement of molecular fluorescence. *Nano Lett.* **2007**, *7*, 496–501.

18 Kelly, K. L.; Coronado, E.; Zhao, L. L.; Schatz, G. C., The optical properties of metal nanoparticles: the influence of size, shape, and dielectric environment. *J. Phys. Chem. B* **2003**, *107*, 668–677.

19 Barnes, W. L.; Dereux, A.; Ebbesen, T. W., Surface plasmon subwavelength optics. *Nature* **2003**, *424*, 824–830.

20 Stewart, M. E.; Anderton, C. R.; Thompson, L. B.; Maria, J.; Gray, S. K.; Rogers, J. A.; Nuzzo, R. G., Nanostructured plasmonic sensors. *Chem. Rev.* **2008**, *108*, 494–521.

21 Eustis, S.; El-Sayed, M. A., Why gold nanoparticles are more precious than pretty gold: noble metal surface plasmon resonance and its enhancement of the radiative and nonradiative properties of nanocrystals of different shapes. *Chem. Soc. Rev.* **2006**, *35*, 209–217.

22 Hutter, E.; Fendler, J. H., Exploitation of localized surface plasmon resonance. *Adv. Mater.* **2004**, *16*, 1685–1706.

23 Lakowicz, J. R., Radiative decay engineering 5: metal-enhanced fluorescence and plasmon emission. *Anal. Biochem.* **2005**, *337*, 171–194.

24 Lakowicz, J. R.; Shen, Y.; D'Auria, S.; Malicka, J.; Fang, J.; Gryczynski, Z.; Gryczynski, I., Radiative decay engineering: 2. Effects of silver island films on fluorescence intensity, lifetimes, and resonance energy transfer. *Anal. Biochem.* **2002**, *301*, 261–277.

25 Truong, K.; Ikura, M., The use of FRET imaging microscopy to detect protein–protein interactions and protein conformational changes in vivo. *Curr. Opin. Struct. Biol.* **2001**, *11*, 573–578.

26 Day, R. N.; Periasamy, A.; Schaufele, F., Fluorescence resonance energy transfer microscopy of localized protein interactions in the living cell nucleus. *Methods* **2001**, *25*, 4–18.

27 Giannetti, A.; Citti, L.; Domenici, C.; Tedeschi, L.; Baldini, F.; Wabuyele, M. B.; Vo-Dinh, T., FRET-based protein-DNA binding assay for detection of active NF-κB. *Sens. Actuators B* **2006**, *113*, 649–654.

28 Kajihara, D.; Abe, R.; Iijima, I.; Komiyama, C.; Sisido, M.; Hohsaka, T., FRET analysis of protein conformational change through position-specific incorporation of fluorescent amino acids. *Nat. Methods* **2006**, *3*, 923–929.

29 Lunz, M.; Zhang, X.; Gerard, V. A.; Gun'ko, Y. K.; Lesnyak, V.; Gaponik, N.; Susha, A. S.; Rogach, A. L.; Bradley, A. L., Effect of metal nanoparticle concentration on localized surface plasmon mediated Forster resonant energy transfer. *J. Phys. Chem. C* **2012**, *116*, 26529–26534.

30 Ozel, T.; Hernandez-Martinez, P. L.; Mutlugun, E.; Akin, O.; Nizamoglu, S.; Ozel, I. O.; Zhang, Q.; Xiong, Q.; Demir, H. V., Observation of selective plasmon-exciton coupling in nonradiative energy transfer: donor-selective versus acceptor-selective plexcitons. *Nano Lett.* **2013**, *13*, 3065–3072.

31 Govorov, A. O.; Lee, J.; Kotov, N. A., Theory of plasmon-enhanced Förster energy transfer in optically excited semiconductor and metal nanoparticles. *Phys. Rev. B* **2007**, *76*, 125308.

32 Lunz, M.; Gerard, V. A.; Gun'ko, Y. K.; Lesnyak, V.; Gaponik, N.; Susha, A. S.; Rogach, A. L.; Bradley, A. L., Surface plasmon enhanced energy transfer between donor and acceptor CdTe nanocrystal quantum dot monolayers. *Nano Lett.* **2011**, *11*, 3341–3345.

33 Osinkina, L. Interactions of molecules in the vicinity of gold nanoparticles, dissertation. Munich: Fakultät für Physik der Ludwig-Maximilians-Universität, **2014**.

34 Darvill, D.; Centeno, A.; Xie, F., Plasmonic fluorescence enhancement by metal nanostructures: shaping the future of bionanotechnology. *Phys. Chem. Chem. Phys.* **2013**, *15*, 15709–15726.

35 Soller, T.; Ringler, M.; Wunderlich, M.; Klar, T.; Feldmann, J.; Josel, H.-P.; Markert, Y.; Nichtl, A.; Kürzinger, K., Radiative and nonradiative rates of phosphors attached to gold nanoparticles. *Nano Lett.* **2007**, *7*, 1941–1946.

36 Glass, A.; Liao, P. F.; Bergman, J.; Olson, D., Interaction of metal particles with adsorbed dye molecules: absorption and luminescence. *Opt. Lett.* **1980**, *5*, 368–370.

37 Malicka, J.; Gryczynski, I.; Fang, J.; Kusba, J.; Lakowicz, J. R., Increased resonance energy transfer between fluorophores bound to DNA in proximity to metallic silver particles. *Anal. Biochem.* **2003**, *315*, 160–169.

38 Gerber, S.; Reil, F.; Hohenester, U.; Schlagenhaufen, T.; Krenn, J. R.; Leitner, A., Tailoring light emission properties of fluorophores by coupling to resonance-tuned metallic nanostructures. *Phys. Rev. B* **2007**, *75*, 073404.

39 Lakowicz, J. R., Radiative decay engineering: biophysical and biomedical applications. *Anal. Biochem.* **2001**, *298*, 1–24.

40 Lakowicz, J.; Fu, Y., Modification of single molecule fluorescence near metallic nanostructures. *Laser Photonics Rev.* **2009**, *3*, 221–232.

41 Han, Y. D.; Lee, J. W.; Park, D. H.; Yang, S. H.; Kim, B. K.; Kim, J.; Joo, J., Core–shell nanoparticle of silver coated with light-emitting rubrene: surface plasmon enhanced photoluminescence. *Synth. Met.* **2011**, *161*, 2103–2106.

42 Kondon, M.; Kim, J.; Udawatte, N.; Lee, D., Origin of size-dependent energy transfer from photoexcited CdSe quantum dots to gold nanoparticles. *J. Phys. Chem. C* **2008**, *112*, 6695–6699.

43 Pompa, P.; Martiradonna, L.; Della Torre, A.; Della Sala, F.; Manna, L.; De Vittorio, M.; Calabi, F.; Cingolani, R.; Rinaldi, R., Metal-enhanced

fluorescence of colloidal nanocrystals with nanoscale control. *Nat. Nanotechnol.* **2006**, *1*, 126–130.
44 Muskens, O.; Giannini, V.; Sanchez-Gil, J.; Gomez Rivas, J., Strong enhancement of the radiative decay rate of emitters by single plasmonic nanoantennas. *Nano Lett.* **2007**, *7*, 2871–2875.
45 Reil, F.; Hohenester, U.; Krenn, J. R.; Leitner, A., Forster-type resonant energy transfer influenced by metal nanoparticles. *Nano Lett.* **2008**, *8*, 4128–4133.
46 Pustovit, V. N.; Shahbazyan, T. V., Cooperative emission of light by an ensemble of dipoles near a metal nanoparticle: the plasmonic Dicke effect. *Phys. Rev. Lett.* **2009**, *102*, 077401.
47 Pustovit, V. N.; Shahbazyan, T. V., Plasmon-mediated superradiance near metal nanostructures. *Phys. Rev. B* **2010**, *82*, 075429.
48 Pustovit, V. N.; Shahbazyan, T. V., Resonance energy transfer near metal nanostructures mediated by surface plasmons. *Phys. Rev. B* **2011**, *83*, 085427.
49 Ditlbacher, H.; Felidj, N.; Krenn, J.; Lamprecht, B.; Leitner, A.; Aussenegg, F., Electromagnetic interaction of fluorophores with designed two-dimensional silver nanoparticle arrays. *Appl. Phys. B* **2001**, *73*, 373–377.
50 Zhang, J.; Fu, Y.; Chowdhury, M. H.; Lakowicz, J. R., Metal-enhanced single-molecule fluorescence on silver particle monomer and dimer: coupling effect between metal particles. *Nano Lett.* **2007**, *7*, 2101–2107.
51 Ming, T.; Chen, H.; Jiang, R.; Li, Q.; Wang, J., Plasmon-controlled fluorescence: beyond the intensity enhancement. *J. Phys. Chem. Lett.* **2012**, *3*, 191–202.
52 Hsieh, Y.-P.; Liang, C.-T.; Chen, Y.-F.; Lai, C.-W.; Chou, P.-T., Mechanism of giant enhancement of light emission from Au/CdSe nanocomposites. *Nanotechnology* **2007**, *18*, 415707.
53 Song, J.-H.; Atay, T.; Shi, S.; Urabe, H.; Nurmikko, A. V., Large enhancement of fluorescence efficiency from CdSe/ZnS quantum dots induced by resonant coupling to spatially controlled surface plasmons. *Nano Lett.* **2005**, *5*, 1557–1561.
54 Bek, A.; Jansen, R.; Ringler, M.; Mayilo, S.; Klar, T. A.; Feldmann, J., Fluorescence enhancement in hot spots of AFM-designed gold nanoparticle sandwiches. *Nano Lett.* **2008**, *8*, 485–490.
55 Kinkhabwala, A.; Yu, Z.; Fan, S.; Avlasevich, Y.; Müllen, K.; Moerner, W., Large single-molecule fluorescence enhancements produced by a bowtie nanoantenna. *Nat. Photonics* **2009**, *3*, 654–657.
56 Dulkeith, E.; Ringler, M.; Klar, T.; Feldmann, J.; Munoz Javier, A.; Parak, W., Gold nanoparticles quench fluorescence by phase induced radiative rate suppression. *Nano Lett.* **2005**, *5*, 585–589.
57 Karthikeyan, B., Fluorescence quenching of rhodamine-6G in Au nanocomposite polymers. *J. Appl. Phys.* **2010**, *108*, 084311.
58 Hövel, H.; Fritz, S.; Hilger, A.; Kreibig, U.; Vollmer, M., Width of cluster plasmon resonances: bulk dielectric functions and chemical interface damping. *Phys. Rev. B* **1993**, *48*, 18178.
59 Maxwell, D. J.; Taylor, J. R.; Nie, S., Self-assembled nanoparticle probes for recognition and detection of biomolecules. *J. Am. Chem. Soc.* **2002**, *124*, 9606–9612.
60 Reineck, P.; Gómez, D.; Ng, S. H.; Karg, M.; Bell, T.; Mulvaney, P.; Bach, U., Distance and wavelength dependent quenching of molecular fluorescence by Au@SiO_2 core–shell nanoparticles. *ACS Nano* **2013**, *7*, 6636–6648.
61 Griffin, J.; Singh, A. K.; Senapati, D.; Rhodes, P.; Mitchell, K.; Robinson, B.; Yu, E.; Ray, P. C., Size-and distance-dependent nanoparticle surface-energy transfer (NSET) method for selective sensing of Hepatitis C virus RNA. *Chem. Eur. J.* **2009**, *15*, 342–351.
62 Broussard, J. A.; Rappaz, B.; Webb, D. J.; Brown, C. M., Fluorescence resonance energy transfer microscopy as demonstrated by measuring the activation of the serine/threonine kinase Akt. *Nat. Protoc.* **2013**, *8*, 265–281.
63 Sapsford, K. E.; Berti, L.; Medintz, I. L., Materials for fluorescence resonance energy transfer analysis: beyond traditional donor–acceptor combinations. *Angew. Chem. Int. Ed.* **2006**, *45*, 4562–4589.
64 Lessard-Viger, M.; Rioux, M.; Rainville, L.; Boudreau, D., FRET enhancement in multilayer core–shell nanoparticles. *Nano Lett.* **2009**, *9*, 3066–3071.
65 Lakowicz, J. R.; Kuśba, J.; Shen, Y.; Malicka, J.; D'Auria, S.; Gryczynski, Z.; Gryczynski, I., Effects of metallic silver particles on resonance energy transfer between fluorophores bound to DNA. *J. Fluoresc.* **2003**, *13*, 69–77.
66 Zhao, L.; Ming, T.; Shao, L.; Chen, H.; Wang, J., Plasmon-controlled Förster resonance energy transfer. *J. Phys. Chem. C* **2012**, *116*, 8287–8296.
67 Ming, T.; Zhao, L.; Yang, Z.; Chen, H.; Sun, L.; Wang, J.; Yan, C., Strong polarization dependence of plasmon-enhanced fluorescence on single gold nanorods. *Nano Lett.* **2009**, *9*, 3896–3903.
68 Komarala, V. K.; Bradley, A. L.; Rakovich, Y. P.; Byrne, S. J.; Gun'ko, Y. K.; Rogach, A. L., Surface plasmon enhanced Förster resonance energy transfer between the CdTe quantum dots. *Appl. Phys. Lett.* **2008**, *93*, 123102.

69 Su, X.-R.; Zhang, W.; Zhou, L.; Peng, X.-N.; Wang, Q.-Q., Plasmon-enhanced Förster energy transfer between semiconductor quantum dots: multipole effects. *Opt. Express* **2010**, *18*, 6516–6521.
70 Su, X.-R.; Zhang, W.; Zhou, L.; Peng, X.-N.; Pang, D.-W.; Liu, S.-D.; Zhou, Z.-K.; Wang, Q.-Q., Multipole-plasmon-enhanced Förster energy transfer between semiconductor quantum dots via dual-resonance nanoantenna effects. *Appl. Phys. Lett.* **2010**, *96*, 043106.
71 Mathieu, L.-V.; Brouard, D.; Boudreau, D., Plasmon-enhanced resonance energy transfer from a conjugated polymer to fluorescent multilayer core–shell nanoparticles: a photophysical study. *J. Phys. Chem. C* **2011**, *115*, 2974–2981.
72 Kochuveedu, S. T.; Son, T.; Lee, Y.; Lee, M.; Kim, D.; Kim, D. H., Revolutionizing the FRET-based light emission in core–shell nanostructures via comprehensive activity of surface plasmons. *Sci. Rep.* **2014**, *4*, 1–8.
73 Aslan, K.; Lakowicz, J. R.; Geddes, C. D., Plasmon light scattering in biology and medicine: new sensing approaches, visions and perspectives. *Curr. Opin. Chem. Biol.* **2005**, *9*, 538–544.

11

Fluorescence Quenching by Plasmonic Silver Nanoparticles

M. Umadevi

Department of Physics, Mother Teresa Women's University, Kodaikanal, India

11.1 Metal Nanoparticles

Investigations of metal nanoparticles (NPs) have attracted significant attention because of their unusual size-dependent optical and electronic properties [1]. Presently there is intense interest in the optical properties of Au and Ag colloids. These colloids display bright colors due to the so-called plasmon absorption, which is in fact due to a combination of absorption and scattering [2].

It possesses unique optical attributes due to their surface plasmon resonance (SPR) which is the collective coherent oscillation of the free electrons in resonance with an electromagnetic wave. The plasmon oscillation is considered essentially as a photon strongly confined to the nanoscale size of the metal particle. The plasmon resonance results in a strong light absorption and scattering by the NPs at the resonance frequency, which has found uses in photonics and biomedicines, including highly sensitive diagnostic assays, thermal ablation, radiotherapy enhancement, drug delivery, and so on [3].

11.2 Fluorescence Quenching

Fluorescence is one of the most leading technologies commonly used in life sciences because of its versatility and widespread potential applications in the areas of luminescence tagging, imaging, medical, diagnostics, multiplexing, and most recently in biosensors.

The fluorescence of fluorophore might be enhanced or quenched due to the presence of nearby metallic NPs. The strength of the enhancement/quenching is influenced by many factors, such as size and shape of the metal NPs, the orientation of the fluorophore dipole moments relative to the NPs, the radiative decay rate, and quantum yield of the fluorophore [4].

A variety of molecular interaction can result in quenching. These include excited-state reactions, molecular rearrangements, energy transfers, ground-state complex formations, and collisional quenching. Fluorescence quenching has been widely studied both as a fundamental phenomenon and as a source of information about biochemical systems. Quenching studies can be used to reveal the localization of fluorophores in proteins and membranes and their permeabilities to quenchers.

Fluorescence quenching has various applications in proteins, membranes, and molecular biology. Quenching of solvent-exposed residues in proteins is a standard tool in characterization of proteins. Some quenchers are known to bind to proteins and induce conformational changes. Quenching membrane probes can be used thoroughly indicating its position in membranes. The quenching is used to determine the location of fluorophore in membranes. It has been used for sensing of a wide variety of analytes, including oxygen, NO, and heavy metals. It is used in green fluorescent protein to study gene expression and also as sensors. In molecular biology, it is used for sensing in DNA analysis [4].

Lakowicz *et al.* reported that the quenching is usually observed if the fluorescence is located at a very short distance (<5 nm) from the metal surface. When the fluorophore–metal distance is increased, both fluorescence quenching and enhancement have been observed [5]. Geddes *et al.* described the effect of silver NPs (Ag NPs) on near the fluorophores [6]. Our groups have also studied the fluorescence quenching of quinone derivatives by Ag NPs [7–11]. This chapter describes the mechanism involved in quenching effect of Ag NPs.

Surface Plasmon Enhanced, Coupled and Controlled Fluorescence, First Edition. Edited by Chris D. Geddes.
© 2017 John Wiley & Sons, Inc. Published 2017 by John Wiley & Sons, Inc.

11.3 Mechanism behind Quenching

Generally, excited-state fluorophore behaves as an oscillating dipole. When these fluorophores are in close proximity to the metal surface, the rate of emission and the spatial distribution of the radiating energy will be modified. The electric fields felt by the fluorophores are affected by the interaction of the incident light with the nearby metal surface. These interactions can increase/decrease the field felt by the fluorophore and then increase/decrease the radiative decay rate [4], resulting in many desirable effects such as increased quantum yield and decreased lifetime.

The energy transfer and electron transfer processes are the major deactivation processes for quenching of excited-state fluorophores on the metal surfaces. The electron transfer mechanism is predominantly for particle sizes of <5 nm. Since the particles do not exhibit any SPR band in the visible region and the metal NPs are <5 nm, electron transfer process is the dominant quenching mechanism [12]. As the Ag NPs are larger than 5 nm, energy transfer dominates the quenching mechanism. In most of the cases, the Ag NPs are larger than 5 nm, in which energy transfer process is the predominant quenching mechanism.

Resonant energy transfer (RET) takes place in the system where the donor molecules are placed in close proximity to the metal surface. If the donor is a fluorescent molecule, RET process is nonradiative where the acceptor may or may not be fluorescent. It is commonly used in biological research to measure the molecular distances or donor to acceptor proximity. It occurs through the dipole–dipole interaction between the excited donor and an acceptor molecule. Energy conservation requires that the energy gap between the ground state and excited state of participating donor and acceptor molecules is nearly the same. This in turn implies that the fluorescence emission spectrum of donor must overlap with absorption spectrum of acceptor, and they should be within a minimal spatial range for a donor to transfer its excitation energy to an acceptor [13].

For example, Figure 11.1 shows the structure of 1,4-dihydroxy-2,3-dimethylanthracene-9,10-dione (DHDMAD) [7]. Figure 11.2 depicts the optical absorption and fluorescence emission spectra of DHDMAD in methanol. Figure 11.3 shows the absorption spectra of Ag NPs prepared by the Lee and Meisel method with different boiling times 60(S1), 70(S2), 80(S3), 90(S4), 100(S5), 110(S6), 120(S7), and 130(S8) min.

Fluorescence resonance energy transfer (FRET) is a distance-dependent interaction between the different electronic excited states of dye molecules in which excitation energy is transferred from one molecule (donor) to another molecule (acceptor) at the cost of emission from the former molecular system. According to Förster's theory, the rate of energy transfer is based on the spectral overlap between emission spectrum of the fluorophore and absorption spectra of the Ag NPs, the relative orientation of the donor and acceptor transition dipoles, the distance between the donor and acceptor transition dipoles, and the fluorescence quantum yield of the donor. It results in long-range dipole–dipole interactions between the donor and acceptor [4, 14, 15].

The degree of quenching depends on the structural details that control proximity between the fluorophore molecules and the Ag NPs core. When a donor molecule is placed in the vicinity of a conductive Ag NP surface, resonance energy transfer between the donor–acceptor takes place. The probability of this energy transfer depends on five factors, such as size, shape of metal NPs, the orientation of the molecular dipole with respect to fluorophore-NPs axis, distance between the fluorophore molecule and the metal NPs, and the overlap of the molecule emission with the NPs absorption spectrum [16].

To understand energy transfer, the distance between NPs and dye molecules using the Förster mechanism of nonradiative energy transfer was calculated. According

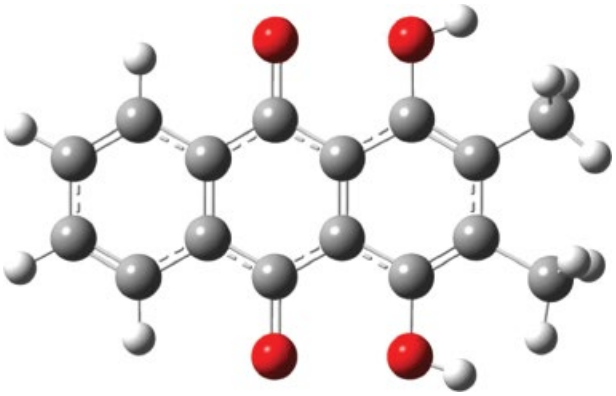

Figure 11.1 Structure of 1,4-dihydroxy-2,3-dimethylanthracene-9,10-dione. Umadevi *et al.* [7]. Reproduced with the permission of Springer.

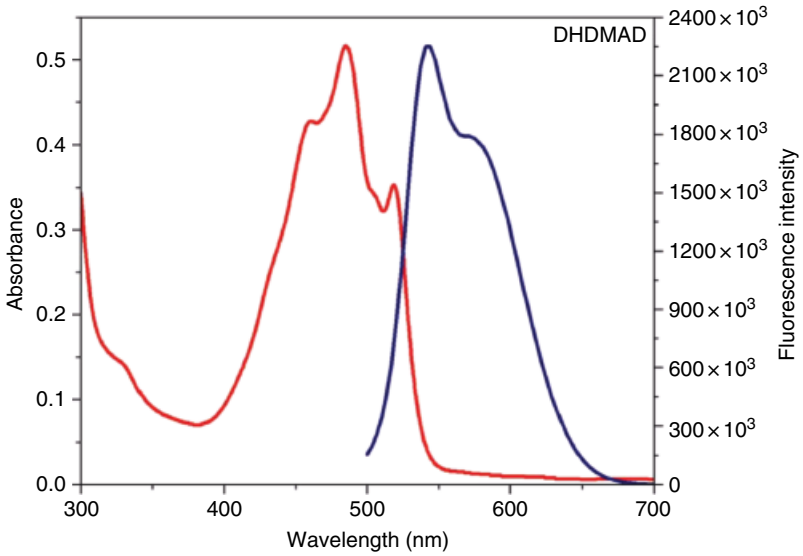

Figure 11.2 Optical absorption and fluorescence emission spectra of DHDMAD in methanol. Umadevi *et al*. [7]. Reproduced with the permission of Springer.

to Förster theory, the energy transfer effect is related not only to the distance (r_0) between the acceptor and donor but also to the critical energy transfer distance (R_0), that is,

$$E = 1 - \frac{F}{F_o} = \frac{R_o^6}{R_o^6 + r_o^6} \tag{11.1}$$

where F is the fluorescence intensity of the donor in the presence of the acceptor, F_0 is the fluorescence intensity of the donor in the absence of the acceptor, and R_0 is the critical distance at which the efficiency of energy transfer is 50%:

$$R_0^6 = 8.8 \times 10^{-25} k^2 n^{-4} \varphi J \tag{11.2}$$

where k^2 is the spatial orientation factor of the dipole, n is the refractive index of the medium, φ is the fluorescence quantum yield of the donor, and J the overlap integral of the fluorescence emission spectrum of the donor and absorption spectra of the acceptor was given by

$$J = \frac{\int_0^\infty F(\lambda)\varepsilon(\lambda)\lambda^4 d\lambda}{\int_0^\infty F(\lambda) d\lambda} \tag{11.3}$$

where $F(\lambda)$ is the fluorescence intensity of the fluorescence donor at wavelength λ and $\varepsilon(\lambda)$ is the molar absorptivity of the acceptor at wavelength (λ). In the case of DHDMAD, it has been reported that $k^2 = 2/3$, $\phi = 0.26905$, and $n = 1.336$. Based on these data, the R_0 and r_0 values were calculated.

The overlap of the optical absorption spectra of Ag NPs and the fluorescence emission spectrum of DHDMAD in methanol were shown in Figure 11.4. The overlap integral (J), critical distance (R_0), energy transfer efficiency (E), and distance (r_0) were shown in Table 11.1. From the overlapping spectrum of the absorption spectra of acceptor and the fluorescence spectrum of DHDMAD, $J(\lambda)$ can be evaluated by integrating the spectra from 500 to 700 nm. By adding the donor molecule into acceptor molecule with increasing heating time, the fluorescence spectra shifts toward shorter wavelength providing a larger value of spectral overlap integral. The increase in $J(\lambda)$ in turn causes an increase in FRET efficiency. The value of $J(\lambda)$ changes from 2.99×10^{-16} $cm^3/L/mol^1$ to 7.36×10^{-15} $cm^3/L/mol^1$ for change in heating time from 60 to 130 min. Accordingly the energy transfer efficiency (E) between Ag NPs and DHDMAD varies from 0.93 (93%) to 1.00 (100%). It is evident that the efficiency of energy transfer is higher in 130 min than that in 60 min. The maximum FRET efficiency was 100% for an acceptor heating time of 130 min. The critical distance (R_0) between Ag NPs and DHDMAD for S1 is 156 nm and 267 nm for S8, respectively. The distance (r_0) between Ag NPs and DHDMAD for S1 is 97 nm and 110 nm for S8, respectively. Interestingly it was observed that the FRET efficiency increases with increase in heating time. Therefore in the present system under investigation the FRET process between donor and acceptor molecule is very heating time sensitive.

In the case of energy transfer from fluorophore to NPs, initially donor state of the system consists of an excited fluorophore molecule and a NP in its ground state. The nonradiative energy transfer from the fluorophore to NP involves simultaneous de-excitation of molecule and collective excitation of compressible

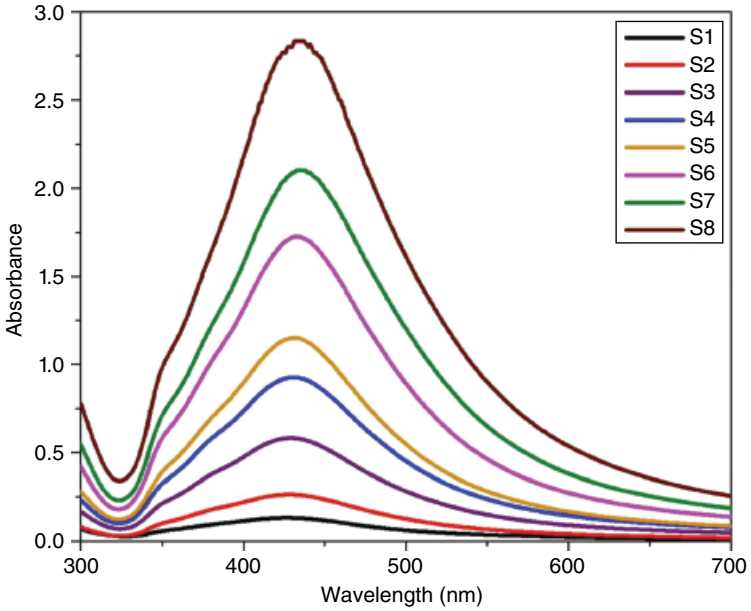

Figure 11.3 Optical absorption spectra of Ag NPs at different heating times. Umadevi *et al*. [7]. Reproduced with the permission of Springer.

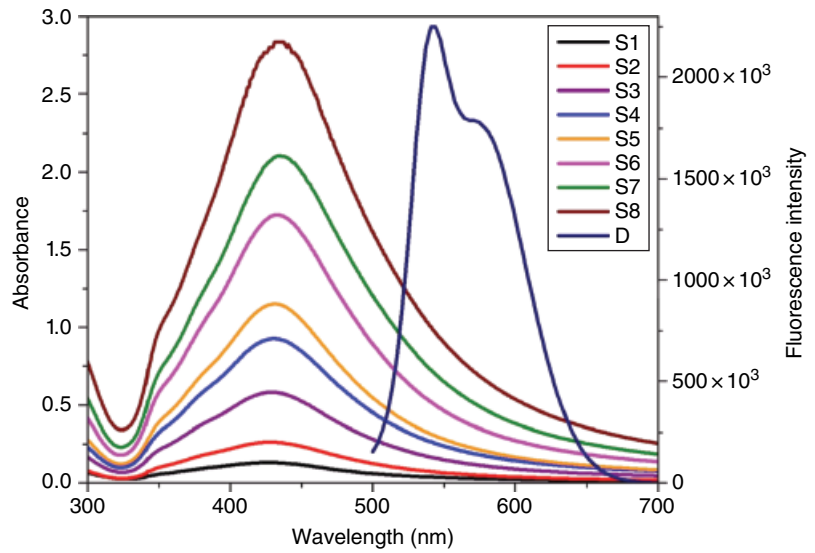

Figure 11.4 Optical absorption spectra of Ag NPs at different heating times and fluorescence emission spectrum of DHDMAD (D) in methanol. Umadevi *et al*. [7]. Reproduced with the permission of Springer. (*See insert for color representation of this figure*.)

electron gas in the NP. The final acceptor state of the system consists of ground-state fluorophore molecule and an NP in its excited state. The rate of excitation energy transfer depends on the strength of Coulombic interactions and the spectral overlap between the emission spectrum of fluorophore and absorption spectrum of NPs.

When a metal NP has been excited and is oscillating in the incident electromagnetic field, the excited fluorophore molecules may have a fluctuating electric dipole moment and cause the radiation. This radiation from dipole moment of excited fluorophore molecule provides the path for radiative decay. On the other hand, the joule heating plasmon absorption caused by these fields provides the path for nonradiative decay. The competition between radiative and nonradiative decay energy transfer affects the fluorescence emission of the fluorophore molecules located near the metal NPs due to joule heating and surface plasmon absorption.

The effect of Coulombic interactions on the energy transfer has been studied in two different ways. First, the Coulombic interactions between fluorophore and NPs depend on the charge densities of fluorophore and NPs. Second, they are based on the interaction within the dipole approximation. This dipole interaction

Table 11.1 Photophysical properties of Ag NPs and energy transfer parameters of DHDMAD in Ag NPs.

S. No.	Heating time (min)	SPR peak of Ag NPs (nm)	J ($cm^3/L/mol^1$)	R_0 (nm)	r_0 (nm)	E (%)
1	60 (S1)	419	2.993×10^{-16}	156	97	93
2	70 (S2)	420	5.472×10^{-16}	173	104	94
3	80 (S3)	424	1.232×10^{-15}	198	118	95
4	90 (S4)	427	1.963×10^{-15}	214	121	96
5	100 (S5)	429	2.310×10^{-15}	220	118	97
6	110 (S6)	431	3.790×10^{-15}	239	118	98
7	120 (S7)	433	5.300×10^{-15}	253	119	99
8	130 (S8)	437	7.363×10^{-15}	267	110	100

Umadevi *et al.* [7]. Reproduced with the permission of Springer.

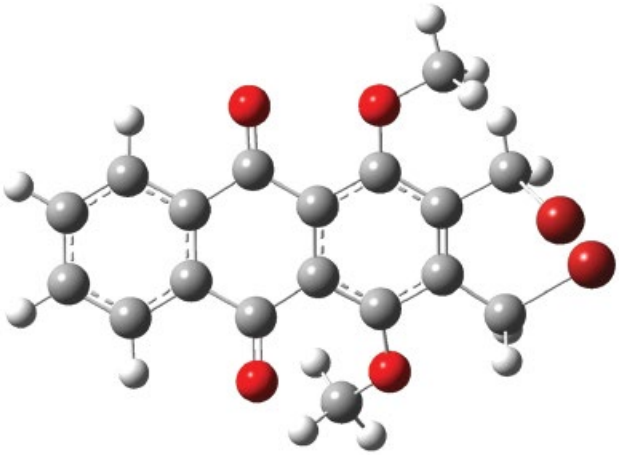

Figure 11.5 Structure of 1,4-dimethoxy-2,3-dibromomethylanthracene-9,10-dione (DMDBMAD). Kavitha *et al.* [11]. Reproduced with the permission of Springer.

mainly depends on the dipole moment of the fluorophores and NPs and the distance between the fluorophores and NPs.

Gersten and Nitzan [17] explained the radiative rate by Hertzian dipole emitters. Hertzian dipole emitters consider the dipole of the entire system. It includes the intrinsic molecular dipole induced by the dipole field of the adjacent NPs and the dipole of the NPs driven by the dipole field of the molecule. By calculating the absorption of the molecular dipole field at the metal surface, the RET taken place in the excited molecule has been predicted.

The quenching rate constant has been calculated from Stern–Volmer plot. The Stern–Volmer equation accounting for both static and dynamic quenching is generally written as $\varphi_0/\varphi = 1 + K_{SV}$ [Ag] [4] where $K_{SV} = K_S + K_D$ and where K_S and K_D are the static and dynamic quenching constants, respectively, and φ_0 and φ are the fluorescence quantum yield of DMDBMAD in the absence and presence of quencher [Ag], respectively. Figure 11.5 shows the structure of 1,4-dimethoxy-2,3-dibromomethylanthracene-9,10-dione (DMDBMAD) [11]. Figure 11.6 shows the plot of φ_0/φ versus silver concentration at constant DMDBMAD concentration. The value of the quenching constant is found as $K_{SV} = 99 \times 10^3/M^1$. The linearity of the Stern–Volmer plot indicates that only one type of quenching occurs in the system. There is no possibility of formation of static quenching complexes via attractive electrostatic interaction between fluorophore–quencher pairs; collisional (dynamic) quenching is effectively possible. In the presence of Ag NPs, there is no change in the peak position in the absorption spectra of the DMDBMAD; the possibility of static quenching is absent. The absence of a new broad band indicates that DMDBMAD has been bound to Ag NPs and so has failed to exhibit excimer and exciplex formation due to intermolecular interactions, or if there is the formation of any trace of the excimer, it is also quenched by the metal. The Stern–Volmer

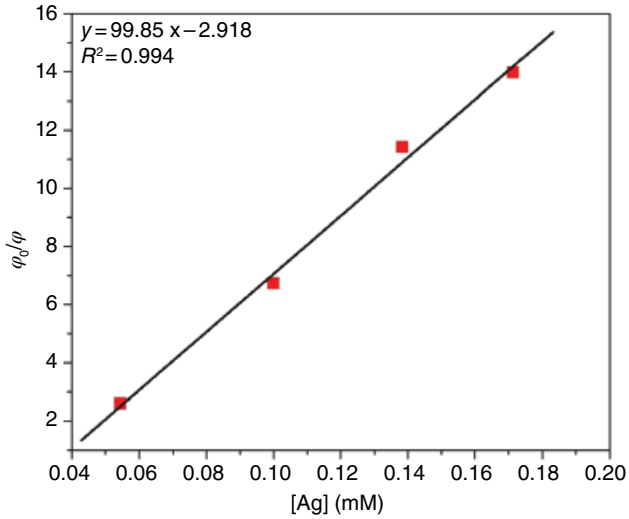

Figure 11.6 Stern–Volmer plot for DMDBMAD. Kavitha *et al*. [11]. Reproduced with the permission of Springer.

quenching constant by Ag NPs in the solution is high indicating the presence of adsorption of the DMDBMAD molecule on the Ag surface.

This chapter elucidated the mechanism involved in fluorescence quenching of fluorophore by Ag NPs.

References

1 Rosi, N.L.; Mirkin, C.A. Nanostructures in biodiagnostics, *Chem. Rev.* **2005**, *105*, 1547–1562.

2 Alivisatos, P. The use of nanocrystals in biological detection, *Nat. Biotechnol.* **2004**, *22*, 47–52.

3 Kah, E.F.; Lin-Yue, L.Y. Localized surface plasmon resonance: a unique property of plasmonic nanoparticles for nucleic acid detection, *Nanoscale* **2013**, *5*, 12043–12071.

4 Lakowicz, J.R. *Principles of Fluorescence Spectroscopy*, 3rd edn., Springer, New York, **2006**.

5 Lakowicz, J.R. Radiative decay engineering 5: metal-enhanced fluorescence and plasmon emission, *Anal. Biochem.* **2005**, *337*, 171–194.

6 Geddes, C.D.; Cao, H.; Gryczynski, I.; Gryczynski, Z.; Fang J.Y.; Lakowicz, J.R. Metal-enhanced fluorescence (MEF) due to silver colloids on a planar surface: potential applications of indocyanine green to in vivo imaging, *J. Phys. Chem. A* **2003**, *107*, 3443–3449.

7 Umadevi, M.; Kavitha S.R.; Vanelle, P.; Terme, T.; Khoumeri, O. Spectral investigations on the fluorescence quenching of 1,4-dihydroxy-2,3-dimethylanthracene-9,10-dione by plasmonic silver nanoparticles, *Plasmonics* **2014**, *9*, 443–450.

8 Umadevi, M.; Kavitha S.R.; Vanelle, P.; Terme, T.; Khoumeri, O. Ground and excited state behaviour of 1,4-dimethoxy-3-methyl-anthracene-9, 10-dione in silver nanoparticles: spectral and computational investigations, *J. Lumin.* **2013**, *142*, 1–7.

9 Umadevi, M.; Kavitha S.R.; Vanelle, P.; Terme, T. Influence of plasmonic silver nanoparticles on fluorescence quenching of 1,4-dihydroxy-3-methylanthracene-9, 10-dione, *Plasmonics* **2013**, *8*, 859–867.

10 Kavitha S.R.; Umadevi, M.; Sridhar, B. Vanelle, P.; Terme, T.; Khoumeri, O. Spectroscopic studies of 1,4-dimethoxy-2,3-dimethylanthracene-9,10-dione on plasmonic silver nanoparticles, *Spectrochim. Acta A* (**2014**), *133*, 472–479.

11 Kavitha S.R.; Umadevi, M.; Vanelle, P.; Terme, T.; Khoumeri, O. Spectral investigations on the influence of silver nanoparticles on the fluorescence quenching of 1,4-dimethoxy-2,3-dibromomethylanthracene-9,10-dione, *Eur. Phys. J. D* **2014**, *68*, 308.

12 Fan, C.; Wang, S.; Hong, J.W.; Bazan, G.C.; Plaxco, K.W.; Heeger, A.J. Beyond superquenching: hyper-efficient energy transfer from conjugated polymers to gold nanoparticles, *Appl. Phys. Sci.* **2003**, *100*, 6297–6301.

13 Clapp, A.R.; Medintz, I.L.; Uyeda, H.T.; Fisher, B.R.; Goldman, E.R.; Bawendi, M.G.; Mattoussi, H. Quantum dot-based multiplexed fluorescence resonance energy transfer, *J. Am. Chem. Soc.* **2005**, *127*, 18212–21.

14 Förster, T. *Modern Quantum Chemistry*, Academic Press, New York, **1965**.

15 Förster, T. Intermolecular energy migration and fluorescence, *Ann. Phys.* **1948**, *2*, 55–75.

16 Wang, Z.L. Transmission electron microscopy of shape-controlled nanocrystals and their assemblies, *J. Phys. Chem. B* **2000**, *104*, 1153–1175.

17 Gersten, J.; Nitzan, A. Spectroscopic properties of molecules interacting with small dielectric particles, *J. Chem. Phys.* **1981**, *75*, 1139–1152.

12

AgO_x Thin Film for Surface-Enhanced Raman Spectroscopy

Ming Lun Tseng[1], Cheng Hung Chu[1,2], Jie Chen[1], Kuang Sheng Chung[1], and Din Ping Tsai[1,2]

[1] *Department of Physics, National Taiwan University, Taipei, Taiwan*
[2] *Research Center for Applied Sciences, Academia Sinica, Taipei, Taiwan*

12.1 Introduction

Surface-enhanced Raman scattering (SERS) has attracted a lot of interests in the nanophotonics and molecule spectroscopy community [1–3]. Raman scattering cross section of molecules nearby the metallic nanostructures is able to be dramatically increased (enhancements of 10^6–10^8) due to the localized surface plasmon resonance on the nanostructure under illumination [1–3]. SERS technology has been used in the fields such as genetics, diseases, and public security for sensing and characterizing the molecules.

Many efforts have addressed the development of plasmonic nanostructures for SERS and sensing. For example, the nanosphere lithography [1, 4, 5] is used to fabricate the well-defined geometric triangular Au nanoparticle array with efficient SERS capability. Asymmetrical split ring resonator nanoslit array is fabricated using focused ion beam technique [6]. Also, electron beam lithography is a versatile tool for obtaining arbitrary metallic nanopatterns as the SERS substrate [7, 8]. However, it is still an important topic for finding a simple way for the fabrication of an efficient SERS-active substrate with high throughput and large area. For achieving this goal, a silver oxide (AgO_x) thin film would be helpful. AgO_x can be decomposed into dense Ag nanoparticles by laser illumination or thermal annealing with following reaction: [9–14]

$$2AgO_x \xrightarrow{\Delta} 2Ag + xO_2 \tag{12.1}$$

The threshold of reaction temperature is around 170°C. Based on this property, AgO_x thin film has been utilized in many important applications, such as ultrahigh density optical data storage [10], molecular sensing [13, 14], super-resolution imaging of nanoobjects [15], plasmon-enhanced photoluminescence [16], and plasmon-enhanced photoelectrochemical water splitting [17].

In this chapter, we review our recent progress on applications of Ag nanostructure reduced from laser-treated and thermal-annealed AgO_x thin films as the useful SERS-active chips. Using the femtosecond laser beam to fabricate the SERS-active micro-pattern as well as the SERS chip on flexible substrate, the relation between SERS capability and the processing laser conditions of the Ag nanostructure is reported. The large-area SERS substrate composed of the annealed AgO_x thin film/dielectric spacer/Au and the modulation of the SERS efficiency by varying the thickness of the spacing layer are reported subsequently.

12.1.1 SERS on the Laser-Treated AgO_x Thin Film

12.1.1.1 Experimental Method

The AgO_x thin films used in this work are prepared by reactive sputtering method. In the reactive sputtering process, the transparent BK7 substrates (Matsunami cover glass, thickness = 1.5 mm) is put into the chamber of the conventional magnetron sputtering machine (Shibaura Mechatronics Corporation). A pure Ag plate is used as the target. The chamber is in an Ar/O_2 (flow ratio = 10/25 m^3/s) mixed-gas atmosphere operation pressure of the gas mixture (= 5×10^{-1} Pa).

Figure 12.1 shows the schematic illustration of the femtosecond laser system [13] used for fabrication of Ag nanostructure from the AgO_x thin film. Femtosecond laser beam from the oscillator (Coherent Inc., λ = 800 nm, pulse duration = 140 fs, repetition rate = 80 MHz) is focused on a 15-nm-thick AgO_x thin film using an oil-immersion objective lens (Zeiss

Surface Plasmon Enhanced, Coupled and Controlled Fluorescence, First Edition. Edited by Chris D. Geddes.
© 2017 John Wiley & Sons, Inc. Published 2017 by John Wiley & Sons, Inc.

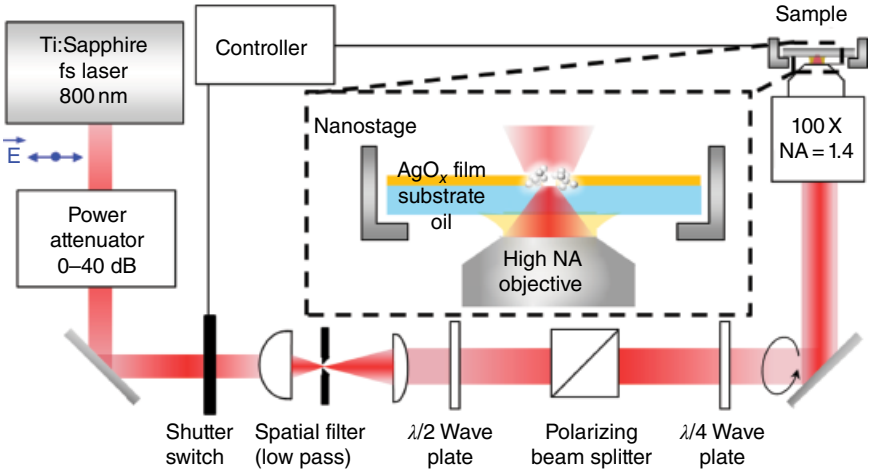

Figure 12.1 Schematic illustration of the femtosecond laser system used for fabrication of the SERS-active nanostructure from AgO_x thin film. Tseng *et al*. [13]. Reproduced with the permission of American Chemical Society.

Plan-Apochromat, 100×, working distance = 0.17 mm, NA = 1.4). The power of laser beam is controlled using the attenuator. The polarization of the laser beam is made circularly polarized using a $\lambda/4$ waveplate. Sample is set on the computer-controlled three-dimensional stage (Mad City Lab. Inc.). By controlling the three-dimensional stage (Mad City Lab. Inc.), specific micro-/nanopatterns are able to be written on the AgO_x thin film by the femtosecond laser beam. The laser-generated nanoparticles are characterized using the high-resolution transmission electron microscope (HR-TEM). Figure 12.2a and b is the TEM and HR-TEM images of the laser-generated Ag nanoparticles, respectively. As shown in Figure 12.2b, the *d*-spacing of the lattice fringes of the nanoparticle is around 0.235 nm, which matches the interspacing of the (111) planes of the face-centered-cubic Ag very well. This result is also in good agreement with that of the Ag bulk crystal (JCPDS no. 89-3722). Figure 12.2c and d is the electron and X-ray diffraction patterns of laser-generated Ag nanostructures, which show the characteristic of polycrystalline.

12.1.1.2 Tunabe SERS Enhancement

As shown in Figure 12.3, a desirable pattern, NTU, is written on AgO_x thin film using femtosecond laser [13]. The three letters in the pattern are made with laser power of 21, 14, and 7 mW. Solution of 10^{-5} M Rhodamine 6G (R6G) molecules are dropped on the surface of the sample. The sample is subsequently purged by pure N_2 gas. Raman intensity map is acquired using a scanning confocal Raman microscope (WITec, CMR200) with a green ($\lambda = 532$ nm) laser [4]. In the Raman intensity mapping, brighter color indicates the stronger Raman signal of the selected peak of the adsorbed R6G molecules. A high brightness contrast between the laser-treated and nontreated area is clearly identified. As shown in Figure 12.3a, the intensity of Raman vibration signal from R6G at each letter is increased with the processing laser power. Figure 12.3c shows the atomic force microscopy (AFM) measurement of the NTU pattern. The surface morphologies of the three letters vary from each other, indicating that the SERS capability of the laser-generated nanostructure is strongly dependent on the laser processing parameters.

As can be seen in Figure 12.4, three rectangular zones on an AgO_x thin film are treated by the femtosecond laser beam with laser power of 21, 14, and 7 mW, respectively [14]. The reflectivity of the laser-processed zone is obviously higher in comparison with the untreated one, indicating the appearance of strong metallic properties at laser-processed zone. In Raman intensity map image, four uniform patterns and obvious levels of R6G Raman intensity are observed. The Raman intensities at the laser-processed regions are much stronger than the ones at untreated region. The Raman intensity at 21-mW processed region is stronger than the ones at 11- and 7-mW regions. Figure 12.4c shows the Raman spectra of R6G adsorbed on zones of laser-processed AgO_x thin film. Peaks associated to the typical vibration modes of R6G at 611, 770, 1358, 1507, and 1647 cm^{-1} are observed in the spectra obtained at the laser-processed zones [18]. Being compared with the unprocessed region, the intensity of the R6G's Raman vibration modes at 611, 770, 1358, 1507, and 1647 acquired from the 21-mW region are enhanced by 46-, 42-, 43-, 40-, 39-fold, respectively.

As shown in Figure 12.5, the surface morphology of the Ag nanostructures made with laser power of 21, 11, and 7 mW is characterized using the AFM [14]. After laser processing, Ag nanoparticles are formed on

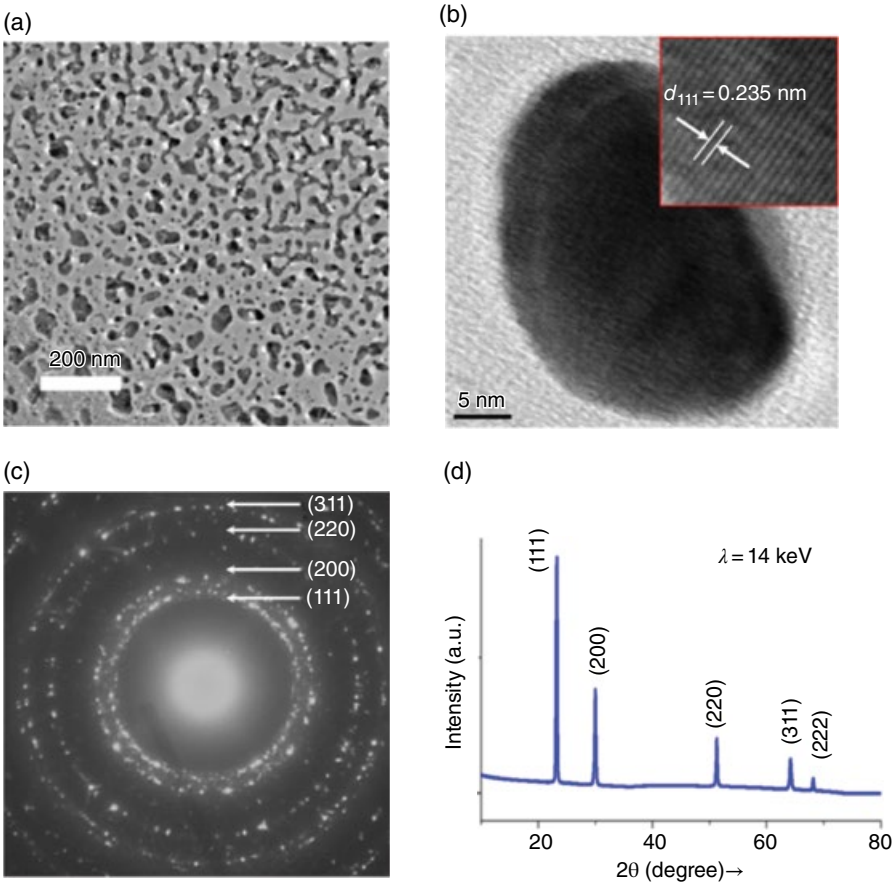

Figure 12.2 (a) TEM image of laser-treated AgO_x thin film. (b) HR-TEM image and (c) electron diffraction pattern of the Ag nanoparticle. (d) X-Ray diffraction of laser-treated AgO_x thin film by laser treatment. Tseng *et al*. [13]. Reproduced with the permission of American Chemical Society.

the substrate. The average sizes of the Ag nanoparticle are found to be decreased with the rise of processing femtosecond laser power. The decline of the average size of the Ag nanoparticles is associated to the laser-induced ablation and reshaping effects in the femtosecond laser processing. The relation between the SERS capability and the surface morphology of Ag nanostructures can be understood using the three-dimensional finite-difference time-domain (FDTD) simulation method. Figure 12.6 shows the FDTD simulation results of the electrical field energy distributions on the Ag nanoparticles made by laser power of 21 mW (Figure 12.6a) and 7 mW (Figure 12.6b). The morphologies of the 1.1 μm × 1.1 μm square region in the lower left corner of AFM image in Figure 12.5a and c are analyzed with the image analysis software IGOR Pro (version 6.3), and the result is subsequently used for the FDTD simulation. Simulation results show that more plasmon-active sites (shown in yellow and red colors) can be observed on the surface of the Ag nanostructure made with laser power 21 mW in comparison with the one made with 7 mW. We can summarize that the Ag structure with higher surface density of plasmonic nanoparticles has more "plasmonic hotspots" over the sample surface. On the fixed probing area in Raman spectroscopy measurement, such nanostructure will provide a better SERS efficiency.

12.1.1.3 SERS-Active Nanostructure Made on Flexible Substrate

The SERS-active Ag nanostructure is able to be easily fabricated on the optical transparent and flexible substrates using the femtosecond laser fabrication technique [14]. The stacked films of 200-nm-thick $ZnS–SiO_2$ (composition ratio ZnS 80% and SiO_2 20%) and 15-nm-thick AgO_x are orderly sputtered on the polycarbonate substrate (thickness = 0.6 mm, refractive index ~ 1.584). $ZnS–SiO_2$ thin film has been used as the protection layer to prevent the laser-induced damage for the polycarbonate substrate in the laser processing [19, 20]. As shown in Figure 12.7a, the stacked films on the polycarbonate substrate are still optical transparent and flexible. A 20× Zeiss Epiplan lens is utilized for the femtosecond laser processing

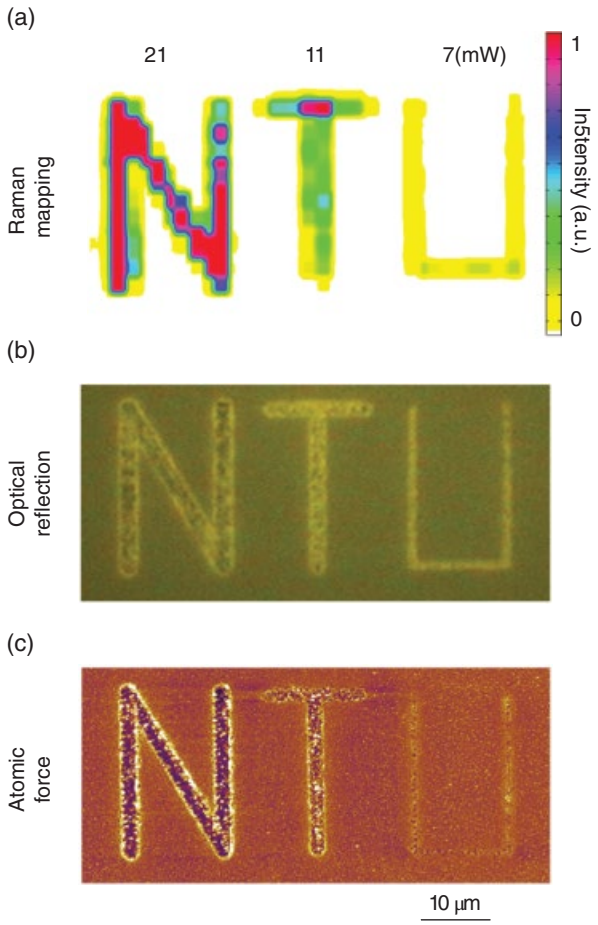

Figure 12.3 Fabrication of the SERS-active micro-pattern on AgO_x thin film. (a)–(c) Raman, optical reflection, and AFM images of "NTU" micro-pattern. From left to right, each letter is written by a femtosecond laser beam with powers of 21, 11, and 7 mW, respectively. Tseng *et al*. [13]. Reproduced with the permission of American Chemical Society. (*See insert for color representation of this figure*.)

on the AgO_x thin film. As shown in Figure 12.7b, the Ag nanostructure is successfully formed on the substrate after laser processing with a laser power of 11 mW. As shown in Figure 12.7c, uniform and obvious SERS for R6G adsorbed over the fabricated nanostructure on the polycarbonate substrate is observed. This result is very important for developing the novel sensing chips with low cost and high throughput.

12.1.2 Annealed AgO_x Thin Film for SERS

Plasmonic Ag nanostructure is also able to be produced from AgO_x thin film using the thermal annealing method [11, 12]. Figure 12.8 shows the scanning electron microscope (SEM) image of the Ag nanoparticles generated from the 15-nm-thick AgO_x thin film treated by thermal annealing at 473 K for 1 h (Ar atmosphere, pressure = 7.5×10^{-6} Pa). Ag nanoparticles are observed on the substrate. The size of the Ag nanoparticle is varied from 10 to 100 nm in diameter with an average size of around 40 nm. Some large irregular nanostructures (denoted as arrows in Figure 12.8) are formed on the surface, which may be associated to the aggregation of nanoparticles in the processing.

For enhancing the SERS capability of the Ag nanostructure, the coupling between localized and propagating surface plasmons in the structure of Ag nanoparticles near an Au film is adopted [21–23]. Using this technique, we are able to efficiently optimize the SERS capability of the sensing chip and fabricate large-area SERS substrate. Here, stacked films $ZnS–SiO_2$(150 nm)/Au(60 nm)/$ZnS–SiO_2$(10–60 nm)/AgO_x(15 nm) are orderly sputtered on the glass substrate (area 1.2 cm × 1.2 cm). The first 150-nm-thick $ZnS–SiO_2$ is used as the adhesion layer for Au thin film and glass substrate. Another $ZnS–SiO_2$ layer is used as the spacing layer for controlling the coupling between the Ag nanostructure and the Au thin film. The thickness of the spacing layer is set as 10, 20, 30, 40, 50, and 60 nm. Figure 12.9 shows the Raman spectra of R6G on the Ag nanostructure/$ZnS–SiO_2$/Au film with different thicknesses of the $ZnS–SiO_2$ layer. The strong modulation of the SERS capability of the Ag nanostructure/$ZnS–SiO_2$/Au film device is observed. The SERS capability of the device is increased when the $ZnS–SiO_2$ spacing layer becomes thicker, and the maximum value is observed when the $ZnS–SiO_2$ spacing layer is 40 nm in thickness. The capability decreases again when the thickness is larger than 40 nm. In comparison with the case with 10-nm-thick $ZnS–SiO_2$ spacing layer, the device with a 60-nm-thick spacing layer shows the obvious enhancements for Raman scattering of R6G. The intensities corresponding to the main vibrational modes of R6G molecule at 770, 1358, 1507, and 1647 cm^{-1} are enhanced to around 19-, 28-, 29-, 29-fold, respectively. The variation of the SERS efficiency is originated from the shifting of the resonant wavelength of the multilayered plasmonic system with different spacing layer thickness [21]. It is thus possible to design the SERS chip for different wavelength excitation by properly selecting the layered structure of the chip.

12.2 Conclusion

In conclusion, the applications of laser-treated and annealed AgO_x thin film for SERS of organic dye molecule have been reported. Experimental results of Raman spectroscopy measurement for R6G on

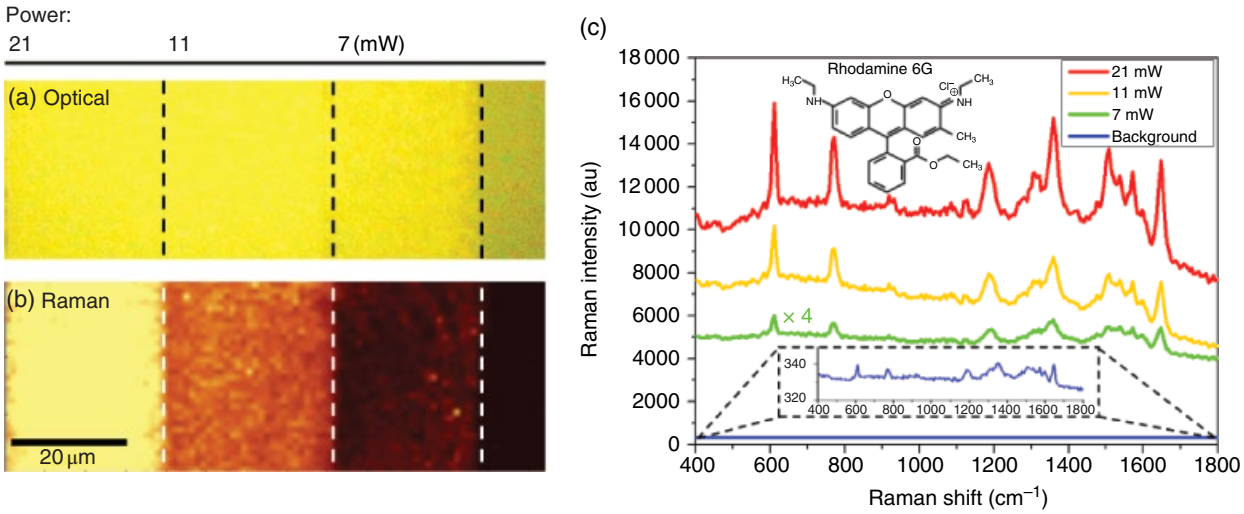

Figure 12.4 (a) Optical reflection image of laser-generated Ag nanostructures made with laser powers 21, 11, and 7 mW. (b) The corresponding Raman intensity map of R6G on the laser-fabricated Ag nanostructures and the untreated AgO_x thin film. The Raman intensity map is obtained from integrating spectral intensity of the R6G Raman peak ranging from 598 to 623 cm^{-1}. (a) and (b) are shown on the same scale. (c) Raman spectra of R6G adsorbed on various zones of laser-processed AgO_x thin film. The molecular structure of R6G molecule is shown as the up insert, and the button one is the magnified Raman spectrum of R6G molecules obtained from the zone of unprocessed AgO_x thin film. Tseng *et al*. [14]. Reproduced with the permission of American Chemical Society. © The Optical Society.

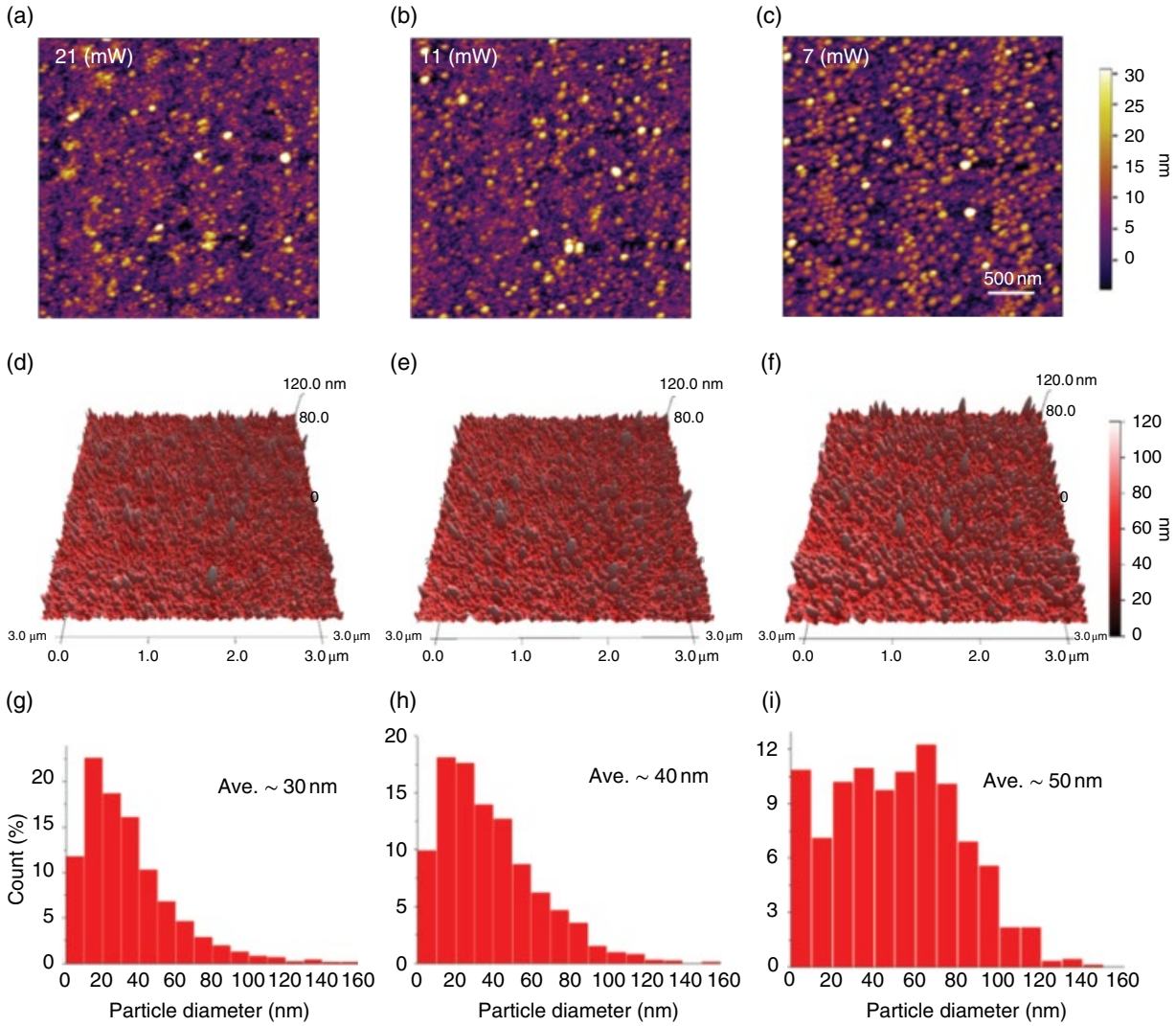

Figure 12.5 (a)–(c) Two-dimensional AFM images of Ag nanoparticle aggregations made with processing laser powers 21, 11, and 7 mW, respectively. The three images are shown on the same scale. (d)–(f) are the corresponding three-dimensional AFM images. The height of morophology is recorded as gray scale. The brighter color is corresponded to the higher height. (g)–(i) are the histograms of Ag nanoparticle diameters made with various laser powers. Tseng *et al*. [14]. Reproduced with the permission of American Chemical Society. © The Optical Society.

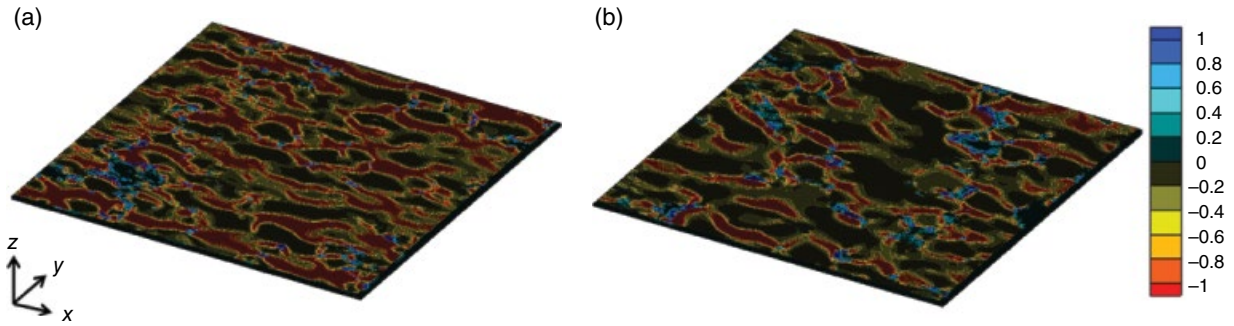

Figure 12.6 Electric-filed energy slice contour (E^*·D/2) at the interface of Ag nanostructure-glass substrate under the illumination of light with a wavelength of 532 nm calculated using FDTD method for the Ag nanostructures made with laser powers (a) 21 mW and (b) 7 mW. Tseng *et al*. [14]. Reproduced with the permission of American Chemical Society. © The Optical Society.

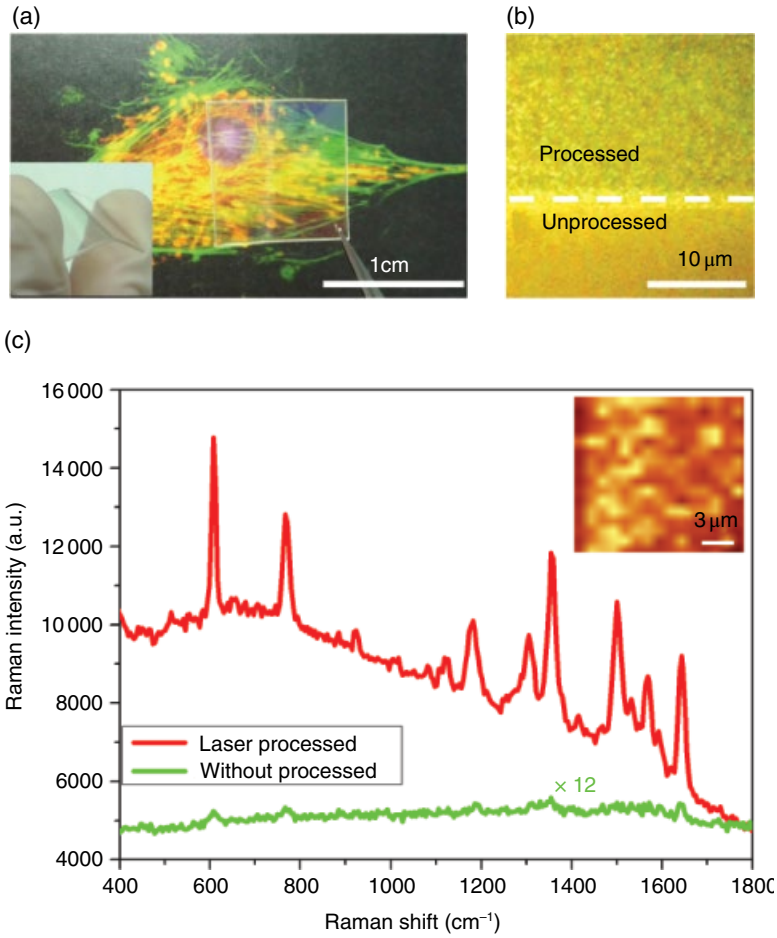

Figure 12.7 (a) Photographs of the as-deposited stacked films on polycarbonate substrate. A photograph of a cell is used as the background for demonstrating the high transparency of the thin films. (b) Optical reflection image of fabricated Ag nanostructures on the polycarbonate substrate. (c) Raman spectra of R6G molecules obtained from the Ag nanostructure and unprocessed AgO_x thin film. The Raman image of intensity map shows the spatial distribution of Raman intensity integrated over the peak in the regime of 598–623 cm^{-1}. Tseng *et al*. [14]. Reproduced with the permission of American Chemical Society. © The Optical Society.

laser-treated AgO_x thin film show the ability for fabrication of the SERS-active micro-pattern with high throughput and efficiency. The relation between the SERS capability of the Ag nanostructure and the laser powers is studied. Fabrication of SERS-active substrate on the flexible polycarbonate substrate is realized. For development of the large-area SERS-active substrate, the devices composed of annealed AgO_x thin film/dielectric layer/Au thin film are present. The enhancement efficiency of the multilayered nanostructure has been tuned by varying the thickness of the ZnS–SiO_2 spacing layer. The best layered structure for the 532-nm excitation is found. Based on the results reviewed in Sections, we believe that the present methodology is thus very promising for future developments of SERS-sensing chips with high throughput and efficiency.

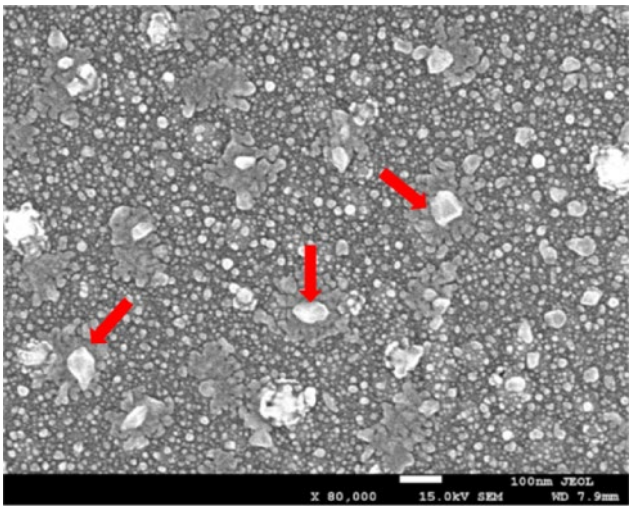

Figure 12.8 SEM image of the Ag nanoparticles generated from the annealed AgO_x thin film.

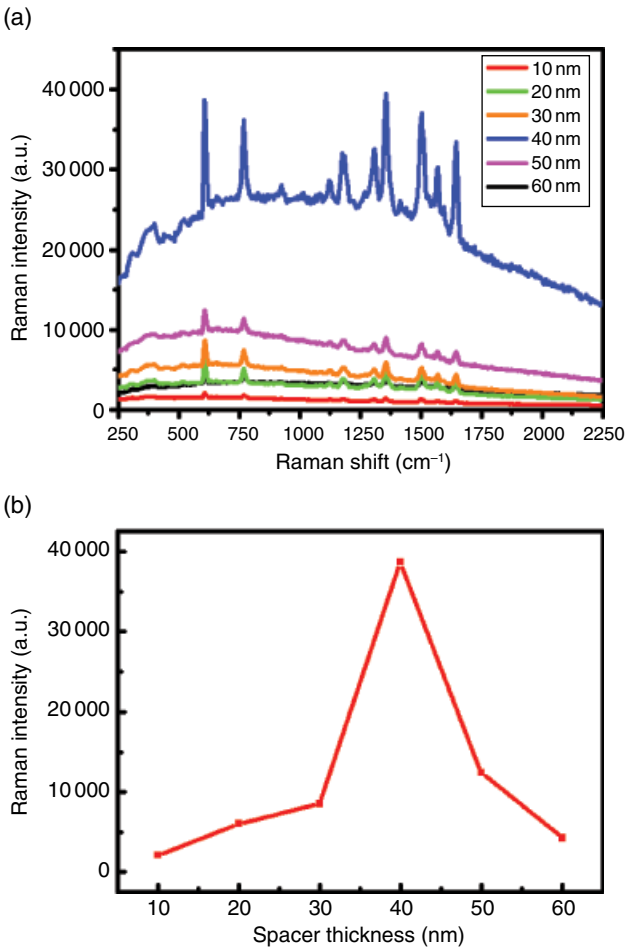

Figure 12.9 (a) Raman spectra of R6G obtained from the multilayered SERS-active nanostructures with different thickness of spacing layers ZnS–SiO_2. (b) Comparison of the Raman intensity at 598 cm^{-1} acquired from the R6G on the multilayered nanostructures with different spacers.

Acknowledgement

The authors acknowledge financial support from Ministry of Science and Technology, Taiwan (Grant No. MOST-105-2745-M-002-005-ASP) and Academia Sinica (Grant No. AS-103-TP-A06). They are also grateful to National Center for Theoretical Sciences, NEMS Research Center of National Taiwan University, National Center for High-Performance Computing, Taiwan, and Research Center for Applied Sciences, Academia Sinica, Taiwan for their supports. C. H. Chu and M. L. Tseng contributed equally to this work.

References

1 Schatz, G. C.; Young, M. A.; Van Duyne, R. P. Electromagnetic Mechanism of SERS. *Top. Appl. Phys.* **2006**, *103*, 19–46.

2 Talley, C. E.; Jackson, J. B.; Oubre, C.; Grady, N. K.; Hollars, C. W.; Lane, S. M.; Huser, T. R.; Nordlander, P.; Halas, N. J. Surface-Enhanced Raman Scattering from Individual Au Nanoparticles and Nanoparticle Dimer Substrates. *Nano Lett.* **2005**, *5*, 1569–1574.

3 Nie, S. M.; Emory, S. R. Probing Single Molecules and Single Nanoparticles by Surface-Enhanced Raman Scattering. *Science* **1997**, *275*, 1102–1106.

4 Lin, W. C.; Huang, S. H.; Chen, C. L.; Chen, C. C.; Tsai, D. P.; Chiang, H. P. Controlling SERS Intensity by Tuning the Size and Height of a Silver Nanoparticle Array. *Appl. Phys. A* **2010**, *101*, 185–189.

5 Willets, K. A.; Van Duyne, R. P. Localized Surface Plasmon Resonance Spectroscopy and Sensing. *Annu. Rev. Phys. Chem.* **2007**, *58*, 267–297.

6 Plum, E.; Fedotov, V. A.; Kuo, P.; Tsai, D. P.; Zheludev, N. I. Towards the Lasing Spaser: Controlling Metamaterial Optical Response with Semiconductor Quantum Dots. *Opt. Express* **2009**, *10*, 8548–8551.

7 Duan, H.; Hu, H.; Kumar, K.; Shen, Z.; Yang, J. K. W. Direct and Reliable Patterning of Plasmonic Nanostructures with Sub-10-nm Gaps. *ACS Nano* **2011**, *5*, 7593–7600.

8 Banaee, M. G.; Crozier, K. B. Mixed Dimer Double-Resonance Substrates for Surface-Enhanced Raman Spectroscopy. *ACS Nano* **2011**, *5*, 307–314.

9 Ho, F. H.; Chang, H. H.; Lin, Y. H.; Chen, B. M.; Wang, S. Y.; Tsai, D. P. Functional Structures of AgO*x* Thin Film for Near-Field Recording. *Jpn. J. Appl. Phys.* **2003**, *42*, 1000–1004.

10 Liu, W. C.; Wen, C. Y.; Chen, K. H.; Lin, W. C.; Tsai, D. P. Near-field images of the AgO_x-type super-resolution near-field structure. *Appl. Phys. Lett.* **2001**, *78*, 685–687.

11 Waterhouse, G. I. N.; Bowmakera, G. A.; Metson, J. B. The Thermal Decomposition of Silver (I, III) Oxide: A Combined XRD, FT-IR and Raman Spectroscopic Study. *Phys. Chem. Chem. Phys.* **2001**, *3*, 3838–3845.

12 Herley P. J., Prout E. G. The Thermal Decomposition of Silver Oxide. *J. Am. Chem. Soc.*, **1980**, *82*, 1540–1543.

13 Tseng, M. L.; Huang, Y. W.; Hsiao, M. K.; Huang, H. W.; Chen, H. M.; Chen, Y. L.; Chu, C. H.; Chu, N. N.; He, Y. J.; Chang, C. M.; Lin, W. C.; Huang, D. W.; Chiang, H. P.; Liu, R. S.; Sun, G.; Tsai, D. P. Fast Fabrication of a Ag Nanostructure Substrate Using the Femtosecond Laser for Broad-Band and Tunable Plasmonic Enhancement. *ACS Nano* **2012**, *6*, 5190.

14 Tseng, M. L.; Chang, C. M.; Cheng, B. H.; Wu, P. C.; Chung, K. S.; Hsiao, M. K.; Huang, H. W.; Huang, D. W.; Chiang, H. P.; Leung, P. T.; Tsai, D. P. Multi-level Surface Enhanced Raman Scattering Using AgO_x Thin Film. *Opt. Express* **2013**, *21*, 24460.

15 Lin, Y. H.; Tsai, D. P. Near-Field Scanning Optical Microscopy Using a Super-Resolution Cover Glass Slip. *Opt. Express* **2012**, *20*, 16205.

16 Tseng, M. L.; Leu, B.-H.; Li, P.-Y.; Chung, K. S.; Chiang, H.-P. Photoluminescence of Organic Dyes using Annealed AgO_x Thin Film. *Plasmonics* **2015**, *10*, 1301–1305.

17 Chen, H.; Chen, C. K.; Tseng, M.; Wu, P.; Chang, C.; Cheng, L.; Huang, H.; Chan, T.; Huang, D.; Liu, R.; Tsai, D. Plasmonic ZnO/Ag Embedded Structures as Collecting Layers for Photogenerating Electrons in Solar Hydrogen Generation Photoelectrodes. *Small* **2013**, *9*, 2926.

18 Hildebrandt, P.; Stockburger, M. Surface-Enhanced Resonance Raman Spectroscopy of Rhodamine 6G Adsorbed on Colloidal Silver. *J. Phys. Chem.* **1984**, *88*, 5935.

19 Tsu, D. V.; Ohta, T. Mechanism of Properties of Noble ZnS–SiO_2 Protection Layer for Phase Change Optical Disk Media. *Jpn. J. Appl. Phys.* **2006**, *45*, 6294.

20 Chu, C. H.; Shiue, C. D.; Cheng, H. W.; Tseng, M. L.; Chiang, H.-P.; Mansuripur, M.; Tsai, D. P. Laser-Induced Phase Transitions of $Ge_2Sb_2Te_5$ Thin Films Used in Optical and Electronic Data Storage and in Thermal Lithography. *Opt. Express* **2010** *18*, 18383–18393.

21 Ye, J. A.; Shioi, M.; Lodewijks, K.; Lagae, L.; Kawamura, T.; Van Dorpe, P. Tuning Plasmonic Interaction Between Gold Nanorings and a Gold Film for Surface Enhanced Raman Scattering. *Appl. Phys. Lett.* **2010**, *97*, 163106.

22 Chen, S. Y.; Mock, J. J.; Hill, R. T.; Chilkoti, A.; Smith, D. R.; Lazarides, A. A. Gold Nanoparticles on Polarizable Surfaces as Raman Scattering Antennas. *ACS Nano* **2010**, *4*, 6535.

23 Farcau, C.; Astilean, S. J. Mapping the SERS Efficiency and Hot-Spots Localization on Gold Film over Nanospheres Substrates. *J. Phys. Chem. C* **2010**, *114*, 11717.

13

Plasmon-Enhanced Two-Photon Excitation Fluorescence and Biomedical Applications

Taishi Zhang, Tingting Zhao, Peiyan Yuan, and Qing-Hua Xu

Department of Chemistry, National University of Singapore, Singapore, Singapore

13.1 Introduction

Noble metal nanoparticles (NPs) have attracted much attention due to their unique optical properties and wide applications in various fields such as chemistry [1, 2], materials [3], biology [4, 5], medicine [6, 7], and optoelectronics [8, 9]. In particular, they display a unique optical property known as localized surface plasmon resonance (LSPR) [10–12], which arises from collective oscillation of electrons in the conduction band. The LSPR of metal NPs strongly depends on the composition, size, shape, and dielectric environment of the metal NPs as well as the coupling between metal NPs [13, 14].

LSPR of metal NPs can modulate optical properties of nearby chromophores and metal NPs themselves. Metal-enhanced optical properties have been extensively studied in the last few decades [2, 15–23]. When the chromophore molecules come to the proximity of metal NPs, metal–chromophore interactions will result in a dramatic change in the optical responses of the chromophores, such as surface-enhanced Raman spectroscopy (SERS) [2, 15], metal-enhanced fluorescence [16–20], and metal-enhanced nonlinear optical responses [21, 22]. SERS has been extensively studied for the last few decades. Metal-enhanced fluorescence has emerged since 1990s as an exciting new research area with a lot of potential applications.

Most of the previous studies on metal-enhanced fluorescence were focused on enhancing the conventional one-photon excitation fluorescence and their applications [24, 25]. Metal-enhanced nonlinear optical responses, in particular metal-enhanced two-photon excitation fluorescence [26, 27], have recently attracted much attention due to the unique advantages of nonlinear optics [28]. Two-photon excitation fluorescence was initiated by absorption of two low-energy photons simultaneously instead of one photon as in the one-photon excitation fluorescence (Figure 13.1a). Two-photon absorption was first theoretically predicted by Göppert-Mayer in 1930 [30] and was experimentally demonstrated by Kaiser and Garrett in the 1960s [31]. Two-photon absorption is a third-order nonlinear optical process with a low absorption cross section. High optical power density excitation sources such as femtosecond lasers are generally required to drive efficient two-photon absorption process. Compared with its one-photon counterpart, two-photon excitation fluorescence exhibits several advantages [28, 29]. First, two-photon excitation is only efficient within the tightly focused spot and falls out quickly out of the focus due to its quadratic incident power dependence (Figure 13.1b). This 3D confined excitation allows for 3D selective treatment, detection, or mapping and minimizes photo-bleaching and photo-damage in the biological applications. Second, two-photon excitation fluorescence uses near-infrared (IR) laser sources, which encounters reduced scattering and absorption by the tissues and hence permits deeper light penetration into biological tissues. Two-photon excitation using near-infrared light also minimizes auto fluorescence from tissue and thus improves signal noise ratio in the bio-imaging applications. Third, the emission wavelength of two-photon excitation fluorescence is well separated from the excitation wavelength with a large anti-Stokes shift, which also improves signal noise ratio. Two-photon excitation fluorescence has been successfully implemented in laser scanning microscope and demonstrated in the *in vivo* tissue imaging [29, 32]. However, chromophores that were used and optimized for one-photon excitation applications have limited two-photon absorption cross sections. To take the attractive advantages of two-photon excitation, it is essential to develop chromophores

Surface Plasmon Enhanced, Coupled and Controlled Fluorescence, First Edition. Edited by Chris D. Geddes.
© 2017 John Wiley & Sons, Inc. Published 2017 by John Wiley & Sons, Inc.

with large two-photon absorption cross sections. Tremendous efforts have been made in synthesizing new two-photon materials [33]. Plasmon-enhanced two-photon excitation fluorescence takes advantage of plasmon engineering to significantly enhance two-photon optical properties of existing chromophores, which offers great convenience and become an attractive alternative approach.

Plasmon-enhanced one-photon excitation fluorescence has been discussed in other chapters and by many other excellent reviewers [34–36]. In this chapter we will focus our discussion on plasmon-enhanced two-photon excitation fluorescence and its applications.

13.2 Metal–Chromophore Interactions

The photophysical processes involving excitation and fluorescence of a typical chromophore are illustrated in Figure 13.1 [37]. When a chromophore is excited by absorption of one or multiple incident photons, the molecule will be promoted from the ground state (S_0) to the excited state (S_1) with the corresponding rate denoted as γ_{EX}. The excited molecules will eventually return back to the ground state through two different deactivation pathways: (i) radiative decay back to the ground state by dissipating the energy as fluorescence (the corresponding rate is denoted as k_R) and (ii) nonradiative decay back to the ground state by dissipating the energy as thermal energy (the corresponding rate is denoted as k_{NR}). As a result of competition between the radiative and nonradiative decay processes, the fluorescence quantum yield (QY) can be obtained as $QY = k_R/(k_R + k_{NR})$. The overall fluorescence intensity is a product of excitation rate and emission QY, that is, $I = \gamma_{EX} \times QY$.

In the absence of interactions with the noble metal, $I = \gamma_{EX0} \times QY_0$ with $QY_0 = k_{R0}/(k_{R0} + k_{NR0})$. When a chromophore comes to the proximity of a metal NP, metal–chromophore interactions can result in a modulation in the rates of both excitation and excited-state decay processes. First, metal NP alters the near-field light distribution and amplifies the local electric field $|E|$, which has been known as local electric field amplification (Figure 13.2a) [38]. The local electric field amplification will result in enhanced excitation rate, γ_{EX}, as it is proportional to $|E|^2$ under unsaturated one-photon excitation. The excitation enhancement factor $f_{EX} = \gamma_{EX}/\gamma_{EX0} = f_E^2$, where f_E is the electric field amplification $f_E = |E|/|E_0|$. Second, the radiative decay rate (k_R) of the chromophore will be enhanced by a factor of f_R due to dipole–dipole interactions [39], which is favorable for improving fluorescence quantum yield ($QY = k_R/(k_R + k_{NR})$ increases with increasing k_R). Third, nonradiative energy transfer will occur from the chromophore to the metal NP, which will introduce an additional nonradiative deactivation channel (k_{ET}) to increase the overall k_{NR} (now equal to $k_{NR0} + k_{ET}$), which is unfavorable for improving QY. Whether quantum yield $QY = k_R/(k_R + k_{NR})$ will be enhanced depends on the relative enhancement of k_R ($=f_R k_{R0}$) over k_{NR} ($=k_{NR0} + k_{ET}$), that is, whether k_R/k_{NR} increases or not. The overall fluorescence intensity is $I = \gamma_{EX} \times QY$ with $\gamma_{EX} = f_{EX}\gamma_{EX0}$ and $QY = f_R k_{R0}/(f_R k_{R0} + k_{NR0} + k_{ET})$.

As all the three aforementioned factors are strongly dependent on the separation distance between the chromophore and metal NP [39–43], the separation distance plays a critical role in the overall fluorescence intensity enhancement. Excitation enhancement f_{EX} is proportional to $|E|^2$ and increases monotonically as the chromophore approaches the surface of metal

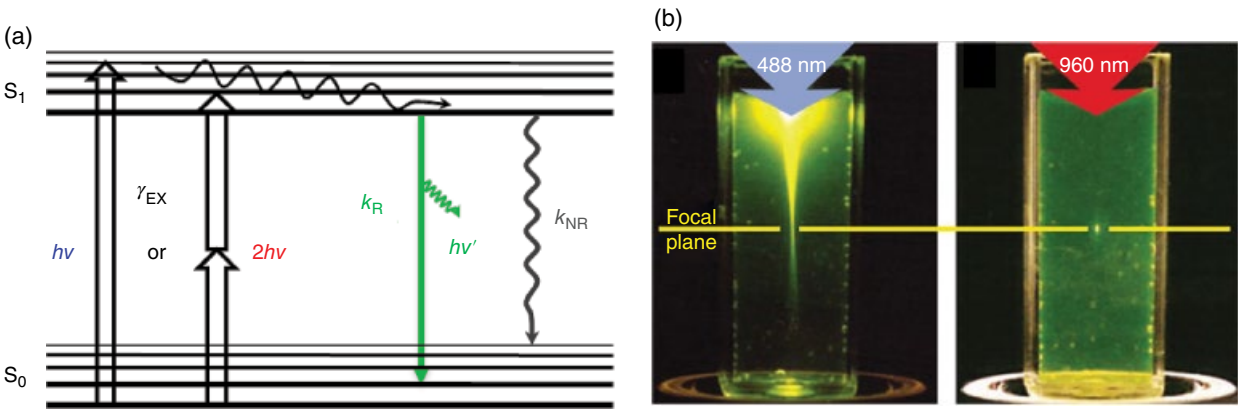

Figure 13.1 (a) Schematic illustration of the photophysical processes in one- and two-photon excitation fluorescence. (b) Pictures of one- and two-photon excitation fluorescence of fluorescein solution. Zipfel *et al*. [29]. Reproduced with the permission of Nature Publishing Group.

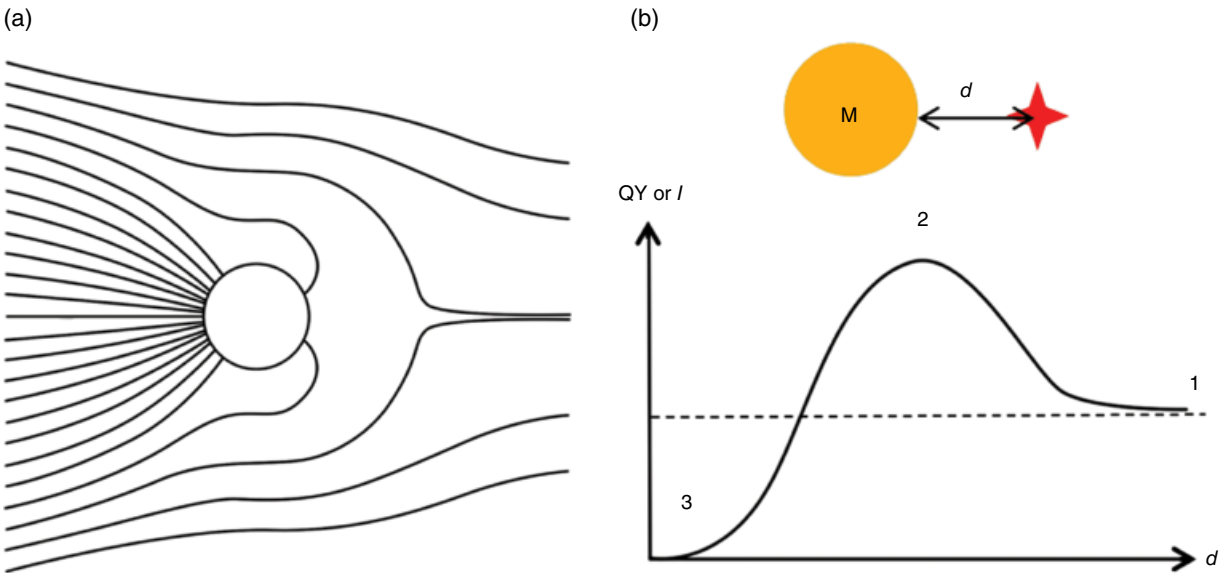

Figure 13.2 Schematic illustration of (a) electric field amplification, reproduced from Bohren and Huffman [38] with permission from John Wiley & Sons, and (b) change in fluorescence intensity or quantum yield of a chromophore (star) in the presence of a metal NP (M) with different separation distances.

NPs. QY enhancement involves the competition between radiative and nonradiative decay processes, both of which will increase monotonically as the chromophore approaches the surface of metal NPs. When a chromophore is at a large distance away from the metal surface (Case 1 in Figure 13.2b), the fluorescence intensity and QY are not affected by the metal NPs, $I = \gamma_{EX0} \times QY_0$ with $QY_0 = k_{R0}/(k_{R0} + k_{NR0})$. As the chromophore moves closer to the metal NP surface ($1 \rightarrow 2$ in Figure 13.2b), both radiative decay and energy transfer processes will increase. For chromophore with a low QY, $k_{NR0} >> k_{R0}$, that is, k_{NR0} is relatively large. k_{ET} is still small compared to k_{NR0} and will play a minor contribution to the total nonradiative decay rate ($k_{NR} = k_{NR0} + k_{ET}$) at this stage. Consequently the extent of increase in nonradiative decay rate will be lagged behind the increase in radiative decay rates ($f_R k_{R0}$). Under such circumstances, both QY and overall fluorescence intensity will increase until reaching the optimum values (Case 2 in Figure 13.2b). As the separation distance further decreases ($2 \rightarrow 3$ in Figure 13.2b), k_{ET} will further increase and become the dominant contributor to k_{NR} to the extent that the increase in k_{NR} starts to overcome the increase in k_R. Under such circumstances, QY will start to decrease. When the decrease in QY cannot be compensated by the increase in γ_{EX}, the overall fluorescence intensity will decrease too, that is, the fluorescence quenching will occur. Consequently, as a molecule with a small initial QY approaches a metal NP with a shortening separation distance, the QY will first increase ($1 \rightarrow 2$), reach an optimum enhancement (Case 2), then decrease ($2 \rightarrow 3$), and become strongly quenched (Case 1). The overall fluorescence intensity of the chromophore will undergo a similar transition and display an enhancement–quenching transition as sketched in Figure 13.2b. However, the transition point for the optimum overall fluorescence is expected to occur at a shorter separation distance than that for optimum QY considering that the enhanced excitation rate increases monotonically with the decreasing separation distance.

The situation for a chromophore with a high quantum yield QY_0 will display slightly different behaviors. As $k_{NR0} << k_{R0}$ (k_{NR0} is relatively small), k_{NR} could become quickly dominated by k_{ET}. The increase in k_R may not overcome the increase in k_{NR}. QY will monotonically decrease as the chromophore approaches the metal NP. The overall fluorescence intensity may display an optimum at intermediate separation distance if the increase in excitation efficiency can overcome the decrease in QY; otherwise overall fluorescence intensity will decrease monotonically with the shortening NP–chromophore separation distance.

Two-photon excitation fluorescence is expected to experience a similar enhancement–quenching transition as the NP–chromophore separation distance decreases. Compared with one-photon excitation, two-photon excitation rate has a stronger dependence on the local electric field amplification since γ_{EX} for two-photon excitation is proportional to $|E|^4$. As electric field amplification increases monotonically as the

separation distance decreases, the optimum two-photon excitation fluorescence is expected to occur at a shorter separation distance compared to that for optimum one-photon excitation fluorescence.

13.3 Plasmon-Enhanced One-Photon Excitation Fluorescence

Plasmon-enhanced one-photon excitation fluorescence has been widely demonstrated in different systems [16, 20, 25, 44]. Metal-enhanced fluorescence was initially discovered on the film substrates [44] and later demonstrated in the colloid solutions [45]. The extent of fluorescence enhancement is strongly dependent on the particle size [46], shape [18], spectral overlap [47, 48], and separation distance [49, 50] between the chromophores and metal NPs. Ag NPs were generally found to give larger fluorescence enhancement compared to Au NPs [42, 51]. In the colloid solution, Au NPs were generally found to quench the fluorescence of chromophores although the fluorescence intensity was found to increase as the separation distance increased [50, 52]. Overall fluorescence enhancement by Au NPs was later demonstrated in Au nanoshells [18], Au nanorods (NRs) [48], and aggregated Au NPs [53]. Fluorescence enhancement of chromophores by Ag NPs of different shapes, Ag nanospheres [20], and nanotriangles [47] have been studied and demonstrated in different systems.

A systematical separation distance-dependent fluorescence enhancement by Ag NPs (Figure 13.3) was demonstrated by Cheng and Xu [20] A fluorescent dye, fluorescein isothiocyanate (FITC), was encapsulated into the SiO_2 matrix shell outside an Ag NP core with a layer of SiO_2 shell serving as a spacer to separate FITC molecules and the Ag NP core. The distance-dependent Ag NP-FITC interactions were studied by adjusting the thickness of the spacer shell from nearly direct contact to ~90 nm. When the distance was <1 nm, fluorescence of FITC was quenched. As the separation distance increased, the fluorescence intensity of FITC gradually increased and became enhanced compared to that without Ag NPs. The FITC fluorescence was enhanced by a maximum of 4.8-fold at a separation

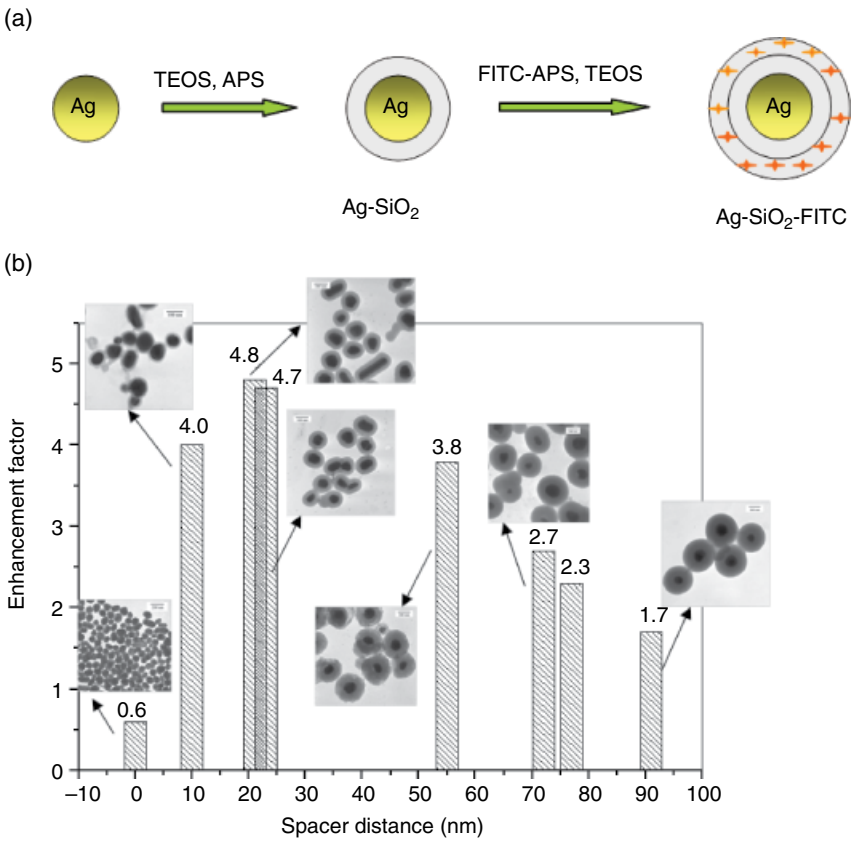

Figure 13.3 (a) Schematic diagram that illustrates Ag-SiO_2-FITC NP preparation process. (b) Distance-dependent fluorescence enhancement with various SiO_2 shell thickness. Cheng and Xu [20]. Reproduced with the permission of Royal Society of Chemistry.

distance of 21 nm. Further increase in the separation distance resulted in a smaller enhancement factor due to the near-field nature of fluorescence enhancement. The results closely follow the trend as predicted in Figure 13.2b.

13.4 Plasmon-Enhanced Two-Photon Excitation Fluorescence

Two-photon excitation fluorescence is expected to experience much larger enhancement than one-photon excitation fluorescence since two-photon excitation fluorescence is proportional to a higher order function of local electric field. Early studies on plasmon-enhanced two-photon excitation fluorescence were usually conducted on the solid substrates [26, 51, 54, 55]. Ag was also found to be generally more effective in enhancing two-photon excitation fluorescence than Au [51, 55]. Kano *et al*. studied two-photon excitation fluorescence of fluorescent dye (LD490) molecules that were dispersed into a poly(methyl methacrylate) (PMMA) film of 100-nm thickness and placed upon the metal film coated onto a BK7 glass prism [51]. Two-photon excitation of LD490 was affected by field-enhancing factors of 270 for Ag films and 80 for Au films. The presence of plasmon resonance introduced a gain of 90 times higher in the experimentally observed fluorescence intensity than that produced from total internal reflection fluorescence. Wenseleers *et al*. reported five orders of magnitude enhancement of two-photon absorption for dyes on Ag NP fractal clusters in films using two-photon excitation fluorescence microscopy measurements [56]. He *et al*. implemented Ag film in total internal reflection fluorescence microscopy and demonstrated improved two-photon excitation fluorescence intensity and contrast on EGFP-labeled cell membranes [26]. Lin *et al*. studied plasmon-enhanced two-photon excitation fluorescence of a layer of dye (Alq3) and a layer of Ag separated by a dielectric spacer. They observed a maximum two-photon excitation fluorescence enhancement of 30-fold compared to that without Ag layer by tuning the distance between Ag film and fluorophore layer [54]. Jung *et al*. studied plasmon-enhanced two-photon excitation fluorescence of Cy5 molecules on a large-scale Au nanopatterned surface prepared by the capillary force lithography method (Figure 13.4) [27]. The separation distance between the Au film and fluorophore was adjusted by the layer-by-layer assembly of PET films. They found that the local field enhancement near metal nanopatterned surface with an appropriate proximity of fluorophore to the metal nanopatterned surface in the range from 5 to 25 nm led to greatly enhanced fluorescence emission. The observed two-photon excitation fluorescence on the gold-patterned surface was enhanced over two orders of magnitude compared with the molecules on the glass surface. The large enhancement in two-photon excitation fluorescence allowed them to develop a DNA detection system with enhanced sensitivity to ultralow concentrations (10^{-11} M) of target molecules.

It is more challenging to achieve overall two-photon excitation fluorescence in the colloid solution owing to the difficulty in preparing highly reproducible nanostructures and controlling the fluorophores around metal NPs. A few available reports on colloid-based systems were mainly focused on plasmon-enhanced two-photon absorption [57–59]. Hernandez *et al*. reported a 157-fold enhancement of two-photon absorption of the chromophores using salt-aggregated spherical Au NPs by using z-scan techniques [57]. A recent report by Sivapalan *et al*. investigated the effect of plasmonic enhancement on the two-photon absorption cross section of an organic chromophore (AF348-3A) attached to polyelectrolyte-coated Au NRs in colloid suspensions (Figure 13.5) [58]. By synthesizing two-, four-, six-, and eight-polyelectrolyte layer-coated Au NRs of a particular aspect ratio (longitudinal LSPR band at 770 nm), the distance dependence of the evanescent electromagnetic field on molecular two-photon absorption was observed. Two-photon absorption enhancements by a maximum of 40-fold were observed for a ~3 nm dye—Au NR separation nearest to the surface. In another report by the same group [59], they studied Au NR enhanced two-photon absorption of AF-348-3A by separating AF348-3A from Au NR surfaces at variable distances using various numbers of polyelectrolyte layers, in which the LSPR of Au NR does not overlap the dye's two-photon absorption maximum. They observed some unusual distance dependence: enhancements in the two-photon cross section were at a minimum at an intermediate distance and rose again at a further distance. With the assistance of the theoretical predictions using finite element analysis, they explained this unusual distance dependence to the constructive and destructive interference effects between polyelectrolyte layers.

It is more difficult to achieve enhanced overall two-photon excitation fluorescence than enhanced two-photon absorption in the colloid-based systems. Overall two-photon excitation fluorescence, generally expressed in terms of two-photon brightness or two-photon action cross section, is a product of two-photon absorption efficiency and emission QY [54]. Two-photon action cross section is the performance indicator

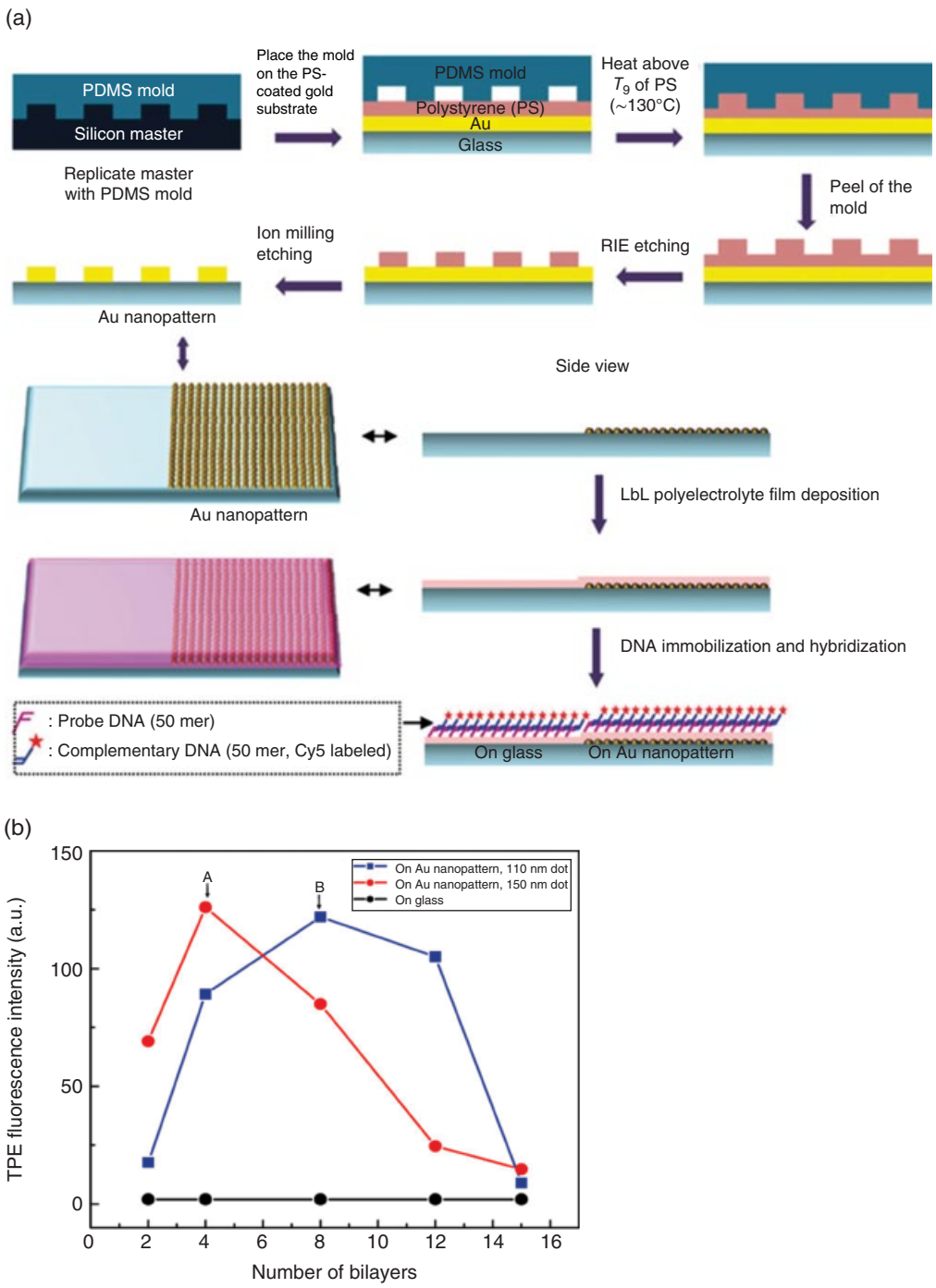

Figure 13.4 (a) Schematic image of enhanced two-photon excitation fluorescence DNA detection using a large-area metal nanopattern. (b) Plot of two-photon excitation fluorescence intensity of Cy5 on the Au nanopatterned surfaces and glass surface as the number of PSS/PAH increases. Jung *et al.* [27]. Reproduced with the permission of John Wiley & Sons.

of materials for applications in two-photon excitation fluorescence imaging. A major difficulty in achieving enhanced overall two-photon excitation fluorescence is that enhanced two-photon excitation efficiency is generally accompanied by decreased QY. Both two-photon excitation efficiency and fluorescence QY are strongly dependent on the separation distance between the chromophores and metal core. A systematical investigation of separation distance-dependent plasmon resonance effect on two-photon excitation fluorescence will help to achieve an overall enhancement in two-photon excitation fluorescence.

Overall two-photon excitation fluorescence in the colloid solution was achieved in the report by Zhao *et al*. by conducting a systematical distance-dependent one- and two-photon excitation fluorescence by Au NRs [23]. In this study, the Au NR core (aspect ratio of 4.25 with longitudinal LSPR at 820 nm) was coated by a layer of SiO_2 shell, while its surface was covalently linked with a layer of porphyrin molecules, T790. The SiO_2 shell served as the spacer between T790 molecule and Au NR. AuNR/SiO_2-T790 NPs with a series of silica shell thickness (13, 20, 28, 34, and 42 nm) were prepared (Figure 13.6a and b) to systematically study distance-dependent enhancement effects. One- and two-photon excitation fluorescence enhancement factors of different AuNR/SiO_2-T790 NPs in DMF solution are summarized in Figure 13.6c and d. Enhanced one- and two-photon excitation fluorescence were both achieved by optimizing the separation distance, and their separation distance dependences were found to closely follow the trend as predicted in Figure 13.2b. The optimum one-photon excitation fluorescence enhancement occurred at a shell thickness of 34 nm with an enhancement factor of 2.1. In contrast, optimum two-photon excitation fluorescence enhancement occurred at a shell thickness of 20 nm with an enhancement factor of 11.8. Larger shell thickness resulted in reduced or nearly no enhancement in one- and two-photon excitation fluorescence. Thinner shell thickness resulted in less enhancement or even quenching in one- and two-photon excitation fluorescence. In this study, excitation enhancement plays a negligible role in one-photon excitation fluorescence enhancement because the excitation wavelength 420 nm falls far away from the LSPR bands of Au NRs. Only the competition of enhanced radiative decay rate and increased nonradiative decay due to resonant energy transfer process needs to be considered for the separation distance-dependent change in one-photon excitation fluorescence, which reflects the change in the fluorescence QY. Two-photon excitation fluorescence will experience an extra contribution from the excitation enhancement since the longitudinal LSPR mode of Au NR (820 nm) is in good overlap with the two-photon excitation wavelength (820 nm). Due to this extra contribution, the enhancement factor of two-photon excitation fluorescence is higher than that of one-photon excitation fluorescence. Since two-photon excitation efficiency is proportional to a higher order function of local electric field compared to one-photon excitation and local electric field amplification monotonically decreases with the increasing separation distance, the optimum separation distance for two-photon excitation will be shorter than that for optimum one-photon excitation fluorescence. The enhanced two-photon excitation efficiency plays a dominant role in the observed overall two-photon excitation efficiency here.

Combined results of distance-dependent fluorescence lifetimes and QYs can reveal more insight on the metal–chromophore interactions. Fluorescence lifetime of T790 was found to become shorter in the presence of

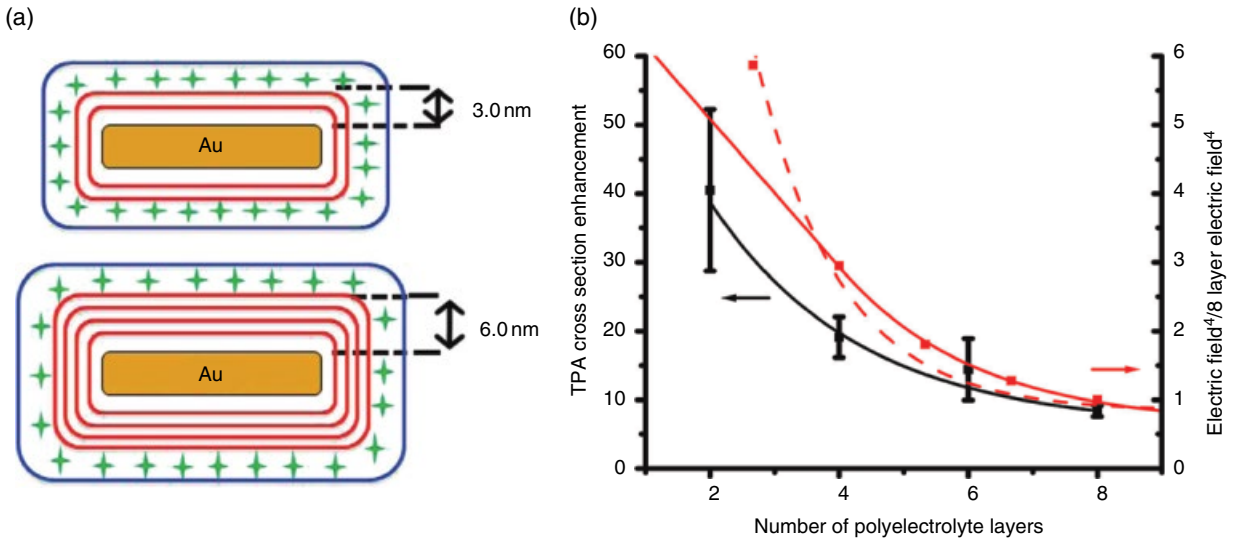

Figure 13.5 (a) Experimental schematic of polyelectrolyte-coated Au NRs with the AF-348-3A chromophore. (b) Two-photon absorption cross section enhancement (left axis) and simulated surface plasmon polariton electric field (right axis) versus distance from the Au NR surface, in terms of polyelectrolyte layers. The black line is an exponential fit to the data. The grey lines are based on calculations of the electric field; the grey dashed line is a single exponential fit including the two-layer data, while the grey solid line does not include two-layer data. Sivapalan *et al*. [58]. Reproduced with the permission of American Chemical Society.

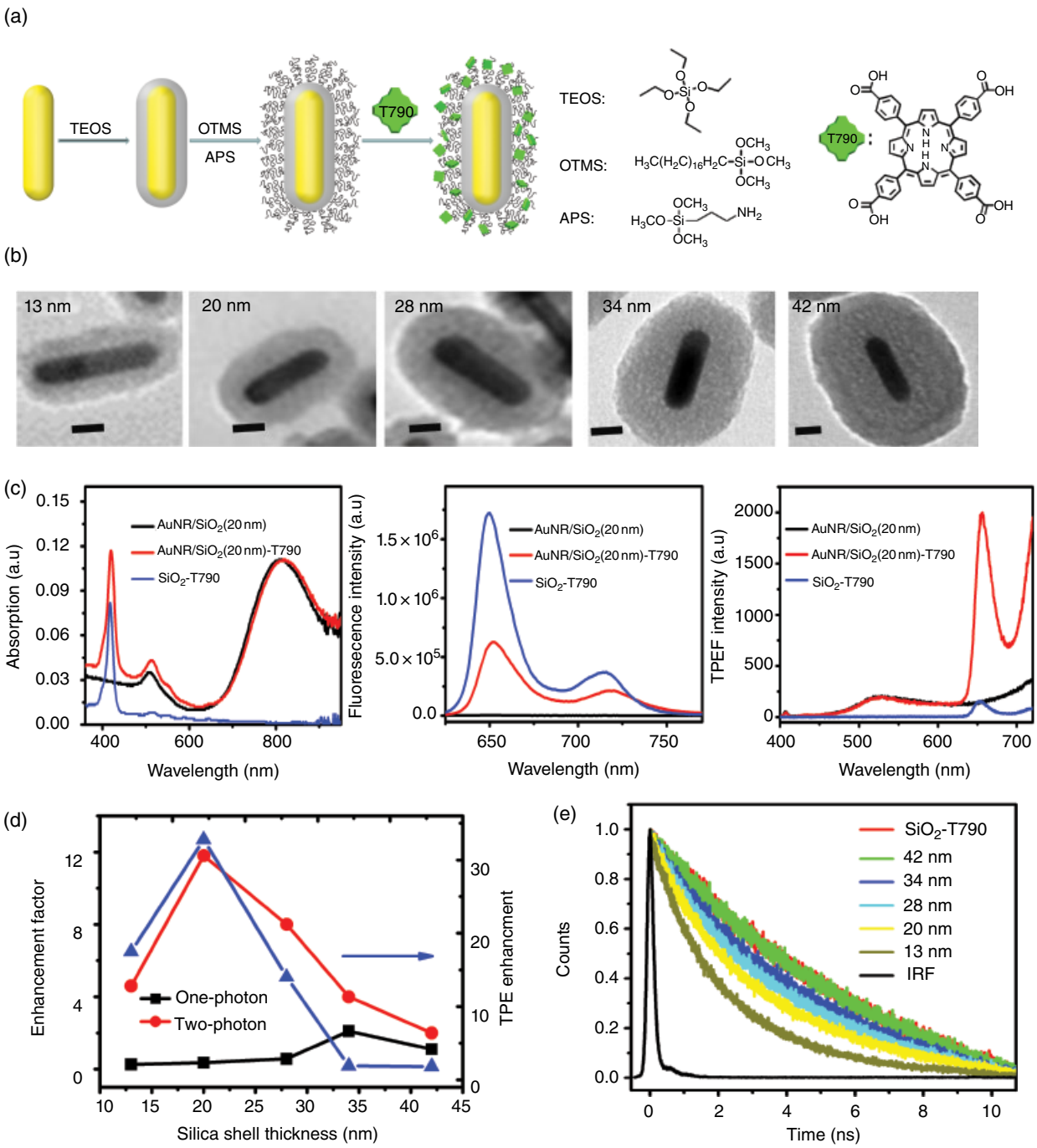

Figure 13.6 (a) Schematic procedures for preparation of AuNR/SiO_2-T790 NPs (b) TEM images of the prepared core-shell NPs. (c) UV-Vis extinction, one- and two-photon excitation fluorescence of one AuNR/SiO_2-T790 sample and controls. (d) Separation distance-dependent enhancement factors of one-and two-photon excitation fluorescence and two-photon excitation efficiency. (e) Fluorescence lifetime of T790 in different NPs. Zhao *et al.* [23]. Reproduced with the permission of American Chemical Society.

Au NR and further decrease as the SiO_2 shell became thinner. Considering the correlation between fluorescence lifetime ($\tau = 1/(k_R + k_{NR})$) and quantum yield ($QY = k_R/(k_R + k_{NR})$), the separation distance dependence of radiative and nonradiative decay rates could be deduced. T790 has a QY of 15% in the DMF solutions [23]. $k_{NR0} >> k_{R0}$, that is, k_{NR0} is relatively large. When the spacer thickness decreased from 42 to 34 nm, fluorescence lifetime became shortened while the QY increased. In this regime, both radiative decay

(k_R) and nonradiative decay ($k_{NR} = k_{NR0} + k_{ET}$) rates of T790 molecules were enhanced through the interactions with Au NR, while the increase in k_R outpaced the increase in k_{NR}. When the spacer thickness decreased from 34 to 13 nm, both fluorescence lifetime and QY decreased. In this regime, resonant energy transfer rate (k_{ET}) will further increase to become the dominant contribution of k_{NR} so that the increase in k_{NR} outpaced the increase in k_R, resulting in fluorescence quenching. These studies confirmed that both the radiative decay (k_R) and nonradiative energy transfer (k_{ET}) rates are enhanced when the chromophore molecule gradually approaches the surface of Au NR.

These plasmon-engineered NPs are attractive agents for biomedical applications such as two-photon imaging and two-photon photodynamic therapy (PDT) (Figure 13.7). Enhanced two-photon excitation fluorescence renders them highly efficient for various two-photon excitation-based applications, while shortened fluorescence or excited-state lifetime helps to improve their photostability. Two-photon excitation imaging capability of AuNR/SiO_2-T790 NPs was subsequently demonstrated in HepG2 cancer cells (Figure 13.7b) by using two-photon laser scanning confocal microscopy under femtosecond laser excitation at 820 nm. These two-photon excitation fluorescence images can be utilized to evaluate the uptake of AuNR/SiO_2-T790 NPs by cancer cells. As the environment inside the cells is mainly aqueous, the observed two-photon emission arises from joint contributions from two-photon photoluminescence of AuNRs and enhanced two-photon excitation fluorescence of T790 molecules.

T790 is a widely investigated hematoporphyrin derivative with singlet oxygen generation yield of 0.47 [60]. Hematoporphyrin derivatives are photosensitizers widely used in PDT processes [61]. Two-photon PDT has been known as a novel noninvasive cancer therapy method with many unique advantages compared to its one-photon counterpart, such as 3D localized treatment area, less side effects, and deep penetration into biological tissues. Effective photosensitizers for two-photon PDT require high singlet oxygen generation under two-photon excitation. Two-photon absorption cross section of T790 is quite small (~2 GM). In the presence of Au NRs, significantly enhanced two-photon excitation efficiency of T790 is beneficial for their applications in two-photon PDT. The capability of singlet oxygen generation of AuNR/SiO_2-T790 under two-photon excitation was evaluated by using a chemical method based on photo-oxidation of 9,10-anthracenediyl-bis

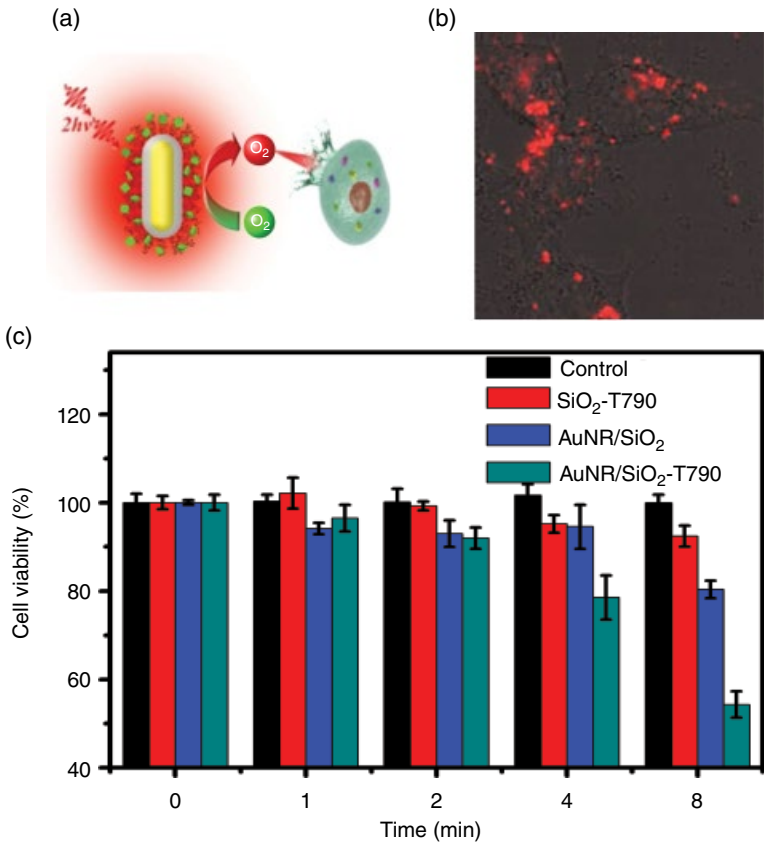

Figure 13.7 Enhanced two-photon excitation fluorescence of AuNR/SiO_2-T790 NPs (a) and their applications in two-photon cell imaging (b) and two-photon PDT (c). Zhao *et al.* [23]. Reproduced with the permission of American Chemical Society. (*See insert for color representation of this figure.*)

(methylene) dimalonic acid (ABDA) [23]. Photooxidation rate of ABDA in the presence of AuNR/SiO_2(20 nm)-T790 under two-photon excitation is much faster (~7.9 times) than that in the presence of SiO_2-T790. Two-photon PDT activity of AuNR/SiO_2(20 nm)-T790 was evaluated on HepG2 cancer cells using the XTT assay (Figure 13.7). The viability of HepG2 cells treated with AuNR/SiO_2(20 nm)-T790 NPs showed significant decrease under femtosecond laser irradiation. Up to 50% of cancer cells were killed after irradiation for 8 min. The significantly improved cancer cell-killing efficiency was ascribed to enhanced singlet oxygen generation of AuNR/SiO_2(20 nm)-T790 compared with SiO_2-T790 under two-photon excitation. These AuNR/SiO_2-T790 NPs thus have great potential in acting as nano-photosensitizers in two-photon PDT.

Lanthanide-doped upconversion NPs (UCNPs) are another type of materials capable of emitting in the visible region upon excitation with a near-IR light source [62, 63]. Similar to two-photon chromophores, UCNPs absorb two low-energy photons and emit one high-energy photon. However, intermediate energy states of UCNPs are real states instead of virtual states as in two-photon excitation case. The excitation of UCNPs involves two sequential one-photon absorption processes. Compared with organic dyes, UCNPs have certain advantages such as narrow and tunable emission range, longer lifetime, and good photostability [64–66]. However, a major drawback of UCNPs is small absorption cross section and low QY. Both the excitation and luminescence efficiency could be enhanced by plasmon resonance of noble metal NPs [67].

Similar to the plasmon-enhanced two-photon excitation fluorescence of organic chromophores, separation distance between UCNP and metal NP are critical for enhancing the photoluminescence of UCNP. A systematical study on separation distance-dependent enhancement of UCNP luminescence was conducted by Yuan *et al*. [67] In their studies, $NaYF_4$:Yb, Er@SiO_2@Ag core-shell NPs were used as the model system. In these core-shell NPs, $NaYF_4$:Yb,Er UCNPs with an average diameter of 45 nm was used as the core and coated with a silica shell of controllable thickness followed by growth of Ag NPs on the outer shell. The distance between UCNPs and Ag NPs could be adjusted by controlling the thickness of the spacer to achieve maximum luminescence enhancement. Four different thicknesses (3, 10, 20, and 30 nm) of the silica shell and two sizes (15 and 30 nm) of Ag NPs were used. These UCNPs can be excited by a 980 nm CW laser to give two upconversion emission bands at 542 nm (corresponding to $^2H_{11/2}/^4S_{3/2}$-$^4I_{15/2}$ transition) and 656 nm (corresponding to $^4F_{9/2}$-$^4I_{15/2}$ transition), respectively. The emission of these UCNPs was found to be strongly modulated by the presence of Ag NPs on the outer shell layer. The extent of modulation depended on the separation distance between Ag NPs and UCNP. The optimum upconversion luminescence enhancement was observed at a separation distance of 10 nm for both 15 nm and 30 nm Ag NPs. In the presence of Ag NPs, both 542 nm and 656 nm emission bands are enhanced. The optimum enhancement factor was 14.4 for emission band peaking at 542 nm and 12.2 for emission band peaking at 656 nm when 15 nm Ag NPs were used as the outer shell. When 30 nm Ag NPs were used, the optimum enhancement factor was 9.5 for emission at 542 nm and 10.8 for emission at 656 nm. Smaller enhancement factors in the upconversion luminescence were obtained for separation distances smaller or larger than 10 nm. Since the excitation wavelength (980 nm) are far off resonance with the LSPR mode of Ag NPs, the contribution from excitation enhancement is negligible, and the enhancement is mainly due to plasmon-modulated emission QY. The competition between enhanced radiative decay and nonradiative decay due to additional resonant energy transfer causes a transition from enhancement to quenching as the separation distance between UCNPs and Ag NPs decreases (Figure 13.8c), consistent with the trend as predicted in Figure 13.2b.

After improving the biocompatibility of these core-shell NPs by surface modification with DNA, the biological imaging capabilities of these core-shell NPs were demonstrated by using B16F0 cells. Compared with other cell-imaging agents such as DAPI (Figure 13.8b (ii)) and Concanavalin A (Figure 13.8b (iii)) that stained the nucleus and cell membranes, respectively, most UCNP@SiO_2@Ag NPs were found to be taken up by the cells and localized at the cytoplasm and the nucleus (Figure 13.8b (i)).

13.5 Conclusions and Outlook

Plasmon-enhanced fluorescence is an emerging research area that have attracted significant scientific interest in fundamental understanding of the metal–chromophore interactions. Metal–chromophore interactions through localized plasmon resonance of noble metal NPs result in huge enhancement in various linear and nonlinear optical responses to allow lots of practical applications to be explored. When a chromophore approaches a metal NP, metal–chromophore interactions cause localized near-field electric field amplification, enhanced radiative decay rate of the chromophores, and resonance energy transfer from the chromophore to metal NP introducing

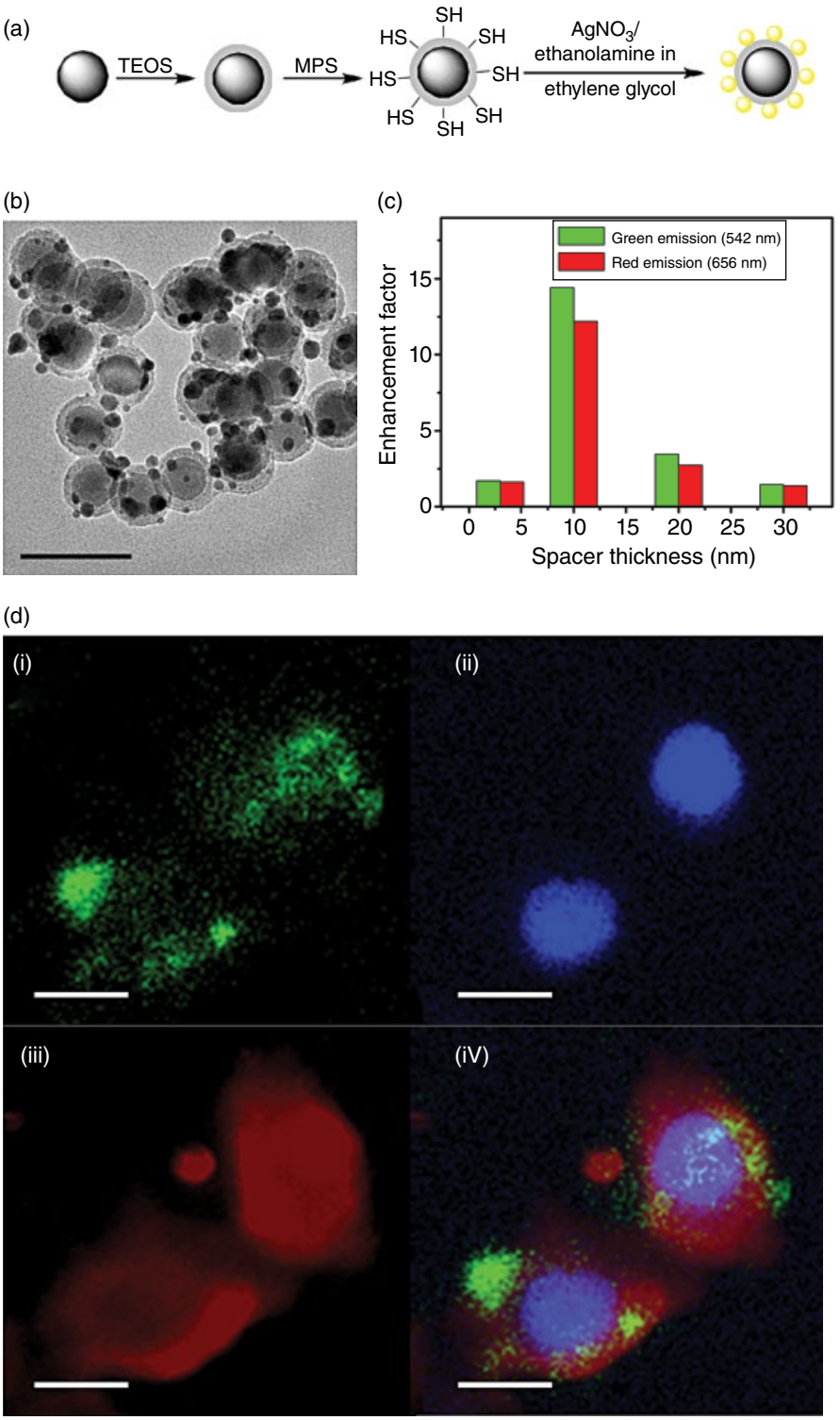

Figure 13.8 (a) Schematic diagram for preparation of UCNP@SiO_2@Ag NPs. (b)TEM images of UCNP@SiO_2(10 nm)@Ag(15 nm) NPs. (c) Distance-dependent luminescence enhancement of UCNPs by 15 nm Ag NPs. (d) Upconversion luminescence image of live B16F0 cells after incubation with DNA-modified UCNP@SiO_2(10 nm)@Ag(15 nm) NPs (i), fluorescence images of the cells counterstained with DAPI (ii) and Concanavalin A (iii) and the merged images (iv). Yuan *et al*. [67]. Reproduced with the permission of Royal Society of Chemistry.

additional nonradiative deactivation pathway. The first effect results in enhanced excitation efficiency of various optical responses, while the competition between the latter two effects result in an enhancement or reduction in the fluorescence QY. Different metal–chromophore separation-dependent behaviors of these three effects make it possible to modulate various linear and nonlinear optical responses through plasmon engineering to fine-tune the interactions between the metal NP and the chromophores. Enhanced one- and two-photon excitation fluorescence could be achieved by adjusting the separation distance between metal NP and chromophores. Metal-enhanced two-photon excitation fluorescence of these composite NPs makes them attractive in various two-photon excitation-based biomedical applications such as two-photon imaging, sensing, and PDT to benefit from the unique advantages of two-photon excitation. These advantages include 3D localized excitation (selective detection or treatment) and mapping, deep tissue penetration to allow *in vivo* applications, and even imaging-guided *in vivo* treatment.

It is challenging to achieve enhanced two-photon excitation fluorescence since a critical balance between enhanced excitation efficiency and modulated QY needs to be carefully controlled. So far enhancement factor of tens of folds was achieved for plasmon-enhanced two-photon excitation fluorescence in the colloid solution [23]. Considering the fact that much larger enhancement factors have been reported in one-photon excitation fluorescence and orders of magnitude enhancement factors in SERS are readily achieved [68], there is still a large room to further enhance two-photon excitation fluorescence. Further efforts could be made in a few directions to achieve further improvement. Experiences in enhanced one-photon excitation fluorescence and SERS can provide good insights in strategy to improve two-photon excitation fluorescence enhancement. Ag NPs generally give much larger enhancement in fluorescence and SERS compared to Au NPs [69, 70]; so far most of the studies on enhanced two-photon excitation fluorescence in the colloid solutions are focused on Au NPs because of the stability and easy preparation of Au NPs [13]. Aggregated metal NPs generally give much larger enhancement factors in one-photon excitation fluorescence and SERS, where hot spot in the gap is expected to provide huge enhancement in the excitation efficiency [1, 17, 68, 71]. So far rare studies have been made in enhanced two-photon excitation fluorescence by aggregated metal NPs. Single particle spectroscopic studies on one-photon excitation fluorescence and SERS generally give much larger enhancement factors compared to the ensemble bulk measurements [16], which suggest inhomogeneous distribution, and large percentage of less optimum nanostructures prevents achieving the largest possible enhancement effects. Significant efforts in nano-engineering are needed to develop homogenous well-controlled nanostructures to achieve the best performance. Single particle spectroscopic studies on metal-enhanced two-photon excitation need to be performed to explore the limit of ideal enhancement.

Enhanced two-photon excitation fluorescence of external chromophores by metal NPs is generally complicated by reduced QY of the chromophores while improving excitation efficiency by shortening the metal–chromophore separation distance. This dilemma could be overcome in enhancing two-photon photoluminescence of metal NPs themselves. Metal NPs have extremely low QY [72], which display moderate change in the aggregated state based on some preliminary studies. As the excitation efficiency will be improved significantly in the aggregated state, two-photon excitation photoluminescence of metal NPs themselves is expected to be significantly enhanced upon formation of nano-aggregates. Aggregation enhanced two-photon photoluminescence of metal NPs is another relevant direction to be explored. Up to hundreds of enhancement in the colloid solution and five orders of magnitude enhancement on the single particle level have been achieved in aggregation enhanced two-photon photoluminescence of metal NPs [73–77]. These studies are still in the relatively preliminary stage, and there is a large room for further improvement with significant efforts in this field.

References

1 Kinkhabwala, A.; Yu, Z.; Fan, S.; Avlasevich, Y.; Müllen, K.; Moerner, W., Large Single-Molecule Fluorescence Enhancements Produced by a Bowtie Nanoantenna. *Nat. Photonics* **2009**, *3*, 654–657.

2 Stiles, P. L.; Dieringer, J. A.; Shah, N. C.; Van Duyne, R. P., Surface-Enhanced Raman Spectroscopy. *Annu. Rev. Anal. Chem.* **2008**, *1*, 601–626.

3 Luk'yanchuk, B.; Zheludev, N. I.; Maier, S. A.; Halas, N. J.; Nordlander, P.; Giessen, H.; Chong, C. T., The Fano Resonance in Plasmonic Nanostructures and Metamaterials. *Nat. Mater.* **2010**, *9*, 707–715.

4 Brolo, A. G., Plasmonics for Future Biosensors. *Nat. Photonics* **2012**, *6*, 709–713.

5 Zijlstra, P.; Paulo, P. M.; Orrit, M., Optical Detection of Single Non-Absorbing Molecules Using the Surface Plasmon Resonance of a Gold Nanorod. *Nat. Nanotechnol.* **2012**, *7*, 379–382.

6 Huang, X.; El-Sayed, I. H.; Qian, W.; El-Sayed, M. A., Cancer Cell Imaging and Photothermal Therapy in the Near-Infrared Region by Using Gold Nanorods. *J. Am. Chem. Soc.* **2006**, *128*, 2115–2120.

7 Huang, X.; Jain, P. K.; El-Sayed, I. H.; El-Sayed, M. A., Plasmonic Photothermal Therapy (PPTT) Using Gold Nanoparticles. *Laser Med. Sci.* **2008**, *23*, 217–228.

8 Chen, H.; Bhuiya, A. M.; Ding, Q.; Toussaint Jr, K. C., Plasmon-Assisted Audio Recording. *Sci. Rep.* **2015**, *5*, 9125.

9 Zijlstra, P.; Chon, J. W.; Gu, M., Five-Dimensional Optical Recording Mediated by Surface Plasmons in Gold Nanorods. *Nature* **2009**, *459*, 410–413.

10 Willets, K. A.; Van Duyne, R. P., Localized Surface Plasmon Resonance Spectroscopy and Sensing. *Annu. Rev. Phys. Chem.* **2007**, *58*, 267–297.

11 Chen, H.; Ming, T.; Zhao, L.; Wang, F.; Sun, L.-D.; Wang, J.; Yan, C.-H., Plasmon-Molecule Interactions. *Nano Today* **2010**, *5*, 494–505.

12 Hutter, E.; Fendler, J. H., Exploitation of Localized Surface Plasmon Resonance. *Adv. Mater.* **2004**, *16*, 1685–1706.

13 Chen, H.; Kou, X.; Yang, Z.; Ni, W.; Wang, J., Shape- and Size-Dependent Refractive Index Sensitivity of Gold Nanoparticles. *Langmuir* **2008**, *24*, 5233–5237.

14 Mayer, K. M.; Hafner, J. H., Localized Surface Plasmon Resonance Sensors. *Chem. Rev.* **2011**, *111*, 3828–3857.

15 Nie, S.; Emory, S. R., Probing Single Molecules and Single Nanoparticles by Surface-Enhanced Raman Scattering. *Science* **1997**, *275*, 1102–1106.

16 Yuan, H.; Khatua, S.; Zijlstra, P.; Yorulmaz, M.; Orrit, M., Thousand-Fold Enhancement of Single-Molecule Fluorescence Near a Single Gold Nanorod. *Angew. Chem. Int. Ed.* **2013**, *52*, 1217–1221.

17 Zhang, T.; Gao, N.; Li, S.; Lang, M. J.; Xu, Q.-H., Single Particle Spectroscopic Study on Fluorescence Enhancement by Plasmon Coupled Gold Nanorod Dimers Assembled on DNA Origami. *J. Phys. Chem. Lett.* **2015**, *6*, 2043–2049.

18 Bardhan, R.; Grady, N. K.; Cole, J. R.; Joshi, A.; Halas, N. J., Fluorescence Enhancement by Au Nanostructures: Nanoshells and Nanorods. *ACS Nano* **2009**, *3*, 744–752.

19 Liu, S.-Y.; Huang, L.; Li, J.-F.; Wang, C.; Li, Q.; Xu, H.-X.; Guo, H.-L.; Meng, Z.-M.; Shi, Z.; Li, Z.-Y., Simultaneous Excitation and Emission Enhancement of Fluorescence Assisted by Double Plasmon Modes of Gold Nanorods. *J. Phys. Chem. C* **2013**, *117*, 10636–10642.

20 Cheng, D.; Xu, Q.-H., Separation Distance Dependent Fluorescence Enhancement of Fluorescein Isothiocyanate by Silver Nanoparticles. *Chem. Commun.* **2007**, *3*, 248–250.

21 Gao, N.; Chen, Y.; Li, L.; Guan, Z.; Zhao, T.; Zhou, N.; Yuan, P.; Yao, S. Q.; Xu, Q.-H., Shape-Dependent Two-Photon Photoluminescence of Single Gold Nanoparticles. *J. Phys. Chem. C* **2014**, *118*, 13904–13911.

22 Cox, J. D.; Garcia de Abajo, F. J., Plasmon-Enhanced Nonlinear Wave Mixing in Nanostructured Graphene. *ACS Photonics* **2015**, *2*, 306–312.

23 Zhao, T.; Yu, K.; Li, L.; Zhang, T.; Guan, Z.; Gao, N.; Yuan, P.; Li, S.; Yao, S. Q.; Xu, Q.-H., Gold Nanorod Enhanced Two-Photon Excitation Fluorescence of Photosensitizers for Two-Photon Imaging and Photodynamic Therapy. *ACS Appl. Mater. Interfaces* **2014**, *6*, 2700–2708.

24 Acuna, G.; Möller, F.; Holzmeister, P.; Beater, S.; Lalkens, B.; Tinnefeld, P., Fluorescence Enhancement at Docking Sites of DNA-Directed Self-Assembled Nanoantennas. *Science* **2012**, *338*, 506–510.

25 Punj, D.; Mivelle, M.; Moparthi, S. B.; van Zanten, T. S.; Rigneault, H.; van Hulst, N. F.; García-Parajó, M. F.; Wenger, J., A Plasmonic 'Antenna-in-Box' Platform for Enhanced Single-Molecule Analysis at Micromolar Concentrations. *Nat. Nanotechnol.* **2013**, *8*, 512–516.

26 He, R.-Y.; Su, Y.-D.; Cho, K.-C.; Lin, C.-Y.; Chang, N.-S.; Chang, C.-H.; Chen, S.-J., Surface Plasmon-Enhanced Two-Photon Fluorescence Microscopy for Live Cell Membrane Imaging. *Opt. Express* **2009**, *17*, 5987–5997.

27 Jung, J. M.; Yoo, H. W.; Stellacci, F.; Jung, H. T., Two-Photon Excited Fluorescence Enhancement for Ultrasensitive DNA Detection on Large-Area Gold Nanopatterns. *Adv. Mater.* **2010**, *22*, 2542–2546.

28 So, P. T.; Dong, C. Y.; Masters, B. R.; Berland, K. M., Two-Photon Excitation Fluorescence Microscopy. *Annu. Rev. Biomed. Eng.* **2000**, *2*, 399–429.

29 Zipfel, W. R.; Williams, R. M.; Webb, W. W., Nonlinear Magic: Multiphoton Microscopy in the Biosciences. *Nat. Biotechnol.* **2003**, *21*, 1369–1377.

30 Göppert-Mayer, M., Über elementarakte mit zwei quantensprüngen. *Annalen der Physik* **1931**, *401*, 273–294.

31 Kaiser, W.; Garrett, C. G. B., Two-Photon Excitation in CaF2: Eu2+. *Phys. Rev. Lett.* **1961**, *7*, 229–231.

32 Denk, W.; Strickler, J. H.; Webb, W. W., Two-Photon Laser Scanning Fluorescence Microscopy. *Science* **1990**, *248*, 73–76.

33 Pawlicki, M.; Collins, H. A.; Denning, R. G.; Anderson, H. L., Two-Photon Absorption and the Design of Two-Photon Dyes. *Angew. Chem. Int. Ed.* **2009**, *48*, 3244–3266.

34 Geddes, C. D.; Lakowicz, J. R., Editorial: Metal-Enhanced Fluorescence. *J. Fluoresc.* **2002**, *12*, 121–129.

35 Lakowicz, J. R., Radiative Decay Engineering: Biophysical and Biomedical Applications. *Anal. Biochem.* **2001**, *298*, 1–24.

36 Aslan, K.; Gryczynski, I.; Malicka, J.; Matveeva, E.; Lakowicz, J. R.; Geddes, C. D., Metal-Enhanced Fluorescence: An Emerging Tool in Biotechnology. *Curr. Opin. Biotechnol.* **2005**, *16*, 55–62.

37 Lakowicz, J. R., *Principles of Fluorescence Spectroscopy, 3rd edition*. Springer Science & Business Media, LLC: New York, **2006**.

38 Bohren, C. F.; Huffman, D. R., *Absorption and Scattering of Light by Small Particles*. WILEY-VCH Verlag GmbH & Co. KGaA, Weinheim, **2004**.

39 Anger, P.; Bharadwaj, P.; Novotny, L., Enhancement and Quenching of Single-Molecule Fluorescence. *Phys. Rev. Lett.* **2006**, *96*, 113002.

40 Dulkeith, E.; Morteani, A.; Niedereichholz, T.; Klar, T.; Feldmann, J.; Levi, S.; Van Veggel, F.; Reinhoudt, D.; Möller, M.; Gittins, D., Fluorescence Quenching of Dye Molecules Near Gold Nanoparticles: Radiative and Nonradiative Effects. *Phys. Rev. Lett.* **2002**, *89*, 203002.

41 Reineck, P.; Gómez, D.; Ng, S. H.; Karg, M.; Bell, T.; Mulvaney, P.; Bach, U., Distance and Wavelength Dependent Quenching of Molecular Fluorescence by Au@SiO_2 Core-Shell Nanoparticles. *ACS Nano* **2013**, *7*, 6636–6648.

42 Bharadwaj, P.; Novotny, L., Spectral Dependence of Single Molecule Fluorescence Enhancement. *Opt. Express* **2007**, *15*, 14266–14274.

43 Kühn, S.; Håkanson, U.; Rogobete, L.; Sandoghdar, V., Enhancement of Single-Molecule Fluorescence Using a Gold Nanoparticle as an Optical Nanoantenna. *Phys. Rev. Lett.* **2006**, *97*, 017402.

44 Lakowicz, J. R.; Shen, Y.; D'Auria, S.; Malicka, J.; Fang, J.; Gryczynski, Z.; Gryczynski, I., Radiative Decay Engineering: 2. Effects of Silver Island Films on Fluorescence Intensity, Lifetimes, and Resonance Energy Transfer. *Anal. Biochem.* **2002**, *301*, 261–277.

45 Aslan, K.; Lakowicz, J. R.; Szmacinski, H.; Geddes, C. D., Metal-Enhanced Fluorescence Solution-Based Sensing Platform. *J. Fluoresc.* **2004**, *14*, 677–679.

46 Stranik, O.; Nooney, R.; McDonagh, C.; MacCraith, B. D., Optimization of Nanoparticle Size for Plasmonic Enhancement of Fluorescence. *Plasmonics* **2007**, *2*, 15–22.

47 Chen, Y.; Munechika, K.; Ginger, D. S., Dependence of Fluorescence Intensity on the Spectral Overlap between Fluorophores and Plasmon Resonant Single Silver Nanoparticles. *Nano Lett.* **2007**, *7*, 690–696.

48 Khatua, S.; Paulo, P. M.; Yuan, H.; Gupta, A.; Zijlstra, P.; Orrit, M., Resonant Plasmonic Enhancement of Single-Molecule Fluorescence by Individual Gold Nanorods. *ACS Nano* **2014**, *8*, 4440–4449.

49 Abadeer, N. S.; Brennan, M. R.; Wilson, W. L.; Murphy, C. J., Distance and Plasmon Wavelength Dependent Fluorescence of Molecules Bound to Silica-Coated Gold Nanorods. *ACS Nano* **2014**, *8*, 8392–8406.

50 Acuna, G. P.; Bucher, M.; Stein, I. H.; Steinhauer, C.; Kuzyk, A.; Holzmeister, P.; Schreiber, R.; Moroz, A.; Stefani, F. D.; Liedl, T., Distance Dependence of Single-Fluorophore Quenching by Gold Nanoparticles Studied on DNA Origami. *ACS Nano* **2012**, *6*, 3189–3195.

51 Kano, H.; Kawata, S., Two-Photon-Excited Fluorescence Enhanced by a Surface Plasmon. *Opt. Lett.* **1996**, *21*, 1848–1850.

52 Dulkeith, E.; Ringler, M.; Klar, T.; Feldmann, J.; Munoz Javier, A.; Parak, W., Gold Nanoparticles Quench Fluorescence by Phase Induced Radiative Rate Suppression. *Nano Lett.* **2005**, *5*, 585–589.

53 Wang, H.; Wang, Y.; Jin, J.; Yang, R., Gold Nanoparticle-Based Colorimetric and "Turn-on" Fluorescent Probe for Mercury (II) Ions in Aqueous Solution. *Anal. Chem.* **2008**, *80*, 9021–9028.

54 Lin, C.-Y.; Chiu, K.-C.; Chang, C.-Y.; Chang, S.-H.; Guo, T.-F.; Chen, S.-J., Surface Plasmon-Enhanced and Quenched Two-Photon Excited Fluorescence. *Opt. Express* **2010**, *18*, 12807–12817.

55 Chiu, K.-C.; Lin, C.-Y.; Dong, C. Y.; Chen, S.-J., Optimizing Silver Film for Surface Plasmon-Coupled Emission Induced Two-Photon Excited Fluorescence Imaging. *Opt. Express* **2011**, *19*, 5386–5396.

56 Wenseleers, W.; Stellacci, F.; Meyer-Friedrichsen, T.; Mangel, T.; Bauer, C. A.; Pond, S. J.; Marder, S. R.; Perry, J. W., Five Orders-of-Magnitude Enhancement of Two-Photon Absorption for Dyes on Silver Nanoparticle Fractal Clusters. *J. Phys. Chem. B* **2002**, *106*, 6853–6863.

57 Cohanoschi, I.; Yao, S.; Belfield, K. D.; Hernández, F. E., Effect of the Concentration of Organic Dyes on Their Surface Plasmon Enhanced Two-Photon Absorption Cross Section Using Activated Au Nanoparticles. *J. Appl. Phys.* **2007**, *101*, 086112.

58 Sivapalan, S. T.; Vella, J. H.; Yang, T. K.; Dalton, M. J.; Swiger, R. N.; Haley, J. E.; Cooper, T. M.; Urbas, A. M.; Tan, L.-S.; Murphy, C. J., Plasmonic Enhancement of the Two Photon Absorption Cross Section of an Organic Chromophore Using Polyelectrolyte-Coated Gold Nanorods. *Langmuir* **2012**, *28*, 9147–9154.

59 Sivapalan, S. T.; Vella, J. H.; Yang, T. K.; Dalton, M. J.; Haley, J. E.; Cooper, T. M.; Urbas, A. M.; Tan, L.-S.; Murphy, C. J., Off-Resonant Two-Photon

Absorption Cross-Section Enhancement of an Organic Chromophore on Gold Nanorods. *J. Phys. Chem. Lett.* **2013**, *4*, 749–752.

60 Gerdes, R.; Wöhrle, D.; Spiller, W.; Schneider, G.; Schnurpfeil, G.; Schulz-Ekloff, G., Photo-Oxidation of Phenol and Monochlorophenols in Oxygen-Saturated Aqueous Solutions by Different Photosensitizers. *J. Photochem. Photobiol. A* **1997**, *111*, 65–74.

61 Fiel, R. J.; Datta-Gupta, N.; Mark, E. H.; Howard, J. C., Induction of DNA Damage by Porphyrin Photosensitizers. *Cancer Res.* **1981**, *41*, 3543–3545.

62 Wang, F.; Liu, X., Recent Advances in the Chemistry of Lanthanide-Doped Upconversion Nanocrystals. *Chem. Soc. Rev.* **2009**, *38*, 976–989.

63 Zhou, J.; Liu, Q.; Feng, W.; Sun, Y.; Li, F., Upconversion Luminescent Materials: Advances and Applications. *Chem. Rev.* **2014**, *115*, 395–465.

64 van de Rijke, F.; Zijlmans, H.; Li, S.; Vail, T.; Raap, A. K.; Niedbala, R. S.; Tanke, H. J., Up-Converting Phosphor Reporters for Nucleic Acid Microarrays. *Nat. Biotechnol.* **2001**, *19*, 273–276.

65 Wang, G.; Peng, Q.; Li, Y., Lanthanide-Doped Nanocrystals: Synthesis, Optical-Magnetic Properties, and Applications. *Acc. Chem. Res.* **2011**, *44*, 322–332.

66 Qian, H. S.; Guo, H. C.; Ho, P. C. L.; Mahendran, R.; Zhang, Y., Mesoporous-Silica-Coated Up-Conversion Fluorescent Nanoparticles for Photodynamic Therapy. *Small* **2009**, *5*, 2285–2290.

67 Yuan, P.; Lee, Y. H.; Gnanasammandhan, M. K.; Guan, Z.; Zhang, Y.; Xu, Q.-H., Plasmon Enhanced Upconversion Luminescence of NaYF4:Yb, Er@SiO_2@Ag Core–Shell Nanocomposites for Cell Imaging. *Nanoscale* **2012**, *4*, 5132–5137.

68 Lee, J.-H.; You, M.-H.; Kim, G.-H.; Nam, J.-M., Plasmonic Nanosnowmen with a Conductive Junction as Highly Tunable Nanoantenna Structures and Sensitive, Quantitative and Multiplexable Surface-Enhanced Raman Scattering Probes. *Nano Lett.* **2014**, *14*, 6217–6225.

69 Lee, K.-S.; El-Sayed, M. A., Gold and Silver Nanoparticles in Sensing and Imaging: Sensitivity of Plasmon Response to Size, Shape, and Metal Composition. *J. Phys. Chem. Lett.* **2006**, *110*, 19220–19225.

70 Rycenga, M.; Hou, K. K.; Cobley, C. M.; Schwartz, A. G.; Camargo, P. H.; Xia, Y., Probing the Surface-Enhanced Raman Scattering Properties of Au-Ag Nanocages at Two Different Excitation Wavelengths. *Phys. Chem. Chem. Phys.* **2009**, *11*, 5903–5908.

71 Xu, L.; Kuang, H.; Xu, C.; Ma, W.; Wang, L.; Kotov, N. A., Regiospecific Plasmonic Assemblies for in situ Raman Spectroscopy in Live Cells. *J. Am. Chem. Soc.* **2012**, *134*, 1699–1709.

72 Dulkeith, E.; Niedereichholz, T.; Klar, T.; Feldmann, J.; Von Plessen, G.; Gittins, D.; Mayya, K.; Caruso, F., Plasmon Emission in Photoexcited Gold Nanoparticles. *Phys. Rev. B* **2004**, *70*, 205424.

73 Guan, Z.; Polavarapu, L.; Xu, Q.-H., Enhanced Two-Photon Emission in Coupled Metal Nanoparticles Induced by Conjugated Polymers. *Langmuir* **2010**, *26*, 18020–18023.

74 Yuan, P.; Ma, R.; Guan, Z.; Gao, N.; Xu, Q.-H., Tuning Two-Photon Photoluminescence of Gold Nanoparticle Aggregates with DNA and its Application as Turn-On Photoluminescence Probe for DNA Sequence Detection. *ACS Appl. Mater. Interfaces* **2014**, *6*, 13149–13156.

75 Yuan, P.; Ma, R.; Gao, N.; Garai, M.; Xu, Q.-H., Plasmon Coupling Enhanced Two-Photon Photoluminescence of Au@Ag Core–Shell Nanoparticles and Applications in Nuclease Assay. *Nanoscale* **2015**, *7*, 10233–10239.

76 Guan, Z.; Gao, N.; Jiang, X.-F.; Yuan, P.; Han, F.; Xu, Q.-H., Huge Enhancement in Two-Photon Photoluminescence of Au Nanoparticle Clusters Revealed by Single-Particle Spectroscopy. *J. Am. Chem. Soc.* **2013**, *135*, 7272–7277.

77 Jiang, X.-F.; Pan, Y.; Jiang, C.; Zhao, T.; Yuan, P.; Venkatesan, T.; Xu, Q.-H., Excitation Nature of Two-Photon Photoluminescence of Gold Nanorods and Coupled Gold Nanoparticles Studied by Two-Pulse Emission Modulation Spectroscopy. *J. Phys. Chem. Lett.* **2013**, *4*, 1634–1638.

14

Fluorescence Biosensors Utilizing Grating-Assisted Plasmonic Amplification

Koji Toma[1], Mana Toma[2], Martin Bauch[3], Simone Hageneder[4], and Jakub Dostalek[4]

[1] *Department of Biomedical Devices and Instrumentation, Institute of Biomaterials and Bioengineering, Tokyo Medical and Dental University, Tokyo, Japan*
[2] *Department of Applied Chemistry for Environment, School of Science and Technology, Kwansei Gakuin University, Sanda, Japan*
[3] *Energy Department, AIT—Austrian Institute of Technology, Vienna, Austria*
[4] *Biosensor Technologies, AIT—Austrian Institute of Technology, Vienna, Austria*

14.1 Introduction

Fluorescence represents arguably the most-spread analytical method for detection and interaction analysis of biomolecules in important areas of life sciences, medicine, and food safety [1, 2]. The performance characteristics of currently used fluorescence analytical technologies can be tremendously advanced by plasmonic-based manipulation of light. Plasmonics emerged as a novel branch of nanophotonics that focuses on the control of propagation and interaction of light at visible and near infrared part of spectrum by its subwavelength confinement [3, 4]. This confinement occurs due to the excitation of surface plasmons (SPs) originating from collective oscillations of charge density and associated electromagnetic field at surfaces of metallic films and metallic nanostructures. The excitation of SPs is accompanied with strongly enhanced field intensity and local density of states (LDOS) which makes them ideally suited for coupling with fluorescence emitters such as organic dyes and quantum dots. The coupling of fluorophores with the confined field of SPs at their absorption (λ_{ab}) and emission (λ_{em}) wavelengths enables enhancing their "brightness." In fluorescence bioassays, fluorophores are used as labels for the measurement of specific capturing of target analyte on a sensor surface with immobilized biomolecular recognition elements such as antibodies [5, 6]. The plasmonic amplification of fluorescence light intensity emitted by these labels allows the analysis of smaller number of target molecules on the surface. This can translate to increased sensitivity and improved limit of detection (LOD) of bioassays and thus open doors for the analysis of trace amounts of biomolecules present in analyzed samples. Such performance is urgently needed in numerous fields including biomarker analysis for early cancer diagnosis and detection of harmful compounds in food.

This chapter deals with surface plasmon-coupled fluorescence emission (SPCE) and its implementations to plasmonically amplified bioassays that utilize diffractive and nondiffractive grating structures. The chapter provides a brief introduction to SPCE relying on reverse Kretchmann configuration and diffraction gratings (Section 14.2) and it discusses the impact of losses of SPs in SPCE studies (Section 14.3), control of SPCE by changing SP dispersion relation by nondiffractive gratings (Section 14.4), extraction of fluorescence light trapped with SPs by diffractive gratings (Section 14.5), and finally it illustrates how these optical phenomena can be employed in fluorescence biosensors for detection of protein analyte (Section 14.6). It should be noted that the chapter does not present a complete review of this field. Rather, it contains a series of examples that were preferably selected from our laboratory and that illustrate recent efforts in the rapidly developing area of plasmonically enhanced fluorescence bioassays.

14.2 SPCE in Vicinity to Metallic Surface

SPs are optical waves at an interface between metal and dielectric that originate from collective oscillations of electron density and associated electromagnetic field. As illustrated in Figure 14.1a, they travel along the interface and their field exponentially decays into both media. The propagation constant of SPs can be expressed as

Surface Plasmon Enhanced, Coupled and Controlled Fluorescence, First Edition. Edited by Chris D. Geddes.
© 2017 John Wiley & Sons, Inc. Published 2017 by John Wiley & Sons, Inc.

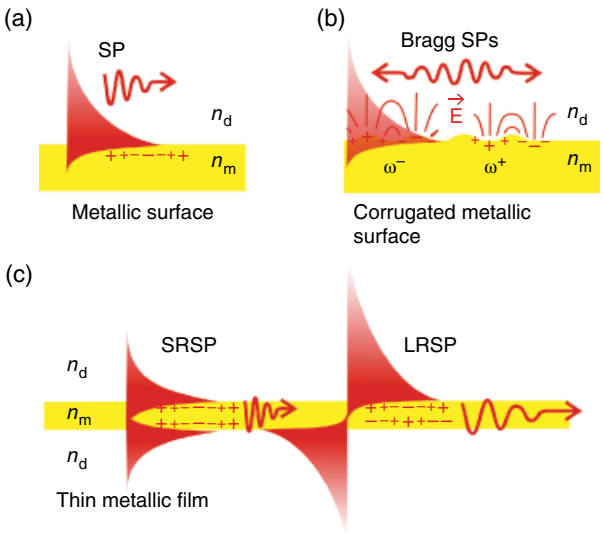

Figure 14.1 (a) SPs traveling along a flat metallic surface, (b) Bragg-scattered SPs on periodically corrugated metallic surface, and (c) long- and short-range SPs on a thin metallic film.

$$k_{SP} = \frac{2\pi}{\lambda}\sqrt{\frac{n_m^2 n_d^2}{n_m^2 + n_d^2}}, \tag{14.1}$$

where λ states for wavelength, n_m is the refractive index of the metal, and n_d is the refractive index of the dielectric. The real part of the propagation constant $\mathrm{Re}\{k_{SP}\}$ represents the momentum of SP and the imaginary part $\mathrm{Im}\{k_{SP}\}$ states for losses of SP due to Ohmic dissipation in the metal. The key characteristics of SPs including the profile of field, dispersion relation, and losses mainly depend on the choice of the SPR-active metal. However, these properties can also be efficiently tuned by using plasmonic structures where multiple SPs couple. For instance, subwavelength periodic corrugation of metallic surface allows for diffraction coupling of counter propagating SPs which leads to opening of a bandgap in SP dispersion relation [7]. This scattering occurs for the corrugation period Λ that fulfills the phase matching condition $2\pi/\Lambda = 2\mathrm{Re}\{k_{SP}\}$. At edges of the induced bandgap, two new Bragg-scattered surface plasmon (BSSP) modes occur as shown in Figure 14.1b. They exhibit standing wave field profile that is weaker confined at the surface and less damped (mode marked as ω^+) or stronger confined at the surface and more damped (mode marked as ω^-).

Another means for tuning the characteristics of SPs provides the near-field coupling of SPs on a thin metallic film, see Figure 14.1c. When such thin metallic film is sandwiched between two dielectrics with similar refractive index n_d, SPs propagating at its bottom and top interfaces interact via their evanescent tails that penetrate through the metal film. This interaction leads to the occurrence of new modes with symmetric and antisymmetric profile of field [8]. The mode with antisymmetric distribution of electric field intensity $E_{||}$ (component parallel to the surface) is referred as to long-range surface plasmon (LRSP). This mode exhibits smaller losses and less confined field compared to those of regular SPs. The complementary mode to LRSPs exhibits symmetric distribution of $E_{||}$ and it is named short-range surface plasmon (SRSP). Its propagation is more damped and field is stronger confined at the metal surface with respect to regular SPs.

Studies of SP-mediated fluorescence date back to 1970s of the last century when luminescence intensity and lifetime of an emitter in vicinity to metallic surfaces were investigated [9, 10]. At distances between an emitter and metal surface d that are below Förster radius, quenching of fluorescence occurs due to dipole–dipole interaction with electrons in the metal. At longer distances that are comparable with penetration depth of SP field into the adjacent dielectric, strong emission via SPs can be observed. As illustrated by simulations in Figure 14.2a, fluorescence emission is strongly quenched at distances $d < 15$ nm (simulations are presented for randomly oriented emitter at gold–water interface with an emission wavelength of $\lambda_{em} = 670$ nm). At distances $d \sim 15$–50 nm, the majority of energy is emitted via SPs. The emission to optical waves propagating into the far field occurs at distances that are further away from the metal $d > 50$ nm and lie outside the SP evanescent field.

Let us note that the majority of fluorescence assays rely on the sandwich detection format using antibodies or antigens for sensing. Antibodies are attached to a solid surface in order to selectively bind target analytes in a sample followed by the binding of detection antibodies that are labeled with a fluorophore, see Figure 14.2b. In such assays, the distance between a fluorophore label and the surface is typically $d = 15$–20 nm when taking into account the size of immunoglobulin G (IgG) antibodies and that of medium-sized protein analytes [11]. Such distance excellently matches the range where strong coupling between fluorescence emission and SPs occurs, see Figure 14.2a.

Photons that are emitted at λ_{em} via SPs from flat interface between semiinfinite metal and dielectric are dissipated due to Ohmic losses. However, the majority of such fluorescence intensity can be recovered by using couplers based on reverse Kretschmann geometry of attenuated total reflection (ATR) method [5, 12, 13] or diffraction on periodically corrugated metal surface [14, 15]. These techniques allow for extracting the emitted fluorescence light

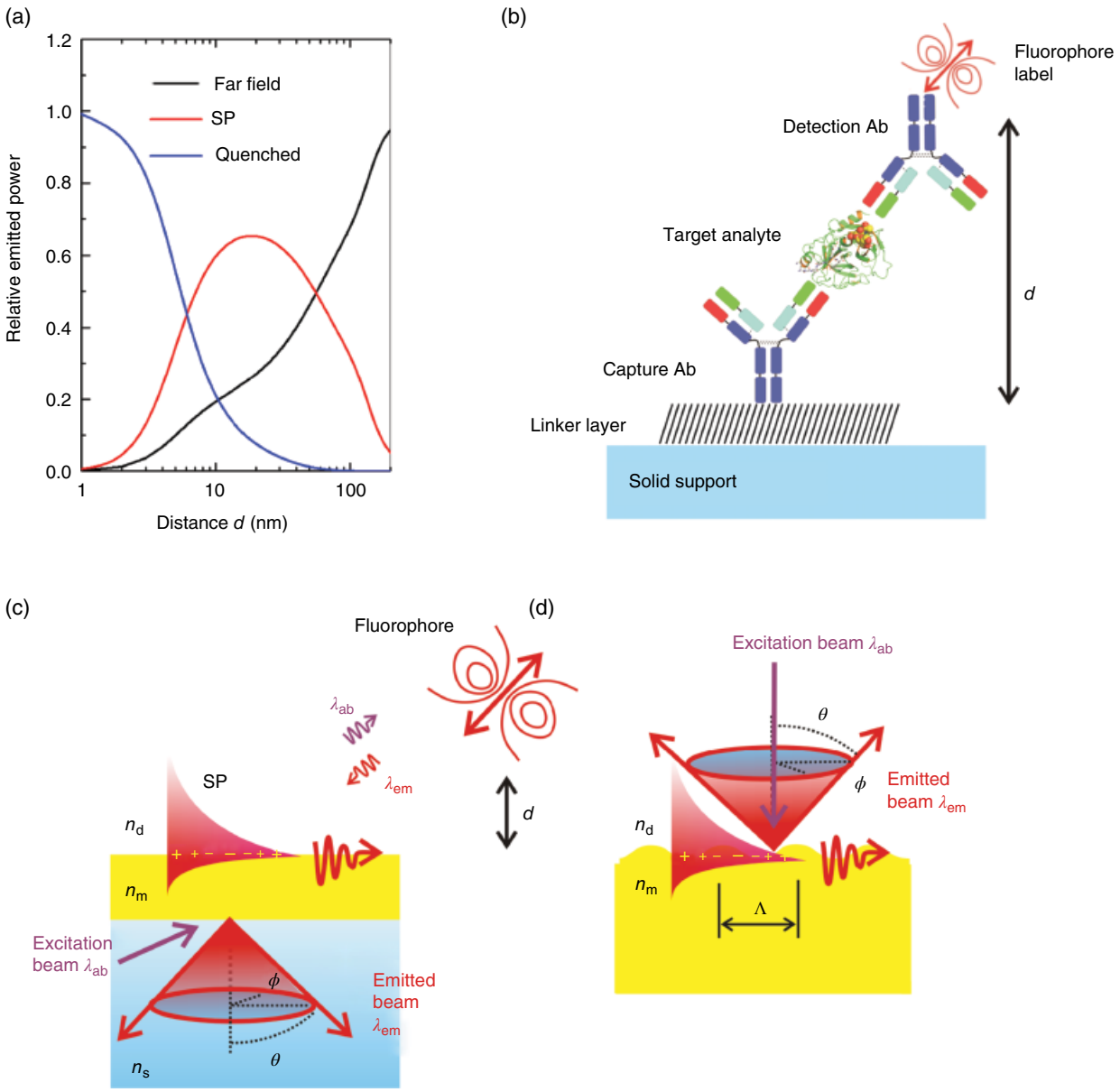

Figure 14.2 (a) Distance dependence of relative power radiated by randomly oriented emitter from a flat gold–water interface at $\lambda_{em} = 670$ nm that is quenched, coupled to SPs, and emitted to the far field. (b) Schematics of sandwich immunoassay utilizing fluorophore labels. Geometry used for out-coupling of SP modes via, (c) reverse Kretschmann geometry of ATR method and (d) by using diffraction on periodically corrugated metallic surface. (*See insert for color representation of this figure.*)

that are trapped by SPs to a highly directional fluorescence beam propagating to the far field. In the reverse Kretschmann configuration depicted in Figure 14.2c, the SPs propagating on a thin metallic film leak into a dielectric substrate with high refractive index n_s. This leakage occurs for narrow range of polar angles θ for which the light beam propagating in the high refractive index dielectric is phase-matched with SPs propagating along the upper interface between the metal and a dielectric with low refractive index n_d.

$$\frac{2\pi}{\lambda} n_s \sin(\theta) = \mathrm{Re}\{k_{SP}\}. \tag{14.2}$$

It should be noted that SPs preferably collect fluorescence light that originates from emitters with emission dipole oriented perpendicular to the surface. The reason is that SP field is transverse magnetically (TM) polarized and its strongest component of electric intensity vector is oriented normal to the surface. For an ensemble of randomly oriented emitters, emission is averaged over the azimuthal angle ϕ and the SPCE

beam in the dielectric substrate with the high index of refraction n_s exhibits a characteristic cone shape defined by the (resonant) polar angle θ.

An alternative means for extracting of fluorescence light energy stored in SPs relies on periodically corrugated interface between a metallic and dielectric (see Figure 14.2d). Diffraction on the periodic corrugation allows for converting SPs to the far field by the grating momentum $G = 2\pi/\Lambda$. This momentum couples the SP-driven emission to an optical wave propagating away from the surface with the polar angle θ and azimuthal angle ϕ that fulfill the following condition:

$$\frac{2\pi}{\lambda} n_d \sin(\theta)\cos(\phi) + m\frac{2\pi}{\Lambda} = \pm \mathrm{Re}\{k_{SP}\}, \quad (14.3)$$

where Λ is the period of the corrugating with the grating vector G oriented in the direction $\phi = 0$.

Besides the coupling of fluorescence emitters with SPs at emission wavelength λ_{em}, the confined SP field can also interact with a fluorophore at its absorption wavelength λ_{ab}. The resonant excitation of SPs generates enhanced field intensity $|E/E_0|^2$ in close vicinity to metallic surface. At λ_{ab}, this field can increase the excitation rate of emitters γ_e which is proportional to the emitted fluorescence signal F when it is far from saturation. In optical instruments supporting fluorescence biosensors, plasmonically increased excitation rate γ_e and controlled angular distribution of emitted fluorescence light $F(\theta,\phi)$ can be preferably combined. These features allow to maximize detected fluorescence signal that originates from the molecular binding at the surface and to minimize parasitic background. The overall enhancement factor of detected fluorescence light intensity EF can be expressed as a product.

$$\mathrm{EF} \propto \left|\frac{E}{E_0}\right|^2 \times \frac{\eta}{\eta^0} \times f, \quad (14.4)$$

Here, η states the quantum yield of the emitter coupled to SPs on a metallic surface and η_0 is the quantum yield of the emitter far from the metal. The term f states the enhanced probability of collecting emitted photons by plasmonic redistribution of emitted fluorescence intensity $F(\theta,\phi)$.

14.3 SPCE Utilizing SP Waves with Small Losses

Decreasing the angular width of directional SPCE beam is beneficial for various kinds of fluorescence measurements as it, for example, allows to better distinguish the specific fluorescence signal originating from the close proximity to a metal surface and the (isotropic) background signal. In order to do so, Toma *et al.* [16] employed LRSPs for mediating fluorescence emission from Alexa Fluor 647 emitters dispersed in a three-dimensional (3D) hydrogel matrix, see Figure 14.3a. These SP waves exhibit lower Ohmic losses compared to regular SPs. When using the reverse Kretschmann geometry, the low losses of LRSPs lead to their resonant coupling with the far-field optical waves at narrow range of polar angles θ that fulfill the condition (14.2). For the geometry with a 19-nm thick gold film deposited on a low refractive index Cytop layer with the thickness of 650 nm, LRSPs provided 4.4-fold higher peak fluorescence intensity and 6-fold narrower full width at half maximum (FWHM) than those of regular SPs when both excitation (at λ_{ab}) and collection of fluorescence light (at λ_{em}) were mediated by SP waves, see Figure 14.3b. The emitters dispersed in the 3D hydrogel matrix were efficiently probed by LRSP field which exhibits less localized field profile, that is, penetrating deeper from the metal film than regular SPs. The average electric field intensity enhancement within 600-nm thick hydrogel film was of $|E/E_0|^2 = 37$ upon the resonant excitation of LRSPs at the wavelength 633 nm, while for regular SPs it was only about 8. In addition, Figure 14.3b shows that LRSP-mediated SPCE occurs at smaller polar angle θ, which, together with the narrower angular distribution, can simplify optics for collecting of SPCE as a smaller numerical aperture (NA) lens can be used.

A recently emerged alternative to SPs for fluorescence enhancement is based on dielectric one-dimensional photonic crystals (1DPC) [17, 18]. These structures can be designed to support the so-called Bloch surface waves (BSWs) that exhibit similar properties to SPs and offer the advantage of versatile tunability. In addition, as the 1DPC comprises a stack of alternating dielectric layers, the losses of BSW are dramatically lower compared to those of SP-based structures. In the work of Toma *et al.* [19], BSWs were employed for the excitation of Alexa Fluor 647 dyes on the surface of a fluorescence biosensor. The schematic of developed BSW-enhanced fluorescence sensor is shown in Figure 14.4a. It relies on Kretschmann configuration for the coupling of an excitation light beam to BSW that probes the interface covered with a 3D hydrogel binding matrix. This matrix features highly open structure due to its swelling in aqueous samples and thus provides huge surface area for the modification with catcher mouse IgG antibodies. The target molecules (antimouse IgG) labeled with Alexa Fluor 647 were affinity bound in the matrix and excited by BSWs. The emitted

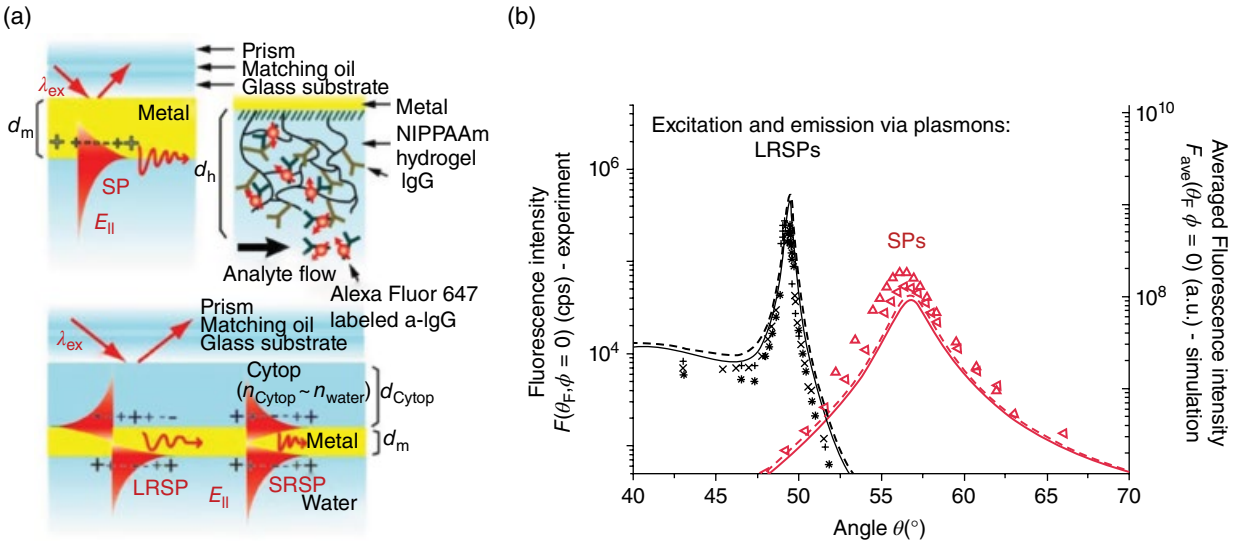

Figure 14.3 (a) Schematic diagrams of the layer architectures for the excitation of regular SPs and LRSPs in order to probe affinity binding of Alexa Fluor 647—labeled antimouse IgG in a 3D hydrogel binding matrix. (b) Angular distribution of SP-coupled emission with (reverse) Kretschmann architecture for the excitation and collection of fluorescence light. Comparison of LRSP and regular SP-coupled emission obtained from experiment (symbols) and simulations (lines) is presented. Toma *et al*. [16]. Reproduced with the permission of The Optical Society.

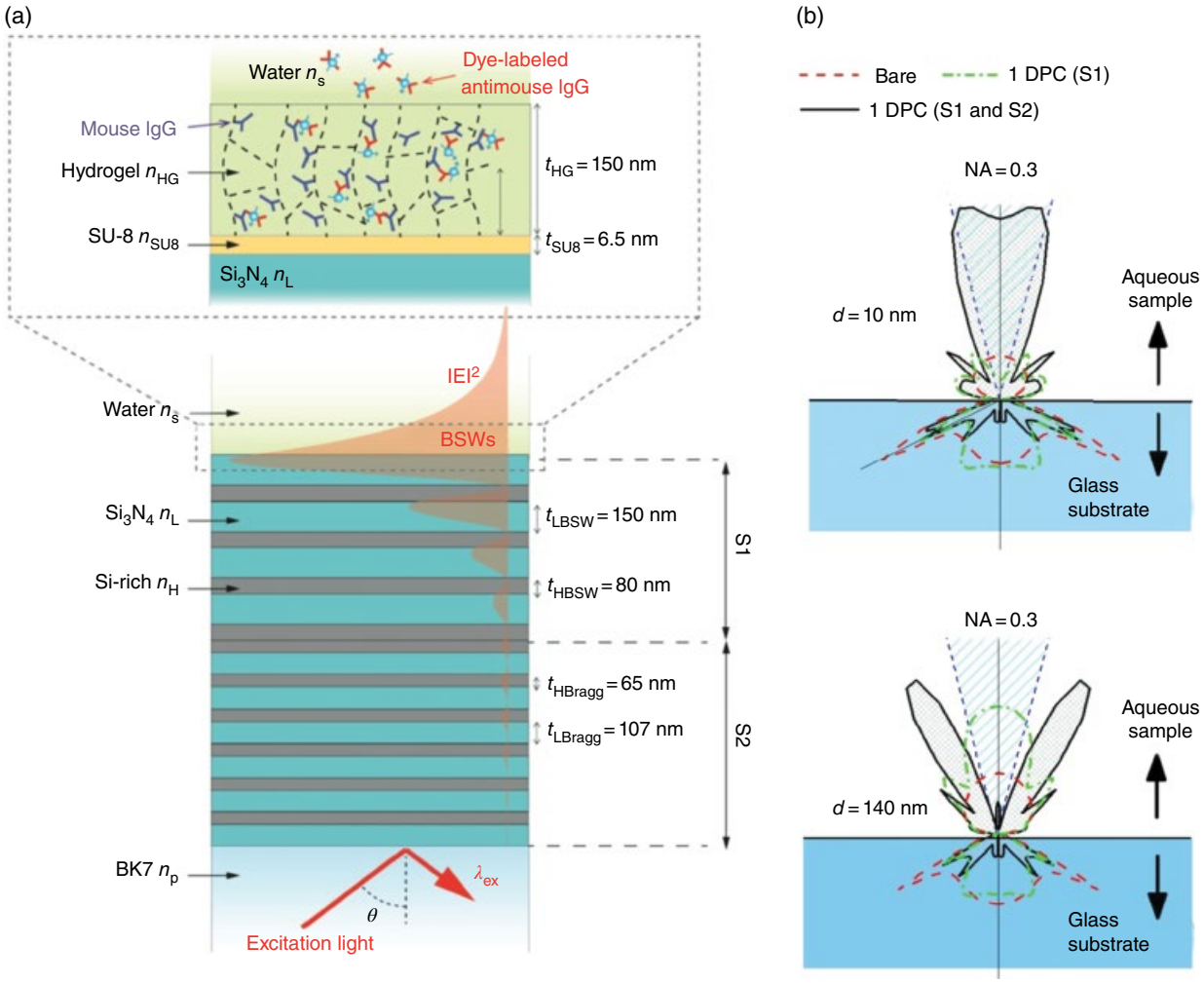

Figure 14.4 (a) Schematics of the surface architecture with periodic stack of dielectric layers that support BSW (S1) and that serves as a Bragg mirror (S2) suppressing the leakage of fluorescence light into the substrate. (b) Simulated angular distribution of emitted light intensity by randomly oriented emitter at the distance from the surface $d = 10$ and 140 nm. Toma *et al*. [19]. Reproduced with the permission of The Optical Society.

fluorescence light was collected with a lens (numerical aperture NA = 0.3) through the aqueous sample and a transparent flow cell. The 1DPC was designed so the BSWs were supported only at λ_{ab}, while no BSW existed at the emission wavelength λ_{em} in order to avoid (in this case unwanted) leaking of fluorescence emission into the glass substrate. Due to the minimized losses of BSW, the maximum electric field intensity enhancement accompanied with the resonant excitation of BSWs of as $|E/E_0|^2 = 300$ was simulated (not taking into account the practical losses due to, for example, scattering on the surface roughness). In order to enhance the collection efficiency of emitted fluorescence light through the aqueous sample *f*, the layer structure comprised two segments: the first segment (S1) served for the resonant excitation of BSWs at λ_{ab} and the second segment (S2) was designed to function as a Bragg mirror at λ_{em} in order to shape the angular distribution of emitted fluorescence light $F(\theta)$. As Figure 14.4b illustrates, Bragg mirror S2 worked not only as a reflector but also provided "beaming" of fluorescence light intensity toward a detector at a water side. The simulated polar angular distribution $F(\theta)$ indicates that the fluorescence light is squeezed in a narrow angular range that matches the acceptance angle of used lens with NA = 0.3 for emitters close to the surface. The fluorescence emission probability within this NA reached about 12% for the distance $d = 10$ nm. Since back-reflected fluorescence from 1DPC gains a different phase-shift when changing the distance, the peak intensity occurs at polar angles θ shifted by about 18° when changing d from 10 to 140 nm.

14.4 Nondiffractive Grating Structures for Angular Control of SPCE

Besides structures periodic in the direction perpendicular to the surface, also periodic corrugation in the direction parallel to the surface allows for control of the angular distribution of SPCE that is extracted by reverse Kretschmann configuration. Toma *et al.* explored SPCE mediated by nondiffractive metallic gratings the split of the dispersion relation of SPs by a plasmonic bandgap [20]. In this study, a 50-nm thick Au layer was sinusoidal modulated with a period of $\lambda = 225$–230 nm and a depth of 10 and 30 nm. The structure was prepared by laser interference lithography and multiple copies were prepared by UV nanoimprint lithography. It was designed for the excitation of BSSPs at edges of the plasmonic bandgap occurring at wavelengths that coincide with the emission wavelength of DiD fluorophore ($\lambda_{em} = 665$ nm). This fluorophore was dispersed in poly(methyl methacrylate) (PMMA) layer deposited on the top Au layer, see Figure 14.5a. Refractive indices of media below and above the Au layer were tuned in order to adjust wavelength position of the plasmonic bandgap. The dispersion relation of SPs was observed from the measurements of reflectivity spectra as a function of polar angle of incidence θ and wavelength λ taken by the ATR method with Kretschmann geometry. In order to observe the angular distribution of fluorescence intensity $F(\theta,\phi)$ that was mediated by BSSPs, the dye-doped PMMA layer was excited by normally incidence beam with $\lambda = 633$ nm hitting the surface from superstrate side, the fluorescence beam leaking into the underneath glass substrate was scattered by an optically matched diffuser, and imaged to a charge coupled device (CCD).

Figure 14.5b shows several examples of SP dispersion relation mediated by the nondiffractive dense grating and corresponding angular distribution of fluorescence intensity $F(\theta,\phi)$. In part (i), SP dispersion relation and corresponding SPCE angular distribution for a reference flat Au layer structure with air on the top (superstrate refractive index $n_6 = 1$) are presented. A continuous dark band in the reflectivity spectrum $R(\lambda,\theta)$ is due to the excitation of SPs at the outer interface with dye-doped PMMA layer. It reveals that SPR occurs at the angle $\theta \sim 39°$ in the LaSFN9 glass substrate for the emission wavelength $\lambda_{em} = 670$ nm. The respective fluorescence angular distribution $F(\theta,\phi)$ displays a characteristic SPCE cone for the similar polar angle of $\theta \sim 38°$.

When the layer structure is corrugated with the modulation depth of 10 nm and the metal surface is brought in contact with water ($n_6 = 1.33$), the resonant coupling to SPs shifts to higher angles and a plasmonic bandgap appears in the dispersion relation. As seen in Figure 14.5b(ii), BSSP modes occur at wavelengths of $\lambda = 670$ nm (ω^+) and 700 nm (ω^-). Therefore, the BSSP ω^+ wavelength matches the fluorescence emission wavelength λ_{em} of used dye which lead to the confinement of SPCE signal in the direction parallel to grating vector *G*. Interestingly, the peak emission via BSSP ω^+ mode was increased by a factor of ~3 compared to that for regular SPCE cone. The reason is the enhanced LDOS associated with the presence of BSSP. It should be noted that the emission via BSSPs occurs only at narrow range of azimuthal angles ϕ as the bandgap blue shifts away from the emission wavelength λ_{em} by increasing ϕ.

Figure 14.5b(iii) shows the dispersion relation and the corresponding SPCE angular distribution $F(\theta,\phi)$

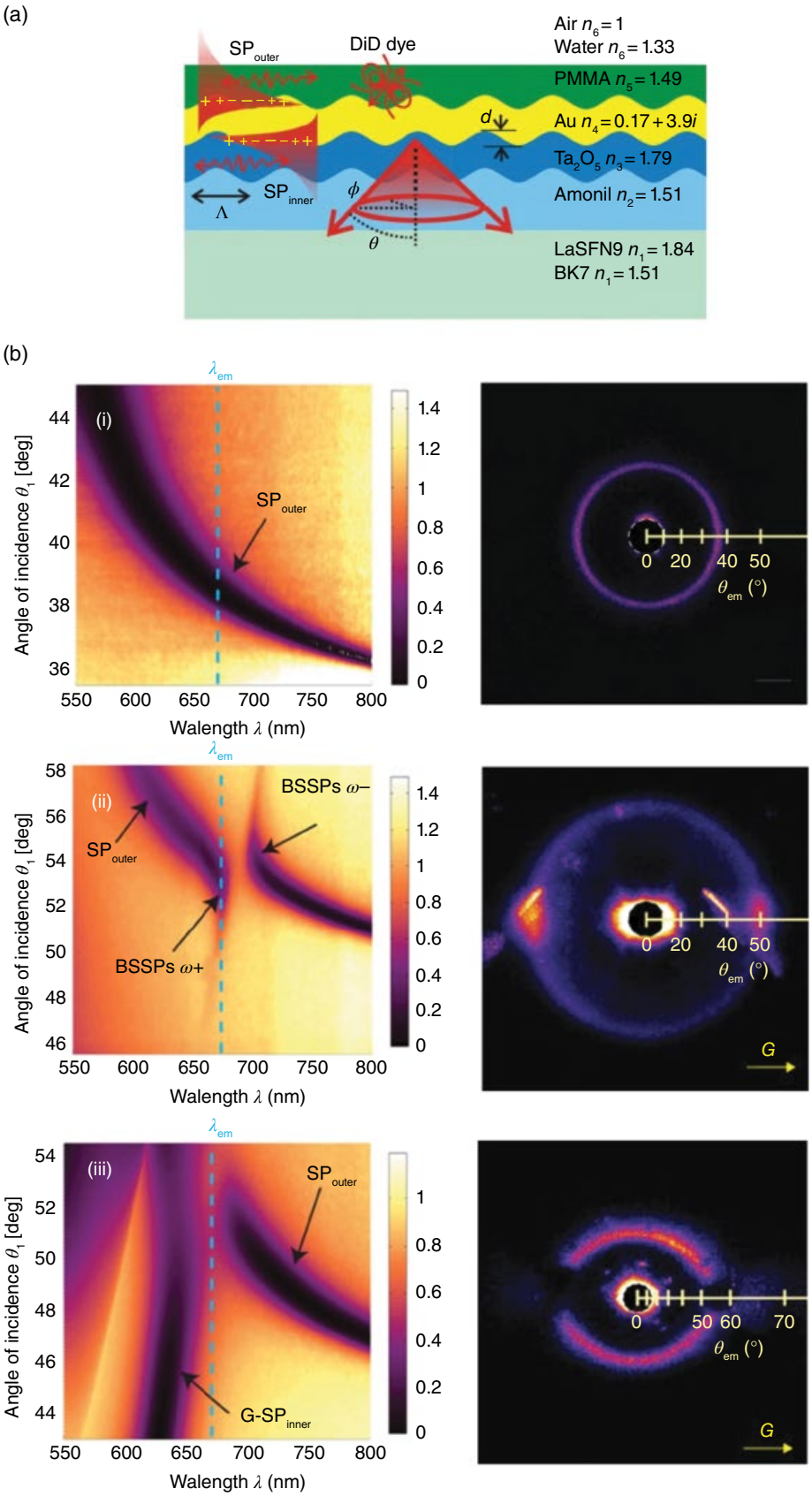

Figure 14.5 (a) Nondiffractive metallic grating structure for probing a thin poly(methyl methacrylate) —PMMA—layer doped with a DiD dye. (b) Examples of SP dispersion relation perturbed by Bragg scattering and respective angular dependence of SPCE $F(\theta,\phi)$ for (i) flat surface, (ii) emission wavelength λ_{em} tuned to the edge of a plasmonic bandgap, and (iii) inside the bandgap. Toma *et al.* [20]. Reproduced with the permission of The Optical Society.

when the grating structure supports SPs that are diffraction coupled across the Au layer. In this experiment, the grating with the modulation depth of 30 nm and without Ta_2O_5 layer was brought into contact with air ($n_6 = 1$). As can be seen from measured data, the dispersion relation of inner SP (that is excited by −1st diffraction order) anticrosses with that of outer SP (excited by ATR and probing the PMMA layer) at the wavelength that coincides with λ_{em} of used DiD dye. Contrary to situation (ii), the anticrossing SP dispersion leads to canceling of the SPCE signal at the direction of parallel with grating vector *G*.

14.5 Diffractive Grating Structures for Angular Control of SPCE

On periodically corrugated metallic surfaces with longer periods Λ, diffraction allows to directly extract fluorescence light emitted via SPs into the far field (see Eq. (14.3)). Bauch *et al.* [21] investigated grating-enhanced fluorescence on crossed periodically corrugated Au surface that is depicted in Figure 14.6a. This structure has been designed to resonantly excite SPs by normally incident laser beam with wavelength λ_{ab} and to diffractively out-couple SPCE at λ_{em} into a narrow emission cone traveling back into direction of the incident excitation beam. Such a design is attractive for the use in fluorescence sensors relying on epifluorescence geometry that is implemented in the majority of fluorescence microarray scanners and fluorescence microscopes [22]. The used structure comprised two superimposed sinusoidal modulations orientated at 90° to each other. It was prepared by laser interference lithography and multiple copies were made by UV nanoimprint lithography which is compatible with mass production technologies. The grating structure was optimized for the amplification of *in situ* fluorescence sandwich immunoassays with Cy5 and Alexa Fluor 647 dyes when the excitation wavelength $\lambda = 633$ nm and the emission is centered at the wavelength $\lambda_{em} = 670$ nm. The grating period was of $\Lambda = 434$ nm and the surface was coated with 4-nm thick adhesion promoting Cr layer and optically thick 100-nm Au film.

Contrary to the Kretschmann configuration, diffraction coupling to SPs on a crossed grating leads to the amplified electric field intensity that varies in lateral direction. The averaged electric field intensity enhancement $|E/E_0|^2$ generated by the resonant excitation of SPs at λ_{ab} is compared with that on a flat Au surface in Figure 14.6b. On a crossed grating, maximum field intensity occurs at the interface between Au and aqueous sample and it exponentially decays into both metal and water media. On a flat surface, the field exhibits minimum intensity at the Au surface and it oscillates when increasing the

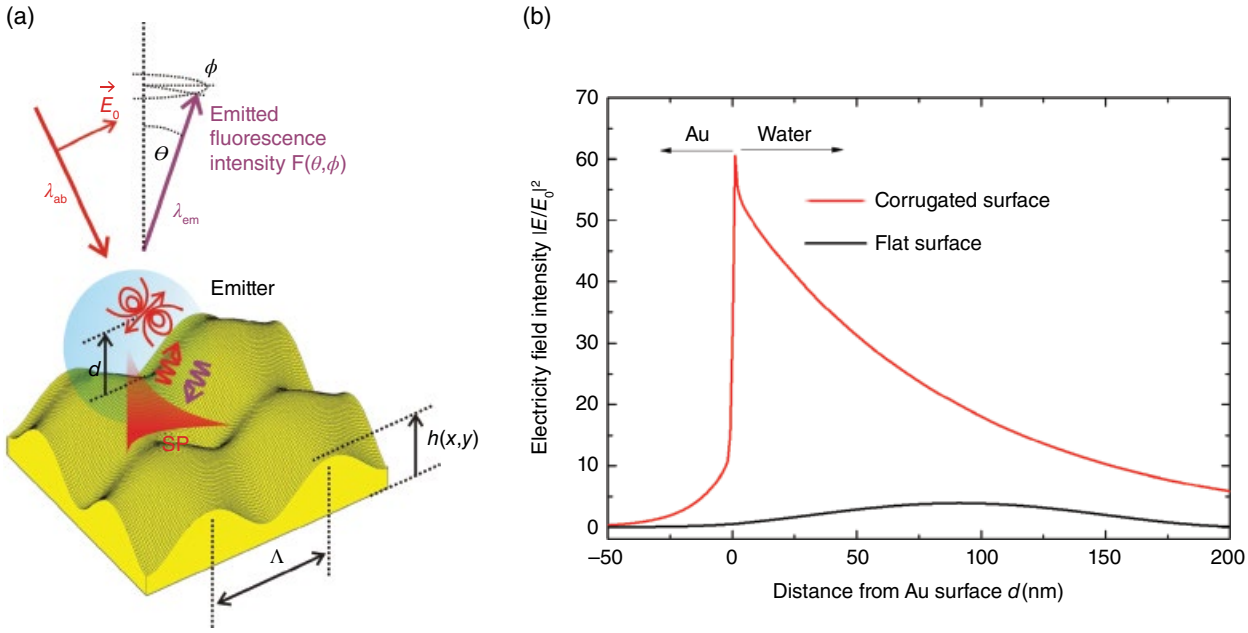

Figure 14.6 (a) Geometry and (b) electric field intensity $|E/E_0|^2$ averaged over the unit cell of the diffractive grating upon the resonant diffractive coupling to SPs. The field strength was calculated as a function of distance *d* from the flat and corrugated gold surfaces. Normally, incident plane wave at the wavelength of $\lambda_{ab} = 633$ nm was assumed. Bauch *et al.* [21]. Reproduced with the permission of The Optical Society.

distance d due to the interference of the incident and reflected beams. The electric field intensity at a distance of $d = 20$ nm that is normalized with the intensity of the incident beam is around $|E/E_0|^2 = 43$ for the resonant coupling to SPs on the corrugated surface. The simulated data on a flat Au surface show much lower field strength $|E/E_0|^2 = 1.36$ at such distance d.

After its excitation, a fluorophore decays back to its ground state by radiative or nonradiative processes. The vicinity of metal alters both the radiative and nonradiative decay rates and therefore changes the quantum yield of the fluorophore η [23]. It should be noted that plasmonic nanostructures have been reported to significantly increase quantum yield of emitters with low intrinsic quantum yield η_0 [24]. However, for the assay that utilizes relatively high intrinsic quantum yield fluorophore Alexa Fluor 647 ($\eta_0 = 0.33$), this effect is weak and rather a small decrease in quantum yield occurs $\eta/\eta_0 = 0.82$. Therefore, mostly the first term $|E/E_0|^2$ and last term f in Eq. (14.4) play important role for maximizing fluorescence assay sensitivity.

The grating-coupled emission of fluorescence light enables controlling the angular distribution of emitted light intensity $F(\theta,\phi)$ at λ_{em} in order to improve fluorescence collection efficiency f. As shown by simulated data in Figure 14.7a, the emission angular distribution $F(\theta,\phi)$ at the flat gold surface is isotropic while that on crossed grating displays series of bright bands due to the first-order diffraction out-coupling of SPCE. These bands lead to a confinement of emitted fluorescence light energy in a narrow cone of polar angles $\theta < 11.5°$ which allows for efficient collecting of fluorescence light by a low numerical aperture lens with NA = 0.2. These simulations predicted that the interplay of plasmonically increased excitation rate by $|E/E_0|^2$ at λ_{ab}, modified quantum yield η/η_0, and increased collection efficiency f at λ_{em} allows to increase fluorescence signal on a crossed Au grating with respect to flat Au surface by a factor EF = 145 for $d = 15$ nm and EF = 96 for $d = 20$ nm.

Figure 14.7b confirms predicted simulations by measurements of fluorescence far-field emission $F(\theta,\phi)$. These measurements were carried out for DiD dye dispersed in a thin PMMA layer deposited on a flat and corrugated Au surfaces. The DiD dye exhibits similar absorption and emission spectra as Alexa Fluor 647 and Cy5 employed in bioassays. The observed behavior qualitatively agrees with the simulated data in Figure 14.7a. The emission bands are broader than those predicted by simulations due to the fact that the emitted light within a spectral range $\lambda_{em} \sim 665$–675 nm was collected and imaged to the detector.

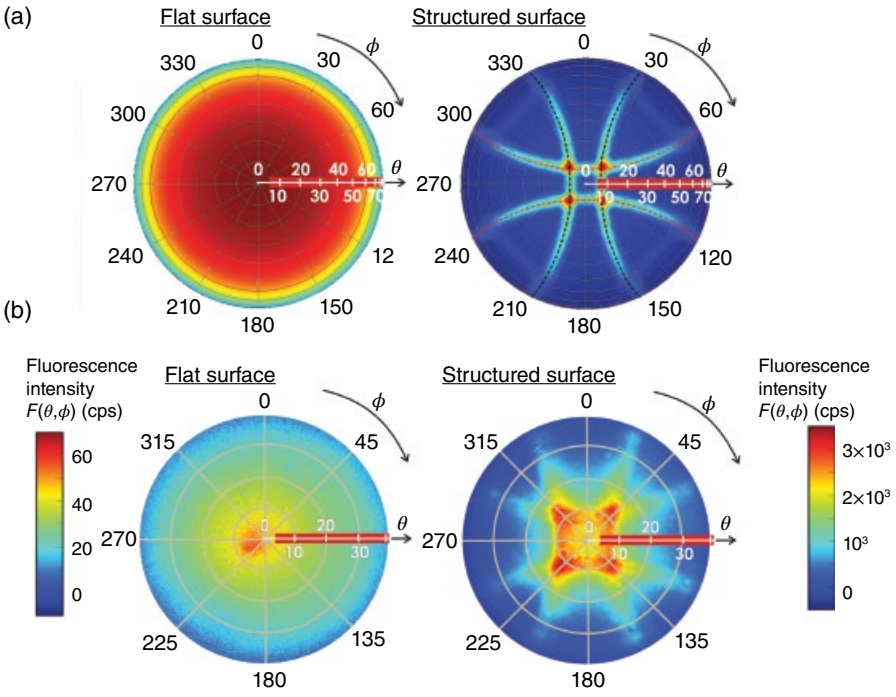

Figure 14.7 (a) Simulated and (b) measured angular distribution of far-field fluorescence intensity $F(\theta,\varphi)$ emitted from randomly oriented DiD dyes dispersed in a poly (methyl methacrylate) layer that was prepared on a flat (*left*) and corrugated (*right*) Au surfaces. The polar angle θ is given in air. Bauch *et al.* [21]. Reproduced with the permission of The Optical Society.

14.6 Implementation of Grating-Assisted SPCE to Biosensors

Bauch *et al.* demonstrated that designed diffractive grating provides enhanced fluorescence signal by a factor EF ~ 10^2 when applied for an immunoassay detection with *in situ* format and epifluorescence readout geometry. As sketched in Figure 14.8a, an optical instrument with a grating sensor chip clamped to a microfluidic device was used for the measurement of affinity binding of biomolecules at the sensor surface. The sensor chip was functionalized with antibodies for specific capture of the medium-sized protein interleukin 6 (IL6) that has been established as an inflammatory biomarker. Detection antibody (dAb) labeled with Alexa Fluor 647 was bound to the captured IL6 in the used sandwich immunoassays and detected by plasmonically amplified fluorescence. Figure 14.8b shows the kinetics of fluorescence signal F measured upon the affinity binding of dAb. It reveals that the selective amplification of fluorescence signal at the grating surface enables distinguishing the fluorescence signal associated with the binding at the surface from that originating from the bulk solution through which the excitation beam passes. On a flat reference surface, the observed change in fluorescence signal F is mostly due to the bulk and it is manifested as a rapid increase in fluorescence signal after the injecting dAb (t = 75 min) and decrease in fluorescence signal after the rinsing (t = 85 min). On the plasmonic grating chip, the relative signal due to the background is massively suppressed and the observed changes in fluorescence signal are virtually attributed only to the analyte bound at the surface that is probed by confined field of SPs.

It should be noted that high numerical aperture optics cannot be easily used for *in situ* epifluorescence measurement when the excitation and collection of fluorescence light are carried out through a microfluidic device. Then, only a low numerical aperture lens can be employed and thus the directional fluorescence emission offers essential advantage of enhanced efficiency in the fluorescence light collection (which otherwise is omnidirectional and only a small fraction of emitted photons are delivered to the detector). However, the majority of currently used fluorescence microarrays scanners are designed for the *ex situ* measurement performed on a dry sensor chip after multiple assay steps. Typically, the excitation beam is scanned over the sensor surface with a high numerical aperture lens that is at the same time used for the collection of fluorescence light. For these optical instruments, the directional SPCE provides limited advantage as the directional emission only redistributes the angular dependence of fluorescence emission within the acceptance cone defined by the maximum polar angle θ_{max} (see Figure 14.8) [25].

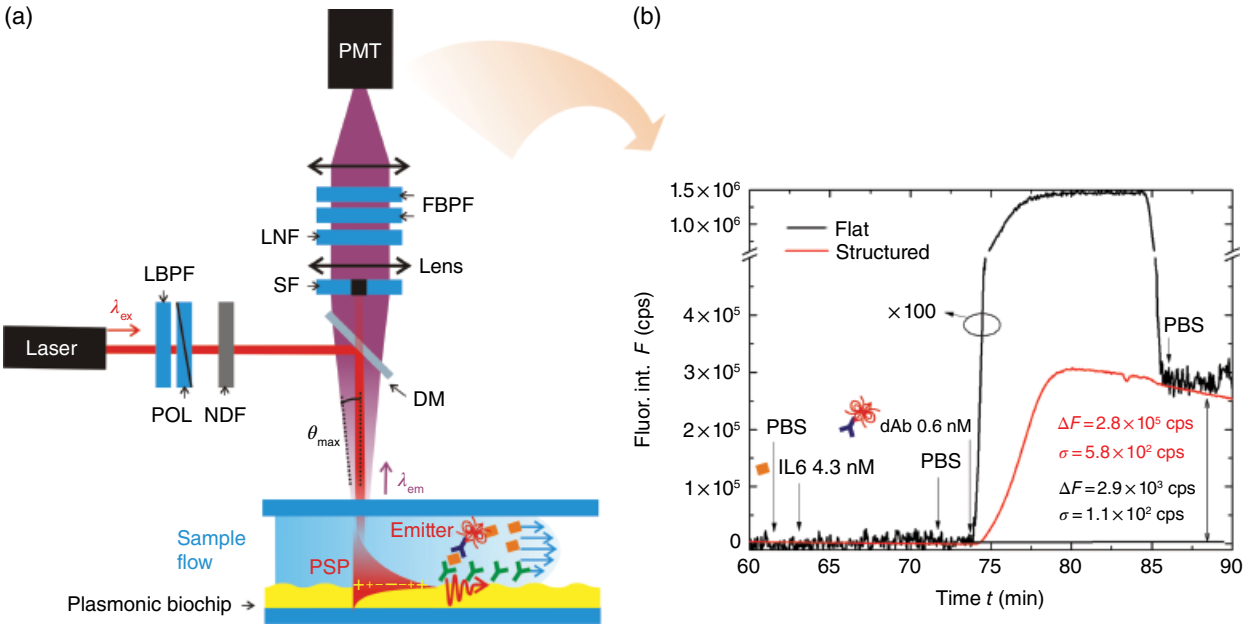

Figure 14.8 (a) Arrangement of an optical instrument for *in situ* fluorescence assay with epifluorescence readout geometry and low numerical aperture lens for the collection of fluorescence light. (b) Example of fluorescence intensity kinetics measured on Au diffraction grating and reference flat Au surface upon the affinity binding of dAb labeled with an Alexa Fluor 647 dye. Bauch *et al.* [21]. Reproduced with the permission of The Optical Society.

Plasmonic biosensor with grating chip for *in situ* sandwich immunoassay detection of inflammation biomarker IL6 was calibrated. In this experiment, a series of buffer samples were spiked with IL6 at concentration c between 10 pg/mL and 100 ng/mL and flown over the sensor chip which carried antibodies against IL6 on its surface. After the IL6 analyte capture, a biotinylated dAb against another epitope of IL6 was injected and bound at the surface. Then, streptavidin labeled with Alexa Fluor 647 was reacted to these biotin moieties, the sensor surface was rinsed with a buffer, and the fluorescence signal difference ΔF before the injection of IL6 analyte and after the streptavidin binding was measured. The whole assay required 50 min including 15-min incubation of the analyzed sample with the capture antibody. Figure 14.9 shows the obtained calibration curves for two assays performed on the structured Au grating chip (gray curve) and a reference flat Au surface (black curve). It demonstrates that plasmonic amplification of fluorescence signal ΔF associated with the capture of IL6 allowed reaching the LOD of 9 pg/mL. This LOD is about 25 times better than that observed on a control flat Au substrate—233 pg/mL. The LOD was determined as an intersection of a linear fit of the measured calibration curve with a background signal ΔF (originating from nonspecific adsorption of labeled streptavidin) plus the 3-fold standard deviation 3σ of measured fluorescence signal. The improvement factor of LOD (25-fold) is lower than the observed EF of the fluorescence intensity (10^2) which is due to the effect of nonspecific adsorption.

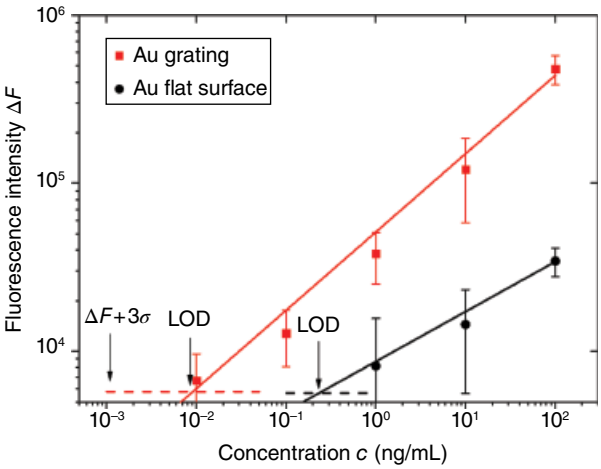

Figure 14.9 Comparison of calibration curves for an IL6 sandwich assay with epifluorescence readout on a structured plasmonic Au surface (gray squares) and a reference flat Au surface (black circles) with corresponding fits and LOD indicated.

As an alternative approach to reverse Kretschmann configuration which typically requires optical matching of a sensor chip to a high refractive index glass prism, Toma *et al.* combined this method with diffractive optical elements [26]. In this work, two gratings were integrated to a compact SPCE sensor chip as depicted in Figure 14.10a. The first one was a linear grating and it served for in-coupling of an excitation light beam to the chip. The excitation beam traveled in the sensor chip and hit the sensing spot at an SP resonance angle for the absorption wavelength of used dye λ_{ab}. The second one was a chirped concentric grating designed for the out-coupling of SPCE cone that propagated in the compact chip. After hitting the concentric grating, the SPCE beam was coupled to −1st diffraction order that traveled away from the sensor chip and converged to a spot below its bottom surface at a distance $D = 15$ mm, see Figure 14.10b. A flat sensing spot was in the center of the concentric grating and it was coated with a 50-nm thick Au film. At this area, the excitation beam generated SPs at the λ_{ab} in order to enhance excitation rate γ_e of fluorescence light that was subsequently collected by SPs at λ_{em}, leaked into the substrate in the form of SPCE cone, and was imaged to a detector by the concentric grating.

A model immunoassay experiment with such a sensor chip was carried out. As seen in Figure 14.10c, this platform offered comparable sensitivity to regular SP-enhanced fluorescence biosensors relying on Kretchmann configuration with a prism coupler. The compact sensor chip platform with the integrated diffractive elements offers the advantage of simpler design that is attractive for portable fluorescence biosensor devices. The designed elements were prepared by using UV nanoimprint lithography from masters fabricated by laser interference lithography which is compatible with mass production technologies and thus suitable for cost effective fabrication.

14.7 Summary

Several approaches for controlling of SPCE by using diffractive and nondiffractive gratings are described. By this means, the angular distribution of fluorescence light that is emitted from close proximity to a metallic surface can be efficiently tailored for maximizing assay sensitivity. In fluorescence bioassays, this approach enables increasing the detected fluorescence intensity that originates from specific capture of target analyte from a liquid sample at the sensor surface. This amplification allows to better discriminate the specific signal from the background

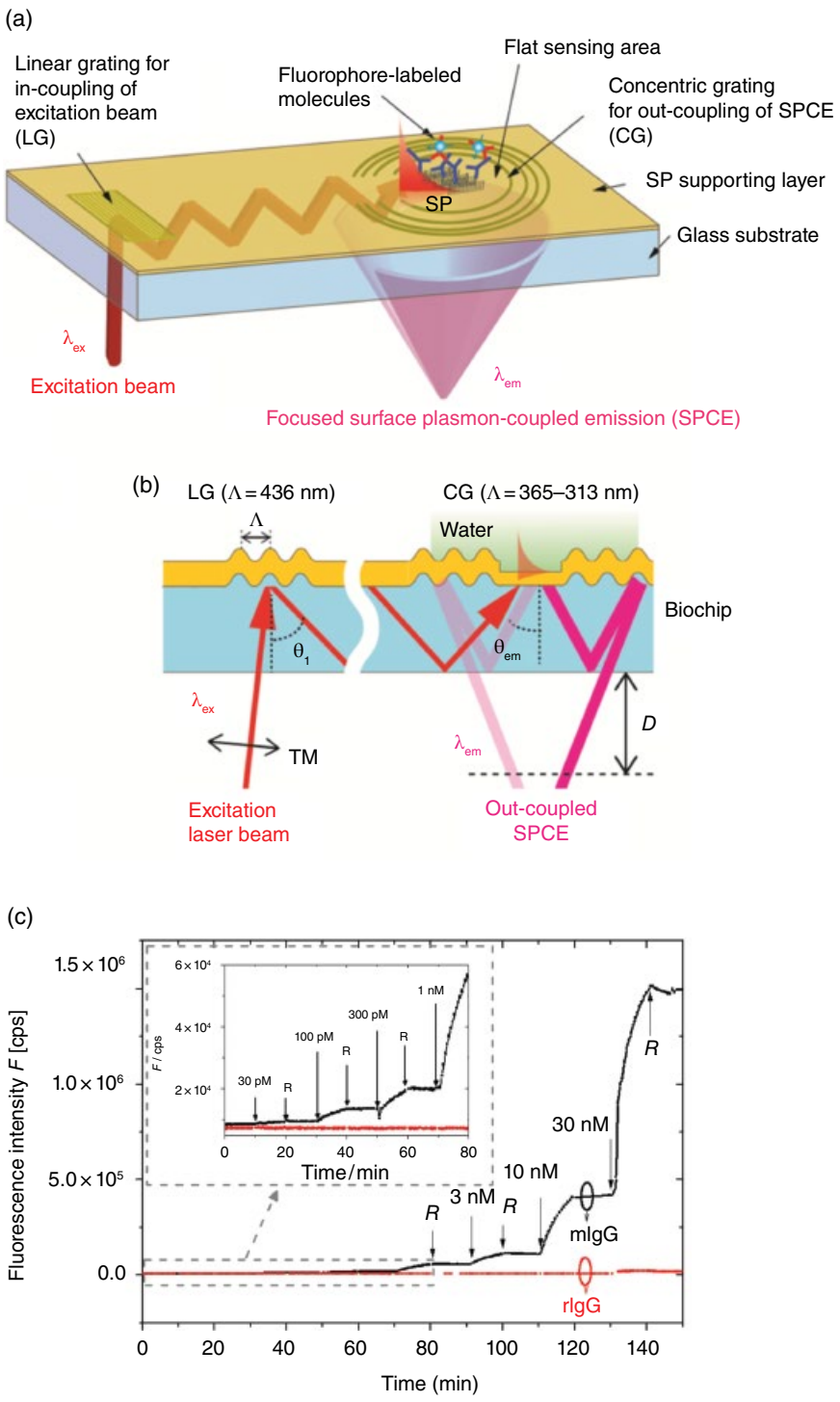

Figure 14.10 (a) Optical geometry for concentric grating-based out-coupling of SPCE from a sensor chip with reverse Kretschmann configuration and (b) its cross section. (c) Example of a model immunoassay experiment with a specific (mouse IgG: mIgG) and a control (rabbit IgG: rIgG) analytes present in analyzed samples. Toma *et al.* [27]. Reproduced with the permission of The Optical Society.

and thus enables improving the assay sensitivity and LOD. The amplification by propagating SPs can be carried out for optical sensors utilizing attenuated total internal reflection fluorescence (TIRF) as well as epifluorescence configuration, and the enhancement factor of fluorescence signal intensity up to 10^2 can be reached. The plasmonically amplified fluorescence assays are particularly attractive for *in situ*

measurements and provide versatile platform where both excitation and collection of fluorescence light can be performed through a dielectric sensor chip [26], through a microfluidic system on the top of the sensor chip [28], or for the excitation and collecting from opposite sides is possible [19].

Acknowledgments

This work was partially supported by Austrian Science Fund (FWF) through the project ACTIPLAS (P244920-N20) and this project has received funding from the European Union's Horizon 2020 research and innovation programme under grant agreement no. 633937, project ULTRAPLACAD.

References

1 Bally, M.; Halter, M.; Voros, J.; Grandin, H. M., Optical microarray biosensing techniques. *Surf. Interface Anal.* **2006**, *38* (11), 1442–1458.
2 Seidel, M.; Niessner, R., Automated analytical microarrays: a critical review. *Anal. Bioanal. Chem.* **2008**, *391* (5), 1521–1544.
3 Schuller, J. A.; Barnard, E. S.; Cai, W. S.; Jun, Y. C.; White, J. S.; Brongersma, M. L., Plasmonics for extreme light concentration and manipulation. *Nat. Mater.* **2010**, *9* (3), 193–204.
4 Novotny, L.; van Hulst, N., Antennas for light. *Nat. Photonics* **2011**, *5* (2), 83–90.
5 Attridge, J. W.; Daniels, P. B.; Deacon, J. K.; Robinson, G. A.; Davidson, G. P., Sensitivity enhancement of optical immunosensors by the use of a surface-plasmon resonance fluoroimmunoassay. *Biosens. Bioelectron.* **1991**, *6* (3), 201–214.
6 Liebermann, T.; Knoll, W., Surface-plasmon field-enhanced fluorescence spectroscopy. *Colloids Surf. A Physicochem. Eng. Asp.* **2000**, *171* (1–3), 115–130.
7 Barnes, W. L.; Preist, T. W.; Kitson, S. C.; Sambles, J. R., Physical origin of photonic energy gaps in the propagation of surface plasmons on gratings. *Phys. Rev. B* **1996**, *54* (9), 6227–6244.
8 Sarid, D., Long-range surface-plasma waves on very thin metal-films. *Phys. Rev. Lett.* **1981**, *47* (26), 1927–1930.
9 Chance, R. R.; Prock, A.; Silbey, R., *Adv. Chem. Phys.* **1978**, *37* (1), 1–65.
10 Weber, W. H.; Eagen, C. F., Energy-transfer from an excited dye molecule to the surface-plasmons of an adjacent metal. *Opt. Lett.* **1979**, *4* (8), 236–238.
11 Vareiro, M. L. M.; Liu, J.; Knoll, W.; Zak, K.; Williams, D.; Jenkins, A. T. A., Surface plasmon fluorescence measurements of human chorionic gonadotrophin: role of antibody orientation in obtaining enhanced sensitivity and limit of detection. *Anal. Chem.* **2005**, *77* (8), 2426–2431.
12 Lakowicz, J. R.; Malicka, J.; Gryczynski, I.; Gryczynski, Z., Directional surface plasmon-coupled emission: a new method for high sensitivity detection. *Biochem. Biophys. Res. Commun.* **2003**, *307* (3), 435–439.
13 Yuk, J. S.; Trnavsky, M.; McDonagh, C.; MacCraith, B. D., Surface plasmon-coupled emission (SPCE)-based immunoassay using a novel paraboloid array biochip. *Biosens. Bioelectron.* **2010**, *25* (6), 1344–1349.
14 Knoll, W.; Philpott, M. R.; Swalen, J. D., Emission of light from Ag metal gratings coated with dye monolayer assemblies. *J. Chem. Phys.* **1981**, *75* (10), 4795–4799.
15 Kitson, S. C.; Barnes, W. L.; Sambles, J. R., Photoluminescence from dye molecules on silver gratings. *Opt. Commun.* **1996**, *122* (4–6), 147–154.
16 Toma, K.; Dostalek, J.; Knoll, W., Long range surface plasmon-coupled emission for biosensor applications. *Opt. Express* **2011**, *19* (12), 11090–11099.
17 Soboleva, I. V.; Descrovi, E.; Summonte, C.; Fedyanin, A. A.; Giorgis, F., Fluorescence emission enhanced by surface electromagnetic waves on one-dimensional photonic crystals. *Appl. Phys. Lett.* **2009**, *94* (23), 231122.
18 Zhang, W.; Ganesh, N.; Mathias, P. C.; Cunningham, B. T., Enhanced fluorescence on a photonic crystal surface incorporating nanorod structures. *Small* **2008**, *4* (12), 2199–2203.
19 Toma, K.; Descrovi, E.; Toma, M.; Ballarini, M.; Mandracci, P.; Giorgis, F.; Mateescu, A.; Jonas, U.; Knoll, W.; Dostalek, J., Bloch surface wave-enhanced fluorescence biosensor. *Biosens. Bioelectron.* **2013**, *43*, 108–114.
20 Toma, M.; Toma, K.; Adam, P.; Vala, M.; Homola, J.; Knoll, W.; Dostalek, J., Surface plasmon-coupled emission on plasmonic Bragg gratings. *Opt. Express* **2012**, *20* (13), 14042–14053.
21 Bauch, M.; Hageneder, S.; Dostalek, J., Plasmonic amplification for bioassays with epi-fluorescence readout. *Opt. Express* **2014**, *22* (26), 32026–32038.
22 Tawa, K.; Hori, H.; Kintaka, K.; Kiyosue, K.; Tatsu, Y.; Nishii, J., Optical microscopic observation of fluorescence enhanced by grating-coupled surface plasmon resonance. *Opt. Express* **2008**, *16* (13), 9781–9790.
23 Bharadwaj, P.; Novotny, L., Spectral dependence of single molecule fluorescence enhancement. *Opt. Express* **2007**, *15* (21), 14266–14274.

24 Kinkhabwala, A.; Yu, Z. F.; Fan, S. H.; Avlasevich, Y.; Mullen, K.; Moerner, W. E., Large single-molecule fluorescence enhancements produced by a bowtie nanoantenna. *Nat. Photonics* **2009**, *3* (11), 654–657.

25 Gogalic, S.; Hageneder, S.; Ctortecka, C.; Bauch, M.; Khan, I.; Preininger, C.; Sauer, U.; Dostalek, J., Plasmonically Amplified Fluorescence Bioassay with Microarray Format. *Proc. SPIE* **2015**, 9506 (Optical Sensors 2015), 95060N.

26 Toma, K.; Adam, P.; Vala, M.; Homola, J.; Knoll, W.; Dostalek, J., Compact biochip for plasmon-enhanced fluorescence biosensor. *Opt. Express* **2013**, *21* (8), 10121–10132.

27 Toma, K.; Vala, M.; Adam, P.; Homola, J.; Knoll, W.; Dostalek, J., Compact surface plasmon-enhanced fluorescence biochip. *Opt. Express* **2013**, *21* (8), 10121–10132.

28 Hageneder, S.; Bauch, M.; Dostalek, J., Plasmonically amplified fluorescence bioassay - total internal reflection vs. epifluorescence geometry, *Talanta* 156–157, 225–231.

15

Surface Plasmon-Coupled Emission

Emerging Paradigms and Challenges for Bioapplication

*Shuo-Hui Cao, Yan-Yun Zhai, Kai-Xin Xie, and Yao-Qun Li**

Department of Chemistry and the MOE Key Laboratory of Spectrochemical Analysis & Instrumentation, College of Chemistry and Chemical Engineering, Xiamen University, Xiamen, China

15.1 Introduction

Fluorescence technology has become one of the most important tools in the fields of bioanalysis, clinical diagnosis, and chemical sensing. There is a dramatic increase in the need of high sensitivity with the rapid development in these applications. Recently, a novel fluorescence technique referred as surface plasmon-coupled emission (SPCE), first described by Lakowicz *et al.* [1–3], has attracted more and more attentions. The unique properties were useful in sensing applications [4].

The typical configuration for SPCE is illustrated in Figure 15.1. The fluorescent molecules are positioned above a continuous metallic nanofilm, which is about 20–50-nm thick, and the distance between the metal and the fluorophores is about 5–200 nm [5]. The excited fluorophores can couple with surface plasmons and result in new emitting species, named as plasmophores [6], to produce highly directional emission. Remarkably, the emission can be seen through a prism attached to the film and it occurs only at a unique angle θ_F measured from the normal of the interface. When a hemisphere prism is used, the emission is observed as a cone around z-axis. This phenomenon is quite different from the classical fluorescence, where the spatial distribution of emission is isotropic. The directional emission in SPCE has the same emission spectrum as the fluorophores, so it can be considered that it originates from the fluorophores. However, the emission is highly p-polarized no matter what kind of polarization of the excitation light, indicating that the emission should reflect the property of the coupled surface plasmons. In fact, the complex emission of plasmophores involved both in fluorophores and surface plasmons can be regarded as the reverse process of surface plasmon resonance (SPR). The most important prerequisite is the matching of wave vectors belonging to fluorophores and surface plasmons, which can be satisfied with a high-index prism attached to the metal surface.

Based on the prism coupling measurement, two modes of configuration can be used in SPCE [4]. As shown in Figure 15.2, the fluorophores can be excited with light incident from either the prism side or the sample side. Through the prism, the incident light at SPR angle can induce the evanescent field and the oscillation of surface plasmons. The fluorophores within near field will be excited by the evanescent field. In this mode, the device is similar to SPR and called as Kretschmann (KR) configuration. On the other hand, the incident light can directly excite the fluorophores from the sample side and the dipoles in near field will couple to surface plasmons, inducing directional emission through the prism. This mode is called as reverse Kretschmann (RK) configuration. In the case of KR configuration, the excited field is enhanced greatly in a resonance with evanescent field [7], so the SPCE intensity will be much higher than that in RK configuration [8]. However, there are more available devices with RK configuration due to its simplicity [4]. For example, a light-emitting diode (LED) has been used in low-cost designs [9]. Collective efficiency can be further enhanced with the setup of a conical mirror around the prism, through which the total signals of the SPCE ring will be reflected into a point and be effectively collected [10]. A miniaturized device can be achieved through modifying the design of a spectrofluorometer [11]. Besides the prism coupling, the metallic grating can also induce the directional emission [12]. SPCE can also be used in chemiluminescence and electrochemiluminescence species [13, 14]. The directional emission has been

*corresponding author

Surface Plasmon Enhanced, Coupled and Controlled Fluorescence, First Edition. Edited by Chris D. Geddes.
© 2017 John Wiley & Sons, Inc. Published 2017 by John Wiley & Sons, Inc.

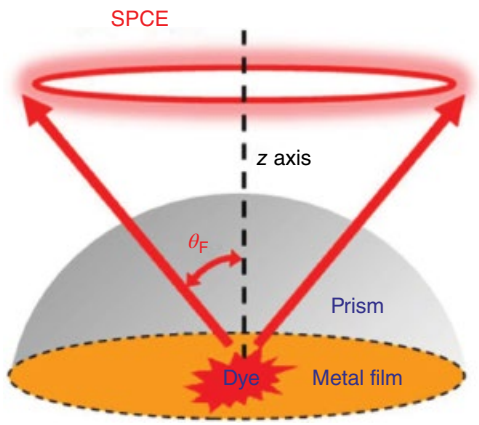

Figure 15.1 Scheme of SPCE.

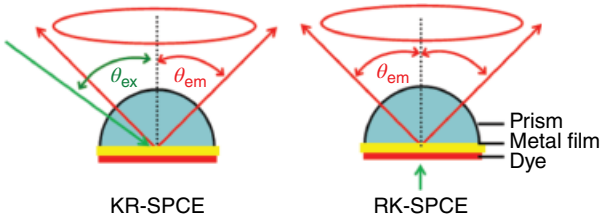

Figure 15.2 The excitation and emission of SPCE in KR and RK configuration.

observed as forms of phosphorescence and two-photon excited fluorescence as well [15, 16].

15.2 Properties of SPCE

The phenomena of SPCE are unique and have attracted more and more interests for recent years [17]. Here, we briefly summarize and analyze the properties of SPCE. Those potentially important for developing novel analytical methods will be especially concerned.

The directional emission is the most important and interesting characteristic of SPCE. It means the signals are almost all concentrated to one direction. Thus, signal collection can be conveniently achieved just with a detector in a defined direction, which brings a great significance in increasing sensitivity. A 50-fold increase is expected with the high collective efficiency compared to the isotropic spontaneous fluorescence. Besides, if KR configuration is used, 10- to 40-fold-enhanced excitation field should be additionally considered, resulting in an overall increased enhancement up to 1000-fold [4]. The remarkable enhancement in SPCE makes it possible to develop ultrasensitive fluorescence assays to monitor extremely low concentrations of analytes, which are significant in biochemistry and biomedical research. On the other hand, the directional emission angle θ_F is relevant to the dielectric properties of metal, the wavelength of fluorophores, and the refractive index of environment [18], which can therefore be an important parameter to monitor analysis systems.

The polarization of SPCE is the most convincing fact that proves the coupling with surface plasmons. As shown in Figure 15.3, for isotropic orientated fluorophore layer within about 100 nm, the SPCE signal is almost p-polarization, while free-space emission (FSE) displays similar intensities for both p- and s-polarization [19]. The characteristic of p-polarized emission provides an approach to identify the coupling of surface plasmons and to exclude the background scattering by a polarizer [1, 5]. The anisotropy emission has been theoretically and experimentally proven to be relative to the orientation of dipoles (the excited fluorophores) [20, 21]. The radiation of vertical dipoles standing up on the surface is pure p-polarized which can efficiently be used to excite surface plasmons. For the horizontal dipoles along surface, the radiation contains the components of both s- and p-polarized [22], but only p-polarized part is the resource of SPCE. As a result, an asymmetry of the SPCE cone will be observed when the dipoles are orientated horizontally [21]. In most cases, the orientation of dipoles is isotropic and the symmetrical SPCE cone can be observed.

The spectral dispersive property of SPCE shows that the angularity of the emission is dependent on the wavelength of the emitting specie, which provides the opportunity to design new approaches and apparatuses. It can be regarded as a format of wavelength resolution. The strong wavelength dependence of surface plasmon coupling at specific angles of observation offers a great potential to investigate complex systems. The mixture of monomer, dimer, and higher order aggregates of Rhodamine-6G has been resolved utilizing SPCE [23]. Fluorescence emissions from protonated, deprotonated, and excimer species of 8-hydroxy-1,3,6-pyrene trisulfonic acid coupling into surface plasmons have been easily separated and observed with 11–14-fold intensity enhancement [24]. Wavelengths are distinguished directly through angular separation without filters, which may be a promising design for miniaturized instruments with remarkable spectral resolution capabilities, meanwhile without the need of additional dispersive optics.

The coupling of SPCE is closely related to the distance between the fluorophore and the metal surface. Within 10 nm, the energy of fluorophores is transferred to metal surface as radiationless transition, so the quenching effect is dominant. While at distance longer than 500 nm, the interference between the far-field emission and its reflection dominates [25–27]. As a result, the appropriate distance for SPCE is

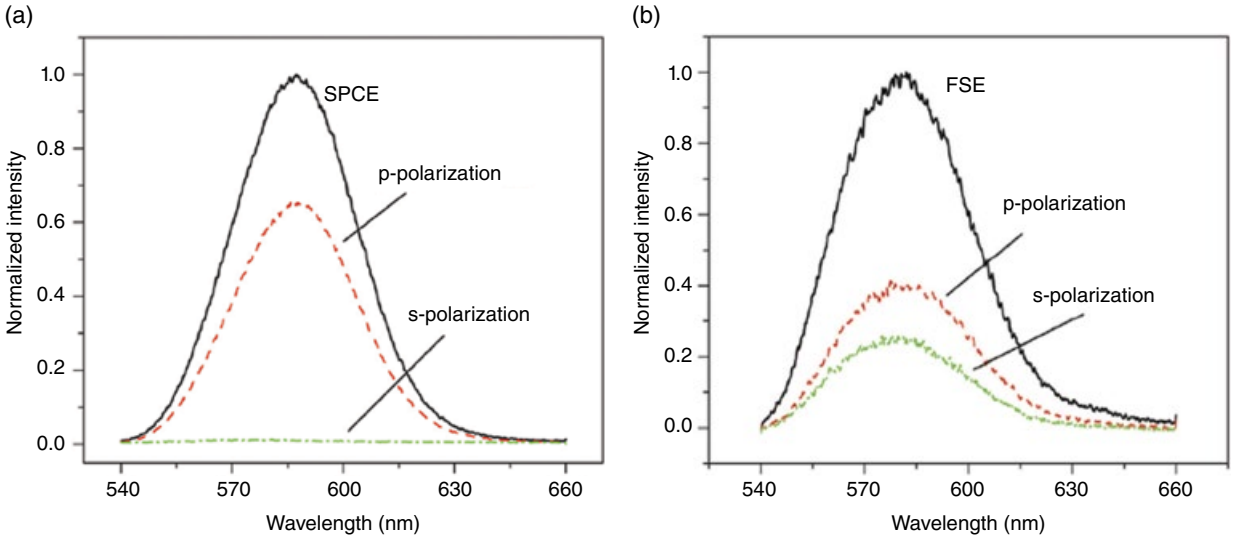

Figure 15.3 (a) SPCE and (b) FSE spectra with p- and s-polarization. Liu *et al*. [19]. Reproduced with the permission of Shanghai Institute of Oraganic Chemistry.

beyond the range of quenching, yet close enough to the surface, usually 20–200 nm, where the excited dipoles can couple to the surface plasmons radiating into the prism [4]. The coupling efficiency experiences a rapid increase with the increase of distance up to 50 nm, and it decreases dramatically over the distance of 200 nm [28, 29]. The maximum of the coupling efficiency can be expected at the optimized position. Because the generation of SPCE is from the interaction of fluorophores and nearby metal film, the signal more distant from the surface will not be produced. It suggests that SPCE presents an approach with the ability of spatial resolution to selectively detect analytes located in near field, and the interference from the bulk solution can be eliminated [5].

15.3 Current Developments of SPCE in Bioanalysis

The great demands for reliable and sensitive detection of various objects, especially biological entities of complexity, have fueled up the development of analytical research. Since SPCE has a potential to become a promising platform in the field of analytical chemistry and biochemistry, increased efforts have been made to enhance the capabilities for the applications. SPCE can be utilized in broad applications, such as nucleic acid, protein, and cell sensing. In this section, the strategies for improving the performance of SPCE are discussed. In this brief review, we will take more space to focus on our recent works as examples for illustration.

15.3.1 New Substrates Designing for Biochip

The generality of SPCE for kinds of fluorophores with different excitation and emission wavelengths is significant in facilitating the development of the technique platforms. Gold and silver are usually used as the films in SPR and SPCE, because their free electrons can form a coherent oscillation at the electromagnetic radiation, while the resonance of other metals with large imaginary part of dielectric constants will be depressed [30]. But the spectral range that gold and silver can be applied to is concentrated in the red spectral region and visible spectral region, respectively [18, 31], which limits the generality of the technique in some assays, such as the protein with fluorescence at ultraviolet. On the other hand, some metals including transition metals have also been proven exciting surface enhancement, though not very strong [32]. The investigations of various metals have been operated in search of a chance to enlarge the optical window where SPCE can be applied. Geddes *et al*. have summarized a general procedure for the selection of a metal thin film to be employed in applications of SPCE [33]. It has been reported that copper [34], aluminum [35], zinc [36, 37], iron [38–40], nickel [41], platinum [42], palladium [43], chromium [33], and rhodium [33] can be used in SPCE. It is worth noting that the whole spectral regions from ultraviolet to infrared can now have the corresponding selections of metal films to be employed. The enlarged optical window makes the approaches more available concerning the use of optional fluorophores, and alternative metals can therefore be expected. Besides, bimetallic chip has

emerged to enhance the SPCE signal by tailoring the metal film composition on the biochip surface.

Many efforts have been made to accelerate the applications of SPCE in biochip. The DNA hybridization was measured foremost between fluorophore-labeled DNA targets and surface-bound capture oligomers in SPCE [44]. If they were complementary, the fluorophore-labeled DNA oligomers localized near the metal surface after hybridization, and a dramatic increase in fluorescence could be observed. In contrast, the noncomplementary fluorophore-labeled DNA oligomers did not cause changes in SPCE. Another advantage of SPCE in DNA detection is the effective rejection of background coming from the molecules not binding to the surface. It is due to the distance-dependent coupling eliminating the emission from fluorphores more distant from surface. Immunoassay based on fluorescence is one important approach to highly sensitive detection of biomarkers through the specific recognition of antigens with antibodies. SPCE provides increased sensitivity and background rejection, enhancing the capability of detection in immunoassays [45]. In SPCE, the successful affinity assays have been reported in forms of direct and sandwich assays [46–48]. The protein interactions near the interface can be sensitively monitored with the coupling effect. Moreover, the protein layer on the interface can effectively act as a spacer because the average protein dimensions can be taken as a few nanometers, natively eliminating the quenching effect [49].

Some substrate designs have been explored to develop SPCE-based biochip. A microwave-accelerated SPCE strategy has been proposed through producing gold disks on glass slides or nanometer-thick equilateral triangles combined with continuous silver films, for fast and sensitive bioassays in buffer, serum, and whole blood [50–52]. Grating-based sensor chip has been achieved for SPR and SPCE dual-mode detection. SPCE has shown the capacity to complement the less sensitive SPR real-time measurements, and the dual-mode detection provides the potential to extend the dynamic range of assays on the same sensor chip [53]. Nanoprint lithography has been used to fabricate compact SPCE biochip with linear grating for in-coupling of excitation beam and concentric grating to focus out-coupling of SPCE. Efficient excitation and collection of fluorescence were implemented for biosensing in a model immunoassay experiment [54].

15.3.2 Optical Switch for Biosensing

In this section, a kind of SPCE-based switchable biosensors will be introduced, demonstrating the advantages of the unique SPCE properties in biosensing designs. Aptamers are single-stranded nucleic acids possessing unique binding characteristics to their targets. Numerous high-affinity and highly specific aptamers have been selected for a wide variety of target molecules including proteins. The configurations of aptamers are specific for the process of binding targets [55]. Considering the conformational changes in aptamers before and after binding proteins, which would cause distance changes in labeled fluorophores, the protein assays based on the distance-dependent coupling effect in SPCE can be expected. We designed a molecular beacon aptamer with fluorophore labeled on the end. In the absence of the target thrombin, the immobilized aptamer formed the stem, and thereby the fluorophore was brought in close proximity to the metal, resulting in the quenching of fluorescence and no signal was detected by SPCE. Upon thrombin binding, the distance between the fluorophore and the gold surface increased due to the conformational change in aptamer (Figure 15.4a) [56]. A detail that should be concerned is that sometimes the change in DNA conformation may not be large enough to extend from quenching zone to enhancement zone. In this case, the conformational change after binding target was just about 2 nm, while the quenching effect dominates around 5 nm near the surface. Therefore, we subtly designed a monomolecular layer of avidin to link the aptamer, warranting the labeled fluorophore placed on the critical zone between quenching and coupling. Consequently, a sensitive response was obtained after binding to target with the conformational change up to the enhancement zone totally. The fluorescence was sharply distributed at a direction, and the SPCE signal was about 6-fold greater than the spontaneous FSE with undesired scattering of light from the light source suppressed (Figure 15.4b and c). It proved that the combination of quenching and coupling for sensing purpose was effective and successful. The design is promising in developing efficient biosensors based on conformational-switching signaling aptamers.

For those charged molecules on metallic film, the electric field can be introduced to control the distribution or conformation of charged molecules near surface to satisfy the uniform and optimum coupling effect in SPCE assays. We proposed the concept of electric field-assisted SPCE (E-SPCE). We chose DNA, a negatively charged molecule, as a model with which to illustrate spatial coupling control in E-SPCE [57]. Hairpin DNA probes labeled with fluorescent dyes were attached to a gold surface, and then exposed to a solution of single-stranded DNA chains. If the strand has a sequence that matches the probe, the hairpin will be unfolded and form a twinned duplex that will position the fluorescent dyes a dozen nanometers

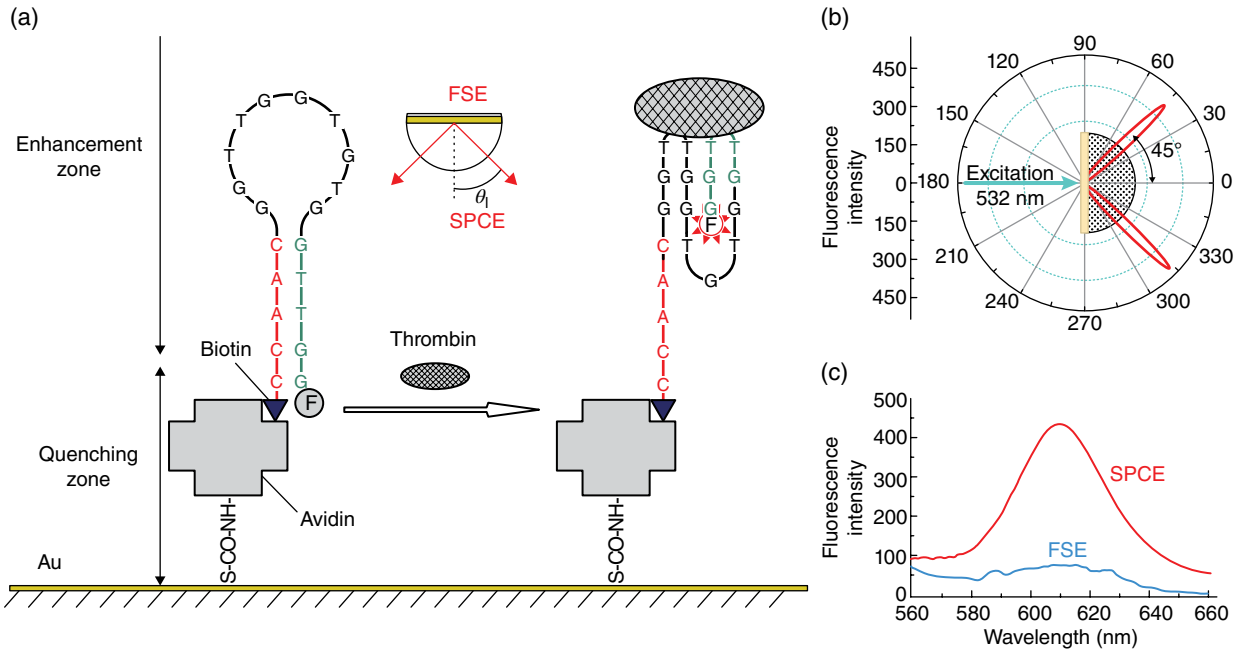

Figure 15.4 (a) The working principle of SPCE based on a conformational switching signaling aptamer. (b) The angular distribution of signaling aptamer after the addition of thrombin. (c) The spectra of SPCE and FSE after the addition of thrombin. Xie *et al.* [56]. Reproduced with the permission of Royal Society of Chemistry.

away from the surface. Therefore, the dyes should strongly interact with oscillating surface plasmons and radiate an amplified fluorescent signal. But, in practice, DNA duplexes anchored to the surface may form a slanted or random orientation, leading to the labeled fluorophores close to the surface, which limits the efficiency of enhancement and results in potential signal deviation with the unpredictable orientation. In addition, the duplex formation involving a single base mismatch may also enhance the fluorescence signal in SPCE, resulting in false positive detection (Figure 15.5a). In our work, we found that E-SPCE could be used to resolve the above problems effectively. With the assistance of appropriate negative potential, the hybrids with matched DNA stood straight up in a uniform way, ensuring all the labeled fluorophores locate in the enhancement zone to the largest extent. On the other hand, most fluorophores were still close to the surface in the mismatched situation, because the mismatched duplexes were less stable and the reaction was hindered at the repulsive potential (Figure 15.5a). As shown in Figure 15.5b and c, by actively modulating the conditions locally at interface with the synergistic effect of intelligently amplifying the right signal and suppressing the wrong signal, E-SPCE has shown a successful application in sensitive DNA sensing with high discriminatory capacity up to 20-fold for a single base mutation in a large concentration range.

In E-SPCE, it was observed that the matched signal was higher at more negative potential within the defined range, suggesting that the coupling efficiency was increased with the more perpendicular orientation of DNA layers. The signal was increased more for the longer DNA chain at the same potential, further confirming that the signal change was correlated to the conformation of DNA. Coupling efficiency increases with the labeled dyes departing from surface as DNA duplexes orientated perpendicularly at negative potential. Thus, larger conformation changes with longer chain produce higher signal responses in the distance-sensitive detection. On the other hand, we also proved the low fluorescence at positive potential with labeled DNA adsorbed to the metal surface. So the coupling efficiency can be controlled spatially by an active way, providing a good opportunity to make the manipulation of the nanometer-scale processes more accessible and detectable. This technique is easy to be applied to a variety of distance-sensitive surface assays. It has the potential to create a new generation of miniaturized high-performance sensing platforms, especially in chip-based microarray assays.

15.3.3 Full-Coupling Effect for Bioapplication

The coupling effect close to the metal surface is dramatically sensitive to the spatial position along the normal to the metal surface, which actually provides

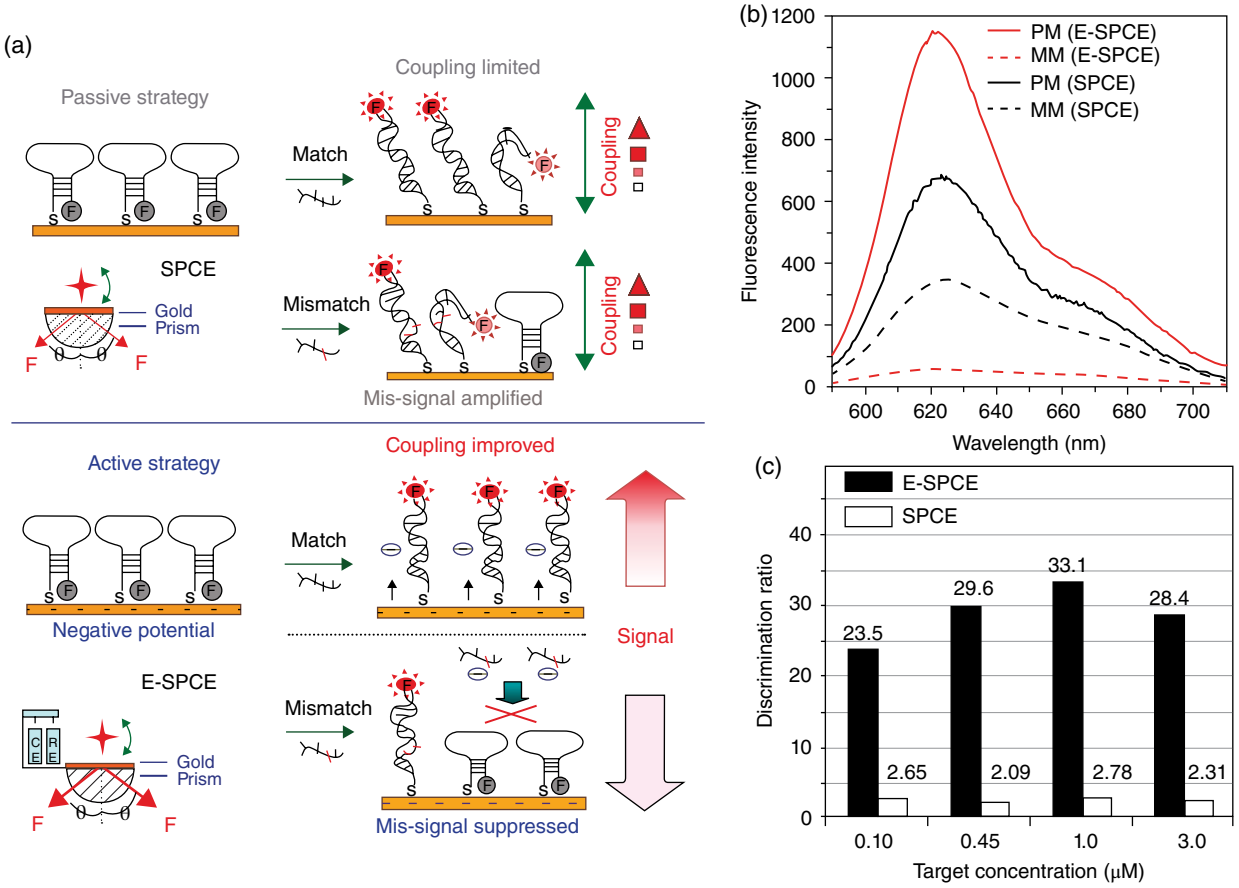

Figure 15.5 (a) The schematic of hairpin molecular beacon signaling match and mismatch in SPCE and E-SPCE. (b) SPCE and E-SPCE fluorescence spectra of DNA hairpin responding to 3.0-μM perfect matches (PM) and single base mismatches (MM). (c) Discrimination ratios with target concentrations ranging from 0.10 to 3.0-μM PM measured in SPCE and E-SPCE. Cao *et al.* [57]. Reproduced with the permission of American Chemical Society. (*See insert for color representation of this figure.*)

chances to develop distance-dependent sensing designs, but meanwhile induces huge challenges in quantitative detection due to the difficulty in ensuring the fluorophores under test uniformly distributed at the expected spatial position. Although numerous efforts have been made to restrict fluorophores at an optimal distance for strong coupling through various spacing layer controls, including Langmuir–Blodgett films [29], polymer [58], SiO_2 [59], and biomolecules [60], some intractable problems still remain. First, the optimized distance is an awkward compromise among the quenching, coupling, and spontaneous emission [61, 62]; consequently, this approach is unsuitable for a generalized platform, because delicate interfacial design must be redesigned once a new system is required. Second, the inconsistent label-to-metal distances caused by the variation of biomolecular orientations and conformations, and the inhomogeneity and roughness of the surface, lead to signal deviation [63]. Third, the coupling at a specific distance results in limited coupling effects because other distances in the coupling dominant region remain unused.

To meet the proposed challenges, we have recently proposed full-coupling SPCE, which not only can improve the utilization of the coupling effect but also can avoid distance fluctuation-induced signal deviation [64]. This concept was demonstrated by collecting the SPCE signal from the fluorescent silica nanoparticle (NP) with a size that matches the entire coupling region. Based on this design, the spatial distribution of the fluorophores was confined by the dimension of the NP. Therefore, these encapsulated fluorophores occupied the maximum coupling dominant region. As shown in Figure 15.6, we have made a comparison between the normal SPCE and the full-coupling SPCE with small fluorophores and fluorescent silica NPs as the labels, respectively. The separation distance between the labels and the metal surface was precisely modulated by adding polyelectrolyte layers, to simulate the distance changes which

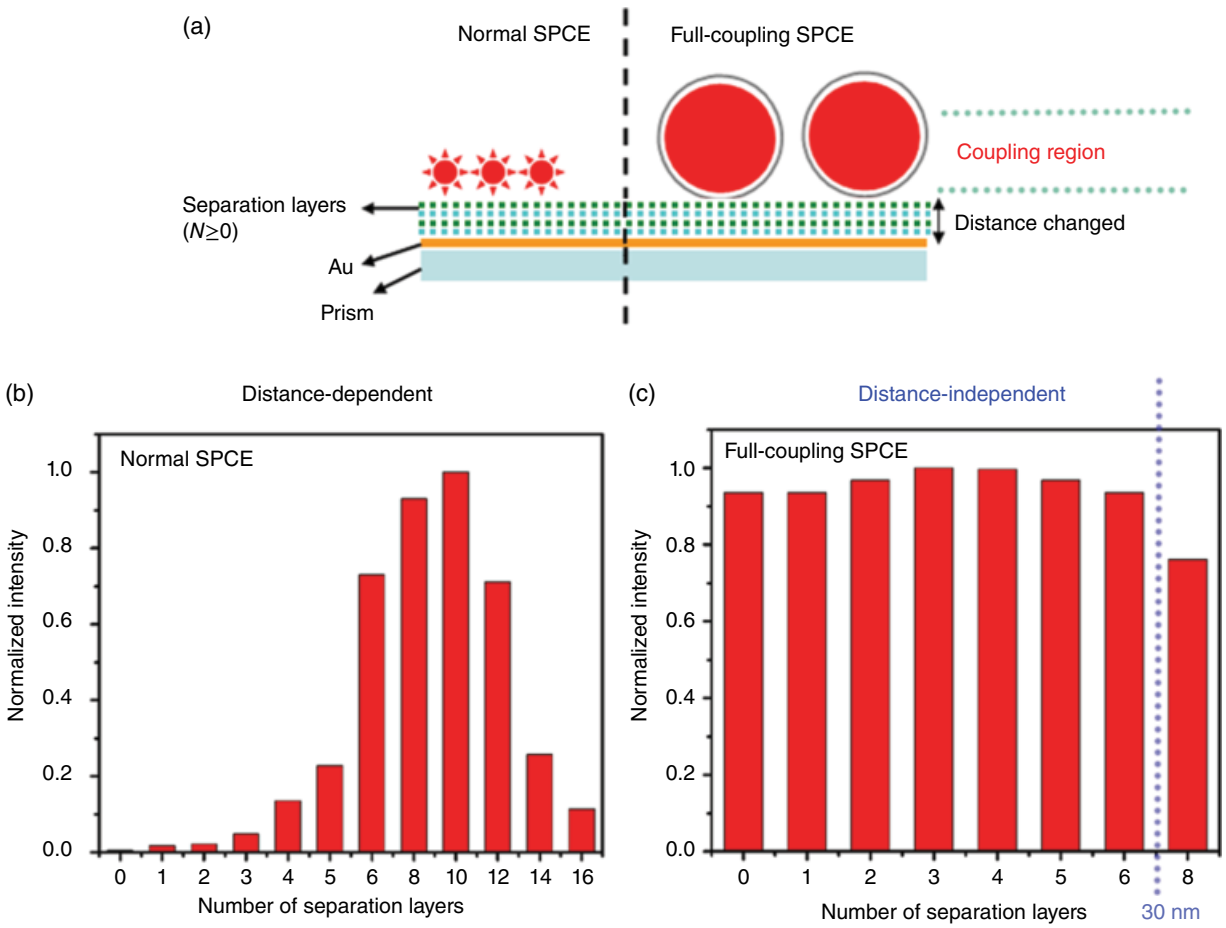

Figure 15.6 (a) Sketch of experiments for the evaluation of signal stability from normal and full-coupling SPCE in response to changing separation layers. (b and c) Normalized SPCE intensity of a monolayer of fluorescent molecules (normal SPCE) and dye-doped silica NPs (full-coupling SPCE) adsorbed on an Au film with increasing numbers of polyelectrolyte separation layers. (b) Normal SPCE. (c) Full-coupling SPCE. Cao *et al*. [64]. Reproduced with the permission of Elsevier.

may be caused by different orientations and conformations in biointeractions. The results showed that the normal SPCE intensity of monolayer fluorophores is critically distance-dependent with a drastic increase and then a decrease over a nanoscale distance range. On the contrary, in full-coupling SPCE, the enhanced fluorescence became nearly independent of distance at a range from 0 to 30 nm. This scale of distances is well suited for many biorecognition events. Therefore, full-coupling SPCE holds promise to solve signal deviation challenges originating from the inconsistent assignments of biomolecules on the nanoscale. As shown in Figure 15.7a and b, the direct immunoassay gives a lower signal and a less sensitive response compared to sandwich immunoassay in normal SPCE, whereas in the full-coupling SPCE, the increasing signal trend is very similar and the intensity is comparable for both immunoassays. It indicates that full-coupling SPCE reports binding events regardless of the immune formats and without loss of sensitivity. As a result, potential unpredicted and uncontrollable changes—such as a single protein's orientation and conformation—will not affect signal report. As shown in Figure 15.7c and d, the signal is sigmoidal versus DNA concentration in normal SPCE; however, the signal in full-coupling SPCE is very different with sustained growth until saturation assuming a Langmuir-type isotherm model. It has been proved that the signal trend in full-coupling SPCE is similar to the cases on glass chips, while the sigmoidal signal trend is related to the lying and standing of duplexs at different concentrations. We thus concluded that full-coupling SPCE readily responds to DNA hybridization with a highly coupled signal and without the interference from the divergence in the DNA conformations at the interface. Avoiding the need of a complicated and rigorous architecture for precise distance control, full-coupling SPCE offers a great promise for a general platform of chip-based biosensing and bioanalysis.

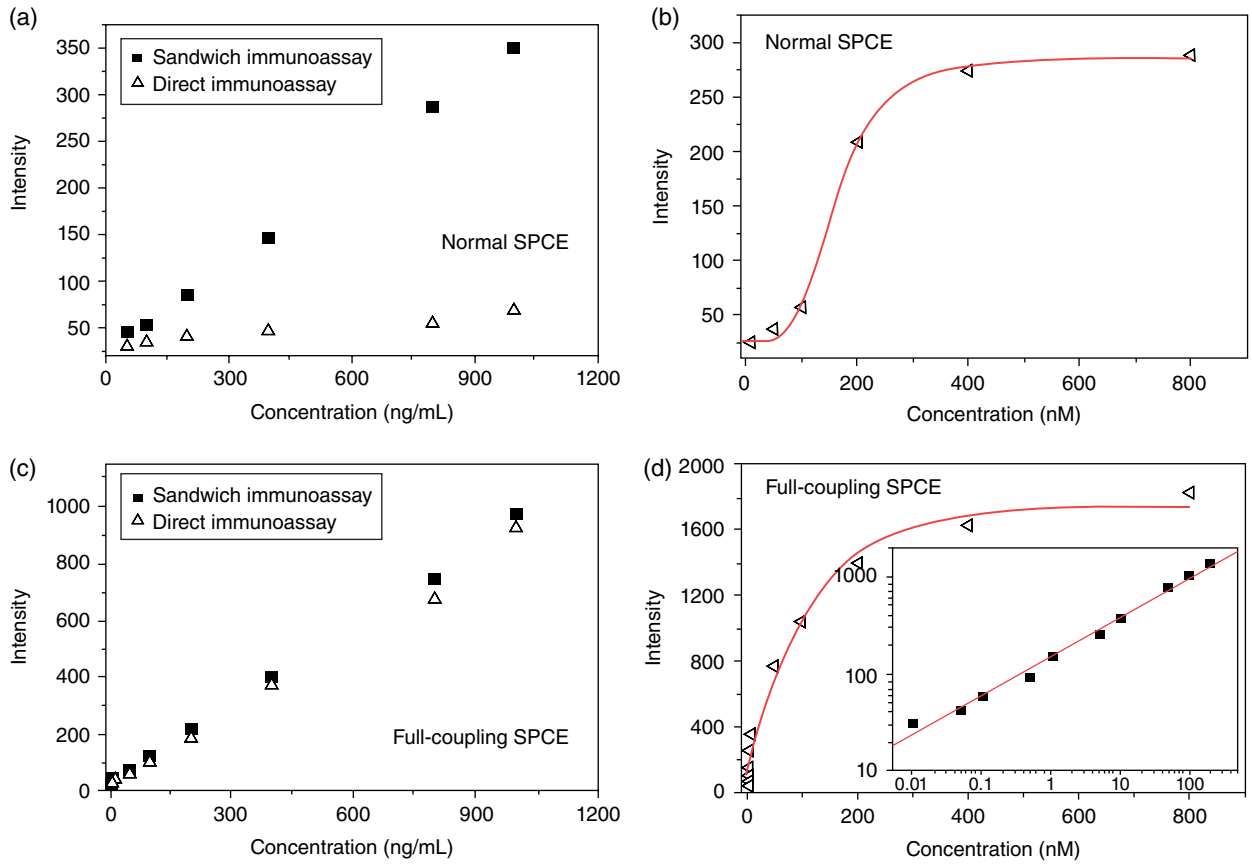

Figure 15.7 (a) Normal and (b) full-coupling SPCE signal response with increasing antigen concentration in sandwich immunoassay (square) and direct immunoassay (triangle). (c) Normal and (d) full-coupling SPCE signal response with increasing DNA target concentration. Cao *et al*. [64]. Reproduced with the permission of Elsevier.

15.3.4 Hot-Spot Nanostructure-Based Biosensor

To further improve the sensing ability of SPCE, plasmonic nanostructures have been expected to be introduced in SPCE platform [65, 66]. A remarkable plasmonic coupling effect has been reported to occur in the nanometer interstices between metallic nanostructures termed as "hot-spot," which has attracted much attention in the area of surface-enhanced spectroscopy [67, 68]. In our recent work, we have proposed a novel SPCE sensing approach with the assistance of hot-spot nanostructure, which can be achieved through the manipulation of plasmonic assembly [69, 70]. In our design, a hot-spot nanostructure of nanoparticle (NP)-dye-film was constructed, with the attachment of metallic NPs to the fluorophores-modified smooth metallic film. The typical results were shown in Figure 15.8. We surprisedly found that the already quenched fluorophores located in the quenching zone of the metallic film were turned on by assembling NPs on the film (Figure 15.10a). We called this special phenomenon as a "dequenching" process. The dequenched signal was distributed at a direction through a prism introduced beneath the film, and the emission was demonstrated to be highly p-polarized (Figure 15.8b and c). As a result, the dequenched signal should be due to SPCE because only a defined angle and p-polarized emission can satisfy the necessary match of plasmon wave vectors. Finite-difference time-domain (FDTD) calculation displayed that the electromagnetic field in the NP–film structure can be dramatically increased compared to that in the individual NP or film. It has been proved that the emission rate has the potential to surpass the nonradiative decay rate at a close emitter–metal spacing, with the emitter radiation coupled to radiative modes [72]. An enhanced electromagnetic field, a net increase in emission efficiency, and an improved collective efficiency from directional radiation contribute to the strong plasmonic coupling emission after the assembly of NPs on the fluorophores-modified film.

Considering that the plasmonic assembly can be realized through the mediation of biorecognition events, we have developed a biosensing approach based on

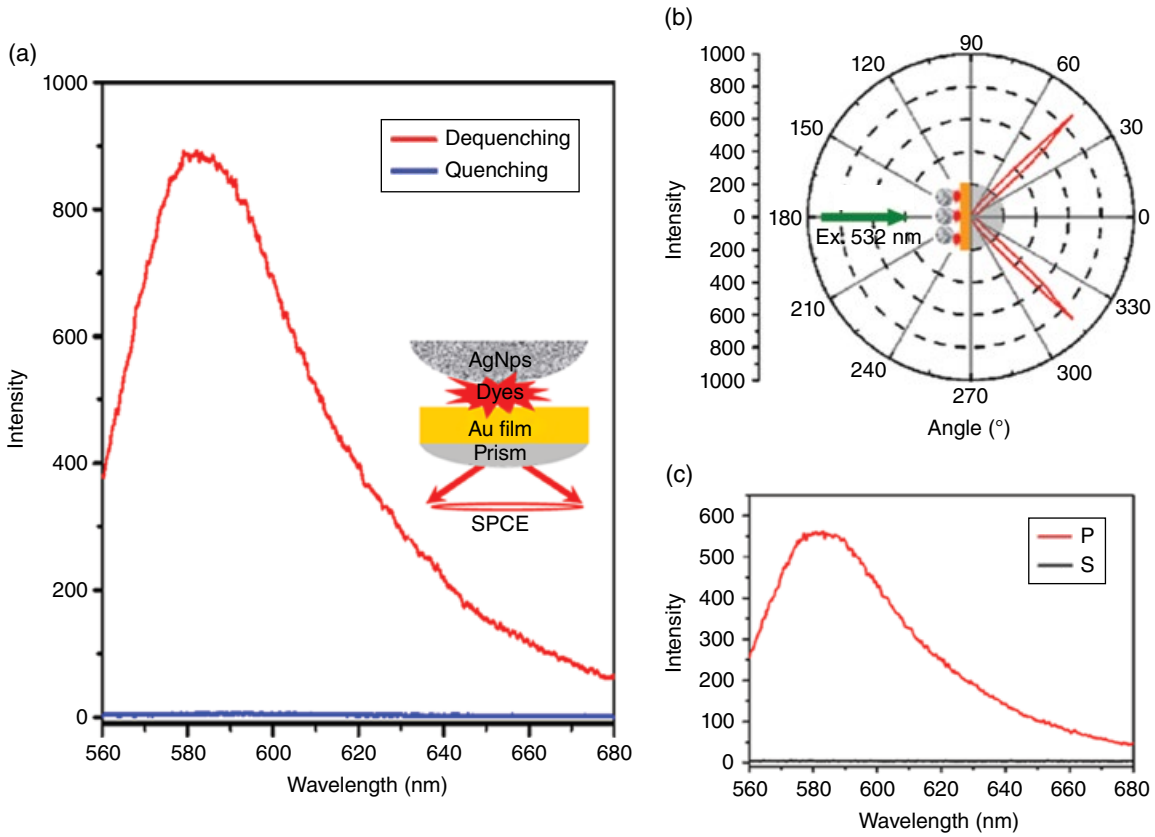

Figure 15.8 (a) SPCE spectra of quenched and dequenched fluorophores. Inset: schematic illustration of dequenched SPCE. (b) Angle distribution of dequenched SPCE. (c) Polarized emission of dequenched SPCE. Cao *et al.* [69]. Reproduced with the permission of Royal Society of Chemistry.

the plasmonic assembly-induced SPCE [70]. Because of the unique properties of SPCE, detectable signal was still found when the gap distances of the NP film were tuned from nanometers to tens of nanometers, in a scale comparable to the size of biomolecules; the assembly of nanostructures through biomolecular binding events (e.g., immunoassay) thus should enable the effective measurement of SPCE for biomarker sensing. In this design, the fluorophores are directly modified on the metal surface, avoiding the intricate operation in labeling fluorophores to biomolecules; a signal-on sensing strategy benefits the effective signal identification through quenching and dequenching fluorescence. It still should be worthy of noting that the SPCE signal shows a trend of rapid decrease as the gap distance increases; as a result, it is of importance to utilize hot-spot with a small gap to improve enhancement capacity. Based on a reasonable interfacial design, we have proposed an ultrathin sensing linker fabricated by a simple electrostatic assembly of one cationic polymer layer and one aptamer layer. The distribution of surface charge in the ultrathin linker would be manipulated by the target sensing to mediate the hot-spot formation with a gap <2 nm. It smartly blocked the adsorption of negatively charged NPs in the absence of targets and actively captured NPs in the presence of targets; the ultrastrong SPCE signal was thus produced to sense target protein. Both the biomolecules and the NPs were completely label free during the sensing processes, ensuring the facility and reliability of the method.

15.3.5 Imaging Apparatus for High-Throughput Detection

The attractive characteristics of SPCE with high collection efficiency and low background play important roles in optical imaging. There have been increased interests in combining the imaging technique with SPCE. The optical imaging based on SPCE will integrate the effects of near-field coupling and the information from microcosmic observation, creating new opportunities to investigate biological issues in a visual way. With the aid of SPCE microscopy, the imaging of muscle fibrils was observed, and the dynamics of interaction between actin and myosin cross-bridges was studied

[73, 74]. The quality of SPCE image was superior to conventional epi-illumination (including total internal reflection fluorescence and epifluorescence excitation). With the background suppression and the selective excitation in near field, the detection zone can be focused only on the motion of 12 actin promoters in a muscle filament. In SPCE, the detection volume is a product of evanescent wave penetration depth and distance-dependent coupling, so 1–2 aL minimized detection volume can be expected supposing 50-nm effective coupling depth and 200-nm lateral diffraction limit [75]. A transparent paraboloid polymer elements coated with thin metal layer was used with the cooperation of the annular aperture to ensure the defined excitation and the selective observation of SPCE through KR configuration in inverted microscopic system, which can be performed as arrays on biochip [76]. However, in those works, a high numerical aperture objective or a paraboloid element is generally involved. Such objective-based SPCE imaging systems are complicated and expensive, while the collective field of vision will be limited.

To improve the feasibility of SPCE technique in imaging research, we propose a prism-based SPCE imaging system in RK configuration [77]. As shown in Figure 15.11a, the laboratory-built setup is composed of a collimation and beam expanding module, an angle-resolution module and a detection module. The excitation light turned into a parallel beam through a spatial filter and a lens in sequence; an attenuator and a diaphragm were positioned on the input path to obtain a rectangular spot, which is uniformly illuminating on the sample surface. A dye-doped microarray chip was investigated in this imaging system, demonstrating its merits of parallelism and multiplexing in high-throughput detection (Figure 15.9b). An angle-scanning detection through the imaging captured by a

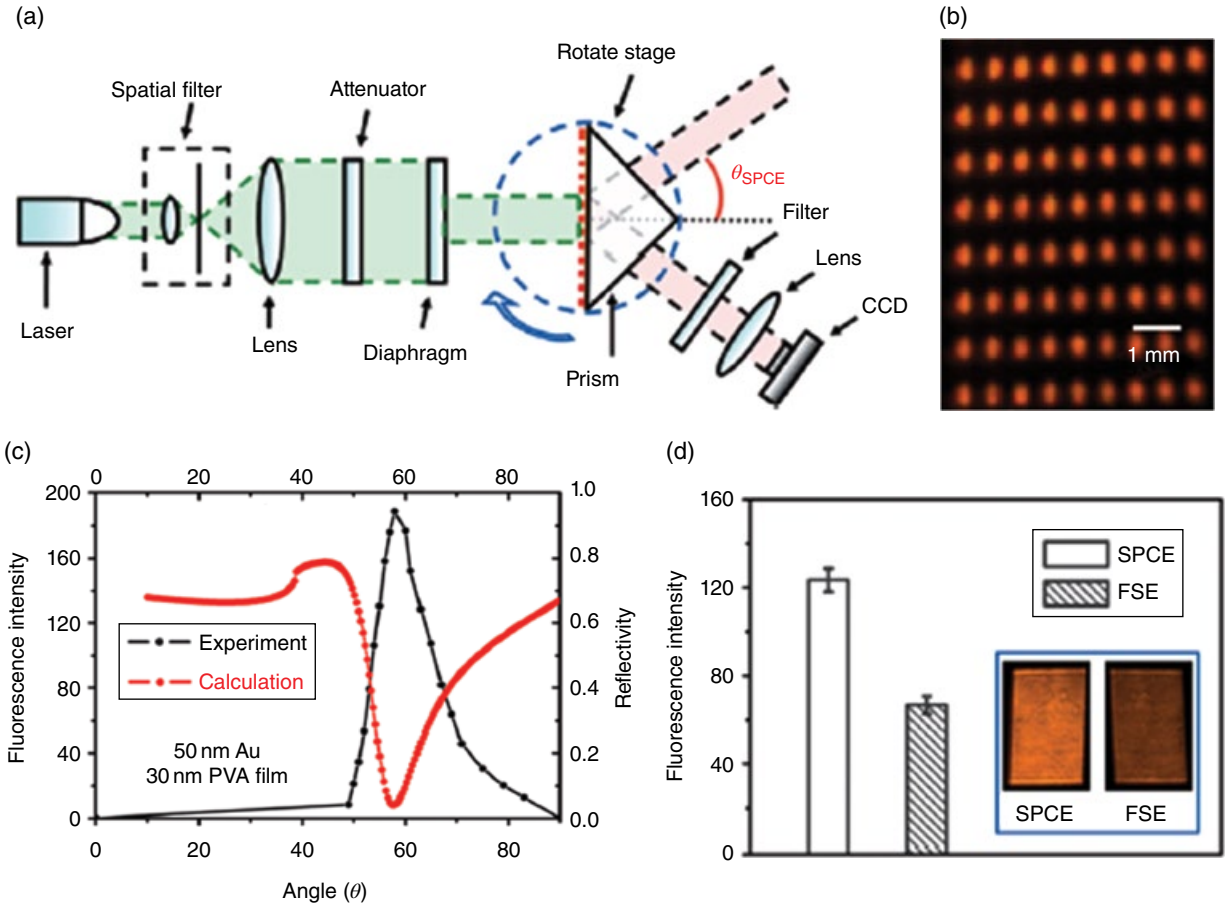

Figure 15.9 (a) The schematic of the prism-based RK configuration of the SPCE imaging apparatus. (b) Typical SPCE images of the fluorescent microarray on the gold surface. (c) Simulated SPR reflectivity (gray dotted line) and experimental SPCE imaging intensity (black dotted line) angular scans. (d) SPCE and FSE intensities from images of dye-doped film on gold surface. Cai *et al.* [77]. Reproduced with the permission of John Wiley & Sons.

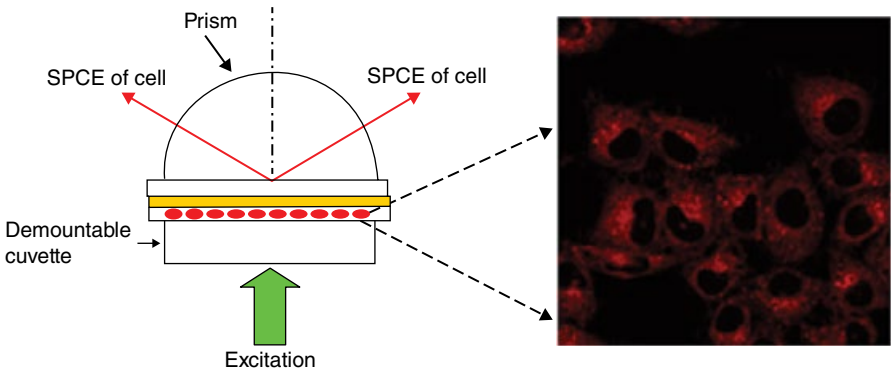

Figure 15.10 The schematic of dye-labeled cells detected by SPCE configuration. Liu *et al*. [71]. Reproduced with the permission of American Chemical Society.

CCD camera presents the signal sharply concentrated to one direction; it agrees well with the corresponding SPR angle through reflectivity simulation (Figure 15.9c). The image of SPCE is obviously much brighter than that of FSE, with the image intensity increased by a 2-fold factor (Figure 15.9d). Compared to the objective-based imaging, where sequential scanning and reconstruction are needed for sample spots in the hundreds-of-microns scale, and paraboloid element-based imaging, where complicated structures are fabricated, our design of prism-based SPCE imaging takes the advantages of low cost, convenient operation and rapid detection, which can detect a mass of arrays simultaneously through capturing a whole image of the microarray sample.

15.3.6 Waveguide Mode SPCE to Widen Detection Region

When referring to the situation with dielectric thickness thicker than 100 nm, the phenomena seem to be more complex. More than one emission ring can be observed in SPCE at one wavelength. That means the emission direction is no longer only one in the case. The polarization and the intensity will show subverted properties, where high directional signal with s-polarized can be observed and the polarization is alternating for rings with different dielectric fluorophore layer thickness [78]. These effects origin from additional surface plasmon modes existed on the metal surface [79]. Considering the thickness of dielectric film comparable to the wavelength, it is possible to have admittance to reverse the phase shift of s-polarized to fit the mode of waveguide [80, 81] or the waveguide can be coupled to plasmon resonance [82]. The multiplex polarization is distinct and is valuable as an obvious analytical parameter to indicate dielectric properties.

In a recent study, we investigated the SPCE properties of fluorophore-labeled micrometer-scale cells [71]. As shown in Figure 15.10, the whole cell was illuminated directly by incident light under RK-SPCE system. We observed that the coupling distance of SPCE can be extended from nanoscale to micrometer scale, due to the presence of plasmon waveguide resonance mode. More than a surface technique, SPCE can thus be used to investigate bulk analytes with the assistance of waveguide. In this work, different subregions of cells, including membrane, cytoplasm, and nucleus, were specifically labeled with fluorophores for SPCE studies. We designed a cell density assay to control the cell thickness and fabricated a series of polymer films in micrometer scale onto metallic film to mimic micrometer-scale samples. The results showed that the SPCE signals were always partially p-polarized and the emission direction maintained unchanged when micrometer-scale samples were measured. We studied the SPCE properties of cell samples on Au, Al, and Ni substrates to check the impact of metallic substrates (Figure 15.11). Compared to Au and Ni substrates, Al substrate presented better performances in polarization and angle distribution. The intensity of the cell samples on Al substrate was comparable to that on Ni substrate, while several folds higher than that on Au substrate. These results demonstrate that the Al substrate can be an optimal choice for SPCE study of cells with micrometer-scale thickness. The real-time detection of the cell labeling process was achieved by monitoring SPCE intensity on Al substrate, indicating the feasibility of SPCE in the observation of cell events. Surface plasmon waveguide-coupled emission technique may be used to study biomolecule interactions inside the cell and provide a promising 3D tool for cell biology.

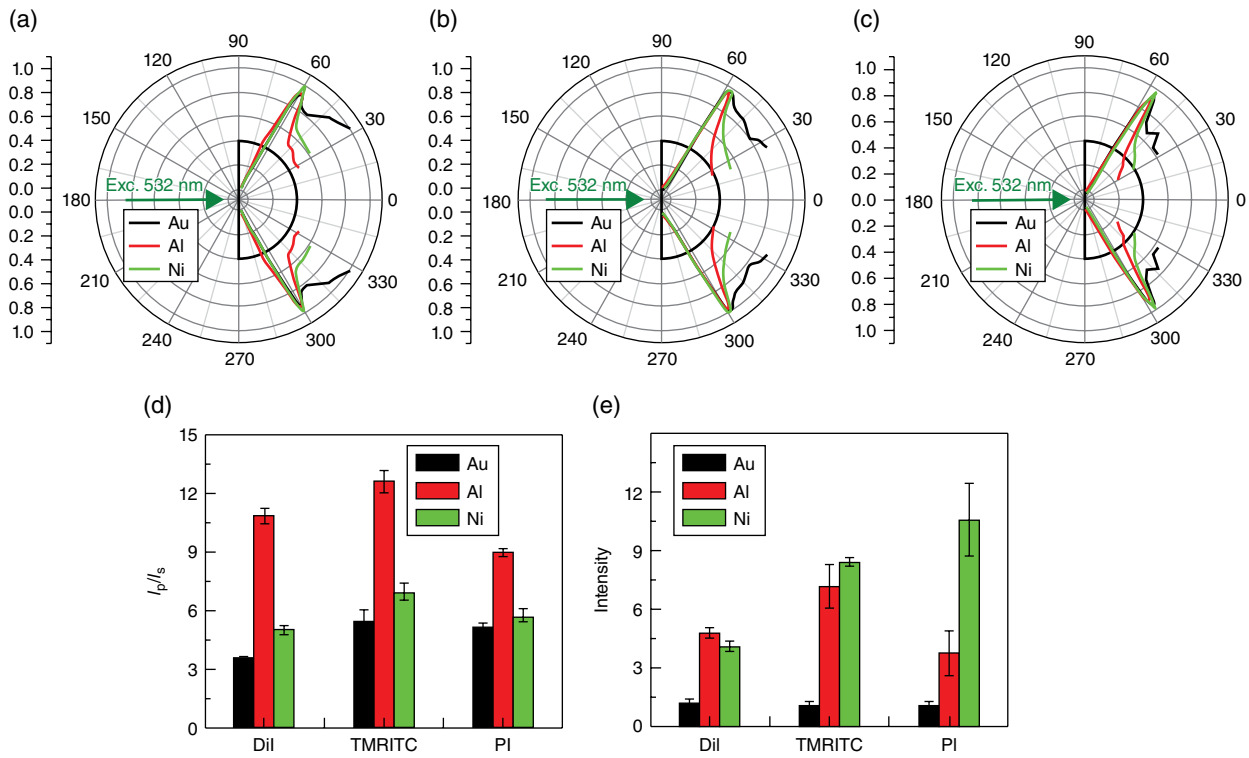

Figure 15.11 Comparison of angle distributions of cells labeled with (a) DiI, (b) TMRITC, and (c) PI on Au (black line), Al (gray line), and Ni (light gray line) substrates. (d) Polarization factor and (e) intensity of cells labeled by 1,1′-Dioctadecyl-3,3,3′,3′-tetramethylindocarbocyanine perchlorate (DiI), Rhodamine B isothiocyanate (TMRITC), and propidium iodide (PI) on Au, Al, and Ni substrates, respectively. The intensity of samples on Al and Ni substrates was normalized to that on Au substrates. Liu *et al.* [71]. Reproduced with the permission of American Chemical Society.

15.4 Perspectives

The combination of fluorescence with SPR has resulted in a paradigm shift for both techniques. There is a steady growth in terms of instruments, devices, and sensors based on SPCE. The processes described for fluorescence emission are readily applicable to other sources of molecular luminescence, such as phosphorescence, chemiluminescence, and electrochemiluminescence. The optical geometry of SPCE also attracts attentions from large scopes. For example, stimulated emission has been investigated in the similar device for potential laser design [83], and enhanced scanning tunneling microscopic light emission has been obtained through the prism at a defined angle [84]. The directional surface-enhanced Raman scattering has been observed [85, 86]; and we have recently demonstrated that the directional Raman scattering can be realized through RK excitation [86]. SPCE creates the platform for the intensive investigation of nanoscale optical properties via plasmon coupling.

However, it is worth noting the complexity of fluorophore–metal interactions, which involves both near- and far-field effects. The coupling between fluorophores and nanostructures with complex geometry is lacking of enough understanding [6, 87]. As a result, it still represents a largely virgin scientific terrain, demanding arduous exploring both in fundamentals and applications. The combination of different optical modes, such as waveguide mode, to SPCE should offer new opportunities for bioscience with the potential to control emission features and extend probing regions. The introduction of novel nanomaterials, nanostructures, and nanooptical devices into SPCE with the active control approach would further modulate SPCE and improve the analytical merits of SPCE, expediting the design of sensors with flexibility and high performance. We have recently observed an enhanced SPCE signal by combining pulse magnetic field with SPCE. As a noninvasive visual technique, SPCE-based imaging will be an emerging tendency; integrating the unique properties of directional emission and microarray imaging, it provides a useful tool to reduce crosstalk interference and to improve the imaging quality. Taking the advantages of the symmetrical distribution of directional emission, we have recently accelerated the process in building up a multichannel optical system to directly capture SPCE through different detectors for realizing simultaneous measurements

of multiplex signals. It is no doubt that the development of SPCE platforms will redound to the field of chip-based biomolecular detection and significantly further the progress in analytical researches for life sciences.

Acknowledgments

Financial supports from the National Science Foundation of China (grant nos. 21375111 and 21127005), the 973 Program of China (2013CB933703), the funds of the Ministry of Education of China (grant no. 20110121110011, PCSIRTIRT13036) are greatly acknowledged.

References

1 Lakowicz JR, Malicka J, Gryczynski I, Gryczynski Z (**2003**) Directional surface plasmon-coupled emission: a new method for high sensitivity detection. *Biochem. Biophys. Res. Commun. 307*: 435–439.
2 Lakowicz JR (**2005**) Radiative decay engineering 5: metal-enhanced fluorescence and plasmon emission. *Anal. Biochem. 337*: 171–194.
3 Geddes CD, Gryczynski I, Malicka J, Gryczynski Z, Lakowicz JR (**2004**) Directional surface plasmon coupled emission. *J. Fluoresc. 14*: 119–123.
4 Lakowicz JR (**2004**) Radiative decay engineering 3. Surface plasmon-coupled directional emission. *Anal. Biochem. 324*: 153–169.
5 Gryczynski I, Malicka J, Gryczynski Z, Lakowicz JR (**2004**) Radiative decay engineering 4. Experimental studies of surface plasmon-coupled directional emission. *Anal. Biochem. 324*: 170–182.
6 Lakowicz JR, Ray K, Chowdhury M, Szmacinski H, Fu Y, Zhang J, Nowaczyk K (**2008**) Plasmon-controlled fluorescence: a new paradigm in fluorescence spectroscopy. *Analyst 133*: 1308–1346.
7 Neumann T, Johansson ML, Kambhampati D, Knoll W (**2002**) Surface-plasmon fluorescence spectroscopy. *Adv. Funct. Mater. 12*: 575–586.
8 Joanna Malicka IG, Gryczynski Z and Lakowicz Joseph R. (**2004**) Use of surface plasmon-coupled emission to measure DNA hybridization. *J. Biomol. Screen. 9*: 208–215.
9 Smith DS, Kostov Y, Rao G, Gryczynski I, Malicka J, Gryczynski Z, Lakowicz JR (**2005**) First observation of surface plasmon-coupled emission due to LED excitation. *J. Fluoresc. 15*: 895–900.
10 Smith DS, Kostov Y, Rao G (**2008**) Signal enhancement of surface plasmon-coupled directional emission by a conical mirror. *Appl. Opt. 47*:5229–5234.
11 Li YQ, Xie TT, Cai WP (**2009**) Surface plasmon coupled fluorescence detection device. Patent. CN ZL200910111882.8.
12 Hung YJ, Smolyaninov II, Davis CC, Wu HC (**2006**) Fluorescence enhancement by surface gratings. *Opt. Express 14*: 10825–10830.
13 Chowdhury MH, Malyn SN, Aslan K, Lakowicz JR, Geddes CD (**2007**) First observation of surface plasmon-coupled chemiluminescence (SPCC). *Chem. Phys. Lett. 435*: 114–118.
14 Zhang J, Gryczynski Z, Lakowicz JR (**2004**) First observation of surface plasmon-coupled electrochemiluminescence. *Chem. Phys. Lett. 393*: 483–487.
15 Previte MJR, Aslan K, Zhang YX, Geddes CD (**2006**) Surface plasmon coupled phosphorescence (SPCP). *Chem. Phys. Lett. 432*: 610–615.
16 Gryczynski I, Malicka J, Lakowicz JR, Goldys EM, Calander N, Gryczynski Z (**2005**) Directional two-photon induced surface plasmon-coupled emission. *Thin Solid Films 491*: 173–176.
17 Mondal PP, Gilbert RJ, So PTC (**2008**) Plasmon enhanced fluorescence microscopy below quantum noise limit with reduced photobleaching effect. *Appl. Phys. Lett. 93*: 093901.
18 Gryczynski I, Malicka J, Gryczynski Z, Lakowicz JR (**2004**) Surface plasmon-coupled emission with gold films. *J. Phys. Chem. B 108*: 12568–12574.
19 Liu XQ, Liu Q, Xie KX, Cao SH, Cai WP, Li YQ (**2012**) Surface plasmon-coupled emission of multicolor quantum dots. *Acta Chim. Sin. 70*: 2220–2225.
20 Calander N (**2004**) Theory and simulation of surface plasmon-coupled directional emission from fluorophores at planar structures. *Anal. Chem. 76*: 2168–2173.
21 Hiep HM, Fujii M, Hayashi S (**2007**) Effects of molecular orientation on surface-plasmon-coupled emission patterns. *Appl. Phys. Lett. 91*: 183110.
22 Penninck L, Mladenowski S, Neyts K (**2010**) The effects of planar metallic interfaces on the radiation of nearby electrical dipoles. *J. Opt. 12*: 075001.
23 Sathish S, Kostov Y, Rao G (**2009**) High-resolution surface plasmon coupled resonant filter for monitoring of fluorescence emission from molecular multiplexes. *Appl. Phys. Lett. 94*: 223113.
24 Sathish RS, Kostov Y, Rao G (**2009**) Spectral resolution of molecular ensembles under ambient conditions using surface plasmon coupled fluorescence emission. *Appl. Opt. 48*: 5348–535.
25 Barnes WL (**1998**) Fluorescence near interfaces: the role of photonic mode density. *J. Mod. Opt. 45*: 661–699.
26 Hellen EH, Axelrod D (**1987**) Fluorescence emission at dielectric and metal-film interfaces. *J. Opt. Soc. Am. B 4*: 337–350.

27 Weber WH, Eagen CF (**1979**) Energy transfer from an excited dye molecule to the surface plasmons of an adjacent metal. *Opt. Lett. 4*: 236–238.

28 Ford GW, Weber WH (**1984**) Electromagnetic interactions of molecules with metal surfaces. *Phys. Rep. 113*: 195–287.

29 Ray K, Szmacinski H, Enderlein J, Lakowicz JR (**2007**) Distance dependence of surface plasmon-coupled emission observed using Langmuir–Blodgett films. *Appl. Phys. Lett. 90*: 251116.

30 Willets KA, Van Duyne RP (**2007**) Localized surface plasmon resonance spectroscopy and sensing. *Annu. Rev. Phys. Chem. 58*: 267–297.

31 Sun YG, Xia YN (**2003**) Gold and silver nanoparticles: a class of chromophores with colors tunable in the range from 400 to 750 nm. *Analyst 128*: 686–691.

32 Tian ZQ, Ren B, Li JF, Yang ZL (**2007**) Expanding generality of surface-enhanced Raman spectroscopy with borrowing SERS activity strategy. *Chem. Commun. 43*: 3514–3534.

33 Aslan K, Geddes CD (**2009**) Directional surface plasmon coupled luminescence for analytical sensing applications: which metal, what wavelength, what observation angle? *Anal. Chem. 81*: 6913–6922.

34 Previte MJR, Zhang YX, Aslan K, Geddes CD (**2007**) Surface plasmon coupled fluorescence from copper substrates. *Appl. Phys. Lett. 91*: 151902.

35 Gryczynski I, Malicka J, Gryczynski Z, Nowaczyk K, Lakowicz JR (**2004**) Ultraviolet surface plasmon-coupled emission using thin aluminum films. *Anal. Chem. 76*: 4076–4081.

36 Asian K, Previte MJR, Zhang YX, Geddes CD (**2008**) Surface plasmon coupled fluorescence in the ultraviolet and visible spectral regions using zinc thin films. *Anal. Chem. 80*: 7304–7312.

37 Aslan K, Geddes CD (**2009**) Surface plasmon coupled chemiluminescence from zinc substrates: directional chemiluminescence. *Appl. Phys. Lett. 94*: 073104.

38 Cao SH, Xie TT, Cai WP, Li YQ (**2010**) Observation of surface plasmon-coupled directional fluorescence using thin iron films. *Chem. J. Chin. Univ. 31*: 61–63.

39 Aslan K, Weisenberg M, Hortle E, Geddes CD (**2009**) Surface plasmon coupled chemiluminescence from iron thin films: directional and approaching fixed angle observation. *J. Appl. Phys. 106*: 014131.

40 Aslan K, Zhang YX, Geddes CD (**2009**) Directional, broad, and fixed angle surface plasmon coupled fluorescence from iron thin films. *J. Phys. Chem. C 113*: 20535–20538.

41 Aslan K, Zhang YX, Geddes CD (**2009**) Surface plasmon coupled fluorescence in the visible to near-infrared spectral regions using thin nickel films: application to whole blood assays. *Anal. Chem. 81*: 3801–3808.

42 Ray K, Chowdhury MH, Lakowicz JR (**2008**) Observation of surface plasmon-coupled emission using thin platinum films. *Chem. Phys. Lett. 465*: 92–95.

43 Aslan K, Weisenberg M, Hortle E, Geddes CD (**2009**) Fixed-angle observation of surface plasmon coupled chemiluminescence from palladium thin films. *Appl. Phys. Lett. 95*: 123117.

44 Malicka J, Gryczynski I, Gryczynski Z, Lakowicz JR (**2003**) DNA hybridization using surface plasmon-coupled emission. *Anal. Chem. 75*: 6629–6633.

45 Lakowicz JR, Malicka J, Matveeva E, Gryczynski I, Gryczynski Z (**2005**) Plasmonic technology: novel approach to ultrasensitive immunoassays. *Clin. Chem. 51*: 1914–1922.

46 Matveeva E, Gryczynski Z, Gryczynski I, Lakowicz JR (**2004**) Immunoassays based on directional surface plasmon-coupled emission. *J. Immunol. Methods 286*: 133–140.

47 Matveeva E, Gryczynski Z, Gryczynski I, Malicka J, Lakowicz JR (**2004**) Myoglobin immunoassay utilizing directional surface plasmon-coupled emission. *Anal. Chem. 76*: 6287–6292.

48 Jin LH, Li SM, Cho YH (**2012**) Enhanced detection sensitivity of pegylated CdSe/ZnS quantum dots-based prostate cancer biomarkers by surface plasmon-coupled emission. *Biosens. Bioelectron. 33*: 284–287.

49 Yuk JS, McDonagh C, MacCraith BD (**2010**) Demonstration of a surface plasmon-coupled emission (SPCE)-based immunoassay in the absence of a spacer layer. *Anal. Bioanal. Chem. 398*: 1947–1954.

50 Aslan K, Malyn SN, Geddes CD (**2007**) Microwave-accelerated surface plasmon-coupled directional luminescence: application to fast and sensitive assays in buffer, human serum and whole blood. *J. Immunol. Methods 323*: 55–64.

51 Aslan K, Previte MJR, Zhang Y, Geddes CD (**2008**) Microwave-accelerated surface plasmon-coupled directional luminescence 2: a platform technology for ultra fast and sensitive target DNA detection in whole blood. *J. Immunol. Methods 331*: 103–113.

52 Previte MJR, Geddes CD (**2007**) Microwave-triggered surface plasmon coupled chemiluminescence. *J. Am. Chem. Soc. 129*: 9850–9851.

53 Yuk JS, Guignon EF, Lynes MA (**2013**) Highly sensitive grating coupler-based surface plasmon-coupled emission (SPCE) biosensor for immunoassay. *Analyst 138*: 2576–2582.

54 Toma K, Vala M, Adam P, Homola J, Knoll W, Dostalek J (**2013**) Compact surface plasmon-enhanced fluorescence biochip. *Opt. Express 21*: 10121–10132.

55 Cho EJ, Lee JW, Ellington AD (**2009**) Applications of aptamers as sensors. *Annu. Rev. Anal. Chem. 2*: 241–264.

56 Xie TT, Liu Q, Cai WP, Chen Z, Li YQ (**2009**) Surface plasmon-coupled directional emission based on a conformational-switching signaling aptamer. *Chem. Commun. 45*: 3190–3192.

57 Cao SH, Xie TT, Cai WP, Liu Q, Li YQ (**2011**) Electric field assisted surface plasmon-coupled directional emission: an active strategy on enhancing sensitivity for DNA sensing and efficient discrimination of single base mutation. *J. Am. Chem. Soc. 133*: 1787–1789.

58 Chi YS, Byon HR, Lee BS, Kong B, Choi HC, Choi IS (**2008**) Polymeric rulers: distance-dependent emission behaviors of fluorophores on flat gold surfaces and bioassay platforms using plasmonic fluorescence enhancement. *Adv. Funct. Mater. 18*: 3395–3402.

59 Guerrero AR, Aroca RF (**2011**) Surface-enhanced fluorescence with shell-isolated nanoparticles (SHINEF). *Angew. Chem. Int. Ed. 50*: 665–668.

60 Zhou LC, Ding F, Chen H, Ding W, Zhang W, Chou SY (**2012**) Enhancement of immunoassay's fluorescence and detection sensitivity using three-dimensional plasmonic nano-antenna-dots array. *Anal. Chem. 84*: 4489–4495.

61 Larmour IA, Graham D (**2011**) Surface enhanced optical spectroscopies for bioanalysis. *Analyst 136*: 3831–3853.

62 Cheng D, Xu QH (**2007**) Separation distance dependent fluorescence enhancement of fluorescein isothiocyanate by silver nanoparticles. *Chem. Commun. 43*: 248–250.

63 Yu F, Persson B, Lofas S, Knoll W (**2004**) Surface plasmon fluorescence immunoassay of free prostate-specific antigen in human plasma at the femtomolar level. *Anal. Chem. 76*: 6765–6770.

64 Cao SH, Zou ZX, Weng YH, Cai WP, Liu Q, Li YQ (**2014**) Plasmon-mediated fluorescence with distance independence: from model to a biosensing application. *Biosens. Bioelectron. 58*: 258–265.

65 Chowdhury MH, Ray K, Geddes CD, Lakowicz JR (**2008**) Use of silver nanoparticles to enhance surface plasmon-coupled emission (SPCE). *Chem. Phys. Lett. 452*: 162–167.

66 Venkatesh S, Ghajesh S, Ramamurthy SS (**2015**) 1-Minute spacer layer engineering for tunable enhancements in surface plasmon-coupled emission. *Plasmonics 10*: 489–494.

67 Halas NJ, Lal S, Chang WS, Link S, Nordlander P (**2011**) Plasmons in strongly coupled metallic nanostructures. *Chem. Rev. 111*: 3913–3961.

68 Camden JP, Dieringer JA, Wang Y, Masiello DJ, Marks LD, Schatz GC, Van Duyne RP (**2008**) Probing the structure of single-molecule surface-enhanced Raman scattering hot spots *J. Am. Chem. Soc. 130*: 12616–12617.

69 Cao SH, Cai WP, Liu Q, Xie KX, Weng YH, Li YQ (**2014**) Turning on fluorescence by plasmonic assembly with large tunable spacing: a new observation and its biosensing application. *Chem. Commun. 50*: 518–520.

70 Cao SH, Cai WP, Liu Q, Xie KX, Weng YH, Huo SX, Tian ZQ, Li YQ (**2014**) Label-free aptasensor based on ultrathin-linker-mediated hot-spot assembly to induce strong directional fluorescence. *J. Am. Chem. Soc. 136*: 6802–6805.

71 Liu Q, Cao SH, Cai WP, Liu XQ, Weng YH, Xie KX, Huo SX, Li YQ (**2015**) Surface plasmon coupled emission in micrometer-scale cells: a leap from interface to bulk targets. *J. Phys. Chem. B 119*: 2921–2927.

72 Russell LJ, Liu TL, Cui S, Hu EL (**2012**) Large spontaneous emission enhancement in plasmonic nanocavities. *Nat. Photonics 16*: 459–462.

73 Borejdo J, Gryczynski Z, Calander N, Muthu P, Gryczynski I (**2006**) Application of surface plasmon coupled emission to study of muscle. *Biophys. J. 91*: 2626–2635.

74 Mettikolla P, Calander N, Luchowski R, Gryczynski I, Gryczynski Z, Borejdo J (**2010**) Kinetics of a single cross-bridge in familial hypertrophic cardiomyopathy heart muscle measured by reverse Kretschmann fluorescence. *J. Biomed. Opt. 15*: 017011.

75 Gryczynski Z, Borejdo J, Calander N, Matveeva EG, Gryczynski I (**2006**) Minimization of detection volume by surface-plasmon-coupled emission. *Anal. Biochem. 356*: 125–131.

76 Yuk JS, Trnavsky M, McDonagh C, MacCraith BD (**2010**) Surface plasmon-coupled emission (SPCE)-based immunoassay using a novel paraboloid array biochip. *Biosens. Bioelectron. 25*: 1344–1349.

77 Cai WP, Liu Q, Cao SH, Weng YH, Liu XQ, Li Y-Q (**2012**) Prism-based surface plasmon coupled emission imaging. *ChemPhysChem 13*: 3848–3851.

78 Gryczynski I, Malicka J, Nowaczyk K, Gryczynski Z, Lakowicz JR (**2004**) Effects of sample thickness on the optical properties of surface plasmon-coupled emission. *J. Phys. Chem. B 108*: 12073–12083.

79 Gryczynski I, Malicka J, Nowaczyk K, Gryczynski Z, Lakowicz JR (**2006**) Waveguide-modulated surface plasmon-coupled emission of Nile blue in poly(vinyl alcohol) thin films. *Thin Solid Films 510*: 15–20.

80 Salamon Z, Macleod HA, Tollin G (**1997**) Coupled plasmon-waveguide resonators: a new spectroscopic tool for probing proteolipid film structure and properties. *Biophys. J. 73*: 2791–2797.

81 Salamon Z, Tollin G (**2001**) Optical anisotropy in lipid bilayer membranes: coupled plasmon-waveguide resonance measurements of molecular orientation, polarizability, and shape. *Biophys. J. 80*: 1557–1567.

82 Calander N (**2005**) Surface plasmon-coupled emission and Fabry–Perot resonance in the sample layer: a theoretical approach. *J. Phys. Chem. B 109*: 13957–13963.

83 Noginov MA, Zhu G, Mayy M, Ritzo BA, Noginova N, Podolskiy VA (**2008**) Stimulated emission of surface plasmon polaritons. *Phys. Rev. Lett. 101*: 226806.

84 Meyer SA, Le Ru EC, Etchegoin PG (**2011**) Combining surface plasmon resonance (SPR) spectroscopy with surface-enhanced Raman scattering (SERS). *Anal. Chem. 83*: 2337–2344.

85 Ahamed JU, Sanbongi T, Katano S, Uehara Y (**2010**) Prism-coupled scanning tunneling microscope light emission spectroscopy of Au film covered with self-assembled alkanethiol monolayer. *Jpn. J. Appl. Phys. 49*: 08LB09.

86 Huo SX, Liu Q, Cao SH, Cai WP, Meng LY, Xie KX, Zhai YY, Zong C, Yang ZL, Ren B, Li YQ (**2015**) Surface plasmon-coupled directional enhanced Raman scattering by means of the reverse Kretschmann configuration. *J. Phys. Chem. Lett. 6*: 2015–2019.

87 Fort E, Gresillon S (**2008**) Surface enhanced fluorescence. *J. Phys. D Appl. Phys. 41*: 013001.

16

Plasmon-Enhanced Luminescence with Shell-Isolated Nanoparticles

Sabrina A. Camacho[1], Pedro H. B. Aoki[2], Osvaldo N. Oliveira, Jr[2], Carlos J. L. Constantino[1], and Ricardo F. Aroca[,1]*

[1] *Faculdade de Ciências e Tecnologia, UNESP Universidade Estadual Paulista, Presidente Prudente, Brazil*
[2] *São Carlos Institute of Physics, University of São Paulo, São Carlos, Brazil*
* *Professor Emeritus, Department of Chemistry and Biochemistry, University of Windsor, Windsor, Canada*

16.1 Introduction

After the discovery of surface-enhanced Raman scattering (SERS) [1, 2] and its proposed connection to plasmons [3], it became clear that *the enhanced phenomenon results from the modified local electromagnetic field experienced by the molecule in the vicinity of protrusions on rough metal substrate* (metallic nanostructures) [4]. The mechanism involving an enhanced local electromagnetic field also implied, in general, that all optical properties of the molecule would be altered. In fact, in 1980, the molecular-enhanced absorption [5] and enhanced luminescence [6] were reported: "*Absorption, luminescence, and excitation luminescence studies of dye molecules adsorbed onto ultrathin, variable-thickness silver films show strong coupling of the particle plasma resonances to the molecules. Luminescence from the dye is increased by excitation transfer from the silver particles for certain film thickness. Increased luminescence has also been observed from dyes on Au and Cu films*" (Glass *et al*. [6]). Enhanced luminescence was also reported in early days for other metals such as indium [7], used as metal island films coated with phthalocyanine dyes. In the case of isolated photoexcited fluorophores, the key elements are: the rate of excitation, the radiative decay (photons emitted), and the nonradiative decay (energy loss channels).

Plasmon-enhanced luminescence (surface-enhanced luminescence [8] or metal-enhanced luminescence [9]) was first characterized for the metal–nanostructure system using these molecular spectroscopic quantities: the radiative decay, the nonradiative decay, and the quantum efficiencies or quantum yields (the ratio of photons emitted to photons absorbed) [4]. Similarly, once the localized surface plasmon resonance (LSPR) in the nanoparticle is excited [10], it can either reradiate into the far field or decay nonradiatively due to internal damping. Experimentally, the fluorescence lifetimes of molecules adsorbed onto metallic nanostructures were drastically shortened [11], and this behavior depends on the shape and size of the nanostructure. These quantities have been measured for several fluorophores on plasmonic nanostructures. For instance, for fluorescein [12] (a fluorophore with quantum yield = 0.95), the molecular lifetime in solution is $\tau_0 = 4.38$ ns, while the measured modified lifetime on the plasmonic nanostructure was $\tau_{mod} = 0.182$ ns, a 24-fold decrease. On the other hand, the radiative decay and the nonradiative decay increased, and fluorescence enhancement was 100-fold. Various spectroscopic measurements confirmed an increased efficiency in the emission (enhanced luminescence) of the molecule–nanostructure system [8, 13, 14]. However, the enhanced luminescence was found to have a strong distance dependence, producing quenching at very short molecule–nanostructure distances, a maximum enhancement at a **critical** distance that drops back to the molecular unperturbed value as separation increases [8]. The interpretation given was based on a competing local field enhancement with losses due to energy transfer to the metal.

The conclusion after 35 years of accumulated data is simply that plasmonic nanoparticles can strongly interact with adjacent chromophores, resulting in plasmon-enhanced luminescence or luminescence quenching. The implication is that there is a very effective energy transfer at short distances (<4 nm) producing quenching, and a far-reaching local field effect that wins at distances >5 nm [15]. The experimental evidence of the distance dependence has been established independently by many groups [16–19]. It should be pointed out that this long-ranged property

Surface Plasmon Enhanced, Coupled and Controlled Fluorescence, First Edition. Edited by Chris D. Geddes.
© 2017 John Wiley & Sons, Inc. Published 2017 by John Wiley & Sons, Inc.

of enhancement is a unique experimental evidence of its electromagnetic nature, which is observed in all enhanced spectroscopic methods and has allowed for the development of new techniques such as TERS (tip-enhanced Raman scattering [20]), SHINERS (shell-isolated nanoparticle-enhanced Raman spectroscopy [21]), and SHINEF (shell-isolated nanoparticle-enhanced fluorescence) [22]. The distance dependence of the enhanced luminescence brings to the forefront the question about the physics of the molecule–nanostructure interactions and energy transfer [18, 23].

In summary, today the understanding is that in a fluorophore-plasmonic system, the fluorescence enhancement arises from an increased excitation rate due to an enhanced local field experienced by the fluorophore, from an increasing coupling efficiency of the fluorescence emission to the far field through nanoparticle scattering, and from modifying the radiative decay rate of the molecule. However, these contributions may be counterbalanced by energy losses due to nonradiative energy transfer to the metal nanostructures [24–26]. The findings under the umbrella of metal-enhanced fluorescence (MEF) are in full agreement: "*The current interpretation of MEF is underpinned using a model whereby non-radiative energy transfer occurs from excited fluorophores (dipoles) to surface plasmons in non-continuous films. The surface plasmons in turn efficiently radiate the emission of the coupling fluorophores, i.e. radiate the coupled quanta*" [19]. Strictly speaking, from the plasmonic point of view, excitation enhancement can be optimized by strong overlapping of the plasmon absorption and molecular extinction, while emission enhancement is maximized by tuning the plasmon with fluorophore emission. Given the broad nature of nanoparticle plasmons, the latter can be partially achieved in most applications in the visible spectrum as illustrated for spherical and nanorods gold nanoparticles coated with silica in Figure 16.1.

Equipped with this understanding, it is possible to plan the experimental conditions to control these processes and optimize the outcome. The challenge is then to manipulate and tune factors such as the size, geometry, and composition of the plasmonic nanoparticle, that is to say, to control the molecule nanoparticle separation and interstitial separation between nanoparticles to increase the contribution of hot spots [27]. One cannot forget important factors, particularly in solution, such as the nanoparticle surface charge and the related molecular adsorption and orientation. There are many good examples on how to increase the emission enhancement by tuning the surface plasmon peak position to the emission peak of the fluorophore [25]. The proof of concept of double tuning with the molecular extinction and emission has been demonstrated using the two plasmon modes of a nanorod [28]. However, it should be kept in mind that fluorescence is a very sensitive function of the environment surrounding the fluorophore, and that plasmon–fluorophore coupling, resulting in fluorescence intensity enhancement, is a complex process, a function of many variables (mentioned above). Correspondingly, the portion on the observed enhancement from contributing factors will change from one experimental condition to another, and one should refrain from one-sided conclusions based on a particular set of results.

Here, we restrict our discussion to findings of plasmon-enhanced fluorescence (PEF) properties using shell-isolated nanoparticles of gold and silver. First, we deal with the fabrication of Au-SHINs and Ag-SHINs. The evident advantages of working with versatile SHINs in different media, liquid, solid, and surfaces allow for a detailed discussion of observed properties in enhanced luminescence experiments. In addition, the future of SHINEF applications is wide open to chemical manipulations of SHINs, including the possibility of dual-mode SHINERS–SHINEF developments [29].

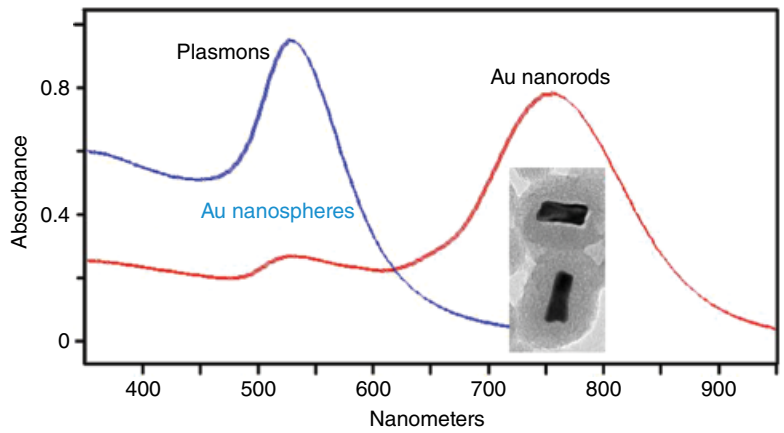

Figure 16.1 Typical surface plasmon spectra of gold nanoparticles coated with silica.

16.2 Synthesis of Shell-Isolated Nanoparticles

There are numerous reports in the literature with specific methods for the preparation of plasmonic nanoparticles, and this intense research is growing in different and profitable directions [30, 31]. The fabrication of SHINs [21, 32] for applications in surface-enhanced spectroscopy begins in wet chemistry with colloidal metal nanoparticles. One of the first methods used trisodium citrate reduction as a method to obtain colloidal gold [33, 34]. Turkevich's method was later perfected by Frens [35], where nanoparticles of different sizes could be produced by varying the citrate-to-gold ratio. In citrate reduction, citrate is oxidized to acetonedicarboxylate, suffering the loss of the carboxyl adjacent to the hydroxyl; the latter is lost as CO_2 which in turn lowers the pH. The reaction generates chloride ions which are neutralized by one of the sodium ions from the citrate. Also, acetonedicarboxylate continues to oxidize to formic acid and CO_2. As part of the equation, Au^{3+} (tetrachloroauric acid, $HAuCl_4$) is reduced to metallic gold, Au^0. It has been suggested that part of the Au^{3+} is not completely reduced, but some is left in the intermediate oxidation state (Au^+). These Au^+ atoms could be found on the surface of the nanoparticle which then acquires a positive surface charge. This charge attracts electrostatically citrate molecules, which end up being adsorbed on the surface of the nanoparticle. The particles finally acquire negative charge and electrostatic repulsion becomes enough to counter the Van der Waals adhesion, becoming nanoparticles. Table 16.1 displays the zeta potential values for typical Au colloids. Notably, the effective surface charge (zeta potential) has positive values for the nanorods coated with cetyltrimethylammonium bromide (CTAB) used during the synthesis.

One of the most cited publications to obtain colloidal silver and gold is that of Lee and Meisel [43]. The latter report presents the first silver colloids synthesized specifically to produce a SERS substrate. It is analogue to the gold citrate reduction, with the difference that the synthesis starts from silver nitrate ($AgNO_3$), and there cannot be a partial reduction of silver; however, there are probably some Ag^+ ions incorporated into the nanoparticle. Leopold and Lendl [44] offer a different approach to produce colloidal silver using hydroxylamine (NH_2OH). In fact, there are many reducing agents to produce silver and gold colloids, and the choice depends on the application of the nanoparticles [45]. In addition, the synthesis can be tuned to fabricate nanoparticles with different shapes, with protocols that commonly include manipulation of the chemical process to orient the nucleation in one direction: "*Mastery over the shape of a nanostructure enables control over its properties and usefulness for a given application*" [46]. Here, we restrict our discussion to Au-SHINs.

Table 16.1 Zeta potential values for typical Au colloids.

Colloid	Zeta potential data (mV)
AuNPs (gold nanospheres) [36]	−45.3
AuNPs (gold nanospheres) [37]	−32.0
AuNPs (gold nanospheres) [38]	−21.3
AuNPs (gold nanospheres) [39]	−16.5
AuNRs (gold nanorods) [40]	+18.0
AuNRs (gold nanorods) [41]	+27.0
AuNRs (gold nanorods) [42]	+49.0 to +71.0

16.2.1 Nanosphere Au-SHINs

Au-SHINs with different core sizes (55 and 120 nm) and shell thickness (1–20 nm) can be synthesized according to Li *et al.* [32]. AuNPs with 55 nm of diameter are prepared using the sodium citrate reduction method [35], with 1.4 mL of sodium citrate (1 weight%) being added quickly to the boiling solution of 200 mL of $HAuCl_4$ (0.01 weight%). The mixture is refluxed for 40 min and then cooled to room temperature. For the silica coating, 30 mL of AuNP (55 nm) solution is stirred with 0.4 mL of APTMS (1 mM) during 15 min. Then, 3.2 mL of sodium silicate solution (0.54 volume% SiO_2 diluted in water and pH ~ 10.2 adjusted with hydrochloric acid (HCl)) is added and kept stirring for an additional 3 min. The mixture is placed in a 90°C water bath and stirred. The heating time depends on the shell thickness desired: 20 min, 1 h, 2 h, 4 h, 8 h, and 20 h results in shell thicknesses of 2 nm, 4 nm, 6 nm, 8 nm, 10 nm, and 20 nm, respectively. The Au-SHINs are transferred to 1.5-mL centrifuge tubes and placed in an ice bath to stop the reaction. The tubes are centrifuged at 2008*g* for 15 min, the supernatant is removed and then 1.5 mL of ultrapure water is added to redisperse the SHINs. This procedure is repeated twice in order to obtain clean and concentrated Au-SHINs [32, 47].

AuNPs with 120 nm of diameter are synthesized from smaller AuNPs (~40 nm of diameter). About 1.0 mL of sodium citrate (1 weight%) is added quickly to the boiling solution of 100 mL of $HAuCl_4$ (0.01 weight%). The solution is kept boiling under stirring for 30 min in a reflux system and then cooled to room temperature [35]. To increase the nanoparticle size, 4.0 mL of the

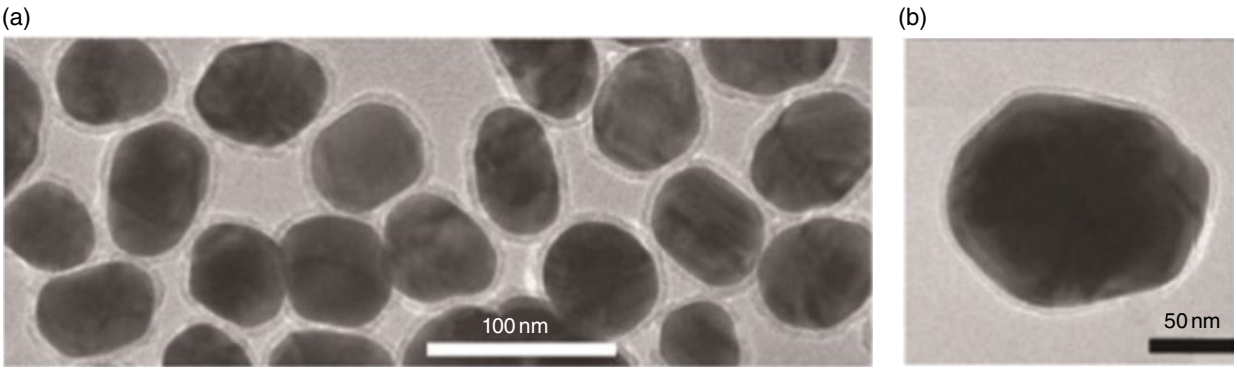

Figure 16.2 HR-TEM images of Au-SHINs with (a) 55 nm of core size and 4 nm of silica shell and (b) 120 nm of core size and 4 nm of silica shell. Li *et al*. [32]. Reproduced with the permission of Nature Publishing Group.

AuNP smaller solution (~40 nm) and 53 mL of Milli-Q water are placed into a round-bottom flask. About 0.9 mL of sodium citrate (1 weight%) is added and stirred for 3 min. Then, 0.9 mL of chloroauric acid (0.01 weight%) is added and stirred for additional 8 min. To prepare monodisperse AuNPs with 120 nm, 1.4 mL of hydroxylamine hydrochloride (10 mM) is added slowly (~1 drop every 10 s) with continuous stirring. The reaction completes after 5 min, but we recommend stirring for 1 h. To the coating with silica, 15 mL of AuNP (120 nm) solution is diluted in 30 mL (adding 15 mL of Milli-Q water) and stirred with 0.5 mL of 3-aminopropyl-triethoxysilane (APTES, 0.5 mM) for 20 min. After that, the same procedure used to coat the AuNPs with 55 nm of diameter is applied, using a lower volume of sodium silicate solution, 2.8 mL, and by centrifuging the SHINs at 598*g* for 10 min [32, 48]. High resolution transmission electron microscopy, HR-TEM images of the Au-SHINs produced by Li *et al*. [32] can be seen in Figure 16.2. For both Au-SHINs, 55 and 120 nm of core sizes, the heating time of 1 h results in 4 nm of silica shell.

We have also prepared Au-SHINs with different core sizes (16 and 40 nm) and silica shell thickness (7 nm and 11 nm, respectively) [22]. The gold cores are synthesized by the sodium citrate reduction method proposed by Grabar *et al*. [49] For the AuNPs with 16 nm of diameter, 250 mL of $HAuCl_4$ (5×10^{-4} M) is added while boiling and stirring, followed by the quick addition of 12.5 mL of sodium citrate (38.8 mM). The color solution changes from yellow to reddish purple and the boiling and stirring continuous for 10 min, then the stirring is kept for 15 min. The mixture is cooled to room temperature. The same experimental conditions are used to prepare AuNPs with 40 nm of diameter, but in this case, we use 150 mL of $HAuCl_4$ (5×10^{-4} M) and 3.4 mL of sodium citrate (38.8 mM). To coat the gold cores (16 and 40 nm), we have employed the method adapted by Li *et al*. [21]. For the coating of AuNPs with 16 nm of diameter, 3 mL of APTMS (1 mM) is added to 50 mL of the AuNP solution under vigorous stirring for 10 min. This mixture is heated in a water bath at 90°C and 95°C, and 6 mL of sodium silicate solution (0.54 volume% SiO_2 diluted in water and pH 10–11 adjusted with HCl) is added. The Au-SHIN samples are collected, cleaned, and concentrated by centrifugation at 12 000 rpm for 7 min. For the coating of AuNPs with 40 nm of diameter, the same experimental conditions are used, but only 25 mL of AuNP solution is coated. The TEM images of the Au-SHINs produced [22] are shown in Figure 16.3. For the Au-SHINs with 16 nm of core size, the heating (or coating) time was 1 h resulting in 7 nm of silica shell and for the Au-SHINs with 40 nm of core size, the heating (or coating) time was 1.5 h resulting in 11 nm of silica shell.

Note that the silica shell thickness is determined by the volume of sodium silicate solution, the pH, and the heating time of the coating. (i) Increasing the volume of sodium silicate solution increases the silica concentration and produces a thicker silica shell. (ii) If the pH is too high (pH > 11), the dissolution of the shell by sodium hydroxide (NaOH) will interfere with its growth and the shell remains very thin. On the other hand, if the pH is too low (pH = 8), the silica shell grows quite rapidly and it can easily become too thick. (iii) One can obtain different silica shell thicknesses by controlling the heating time of the coating. The longer the heating time, the thicker the silica shells.

16.2.2 Nanorod Au-SHINs

Nanorod Au-SHINs, with a core size of 12 nm in width (*w*) and 52 nm in length (*l*) coated with 10, 20,

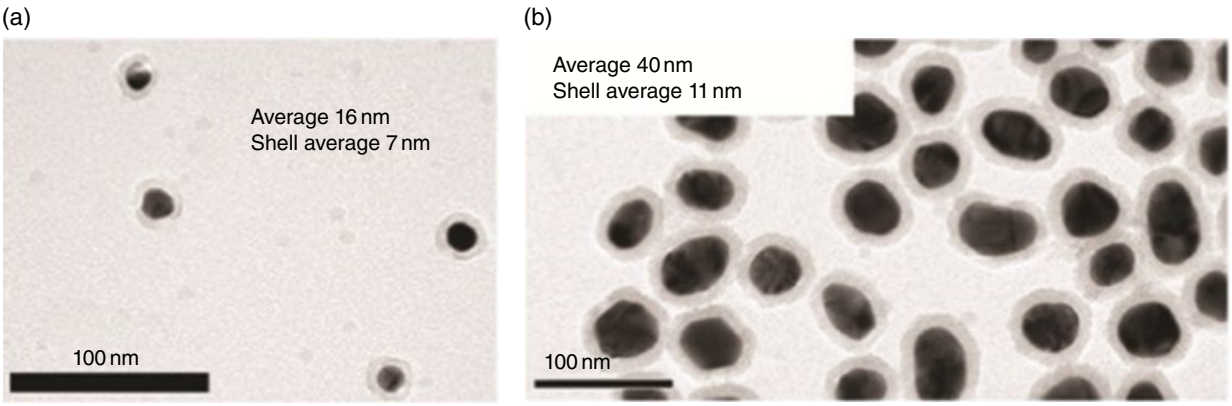

Figure 16.3 TEM images of Au-SHINs with (a) 16 nm of core size and 7 nm of silica shell and (b) 40 nm of core size and 11 nm of silica shell. Guerrero and Aroca [22]. Reproduced with the permission of John Wiley & Sons.

30, and 40 nm of silica shell, have been prepared according to Liu *et al.* [50]. AuNRs are synthesized as proposed by Li *et al.* [51]. In the first step, 10 mL of cetyltrimethyl ammonium bromide (CTAB, 0.1 M) is mixed with 0.05 mL of $HAuCl_4$ (0.05 M). Then, 0.6 mL of sodium tetrahydridoborate ($NaBH_4$, 0.01 M) is added into the mixture under vigorous stirring. Within 1 day, the color of the solution changes from brownish to red, indicating the formation of Au seeds. In the second step, the growth solution is prepared by successively adding 0.24 mL of $AgNO_3$ (0.02 M), 0.5 mL of $HAuCl_4$ (0.05 M), and 0.13 mL of l-ascorbic acid (AA, 0.1 M) into 49 mL of CTAB solution (0.1 M). Then, 0.06 mL of the Au seeds solution is added into the growth solution leading to the growth of AuNRs. About 12 h later, the sample is centrifuged and dispersed with water to purify the AuNR colloid. For the silica shell coating (10, 20, 30, and 40 nm), Liu *et al.* [50] have used the Stöber methodology according to Gorelikov *et al.* [52], with some modifications. About 4 mL of AuNR solution is mixed with 0.04 mL of NaOH (0.1 M) under stirring. In this step, 0.3 mL of CTAB (0.1 M) is placed into the AuNR colloid. The authors found an amount of CTAB covering the AuNR surface and observed that the addition of CTAB is fundamental for the silica coating. An adequate volume of tetraethoxysilane-TEOS (in this case, 0.04 mL of TEOS is mixed with a volume of ethanol) is then added into AuNR colloid under gentle agitation ensuring the hydrolysis of TEOS and the silica coating. Au-SHINs are obtained 20 h later, washed three times (with ethanol) by centrifugation at 5000 rpm for 15 min and dispersed in Milli-Q water. The geometry and TEM images of the nanorod Au-SHINs coated with different silica thicknesses are displayed in Figure 16.4. Increasing the volume of TEOS/ethanol increases the silica shell thickness (10, 20, 30, and 40 nm).

Nanorod Au-SHINs with different core sizes (length × width) and silica shell thickness of ~3, 4.3, and 7 nm have been reported by Zhang *et al.* [53] The AuNRs are synthesized using a standard methodology proposed by Nikoobakht *et al.* [54] and adapted by Wang *et al.* [55]. Initially, the Au seeds are prepared by the mixture of 0.25 mL of $HAuCl_4$ (0.01 M) and 9.75 mL of CTAB (0.1 M) into a 25-mL round-bottom flask under stirring. Then, 0.60 mL of freshly prepared and ice-cold $NaBH_4$ (0.01 M) is quickly added, under vigorous stirring. The color of the solution changes to brownish yellow. The solution is stirred for further 2 min and then kept standing for 2 h at room temperature. In the second step, the growth solution is prepared in six 50-mL tubes filled with 40 mL of CTAB (0.1 M) and 2 mL $HAuCl_4$ (0.01 M), mixed homogenously. Followed by 0.40 mL of $AgNO_3$ (0.01 M), 0.80 mL HCl (1.0 M) used to regulate pH = 2 and 0.32 mL of ascorbic acid (0.1 M). The solution is kept under stirring until it becomes colorless. To grow different sizes of AuNRs, different volumes of Au seeds (80, 50, 30, 20, 10, and 5 mL) are added into the six tubes and mixed uniformly. These final mixtures are incubated for more than 6 h at room temperature. Then, the colloid with AuNRs is purified twice (with Milli-Q water) by centrifugation at 6000 rpm for 15 min. The SEM images of the AuNRs obtained by the addition of different volumes of Au seeds solution are shown in Figure 16.5. The lesser the amount of Au seeds used, the larger the size of AuNRs produced. For the silica coating, Zhang *et al.* [53] applied the SHINERS method [32]. About 10 mL of AuNR colloid is mixed with 0.5 mL of APTES (1 mM) under vigorous stirring. After 30 min, 1.6 mL of sodium silicate solution

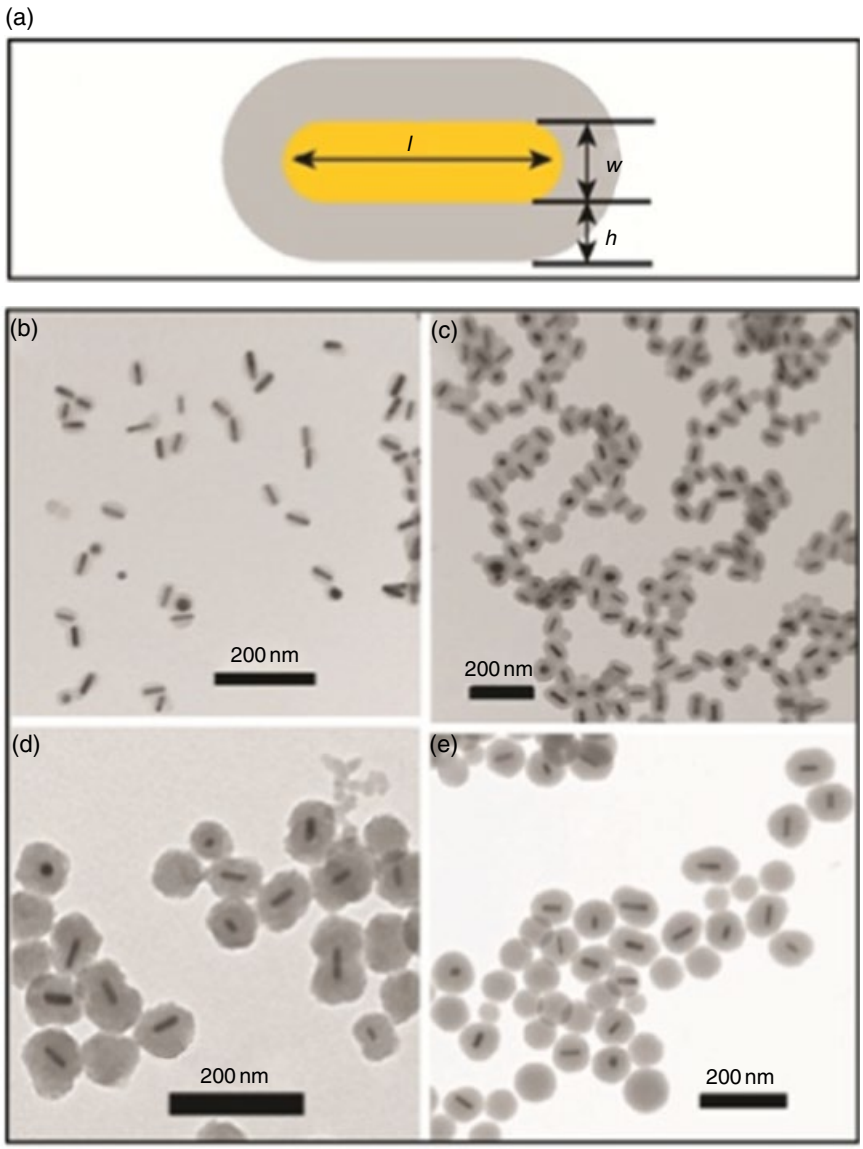

Figure 16.4 (a) Geometry and geometrical parameters of the nanorod Au-SHINs ($l = 52$ nm, $w = 12$ nm, $h = 10$, 20, 30, 40 nm). TEM images of the nanorod Au-SHINs with different thicknesses of silica shell: (b) 10 nm, (c) 20 nm, (d) 30 nm and (e) 40 nm. Liu *et al.* [50]. Reproduced with the permission of Springer.

(0.54 volume% SiO_2 diluted in water and pH 10 adjusted with HCl) is added and the mixture is stirred for additional 5 min. Then, the mixture is stirred in a 90°C water bath during 5 (20) min to coat the AuNRs with ~3 (4.3) nm silica thickness. The nanorod Au-SHINs are then cooled at room temperature in a water bath and centrifuged at 4000 rpm for 10 min. To prepare nanorod Au-SHINs with thicker silica shell (~7 nm), the AuNRs coated with 4.3 nm of silica are put into 9 mL of ethanol (1 : 3 water/ethanol), into which are added 20 mL of ammonia and 3 mL of TEOS [56]. The solution is kept under gentle stirring for 12 h and then centrifuged at 4000 rpm for 10 min. The TEM images of the nanorod Au-SHINs obtained with different shell thicknesses can be seen in Figure 16.6.

16.3 Plasmon-Enhanced Luminescence in Liquid Media

SHINs permit to work in aqueous solutions as well as other organic solvents. In a recent report [57], we demonstrated in experiments carried out in aqueous solution that with far-field measurements of Raman

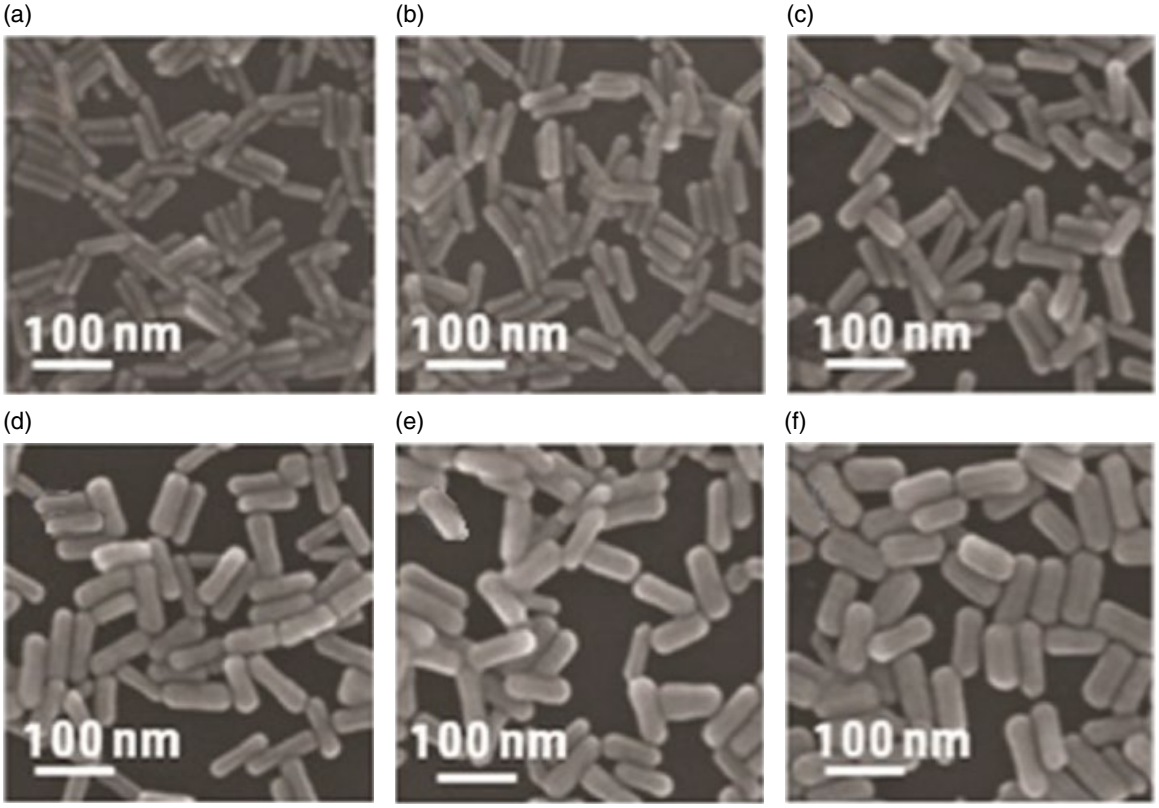

Figure 16.5 SEM images of AuNRs with different shell thicknesses prepared by the addition of different volumes of Au seed solutions: (a) 80 mL ($l = 65$; $w = 18$), (b) 50 mL ($l = 71$ nm; $w = 20$ nm), (c) 30 mL ($l = 73$ nm; $w = 24$ nm), (d) 20 mL ($l = 79$ nm; $w = 29$ nm), (e) 10 mL ($l = 84$ nm; $w = 32$ nm) and (f) 5 mL ($l = 91$ nm; $w = 42$ nm). Zhang *et al*. [53]. Reproduced with the permission of John Wiley & Sons.

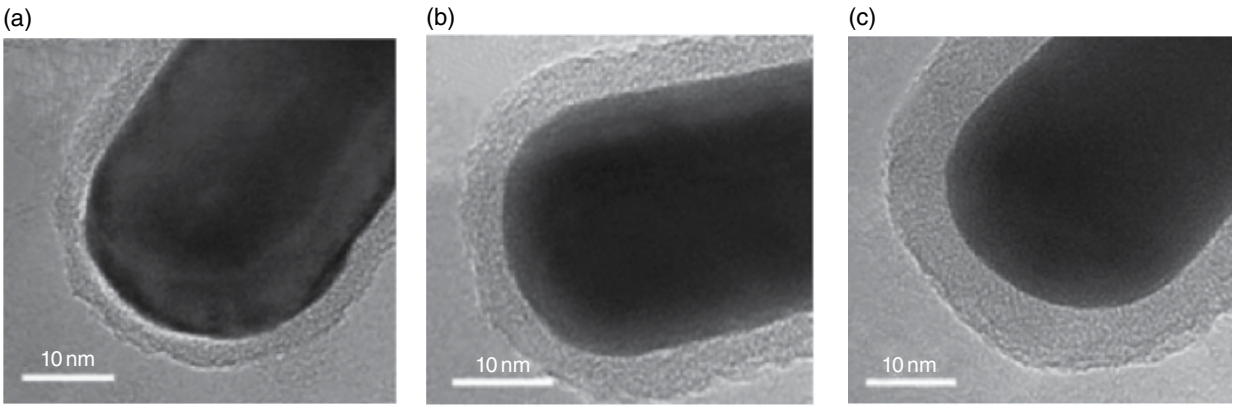

Figure 16.6 TEM images of the nanorod Au-SHINs with different shell thicknesses: (a) 3 nm, (b) 4.3 nm and (c) 7 nm. Zhang et al. [53]. Reproduced with the permission of John Wiley & Sons.

scattering and fluorescence from the same molecular system, it is possible to confirm the scattering scales as the fourth power of the local field enhancement, while the fluorescence is proportional to the square of the local field enhancement [26]. In brief, when E_0 is the incident field and E_{loc} is the enhanced local field at the plasmonic nanostructure, it leads to an enhancement $|E| = |E_{loc} / E_0|$. For scattering, the enhancement is proportional to the fourth power of the $|E|$ factor, providing the $|E|^4 = |E_{loc} / E_0|^4$ approximation, extensively discussed and used even for nanostructures other than spheres [58]. However, surface-enhanced

emission can only benefit once from the enhanced local field and should be proportional to $|E|^2 = |E_{loc} / E_0|^2$, with much more modest enhancement factors (EFs) if compared to SERS. Experiments have been carried out with molecules that provide both SHINERS and SHINEF (dual-mode) in the same collected spectrum. The latter was achieved with low quantum yield molecules, with which both Raman and fluorescence were observed within the same spectrum. Molecules with very low quantum yield, such as crystal violet (CV) [57] and malachite green (MG) [59], have been used. The SHINERS + SHINEF spectrum of MG recorded from a 2.5×10^{-5} M solution of MG with silver SHINs and excited with the 514.5-nm laser line is shown in Figure 16.7.

A typical plasmon absorption spectrum of Ag-SHINs is given in Figure 16.8, together with the extinction spectrum of MG. The 514.5-nm laser line can excite both molecule and nanoparticle. The Ag-SHIN extinction is in the blue range of the electromagnetic spectrum, but silver nanostructures provide strong enhancement throughout the visible and even in the near-infrared spectral regions [60]. Therefore, the observation of SHINEF at about 750 nm is in agreement with former studies, where plasmonic silver structures provided extremely high enhancement level in the near infrared used for single-molecule detection [61]. Notably, with Ag-SHINs, and thanks to the spacer layer, the plasmon-enhanced vibrational Raman scattering in Figure 16.7 is observed unperturbed from the reference spectrum in solution. SHINEF is collected for molecules located outside the zone of strong quenching or dramatic changes in the lifetime. In addition, by working in solution reproducible average properties are measured. The experimentalist working in SHINEF may profit from the extensive experience accumulated in the field of colloidal SERS: SHINs are electrostatically charged nanoparticles that can be functionalized or aggregated. Following the methodology of metal colloids [62], SHIN's aggregation can also be induced in a colloidal dispersion by adding electrolytes such as NaCl or KCl. The aggregates deliver hot spots that help to increase the associated EFs in SHINEF by about an order of magnitude [59], with EF > 50, in the footsteps of the colloidal silver aggregates that led to single-molecule detection [61]. In recent studies [63], we have extended this work to large gold SHINs (core of ~100 nm in diameter) and CV in solution, and compare the SHINEF enhancement with smaller Au-SHINs of Au core in the 40-nm range. The small Au-SHINs aggregated with NaCl in solution produce an EF > 50-fold, similar to silver [59]. However, the large Au-SHINs, after aggregation led to an enhancement EF = 155, the highest we have observed in solution experiments. The results are illustrated in Figure 16.9. Similar experiments with Ag-SHINs are in progress.

The preliminary conclusion is that SHINs with large Au core, with a predominant dipole excitation (~100 nm diameter), provide higher EFs. Clearly, much work remains to be done to correspondingly optimize the thickness of SiO_2 coating. The new results are in agreement with reported stronger SHINERS enhancement using silica shell Au-SHINs with a 120-nm gold core [48]. This very active field of research includes different bottom-up approaches [45]. For instance, there are reports on quantum dots assembly on gold plasmonic nanorods with controlled spacing and quantum dot/nanorod ratio, which have been further encapsulated in a protective silica shell. A 5-fold enhancement was obtained in solution.

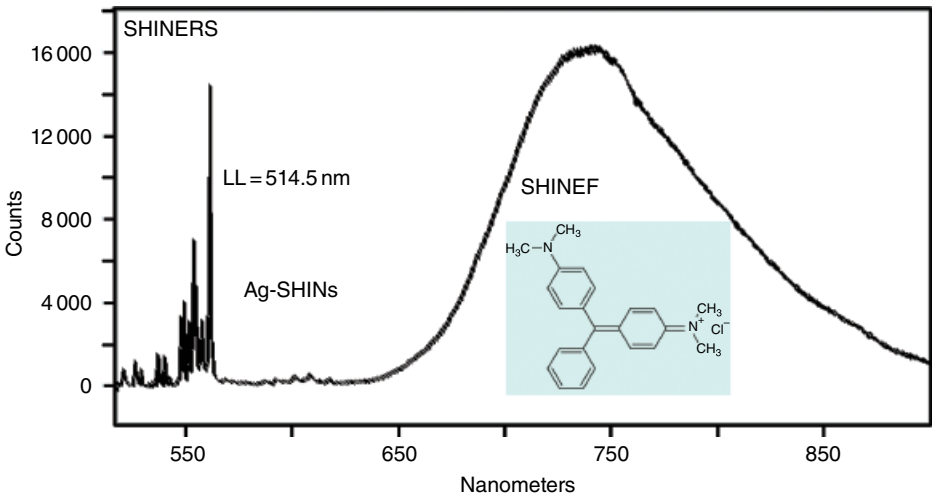

Figure 16.7 SHINERS + SHINEF spectrum of malachite green in solution, excited with the 514.5-nm laser line.

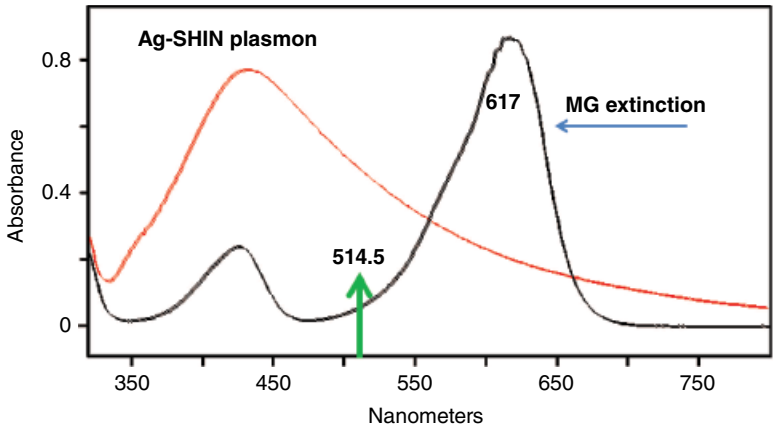

Figure 16.8 Ag-SHIN plasmon absorption and molecular extinction spectra of malachite green.

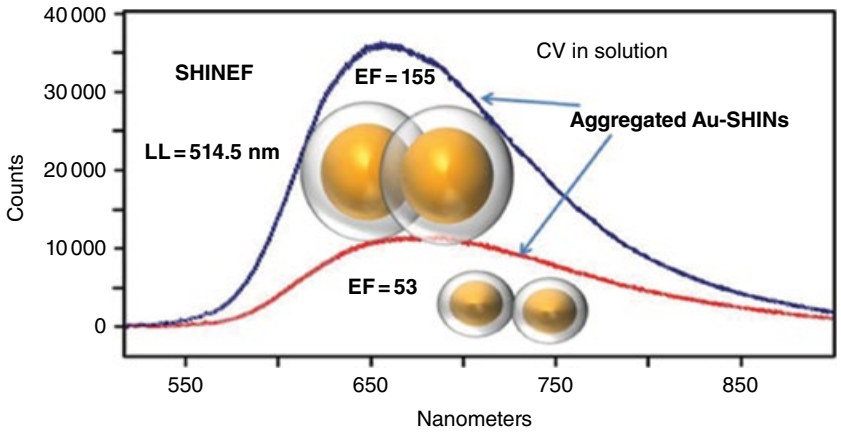

Figure 16.9 SHINEF EF for crystal violet in solution after Au-SHIN's aggregation with NaCl. Large Au-SHINs with central core of about 100 nm and SiO_2 coating of ~10 nm. Smaller SHINs with a core of ~40 nm and a coating of ~10 nm. EF: enhancement factor. (*See insert for color representation of this figure.*)

16.4 Enhanced Luminescence on Solid Surfaces and Spectral Profile Modification

The original idea of spreading SHINs as "smart dust" over a solid surface [21] has been very profitable for both SHINERS and SHINEF. SHINs casting [64] and spraying [59] are commonly used, although the fabrication of two- (or three-) dimensional substrates for SHIN is also an avenue for specific applications [65]. Layer-by-layer (LbL) surfaces have been prepared with quantum dots and different fluorescent groups to be probed by spreading SHINs of silver and gold. For instance, in a recent report, LbL surfaces of CdTe-green and CdTe-orange quantum dots were probed with Ag-SHINs. Quantum yields (QY) determined for CdTe QDs green and orange are 0.15 and 0.48, respectively. The corresponding EFs measured were 12-fold for CdTe-green and 35-fold for CdTe-orange [66]. Similarly, a high PEF EF of 45-fold and 41.23% decrease in fluorescence lifetimes were reported for heavy-metal-free Cu–In–Zn–S quantum dots [67] on plasmonic silver films. The LbL technique has also been used to probe fluorophores such as eosin and crystal violet by spraying Au-SHINs [59]. For eosin, the best EF was 9-fold as shown in Figure 16.10. The plasmon fluorescence enhancement of eosin has been measured on several enhancing structures. (i) Gold nanostructures fabricated on glass substrates using high-resolution electron beam lithography and spacer layers of Al_2O_3; a 3.5-fold EF was reported [68]. (ii) Eosin in close proximity to silver island films showed a 3-fold EF [69]. (iii) An EF = 4.3 has been reported for eosin on a nanoplasmonic silver structure [12]. (iv) A 9-fold enhancement in fluorescence has also been measured for eosin in anhydrous glycerol close to an

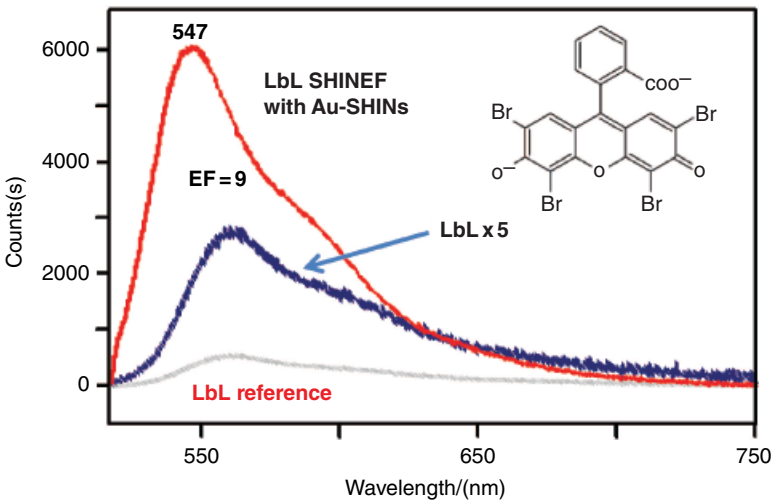

Figure 16.10 SHINEF obtained by spraying Au-SHINs onto an LbL film containing eosin. The LbL reference fluorescence and the LbL reference ×5 are also included. Osorio-Roman *et al*. [59]. Reproduced with the permission of American Chemical Society.

SiO_x-coated silver island film, with respect to a control sample containing no silver [19].

The SHIN experiments in solution clearly show that higher enhancements are possible thanks to nanoparticle aggregation. The spraying experiments confirm the aggregation effect; however, when using aggregates of the "smart dust," it is important to remember that clumping ought to be avoided, since reabsorption may lead to lower EFs. Another important detail in Figure 16.10 is that the maximum of the emission is blue shifted with respect to the LbL reference by about 13 nm. This spectral profile modification (SPM) [64, 70] is consistent with the observation of the Au-SHIN plasmon at 531 nm, blue shifted with respect to the eosin fluorescence with a maximum at ~560 nm. Since the enhanced spectrum has a contribution proportional to the coupling efficiency of the fluorescence emission to the far field through nanoparticle scattering, it is evident that the plasmon signature will be part of the observed spectral profile. In other words, SPM in emission enhancement is the result of the mismatch in the overlapping of the plasmon with fluorophore emission.

16.4.1 SHINEF on Langmuir–Blodgett Films

Langmuir–Blodgett (LB) films are monolayers or multilayers films transferred from the liquid–gas interface onto a solid substrate [71]. The advantage of working with LB monolayers is the control of the target molecules in neat homogenous monolayers, or doping a spectroscopic silent background molecule with a fluorophore to form mixed LB monolayers. To illustrate the effect, we prepared a mixed LB monolayer of bis(pentadecylimido) perylene (15C-PTCD, MM = 811.21 g/mol) and stearic acid (SA) [$CH_3(CH_2)_{16}COOH$]. The LB mixed monolayer of 15C-PTCD/SA was obtained by spreading a volume of 200 µL 1:1000 molecular ratio of 15C-PTCD:SA solution (10% in volume of trifluoroacetic acid and 90% of dichloromethane) at the air/ultrapure water interface. LB monolayers were fabricated using a Langmuir trough, KSV model 2000, using ultrapure water subphase (pH 5.6) at room temperature. After spreading, a waiting time of 20 min was required to ensure complete evaporation of the solvents used. The monolayer was then symmetrically compressed under a constant barrier speed at 10 mm/min, forming a Langmuir monolayer at the air/ultrapure water interface. The structure of the target molecule and the pressure area isotherm for the mixed monolayer of 15C-PTCD/SA is shown in Figure 16.11. Since the perylene tetracarboxylic diimide (PTCD) chromophore has a molecular area of 130 $Å^2$, the dilute mixed isotherm is dominated by the molecular area of the fatty acid [71].

Since this pressure area isotherm corresponds to a very dilute (1:1000) solution of the target molecule, the area per molecule is mainly that of SA. The surface pressure was kept constant at 30 mN/m during the transfer of the monolayer to a quartz slide with upstroke speed at 5 mm/min. For the SHINEF experiments, 5 µL of small and large Au-SHINs was spread onto the LB monolayers. The results are shown in Figure 16.12.

The families of PTCD dyes are fluorophores with high quantum efficiency, and we have used them to study SHINEF properties in LB films with Au- and Ag-SHINs. For instance, Au-SHINs spread over mixed LB of bis(*n*-butylimido)perylene (*n*BPTCD) with *n*-eicosanoic acid or arachidic acid (AA) produces a ~20-fold EF [22], in agreement with the EF for 15C-PTCD with small Au-SHINs in Figure 16.12, with gold core size between 40 and 50 nm. A large

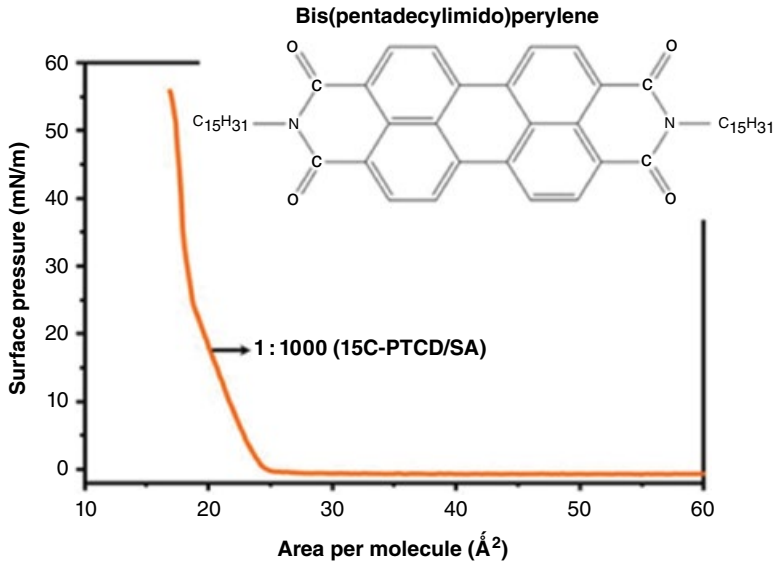

Figure 16.11 Surface pressure-area isotherms for the mixed 15C-PTCD/SA Langmuir monolayer.

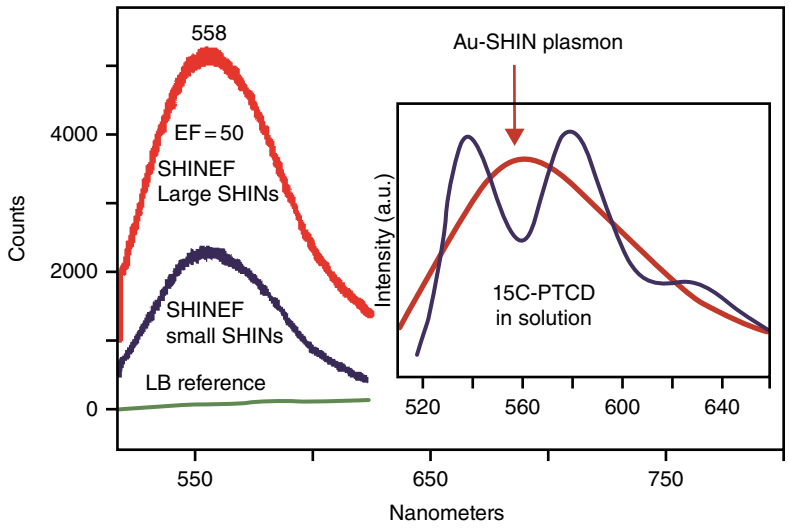

Figure 16.12 SHINEF of 15C-PTCD/SA mixed LB monolayer with two core sizes for Au-SHINs. The inset shows the plasmon of large SHINs and the fluorescence emission of 15C-PTCD in solution.

enhancement (~20-fold) was also found for another high quantum yield fluorophore in an LB mixed film of octadecyl rhodamine B (R18)/AA and Au-SHINs [22, 59]. The same R18 LB film produces more than 90-fold EF with Ag-SHINs [57]. As shown in Figure 16.12, the EF for LB films of 15C-PTCD can be further increased by using large Au-SHINs with gold core sizes of ~100 nm, providing a 50-fold EF [63]. The inset in Figure 16.12 illustrates the structure in the fluorescence spectrum of 15C-PTCD monomers which is predominant in solution as has been previously reported [64]. The inset also shows the plasmon spectrum of large Au-SHINs. Here again, it can be seen in the SHINEF spectrum the contribution due to the coupling of the fluorescence emission to the far field through nanoparticle scattering. The effect of SPM is commonplace in plasmon-enhanced luminescence, being also referred to as plasmon-induced modulation of the emission spectra of the fluorescent molecules [72].

In summary, the "smart dust" idea using SHINs has opened a new avenue for plasmon-enhanced luminescence (fluorescence—SHINEF or phosphorescence—SHINEP) that is rapidly growing parallel to other substrate developments for PEF applications. Similar to SERS, gold and silver cores are the preferred metals for Au-SHIN and Ag-SHIN fabrication. The most common shapes for the metal core are nanospheres and nanorods; but there is plenty of room to explore other shapes for enhancing properties or specific applications. SiO_2 is the default coating material; however, other oxides such as Al_2O_3 and MnO_2 are also explored

together with bio-organic coating materials. In each case, it will be necessary to determine the SHIN's stability and optimize the thickness of the spacer layer. It has become clear, for nanospheres, that large metallic cores (diameter ~ 100 nm) are more efficient enhancers. In fact, small gold and silver nanoparticles (diameter ~5 to 10 nm) are excellent absorbers and are used for quenching applications. In practice, the nanoparticle size and shape together with the coating material and thickness of the spacer layer may be seen as experimental variables in the hands of the experimentalist to increase the emission enhancement by tuning the surface plasmon peak position to the emission peak of the luminophore.

Acknowledgments

The authors acknowledge the financial support from FAPESP and CNPq of Brazil.

References

1 Albrecht, M. G.; Creighton, J. A. Anomalously intense Raman-spectra of pyridine at a silver electrode. *Journal of the American Chemical Society* **1977**, *99*, 5215–5217.
2 Jeanmaire, D. L.; Van Duyne, R. P. Surface Raman spectroelectrochemistry. Part I. Heterocyclic, aromatic, and aliphatic amines adsorbed on the anodized silver electrode. *Journal of Electroanalytical Chemistry and Interfacial Electrochemistry* **1977**, *84*, 1–20.
3 Moskovits, M. Surface-roughness and enhanced intensity of Raman-scattering by molecules adsorbed on metals. *Journal of Chemical Physics* **1978**, *69*, 4159–4161.
4 Gersten, J.; Nitzan, A. Spectroscopic properties of molecules interacting with small dielectric particles. *Journal of Chemical Physics* **1981**, *75*, 1139–1152.
5 Hartstein, A.; Kirtley, J. R.; Tsang, J. C. Enhancement of the infrared-absorption from molecular monolayers with thin metal overlayers. *Physical Review Letters* **1980**, *45*, 201–204.
6 Glass, A. M.; Liao, P. F.; Bergman, J. G.; Olson, D. H. Interaction of metal particles with absorbed dye molecules—absorption and luminescence. *Optics Letters* **1980**, *5*, 368–370.
7 Loutfy, R. O.; Aroca, R. Interaction of indium metal with phthalocyanine molecules: luminescence enhancement. *Journal of Luminescence* **1982**, *26*, 359–366.
8 Wokaun, A.; Lutz, H. P.; King, A. P.; Wild, U. P.; Ernst, R. R. Energy transfer in surface enhanced luminescence. *Journal of Chemical Physics* **1983**, *79*, 509–514.
9 Geddes, C. D.; Lakowicz, J. R. Metal-enhanced fluorescence. *Journal of Fluorescence* **2002**, *12*, 121–129.
10 Maier, S. A. *Plasmonics: Fundamentals and Applications*. Springer: New York, **2007**.
11 Weitz, D. A.; Garoff, S.; Hanson, C. D.; Gramila, T. J.; Gersten, J. I. Fluorescent lifetimes and yields of molecules adsorbed on silver-island films. *Journal of Luminescence* **1981**, *24–5*, 83–86.
12 Gartia, M. R.; Eichorst, J. P.; Clegg, R. M.; Liu, G. L. Lifetime imaging of radiative and non-radiative fluorescence decays on nanoplasmonic surface. *Applied Physics Letters* **2012**, *101*, 023118.
13 Weitz, D. A.; Garoff, S.; Gersten, J. I.; Nitzan, A. The enhancement of Raman-scattering, resonance Raman-scattering, and fluorescence from molecules adsorbed on a rough silver surface. *Journal of Chemical Physics* **1983**, *78*, 5324–5338.
14 Le Ru, E. C.; Etchegoin, P. G. *Principles of Surface Enhanced Raman Spectroscopy (and related plasmonic effects)*. Elsevier: Amsterdam, **2009**.
15 Anger, P.; Bharadwaj, P.; Novotny, L. Enhancement and quenching of single-molecule fluorescence. *Physical Review Letters* **2006**, *96*, 113002-1–113002-4.
16 Aroca, R. F. Plasmon enhanced spectroscopy. *Physical Chemistry Chemical Physics* **2013**, *15*, 5355–5363.
17 Akbay, N.; Lakowicz, J. R.; Ray, K. Distance-dependent metal-enhanced intrinsic fluorescence of proteins using polyelectrolyte layer-by-layer assembly and aluminum nanoparticles. *Journal of Physical Chemistry C* **2012**, *116*, 10766–10773.
18 Saini, S.; Srinivas, G.; Bagchi, B. Distance and orientation dependence of excitation energy transfer: from molecular systems to metal nanoparticles. *Journal of Physical Chemistry B 2009*, 113, **1817–1832**.
19 Mishra, H.; Mali, B. L.; Karolin, J.; Dragan, A. I.; Geddes, C. D. Experimental and theoretical study of the distance dependence of metal-enhanced fluorescence, phosphorescence and delayed fluorescence in a single system. *Physical Chemistry Chemical Physics* **2013**, *15*, 19538–19544.
20 Pettinger, B. Single-molecule surface- and tip-enhanced Raman spectroscopy. *Molecular Physics* **2010**, *108*, 2039–2059.
21 Li, J. F.; Huang, Y. F.; Ding, Y.; Yang, Z. L.; Li, S. B.; Zhou, X. S.; Fan, F. R.; Zhang, W.; Zhou, Z. Y.; Wu, D. Y.; Ren, B.; Wang, Z. L.; Tian, Z. Q. Shell-isolated

nanoparticle-enhanced Raman spectroscopy. *Nature* **2010**, *464*, 392–395.
22 Guerrero, A. R.; Aroca, R. F. Surface-enhanced fluorescence with shell-isolated nanoparticles (SHINEF). *Angewandte Chemie International Edition* **2011**, *50*, 665–668.
23 Chen, H.; Schatz, G. C.; Ratner, M. A. Experimental and theoretical studies of plasmon-molecule interactions. *Reports on Progress in Physics* **2012**, *75*, 096402.
24 Hoppener, C.; Novotny, L. Exploiting the light-metal interaction for biomolecular sensing and imaging. *Quarterly Reviews of Biophysics* **2012**, *45*, 209–255.
25 Tam, F.; Goodrich, G. P.; Johnson, B. R.; Halas, N. J. Plasmonic enhancement of molecular fluorescence. *Nano Letters* **2007**, *7*, 496–501.
26 Moskovits, M. Surface-enhanced spectroscopy. *Reviews of Modern Physics* **1985**, *57*, 783–826.
27 Kleinman, S. L.; Frontiera, R. R.; Henry, A.-I.; Dieringer, J. A.; Van Duyne, R. P. Creating, characterizing, and controlling chemistry with SERS hot spots. *Physical Chemistry Chemical Physics* **2013**, *15*, 21–36.
28 Liu, S. Y.; Huang, L.; Li, J. F.; Wang, C.; Li, Q.; Xu, H. X.; Guo, H. L.; Meng, Z. M.; Shi, Z.; Li, Z. Y. Simultaneous excitation and emission enhancement of fluorescence assisted by double plasmon modes of gold nanorods. *Journal of Physical Chemistry C* **2013**, *117*, 10636–10642.
29 Fang, P. P.; Lu, X. H.; Liu, H.; Tong, Y. X. Applications of shell-isolated nanoparticles in surface-enhanced Raman spectroscopy and fluorescence. *Trends in Analytical Chemistry* **2015**, *66*, 103–117.
30 Rycenga, M.; Cobley, C. M.; Zeng, J.; Li, W. Y.; Moran, C. H.; Zhang, Q.; Qin, D.; Xia, Y. N. Controlling the synthesis and assembly of silver nanostructures for plasmonic applications. *Chemical Reviews* **2011**, *111*, 3669–3712.
31 Giner-Casares, J. J.; Liz-Marzan, L. M. Plasmonic nanoparticles in 2D for biological applications: toward active multipurpose platforms. *Nano Today* **2014**, *9*, 365–377.
32 Li, J. F.; Tian, X. D.; Li, S. B.; Anema, J. R.; Yang, Z. L.; Ding, Y.; Wu, Y. F.; Zeng, Y. M.; Chen, Q. Z.; Ren, B.; Wang, Z. L.; Tian, Z. Q. Surface analysis using shell-isolated nanoparticle-enhanced Raman spectroscopy. *Nature Protocols* **2013**, *8*, 52–65.
33 Turkevich, J.; Stevenson, P. C.; Hillier, J. A study of the nucleation and growth processes in the synthesis of colloidal gold. *Discussions of the Faraday Society* **1951**, *11*, 55–75.
34 Enüstün, B. V.; Turkevich, J. Coagulation of colloidal gold. *Journal of the American Chemical Society* **1963**, *85*, 3317–3328.
35 Frens, G. Controlled nucleation for regulation of particle-size in monodisperse gold suspensions. *Nature Physical Science* **1973**, *241*, 20–22.
36 Chen, S. H.; Kimura, K. Synthesis and characterization of carboxylate-modified gold nanoparticle powders dispersible in water. *Langmuir* **1999**, *15*, 1075–1082.
37 Nikov, R. G.; Nikolov, A. S.; Nedyalkov, N. N.; Dimitrov, I. G.; Atanasov, P. A.; Alexandrov, M. T. Stability of contamination-free gold and silver nanoparticles produced by nanosecond laser ablation of solid targets in water. *Applied Surface Science* **2012**, *258*, 9318–9322.
38 Guo, M. X.; Li, W.; Yang, F.; Liu, H. H. Controllable biosynthesis of gold nanoparticles from a *Eucommia ulmoides* bark aqueous extract. *Spectrochimica Acta Part A: Molecular and Biomolecular Spectroscopy* **2015**, *142*, 73–79.
39 Tian, F.; Bonnier, F.; Casey, A.; Shanahan, A. E.; Byrne, H. J. Surface enhanced Raman scattering with gold nanoparticles: effect of particle shape. *Analytical Methods* **2014**, *6*, 9116–9123.
40 Huang, C. C.; Huang, C. H.; Kuo, I. T.; Chau, L. K.; Yang, T. S. Synthesis of silica-coated gold nanorod as Raman tags by modulating cetyltrimethylammonium bromide concentration. *Colloids and Surfaces A: Physicochemical and Engineering Aspects* **2012**, *409*, 61–68.
41 Wang, X. H.; Li, Y. A.; Wang, H. F.; Fu, Q. X.; Peng, J. C.; Wang, Y. L.; Du, J. A.; Zhou, Y.; Zhan, L. S. Gold nanorod-based localized surface plasmon resonance biosensor for sensitive detection of hepatitis B virus in buffer, blood serum and plasma. *Biosensors & Bioelectronics* **2010**, *26*, 404–410.
42 Sau, T. K.; Murphy, C. J. Self-assembly patterns formed upon solvent evaporation of aqueous cetyltrimethylammonium bromide-coated gold nanoparticles of various shapes. *Langmuir* **2005**, *21*, 2923–2929.
43 Lee, P. C.; Meisel, D. Adsorption and surface-enhanced Raman of dyes on silver and gold sols. *Journal of Physical Chemistry* **1982**, *86*, 3391–3395.
44 Leopold, N.; Lendl, B. A new method for fast preparation of highly surface-enhanced Raman scattering (SERS) active silver colloids at room temperature by reduction of silver nitrate with hydroxylamine hydrochloride. *Journal of Physical Chemistry B* **2003**, *107*, 5723–5727.
45 Liz-Marzan, L. M. Nanometals formation and color. *Materials Today* **2004**, *7*, 26–31.
46 Wiley, B.; Sun, Y.; Xia, Y. Synthesis of silver nanostructures with controlled shapes and properties. *Accounts of Chemical Research* **2007**, *40*, 1067–1076.

47 Li, J. F.; Li, S. B.; Anema, J. R.; Yang, Z. L.; Huang, Y. F.; Ding, Y.; Wu, Y. F.; Zhou, X. S.; Wu, D. Y.; Ren, B.; Wang, Z. L.; Tian, Z. Q. Synthesis and characterization of gold nanoparticles coated with ultrathin and chemically inert dielectric shells for SHINERS applications. *Applied Spectroscopy* **2011**, *65*, 620–626.

48 Tian, X. D.; Liu, B. J.; Li, J. F.; Yang, Z. L.; Ren, B.; Tian, Z. Q. SHINERS and plasmonic properties of Au Core SiO_2 shell nanoparticles with optimal core size and shell thickness. *Journal of Raman Spectroscopy* **2013**, *44*, 994–998.

49 Grabar, K. C.; Freeman, R. G.; Hommer, M. B.; Natan, M. J. Preparation and characterization of Au colloid monolayers. *Analytical Chemistry* **1995**, *67*, 735–743.

50 Liu, J. S.; Kan, C. X.; Cong, B.; Xu, H. Y.; Ni, Y.; Li, Y. L.; Shi, D. N. Plasmonic property and stability of core–shell Au@SiO_2 nanostructures. *Plasmonics* **2014**, *9*, 1007–1014.

51 Li, H. C.; Kan, C. X.; Yi, Z. G.; Ding, X. L.; Cao, Y. L.; Zhu, J. J. Synthesis of one dimensional gold nanostructures. *Journal of Nanomaterials* **2010**, *2010*, 1–8.

52 Gorelikov, I.; Matsuura, N. Single-step coating of mesoporous silica on cetyltrimethyl ammonium bromide-capped nanoparticles. *Nano Letters* **2008**, *8*, 369–373.

53 Zhang, B. Q.; Li, S. B.; Xiao, Q.; Li, J.; Sun, J. J. Rapid synthesis and characterization of ultra-thin shell Au@SiO_2 nanorods with tunable SPR for shell-isolated nanoparticle-enhanced Raman spectroscopy (SHINERS). *Journal of Raman Spectroscopy* **2013**, *44*, 1120–1125.

54 Nikoobakht, B.; El-Sayed, M. A. Preparation and growth mechanism of gold nanorods (NRs) using seed-mediated growth method. *Chemistry of Materials* **2003**, *15*, 1957–1962.

55 Ming, T.; Feng, W.; Tang, Q.; Wang, F.; Sun, L. D.; Wang, J. F.; Yan, C. H. Growth of tetrahexahedral gold nanocrystals with high-index facets. *Journal of the American Chemical Society* **2009**, *131*, 16350–16351.

56 Liz-Marzan, L. M.; Giersig, M.; Mulvaney, P. Synthesis of nanosized gold–silica core–shell particles. *Langmuir* **1996**, *12*, 4329–4335.

57 Guerrero, A. R.; Zhang, Y.; Aroca, R. F. Experimental confirmation of local field enhancement determining far-field measurements with shell-isolated silver nanoparticles. *Small* **2012**, *8*, 2964–2967.

58 Le Ru, E. C.; Etchegoin, P. G. Rigorous justification of the $|E|^4$ enhancement factor in surface enhanced Raman spectroscopy. *Chemical Physics Letters* **2006**, *423*, 63–66.

59 Osorio-Roman, I. O.; Guerrero, A. R.; Albella, P.; Aroca, R. F. Plasmon enhanced fluorescence with aggregated shell-isolated nanoparticles. *Analytical Chemistry* **2014**, *86*, 10246–10251.

60 Kneipp, K.; Kneipp, H. Single molecule Raman scattering. *Applied Spectroscopy* **2006**, *60*, 322A–334A.

61 Kneipp, K.; Wang, Y.; Kneip, H.; Perelman, L. T.; Itzkan, I.; Dasari, R. R.; Feld, M. Single molecule detection using surface-enhanced Raman scattering. *Physical Review Letters* **1997**, *78*, 1667–1670.

62 Kruszewski, S.; Cyrankiewicz, M. Aggregated silver sols as SERS substrates. *Acta Physica Polonica A* **2012**, *121*, A68–A74.

63 Camacho, S. A.; Aoki, P. H. B.; Albella, P.; Oliveira Jr., O. N.; Aroca, R. F.; Constantino, C. J. L. Increasing the enhancement factor in plasmon enhanced fluorescence with shell-isolated nanoparticles. *Journal of Physical Chemistry C* **2016**, *120*(37), p. 20530–20535.

64 Aroca, R. F.; Teo, G. Y.; Mohan, H.; Guerrero, A. R.; Albella, P.; Moreno, F. Plasmon-enhanced fluorescence and spectral modification in SHINEF. *Journal of Physical Chemistry C* **2011**, *115*, 20419–20424.

65 Volpati, D.; Alsaleh, A.; Constantino, C. J. L.; Aroca, R. Plasmon-Enhanced scattering and fluorescence used for ultrasensitive detection in Langmuir–Blodgett monolayers. In *Frontiers of Surface-Enhanced Raman Scattering*, Ozaki, Y.; Kneipp, K.; Aroca, R., Eds. John Wiley & Sons Ltd.: Chichester, **2014**; pp 243–255.

66 Ramirez-Maureira, M.; Vargas, C. V.; Riveros, A.; Goulet, P. J. G.; Osorio-Roman, I. O. Shell-isolated nanoparticle-enhanced fluorescence (SHINEF) of CdTe quantum dots. *Materials Chemistry and Physics* **2015**, *151*, 351–356.

67 Kong, W. G.; Zhang, B. P.; Li, R. F.; Wu, F. F.; Xu, T. N.; Wu, H. Z. Plasmon enhanced fluorescence from quaternary Cu–In–Zn–S quantum dots. *Applied Surface Science* **2015**, *327*, 394–399.

68 Teng, Y.; Ueno, K.; Shi, X.; Aoyo, D.; Qiu, J. R.; Misawa, H. Surface plasmon-enhanced molecular fluorescence induced by gold nanostructures. *Annalen Der Physik* **2012**, *524*, 733–740.

69 Zhang, Y.; Aslan, K.; Previte, M. J. R.; Geddes, C. D. Metal-enhanced e-type fluorescence. *Applied Physics Letters* **2008**, *92*, 013905.

70 Le Ru, E. C.; Etchegoin, P. G.; Grand, J.; Felidj, N.; Aubard, J.; Levi, G. Mechanisms of spectral profile modification in surface-enhanced fluorescence. *The Journal of Physical Chemistry C* **2007**, *111*, 16076–16079.

71 Roberts, G. *Langmuir–Blodgett Films*. Plenum Press: New York, **1990**.

72 Zhao, L.; Ming, T.; Chen, H. J.; Liang, Y.; Wang, J. F. Plasmon-induced modulation of the emission spectra of the fluorescent molecules near gold nanorods. *Nanoscale* **2011**, *3*, 3849–3859.

17

Controlled and Enhanced Fluorescence Using Plasmonic Nanocavities

Gleb M. Akselrod[1,2], David R. Smith[1,2,3], and Maiken H. Mikkelsen[1,2,3]

[1] *Center for Metamaterials and Integrated Plasmonics, Duke University, Durham, NC, USA*
[2] *Department of Electrical and Computer Engineering, Duke University, Durham, NC, USA*
[3] *Department of Physics, Duke University, Durham, NC, USA*

17.1 Introduction to Plasmonic Nanocavities

Fluorescence from molecular and nanoscale emitters is critical to optoelectronic devices such as lasers, light-emitting diodes (LEDs), and single-photon sources, as well as for biological imaging and detection. Often these, applications are limited by the intrinsically weak interaction between emitters and light which is manifested in a number of poor optical properties, including weak absorption, slow spontaneous emission, and nondirectional emission. Over the past two decades, dielectric [1–6] and plasmonic nanostructures have been developed that structure the electromagnetic environment around fluorescent emitters in order to enhance and control their interaction with light. Plasmonic nanocavities are particularly powerful for enhancing the optical properties of emitters due to their small optical mode volumes and relatively broad resonances that are well matched to the broad emission and absorption spectral features of molecules. In particular, plasmonic nanocavities have been used for absorption enhancement [7, 8], spontaneous emission rate enhancement [7, 9–11], and modification of the emission directionality [12–14]. Control of these fundamental properties has given rise to a number of proof-of-principle optical devices based on plasmonic enhancement of absorption and fluorescence, including single-photon sources [10, 15, 16], nanolasers [17, 18], biomolecule sensors [19], and photodetectors [20–22].

Central to achieving large enhancements in the properties of fluorescent emitters is the ability to create metal nanostructures with small optical mode volumes. The best mode confinement occurs in metal–insulator–metal structures with nanoscale gaps, such as the bowtie nanoantenna [7] or other metal dimers [23]. However, these structures are often made using nanofabrication techniques such as electron beam lithography [7, 23] or ion beam milling [24], making it difficult to create the sub-10-nm gaps in which the largest electric field enhancements occur. At the same time, these nanocavities must also act as efficient optical antennas by efficiently radiating the fluorescence coupled to the structure into free space or a waveguide. A promising geometry that overcomes the fabrication challenge and has the simultaneous advantages of a nanocavity and an optical antenna is the nanopatch antenna [14, 16, 25, 26]. This structure consists of a metal disk or flat metal nanoparticle situated over a metal ground plane, separated vertically by a dielectric spacer. This geometry enables a planar fabrication technique, which allows the metal–insulator–metal gap to be controlled with nanometer [27] and even with subnanometer [28] precision. Microfabricated patch antennas with micrometer diameters have been used to enhance the spontaneous emission rate by a factor of ~80 and showed directional emission, although the radiative quantum efficiency was poor [14]. The optical patch antenna has also been theoretically proposed as an efficient single-photon source with a high repetition rate [16].

Recently, our group developed a nanopatch antenna based on colloidal silver nanocubes that has proved to be a versatile and well-controlled system for manipulating the absorption and emission rate of fluorescent emitters. The structure consists of a metal nanocube situated over a metal film, separated by a ~10-nm dielectric spacer, forming a plasmonic nanocavity with an ultrasmall effective mode volume of $V_{\text{eff}} \approx 0.001(\lambda/n)^3$ and a typical quality factor of $Q \approx 15$ (Figure 17.1a). Fluorescent emitters embedded into this nanocavity

Surface Plasmon Enhanced, Coupled and Controlled Fluorescence, First Edition. Edited by Chris D. Geddes.
© 2017 John Wiley & Sons, Inc. Published 2017 by John Wiley & Sons, Inc.

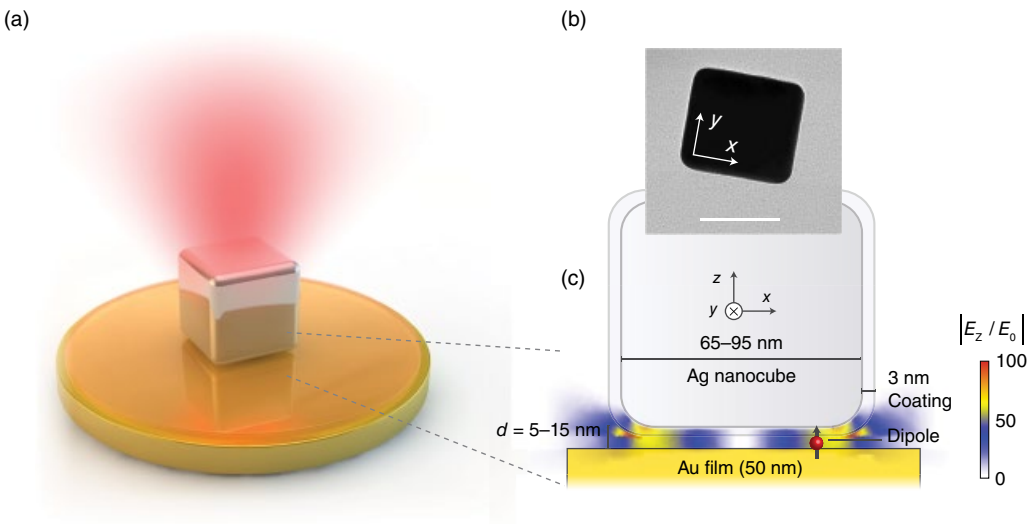

Figure 17.1 (a) Schematic of the nanocavity formed by a colloidal silver nanocube situated over a metal ground plane, separated by a dielectric spacer. Upward beam illustrates the directional emission from the cavity due to its action as a nanopatch antenna. (b) Transmission electron micrograph of a single nanocube, showing atomically flat facets. Scale bar: 50 μm. (c) Cross-sectional schematic of the nanocavity, showing the electric field enhancement in the *z*-direction at the fundamental resonance of the structure. An optimally oriented and positioned dipole is illustrated. Akselrod *et al*. [30]. Reproduced with the permission of Nature Publishing Group.

have shown fluorescence intensity enhancement of up to a factor of 30 000 [29] as well as ~1000-fold enhancements in the spontaneous emission rate [30, 31]. The purpose of this chapter is to review the properties of this structure and the experimental demonstrations of fluorescence control and enhancement.

The film-coupled nanocube structure can be considered a Fabry–Pérot resonator that supports a half-wavelength fundamental mode. The mode is confined laterally by the edges of the nanocubes and vertically by the nanoscale gap formed between the nanocube's bottom facet and the metal film (Figure 17.1a and b). This unique plasmonic mode has four key advantages: (i) The nanoscale gap creates electric field enhancements of up to ~100-fold over a large fraction of the nanocavity [27] (Figure 17.1c). These large field enhancements can subsequently be used for absorption enhancement or for spontaneous emission rate enhancement (Purcell enhancement) of emitters [30, 32]. (ii) The resonance wavelength can be tuned over a wide wavelength range by changing the thickness of the spacer layer in the gap or by changing the nanocube size [27, 33]. (iii) Despite the large field enhancements and the proximity of emitters to metal surfaces, the radiative quantum yield of the structure is high, up to ~50%, due to the antenna action of the nanocavity [29, 30, 34]. (iv) The patch antenna emission is directional, with a calculated collection efficiency of 84% using a standard microscope objective [30].

In the chapter, we first discuss the general procedure for fabricating the nanocavities (Section 17.2). In Section 17.3, we discuss the properties of the nanocavity modes, the tunability of these modes, and the directional emission from the structure. In Section 17.4, we present the theory of emitters coupled to the nanocavity and the simulation techniques used to quantify absorption and fluorescence enhancement. Section 17.5 presents a demonstration of large fluorescence enhancement from dye molecules coupled to the nanocavity. In Section 17.6, we discuss how the nanocavity can be used to enhance the spontaneous emission rate of molecules by a factor of ~1000. In Section 17.7, the same approach is used to enhance the emission rate from colloidal quantum dots (QDs) in order to obtain an ultrafast source of spontaneous emission. Section 17.8 focuses on utilizing both the fundamental and second-order resonance of the nanocavity in order to simultaneously enhance the absorption and fluorescence quantum yield of a MoS_2 monolayer. Finally, Section 17.9 provides conclusions and outlook on future directions.

17.2 Summary of Fabrication

While fabrication procedures varied slightly between the different experiments described in this chapter, here we give a general summary of the techniques used [29, 30]. The key features that enables fabrication of reproducible plasmonic nanocavities with small mode volumes is the use of colloidally synthesized silver nanocubes and the nanometer-precision polymer spacer layer. The nanocubes, originally developed

by Sun *et al.* [35], are crystalline with pristine facets of tunable size that form one side of the nanocavity. For the nanocavity experiments described subsequently, the nanocubes are chemically synthesized using CF_3COOAg as a precursor using the method described by Zhang *et al.* [36]. As a byproduct of the synthesis, the nanocubes are coated with a ~3-nm thick layer of poly(vinyl pyrrolidone) (PVP), which contributes to the volume of nanocavities formed with the nanocubes.

The nanocavities are fabricated by first depositing a 50–75-nm thin film of Au or Ag on a glass substrate by electron beam evaporation, using a 5-nm Ge or Cr adhesion layer. The spacer layer between the nanocube and the metal, which constitutes the volume of the nanocavity, is composed of a polymer film assembled using a layer-by-layer dip coating technique. To form this polymer film, the metal films are immersed in alternating solutions of cationic poly(allylamine) hydrochloride (PAH) (3 mM) and anionic polystyrenesulfonate (PSS) (3 mM) for 5 min each, with a water rinse between each polymer deposition. The alternating charge of each polyelectrolyte (PE) layer insures that a single monolayer of polymer is deposited at each step. The thickness of the spacer layer is determined by the number of PE layers used and is measured using variable angle spectroscopic ellipsometry. Each PAH–PSS bilayer contributes a thickness of ~2 nm. This vertical assembly technique for forming the cavity spacer gives nanometer control of the cavity dimensions, which is not possible with lithographic techniques. The films are terminated with a positively charged PAH layer to allow for adhesion of the negatively charged nanocubes. In order to integrate molecular emitters into the cavity, the polymer films are immersed in an aqueous solution of Cy5 dye (Section 17.5) or Ru dye (Section 17.6), which intercalate into the top layers of the polymer film. To complete the nanocavities, a solution of nanocubes is deposited on the polymer film allowing the negatively charged nanocubes to attach to the PAH layer. The concentration of nanocubes in solution and the deposition time is controlled such that the final surface density gives a mean separation of >3 μm, allowing each nanocavity to be addressed optically with a focused laser beam.

17.3 Properties of the Nanocavity

The nanocavity formed by the film-coupled silver nanocubes has a number of unique features that make it suitable for enhancement of fluorescence, which will be reviewed in this section. The gap between the nanocube and metal film can be considered a Fabry–Pérot resonator, with the horizontal (longitudinal) length of the resonator, and hence the fundamental resonance wavelength, determined by the side length of the nanocube. The vertical (transverse) dimension of the nanocavity is determined by the thickness of the polymer spacer layer. The optical properties can be predicted theoretically using a coupled-mode theory recently developed by our group [37]. Alternatively, the structure can be interpreted using transmission line theory, in analogy with microwave transmission lines [38]. In this chapter, we consider only the optical properties of the structure as obtained from full-wave simulations [34].

17.3.1 Nanocavity Resonances

To analyze the modes of this nanocavity, Lassiter *et al.* [27] employed full-wave numerical simulations using COMSOL Multiphysics, the details of which are described in Section 17.4.1. The calculated scattering spectrum of a nanocavity formed with an $L = 81$ nm nanocube and a $d = 8$ nm gap shows several narrowband resonances (Figure 17.2a), which have the same spectral positions under TM- and TE-polarized excitation. The fundamental mode of the cavity has a Lorentzian line shape with a resonance at $\lambda = 675$ nm and a linewidth of ~35 nm. These modes are analogous to waveguide cavity modes that have been observed in other plasmonic structures having a metal–insulator–metal structure [33, 39–41]. The modes can be excited from free space and simultaneously observed in the scattering spectrum due to the leaky nature of the waveguide. Modes 1–3, occurring at shorter wavelengths in the scattering spectrum, correspond to higher order modes that have multiple field nodes. These modes have strong spectral overlap with each other but are distinct from the fundamental resonance (mode 4). To visualize these modes, the normal component of the electric displacement field on the surface of the nanocube is plotted in Figure 17.2b. The complex pattern of mode 3 is attributed to both x and y propagating components. The modes have nearly identical profiles for both TE- and TM-polarized excitation, indicating that these modes are independent of polarization.

The cavity mode that has been the focus of most experimental work is the fundamental resonance (mode 4). The electric field distribution of this mode has dipolar character, with the maximum electrical field near the edges of the cavity (Figure 17.3a and c). The dominant electric field is in the vertical direction, normal to the metal surfaces. This mode roughly satisfies the half-wavelength criterion of an analogous dielectric resonator, but modified here by the plasmonic

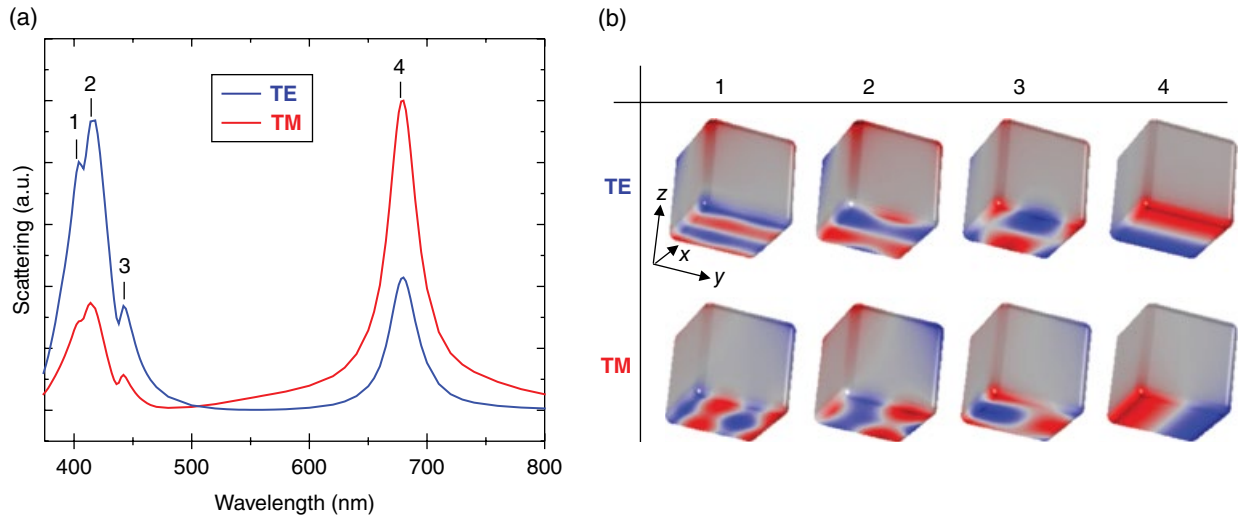

Figure 17.2 (a) Simulated scattering spectrum of a typical nanocavity under TM and TE excitations, showing multiple resonances. Peak 4 is the fundamental resonance of the nanocavity, while peaks 1, 2, and 3 are the second-order modes. (b) Electric displacement fields on the surface of the nanocube at the resonance wavelength indicated in (a).

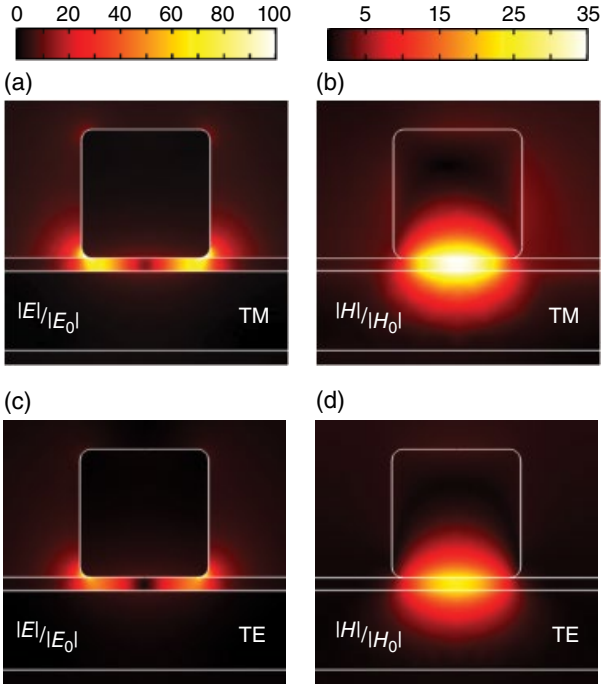

Figure 17.3 (a and c) Electric field enhancement and (b and d) magnetic field enhancement relative to free space at the fundamental resonance of the nanocavity. The field enhancement is higher under (a and b) TM excitation, as compared to (c and d) TE excitation.

dispersion of the metal–insulator–metal structure. The maximum field enhancement relative to free space is ~100×, corresponding to an intensity enhancement of 10 000×. While the field distribution is found to be similar for TE and TM excitations, TM excitation results in larger field enhancements. Unlike the electric field, the magnetic field distribution has a maximum in the center of the cavity with the dominant field oriented in the plane, parallel to the metal surfaces (Figure 17.3b and d).

17.3.2 Tuning the Resonance

The resonance of the fundamental mode can be precisely tuned by independently varying the nanocube size or the spacer thickness. Figure 17.4 shows the measured and simulated scattering spectra obtained from nanocavities with varying spacer thickness. The scattering spectra are obtained using darkfield illumination with white light, followed by collection and detection of the scattered light onto an imaging spectrograph. The left column shows spectra from three individual nanocubes coupled to a silver film, each with a different spacer layer but a nearly identical nanocube size. Meanwhile, the right column shows three individual nanocubes coupled to a gold film. In addition to the PE layers, a 3-nm coating of residual polymer on the nanocubes contributes to the nanocavity spacer thickness. With increasing spacer thickness, the resonance moves to shorter wavelengths, a trend which is observed both in experiments and simulations. This behavior is to be expected for a coupled system in which the coupling strength increases with reduced spacing of the coupled elements, thus red-shifting the resonance. The spacer thickness in the simulations was varied in order to match the experimentally observed resonance wavelength. This was the only fit parameter used in the simulations. The fitted spacer thicknesses from simulations were found to agree well with the measured spacer thickness.

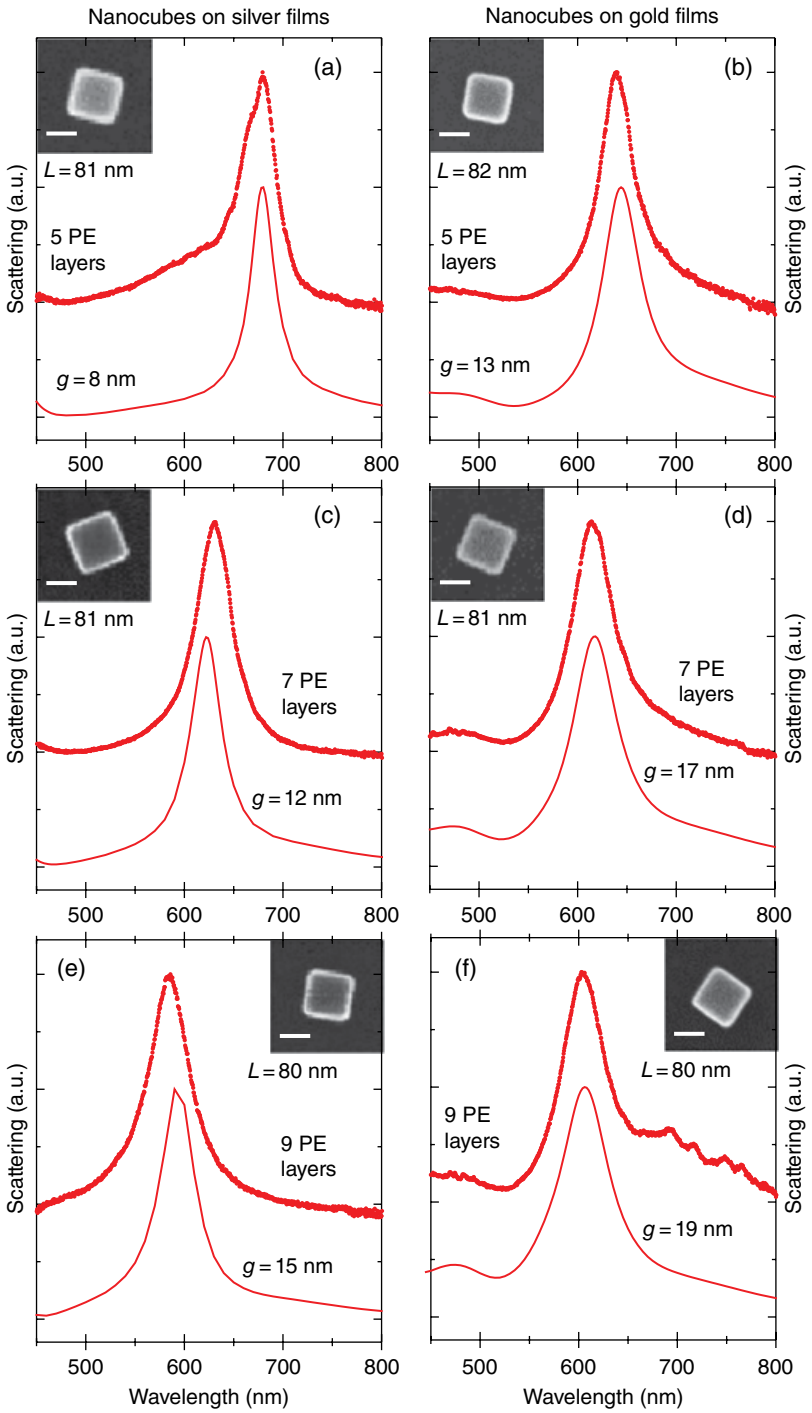

Figure 17.4 Experimental and simulated scattering spectra from nanocubes on varying spacer thicknesses. (a, c, and e) Nanocubes coupled to a silver film. (b, d, and f) Nanocubes coupled to a gold film. In each plot, the bottom spectrum is simulated and the top spectrum is measured, obtained from darkfield microscopy. The inset shows an SEM image of the same nanocube from which the scattering spectrum is obtained. Scale bar is 55 nm. The measured and simulated spectra are obtained under TM-polarized excitation. The size of each nanocube, *L*, is indicated under the SEM images. The spacer layer thickness for the experimental structures is indicated by the number of PE layers, with five PE layers corresponding to an alternating stack of three PAH and two PSS layers, terminating with PAH. The gap size for each simulation is indicated by *g*. Reproduced with the permission of American Chemical Society.

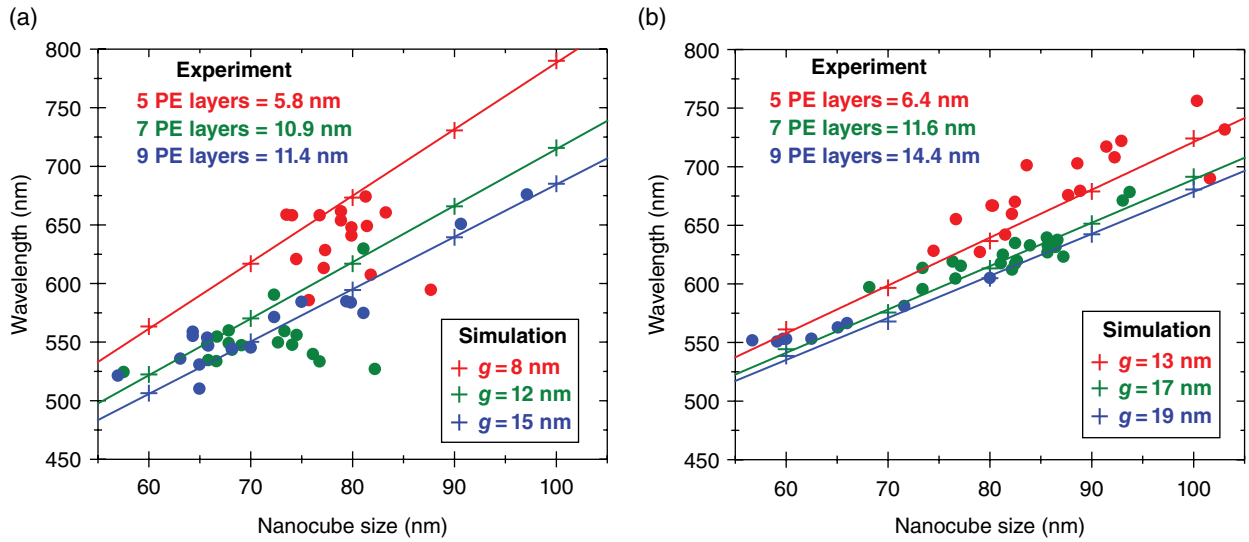

Figure 17.5 Nanocavity fundamental resonance wavelength as a function of nanocube size, (a) on a silver film and (b) on a gold film. Experimental values are shown as circles while simulation values are shown as crosses. Lines are linear fits to the simulated data points.

In addition to varying the spacer thickness, the resonance wavelength can also be tuned by changing the nanocube size. Figure 17.5 shows the correlation between nanocube size, measured by scanning electron microscopy (SEM), and the fundamental resonance wavelength, measured by darkfield scattering spectroscopy. SEM and optical measurements were done on the same individual nanocubes by creating alignment marks on the sample and using the spatial distribution of nanocubes on the surface to locate particular nanocubes in each instrument. With increasing nanocube size, the resonance wavelength increases, consistent with the film-coupled nanocube acting as a half-wavelength Fabry–Pérot resonator. In contrast, increasing the vertical dimension of the nanocavity through the spacer thickness decreases the resonance wavelength. The correlation between nanocube size and resonance wavelength is found to be better in the case of a gold ground plane as compared to a silver ground plane. The large variation in resonances with the silver film is attributed to the rapid oxidation of the silver, creating a rougher film and hence an inconsistent nanocavity geometry. The simulations of the resonance wavelength show good agreement with the measured values for both ground plane metals and for all three spacer thicknesses. The spacer thicknesses for the simulations are obtained by fitting the simulated resonance wavelength to the measured resonance wavelength for $L = 80$ nm cubes, as in Figure 17.4.

17.3.3 Directional Scattering and Emission

While large field enhancement has been observed in other metal–insulator–metal structures [7, 42], the film-coupled nanocube system is fundamentally different in its ability to couple the confined plasmons to free space by acting as an efficient antenna. Figure 17.6 shows schematics of two well-studied plasmonic antenna geometries—the bowtie antenna and the film-coupled sphere—and their free-space radiation patterns, with a comparison to the film-coupled nanocube. The plasmonic modes in these structures result from the hybridization of plasmonic resonances that occur in each of the constituent elements. This hybridization creates either symmetric or antisymmetric modes. The highly confined antisymmetric mode couples to free space, having the radiation pattern of an electric dipole. In the case of the bowtie antenna on glass, the image dipole is weak, and most of the radiation couples to the glass substrate, although the main emission lobe is normal to the antenna. The film-coupled sphere system has a vertical effective electric dipole with a strong image dipole. These electric dipoles radiate primarily along the substrate, making collection with free-space optics difficult.

In contrast, the film-coupled nanocube has an effective magnetic dipole due to the opposed currents in the top and bottom surface of the cavity. Two degenerate magnetic dipoles are present, one along each in-plane axis. These dipoles radiate out of plane, with the radiation lobe perpendicular to the surface and emitting into free space. This geometry is analogous to the microwave patch antenna and has similar radiation characteristics. Consequently, the film-coupled nanocube is also referred to as a nanopatch antenna. This feature of the film-coupled nanocube is critical: the small gap between the nanocube and the

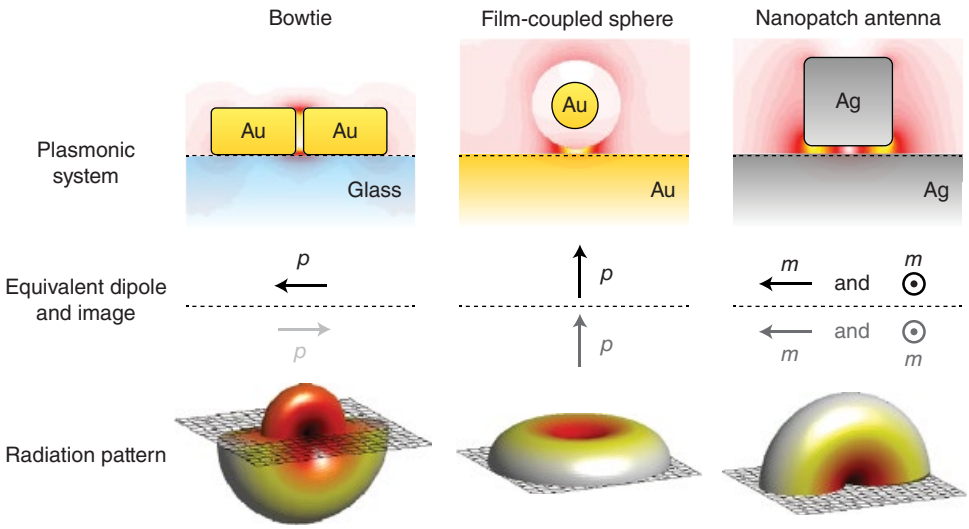

Figure 17.6 Geometries and the radiation patterns of two plasmonic antenna geometries—bowtie antenna and film-coupled sphere—and their radiation patterns as compared to the film-coupled nanocube (nanopatch antenna). The effective dipole for each structure and its image dipole in the substrate are shown. The nanopatch antenna, which has an effective magnetic dipole, shows the highest coupling into free space. Reproduced with the permission of American Chemical Society.

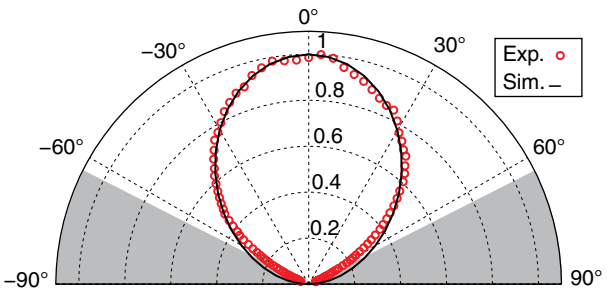

Figure 17.7 Measured and simulated radiation pattern from a single nanopatch antenna with $L = 75$ nm and $g = 8$ nm. Gray regions indicate angular regions outside the collection of the objective lens. Using an objective lens with NA = 0.9, it is estimated that 84% of light is collected, based on the simulations. Reproduced with the permission of Nature Publishing Group.

film forms a small mode volume nanocavity with large field enhancement *and* couples favorably to free space due to the antenna action of the structure.

The radiation pattern of a single nanopatch antenna was investigated using Fourier space imaging of scattered light resonant with the fundamental mode [30]. The measurement technique involves imaging the back aperture of the objective lens onto a CCD, and subsequently converting pixel position into emission angle [43]. The measured radiation pattern shows good agreement with the simulated pattern obtained from CST Microwave Studio (Figure 17.7). Using an objective lens with NA = 0.9, it is estimated that 84% of plasmons that decay as free-space photons can be collected by the objective.

17.4 Theory of Emitters Coupled to Nanocavity

To understand the coupling of fluorescent emitters to the film-coupled nanocube, we approximate the emitters as four-level systems (Figure 17.8), as is typical of organic dyes and colloidal semiconductor QDs. In absence of the plasmonic structure, excitation occurs at a rate γ_{ex}^0 from the ground state (i) to the excited state (ii), with transition energy $\hbar\omega_{ex}$. In the case of molecular emitters, this absorption is followed by vibrational relaxation to the relaxed excited state (iii), which typically occurs on the picosecond timescale. The relaxed excited state can subsequently decay back to the ground state radiatively by spontaneously emitting a photon with energy $\hbar\omega_{sp}$ at a rate γ_r^0, or nonradiatively with an internal decay rate γ_{int}^0 by emitting phonons. This spontaneous decay transition occurs at an energy less than the excitation energy, allowing for control the two processes independently by tuning the plasmonic resonance (Section 17.8). The internal nonradiative decay is an intrinsic property of the emitter that is determined by factors such as the solid-state environment or coupling of the excited electron to the vibrational states of the molecule. The intrinsic radiative quantum yield (QY_0), sometimes referred as the quantum efficiency, is defined as the fraction of excited molecules that emit a photon, given by

$$QY_0 = \frac{\gamma_r^0}{\gamma_r^0 + \gamma_{int}^0} = \frac{\gamma_r^0}{\gamma_{sp}^0}, \tag{17.1}$$

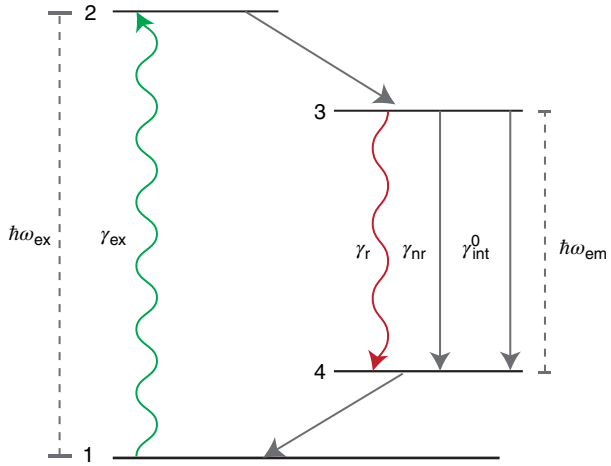

Figure 17.8 Energy diagram of a four-level system, which represents typical emitters such as molecular dyes. Wavy lines indicate radiative transitions, while straight lines indicate nonradiative transitions. The relevant rates in the system are labeled, including the excitation rate γ_{ex}, the radiative decay rate due to the plasmonic structure γ_r, the nonradiative decay rate due to the plasmonic structure γ_{nr}, and the internal decay rate of the emitter γ^0_{int}. The excitation transition energy is $\hbar\omega_{ex}$, while the emission transition energy is $\hbar\omega_{em}$.

where γ^0_{sp} is the intrinsic spontaneous decay rate, also referred to as the spontaneous emission rate.

17.4.1 Simulation of Nanocavity

When the emitter is coupled to the nanocavity, both the excitation rate and the emission rate can be enhanced, depending on the spectral overlap between the nanocavity resonance and the transition energies of the emitter. To quantify both processes, a full understanding of the emitters' electromagnetic environment is needed, which is obtained from finite-element simulations of the structure in COMSOL Multiphysics. In this section, we describe the general approach for the simulations used to support the experimental results described in Refs. [29, 30, 44], although details varied slightly in each of these works.

In order to obtain the scattering spectrum and the spatial maps of the field enhancement, the nanocavity structure was analyzed in the scattering formalism. In this formalism, the analytical solution for the incident fields in the absence of the nanocube is used as the background field. In the presence of the nanocube, modifications to this background field are then attributed to the nanocavity structure. With this method, it is possible to obtain the enhancement of the electric and magnetic fields relative to the free-space values, which is a convenient feature for comparison with experimental results. To model the nanocavity, a spherical domain was created around a single nanopatch antenna, and scattering boundary conditions were utilized to simulate an open boundary. The dispersive permittivity of the silver and gold was obtained from Palik [45]. When simulating with a silver back plane, the imaginary part of the permittivity was increased by a factor of 1.75 to account for film roughness and oxidation. This results in the simulated resonance linewidth matching the measured linewidth [29]. The corners of the nanocube were given a radius of curvature of ~8 nm, in accordance with the corner radius obtained from transmission electron microscopy images of the silver nanocubes. A 3-nm shell with a refractive index of $n = 1.45$ was placed around the nanocube to simulate the PVP layer which remains after chemical synthesis. The spacer layer was simulated as a lossless dielectric with a refractive index of $n = 1.45$. The spacer layer thickness and nanocube size were varied to match the experimental conditions as determined by ellipsometry and SEM analysis. The thickness of the metal ground plane is not found to be critical as long as the thickness is greater than ~50 nm. The substrate under the metal film is semi-infinite glass with a refractive index $n = 1.47$. The excitation was accomplished with a monochromatic plane wave either at normal incidence, or at ~62° relative to normal with TM polarization. The excitation angle was not found to affect the resonance wavelength or the electric field spatial distribution, but it does affect the maximum field enhancement [27]. This simulation domain was also used to simulate the spontaneous emission rate enhancement based on the Green's function formalism.

The simulations produce maps of the magnetic and electric field enhancements as a function of position in the nanocavity, as in Figure 17.3. The excitation rate enhancement for a molecule placed in the nanocavity at a position $\mathbf{r}$ is related to the field enhancement by

$$\frac{\gamma_{ex}(\mathbf{r})}{\gamma^0_{ex}(\mathbf{r})} = \frac{\left|\mathbf{E}_{ex}(\mathbf{r})\cdot\hat{\mathbf{n}}_p\right|^2}{\left|\mathbf{E}^0_{ex}(\mathbf{r})\cdot\hat{\mathbf{n}}_p\right|^2} \tag{17.2}$$

where γ_{ex} is the excitation rate in the cavity, $\mathbf{E}^0_{ex}$ is the electric field experienced for the molecule in free space or on a reference substrate, $\mathbf{E}_{ex}$ is the excitation rate in the nanocavity, and $\hat{\mathbf{n}}_p$ is the orientation vector of the molecules absorption transition dipole moment. The absorber/emitter molecules are assumed to be small perturbations to the cavity system and hence are not included in the simulations.

17.4.2 Enhancement in the Spontaneous Emission Rate

Since absorption and spontaneous emission in a four-level system are incoherent, we can treat these

processes independently. To simulate the spontaneous emission (fluorescence) dynamics of emitters coupled to the nanocavity, we employ the Green's function formalism [11, 34]. In this analysis, collective effects of multiple emitters will be neglected and the system is assumed to be in the weak coupling regime. The weak coupling assumption is valid, as discussed in Ref. [31]. According to Fermi's golden rule, the spontaneous emission rate for a point dipole at position **r** is

$$\gamma_{\mathrm{sp}} = \frac{\pi\omega}{3\hbar\varepsilon_0}|\mathbf{p}|^2\,\rho(\mathbf{r},\,\omega_{\mathrm{em}}) + \gamma_{\mathrm{int}}^0 \tag{17.3}$$

where ω_{em} is the transition frequency, **p** is the transition dipole moment, and $\rho(\mathbf{r},\omega)$ is the local density of optical states (LDOS). The first term in Eq. (17.3) constitutes the coupling of the transition dipole moment to free space or a photonic structure, while γ_{int}^0 is the internal decay rate of the dipole, which is not affected by the electromagnetic environment. The LDOS can be expressed in terms of the dyadic Green's function, **G**,

$$\rho(\mathbf{r},\omega) = \frac{6\omega}{\pi c^2}\left[\hat{\mathbf{n}}_{\mathrm{p}}\cdot\mathrm{Im}\{\mathbf{G}(\mathbf{r},\mathbf{r})\}\cdot\hat{\mathbf{n}}_{\mathrm{p}}\right] \tag{17.4}$$

where $\hat{\mathbf{n}}_{\mathrm{p}}$ is the unit vector for the transition dipole orientation. The Green's function is obtained from

$$\nabla\times\nabla\times\mathbf{G}(\mathbf{r},\mathbf{r}_0) - \varepsilon(\mathbf{r})k_0^2\mathbf{G}(\mathbf{r},\mathbf{r}_0) = \mathbf{I}\delta(\mathbf{r}_0) \tag{17.5}$$

where ε is the spatially dependent permittivity in the structure and k_0 is the free-space wavevector.

In free space, the LDOS is $\rho_0(\omega) = \omega^2/(\pi^2c^3)$, which gives the free-space spontaneous emission rate

$$\gamma_{\mathrm{sp}}^0 = \gamma_{\mathrm{r}}^0 + \gamma_{\mathrm{int}}^0 = \frac{\omega^3|\mathbf{p}|^2}{3\hbar\pi\varepsilon_0 c^3} + \gamma_{\mathrm{int}}^0. \tag{17.6}$$

In the presence of plasmonic structure, rather than decaying directly into free space, the emitter decays by generating a plasmon. Subsequently, this plasmon can decay itself by emitting a photon into free space with a radiative rate γ_{r}, or decay by Ohmic losses in the metal with a rate γ_{nr}. The total spontaneous decay rate of the emitter coupled to the nanocavity is then

$$\gamma_{\mathrm{sp}} = \gamma_{\mathrm{r}} + \gamma_{\mathrm{nr}} + \gamma_{\mathrm{int}}^0. \tag{17.7}$$

In a lossy environment such as the plasmonic nanocavity, the aforementioned Green's function formalism does not make it possible to distinguish between the radiative and nonradiative decay. Instead, only the total coupling rate to the plasmonic mode can be calculated, as given by

$$\gamma_{\mathrm{r}} + \gamma_{\mathrm{nr}} = \frac{2\omega^2}{\hbar\varepsilon_0 c^2}\left[\hat{\mathbf{n}}_{\mathrm{p}}\cdot\mathrm{Im}\{\mathbf{G}(\mathbf{r},\mathbf{r})\}\cdot\hat{\mathbf{n}}_{\mathrm{p}}\right]|\mathbf{p}|^2. \tag{17.8}$$

To determine the radiative and nonradiative rates explicitly, the Ohmic losses in the plasmonic structure can be calculated directly by integrating the absorbed power over the entire simulation domain **Ω**

$$\gamma_{\mathrm{nr}} = \frac{1}{2}\frac{\gamma_{\mathrm{r}}^0}{W_{\mathrm{r}}^0}\int_{\Omega}\mathrm{Re}\{\mathbf{J}^*\cdot E\}\,dV \tag{17.9}$$

where **J** is the current density in the metal induced by the oscillating molecular dipole, and $W_{\mathrm{r}}^0 = \omega^4|\mathbf{p}|^2/(12\pi\varepsilon_0 c^3)$ is the total power radiated by a dipole in free space. By knowing the nonradiative losses, the radiative decay rate can be calculated from $\gamma_{\mathrm{r}} = \gamma_{\mathrm{sp}} - \gamma_{\mathrm{nr}} - \gamma_{\mathrm{int}}^0$ and the quantum yield for emission of a photon from a nanocavity-coupled emitter is

$$\mathrm{QY} = \frac{\gamma_{\mathrm{r}}}{\gamma_{\mathrm{r}} + \gamma_{\mathrm{nr}} + \gamma_{\mathrm{int}}^0}. \tag{17.10}$$

The enhancement in the spontaneous emission rate for an emitter coupled to the nanocavity relative to free space or a control substrate is $\gamma_{\mathrm{sp}}/\gamma_{\mathrm{sp}}^0$. This value is often referred to as the Purcell factor, although this terminology has more precise meaning in the context of low-loss dielectric cavities, in which the enhancement in the total spontaneous emission rate is equal to the enhancement in the radiative decay rate, $\gamma_{\mathrm{r}}/\gamma_{\mathrm{r}}^0$. In the context of emitters coupled to plasmonic structures, the Purcell factor in most works refers to the enhancement in the total rate. We follow this convention in Sections 17.6, 17.7 and 17.8. However, plasmonic structures often have large nonradiative losses, making a short decay lifetime an insufficient metric of the radiative performance of the nanocavity. Instead, it is also important to calculate the complementary metrics of radiative rate enhancement and the radiative quantum yield, QY, as measures of how well the structure enhances and radiates the fluorescence into free space.

To simulate the quantum yield and Purcell enhancement, the emitters were modeled as monochromatic point dipoles in COMSOL Multiphysics. These dipole sources were swept in a grid pattern laterally across the nanocavity, calculating the Green's function and decay rates at each position. The same geometry was used to calculate both the scattering and absorption properties, and the emission rates. The 4-fold symmetry of the structure was used to reduce the number of simulation points.

In Sections 17.5, 17.6, 17.7, and 17.8, we explore an experimental demonstration of large absorption

enhancement in these plasmonic nanocavities as well as their large Purcell enhancement and high radiative quantum yield.

17.5 Absorption Enhancement

To investigate absorption and Purcell enhancement, Rose *et al.* [29] demonstrated the coupling of the molecular dye Cy5 to the plasmonic nanocavities, which will be reviewed in this section. We first present the experimental results on how fluorescence enhancement can be controlled by tuning the nanocavity resonance, followed by a comparison with the predictions from simulations using the formalism developed in Section 17.4.

The nanocavities are fabricated on a 50-nm silver film, following the process described in Section 17.2. After deposition of the five PE layers (5.0-nm thickness), the samples are immersed in a 25-μM solution of the Cy5 dye (sulfo-Cy5 carboxylic acid) for 10 min, followed by deposition of the silver nanocubes. The nanocube density is controlled such that individual nanocavities can be addressed optically in the darkfield microscope (Figure 17.9a). The fluorescence enhancement measurements were done on 48 isolated nanocavities with nanocube sizes ranging from 50 to 100 nm. Each nanocavity was first identified using darkfield imaging (Figure 17.9a) using a 50×, 0.55 NA microscope objective. The scattered light from each selected nanocavity was then collected and dispersed on a CCD spectrograph to identify the resonance wavelength (Figure 17.9b). The resonance linewidth (full-width at half-maximum) was found to be ~35 nm. The scattering spectra of two representative nanocavities are shown in Figure 17.9b. The nanocube size for each nanocavity was determined by SEM analysis of the same nanocubes by using alignment marks on the sample. Simulations and measurements of the scattering spectra show good agreement in the resonance shape and position.

To investigate the fluorescence enhancement, individual nanocavities were excited with $\lambda = 633$ nm HeNe continuous-wave laser at an angle of 62° relative to normal. The fluorescence was collected through the microscope objective and imaged onto a pinhole confocal with the nanocavity. The area of the pinhole is $A_c = 8.2\,\mu m^2$ when imaged back onto the sample plane, which is smaller than the defocused excitation spot. The fluorescence passing through the pinhole is imaged onto the spectrograph. To quantify the fluorescence enhancement, a control sample consisting of glass coated with the same number PE layers and embedded with Cy5 molecules was also fabricated

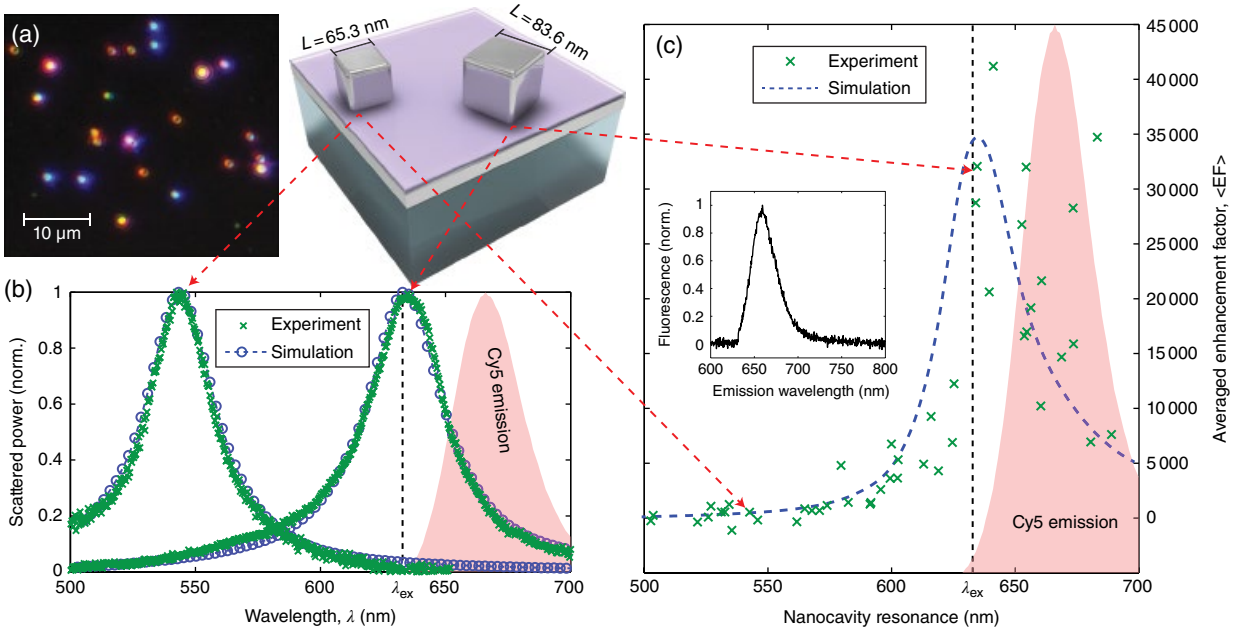

Figure 17.9 Experimentally measured fluorescence enhancement of Cy5 molecules coupled to nanocavities. (a) Darkfield scattering image on a color camera of multiple nanocavities, each with a different resonance wavelength, as apparent by the colors. (b) Scattering spectra of two representative nanocavities, with nanocube side lengths of $L = 65$ and 84 nm, along with simulated scattering spectra of the same geometries. (c) The measured and simulated enhancement factor as a function of nanocavity resonance wavelength. The measurements were done on 48 individual nanocavities. Inset shows a typical emission spectrum from a single nanocavity. Reproduced with the permission of American Chemical Society.

and measured under the same conditions. The average fluorescence enhancement factor per unit area can now be defined as

$$\langle \mathrm{EF} \rangle = \frac{I_{\mathrm{cav}}}{I_{\mathrm{glass}}} \frac{A_{\mathrm{c}}}{A_{\mathrm{cav}}} \tag{17.11}$$

where I_{cav} is the fluorescence intensity from the nanocavity, I_{glass} is the fluorescence intensity from the control sample, and A_{cav} is the lateral area of the nanocavity. The nanocavity area is the area of one nanocube facet, which is obtained by SEM analysis of the same nanocubes. The area normalization is done in order to obtain the fluorescence enhancement per unit area, or equivalently, per fluorescent molecule. It was found that on the nanocavity sample, regions outside the nanocubes showed extremely weak fluorescence due to quenching by the silver film, and this contribution could be neglected. On the other hand, on the control sample, the entire area A_{c} imaged by the pinhole is collected, which necessitates the area normalization.

Figure 17.9c shows the fluorescence enhancement factors for 48 individual nanocavities as a function of the fundamental resonance wavelength. Despite the statistical fluctuations, a clear trend is seen with the largest enhancement of $\langle \mathrm{EF} \rangle \approx 30000$ observed at resonance wavelengths from 635 to 675 nm. Rather than being centered about the excitation wavelength of 633 nm, the largest enhancements are centered about 655 nm. This is attributed to the fact that the quantum yield for radiative emission in plasmonic structures is typically higher for on-resonance emitters [8]. This has the effect of shifting the largest enhancements toward the emission spectrum, which is peaked at 665 nm. The scatter in the data can be attributed to a number of mechanisms including spatial variation in the density of Cy5 molecules and surface roughness of the evaporated silver film. While these steady-state measurements do not elucidate the emission rate enhancement, the large magnitude of the fluorescence increase suggests that the nanocavity is radiating efficiently as an antenna and that metal quenching is not a dominant mechanism.

To quantitatively understand the mechanisms responsible for the 30 000-fold fluorescence enhancement, we return to simulations of the plasmonic nanocavity. The enhancement in fluorescence can be decomposed into three contributions: (i) enhancement in the collection efficiency, (ii) enhancement in the excitation rate, and (iii) enhancement in the spontaneous emission quantum yield. The product of these factors gives the local fluorescence enhancement at position $\mathbf{r}$ in the cavity

$$\mathrm{EF}(\mathbf{r}) = \frac{\eta}{\eta_0} \frac{\gamma_{\mathrm{ex}}(\mathbf{r})}{\gamma_{\mathrm{ex}}^0} \frac{\mathrm{QY}(\mathbf{r})}{\mathrm{QY}_0} \tag{17.12}$$

The collection efficiency, η, is the fraction of fluorescence emitted from the nanoantenna that is collected by the objective which is 84% in our case (Section 17.3.3), and $\eta_0 = 15\%$ is the calculated collection efficiency from the control sample. The excitation rate and emission rate enhancements are calculated using the simulation method described in Section 17.4. Figure 17.10a shows the excitation rate enhancement for a vertically oriented molecule as a function of lateral position in the nanocavity for an $L = 84$ nm nanocube and a 5-nm polymer spacer (plus a 3-nm polymer coating on the nanocube). The vertical position probed is at the top of the polymer spacer, below the nanocube coating, although the field between the metal surfaces is not highly sensitive to the vertical position. Due to the ~100-fold field enhancement, the maximum excitation rate enhancement for vertically oriented dipoles is ~10 000-fold when the excitation is at the fundamental resonance wavelength of 633 nm. The spatial profile of the enhancement mirrors that of the field enhancement (Figure 17.3), with the largest enhancements near the sides of the nanocube. Figure 17.10e shows the spatially averaged excitation rate enhancement as a function of nanocavity resonance, which is obtained by sweeping the nanocube size. The spatial averaging assumes a random spatial distribution of molecules under the nanocube and a random angular orientation ($\hat{\mathbf{n}}_{\mathrm{p}}$).

The Purcell enhancement for emission was calculated by modeling the Cy5 molecules as monochromatic point sources emitting at $\lambda_{\mathrm{sp}} = 665$ nm and sweeping the dipole in a grid pattern through the nanocavity. Figure 17.10b shows a spatial map of the enhancement in the spontaneous emission rate at a nanocavity resonance of $\lambda_{\mathrm{cav}} = 633$ nm. Although the emission is nonresonant with the nanocavity, a >1000-fold enhancement in the spontaneous emission rate is still observed for vertically oriented emitters near the corners of the cavity. In the calculation of the total rate enhancement, it was assumed that the intrinsic quantum yield of Cy5 embedded in the polymer film is $\mathrm{QY}_0 = 20\%$. Knowing the enhancement in the total emission rate and by calculating the Ohmic losses in the metal, it is possible to calculate the radiative quantum yield (QY), following Eqs. (17.8–17.10) (Figure 17.10c). The quantum yield is found to be ~40% in the regions where the largest Purcell enhancements occur, with slightly lower values in the center of the nanocavity. This quantum yield is determined by the radiative and nonradiative decay rates of the plasmon, which are much faster than the internal decay rate of the molecule, γ_{int}^0.

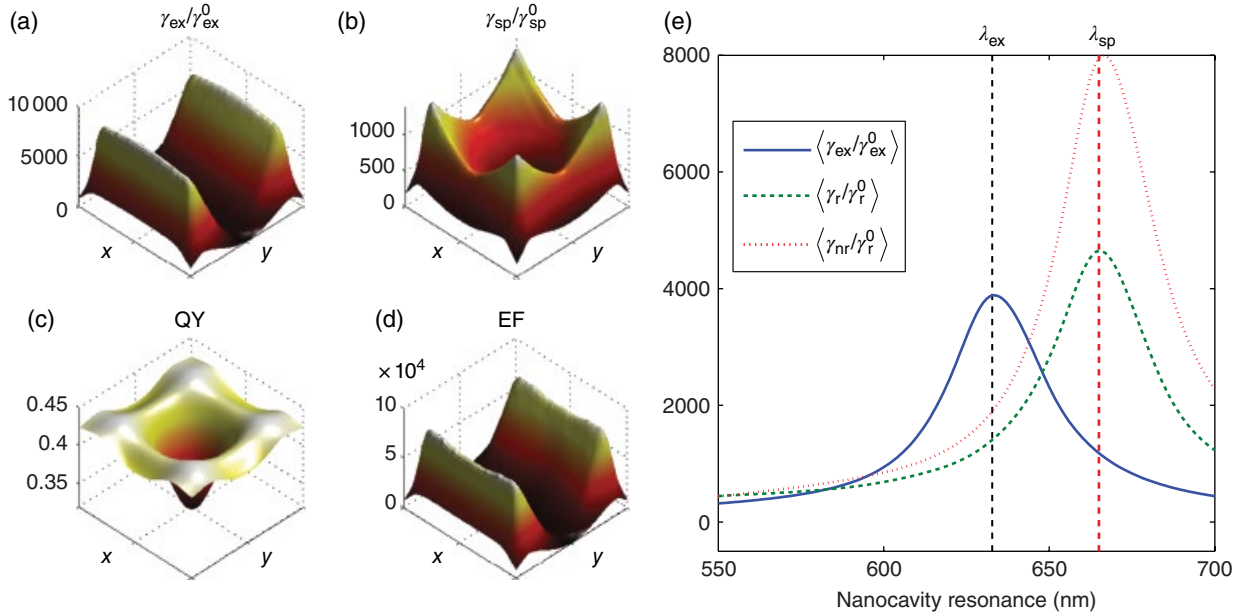

Figure 17.10 Spatial maps of the (a) excitation rate enhancement, (b) spontaneous emission rate enhancement, (c) quantum yield, and (d) fluorescence enhancement factor, as a function of position of the absorber/emitter molecule in the nanocavity. Simulations are done for $L = 84$ nm nanocube, $g = 5$ nm spacer (+3 nm nanocube coating), at the resonance wavelength of 633 nm. The emitters are assumed to be monochromatic, at a wavelength of 665 nm, off-resonance with the nanocavity.

Figure 17.10e shows the radiative rate and nonradiative rate enhancement relative to the free-space radiative rate, γ^0_r, as a function of nanocavity resonance. The largest rate enhancements occur when the nanocavity is resonant with the emission wavelength of the dipole. Critically, the radiative and nonradiative rates increase in concert as the nanocavity moves on-resonance with the emission, which is reflected in the high quantum yield of the structure. This feature of the film-coupled nanocube nanocavity is in contrast to the many plasmonic structures that increase the nonradiative decay channels, such as a molecule on a planar metal surface, without increasing the radiative decay rate [46]. Combining the simulated excitation rate and quantum yield, it is now possible to calculate the fluorescence enhancement factor as a function of position in the cavity, $\langle EF \rangle$, following Eq. (17.12) (Figure 17.10d). Figure 17.9c shows the predicted enhancement factor as a function of nanocavity resonance, with the largest enhancement of $\langle EF \rangle = 35\,000$ observed for a nanocavity resonance of $\lambda_{cav} = 633$ nm, at the excitation wavelength. This simulated value is in good agreement with the enhancement factors obtained experimentally.

17.6 Purcell Enhancement

The aforementioned discussion demonstrated the capability of the nanocavity to enhance the steady-state amount of fluorescence from molecules by increasing the absorption, increasing the directionality, and modifying the radiative quantum yield. Now, we turn to the question of how the nanocavity affects the emission dynamics from embedded molecules. Measuring large Purcell factors with conventional emitters such as fluorescent molecules and semiconductor QDs is challenging due to their short intrinsic fluorescence lifetimes of 1–10 ns. The expected 4500-fold Purcell enhancement for optimally coupled emitters in the nanocavity would result in spontaneous emission lifetimes of several picoseconds, which is beyond the resolution limit of single-photon detectors with a temporal response of ~30 ps. This temporal resolution barrier was encountered in the time-resolved measurements in the work by Rose *et al.* [29].

To overcome this challenge, Akselrod *et al.* [30] integrated into the nanocavity a phosphorescent ruthenium metal complex with an intrinsically long lifetime of $\tau_0 = 600$ ns. This dye was also chosen due to its large spectral shift between absorption and emission, such that only the emission process can be enhanced without dramatically enhancing the absorption. To fabricate the nanocavities, a 50-nm gold film was coated with PE layers ranging in thickness from 2 to 12 nm, followed by immersion in a solution of the Ru dye, which intercalates into the polymer film (Figure 17.11a). This was followed by deposition of the silver nanocubes with a typical size of $L = 75$ nm. The transition dipole moment of the molecules was found to be oriented at ~75° relative to normal, as is

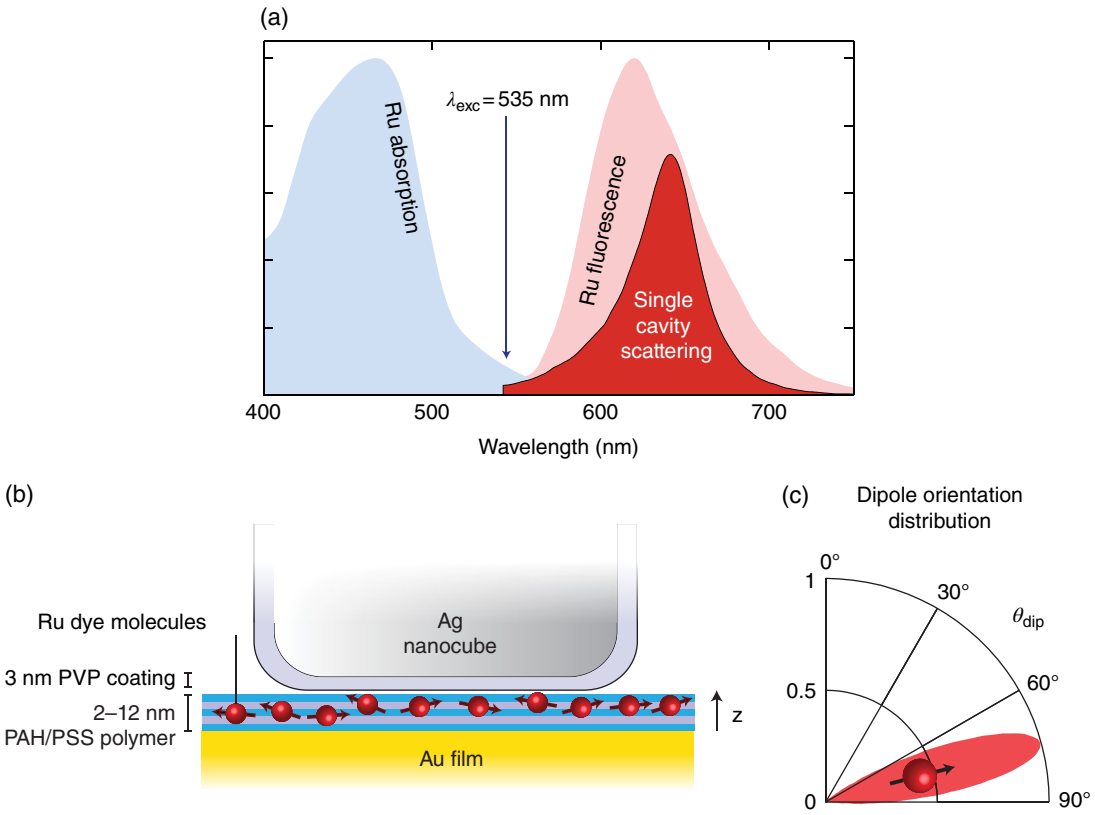

Figure 17.11 (a) Absorption and emission spectra of the Ru dye, showing overlap between the emission spectrum and the nanocavity scattering spectrum. (b) Schematic of the nanocavity structure with embedded Ru dye molecules. The arrows represent the orientation of their transition dipole moments. (c) Measured distribution of orientations of the Ru transition dipole moments.

illustrated in Figure 17.11b and c. This orientation distribution was found to be critical to accurately modeling the emission dynamics, as will be discussed in the following section. The nanocavities were excited through an objective lens nonresonantly with the nanocavities at $\lambda_{ex} = 535\,\text{nm}$ with a pulsed laser producing 150-fs pulses at a repetition rate of 20 MHz. The fluorescence was collected by the same objective lens, passed through a long-pass filter and detected using time-resolved single-photon counting. Only nanocavities with a resonance of $\lambda_{cav} \approx 620 - 650\,\text{nm}$ were selected, regardless of the spacer layer thickness. The relationship between nanocube size, spacer thickness, and resonance wavelength was discussed in Section 17.3.2.

Figure 17.12a shows a representative emission decay curve from a nanocavity with an 8-nm total gap thickness (including PVP layer surrounding the nanocube). In contrast to the long intrinsic decay with a lifetime of $1/\gamma_{sp}^{0} = \tau_0 = 600\,\text{ns}$ on glass, the nanocavity displays a much faster decay with a highly nonexponential time dependence. The fast initial decay is attributed to molecules that are optimally positioned within the cavity and have the most favorable angular orientation. The nonexponential decay occurs because each molecule coupled to the nanocavity experiences a different emission rate depending on its position and orientation. To obtain the underlying distribution of rates, the decay curve can be fitted to a stretched exponential function, a standard technique for analyzing time-resolved fluorescence in complex environments [47]. The decay constant for the stretched exponential fit is found to be $1/\gamma_{sp}^{max} = \tau_{max} = 0.7\,\text{ns}$, which characterizes the fastest decay rate present in the distribution of rates. This maximum decay corresponds to a Purcell factor of $\gamma_{sp}^{max}/\gamma_{sp}^{0} = 860$. A Laplace transform is then applied to the stretched exponential to obtain the entire distribution of decay rates (Figure 17.12b). This distribution shows that while a small fraction of molecules are optimally coupled to the cavity, the most likely emission occurs with a Purcell factor of ~60.

An important parameter in correctly simulating the emission dynamics is the orientation of the emitter transition dipole moment in the cavity. The orientation is critical because the emitter–cavity coupling scales with $\cos^2\theta$, where θ is the angle between the dipole direction and the electric field direction. In many studies of plasmon-enhanced fluorescence, the distribution of orientations is assumed to be isotropic

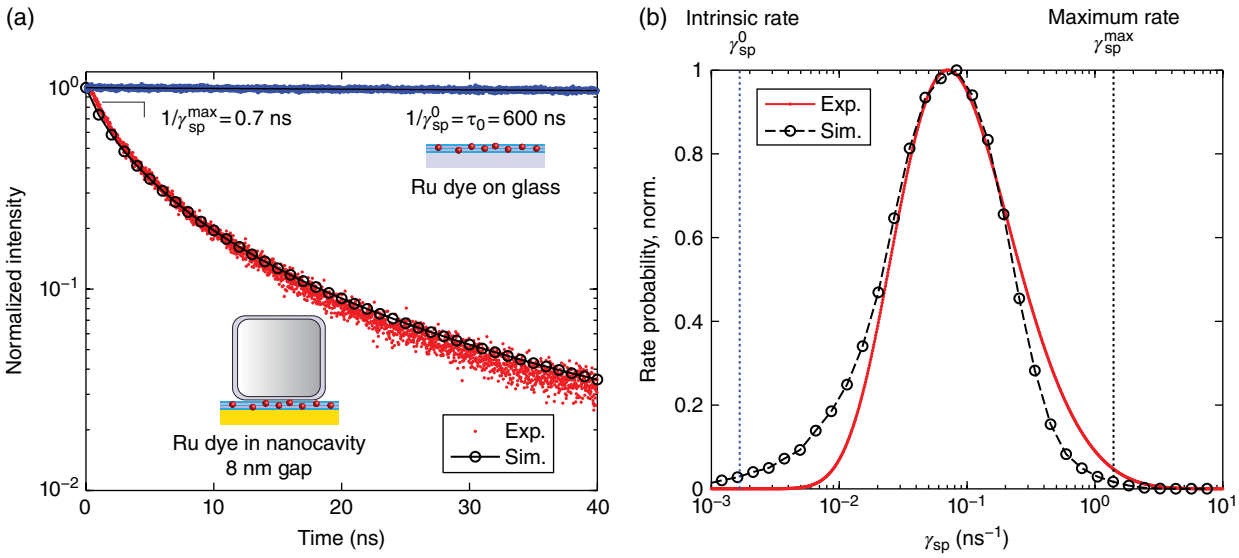

Figure 17.12 (a) Measured and simulated decay dynamics from Ru dye molecules coupled to a nanocavity with an 8-nm spacer thickness. Also shown is the intrinsic decay of Ru dye on glass, having a lifetime of 600 ns. (b) Distribution of decay rates obtained from time-resolved emission data in (a). Experimental distribution is obtained from a stretched exponential fit, while the simulated distribution is obtained from the spatial map of the spontaneous emission decay rate.

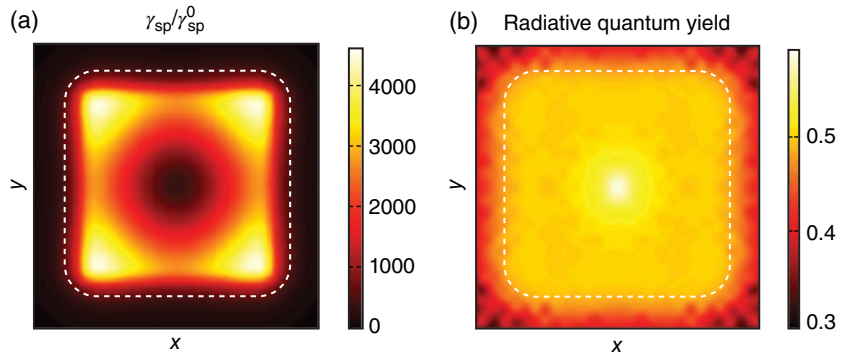

Figure 17.13 Simulated map of the (a) spontaneous emission rate enhancement and the (b) radiative quantum yield, as a function of position in a nanocavity with an 8-nm spacer and a resonance of $\lambda_{cav} = 650$ nm. The dipole orientation is assumed to be vertical, along the direction of the dominant field. White dashed outlines represent lateral extent of the nanocube.

[8, 14] or to have an optimal orientation [48]. In our work, an experimental technique was used to directly measure the distribution of Ru dipole orientations. To measure the dipole orientation, a sample was prepared consisting of a five PE layer polymer films embedded with Ru dye deposited on a Si wafer with ~1000-nm thermal oxide layer. Fluorescence from this sample was measured as a function of incidence angle, observation angle, and polarization using a goniometer setup as described in Ref. [49]. Based on these measurements, it was determined that most of the molecular emission dipoles are oriented at 75° relative to the surface normal, with a distribution width of ±15°.

In order to predict the emission dynamics, the structure was simulated following the procedure outlined in Section 17.4. Figure 17.13 shows the spontaneous emission rate enhancement, $\gamma_{sp}/\gamma_{sp}^{0}$, and the radiative quantum yield, QY, as a function of position in a nanocavity with an 8-nm total gap thickness and a $\lambda_{cav} = 650$ nm resonance. The largest Purcell enhancement from these simulations is ~4500 for a vertically oriented dipole located near the corners of the nanocavity. The exponential decay for a molecule located at a position $\mathbf{r}$ in the nanocavity and oriented at an angle θ relative to normal is given by

$$I(\mathbf{r},\theta,t) \propto \gamma_r(\mathbf{r}) \exp\left[-\gamma_{sp}(\mathbf{r}) \cos^2\theta\, t\right]. \qquad (17.13)$$

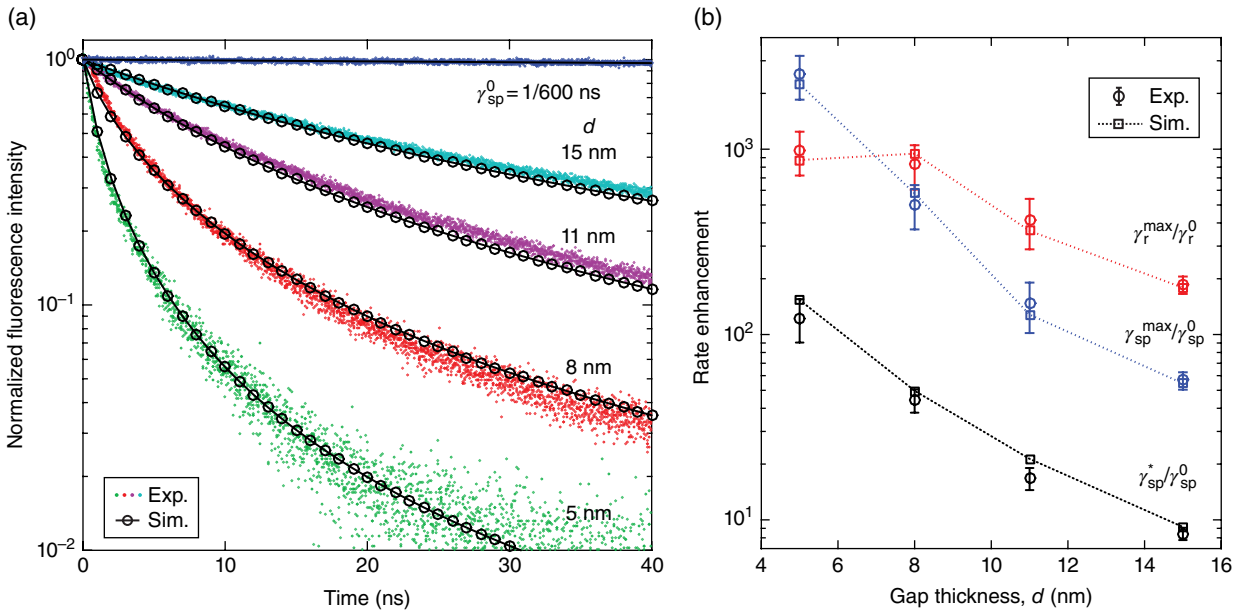

Figure 17.14 (a) Time-resolved emission from four representative nanocavities with varying gap sizes from 5 to 15 nm. Simulated emission dynamics (black lines with open circles) show good agreement with the experiment. (b) Enhancement in the maximum spontaneous emission rate $\gamma_{sp}^{max}/\gamma_{sp}^0$, enhancement in the mostly likely rate $\gamma_{sp}^*/\gamma_{sp}^0$, and enhancement in the radiative rate, $\gamma_r^{max}/\gamma_r^0$, as a function of gap thickness.

By performing averaging over all dipole positions and over the measured orientation distribution, it is possible to predict the emission dynamics from the nanocavity. Averaging was also performed over the vertical positions of the emitters, which were assumed to be in the top 2 nm of the polymer film. The calculated dynamics for a cavity with an 8-nm gap shows excellent agreement with the experimental data (Figure 17.12a and b). To obtain these decay curves, no fit parameters were used other than normalization. The simulated emission rates can be plotted as a distribution of rates, which also shows good agreement with the distribution extracted from the stretched exponential fit. As seen in Figure 17.12b, a fraction of molecules are expected to have Purcell factor of ~1000.

To further demonstrate the control over spontaneous emission, nanocavities were fabricated with gap thicknesses ranging from 5 to 15 nm. Figure 17.14a shows the measured time-resolved emission from a representative nanocavity for each gap thickness. With decreasing gap thickness, a strong decrease in the initial emission lifetime is observed. The maximum Purcell enhancement reaches a value of ~2000 for $d = 5$ nm gap thickness (Figure 17.14b). The most likely rate enhancement $\gamma_{sp}^*/\gamma_{sp}^0$ shows a similar trend, but with lower values due to the nonoptimal position of most emitters.

A critical question to answer in metal-enhanced fluorescence experiments is whether short emission lifetimes, as those observed in this system, are the result of nonradiative quenching or radiative rate enhancement. While radiative quantum yield cannot be measured directly, it can be inferred from a combination of simulations and a measurement of the fluorescence enhancement factor, as defined in Eq. (17.12). Figure 17.15a and b shows the calculated excitation rate enhancement and QY as a function of gap thickness, averaged over the nanocavity. The excitation rate enhancement is largest for small gap sizes, but modest as compared to the enhancements observed with the Cy5 dye in Section 17.5 due to the nonresonant excitation. The simulated QY, in contrast, is highest for larger gap sizes, with quenching occurring for gaps $d < 8$ nm. The intrinsic quantum yield of the dye in the polymer film is assumed to be 20%. Using the calculated collection efficiency from the antenna of $\eta = 84\%$ and the collection efficiency from dipoles of $\eta_0 = 15\%$, the spatially averaged fluorescence enhancement factor is calculated (Figure 17.15c). To obtain the experimental values for $\langle EF \rangle$, the same polymer films embedded with Ru dye were deposited on a glass substrate and the fluorescence was measured under the same experimental conditions as the nanocavities. The experimentally measured enhancement factor as a function of gap thickness is shown in Figure 17.15c, normalized for measurement area following Eq. (17.11). The excellent agreement between the measured and predicted enhancement factor implies the accuracy of

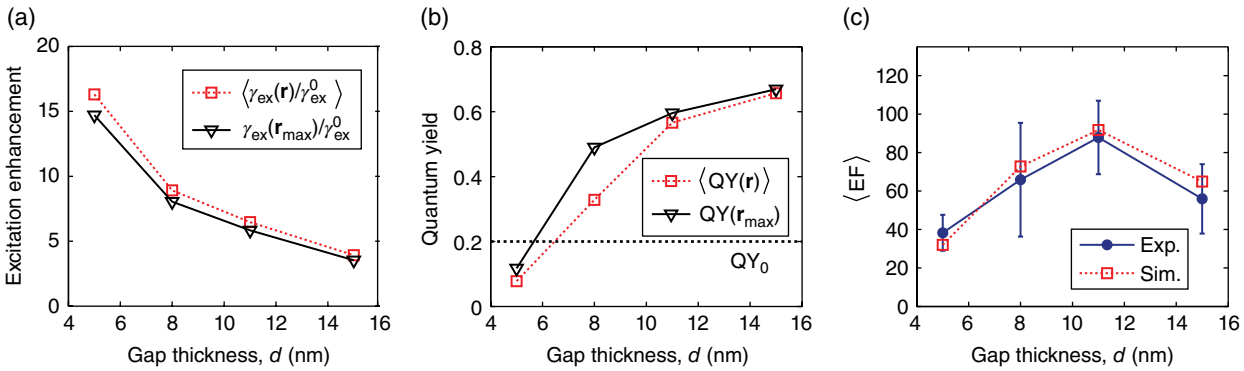

Figure 17.15 Simulated spatially averaged enhancement in the (a) excitation rate at $\lambda_{ex} = 535$ nm, (b) quantum yield at the emission wavelength of $\lambda = 650$ nm (squares). Also shown is the excitation enhancement and quantum yield at the position of maximum Purcell enhancement (triangles). (c) The total fluorescence enhancement factor obtained from simulations (Eq. (17.12)) and experiments, as a function of gap thickness.

the constituent simulations—namely the excitation rate enhancement and radiative quantum yield. Consequently, knowing the QY of the nanocavities, which is >50% for gap sizes $d > 8$ nm, it is now possible to calculate the radiative rate enhancement based on the measured total emission rate. Figure 17.14b shows that the maximum radiative rate enhancement of $\gamma_r^{max}/\gamma_r^0 \approx 1000$ occurs for gap sizes of $d = 5$ and 8 nm.

17.7 Ultrafast Spontaneous Emission

Integrating Ru dye into the nanocavities demonstrated the capability of this plasmonic structure for achieving large Purcell enhancements while maintaining a high quantum yield due to the antenna action of the cavity. For future device applications such as modulated LEDs and single-photon sources, it is important to develop ultrafast spontaneous emission sources based on a stable and technologically relevant material. One such set of materials is colloidal semiconductor QDs. These emitters have a wavelength-tunable room temperature emission, have excellent photostability, and can be easily integrated with other materials due to their solution processability [50]. For example, QDs have been used as stable, room-temperature single-photon sources [51], but their intrinsic radiative lifetime of ~20 ns limits the obtainable repetition rate. Likewise, LEDs are not suitable for high data rate telecommunications due to the slow switching time of LEDs, limited by the spontaneous emission lifetime.

Various plasmonic structures have been used over the past several years to control the spontaneous emission from QDs, but so far Purcell factors of at most 145 have been demonstrated [14, 26, 52–54]. However, these Purcell enhancements are often accompanied by large nonradiative losses. For example, structures assembled by atomic force microscopy consisting of a QD coupled to a Au nanoparticle shows a Purcell factor of up to 145, but the radiative decay enhancement is only ~8×.

In our recent work [31], we demonstrated the coupling of QDs to the nanocube nanocavities, resulting in ultrafast spontaneous emission with a lifetime of <11 ps, corresponding to Purcell factors of 880. While a similar Purcell enhancement was achieved in this work as compared to the work on Ru dye enhancement, the enhancement of QDs results in an absolute lifetime in the picosecond time regime. This produces a source of spontaneous emission that operates at ultrafast frequencies and with high radiative efficiency. The structures are produced by first depositing a single PAH layer on a 50-nm gold film which is evaporated on a glass substrate. CdSe/ZnS QDs core-shell QDs, with an emission spectrum centered at $\lambda_{em} = 620$ nm, are spin coated on the PAH film at a density such that ~10 QDs are located in each nanocavity. The QD-coated sample is then immersed in a solution of nanocubes which adhere to the top of the QDs, completing the nanocavities (Figure 17.16a). The nanocavities with a resonance of $\lambda_{cav} = 625$–635 nm were identified using darkfield microscopy.

To demonstrate the overall fluorescence enhancement of the QDs, the nanocavities were excited with a continuous-wave laser nonresonantly at $\lambda_{ex} = 514$ nm. Figure 17.16b shows the fluorescence intensity as a function of excitation power from three representative nanocavities as well as a control sample consisting of the QDs on glass. The fluorescence intensity from QDs coupled to the nanocavity is substantially higher than from QDs on the control sample. A linear dependence between excitation power and fluorescence intensity is observed over the power regime probed. At higher excitation powers, permanent

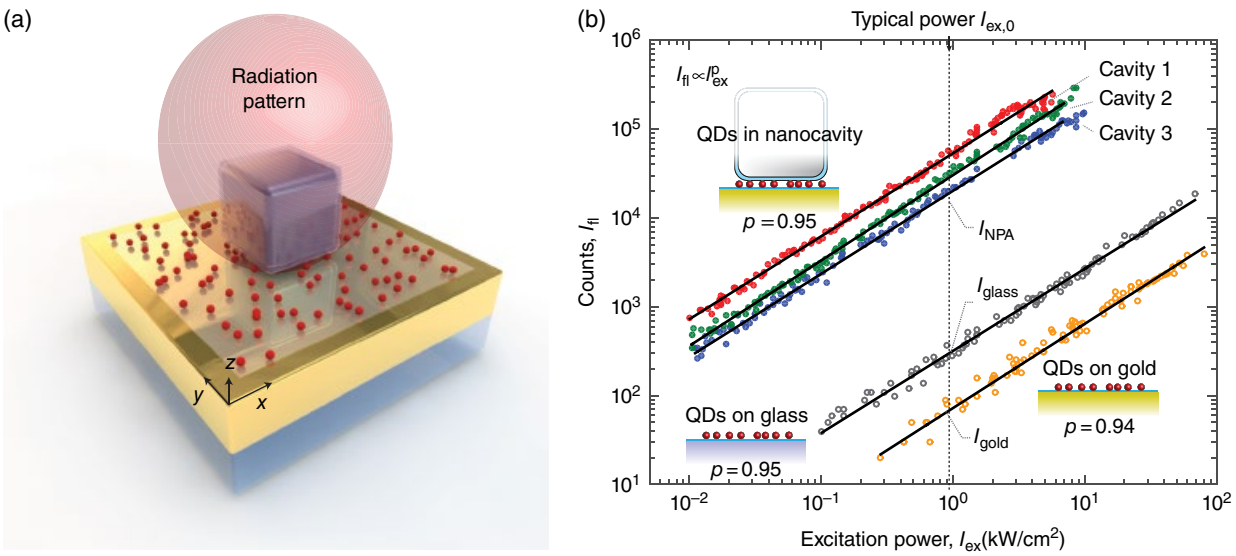

Figure 17.16 (a) Schematic structure of colloidal QDs integrated into the nanocavity, showing the directional radiation pattern of the structure. (b) Fluorescence intensity as a function of excitation power with a continuous-wave laser for QDs coupled to three representative nanocavities, as well as for QDs on glass, and QDs on a gold film. Fits are to power laws, where p is the exponent. The vertical dashed line indicates the power at which the time-resolved measurements were performed.

photobleaching of the QDs occurs, before the saturation regime can be reached. QDs that are on the gold film but coupled to a nanocavity show fluorescence quenching of 70% as compared to the control sample. Using Eq. (17.11), the spatially averaged fluorescence enhancement factor is found to vary from 177 to 2300, with an average value of $\langle \mathrm{EF} \rangle_{\mathrm{avg}} = 831$. This variation in $\langle \mathrm{EF} \rangle$ is attributed to (i) the random spatial distribution of the small number of QDs (~10) within the nanocavity, with different QDs near the cavity edges experiencing higher field enhancements (Figure 17.3); and (ii) the random orientation of the QD transition dipoles, with optimally oriented QDs experiencing larger enhancement. As with the Cy5 and Ru molecular dyes, this enhancement is attributed to an increased excitation rate, modified quantum yield, and a higher collection efficiency. To compare with the predicted enhancement factor, the structure was simulated using the same method as in Section 17.6. Assuming an intrinsic quantum yield for QDs on glass of 10%, the spatially averaged enhancement factor was found to be $\langle \mathrm{EF} \rangle = 660$, which is in good agreement with the experimentally obtained value for ~10 different nanocavities of $\langle \mathrm{EF} \rangle_{\mathrm{avg}} = 831$. This agreement indicates that the high quantum yield of ~50% predicted by simulations is close to the value observed in the experimental system.

Having established the emission efficiency, we now turn to the emission dynamics. Figure 17.17a shows the time-resolved emission from a nanocavity with embedded QDs under pulsed excitation at $\lambda_{ex} = 535$ nm, as well as emission from QDs on glass. The control sample shows emission with a single-exponential lifetime of =9.7 ns. For QDs on the Au film without the presence of nanocubes, the emission has a lifetime of =0.8 ns, but with a substantially reduced intensity, as seen in Figure 17.16b. When the QDs are coupled to the nanocavity, the emission is dramatically shorter than from the control sample, which occurs concurrently with a large intensity increase (Figure 17.16b). The spatial and orientational distribution of the QDs is expected to produce a nonexponential decay curve, as observed with Ru dye coupled to the nanocavity (Section 17.6) [30]. However, the instrument response function (IRF) of the avalanche photodiode used to detect the fluorescence has ~30-ps resolution, which prevents the extraction of the entire decay distribution. Instead, a biexponential function convolved with the IRF is used to extract the dominant decay components. This fitting results in a fast decay lifetime of =11 ps and slow decay time of =981 ps. The fast component, which contributes approximately 50% of the emission, corresponds to a Purcell factor of $F_{\mathrm{p}} = \tau_{\mathrm{glass}} / \tau_{\mathrm{NPA}}^{\mathrm{fast}} = 880$. This Purcell factor is only a lower bound due to the limits of the detector and the amount of deconvolution that can be performed. The lifetimes and the relative fluorescence contributions of the fast and slow components were measured for ~30 other nanocavities (Figure 17.17b and c). All nanocavities showed a fast decay lifetime between 11 and 51 ps, corresponding to Purcell factors of 190–880. Some nanocavities were found not to have a

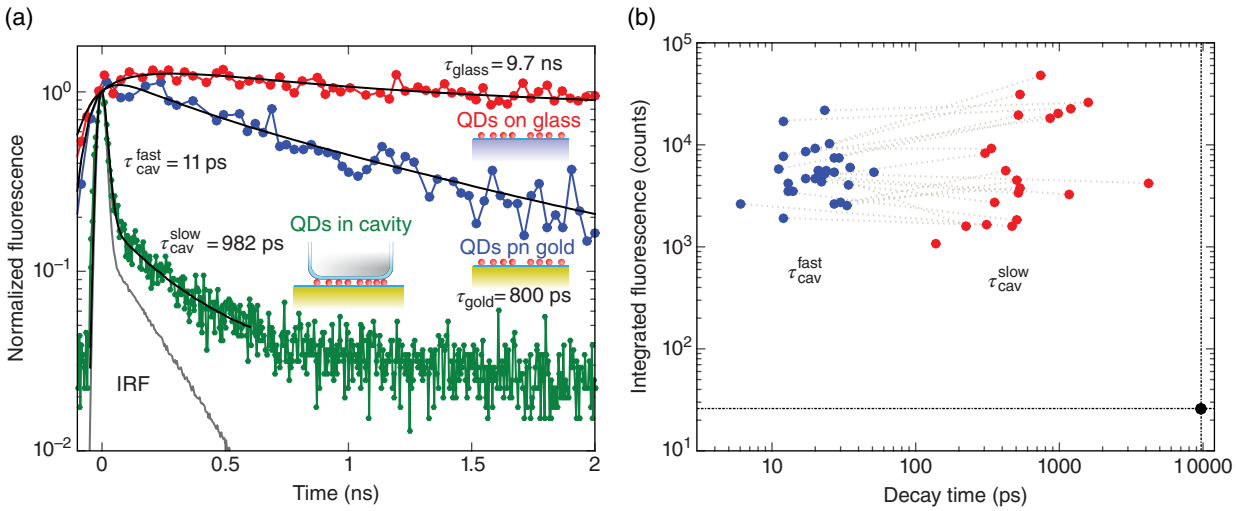

Figure 17.17 (a) Normalized time-resolved emission from QDs coupled to a nanocavity, QDs on glass, and QDs on gold (without nanocubes). The IRF is shown in gray. A biexponential function convolved with the IRF is used to fit the nanocavity emission, while a single exponential convolved with the IRF is used to fit emission from the other two samples. (b) Fast and slow components of the fluorescence decay times for ~30 nanocavities. Some decays showed more robust fits to a single-exponential function, in which case the slow component is absent.

slower component, perhaps due to the absence of QDs that are poorly coupled to the cavity. On average, the fast and slow components contribute equal amounts of fluorescence, when integrated over time.

The simulated Purcell factor was obtained by calculating the Purcell factor at each position for a randomly orientated QD dipole, and then by performing averaging over all positions. This results in an average Purcell enhancement of $F_p = 990$, corresponding to a lifetime of ~10 ps, which agrees well with the measured fast decay lifetime. However, the simulations predict Purcell enhancements of 4000× for optimally positioned and oriented QDs. This suggests that such large enhancements are occurring in the experimental system but are not resolved by the current fluorescence detection system.

17.8 Harnessing Multiple Resonances for Fluorescence Enhancement

As discussed in Section 17.3, the nanocavity possesses a second-order mode that is spectrally distinct from the fundamental mode. Such nanostructures with multiple, spectrally separated harmonics are desirable for the control of optical processes where field enhancement is needed at two or more distinct wavelengths. For example, nonlinear processes such as second harmonic generation can be enhanced by a nanocavity with resonances at the fundamental wavelength and at the second harmonic wavelength [55–58]. Multiresonant cavities could also be used to enhance entangled photon generation by tuning one resonance to the single-exciton transition and another to the biexciton transition of a quantum emitter [59]. In the context of fluorescence enhancement, a higher order resonance can be used to enhance the absorption, while a lower energy resonance can be used to enhance the quantum yield via the Purcell effect.

In this section, we describe how the nanocube cavities can be used to enhance the fluorescence from monolayer MoS_2 by simultaneously increasing the absorption and quantum yield using two independent resonances [44]. Monolayer MoS_2 is a promising two-dimensional (2D) material for optoelectronic applications due to its direct bandgap fluorescence. However, the intrinsic optical properties of MoS_2 are poor, with typical single-pass optical absorption of ~3% [60] combined with a low quantum yield of ~0.5% [61], making optical strategies for enhancing these properties highly desirable. The nanocube cavity is particularly suited to the enhancement of MoS_2 due to the excellent spectral overlap between the nanocavity resonances and the spectral features of the material (Figure 17.18). For a typical nanocavity, the quadrupolar second-order resonance at $\lambda = 420$ nm overlaps well with the absorption peak of MoS_2 at $\lambda = 430$ nm, corresponding to the quasiparticle at the K point [62] (Figure 17.18c and d). At the same time, the dipolar fundamental resonance at $\lambda = 660$ has good spectral overlap with the excitonic emission spectrum, so that enhancement of spontaneous emission rate and quantum yield can occur by the Purcell effect. Importantly,

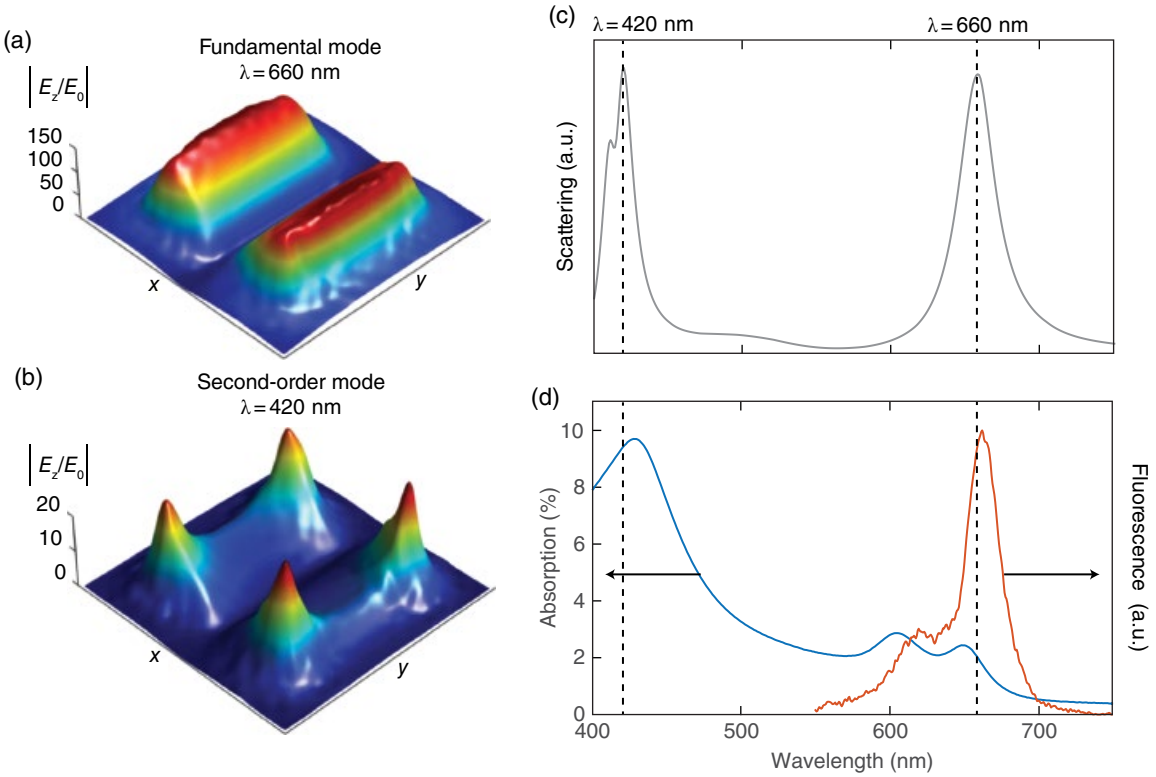

Figure 17.18 (a) Electric field enhancement as a function of position in the cavity at the (a) fundamental resonance and (b) second-order resonance. (c) Simulated scattering spectrum of the nanocavity, showing two resonances. (d) Absorption and emission spectra of monolayer MoS_2, showing good overlap between these spectral features and the nanocavity modes. Reproduced with the permission of American Chemical Society.

absorption and emission of MoS_2 can be enhanced simultaneously because the two modes of the nanocavities have good spectral separation yet good spatial overlap.

The nanocavities consist of a 50-nm gold film evaporated on glass, followed by the layer of HfO_2 deposited by atomic layer deposition, with thickness ranging from 2 to 15 nm (Figure 17.19a). MoS_2 monolayers, grown by a seeding-promoter-assisted chemical vapor deposition method, were dry transferred onto the HfO_2 layer. The HfO_2 is then coated with a layer of PAH, followed by the deposition of nanocubes. A control sample was also fabricated which consists of MoS_2 on the native growth substrate of thermal oxide on silicon. Nanocavities with a resonance wavelength of ~650 nm were identified by dark-field imaging, where the edges of the MoS_2 can also be seen (Figure 17.19b). Under defocused laser illumination, the fluorescence from a single nanocavity-coupled MoS_2 appears as a bright, diffraction limited spot (Figure 17.19b). At an excitation wavelength of $\lambda_{ex} = 420$ nm, the MoS_2 coupled to the nanocavity shows a 56-fold increase in fluorescence intensity relative to the same diffraction-limited excitation spot (~350 nm) on the control sample (Figure 17.19c). The shape of the fluorescence spectrum is also modified by nanocavity, resulting in a narrower and slightly redshifted emission spectrum relative to the control sample (Figure 17.19c inset). Because the resonance of the nanocavity is at $\lambda = 675$ nm, the effect of coupling MoS_2 to the cavity is to redshift the emission spectrum from its intrinsic peak at 660 nm toward the cavity resonance. By tuning the nanocavity resonance, various components of the MoS_2 emission spectrum—which consists of exciton and trion emission—could be suppressed or enhanced in future work.

To reveal the effect of nanocavity resonances on the fluorescence enhancement, the excitation wavelength was swept from $\lambda_{ex} = 400$ to 650 nm on a single nanocavity (Figure 17.20). The same measurement was performed on the control sample to obtain the spatially averaged fluorescence enhancement factor as a function of excitation wavelength, following Eq. (17.11). The enhancement factor spectrum (Figure 17.20) follows the scattering spectrum of the nanocavity (Figure 17.18b), consistent with the largest excitation enhancement occurring at the resonances of the nanocavity. The highest enhancement of

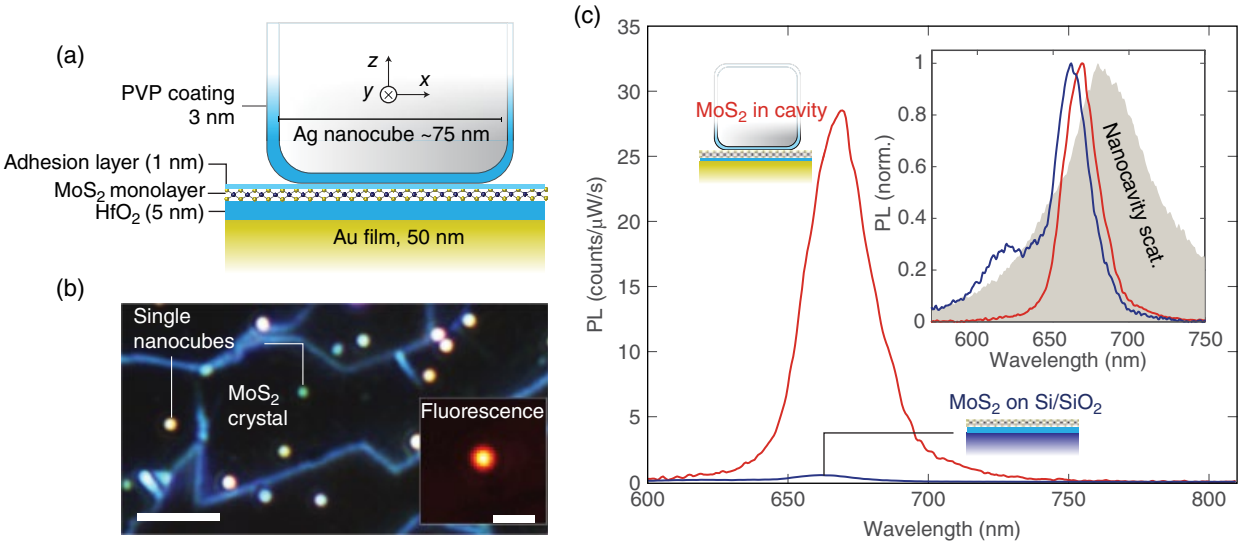

Figure 17.19 (a) Schematic of the fabricated nanocavity integrated with monolayer MoS_2. (b) Darkfield microscope image of the sample. Bright outlines are edges of the MoS_2 monolayers, while the bright spots are individual nanocavities. The scale bar is 5 μm. Inset shows fluorescence from a single nanocavity, which is much stronger than the background MoS_2 emission. The scale bar is 1.5 μm. (c) Fluorescence spectrum from nanocavity-coupled MoS_2 and from MoS_2 on the control sample, using the same diffraction limited excitation spot at $\lambda_{ex} = 420$ nm. Inset shows the same spectra normalized, along with the nanocavity scattering spectrum in gray. Reproduced with the permission of American Chemical Society.

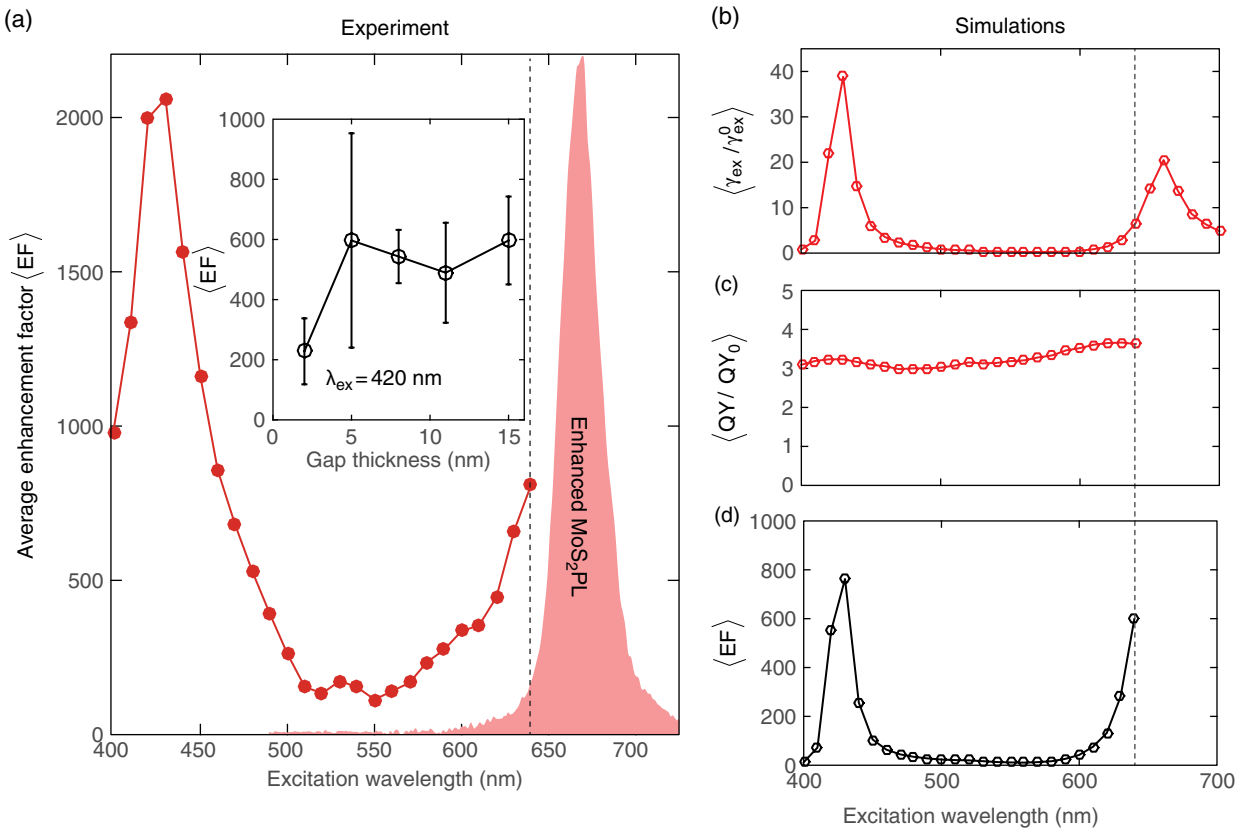

Figure 17.20 (a) Fluorescence enhancement factor for MoS_2 coupled to a nanocavity as a function of excitation wavelength. The largest enhancements occur at the second-order resonance wavelength and near the fundamental resonance wavelength. Inset shows the average enhancement factor with varying HfO_2 spacer thickness (excluding PVP layer), with ~6 nanocavities measured at each thickness. Error bars represent one standard deviation. (b and c) Spatially averaged enhancement in the (b) excitation rate, and (c) quantum yield, due to the in-plane cavity fields. (d) Calculated fluorescence enhancement factor relative to the control sample of MoS_2 on thermal oxide.

$\langle EF \rangle = 2000$ occurs at $\lambda_{ex} = 420$ nm, at the second-order resonance of the nanocavity, while near the fundamental resonance, the enhancement factor is $\langle EF \rangle = 800$. The presence of the two modes provides flexibility in how the MoS_2 is enhanced: excitation at the fundamental resonance, which both increases absorption and emission quantum yield, or by excitation at the second-order resonance, which increases absorption while the emission is again enhanced by the fundamental resonance.

Fluorescence enhancement measurements were also done on nanocavities with varying HfO_2 spacer thicknesses, ranging from 2 to 15 nm (Figure 17.20a inset). Under 420-nm excitation, the average enhancement factor for ~6 nanocavities at each spacer thickness $d > 2$ nm was found to be nearly constant, with $\langle EF \rangle \approx 550$. The nanocavity for which spectral dependence data is shown in Figure 17.20a had one of the highest enhancement factors observed in our measurements. For $d = 2$ nm, the average enhancement factor is smaller, which is attributed to nonradiative quenching, as was observed for smaller gaps with Ru dye embedded in the nanocavity. The variation in the enhancement factor for a given sample could be caused by variation in the cavity resonance relative to the fluorescence spectrum, roughness in the gold film, or spatial nonuniformity of the intrinsic quantum yield of MoS_2.

The large fluorescence enhancement can be understood through simulations, using the approach outlined in Section 17.5. Due to the 2D nature of the material, MoS_2 is believed to have a purely in-plane absorption dipole and exciton dipole orientation [63]. Although the dominant electric field in the nanocavity is vertical, normal to the MoS_2 monolayer, the in-plane cavity fields are still significant, especially near the edges of the cavity where fringing fields occur [44]. From simulations of the in-plane fields, Figure 17.20b shows the spatially averaged enhancement in the excitation rate as a function of excitation wavelength, demonstrating that excitation enhancement is highest near the two cavity resonances. We note that this excitation enhancement is relative to the control sample, which has a lower absorption than MoS_2 would in free space due to interference effects [44]. Meanwhile, the quantum yield enhancement is ~3-fold and is relatively insensitive to the excitation wavelength since emission is incoherent with the absorption process (Figure 17.20c). The calculated enhancement in quantum yield is equivalent to the enhancement in the emission rate since the internal decay rate in the material is dominant. However, measurement of the emission dynamics was not possible due to the very short exciton lifetime in MoS_2. Combining excitation enhancement, quantum yield enhancement, and modification of collection efficiency following Eq. (17.12), the total fluorescence enhancement is predicted to the $\langle EF \rangle = 800$ at the second-order resonance and $\langle EF \rangle = 600$ near the fundamental resonance (Figure 17.20d), values which are in qualitative agreement with experiments.

17.9 Conclusions and Outlook

In conclusion, the film-coupled nanocube is a versatile system for dramatic fluorescence enhancement of a wide variety of emitters such as molecules, QDs, and 2D semiconductors. By tuning the nanocavity, the system can be moved from the regime of excitation enhancement to the regime of Purcell enhancement, or both processes can simultaneously use multiple cavity modes. The fine control over fluorescence processes is enabled by the nanometer-precision control over the nanocavity fabrication, which is highly reproducible and does not rely on nanolithography. The well-defined geometry and dimensions allow the structure to be accurately simulated, producing quantitative predictions that agree well with experiments of parameters such as absorption enhancement, Purcell enhancement, quantum yield, and the radiation pattern. Future work will improve on the current theoretical understanding of the structure by including possible losses from the nanocavity into surface plasmons, as was recently discussed by Pors *et al.* [64].

Even larger enhancements could be enabled by controlling the orientation and position of the emitter dipoles in the nanocavity using chemical or nanofabrication methods. In principle, for optimally positioned and oriented dipoles, Purcell enhancements of ~10 000 are possible, corresponding to terahertz-frequency modulation of fluorescence using an emitter with a 10-ns intrinsic lifetime. Using electric excitation, such a device could function as an LED or as a high repetition rate single-photon source, if only one dipole is coupled to the cavity. The nanocavity could also be used as a sensor, by enhancing emitters with an intrinsically very low fluorescence quantum yield, as was demonstrated with MoS_2.

References

1 Yablonovitch, E. (**1987**) Inhibited spontaneous emission in solid-state physics and electronics. *Phys. Rev. Lett. 58* (20), 2059–2062.

2 Claudon, J., Bleuse, J., and Malik, N. (**2010**) A highly efficient single-photon source based on a quantum dot in a photonic nanowire. *Nat. Photonics 4*, 174–177.

3 Hennessy, K., Badolato, A., Winger, M., *et al.* (**2007**) Quantum nature of a strongly coupled single quantum dot-cavity system. *Nature 445* (7130), 896–899.

4 Englund, D., Fattal, D., Waks, E., *et al.* (**2005**) Controlling the spontaneous emission rate of single quantum dots in a two-dimensional photonic crystal. *Phys. Rev. Lett. 95* (1), 013904.

5 Gérard, J., Sermage, B., Gayral, B., *et al.* (**1998**) Enhanced spontaneous emission by quantum boxes in a monolithic optical microcavity. *Phys. Rev. Lett. 81* (5), 1110–1113.

6 Bleuse, J., Claudon, J., Creasey, M., *et al.* (**2011**) Inhibition, enhancement, and control of spontaneous emission in photonic nanowires. *Phys. Rev. Lett. 106* (10), 103601.

7 Kinkhabwala, A., Yu, Z., Fan, S., *et al.* (**2009**) Large single-molecule fluorescence enhancements produced by a bowtie nanoantenna. *Nat. Photonics 3* (11), 654–657.

8 Chen, Y., Munechika, K., and Ginger, D.S. (**2007**) Dependence of fluorescence intensity on the spectral overlap between fluorophores and plasmon resonant single silver nanoparticles. *Nano Lett. 7* (3), 690–696.

9 Russell, K., Liu, T., Cui, S., and Hu, E. (**2012**) Large spontaneous emission enhancement in plasmonic nanocavities. *Nat. Photonics 6*, 459–462.

10 Choy, J., Hausmann, B., and Babinec, T. (**2011**) Enhanced single-photon emission from a diamond-silver aperture. *Nat. Photonics 5*, 738–743.

11 Anger, P., Bharadwaj, P., and Novotny, L. (**2006**) Enhancement and quenching of single-molecule fluorescence. *Phys. Rev. Lett. 96* (11), 3–6.

12 Curto, A.G., Volpe, G., Taminiau, T.H., *et al.* (**2010**) Unidirectional emission of a quantum dot coupled to a nanoantenna. *Science 329* (5994), 930–933.

13 Kosako, T., Kadoya, Y., and Hofmann, H. (**2010**) Directional control of light by a nano-optical Yagi–Uda antenna. *Nat. Photonics 4*, 312–215.

14 Belacel, C., Habert, B., Bigourdan, F., *et al.* (**2013**) Controlling spontaneous emission with plasmonic optical patch antennas. *Nano Lett. 13* (4), 1516–1521.

15 Schietinger, S., Barth, M., Aichele, T., and Benson, O. (**2009**) Plasmon-enhanced single photon emission from a nanoassembled metal–diamond hybrid structure at room temperature. *Nano Lett. 9* (4), 1694–1698.

16 Esteban, R., Teperik, T.V., and Greffet, J.J. (**2010**) Optical patch antennas for single photon emission using surface plasmon resonances. *Phys. Rev. Lett. 104* (2), 026802.

17 Noginov, M.A., Zhu, G., Belgrave, A.M., *et al.* (**2009**) Demonstration of a spaser-based nanolaser. *Nature 460* (7259), 1110–1112.

18 Oulton, R.F., Sorger, V.J., Zentgraf, T., *et al.* (**2009**) Plasmon lasers at deep subwavelength scale. *Nature 461* (7264), 629–632.

19 Punj, D., Mivelle, M., Moparthi, S.B., *et al.* (**2013**) A plasmonic "antenna-in-box" platform for enhanced single-molecule analysis at micromolar concentrations. *Nat. Nanotechnol. 8* (7), 512–6.

20 Brongersma, M.L., Halas, N.J., and Nordlander, P. (**2015**) Plasmon-induced hot carrier science and technology. *Nat. Nanotechnol. 10* (1), 25–34.

21 Sobhani, A., Knight, M.W., Wang, Y., *et al.* (**2013**) Narrowband photodetection in the near-infrared with a plasmon-induced hot electron device. *Nat. Commun. 4*, 1643.

22 Li, W., and Valentine, J. (**2014**) Metamaterial perfect absorber based hot electron photodetection. *Nano Lett. 14* (6), 3510–4.

23 Aćimović, S.S., Kreuzer, M.P., González, M.U., and Quidant, R. (**2009**) Plasmon near-field coupling in metal dimers as a step toward single-molecule sensing. *ACS Nano 3* (5), 1231–1237.

24 Kollmann, H., Piao, X., Esmann, M., *et al.* (**2014**) Toward plasmonics with nanometer precision: Nonlinear optics of helium-ion milled gold nanoantennas. *Nano Lett. 14* (8), 4778–4784.

25 Yi, M., Zhang, D., Wang, P., *et al.* (**2011**) Plasmonic interaction between silver nano-cubes and a silver ground plane studied by surface-enhanced Raman scattering. *Plasmonics 6* (3), 515–519.

26 Yuan, C., Wang, Y., and Cheng, H. (**2013**) Modification of fluorescence properties in single colloidal quantum dots by coupling to plasmonic gap modes. *J. Phys. Chem. C 117* (24), 12762–12768.

27 Lassiter, J.B., McGuire, F., Mock, J.J., *et al.* (**2013**) Plasmonic waveguide modes of film-coupled metallic nanocubes. *Nano Lett. 13* (12), 5866–5872.

28 Ciracì, C., Hill, R.T., Mock, J.J., *et al.* (**2012**) Probing the ultimate limits of plasmonic enhancement. *Science 337* (6098), 1072–4.

29 Rose, A., Hoang, T.T.B., McGuire, F., *et al.* (**2014**) Control of radiative processes using tunable plasmonic nanopatch antennas. *Nano Lett. 14* (8), 4797–4802.

30 Akselrod, G., Argyropoulos, C., Hoang, T., *et al.* (**2014**) Probing the mechanisms of large Purcell enhancement in plasmonic nanoantennas. *Nat. Photonics 8*, 835–840.

31 Hoang, T.B., and Akselrod, G.M. (**2015**) Ultrafast spontaneous emission source based on plasmonic nanopatch antenna. *Nat. Commun. 6*, 7788.

32 Rose, A., Huang, D., and Smith, D.R. (**2011**) Controlling the second harmonic in a phase-matched negative-index metamaterial. *Phys. Rev. Lett. 107* (6), 063902.

33 Moreau, A., Ciracì, C., Mock, J.J., *et al.* (**2012**) Controlled-reflectance surfaces with film-coupled colloidal nanoantennas. *Nature 492* (7427), 86–89.

34 Ciraci, C., Rose, A., Argyropoulos, C., and Smith, D. (**2014**) Numerical studies of the modification of photodynamic processes by film-coupled plasmonic nanoparticles. *J. Opt. Soc. Am. B 31*, 2601–2607.

35 Sun, Y., and Xia, Y. (**2002**) Shape-controlled synthesis of gold and silver nanoparticles. *Science 298* (5601), 2176–2179.

36 Zhang, Q., Li, W., Wen, L.-P., *et al.* (**2010**) Facile synthesis of Ag nanocubes of 30 to 70 nm in edge length with CF(3)COOAg as a precursor. *Chem. Eur. J. 16* (33), 10234–10239.

37 Bowen, P.T., and Smith, D.R. (**2014**) Coupled-mode theory for film-coupled plasmonic nanocubes. *Phys. Rev. B 90*, 195402.

38 Ciracì, C., Britt Lassiter, J., Moreau, A., and Smith, D.R. (**2013**) Quasi-analytic study of scattering from optical plasmonic patch antennas. *J. Appl. Phys. 114* (16), 163108.

39 Dionne, J. A., Lezec, H.J., and Atwater, H.A. (**2006**) Highly confined photon transport in subwavelength metallic slot waveguides. *Nano Lett. 6*, 1928–1932.

40 Hill, M.T., Marell, M., Leong, E.S.P., *et al.* (**2009**) Lasing in metal-insulator-metal sub-wavelength plasmonic waveguides. *Opt. Express 17* (13), 11107–11112.

41 Gordon, R. (**2006**) Light in a subwavelength slit in a metal: Propagation and reflection. *Phys. Rev. B 73*, 8–10.

42 Zhang, J., Fu, Y., Chowdhury, M.H., and Lakowicz, J.R. (**2007**) Metal-enhanced single-molecule fluorescence on silver particle monomer and dimer: Coupling effect between metal particles. *Nano Lett. 7*, 2101–2107.

43 Richard, M., Kasprzak, J., Romestain, R., *et al.* (**2005**) Spontaneous coherent phase transition of polaritons in CdTe microcavities. *Phys. Rev. Lett. 94* (18), 187401.

44 Akselrod, G.M., Ming, T., Argyropoulos, C., *et al.* (**2015**) Leveraging nanocavity harmonics for control of optical processes in 2D semiconductors. *Nano Lett. 15* (5), 3578–3584.

45 Palik, E.D. (**2012**) *Handbook of Optical Constants of Solids*, Academic Press, Cambridge, MA.

46 Chance, R.R. (**1975**) Comments on the classical theory of energy transfer. *J. Chem. Phys. 62*, 2245.

47 Berberan-Santos, M.N., Bodunov, E.N., and Valeur, B. (**2005**) Mathematical functions for the analysis of luminescence decays with underlying distributions 1. Kohlrausch decay function (stretched exponential). *Chem. Phys. 315* (1–2), 171–182.

48 Cang, H., Liu, Y., Wang, Y., *et al.* (**2013**) Giant Suppression of photobleaching for single molecule detection via Purcell effect. *Nano Lett. 13* (12), 5949–5953.

49 Barritault, P., Gétin, S., Chaton, P., *et al.* (**2002**) Determination of surface-bound-fluorophore orientation by goniometric fluorescence polarization: Application to quantification of DNA-chip readouts. *Appl. Opt. 41* (22), 4732–4738.

50 Kim, J.Y., Voznyy, O., Zhitomirsky, D., and Sargent, E.H. (**2013**) 25th anniversary article: Colloidal quantum dot materials and devices: A quarter-century of advances. *Adv. Mater. 25*, 4986–5010.

51 Vittorio, M. De, Pisanello, F., Martiradonna, A., *et al.* (**2010**) Recent advances on single photon sources based on single colloidal nanocrystals. *Opto-Electron. Rev. 18* (1), 1–9.

52 Ureña, E.B., Kreuzer, M.P., Itzhakov, S., *et al.* (**2012**) Excitation enhancement of a quantum dot coupled to a plasmonic antenna. *Adv. Mater. 24*, 314–320.

53 Ratchford, D., Sha, F., Kim, S., *et al.* (**2011**) Manipulating coupling between a single semiconductor quantum dot and single gold nanoparticle. *Nano Lett. 11*, 1049–1054.

54 Okamoto, K., Vyawahare, S., and Scherer, A. (**2006**) Surface-plasmon enhanced bright emission from CdSe quantum-dot nanocrystals. *J. Opt. Soc. Am. B 23* (8), 1674.

55 Thyagarajan, K., Rivier, S., Lovera, A., and Martin, O.J.F. (**2012**) Enhanced second-harmonic generation from double resonant plasmonic antennae. *Opt. Express 20* (12), 12860.

56 Rodriguez, A., Soljacic, M., Joannopoulos, J.D., and Johnson, S.G. (**2007**) Chi((2)) and Chi((3)) harmonic generation at a critical power in inhomogeneous doubly resonant cavities. *Opt. Express 15* (12), 7303–7318.

57 Buckley, S., Radulaski, M., Zhang, J.L., *et al.* (**2014**) Nonlinear frequency conversion using high quality modes in GaAs nanobeam cavities. *Opt. Lett. 39* (19), 5673–5676.

58 Celebrano, M., Wu, X., Baselli, M., *et al.* (**2015**) Mode matching in multiresonant plasmonic nanoantennas for enhanced second harmonic generation. *Nat. Nanotechnol. 10* (5), 412–417.

59 Benson, O., Santori, C., Pelton, M., and Yamamoto, Y. (**2000**) Regulated and entangled photons from a single quantum dot. *Phys. Rev. Lett. 84*, 2513–2516.

60 Mak, K., He, K., Lee, C., *et al.* (**2013**) Tightly bound trions in monolayer MoS_2. *Nat. Mater. 12*, 207–211.

61 Mak, K.F., Lee, C., Hone, J., *et al*. (**2010**) Atomically thin MoS_2: A new direct-gap semiconductor. *Phys. Rev. Lett. 105* (13), 136805.

62 Li, W., Birdwell, A., Amani, M., *et al*. (**2014**) Broadband optical properties of large-area monolayer CVD molybdenum disulfide. *Phys. Rev. B 90*, 195434.

63 Schuller, J. A., Karaveli, S., Schiros, T., *et al*. (**2013**) Orientation of luminescent excitons in layered nanomaterials. *Nat. Nanotechnol. 8* (4), 271–276.

64 Pors, A., and Bozhevolnyi, S.I. (**2015**) Quantum emitters near layered plasmonic nanostructures: Decay rate contributions. *ACS Photonics 2* (2), 228–236.

18

Plasmonic Enhancement of UV Fluorescence

Xiaojin Jiao, Yunshan Wang, and Steve Blair

Department of Electrical and Computer Engineering, University of Utah, Salt Lake City, USA

18.1 Introduction

Plasmonics is based on the interaction between electromagnetic radiation and conduction electrons at metallic interfaces or in metallic nanostructures [1]. One unique property of metallic nanostructures is their ability to strongly enhance the electromagnetic field via localized surface plasmons (LSPs)—the collective electron oscillations at a bounded metal surface. This property is, therefore, called plasmonic enhancement (PE). PE-based applications cover a broad spectrum from visible-to-near infrared, including biosensing [2, 3], spectroscopy [4], photovoltaics [5], and so on. However, there remains a gap in this activity in the ultraviolet (UV, <400 nm), where significant opportunity exists for both fundamental and applications research. The study of UV plasmonics is motivated by applications such as label-free biomolecular detection, resonant Raman spectroscopy, and control of photochemical reactions on the nanometer scale. This chapter will be devoted to the first application.

Fluorescence-based spectroscopy is a fundamental research tool in biochemistry and biophysics [6]. Typically, an additional step called labeling is usually required, in which fluorescent dye molecules are attached to the species of interest. Labeling introduces complexity into both sample preparation and data analysis. By directly accessing the native fluorescence of biomolecules, it is possible to achieve biomolecular detection without labeling (label-free). Some important biomolecules such as proteins and DNA contain residues that absorb in the UV part of the spectrum (220–280 nm) [7, 8]. However, their brightness is several orders of magnitude lower compared to dye molecules in the visible due to smaller fluorescence quantum yield (QY) and molecular extinction [7, 9]. PE can be a key factor to enable label-free detection with native UV fluorescence, whose potential has been investigated by a number of groups [10–27].

In the chapter, the research on PE of UV fluorescence will be reviewed.

18.2 Plasmonic Enhancement

Surface plasmon polaritions (SPPs) arise from the interactions between electromagnetic radiation and conduction electrons at metal–dielectric interfaces or at the surface of metallic nanostructures [1]. PE is usually described as the ratio of electric field intensity with to without the plasmonic structure. We will use PE as a figure of merit, or FOM. Considering a three-layer structure with a metal film sitting atop a substrate and covered by another dielectric (e.g., air), the FOM of SPPs (PE_{SPP}) at the metal/covering interface as equation (18.1), [28]

$$\mathrm{FOM}_{\mathrm{SPP}} = \frac{1}{\varepsilon_c}\frac{2\left|\varepsilon_m^{'}\right|^2}{\varepsilon_m^{''}}\frac{a}{1+\left|\varepsilon_m^{'}\right|} \tag{18.1}$$

where $a^2 = \left|\varepsilon_m^{'}\right|\left(\varepsilon_s - 1\right) - \varepsilon_s$, $\varepsilon_m^{'}$ and $\varepsilon_m^{''}$ are the real and imaginary parts of permittivity of metal, and ε_s and ε_c are the permittivities of the substrate and covering material.

For LSPs, the situation is more complicated, because PE is also determined by the size and shape of the metallic nanostructure, in addition to the permittivity. If the simplest structure—a nanosphere with a diameter much smaller than wavelength—is considered, LSPs can be analytically analyzed under the dipole approximation. The corresponding FOM of LSPs (PE_{LSP}) can be described by equation (18.2) [29]

$$\mathrm{FOM}_{\mathrm{LSP}} = \left|1 + \frac{2\left(\varepsilon_m - \varepsilon_d\right)}{2\varepsilon_d + \varepsilon_m}\right| \approx \frac{-3\varepsilon_m^{'}}{\varepsilon_m^{''}} \tag{18.2}$$

Surface Plasmon Enhanced, Coupled and Controlled Fluorescence, First Edition. Edited by Chris D. Geddes.
© 2017 John Wiley & Sons, Inc. Published 2017 by John Wiley & Sons, Inc.

where ε_d is the permittivity of the medium surrounding the nanosphere. The latter approximation only holds when the nanosphere is under resonance, that is, $\varepsilon_m' = -2\varepsilon_d$.

In order to give a straightforward feeling of the magnitude of PE of both cases, we can calculate PE by considering two practical cases: aluminum (Al) thin-film atop a quartz substrate and covered by water, and an Al nanosphere with a radius of 20 nm surrounded by water. The wavelength is 270 nm corresponding to the absorption peak of a typical biomolecule, such as tryptophan. At this wavelength, $\varepsilon_m = -10.36941 + i1.44545$, $\varepsilon_d = \varepsilon_c = 1.914$, and $\varepsilon_s = 2.244$ from handbook data [30], and the FOMs can be calculated as equation (18.3)

$$\mathrm{FOM_{SPP}} = 22; \quad \mathrm{FOM_{LSP}} = 5(22) \tag{18.3}$$

One can see that SPPs have a higher FOM (22) compared to $\mathrm{FOM_{LSP}}$ (5), which is due to the fact that the nanosphere is not under the resonant condition. $\mathrm{FOM_{LSP}}$ becomes the same (22) in this case under resonance.

18.3 Analytical Description of PE of Fluorescence

Strong PE can improve the efficiency of electromagnetic-related processes, such as absorption and emission. However, only considering that PE is not enough to describe the enhancement of fluorescence, due to the fact that fluorescence radiation includes two procedures: excitation and emission. More analytical consideration is required to fully understand the PE of fluorescence.

Fluorescence can be described by a system of three energy levels shown in Figure 18.1—singlet ground state S_0, first excited singlet state S_1, and first excited triplet (dark, nonfluorescing) state T_1. Upon absorbing light, a molecule is excited from the ground state to the excited singlet state. The molecule can relax back to the ground state by emitting a photon. It can also make a transition to the triplet state through intersystem crossing, where the transition from triplet state to ground state is forbidden; however, this transition can still occur on a slow time scale by phosphorescence. The difference between fluorescence and phosphorescence can be found from the lifetime. The lifetime (τ) is the average time a molecule spends in the excited state before returning to the ground state. Lifetime of fluorescence is usually on the order of nanoseconds, while that of phosphorescence is typically milliseconds or longer.

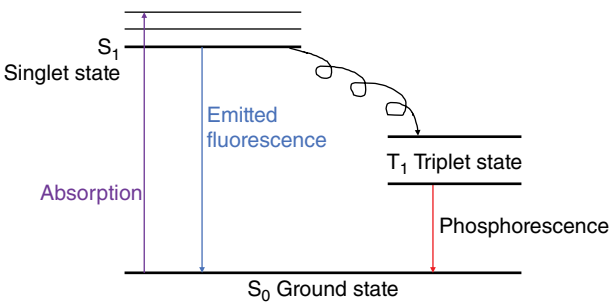

Figure 18.1 Diagram of system of three energy levels for fluorescence.

Fluorescence and phosphorescence represent the radiative channel of a molecule's relaxation from the excited state. Molecules can also return to the ground state without emitting any light, that is, through nonradiative channels. Usually, rate constants are used to describe how fast certain relaxations happen. For example, $k_{tot} = k_{rad} + k_{nr}$ is the total relaxation rate from S_1 to S_0, where k_{rad} and k_{nr} stand for the rate constants for radiative and nonradiative relaxations. The fluorescence, or spontaneous emission, lifetime (τ), is given by $k_{tot} = 1/\tau$.

The quantum yield (QY, ϕ) is the ratio of the number of photons emitted to the number of photons absorbed by a molecule, which measures how efficient the molecule is in terms quantum yield can be expressed as equation (18.4) of fluorescence emission. In terms of rate constants,

$$\phi = \frac{k_{rad}}{k_{tot}} = \frac{k_{rad}}{k_{rad} + k_{nr}} \tag{18.4}$$

The fluorescence emission of a single molecule at steady state can be described as count rate per molecule (CRM), which is given by equation (18.5), [31, 32]

$$\mathrm{CRM} = k_c \phi \frac{\sigma I_e}{1 + I_e / I_s} \tag{18.5}$$

where k_c is the light collection efficiency (combination of optical system and radiation profile), I_e is the net excitation rate, σ is the absorption cross-section, and the saturation intensity $I_s = k_{tot}/[\sigma(1 + k_{isc}/k_d)]$, where k_{isc} and k_d are the rate constants for intersystem crossing to the triplet state and relaxation to the ground state, respectively.

Energy transfer between the molecule and the plasmonic structure is mediated through the radiative transition of the molecule (with the internal nonradiative rate k_{nr} unchanged). We denote k_{rad}' as the effective radiative rate of the structure and k_{nr}' as the dissipation rate of the structure, and define the Purcell factor [31] $\zeta = (k_{rad}' + k_{nr}')/k_{rad}$ to represent the change in total emission rate or lifetime of a perfect dipole emitter (i.e., one with no internal resistive losses, with unity native QY ϕ_0). This factor can readily be obtained from simulation [24, 25, 33] and does not change with the

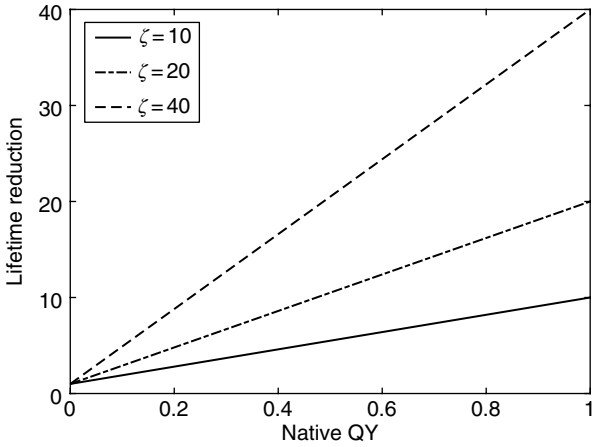

Figure 18.2 Lifetime reduction versus native QY for structures giving different ζ.

particular value of k_{rad}. The reduction in lifetime of a real molecule [34], that is, change of total spontaneous emission rate, is defined as equation (18.6)

$$f_\tau = \frac{\tau}{\tau'} = \frac{k'_{rad} + k'_{nr} + k_{nr}}{k_{rad} + k_{nr}} = 1 + \phi_0(\zeta - 1) \quad (18.6)$$

The change in QY can then be expressed as $f_\varphi = f_{rad} / f_\tau$, where $f_{rad} = k'_{rad} / k_{rad}$ is the ratio of the effective radiative rate with to without the influence of the plasmonic structure.

It is clear from Eq. (18.6) that the lifetime reduction for a nonideal emitter depends on its native QY ϕ_0. Stated differently, two emitters with different native QYs will experience different Purcell factors within the same electromagnetic environment (Figure 18.2). For an emitter with low ϕ_0, k_{nr} dominates k_{rad}, and since the structure acts through k_{rad}, ζ must be large to effect a decrease in lifetime. For the same emitter, f_ϕ is roughly proportional to f_{rad}. In contrast, for a high ϕ_0 emitter, k_{rad} dominates k_{nr}, and lifetime reduction is roughly proportional to ζ. However, since $f_{rad} \ll \zeta$, then $f_\phi \ll 1$. This is the origin of increased net fluorescence enhancement for molecules with low QYs [31, 33], and also leads to the practical conclusion that it takes a poor emitter in the first place in order to realize enhancement via f_{rad}.

The expression for CRM can be simplified under saturated ($I_e \gg I_s$) and unsaturated ($I_e \ll I_s$) conditions

$$\mathrm{CRM}\big|_{I_e \gg I_s} \propto k_c k_{rad} \Rightarrow \mathrm{NE}\big|_{I_e \gg I_s} \propto f_c f_{rad} \quad (18.7)$$

$$\mathrm{CRM}\big|_{I_e \ll I_s} \propto k_c \varphi \sigma I_e \Rightarrow \mathrm{NE}\big|_{I_e \ll I_s} \propto f_c f_I f_\varphi = f_c f_I \frac{f_{rad}}{f_\tau} \quad (18.8)$$

where NE represents the net fluorescence enhancement in each limit, f_I is the excitation enhancement, and f_c is the change in collection efficiency.

18.4 Overview of Research on Plasmon-Enhanced UV Fluorescence

Plasmon-enhanced UV fluorescence (PEUVF) has its unique advantage compared with its counterpart in the visible, which is due to the ability of direct access to the native fluorescence of biomolecules. However, the study of PEUVF is still at the early stages. Table 18.1 summarizes the published experimental research in this area in chronological order. We will review the research on PEUVF from the perspectives of material choice, structure fabrication, and experimental measurement.

18.4.1 Material Selection

Materials with negative real part of the permittivity ($\varepsilon'_m < 0$) are required for excitation of SPPs [1]. Metals, as natural materials with negative ε'_m, have been used as plasmonic materials for many applications in the visible and near-infrared. However, their intrinsic ohmic losses always impair the device performance. This becomes a more serious issue in the UV, because conventional plasmonic materials, such as gold and silver, suffer from the influence of interband transitions near the blue part of the spectrum. Searching for better plasmonic materials is an ongoing effort that has attracted increasing attention [35–40]. From Table 18.1, one can see that Al is the dominant material [11–20]. Al has a relatively low material loss in the UV due to the fact that its interband transition is in the near-infrared. Furthermore, Al is a relatively inexpensive material. These properties make Al the first choice for UV plasmonic applications [41], not only limited to PEUVF.

However, Al has higher ohmic loss in the UV compared with Ag and Au in the visible, which is due to its high density of free electrons, which limits the performance of Al-based UV plasmonic structures. Furthermore, Al is easily oxidized. Even though a 3-nm self-protective oxide layer forms, the surface and bulk oxidation will still change the plasmonic resonance and near-field enhancement due to the high sensitivity of plasmonic resonance to the presence of Al oxidation [42]. Because of these drawbacks, several efforts have been made to identify alternative materials. Silver (Ag) has been used to demonstrate the PEUVF of DNA and tryptophan for the first time with

Table 18.1 Summary of experimental study of PE of UV fluorescence.

Species	$\frac{\lambda_{ex}}{\lambda_{em}}$ (nm)	Materials	Structures (λ_{res})	Fluorescence enhancement	Lifetime reduction	References
DNA	287/340	Ag	Islands (420 nm)	80	3	10
DNA	300/380	Al	20 nm film (NA)	NA	1.2	12
2-AP	300/370	Al	10 nm islands (680 nm)	9	3.8	13
7-HC	300/450			6	2	
7-HC	405/470	Zn	10 nm islands (380 nm)	8	NA	21
Tryptophan	280/340	Al	10 nm islands (680 nm)	14	6	14
Tryptophan	280/340	Ag	Islands (450 nm)	1.5	2	11
Tryptophan	280/340	Al	10 nm islands (680 nm)	11	2	15
NATA-tys	280/340	Ag/Al	10-nm islands (620 nm)	10	3	16
NATA	280/340			2	2.5	
Water	204/450	Al	21-nm film (NA)	NA	NA	17
Nucleotides	280/340	Pt	10 nm islands (>400 nm)	20	3	22
DNA	280/340			5	2.5	
Crystal violet	325/590	Ga	70 nm NPs (590 nm)	18	NA	23
CdS QDs	266/380	Al	18 nm Al film (NA)	NA	NA	18
DBMBF2	385/590	Al	Hole arrays (440 nm)	3.8	1.14	19
p-Terphenyl	266/340	Al	Single hole (NA)	NA	3.5	20
Tryptophan	266/340				1.7	

Lakowicz *et al.* [10]. Reproduced with the permission of Elsevier.

island-like structure [10, 11]. However, Ag's working range is limited down to about 350 nm due to the interband transition. Further, Ag degrades relatively quickly and has a large thickness threshold to form a uniform continuous film, which is around 12–23 nm [36]. Other metals that have been experimentally studied are zinc (Zn), platinum (Pt), and gallium (Ga). Zn nanoparticles (NPs) can enhance the fluorescence by 5-fold near the UV edge [21]. Enhancement up to 20-fold of intrinsic fluorescence of nucleic acid around 340 nm by Pt NPs has been observed [22]. Hemispherical Ga NPs deposited on a sapphire substrate have been used as a plasmonic substrate to achieve 18-fold fluorescence enhancement with excitation at 325-nm wavelength [23]. Besides pure metals, alloys are another choice as low-loss plasmonic materials. Ag/Al bimetallic NPs have been used to achieve up to 10-fold of enhancement of intrinsic UV fluorescence [16]. By alloying Al and Ag, it is possible to achieve both the enhancement comparable to Ag and the working range similar to Al.

The material choice for all UV plasmonics applications, not only PEUVF, is still limited. More materials need to be explored. In order to screen the material candidates for different plasmonic applications, researchers have proposed the concept of the FOM, which relates the permittivity to the device performance [35, 36]. For PE-based application, such as PEUFV, the LSP FOM is primarily considered. FOM_{LSP} is defined by calculating the electric field enhancement at the surface of a subwavelength sphere, which is given by Eq. (18.2). Furthermore, SPPs have also be used to enhance UV fluorescence [12, 17, 18], so it is useful to consider FOM_{SPP}, as described by Eq. (18.1).

Here, we survey several materials that are metallic ($\varepsilon_m' < 0$) in the UV range. FOM_{LSP} and FOM_{SPP} of these materials in the UV range are plotted in Figure 18.3. Practical structures close to typical experiments are considered in the calculation. For FOM_{SPP}, an Al film is covered by water, while for FOM_{LSP}, a nanosphere with 20-nm radius is considered. The material data are extracted from the Palik handbook [30]. Figure 18.3a shows the FOM_{LSP} versus wavelength assuming that the sphere is surrounded by water, while Figure 18.3b shows FOM_{LSP} assuming that the nanosphere is always under resonance, that is, $\varepsilon_m' = -\varepsilon_d$. One can see that Figure 18.3a and b shows an obvious difference. Mg and Ag have peaks at 260 nm and 400 nm in the plot of FOM_{LSP}, respectively, at which they have similar values to the plot of resonant FOM_{LSP} because the resonant condition is satisfied. In addition, the best three metals shown by FOM_{LSP} in Figure 18.3a are Mg, In, and Sn, while those shown by resonant FOM_{LSP} in Figure 18.3b are Mg, Al, and In. On the other hand, FOM_{SPP} in Figure 18.3c shows that the best three metals are Al, Mg, and In.

Considering the FOM_{LSP} in Figure 18.3a, one can see that the alkali metal, magnesium (Mg), has the largest FOM_{LSP} due to the fact that its resonance wavelength in water lies in the mid-UV. Appusamy *et al*. have studied the influence of film thickness on the optical constants of Mg thin film [43]. By comparing the FOM_{LSP} of Mg and Al, they showed that 910-nm thick Mg film on glass substrate has the best plasmonic property, which is superior or comparable to Al in the UV. However, 910 nm is too thick to be used for the nanofabrication of many UV plasmonic structures. Recently, they have demonstrated a method to improve the plasmonic property of 100-nm thick Mg film by using a 10-nm Al seed layer [44]. Nevertheless, the issue with Mg is that it can keep growing an oxide layer of MgOH under a humid environment, even though it also forms a self-protective MgO layer of 20–50 nm [45]. So, Mg can be a practical candidate only if the humidity of the environment is controlled. Another way to improve Mg"s property is by alloying with other metals. It has been demonstrated that Ga/Mg NPs have tunable plasmonic resonance with varying Mg contents, and also better thermal stability compared with Mg [46]. It is unexpected that indium (In) and tin (Sn) outperform aluminum (Al) according to FOM_{LSP} in Figure 18.3a, although their values are very small. Recently, Kumamoto *et al*. have demonstrated that an indium-coated substrate can generate 11× higher Raman signal when excited at 266 nm [47]. There is still no experimental study on Sn, besides the theoretical work [48]. Recent study also shows that a special semiconductor material, $Bi_{1.5}Sb_{0.5}Te_{1.8}$, known as a topological insulator, is a possible plasmonic material in the blue-UV range [49]. Gratings with varied periods made from it can have varied plasmonic resonance from 350 to 550 nm.

In addition, theoretical research has also been carried out to compare materials. Mahdavi *et al*. simulated the net enhancement of UV fluorescence from a single tryptophan molecule placed inside a nanoaperture made from gold, silver, and aluminum. This work demonstrated that the aluminum nanoaperture provides the greatest fluorescence enhancement (10× net enhancement) [24]. Performance of the so-called "poor" metals (Al, Ga, In, Sn, Tl, Pb, and Bi) has been studied by calculating the near-field enhancement of single nanosphere and dimers made from them [48]. All of them, except Bi, generate more than 10^3 enhancement in the UV range, which is comparable to or higher than that of Ag and Au in the visible. The

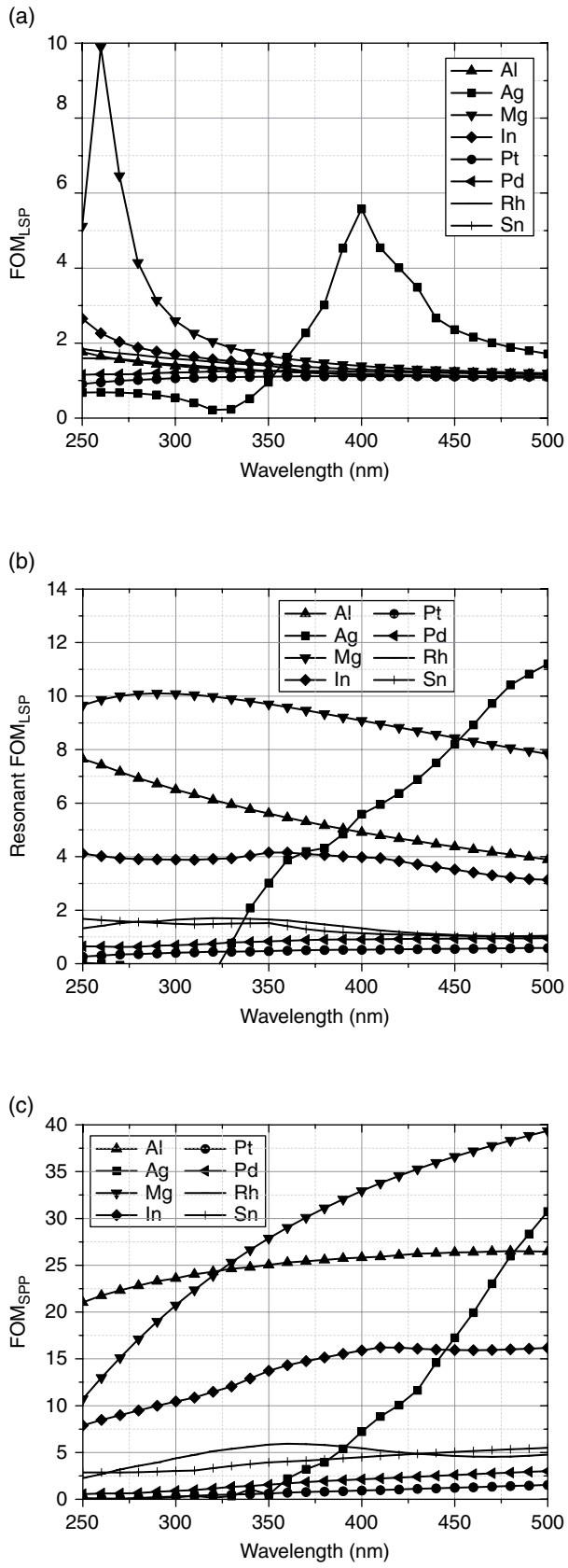

Figure 18.3 FOM of possible UV plasmonic materials versus wavelength. (a) FOM_{LSP} (Eq. (18.2)), (b) FOM_{LSP} under resonance, and (c) FOM_{SPP} (Eq. (18.1). An Al film supported by a quartz substrate and covered with water is considered for FOM_{SPP}. A 20-nm Al nanosphere surrounded by water is considered for FOM_{LSP}.

optimal electric field enhancement of Al and In dimers has been calculated and compared with Au and Ag [50]. This research demonstrated that Al and In dimers can give comparable enhancement to that of Au and Ag in the visible, which further confirms the potential of "poor" metals in UV plasmonic applications.

Oxidation is another important factor to be considered for some metals such as Al and Mg. It has been found that oxidation can totally degrade the LSP resonance of 20-nm Mg NPs [51]. Al and Mg nanoapertures have been numerically studied for PEUVF [27]. The presence of the native oxide red-shifts the resonance for both materials. In order to improve fluorescence enhancement using either metal, avoiding bulk/surface oxidation during film deposition is important, along with the development of surface passivation schemes.

In summary, the research of PEUVF so far has proven that Al is still the dominant material. Zinc, platinum, and gallium have also been experimentally demonstrated to be possible candidates. Besides them, magnesium and indium could be other possible materials according to the comparison of FOM; however, further experimental studies of nanostructures made from those materials are still required in order to validate their performance with PEUVF.

18.4.2 Structure Choice

Plasmon-enhanced fluorescence (PEF) or metal-enhanced fluorescence (MEF) [52] has been proven as a promising means to improve the fluorescence signal in the visible. Many plasmonic structures have been investigated, including NPs, nanoapertures, bullseyes, dipole antenna/aperture, and so on. However, from Table 18.1, one can see that only few structures have been studied in the UV.

Most of the studies [10–18, 21, 22] were performed on the simplest structure: a thin film. The thin film can be deposited with "wet" chemical method [10–12, 21] or "dry" evaporation [13–18] and sputtering [22] methods. With the smooth thin film, it has been demonstrated that UV illumination can excite SPPs, which can in turn effectively excite the UV fluorescence emission [12, 17, 18]. However, there is still no detailed characterization of enhancement. A variation of the thin film is the particulate film or islands. Ray *et al*. studied the UV-blue fluorescence of DNA enhanced by Al islands [13]. LSPs play an important role in this case. By varying the thickness of Al thin film from 2 to 80 nm, the surface morphology can be controlled. Figure 18.4a demonstrates the change in Al island morphology with the increase in film thickness. Figure 18.4b presents the enhancement of fluorescence of two probes (2-AP and 7-HC) versus film thickness. The 10-nm-thick Al film generates the highest enhancement up to 9× for 2-AP and 6× for 7-HC. The maximal enhancement achieved by this kind of structure is reported as 80× with Ag islands [10]. The island structure is relatively easy to prepare over a large area. But the lack of control of island sizes limits its performance in terms of fluorescence enhancement. Due to the nonuniformity of island sizes, the resonant peak is usually very broad. Figure 18.5 shows the absorption spectra of Ag [10], Al [13], Zn [21], and Pt [22] islands. One can see that all of them have broad peaks and do not have resonances in the UV range. Among them, Ag islands have the narrowest peak, which is also closest to the wavelength studied. That is why they give the highest enhancement even though Al performs better in terms of FOM_{LSP} as discussed in the previous section.

Another structure that has been studied extensively is the nanoaperture [19, 20]. The main advantage of the nanoaperture is that its small physical volume allows single molecule to be isolated for optical analysis at high concentration. It has found many applications such as real-time imaging of protein–protein interaction, real-time observation of enzymatic activity, and membrane-bound diffusion [53]. By applying advanced fabrication techniques, the physical size of nanoapertures can be accurately controlled. Schmidt *et al*. [19] fabricated the Al hole arrays with colloidal lithography, which is shown in Figure 18.6a. Figure 18.6b shows the extinction spectra of Al hole arrays with different center-to-center distance and hole sizes. One can see that modification of geometrical parameters of the structure can effectively tune the plasmonic resonances of Al hole arrays. They also demonstrated that SPPs and LSPs give different contributions to the fluorescence enhancement of $DBMBF_2$ monomers and exciplexes. Jiao fabricated nanohole using focused ion beam, which has control of the size of the hole and spacing better than NP lithography [19]. Jiao has measured the lifetime change in UV dyes diffusing from free solution into nanoapertures, which was the first time in the literature. This work demonstrated a factor of 3.5 lifetime reduction for *p*-terphenyl.

Nanoparticles (NPs) are important structures for LSP-based fluorescence enhancement in the visible, but only Ga NPs have been investigated to demonstrate their potential for surface-enhanced Raman spectroscopy and fluorescence in the UV [23]. The hemispherical Ga NPs were deposited on sapphire substrate with molecular beam epitaxy. By controlling the mean size of NPs, the LSP resonance peak can be tuned from blue to red. Fluorescence enhancement up to 18× has been demonstrated.

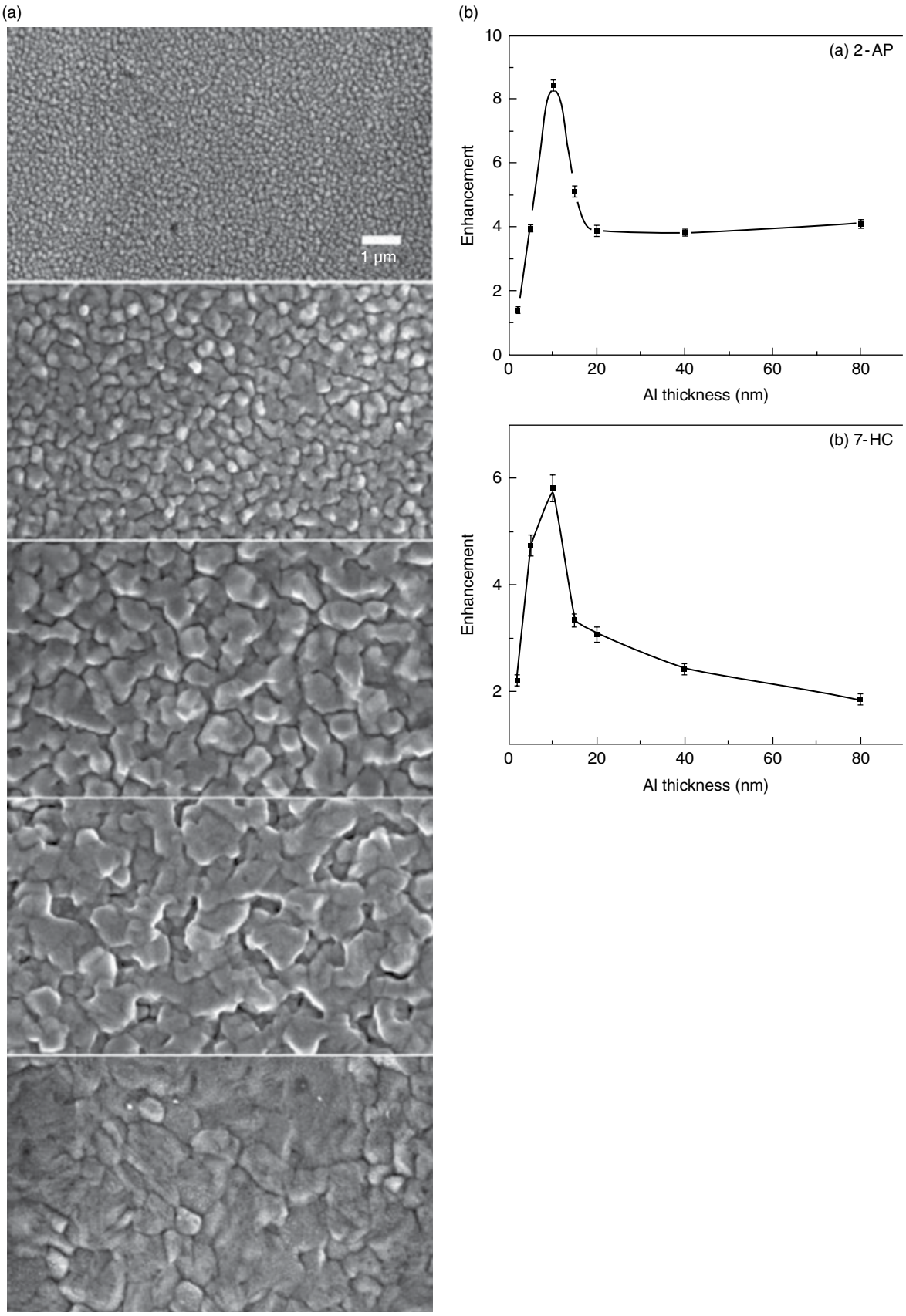

Figure 18.4 UV fluorescence enhanced by Al islands. (a) Scanning Electron Microscopy (SEM) images of thermally evaporated Al films on quartz substrates with thicknesses increasing from top down (2, 5, 10, 20, 80 nm). (b) Dependence of fluorescence intensity enhancement of 1-AP and 7-HC on AL film thickness. Ray *et al*. [13]. Reproduced with the permission of American Chemical Society.

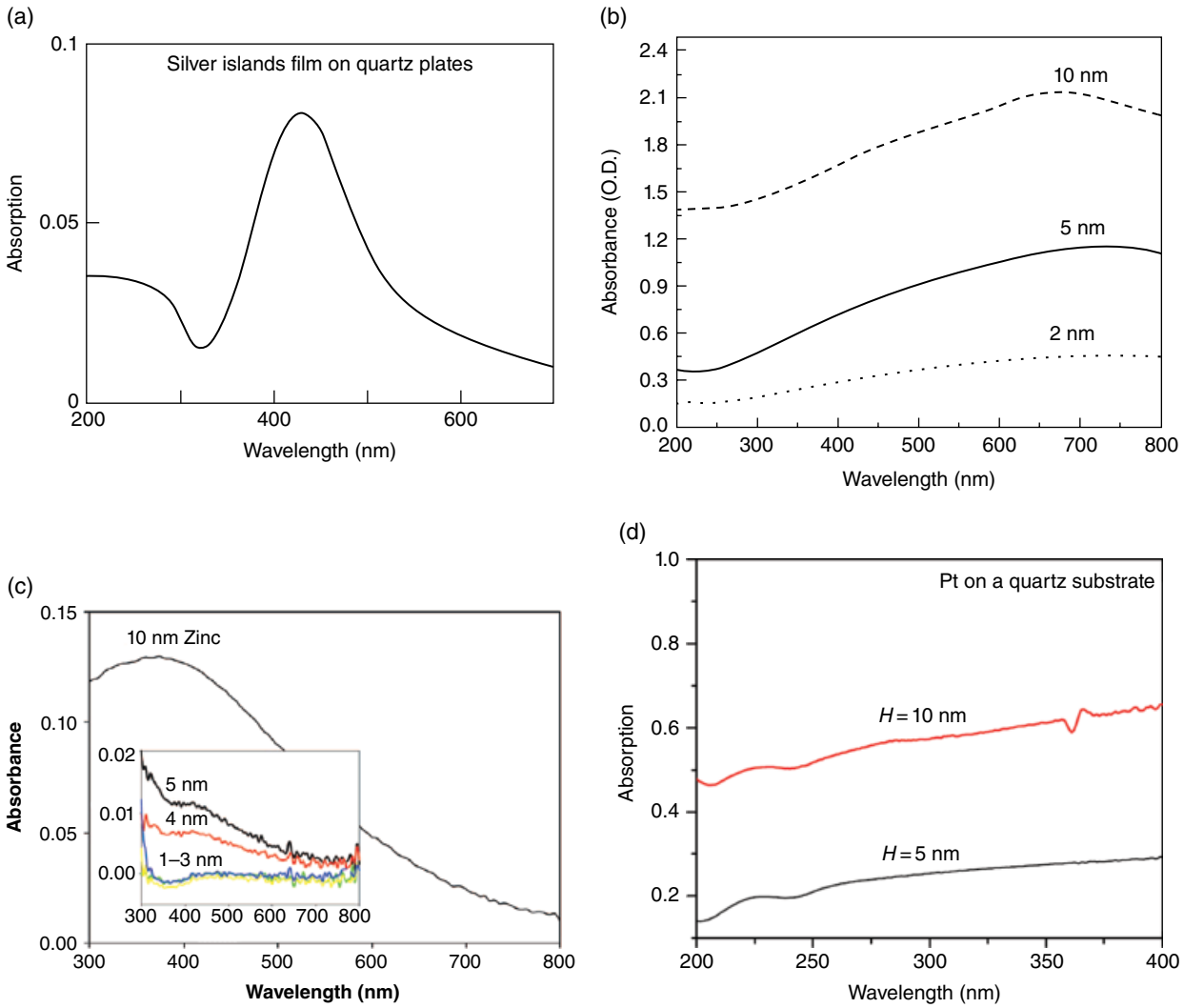

Figure 18.5 Absorption spectra of (a) Ag, (b) Al, (c) Zn, and (d) Pt island films. Figure 18.5a: Lakowicz *et al*. [10]. Reproduced with the permission of Elsevier. Figure 18.5b: Ray *et al*. [13]. Reproduced with the permission of American Chemical Society. Figure 18.5c: Aslan *et al*. [21]. Reproduced with the permission of American Chemical Society.

There are other possible structures for PEUVF. Jiao *et al*. numerically analyzed the PEUVF of three common plasmonic structures: dipole antenna, bullseye, and nanoaperture. They found that an Al bullseye can give more than 100x net enhancement of UV fluorescence [25], while the dipole antenna gives largest Purcell factor of 11. Rodriguez *et al*. numerically demonstrated that Al nanocrescent antennas can have plasmonic resonance in the UV [54], which is another promising structure for PEUVF.

18.4.3 Experimental Measurement

18.4.3.1 Characterization of SPR Properties

Several experimental configurations were employed to characterize plasmonic properties of the structures in UV range, such as the Kretschmann configuration [17, 18], the reverse Kretschmann configuration [12], dark-field extinction spectroscopy [42], and UV-Vis spectroscopy with an integrating sphere [19]. Different configurations are chosen depending on the type of material and geometry that need to be characterized. Front-face illumination and collection schemes are suitable for NPs or particulate films when LSPR is excited and the angle of incident light does not matter. These particulate films are typically very thin, around 10 nm in thickness. As the film becomes thicker, the enhancement factor reduces as the film becomes continuous, as studied by Ray *et al*. [13]. For continuous metal films, the Kretschmann configuration is utilized to determine resonant wavelengths and angles. Optical constants of continuous metal film can be determined by variable-angle ellipsometry [43] and elemental information from

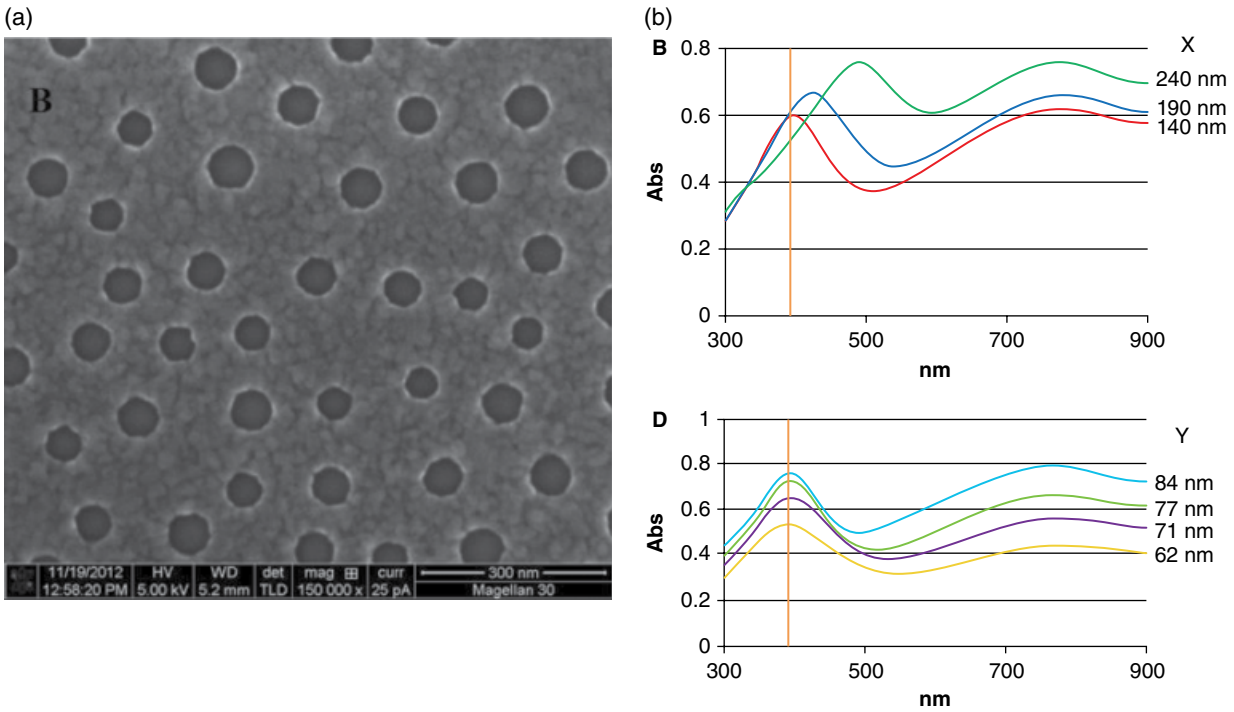

Figure 18.6 (a) SEM images of 67-nm hole array in 20-nm Al. (b) Extinction spectra of Al hole arrays with different center-to-center distance and hole sizes. Schmidt *et al*. [19]. Reproduced with the permission of American Chemical Society.

X-ray photoelectron spectroscopy (XPS) data can be used to interpret ellipsometry data. To characterize NPs or nanoaperture arrays, extinction/absorption spectrum measurement was carried out using dark-field microscopy [42] or UV-Vis with integrating sphere [19]. These measurement schemes can help determine plasmonic resonant conditions of the structures (excitation wavelength, incident angle, polarization, etc.), thus facilitating fluorescent enhancement experiments.

18.4.3.2 Fluorescence Enhancement

The fluorescence enhancement factor is the ratio of fluorescence intensity with metal structures to the fluorescence without the metal structures, based on the same number of molecules. Similar to SPR characterizations, front-face illumination/collection or Kretschmann configurations are chosen for fluorescent quantification based on the type of metal structures. Kretschmann configurations are typically used for fluorescent enhancement on continuous films. In addition to varying incident angles to match SPP excitation angles, collections angles can also be chosen to match surface plasmon-coupled emission (SPCE) angles . Due to the small absorption cross-sections of most UV fluorophores, fewer number of photons are collected compared to visible fluorophores. Therefore, extra care needs to be taken to maximize collection efficiency and minimize background noise. Confocal microscopy and large NA objective are some ways to improve collection efficiency and reduce background noise.

Quantitatively determining the enhancement factor can be challenging. First of all, the density of molecules before and after adding metal structures needs to be the same to ensure a fair comparison. Second, quenching due to metallic film can compete with enhancement effects, thus careful placing of molecules at certain distance from metal surface is necessary. Spin coating of molecules on metal film coated with a thin layer of dielectric film is one approach so far used to meet these challenges. However, this method can only provide an average enhancement factor over a large area that consists of molecules with all orientations and metal particles with a range of size distribution. Jiao studied fluorescent enhancement inside a nanoaperture [20] and significantly reduced the number of observed molecules to fewer than 100 in a small aperture. In addition, this approach allows the analysis of freely diffusing molecules rather than molecules fixed on a substrate. The former scenario not only better resembles biological conditions but also reduces quenching and photobleaching.

18.4.3.3 Lifetime Measurement

To gain knowledge of the radiative rate of a molecule, fluorescence lifetime measurement is often used in conjunction with measurement of the QY. Lifetime measurement has been performed using two approaches: frequency-domain fluorometer [10, 12] and time-domain fluorometer [13, 20]. The former approach requires sweeping of modulation frequency at a wavelength near the absorption peak, while the latter approach is typically performed with a pulsed laser. Lifetime measurements have been mostly performed on spin-coated molecules on metal films [11–13, 15, 16, 18, 19], in which case the molecules are fixed onto the substrate and are more prone to photobleaching. Jiao *et al*. has performed lifetime modification of freely diffusing molecules in nanoapertures. Since molecules can freely diffuse in and out of nanoapertures, the probability of photobleaching is relatively small compared to fixed molecules. Jiao has observed 3.5× reduction of lifetime for 60-nm diameter nanoapertures. Larger lifetime reduction (~10) is expected for smaller apertures (30-nm diameter) and even larger lifetime reduction is expected for Mg nanoapertures [27].

18.4.3.4 Toward Quantitative Florescence Analysis

To differentiate the contribution of excitation and emission enhancement in PEUVF, lifetime measurements or fluorescent intensity measurements are not enough. The count rate per molecule (CRM) has to be known. Combining Fluorescence Correlation Spectroscopy (FCS) analysis and lifetime measurements, the contribution of excitation enhancement and radiative enhancement can be derived [55], where FCS allows quantitative determination of the number of molecules being interrogated. FCS measurements in the UV range are challenging due in part to the short transit time of dye molecules in structures with small feature size. UV dyes also tend to have lower brightness compared to visible dyes. Design of novel plasmonic structures to further enhancement fluorescence and improve collection efficiency is therefore needed.

From Table 18.1, one can spot an interesting phenomenon. The same plasmonic structure can give different fluorescence enhancement and lifetime reduction for different molecules [13, 16, 22]. This implies that the enhancement depends on the intrinsic properties of the molecule. According to the discussions in the previous sections, we know that this is due to the fact that lifetime reduction and total emission enhancement depend on the native QY of the molecule. Even though this has been implied in several studies, the direct experimental demonstration and analysis have only been carried out recently [20]. Jiao *et al*. studied excited-state lifetime modification of diffusing molecules by Al nanoapertures in the UV using two molecules with different native QYs: *p*-terphenyl and tryptophan. Figure 18.7a shows the Scanning Electron Microscopy (SEM) image of Al nanoapertures with different diameters. Figure 18.7b shows the measured lifetime reduction versus diameter for the two molecules. It is clear

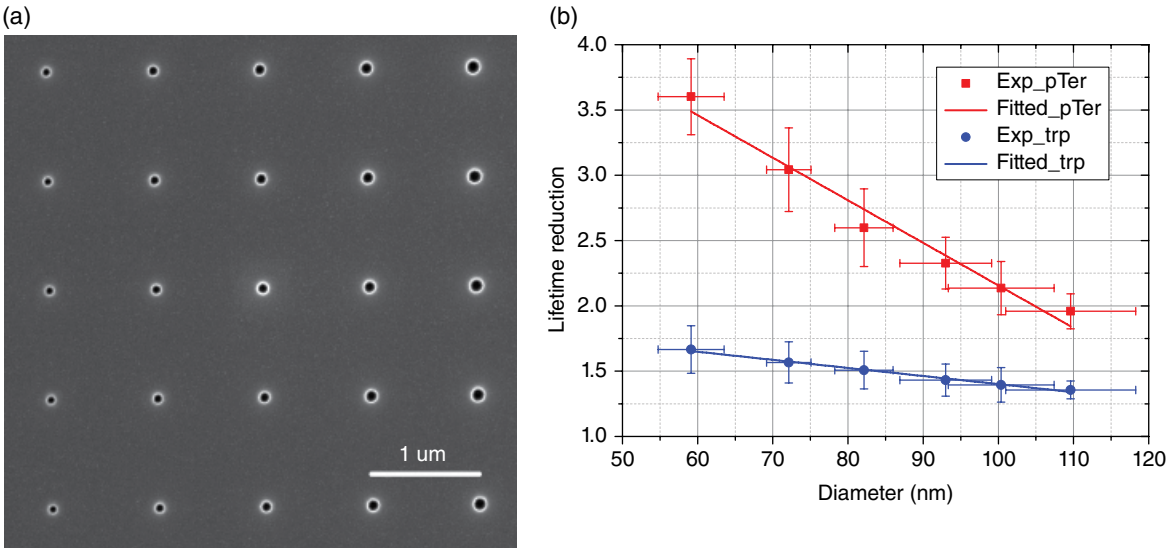

Figure 18.7 (a) SEM images of Al nanoaperture sample. Aperture size varies along the horizontal direction from 60- to 110-nm diameter. Milling dose varies along the vertical direction. (b) Measured lifetime reduction versus diameter for *p*-terphenyl (red dots) and tryptophan (blue dots). Linear fits (solid lines) are shown for the experimental data points. Jiao *et al*. [20]. Reproduced with the permission of American Chemical Society.

that two molecules experience different lifetime modifications. Larger lifetime reductions of ~3.5× were observed for high QY laser dye *p*-terphenyl in a 60-nm diameter aperture, while lower lifetime reduction of ~1.7 was observed for low QY molecule tryptophan, following Eq. (18.6).

18.5 Summary

In the chapter, we introduced the basics of PE of UV fluorescence. PEUVF research was also reviewed from the perspectives of material selection, structure choice, and experimental measurement.

Acknowledgment

The authors acknowledge support from NSF MRSEC grant DMR-1121252.

References

1 Maier, S. *Plasmonics: Fundamentals and Applications*; Springer: New York, **2007**.
2 Anker, J. N.; Hall, W. P.; Lyandres, O.; Shah, N. C.; Zhao, J.; Van Duyne, R. P. Biosensing with Plasmonic Nanosensors. *Nat. Mater.* **2008**, *7* (6), 442–453.
3 Brolo, A. G. Plasmonics for Future Biosensors. *Nat. Photonics* **2012**, *6* (11), 709–713.
4 Aroca, R. F. Plasmon Enhanced Spectroscopy. *Phys. Chem. Chem. Phys.* **2013**, *15* (15), 5355–5363.
5 Atwater, H. A.; Polman, A. Plasmonics for Improved Photovoltaic Devices. *Nat. Mater.* **2010**, *9* (3), 205–213.
6 Lakowicz, J. Principles of Fluorescence Spectroscopy, 3rd edition; Science Press: Beijing, **2008**; Chaps. 16–25.
7 Chen, R. F. Fluorescence Quantum Yields of Tryptophan and Tyrosine. *Anal. Lett.*, **1967**, *1*, 35–42.
8 Edelhoch, H. Spectroscopic Determination of Tryptophan and Tyrosine in Proteins. *Biochemistry* **1967**, *6* (7), 1948–1954.
9 Fasman, G. D., Ed. *Practical Handbook of Biochemistry and Molecular Biology*; CRC Press: Boca Raton, FL, **1989**.
10 Lakowicz, J. R.; Shen, B.; Gryczynski, Z.; D'Auria, S.; Gryczynski, I. Intrinsic Fluorescence from DNA Can Be Enhanced by Metallic Particles. *Biochem. Biophys. Res. Commun.* **2001**, *286* (5), 875–879.
11 Szmacinski, H.; Ray, K.; Lakowicz, J. R. Metal-Enhanced Fluorescence of Tryptophan Residues in Proteins: Application toward Label-Free Bioassays. *Anal. Biochem.* **2009**, *385* (2), 358–364.
12 Gryczynski, I.; Malicka, J.; Gryczynski, Z.; Nowaczyk, K.; Lakowicz, J. R. Ultraviolet Surface Plasmon-Coupled Emission Using Thin Aluminum Films. *Anal. Chem.* **2004**, *76* (14), 4076–4081.
13 Ray, K.; Chowdhury, M. H.; Lakowicz, J. R. Aluminum Nanostructured Films as Substrates for Enhanced Fluorescence in the Ultraviolet-Blue Spectral Region. *Anal. Chem.* **2007**, *79* (17), 6480–6487.
14 Ray, K.; Szmacinski, H.; Lakowicz, J. R. Enhanced Fluorescence of Proteins and Label-Free Bioassays Using Aluminum Nanostructures. *Anal. Chem.* **2009**, *81* (15), 6049–6054.
15 Chowdhury, M. H.; Ray, K.; Gray, S. K.; Pond, J.; Lakowicz, J. R. Aluminum Nanoparticles as Substrates for Metal-Enhanced Fluorescence in the Ultraviolet for the Label-Free Detection of Biomolecules. *Anal. Chem.* **2009**, *81* (4), 1397–1403.
16 Chowdhury, M. H.; Chakraborty, S.; Lakowicz, J. R.; Ray, K. Feasibility of Using Bimetallic Plasmonic Nanostructures to Enhance the Intrinsic Emission of Biomolecules. *J. Phys. Chem. C. Nanomater. Interfaces* **2011**, *115* (34), 16879–16891.
17 Crosbie, S.; Zerulla, D. Long Range Surface Plasmon Resonance and Enhanced Fluorescence near the Ultra-Violet Vacuum Cutoff Limit. *J. Appl. Phys.* **2012**, *111* (8), 084702.
18 Ono, A.; Kikawada, M.; Akimoto, R.; Inami, W.; Kawata, Y. Fluorescence Enhancement with Deep-Ultraviolet Surface Plasmon Excitation. *Opt. Express* **2013**, *21* (15), 17447–17453.
19 Schmidt, T. M.; Bochenkov, V. E.; Espinoza, J. D. A.; Smits, E. C. P.; Muzafarov, A. M.; Kononevich, Y. N.; Sutherland, D. S. Plasmonic Fluorescence Enhancement of DBMBF2 Monomers and DBMBF2–Toluene Exciplexes Using Al-Hole Arrays. *J. Phys. Chem. C* **2014**, *118* (4), 2138–2145.
20 Jiao, X.; Peterson, E. M.; Harris, J. M.; Blair, S. UV Fluorescence Lifetime Modification by Aluminum Nanoapertures. *ACS Photonics* **2014**, *1* (12), 1270–1277.
21 Aslan, K.; Previte, M. J. R.; Zhang, Y.; Geddes, C. D. Metal-Enhanced Fluorescence from Nanoparticulate Zinc Films. *J. Phys. Chem. C. Nanomater. Interfaces* **2008**, *112* (47), 18368–18375.
22 Akbay, N.; Mahdavi, F.; Lakowicz, J. R.; Ray, K. Metal-Enhanced Intrinsic Fluorescence of Nucleic Acids Using Platinum Nanostructured Substrates. *Chem. Phys. Lett.* **2012**, *548*, 45–50.

23 Yang, Y.; Callahan, J. M.; Kim, T.-H.; Brown, A. S.; Everitt, H. O. Ultraviolet Nanoplasmonics: A Demonstration of Surface-Enhanced Raman Spectroscopy, Fluorescence, and Photodegradation Using Gallium Nanoparticles. *Nano Lett.* **2013**, *13* (6), 2837–2841.

24 Mahdavi, F.; Blair, S. Nanoaperture Fluorescence Enhancement in the Ultraviolet. *Plasmonics* **2010**, *5* (2), 169–174.

25 Jiao, X.; Blair, S. Optical Antenna Design for Fluorescence Enhancement in the Ultraviolet. *Opt. Express* **2012**, *20* (28), 29909.

26 Forestiere, C.; Handin, A.; Dal Negro, L. Enhancement of Molecular Fluorescence in the UV Spectral Range Using Aluminum Nanoantennas. *Plasmonics* **2014**, *9* (3), 715–725.

27 Jiao, X.; Wang, Y.; Blair, S. UV Fluorescence Enhancement by Al and Mg Nanoapertures. *J. Phys. D Appl. Phys.* **2015**, *48* (18), 184007.

28 Raether, H. *Surface Plasmons on Smooth and Rough Surfaces and on Gratings*; Springer: Berlin, **1988**.

29 Sarid, D.; Challener, W. *Modern Introduction to Surface Plasmons: Theory, Mathematica Modeling, and Applications*; Cambridge University Press: Cambridge, UK, **2010**.

30 Palik, E. D., Ed. *Handbook of Optical Constants of Solids*; Academic Press: London, **1985**.

31 Wenger, J.; Aouani, H.; Gérard, D.; Blair, S.; Ebbesen, T. W.; Rigneault, H. Enhanced Fluorescence from Metal Nanoapertures: Physical Characterizations and Biophotonic Applications. In *Proc. SPIE 7577, Plasmonics in Biology and Medicine VII, 75770J*; Vo-Dinh, T., Lakowicz, J. R., Eds.; **February 16, 2010**; pp. 75770J1–J75770J8. doi:10.1117/12.840042.

32 Blair, S.; Wenger, J. Enhancing Fluorescence with Sub-Wavelength Metallic Apertures. In *Metal-enhanced Fluorescence*; Geddes, C. D., Ed.; John Wiley & Sons: Hoboken, NJ, **2010**; p. 489.

33 Kinkhabwala, A.; Yu, Z.; Fan, S.; Avlasevich, Y.; Müllen, K.; Moerner, W. E. Large Single-Molecule Fluorescence Enhancements Produced by a Bowtie Nanoantenna. *Nat. Photonics* **2009**, *3* (11), 654–657.

34 Purcell, E. M. Spontaneous Emission Probabilities at Radio Frequencies. *Phys. Rev.* **1946**, *69*, 681.

35 Blaber, M. G.; Arnold, M. D.; Ford, M. J. A Review of the Optical Properties of Alloys and Intermetallics for Plasmonics. *J. Phys. Condens. Matter* **2010**, *22* (14), 143201.

36 West, P. R.; Ishii, S.; Naik, G. V.; Emani, N. K.; Shalaev, V. M.; Boltasseva, A. Searching for Better Plasmonic Materials. *Laser Photon. Rev.* **2010**, *4* (6), 795–808.

37 Boltasseva, A.; Atwater, H. A. Low-Loss Plasmonic Metamaterials. *Science* **2011**, *331* (6015), 290–291.

38 Naik, G. V.; Kim, J.; Boltasseva, A. Oxides and Nitrides as Alternative Plasmonic Materials in the Optical Range [Invited]. *Opt. Mater. Express* **2011**, *1* (6), 1090.

39 Tassin, P.; Koschny, T.; Kafesaki, M.; Soukoulis, C. M. A Comparison of Graphene, Superconductors and Metals as Conductors for Metamaterials and Plasmonics. *Nat. Photonics* **2012**, *6* (4), 259–264.

40 Naik, G. V.; Shalaev, V. M.; Boltasseva, A. Alternative Plasmonic Materials: Beyond Gold and Silver. *Adv. Mater.* **2013**, *25* (24), 3264–3294.

41 Gérard, D.; Gray, S. K. Aluminium Plasmonics. *J. Phys. D Appl. Phys.* **2015**, *48* (18), 184001.

42 Knight, M. W.; King, N. S.; Liu, L.; Everitt, H. O.; Nordlander, P.; Halas, N. J. Aluminum for Plasmonics. *ACS Nano* **2014**, *8* (1), 834–840.

43 Appusamy, K.; Blair, S.; Nahata, A.; Guruswamy, S. Low-Loss Magnesium Films for Plasmonics. *Mater. Sci. Eng. B* **2014**, *181*, 77–85.

44 Appusamy, K.; Jiao, X.; Blair, S.; Nahata, A.; Guruswamy, S. Mg Thin Films with Al Seed Layers for UV Plasmonics. *J. Phys. D. Appl. Phys.* **2015**, *48* (18), 184009.

45 Song, Y.; Shan, D.; Chen, R.; Han, E.-H. Investigation of Surface Oxide Film on Magnesium Lithium Alloy. *J. Alloys Compd.* **2009**, *484* (1-2), 585–590.

46 Wu, P. C.; Kim, T.-H.; Suvorova, A.; Giangregorio, M.; Saunders, M.; Bruno, G.; Brown, A. S.; Losurdo, M. GaMg Alloy Nanoparticles for Broadly Tunable Plasmonics. *Small* **2011**, *7* (6), 751–756.

47 Kumamoto, Y.; Taguchi, A.; Honda, M.; Watanabe, K.; Saito, Y.; Kawata, S. Indium for Deep-Ultraviolet Surface-Enhanced Resonance Raman Scattering. *ACS Photonics* **2014**, *1* (7), 598–603.

48 McMahon, J. M.; Schatz, G. C.; Gray, S. K. Plasmonics in the Ultraviolet with the Poor Metals Al, Ga, In, Sn, Tl, Pb, and Bi. *Phys. Chem. Chem. Phys.* **2013**, *15* (15), 5415–5423.

49 Ou, J.-Y.; So, J.-K.; Adamo, G.; Sulaev, A.; Wang, L.; Zheludev, N. I. Ultraviolet and Visible Range Plasmonics in the Topological Insulator $Bi_{1.5}Sb_{0.5}Te_{1.8}Se_{1.2}$. *Nat. Commun.* **2014**, *5*, 5139.

50 Ross, M. B.; Schatz, G. C. Aluminum and Indium Plasmonic Nanoantennas in the Ultraviolet. *J. Phys. Chem. C* **2014**, *118* (23), 12506–12514.

51 Sanz, J. M.; Ortiz, D.; Alcaraz de la Osa, R.; Saiz, J. M.; González, F.; Brown, A. S.; Losurdo, M.; Everitt, H. O.; Moreno, F. UV Plasmonic Behavior of Various

Metal Nanoparticles in the Near- and Far-Field Regimes: Geometry and Substrate Effects. *J. Phys. Chem. C* **2013**, *117*, 19606–19615.

52 C.D. Geddes, Ed.; *Metal-Enhanced Fluorescence*; John Wiley & Sons: Hoboken, NJ, **2010**.

53 Zhu, P.; Craighead, H. G. Zero-Mode Waveguides for Single-Molecule Analysis. *Annu. Rev. Biophys.* **2012**, *41*, 269–293.

54 Rodriguez, M.; Furse, C.; Shumaker-Parry, J. S. and Blair S. Scaling the Response of Nanocrescent Antennas into the Ultraviolet. *ACS Photonics* **2014**, *1*, 496–506.

55 Wenger, J.; Gérard, D.; Dintinger, J. Emission and Excitation Contributions to Enhanced Single Molecule Fluorescence by Gold Nanometric Apertures. *Opt. Express* **2008**, *16* (5), 8855–8865.

Index

a

adenosine triphosphate (ATP) 123
AEF *see* average enhancement factor (AEF)
Ag-coated Au nanorod–fluorescein composites 7
Ag–Cu bimetallic nanoparticles
  average size 75
  finite-difference time-domain calculations 85–87
  fluorescence spectroscopy 76, 78–79
  high-resolution transmission electron micrograph 75
  particle characterization 75–76
  particle density 76
  polyol synthesis process 74–75
  SEM and AFM images 75–77
  sputtering and annealing synthesis technique 74
  STEM-EDS spectra 75, 76
  transmission electron microscopy 75, 76
Ag–fluorescein composite
  average lifetimes 8
  fluorescence quantum yield 7
Ag NS, average enhancement factor of 52–53
Ag NS@SiO_2
  absorption cross section of 58–59
  AEF distribution *vs.* distances 61, 63
  AEF *vs.* wavelengths for 64–66
  configuration of 38–39
  EEF *vs.* molecular positions for 61, 63–64
  EF *vs.* dipole orientations for 61–63, 65
  excitation rates of 61
  extinction cross section of 58–59
  scattering cross section of 58–59
Ag plate–fluorescein composite, average lifetimes of 8
Ag@SiO_2
  AEF *vs.* distances 48–49
  AEF *vs.* emission for 49
  AEF *vs.* wavelengths for 49
  ECSs of 46
  EEF *vs.* molecule positions for 48
  EF *vs.* dipole orientations 46, 47
  theoretical AEF of 49–50
Ag-SiO_2-fluorescein isothiocyanate NP preparation process 214
Alexa488
  absorption and emission spectra of 117, 118
  distance-dependent excitation rate 119, 120
  spectral overlap 119
Alexa Fluor 430 30, 31
Alexa Fluor 488 74, 78, 79
Alexa Fluor 594 74, 78, 79
aluminum phthalocyanines (AlPcS) 126–127
annealed AgO_x thin film 206, 208, 209
antigen–antibody interaction 129
aptamers 123, 130, 244
aptasensor 123
asymmetrical split ring resonator nanoslit array 203
Atto655 128
Au colloid-modified PVDF membrane 26, 27
Au colloids 14–16
  zeta potential values for 259
Au core–Ag shell nanostructures 14, 15
Au–fluorescein composite
  average lifetimes 8
  fluorescence quantum yield 7
Au nanoparticle substrates 16–18
Au nanorod–fluorescein composite
  average lifetimes 8
  fluorescence quantum yield 7
AuNR/SiO_2-T790 NPs
  9,10-anthracenediyl-bis (methylene) dimalonic acid, photo-oxidation of 219–220
  enhanced two-photon excitation fluorescence 219
  preparation 217, 218
  singlet oxygen generation 219, 220
Au NS, average enhancement factor of 50–52
Au NS@SiO_2
  AEF *vs.* emission wavelengths 58, 59
  AEF *vs.* wavelength for 55, 57–58
  distribution of AEF *vs.* distances 55, 57
  EEF *vs.* molecular positions for 54–55, 57
  EF *vs.* dipole orientations 54, 56
  SCS, ACS, and ECS of 54
Au-SHIN
  nanorod synthesis 260–263
  nanosphere synthesis 259–261
Au@SiO_2
  AEFs *vs.* emission wavelength for 44–45
  distance *vs.* AEF distribution 43, 45
  ECSs *vs.* wavelengths for 41
  EEF *vs.* molecular positions for 42–43
  EF *vs.* dipole orientations 41–42

Surface Plasmon Enhanced, Coupled and Controlled Fluorescence, First Edition. Edited by Chris D. Geddes.
© 2017 John Wiley & Sons, Inc. Published 2017 by John Wiley & Sons, Inc.

average enhancement factor (AEF) 39
Ag NS@SiO_2 61, 63–66
Ag@SiO_2 48–50
Au NS@SiO_2 55, 57–59
Au@SiO_2 43–45

b

bacterial adhesion quantification 126
Bergman's theory 80–81
BHHCT-Eu-DPBT-doped Ag@SiO_2 nanoparticles 33, 34
bio-barcode amplification 123
biochip, substrate design for 243–244
biomolecules, sensing of 169–171
biosensors
grating-assisted SPCE implemetation 236–238
SPCE-based 244–245
biotin–avidin interaction 129
Bloch surface waves (BSWs) 230–232
bovine serum albumin (BSA) 18, 27
(Deep Purple™)-bovine serum albumin (DP-BSA) monolayers 16, 23, 25
FLIM images of 19
fluorescence measurements of 24
bowtie antenna 276, 277
Bragg-scattered surface plasmon (BSSP) modes 228
BSA *see* bovine serum albumin (BSA)

c

cathodoluminescence characterization, of Klarite substrate 19
CEF *see* copper-enhanced fluorescence (CEF)
Chance, Prock, and Silbey (CPS) 139
chelate-enhanced fluorescence (CHEF) 155
chip sensor 125
coinage metal nanoparticles, MEF 153–154
collective effects, in NP films 138
colloidal semiconductor quantum dots 286
composite nanoparticles
magnetic-fluorescent (*see* magnetic-fluorescent composite nanoparticles)
plasmonic-fluorescent (*see* plasmonic-fluorescent composite nanoparticle)
with properties and application potentials 3, 5
concanavalin A (Con A) 8, 220, 221
conformational-switching signaling aptamers 244, 245
copper-enhanced fluorescence (CEF) 165–166
copper nanoparticles (CuNPs) 154
core–shell approach 14–15
corrugated Au surface, grating-enhanced fluorescence on 234
count rate per molecule (CRM) 296, 297
cyanine 5 (Cy5) 122, 130, 280, 281
Cy3 fluorophores
experimentally observed luminescence enhancement ratio 83, 84
fluorescence intensity of 79, 80
overall luminescence quantum efficiency enhancement ratio 83, 84
quantum efficiency enhancement ratio 84, 85

d

decay length, surface electromagnetic field 128
density of states 137
dequenched fluorophores, SPCE spectra 248, 249
detection antibody (dAb) 236
Dicke effect 182
dielectric/metal/dielectric planar structures 112
dielectric one-dimensional photonic crystals (1DPC) 230, 232
diffractive grating structures, for angular control 234–235
1,4-dihydroxy-2,3-dimethylanthracene-9,10-dione (DHDMAD)
energy transfer parameters, in Ag NPs 199, 201
fluorescence emission spectra 198, 199
optical absorption spectra 198, 199
structure 198
diiminic Schiff bases (DSBs)
CEF 165–166
silver-enhanced fluorescence 161–165
1,4-dimethoxy-2,3-dibromomethylanthracene-9,10-dione (DMDBMAD)
Stern–Volmer plot 201–202
structure 201
distance controlling 130
distance-dependent feature, MEF 126, 138
DNA detection 122, 123, 244
dopamine (DA) 169–171
Drude theory 80
DSBs *see* diiminic Schiff bases (DSBs)
dual-aptamer-based strategy,123
dye-doped microarray chip 250
dye-doped poly(methyl methacrylate) layer
far-field fluorescence intensity, angular distribution of 235
nondiffractive metallic grating structure for 232, 233

e

EF *see* enhancement factor (EF)
electric field-assisted SPCE (E-SPCE) 244–246
electron beam evaporation 130
electron beam lithography 203
electrostatic adsorption 130–132
emission enhancement 17, 18
emission linewidth 143–147
emission wavelength 143–147
energy transfer process 128
Coulombic interactions, effects of 200–201
efficiency 199
fluorescence resonance energy transfer 198
from fluorophore to nanoparticles 199–200
resonant energy transfer 198
enhanced luminescence 257
on solid surfaces and spectral profile modification 265–268
plasmon-enhanced (*see* plasmon-enhanced luminescence)
enhancement factor (EF) 39
Ag NS@SiO_2 61–63, 65
Ag@SiO_2 46, 47

Au NS@SiO_2 54, 56
Au@SiO_2 41–42
on fluorescence 40–41
enhancing substrate 123
ESEM, of silver structure 20, 22
Eu3+ complexes 139
excitation enhancement, values of 17, 18
excited-state fluorophores 198

f

FDTD *see* finite-difference time-domain (FDTD)
femtosecond laser system, illustration of 203, 204
figure of merit (FOM), of LSP 295–296
film-coupled silver nanocube structure 272, 273, 276, 277, 282 *see also* plasmonic nanocavities
film-coupled sphere system 276, 277
finite-difference time-domain (FDTD) 50, 85–87, 127, 166, 168, 205, 208, 248
FITC-HSA monolayer
fluorescence emission intensity of 16
laser scanning microscopy 14, 15
FLIM images 19
of fluorescent monolayers 20, 22
flow cytometry 13
beads, MIFE with 30–34
fluorescein isothiocyanate (FITC) 122, 123, 125, 127, 214–215
fluorescence *see also* plasmon-enhanced UV fluorescence (PEUVF)
enhancement factor on 40–41
lifetime 296
and phosphorescence 296
quantum yield 296–297
three energy levels for 296
fluorescence-based spectroscopy 295
fluorescence enhancement *see also* metal-induced fluorescence enhancement (MIFE)
for DP-BSA 16
origin of 17
of silver structures 22–23
fluorescence lifetime ratios, for DP-BSA fluorophore 24
fluorescence quantification 151
fluorescence quenching
applications 197
fluorescence resonance energy transfer (FRET) 123, 162, 198
fluorescence spectra
of fluorescein-based composite nanomaterials 5–7
QD-based composite nanomaterials 6, 7
fluorescent monolayers 20–22
fluoroimmunoassay 122
fluorophores *see also* Cy3 fluorophores
in absence of metal 152
Deep Purple 18
electron–hole recombination options 1, 2
emission characteristics 151
excited-state 198
in free space 153
intrinsic radiative decay rate 163
lifetime study 7–8
oscillating dipoles 152
RP model 166
simplified energy diagram 112–113
and SPB 163–164
total excited-state lifetime 111–112
Förster resonance energy transfer (FRET) 114, 115
Au nanoparticle concentration 190
description 185
efficiency 186–188
plasmonic nanostructures 189–191
requisites 181
Förster's theory 198, 199
frequency-domain fluorometer 305
frequency shift 144
full-coupling surface plasmon-coupled emission 245–248
full-wave numerical simulations 273

g

Galvanic replacement reaction 128
gold-enhanced fluorescence (GEF) 155, 157–160
gold nanoparticles (AuNPs) 154–155
grating-assisted SPCE *see* surface plasmon–coupled emission (SPCE)
Green's functions, of multilayered sphere 40

h

hairpin molecular beacon signaling match and mismatch 245, 246
half-wavelength fundamental mode 272
hematoporphyrin derivatives 219
Hertzian dipole emitters 201
H5N1 influenza virus 129, 130
homogeneous substrates, MIFE
Au nanoparticle substrates 16–18
core–shell approach 14–15
Klarite™ substrate 18–19
hot-spot nanostructure-based biosensor 248–249
hotspots 125, 127–128
HSA-FITC complex 20
human immunoglobulin E (IgE) 130
human immunoglobulin G (IgG) 127
hyaluronic acid (HA) 131
hyperlens 112

i

IGEPAL cyclohexane-based reverse micelle solution 3
image theory 144
immunoassay, on glass slide 13, 14
indocyanine green 125
Influenza A virus 126
inherent fluorescence 151
in situ fluorescence assay, optical instrument for 236
in situ photoreduction 131
interference 138
interference lithography 95–96
interleukin 6 (IL6) 237
internal conversion (IC) process 179
intersystem crossing (ISC) 179, 180
intracellular protein imaging 123
intrinsic fluorescence
bacterial 126
biomolecule 122
intrinsic radiative quantum yield 277–278

j

Jablonski diagram 151, 152, 179, 180

k

Klarite™ substrate 18–19
Kretschmann (KR) configuration 241, 303, 304

l

labeling 295
Langmuir–Blodgett (LB) films 266–268
lanthanide-doped upconversion NPs 220
laser scanning microscopy
  FITC-HSA monolayer on nanoparticles and glass surface 14, 15
  fluorescent protein monolayer 20, 21
laser-treated AgO_x thin film
  adsorbed R6G, Raman spectra of 204, 207
  Ag nanoparticle aggregation, AFM 204, 205, 207
  finite-difference time-domain simulation method 205, 208
  HR-TEM image 204, 205
  reactive sputtering method 203
  SERS-active micro-pattern fabrication 204, 206
  TEM image 204, 205
  X-ray diffraction 204, 205
lattice fringe 155, 156, 174
layer-by-layer (LbL) assembly 130–132
leukemia cell imaging 123
ligand exchange approach 4–5
lightening rod effect 155, 163, 166
limit of detection (LOD) 151, 237–238
local electric field 127
localized surface plasmon resonance (LSPR) 211
localized surface plasmons (LSPs) 180, 295
  AuNRs 126
  polaritons, in metallic arrays 93–94
LOD *see* limit of detection (LOD)
long-range surface plasmon (LRSP) 228
long-range surface plasmon polariton modes (LRSPPs) 115
Lorentz theory 80

m

magnetic-fluorescent composite nanoparticles
  fluorophore lifetime study 7–8
  functionalization and labeling application 8
  ligand exchange approach 4–5
  optical property 5–7
  polyacrylate coating method 3–4
magnetic resonance imaging (MRI) 128
magnetic separation 123
malachite green 264
Maxwell Garnett (MG) theory 80–81
MEF *see* metal-enhanced fluorescence (MEF)
MEF-based bioassay, sonication-accelerated 122
mercuric ion detection 123
metal-based superlenses 112
metal–chromophore interactions 214
  enhancement–quenching transition 213
  local electric field amplification 212, 213
  near-field light distribution 212
  nonradiative energy transfer 212
  quantum yield 212, 213
  radiative decay rate 212
  separation distance 212
metal-enhanced fluorescence (MEF) 121, 151, 180, 211, 258
  see also Ag–Cu bimetallic nanoparticles
  advantage 181
  applications of 169–174
  biomolecules, sensing of 169–171
  coinage metal nanoparticles 153–154
  complementary effects 153, 155
  copper-enhanced fluorescence 165–166
  description 73
  FDTD calculations 85–87
  gold-enhanced fluorescence 154–155
  interpretation of 153
  lightening rod effect 155
  near-field enhancement 181
  nonradiative decay 182
  resonance energy transfer 180–181
  for silver 153
  silver-enhanced fluorescence 154–165
  in solution phase 154–169
  toxic metals, sensing of 171–174
  tuning of 166–169
metal-enhanced fluorescence modified Gersten–Nitzan model 81–85
metal-induced fluorescence enhancement (MIFE) 13
  homogeneous protein sensing 14–19
  silver fractal structures 19–25
  with flow cytometry beads and single particle imaging 30–34
  with membranes for protein dot blots 25–30
metal-induced quenching
  adverse effect 2
  in fluorescence-based experiments 1
metallic hole arrays, decay lifetimes 97–98
metal nanoparticles (MNPs) 151–152 *see also* silver (Ag) nanoparticles
  localized surface plasmon resonance 211
  quenching effect 153
  SPR modeling, using Mie theory 79–81
  surface plasmon resonance 197
microfabricated patch antenna 271
microwave acceleration 123
Mie theory 39, 79–81
MIFE *see* metal-induced fluorescence enhancement (MIFE)
mirror 139
mixed 15C-PTCD/SA Langmuir monolayer
  SHINEF 266, 267
  surface pressure-area isotherms 266, 267
MNPs *see* metal nanoparticles (MNPs)
modified Maxwell's equation 151

molecule beacon 123
molecule-doped core–shell 37
  $Ag@SiO_2$ 46–50
  $Au@SiO_2$ 41–45
  configuration of 38
MoS_2 monolayer
  absorption and emission spectra 289
  fluorescence enhancement factor 289–291
  intrinsic optical properties 288
  nanocavity-coupled MoS_2 289–291
multilayered smooth metallic/dielectric structures 112
multilayered sphere
  excited dipole interacting with 40
  plane wave interacting with 39–40
multiligand binding 129

n

nanometal surface energy transfer (NSET) mechanism 185
nanoparticle film 138
nanopatch antenna 276
  description 271
  measured and simulated radiation pattern 277
nanorod Au-SHIN 260
  geometry and geometrical parameters 261, 262
  Stöber methodology 261
  TEM images 261–263
nanoshelled nanocavity
  Ag NS 52–53
  Au NS 50–52
nanosphere Au-SHIN
  HR-TEM images 260
  sodium citrate reduction method 259–260
  TEM images 260, 261
nanowire structures, high enhancement factors in 19–22
$NaYF_4$:Yb, $Er@SiO_2@Ag$ core-shell NPs 220, 221
near-field enhancement (NFE) 181, 183
near-infrared (NIR) fluorescence 37
noble metal nanoparticle-based hybrid nanoprobes 2
noble metal nanoparticles 179, 211
nondiffractive grating structures, for angular control 232–234
$NS@SiO_2$ 53–54
  Ag $NS@SiO_2$ 58–66
  Au $NS@SiO_2$ 54–59

o

Ochratoxin A (OTA) 125
oleyl-functionalized Au nanorod–fluorescein composite 8, 9
oleyl-functionalized γ-Fe_2O_3–CdSe/ZnS nanocomposite 8, 9
oligonucleotides 185
optical patch antenna 271

p

perfect lens 112
PEUVF *see* plasmon-enhanced UV fluorescence (PEUVF)
phosphorescent ruthenium metal complex 282
photodynamic therapy 126
photoluminescence mapping *vs.* dispersion relation 100–102
photonic mode density 137, 152, 155
photosensitizer 126
plasmon decay length 138
plasmon-enhanced fluorescence
  one-photon excitation fluorescence 214–215
  two-photon excitation fluorescence 215–220
plasmon-enhanced luminescence
  in liquid media 262–265
  nanorod Au-SHIN 260–263
  nanosphere Au-SHIN 259–260
plasmon-enhanced UV fluorescence (PEUVF)
  advantage 297
  dipole antenna 303
  experimental studies 297, 298
  fluorescence enhancement factor 304
  Ga nanoparticles 301
  island structure 301–303
  lifetime measurements 305
  material selection 297, 299–301
  nanoaperture 299, 301, 303
  quantum yield-dependency 305–306
  SPR properties, characterization of 303–304
  structure selection 301–303
plasmonic assembly-induced SPCE 249
plasmonic biosensor with grating chip, for IL6 detection 237
plasmonic enhancement (PE) 295
plasmonic-fluorescent composite nanoparticle
  fluorophore lifetime study 7–8
  functionalization and labeling application 8
  ligand exchange approach 4–5
  optical property 5–7
  polyacrylate coating method 3–4
plasmonic nanocavities 271–272
  absorption enhancement 280–282
  colloidal silver nanocube 272
  coupling of fluorescent emitters 277–280
  Cy5 molecular dye 280, 281
  directional scattering and emission 276–277
  electron beam evaporation 273
  fabrication procedures 272–273
  fluorescence enhancement 288–291
  fundamental resonance wavelength *vs.* nanocube size 276
  Green's function formalism 278, 279
  intrinsic radiative quantum yield 277–278
  layer-by-layer dip coating technique 273
  Lorentzian line shape 273
  measured and simulated scattering spectra 274, 275
  nanocavity resonances 273–274
  phosphorescent ruthenium metal complex 282
  properties 273–277
  Purcell enhancement 282–286
  resonance tuning 274–276
  simulation 278
  spontaneous emission rate enhancement 278–280
  ultrafast spontaneous emission 286–288
plasmonic nanostructures, in FRET system 189–191
plasmonics 227, 295
plasmophores 241
poly(3-hexylthiophene) (P3HT) 125

polyacrylate-coated hydrophilic quantum dots 5
polyacrylate coating-based composite
CdSe/ZnS quantum dots 3
inorganic semiconductor nanoparticles 3–4
of nanoparticle and organic dye 3
polyelectrolyte multilayer 139
polyethyleneimine (PEI) 131
poly(allylamine) hydrochloride (PAH) layer 273
polymer fluorescein, lifetime data for 7
polystyrene sulfonate (PSS) layer 273
polyvinylidene fluoride (PVDF) membranes 30
Au colloid-modified 26
dot blots on 27, 29
P-polarization Fresnel coefficient 116
P-polarization reflection coefficient, Si_3N_4 layers 116, 117
prism-based SPCE imaging system 250–251
propagating surface plasmons (PSPs) 93–94, 180
Protein A 127
protein dot blots, MIFE with membranes for 25–30
protein–ligand interaction 123
Purcell enhancement 282–286
Purcell factors 296, 297, 303

q

quantum efficiency 277–278
quantum yield, of quantum dots 179

r

radiating plasmon (RP) 153, 166, 182
radiative decay engineering (RDE) 163
recombinant hemagglutinin (rHA) 130
resonance energy transfer (RET) 162, 198
reverse Kretschmann (RK) configuration 229, 232, 237, 238, 241
reverse micelle 3
Rhodamine 6G (R6G) molecules 204
on Ag nanostructure/ZnS-SiO_2/Au film 206, 209
RNA detection 122
Ru dyes 282–286

s

semiconductor nanoparticle QD-based composites 7
semiconductors, photoluminescence process 179, 180
SERS *see* surface-enhanced Raman scattering (SERS)
Sgc8 123
shell-isolated nanoparticle-enhanced fluorescence (SHINEF) 258
crystal violet 264, 265
Langmuir–Blodgett films 266–268
shell-isolated nanoparticle-enhanced Raman spectroscopy (SHINERS) 258, 264
short-range surface plasmon (SRSP) 228
signal intensity histograms
of silica beads and Ag nanostructures 32
of stained Giardia lamblia cells 32, 33
silica beads 30–34
silver dendritic nanostructures 22–26
silver-enhanced beads, bioimaging with 33
silver-enhanced fluorescence (SEF) 154–155
diiminic Schiff bases 161–165
selectivity for 157–161
silver film over nanosphere (AgFON) 125
silver fractal structures
deposited on membranes (tree-like structures) 26, 28
enhancement factors in nanowire structures 19–22
silver dendritic nanostructures 22–26
silver island films (SIFs) 153
silver (Ag) nanoparticles 155
optical absorption spectra 198, 200
photophysical properties 199, 201
silver nanostructure-coated silica microspheres 30–32
Si_3N_4 dielectric coating layers 116, 117
single-molecule spectroscopic study 128
single particle imaging, MIFE 30–34
sinusoidal oscillation 145
sodium citrate reduction method 259–261
SPB *see* surface plasmon band (SPB)
SPCE *see* surface plasmon–coupled emission (SPCE)
spectral overlap 119, 145
spontaneous decay, of excited fluorophore 19
SPR *see* surface plasmon resonance (SPR)
SPR-induced enhanced FRET 188–191
sputtered and annealed Ag–Cu NPs 74, 76, 78
standard electron beam lithographic technique 126
Stern–Volmer plot 201, 202
Stokes-shift effect
Ag NS 52
Ag NS@SiO_2 64
Ag@SiO_2 49
Au NS 50
Au NS@SiO_2 54
Au@SiO_2 44
substrates, noble metal nanomaterials
Ag colloids 123
aluminum particle 130–131
core-shell Ag@SiO_2 nanoflares 130
core-shell Ag@SiO_2 NPs 123
core-shell bimetallic (Au^0-Ag^0) NPs embedded glasses 128
decahedral AgNPs 123
disk-coupled dots-on-pillar antenna-array (D2PA) 127
extinction spectrum, silver nanostructures 122
Fe_3O_4 NP core 127
gold nanocubes 126–127
gold NPs (AuNPs) 127
gold NRs (Au NRs) 125–126
gold/silica thin film 126, 130
hybrid magnetic NP/nanogold clusters (HMNCs) 127
hybrid metallic materials 127
magnetic NPs seeded with AgNPs 123–124
nano-antenna dot array 127
nanoporous gold leaf (NPGL) 126
plasmon absorption, silver nanostructures 121
polymer-coated AgNPs 123
silica-coated Au/Ag alloy NPs 128
silica-coated NPs 129
silver aggregates 125

silver film over nanosphere (AgFON) 125
silver-gold nanocomposite structure 128
silver island films (SIFs) 122–123
silver nanocubes 125
silver nanoparticles 123–125
silver nanorods (Ag NRs) 125
silver nanowires 125
triangular silver nanoplates 125
surface-enhanced fluorescence (SEF) 37
surface-enhanced Raman scattering (SERS) 37, 123
annealed AgO_x thin film 206, 208, 209
laser-treated AgO_x thin film 203–208
surface plasmon band (SPB) 153
surface plasmon–coupled emission (SPCE) 153
angular control
diffractive grating structures 234–235
nondiffractive grating structures 232–234
concentric grating-based out-coupling 237, 238
configuration for 241, 242
coupling efficiency 243
directional emission 242
DNA hybridization 244
dye-labeled cells 251
excitation and emission 241, 242
full-coupling effect 245–248
high-throughput detection, imaging apparatus for 249–251
hot-spot nanostructure-based biosensor 248–249
metallic surface 227–230
optical geometry 252
optical switch, for biosensing 244–245
plasmonically amplified bioassays 236–238
polarization 242
spectral dispersive property 242
SP waves with small losses 230–232
substrate design, for biochip 243–244
waveguide mode 251, 252
working principle 244, 245
surface plasmon-mediated emission (SPME)
dispersion relation 93
excitation in periodic metallic arrays 93–94
from periodic arrays 95
process 91–92
propagating and localized SPPs 93
resonant photoluminescence enhancement 91–92
surface plasmon polaritons (SPPs) 295
angle-resolved measurements 96–97
coupling efficiency 102–104
decay lifetimes
dependence on hole size 98–100
of metallic hole arrays 97–98
fluorescence decay lifetime on hole size 105–107
interference lithography 95–96
LEM 96–97
photoluminescence
dependence on hole size 104–105
mapping *vs.* dispersion relation 100–102
scanning electron microscopy 95–96
SPME (*see* surface plasmon-mediated emission (SPME))
thin metal films 115
surface plasmon resonance (SPR) 37, 179
emission enhancement 182–184
Förster resonance energy transfer process 185–189, 191
localized 152
of metallic NPs using Mie theory 79–81
in photoluminescence 181–182
pictorial depiction of 152
quenching of emission 184–185, 188
surface plasmon resonance (SPR)-enhanced Förster resonance energy transfer (FRET) 37
surface plasmons (SPs) 179–180, 229, 230
characteristics 228
diffraction, on periodically corrugated metallic surface 229, 230
gold NPs coated with silica 258
propagation constant 227–228
SP waves with small losses 230–232
surfactant-coated hydrophobic iron oxide nanoparticle 5

t

TAMRA 122
T–Hg^{2+}–T structure 123
thiazole orange (TO) 130
thiol chemistry 122–123, 130
thrombin 123
time-domain fluorometer 305
tip-enhanced Raman scattering (TERS) 258
toxic metals, sensing of 171–174
trisodium citrate reduction method, for shell-isolated nanoparticles 259
tris(bipyridine)ruthenium(II) 138–139
two-photon absorption 211
two-photon excitation fluorescence of fluorescein solution. 211, 212
schematic illustration 211, 212
two-photon photodynamic therapy 219, 220

u

UCNP@SiO_2@Ag NPs 220, 221
unamplified human genomic DNA 123
up-conversion fluorescence 128
UV–Vis spectra
of fluorescein-based composite nanomaterials 5–7
QD-based composite nanomaterials 6, 7
sputtered and annealed Ag–Cu NPs 76, 78

v

vancomycin-functionalized γ-Fe_2O_3–CdSe/ZnS nanocomposite 8, 9

w

waveguide mode SPCE 251, 252

x

X-ray photoelectron spectroscopy (XPS) 155, 156, 174

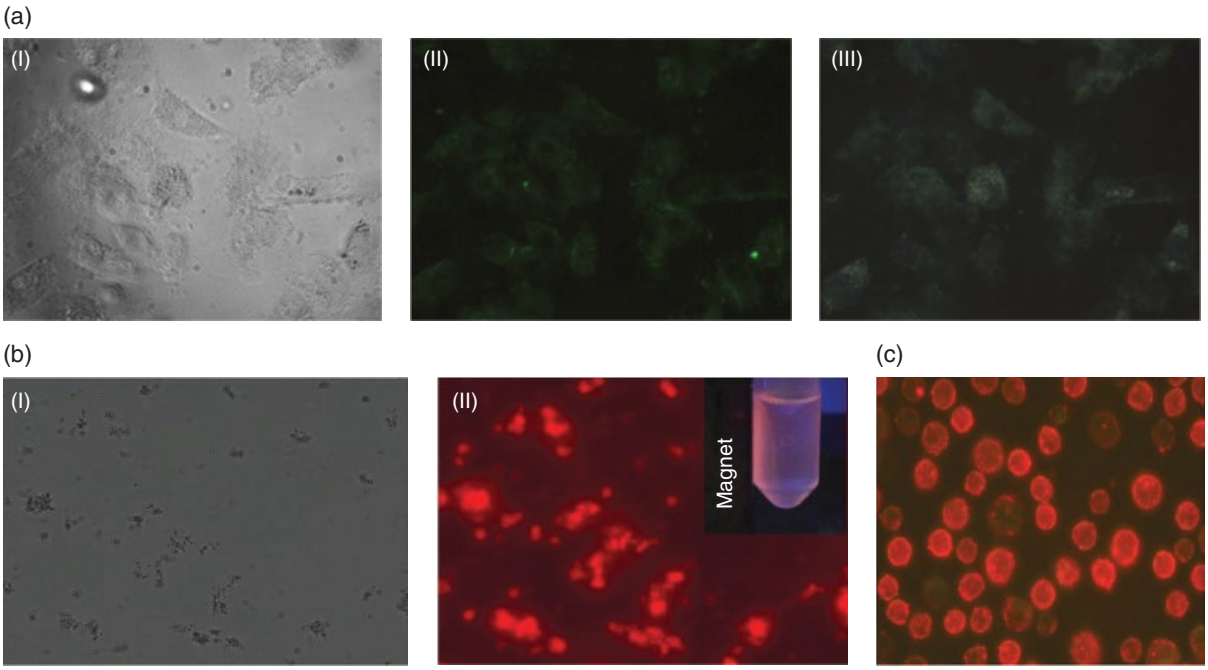

Figure 1.3 (a) H9C2 cells treated with oleyl-functionalized Au nanorod–fluorescein composite. (I) Bright field image, (II) fluorescence image, and (III) dark field image. (b) *Bacillus subtilis* bacteria treated with vancomycin-functionalized γ-Fe_2O_3–CdSe/ZnS nanocomposite (I) bright field image and (II) fluorescence image (inset magnetic separation of bacteria). (c) Fluorescence image of EAC cell treated with oleyl-functionalized γ-Fe_2O_3–CdSe/ZnS nanocomposite.

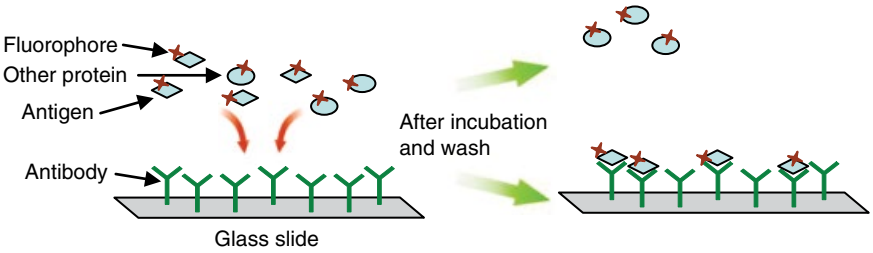

Figure 2.1 Schematic illustration of immunoassay on a glass slide.

Figure 3.1 Configuration of a molecule-doped core–shell (Au@SiO_2 or Ag@SiO_2) irradiated by a plane wave. The radii of metal core and silica shell are denoted by a_2 and a_1, respectively. Points A, B, C, and D are four typical locations for a single molecule embedded in the middle of the outer silica shell.

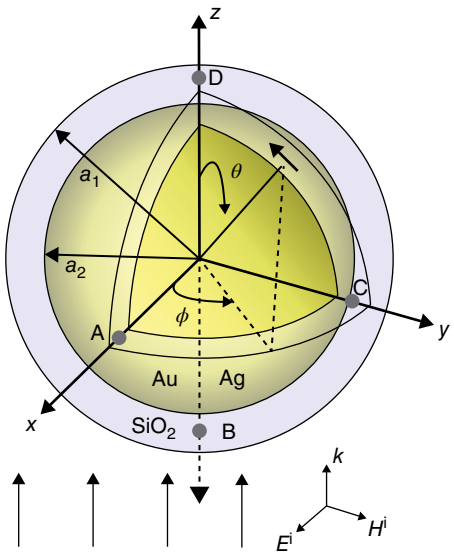

Surface Plasmon Enhanced, Coupled and Controlled Fluorescence, First Edition. Edited by Chris D. Geddes.
© 2017 John Wiley & Sons, Inc. Published 2017 by John Wiley & Sons, Inc.

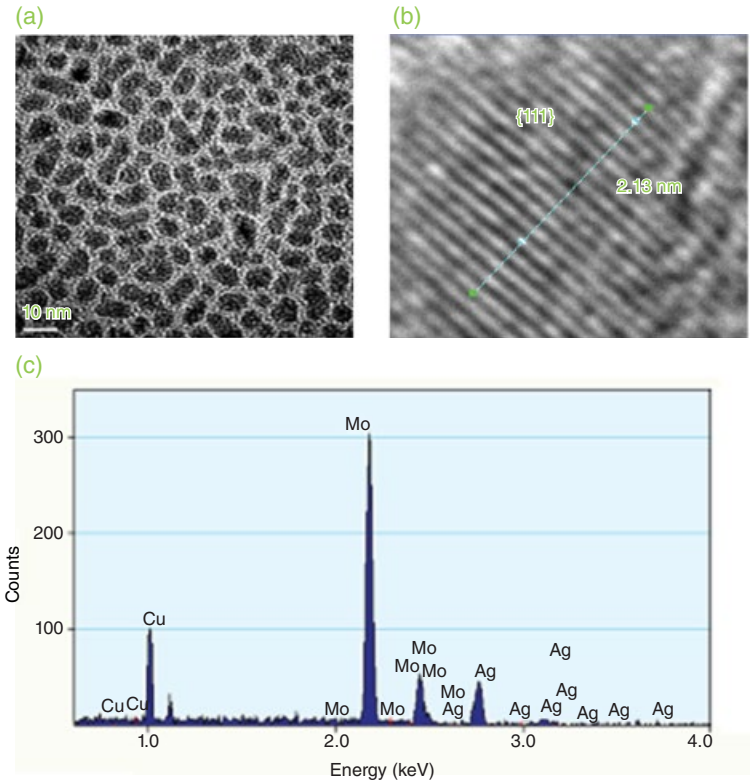

Figure 4.1 (a and b) High-resolution transmission electron micrograph and (c) STEM-EDS spectra, for the Ag–Cu alloy nanoparticles as synthesized using the sputtering technique. Jeremie *et al*. [24]. Reproduced with the permission of Hindawi Publication Corporation.

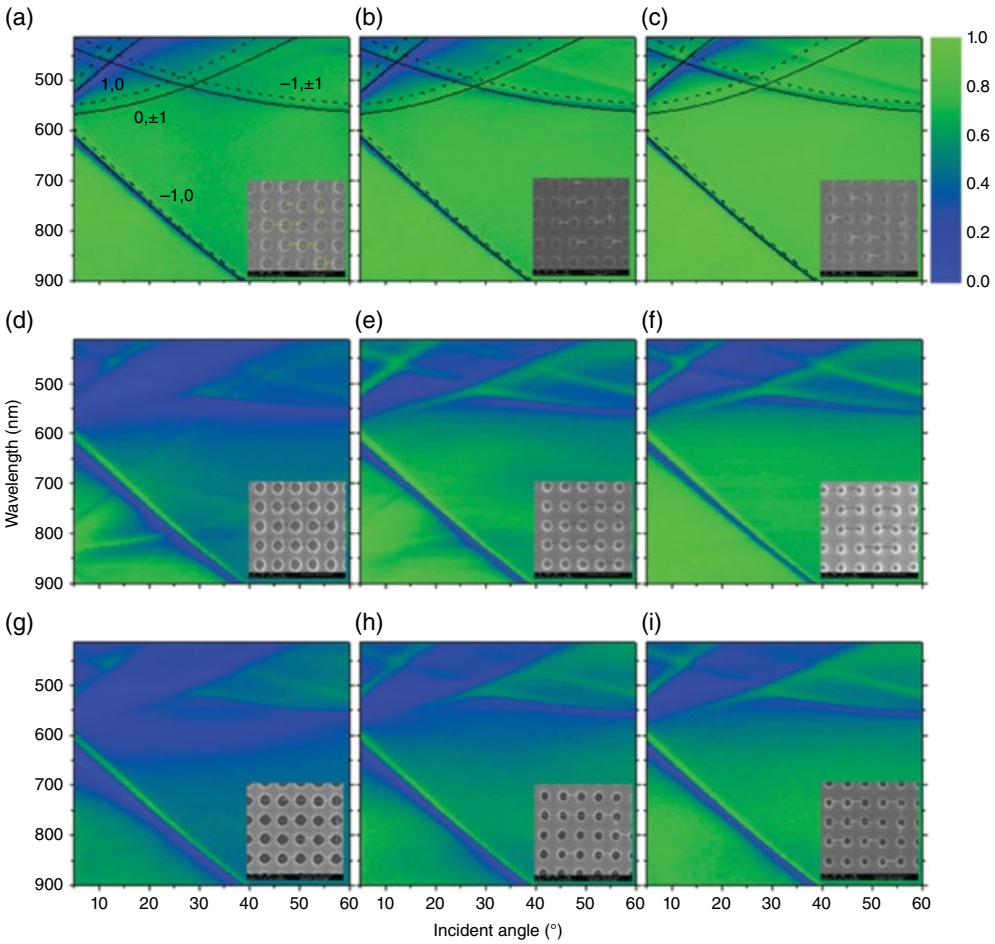

Figure 5.9 The p-p angle-dependent reflectivity mapping (dispersion relations) of each 2D grating was measured in Γ–X direction. The SEM images of the circular hole arrays having cubic lattice with period = 550 nm are shown in the insets of Figure 5.9. The height H of the grooves are (a)–(c) 200 nm, (d)–(f) 300 nm, and (g)–(i) 480 nm, respectively, for shallow, medium depth, and thick holes. The radius R of the holes for different H range from (a), (d), and (g) 101 nm to (c), (f), and (i) 166 nm. The solid lines deduced from Eq. (5.6) indicate the excitation of $(-1,0)$, $(1,0)$, $(0,\pm 1)_s$, and $(-1,\pm 1)_s$ Bloch-like propagating SPPs modes. Wood's anomalies (dashed lines) deduced from replacing $\sqrt{\varepsilon_m\varepsilon_d/\varepsilon_m+\varepsilon_d}$ with $\sqrt{\varepsilon_d}$ in Eq. (5.6) are also observed as bright bands.

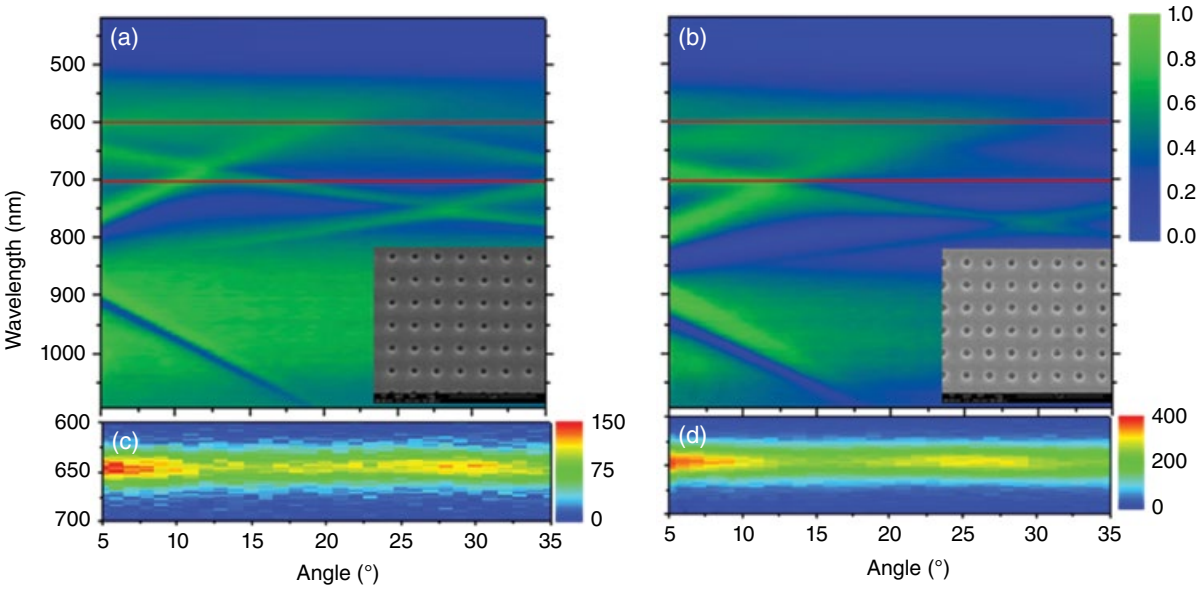

Figure 5.21 The p-p dispersion relations in Γ–X direction for (a) $R = 70$ nm and (b) 120 nm. Several SPP modes such as (1,0), (−2,0), and $(-1,\pm1)_s$ are seen at the region of 600–700 nm, indicated by the solid lines. The corresponding PL detection mappings in Γ–X direction for (c) $R = 70$ nm and (d) 120 nm are measured when the 514 nm laser is incident on metal surface at 40°.

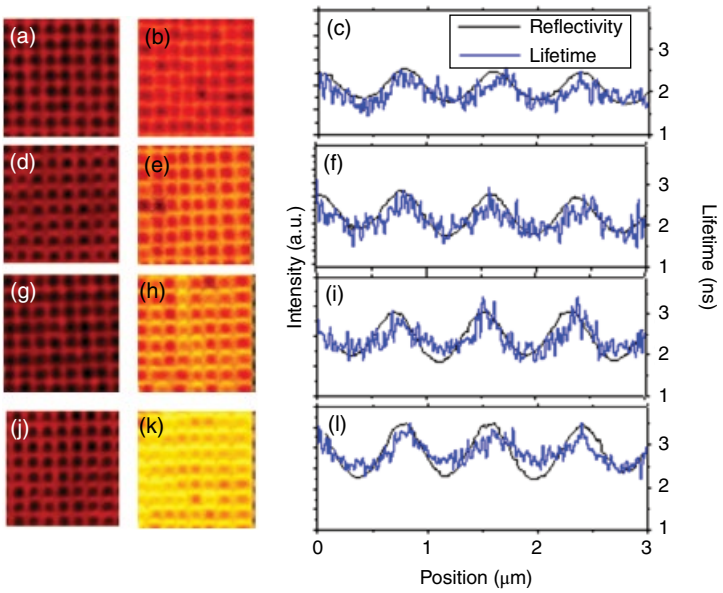

Figure 5.22 The confocal reflection and lifetime images of the arrays with (a, b) $R = 170$ nm, (d, e) 120 nm, (g, h) 70 nm, and (j, k) 60 nm. Their corresponding cuts in reflectivity (black) and lifetime (blue) shown in (c), (f), (i), and (l), respectively, reveal that high reflection regions (i.e., array surfaces) always give longer lifetime.

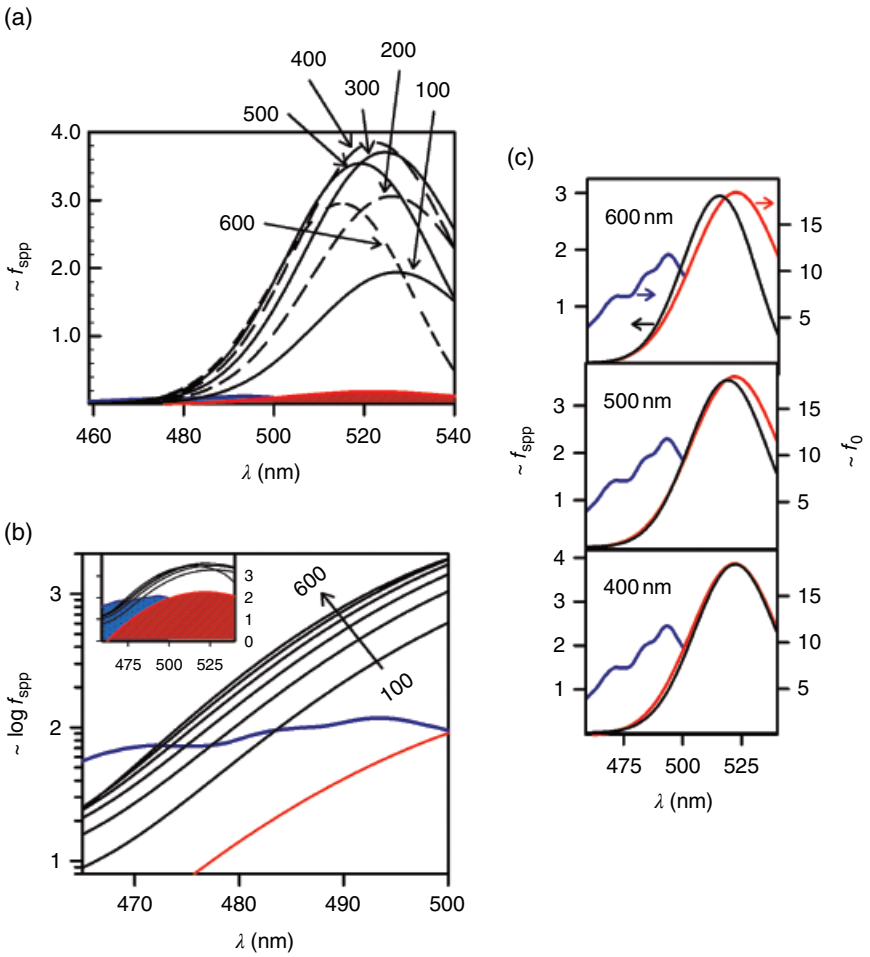

Figure 6.9 Same as Figure 6.8 but for larger distances from the substrate. (Numbers on plots are the distances in nm.) (a) On linear axis, (b) on log axis showing the short wavelength region overlap with the absorption spectrum. (c) Same as (a) but on separate plots and scales so that peak coincides with free-space emission spectrum used for calculation [red line].

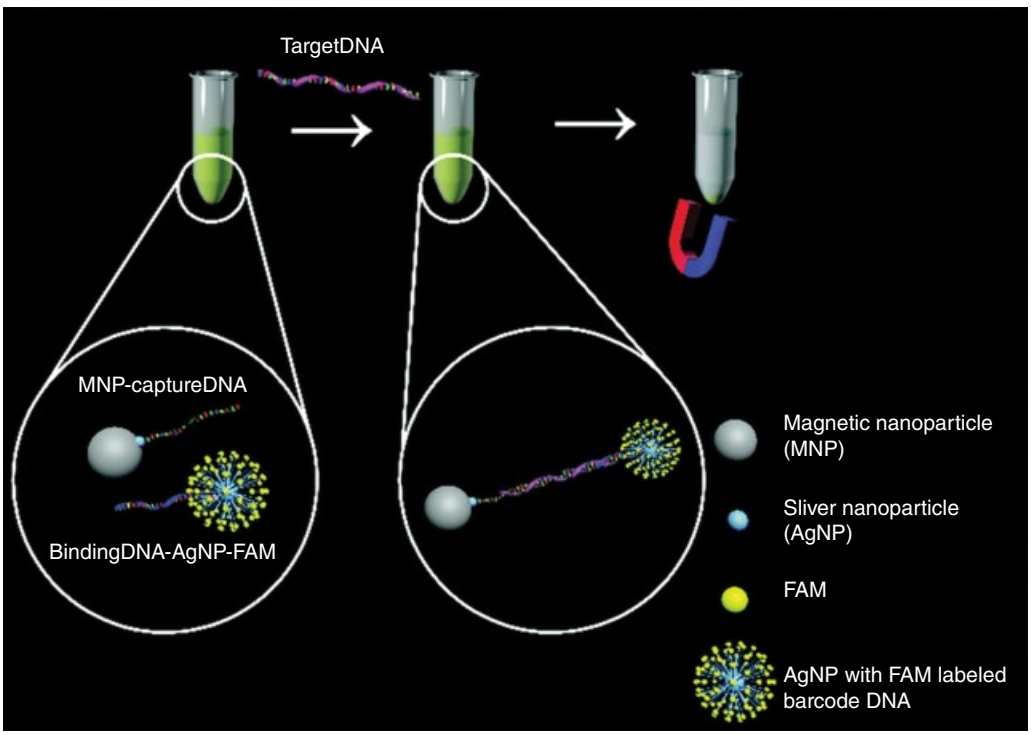

Figure 7.3 Schematic illustration of the assay rationale of the dual amplification strategy for DNA detection. Copyright from 2014 the Royal Society of Chemistry.

Figure 8.5 (a) Fluorescence decay curves for a control slide and three 100 nm AuNP samples, coated with spacers of different thicknesses (indicated) and $[Ru(bpy)_3]^{2+}$, excited at a wavelength of 355 nm.

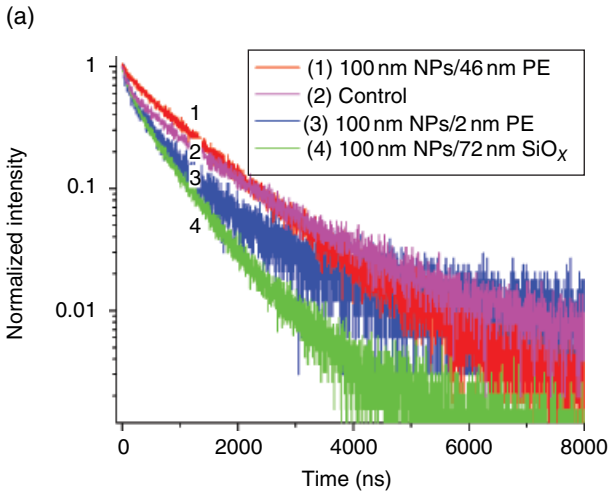

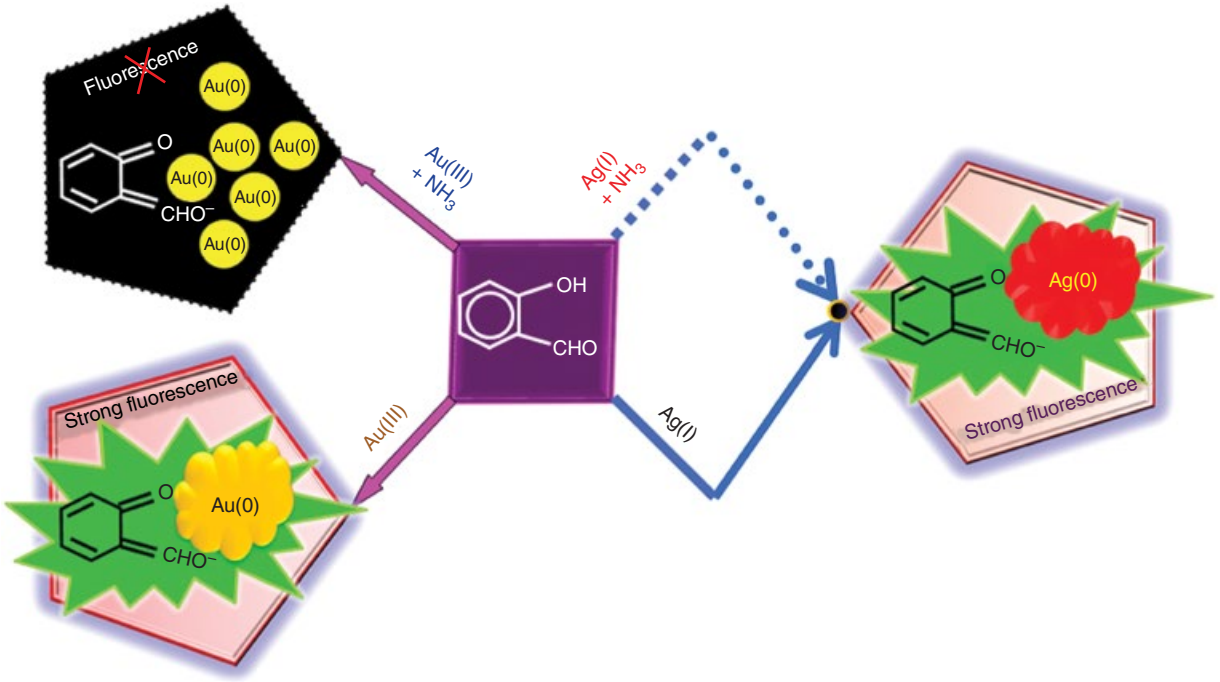

Figure 9.6 Intriguing gold- and silver-enhanced fluorescence from SL. Introduction of ammonia destroys gold-enhanced fluorescence selectively. Ganguly *et al*. [4]. Reproduced with the permission of Royal Society of Chemistry.

Scheme 10.3 Schematic of plasmon oscillation for a sphere, showing the displacement of the conduction electron charge cloud relative to the nuclei. Kelly *et al*. [18]. Reproduced with the permission of American Chemical Society.

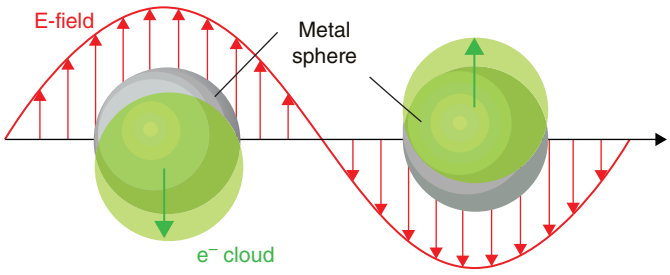

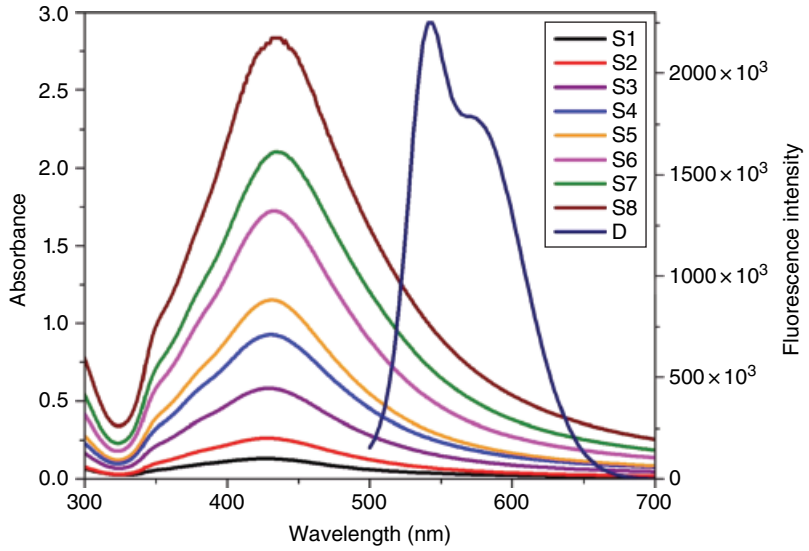

Figure 11.4 Optical absorption spectra of Ag NPs at different heating times and fluorescence emission spectrum of DHDMAD (D) in methanol. Umadevi *et al*. [7]. Reproduced with the permission of Springer.

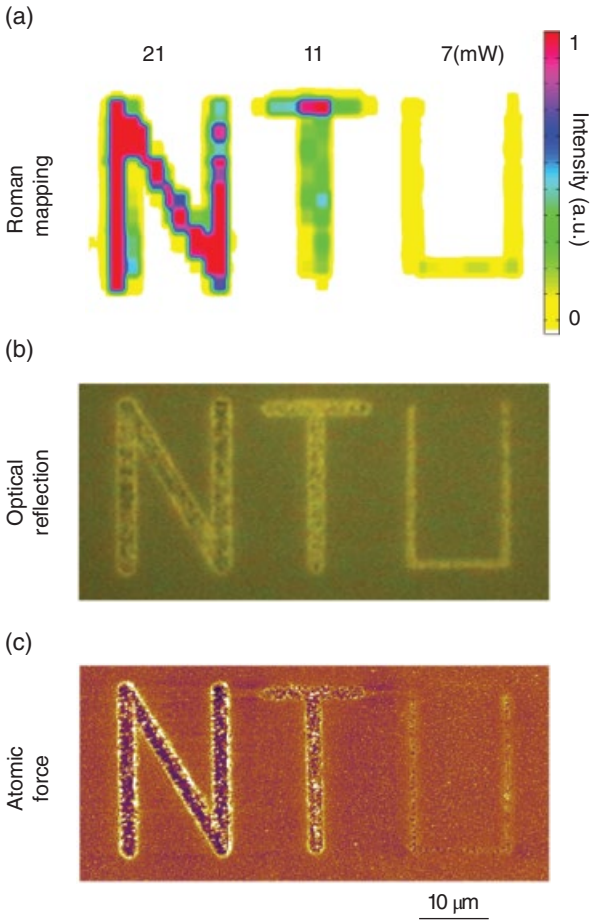

Figure 12.3 Fabrication of the SERS-active micro-pattern on AgO_x thin film. (a)–(c) Raman, optical reflection, and AFM images of "NTU" micro-pattern. From left to right, each letter is written by a femtosecond laser beam with powers of 21, 11, and 7 mW, respectively. Tseng *et al*. [13]. Reproduced with the permission of American Chemical Society.

Figure 13.7 Enhanced two-photon excitation fluorescence of AuNR@SiO_2-T790 NPs (a) and their applications in two-photon cell imaging (b) and two-photon PDT (c). Zhao *et al*. [23]. Reproduced with the permission of American Chemical Society.

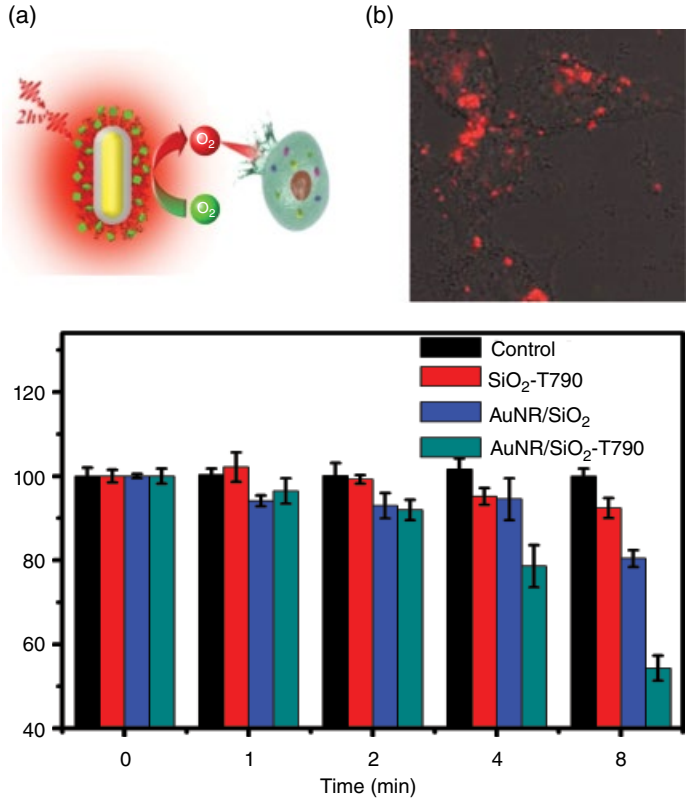

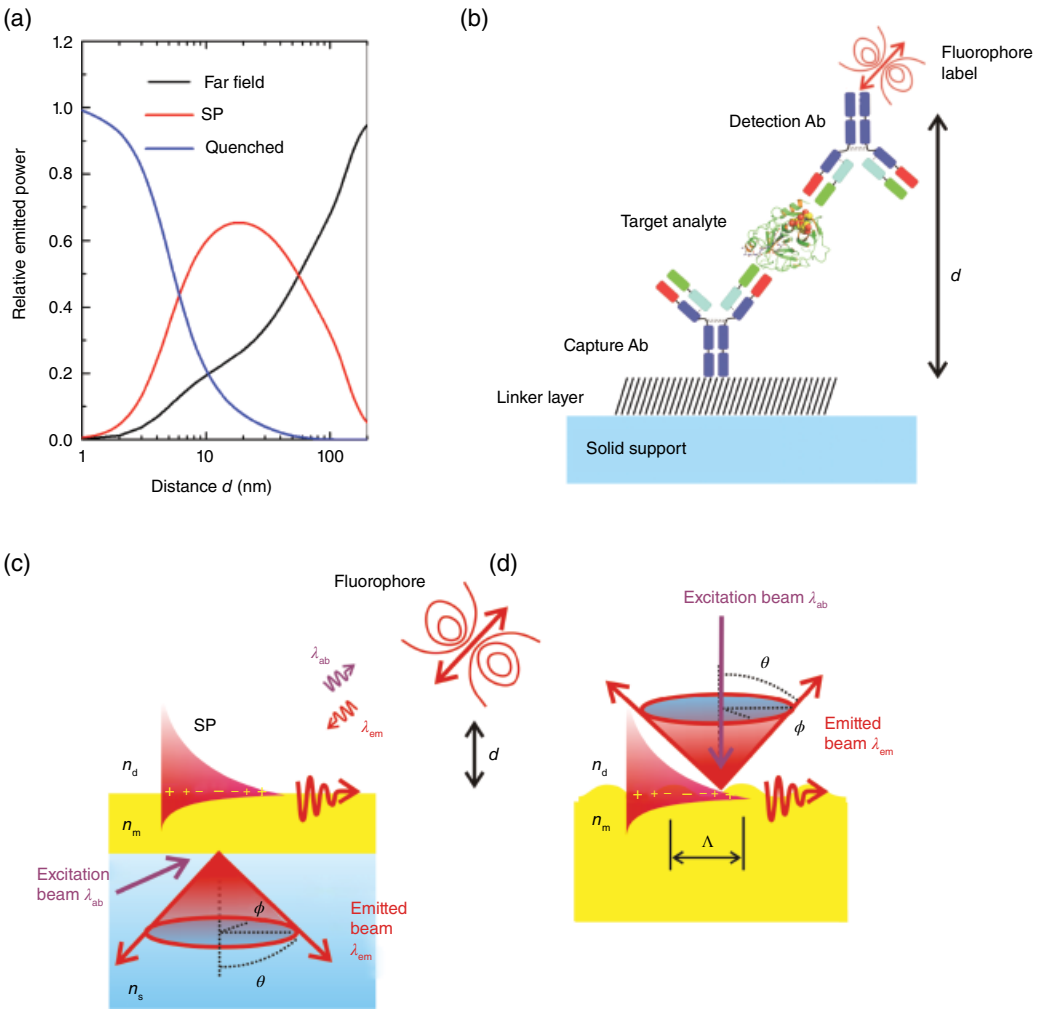

Figure 14.2 (a) Distance dependence of relative power radiated by randomly oriented emitter from a flat gold–water interface at $\lambda_{em} = 670$ nm that is quenched, coupled to SPs, and emitted to the far field. (b) Schematics of sandwich immunoassay utilizing fluorophore labels. Geometry used for out-coupling of SP modes via, (c) reverse Kretschmann geometry of ATR method and (d) by using diffraction on periodically corrugated metallic surface.

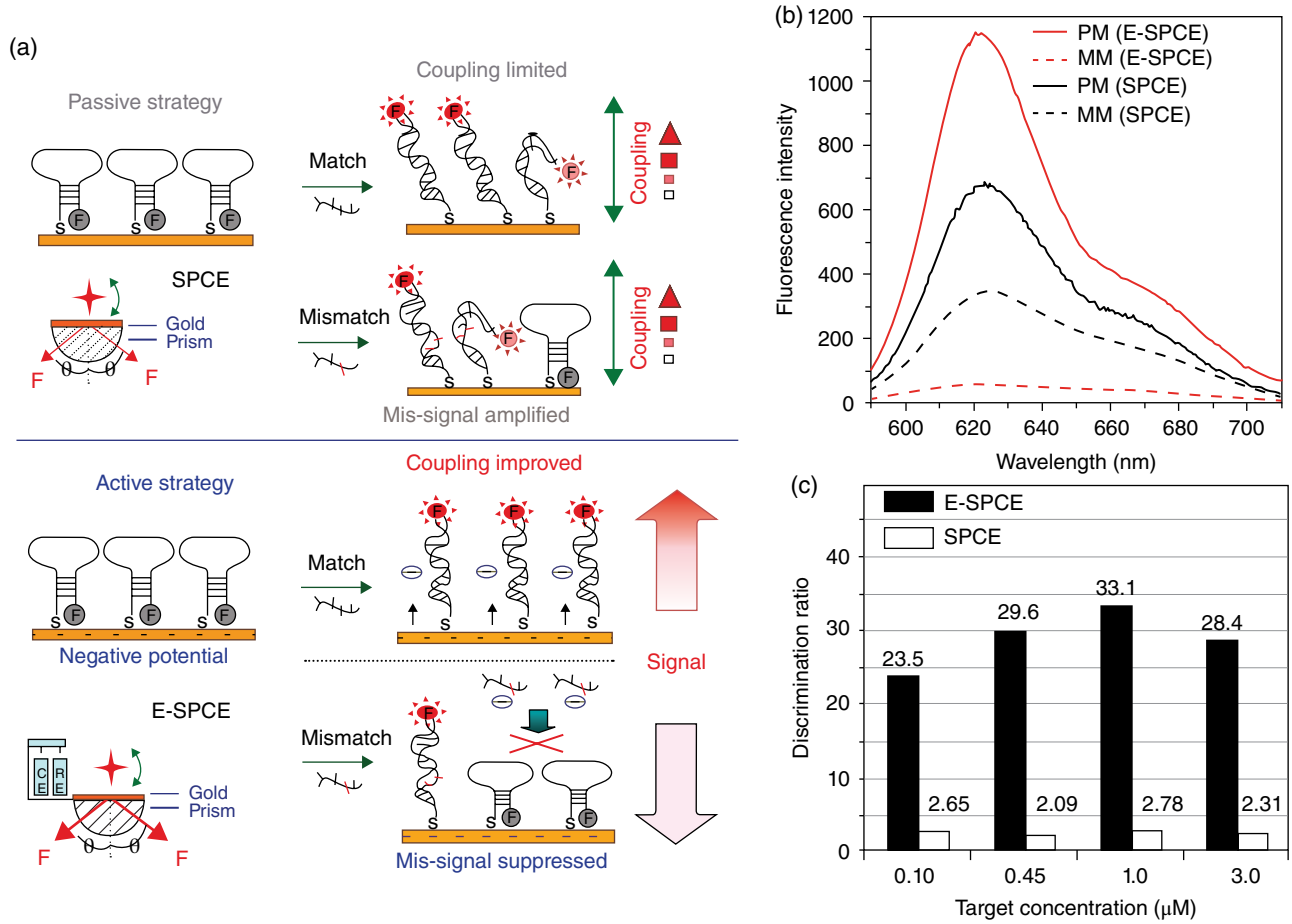

Figure 15.5 (a) The schematic of hairpin molecular beacon signaling match and mismatch in SPCE and E-SPCE. (b) SPCE and E-SPCE fluorescence spectra of DNA hairpin responding to 3.0-μM perfect matches (PM) and single base mismatches (MM). (c) Discrimination ratios with target concentrations ranging from 0.10 to 3.0-μM PM measured in SPCE and E-SPCE. Cao *et al.* [57]. Reproduced with the permission of American Chemical Society.

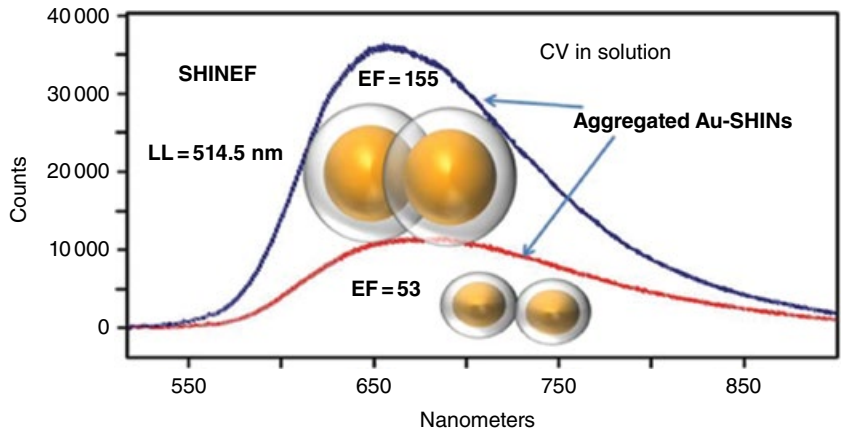

Figure 16.9 SHINEF EF for crystal violet in solution after Au-SHIN's aggregation with NaCl. Large Au-SHINs with central core of about 100 nm and SiO_2 coating of ~10 nm. Smaller SHINs with a core of ~40 nm and a coating of ~10 nm. EF: enhancement factor.